UC Berkeley
UC Berkeley Electronic Theses and Dissertations

Title
Engineering measurement tools to advance quantitative single-cell biology and pathogen inactivation

Permalink
https://escholarship.org/uc/item/6nh584rr

Author
Geldert, Alisha M

Publication Date
2021

Peer reviewed|Thesis/dissertation

eScholarship.org Powered by the California Digital Library
University of California

Engineering measurement tools to advance quantitative single-cell biology and pathogen inactivation

by

Alisha M Geldert

A dissertation submitted in partial satisfaction of the

requirements for the degree of

Joint Doctor of Philosophy
with the University of California, San Francisco

in

Bioengineering

in the

Graduate Division

of the

University of California, Berkeley

Committee in charge:

Professor Amy E. Herr, Chair
Professor Bo Huang
Professor Haiyan Huang

Summer 2021

Engineering measurement tools to advance quantitative single-cell biology and pathogen inactivation

Copyright 2021

By

Alisha M Geldert

Abstract

Engineering measurement tools to advance quantitative single-cell biology and pathogen inactivation

by

Alisha M Geldert

Joint Doctor of Philosophy in Bioengineering
with the University of California, San Francisco

University of California, Berkeley
Professor Amy E. Herr, Chair

Quantitative measurement techniques are critical to new biological discoveries and reproducibility in science and medicine. Research advances are often driven by novel measurement capabilities or improvements in the sensitivity, specificity, or multiplexing of existing approaches. Improvements in throughput and precision can enable more accessible and accurate validation techniques to support reproducibility. Here, we introduce and optimize measurement approaches to advance two fields of quantitative biology: (1) single- and few-cell molecular profiling, and (2) germicidal ultraviolet-C (UV-C) pathogen inactivation. The measurement techniques developed here support research to understand the cellular heterogeneity driving development and disease, as well as safe and effective UV-C decontamination in clinical settings.

First, we focus on advancing proteomic characterization of single cells with high specificity. Different proteoforms – different molecular forms of a protein arising from the same gene – often have unique roles in disease progression and other important biological processes. However, many assays cannot distinguish between proteoforms due to a lack of proteoform-specific antibodies. Electrophoretic cytometry increases proteoform specificity by using electrophoretic separations to spatially resolve proteoforms by mass or charge prior to antibody-based detection. To facilitate quantitative comparison of the ~100s of single-cell protein measurements which can be made on a single electrophoretic cytometry device, is it important to characterize and minimize measurement error. Here, we first investigate approaches to minimize and control for technical variation in both protein abundance and molecular mass measurements made by electrophoretic cytometry. We identify physicochemical mechanisms which contribute to intra-assay technical variation in protein immobilization and antibody binding within the electrophoretic sieving matrix, and use this fundamental understanding to develop strategies to improve the precision of single-cell protein abundance measurements. To improve the precision of molecular mass measurements, we develop protein-loaded microparticles which can be co-loaded with single-cells to act as a molecular mass ladder and control for technical variation in protein electromigration. Overall, these strategies allow finer biological differences in protein abundance and proteoform molecular mass to be distinguished.

Next, we extend electrophoretic cytometry approaches to a range of biological sample types and incorporate multimodal detection capabilities. First, to support study of the roles of different proteoforms in mammalian development, we develop and apply an electrophoretic cytometry approach to characterize proteins expressed in single mouse embryos and blastomeres. To understand the relationship between protein expression and upstream nucleic acids (DNA, mRNA), we also develop an approach to fractionate a single cell or embryo and measure both cytoplasmic proteins and nuclear DNA or mRNA from the same single cell or embryo. While these platforms advance molecular profiling of detached cells in suspension, measurements of adherent cells are also valuable to understand spatial variation in protein expression and to understand cell-microenvironment interactions. To characterize proteoforms from adherent cells while preserving information about the starting cell locations, we investigate the use of projection electrophoresis to separate proteoforms in the Z-dimension while maintaining spatial context information in the X-Y plane. Because adherent cell projection electrophoresis has a different assay geometry and boundary conditions than traditional electrophoretic cytometry platforms in which detached cells are isolated and lysed within microwells, we compare the sensitivity and lateral spatial resolution of adherent cell and microwell-based projection electrophoresis platforms using simulation and fluorescent protein imaging. Informed by this characterization, we demonstrate a proof-of-concept projection electrophoretic separation of subconfluent adherent breast cancer cells. Overall, this work extends electrophoretic cytometry to new sample types and offers a new approach to couple nucleic acid and proteoform measurements from the same single or few cells.

In addition to advancing techniques to measure biological samples directly, we also advance research and implementation of germicidal UV-C pathogen inactivation through the development of quantitative, high-throughput, and accessible UV-C dosimetry techniques. To address shortages induced by the COVID-19 pandemic, UV-C decontamination has been identified as a promising approach to decontaminate N95 respirators for emergency reuse. Both pathogen inactivation and N95 degradation depend on UV-C dose. However, it is challenging to measure UV-C dose on N95 surfaces, as radiometers and other standard UV-C dose measurement techniques have insufficiently small form factor, and often have nonideal angular response. Here, we develop a high-throughput quantitative UV-C dosimetry approach using colorimetric indicators, characterize the impact of optical attenuators on dosimeter dynamic range and angular response, and apply the dosimetry approach to make first-in-kind paired measurements of on-N95 UV-C dose and SARS-CoV-2 viral inactivation. Improved UV-C dose measurement techniques facilitate research of UV-C pathogen inactivation and validation of UV-C decontamination protocols.

Taken together, the work covered in this dissertation advances the range and precision of measurements important to studying single-cell biology and pathogen inactivation, supporting a variety of research and clinical applications.

Table of Contents

List of Figures

List of Tables

To my family.

Acknowledgments

This dissertation is the product of work made possible from the mentorship, financial, administrative, technical, and emotional support of so many people that I am grateful for. First of all, there are many people to thank for putting me on a path toward a PhD in the first place. K-12 teachers often do not get enough credit for the hugely impactful role they play in setting students up for success. I am thankful for the several fantastic math and science teachers I have had in middle school and high school – these are the people who first inspired me to pursue degrees and a career in STEM, and who helped me establish strong fundamentals in math and science. I am also grateful to the professors and research mentors who played an integral role in helping me get to graduate school. In particular, Professors Dana Elzey, Richard Price, Chwee Teck Lim, and Drs. Nicole Morgan and Matt Eames inspired me to pursue bioengineering, gave me valuable opportunities to gain research experience, and wrote many letters of recommendation in support of my graduate school applications.

I feel so fortunate to have had the opportunity to be mentored by and work with Professor Amy Herr throughout my Ph.D. Amy is an inspiration in more ways than can be described here, but her work ethic and enthusiasm are, in particular, unparalleled. I am thankful for all the ways that Amy has helped me grow as a scientist – from her prompt manuscript revisions with dozens (or hundreds) of comments, to her frank and thoughtful career advice, to her support to attend numerous conferences, trainings, and other professional development opportunities. I would also like to thank Professors Lydia Sohn and Aaron Streets for providing helpful feedback as members of my qualifying exam committee, and Professors Bo Huang and Haiyan Huang for providing valuable insight over the years as members of both my qualifying exam and dissertation committees.

I am also thankful to all the members of the Herr Lab (past and present), who have been fantastic mentors, labmates, and friends. I have learned so much from other lab members through all the questions asked during lab meeting presentations, collaborations and trainings I have received, and informal breakroom conversations. In particular, Dr. Samantha Grist and Dr. Julea Vlassakis have been key role models and mentors to me, setting great examples of scientific rigor in experimental design and analysis. I also feel incredibly lucky to have had Ali, Kristine, Andoni, and Anjali as labmates through my entire time in the Herr Lab. They have been a huge source of support as we have gone through classes, quals, GSI-ing, dissertation writing, and other milestones of the Ph.D. together. In particular, I am thankful to have had the chance to work closely with Ali as both classmates and coauthors – Ali's attention to detail and hardworking nature has made me a better scientist, and she has been a fantastic collaborator as well as supportive friend over the course of the Ph.D.

My Ph.D. experience has also been enriched by collaborations with incredible researchers from other departments and institutions. I am thankful to all my coauthors and collaborators for sharing their expertise in developmental biology, virology, optics, and other fields with me, and for being curious and interested to learn more about and work with the Herr Lab's technology. And while I wish the COVID-19 pandemic and associated N95 shortages had not been an issue over the past year and a half, I am grateful to have had the opportunity to work with the N95DECON consortium. The way in which consortium members from wide-ranging fields across academia and medicine worked together and valued every members' opinion was an inspiration.

My Ph.D. would not have been possible without the technical, administrative, and financial support of many different teams. Thank you to the core facilities managers – Paul Lum and Naima

Azgui at the BNC, Holly Aaron and Feather Ives at the MIC, and Mary West and Tram Do at the CTAF – for keeping many of the instruments critical to my experiments up and running smoothly. I am also thankful to all the administrators in the bioengineering program who keep aspects related to purchasing, academic program requirements, and other matters on track – thank you to Rocio Sanchez, Kristin Olson, Victoria Ross, SarahJane Taylor, Catherine Dea, April Alexander, and Kathleen Sutton, among others. Our research would also not be possible without the incredible team at Stanley Hall. Thank you to Thom Opal for responding to my several safety questions over the years, to Kris Thompson, Harry Stark, Cherry Chung, Geoff Bingaman, and Dave Rogers for keeping the building running smoothly, to Mike Bentley, Chris Hardin, and all the shipping and receiving staff for handling our many, many deliveries, and to the custodial staff for keeping Stanley safe and clean.

I also thank my funding sources, without which this research would not be possible. I am thankful for support from the National Defense Science and Engineering Graduate (NDSEG) Fellowship and National Institutes of Health (NIH) training grant, as well as to the Chan Zuckerberg Biohub, NIH, and UC Berkeley College of Engineering Dean's COVID-19 Emergency Research Fund, among other sources, for supporting Herr Lab research. For the N95 decontamination research in particular, numerous parties also donated equipment and provided helpful discussion to support this time-sensitive research. We greatly appreciate the generous donation of the following materials: all UV-C chambers and bulbs (Betty Chang at Spectro-UV), handheld UV point lamp/source (Daniel Tristan at Spectroline), 3M 1860 N95s (Kristen Bole, Dr. Aenor Sawyer, and Dr. Nichole Starr at University of California, San Francisco) and Zemax OpticStudio Professional license (S. Subbiah and David Lineberger). We also thank the Streets Lab at University of California, Berkeley for kindly loaning the rotation platform used for angular response measurements. We thank Douglas Fox for assistance with our Biological Use Authorization application for the SARS-CoV-2 experiments, Brian Heimbuch for helpful discussion on viral inactivation measurements, Clarence Zarobila, Henry Pinkard, Dr. Cameron Miller, and Prof. Bo Huang for helpful discussion on the optical attenuator research, as well as Csilla Timar-Fulep for assistance with Zemax Opticstudio.

Finally, I am grateful to all the people who kept me sane and supported me outside of lab. First and foremost, I would not be where I am today without my family. I am so thankful to my parents for prioritizing my education while never pressuring me to perform in a certain way or to choose a certain field of study. My parents have been constant sources of support, strong role models, and have helped me keep the bigger picture in perspective. I also thank my brother, Aaron – his intellectual curiosity and wholehearted enthusiasm for any of his projects or goals is inspiring, and our conversations are always bound to make me laugh and lift my mood. And though I do not get to see my extended family often, I appreciate the love and support they send all the way from Minnesota and Taiwan. I am also thankful for Kenry for his constant support throughout my Ph.D. – I admire his resilience and determination, and he has always provided a listening ear and calm, positive perspective through the ups and downs over the past few years. Thank you also to my friends – both from Berkeley and afar – for all the fun times and emotional support they have provided throughout the Ph.D. There are so many friendships that I value, but in particular, I am grateful to Kristine and Priya for being kind and generous housemates who have made our apartment such a comfortable place to come home to over the past several years. Yiqi, Natalie, Tanya, and Kevin – I am so thankful for our friendship over the past ten years and for the fact that we can always pick up right where we left off, even if we do not get the chance to see each other often.

The work covered in this dissertation truly would not have been possible without these people and organizations, and I am so grateful for everyone who has helped me along this journey.

Chapter 1

Introduction

1.1 Dissertation overview

Measurement tools are critical to biology and medicine, forming the foundation of both fundamental biological research and clinical implementation of diagnostics and therapies. New measurement capabilities drive new biological discoveries and translational advances, as demonstrated in recent decades by the impact of lightsheet microscopy[1,2], sequencing[3,4], and other techniques on fields ranging from developmental biology to genetic testing. Improvements in the sensitivity, specificity, and multiplexing of measurement techniques can be equally impactful; for example, the increased sensitivity afforded by single-cell sequencing technologies[5] has revolutionized study of rare cell subpopulations, such as circulating tumor cells[6,7] and antibiotic-resistant bacteria[8], which may be undetectable with bulk sequencing methods. In addition to enabling new discoveries, quantitative techniques and characterization of associated measurement uncertainty are critical to scientific reproducibility and rigor[9–11]. For example, development of standard reference materials and methods for blood cholesterol testing improved the precision and accuracy of clinical laboratory measurements, saving millions of dollars in healthcare costs[11–14]. Overall, advances in biomedical measurements are key to both novel discoveries and reproducibility in research and medicine.

In this dissertation, we introduce technologies and analytical workflows to advance two fields of biomedical measurements: (1) single- and few-cell molecular profiling, and (2) germicidal ultraviolet-C (UV-C) dose quantification. First, we advance molecular profiling methods by quantifying and reducing technical variation of massively parallel single-cell proteoform measurements (Chapters 2-4), and by developing new electrophoretic cytometry-based tools for proteomic and/or multiomic measurements of diverse cell types (Chapters 5-7). Next, we review a measurement need recently highlighted by the COVID-19 pandemic: the need for accurate germicidal UV-C dose quantification to validate N95 respirator decontamination (Chapters 8-9). To address this need, we introduce a method for quantitative on-N95 UV-C dosimetry and apply this technique to make first-in-kind paired measurements of UV-C dose and pathogen inactivation on-N95 (Chapters 10-12). Taken together, the measurement techniques covered in this dissertation advance quantitative single-cell biology and pathogen inactivation research.

For the remainder of this chapter, we provide an overview of the motivation for and fundamental physicochemical phenomena underlying the measurement approaches at the focus of this dissertation.

1.2 Motivation for electrophoretic cytometry

Cell-to-cell heterogeneity – even among cells from the same organ or tissue type – plays a key role in driving development, immune response, cancer metastasis, and many other important biological processes. Single-cell analysis (i.e., cytometry) is key to identifying and understanding variation between cells. Cell populations with the same mean expression of a molecule (as determined by bulk analysis) can have drastically different distributions of expression when

characterized at the single-cell level. Single-cell analysis facilitates identification of rare cell subpopulations, bimodal expression patterns, and other heterogeneity that is averaged out in bulk measurements[15].

Multiple types of biomolecules can be measured from each individual cell. The core workings of a cell are governed by the central dogma of molecular biology, which dictates that information in DNA is transcribed into mRNA transcripts, which are then translated into proteins[16]. Proteins are the functional units of the cell, playing critical roles in cell structure, metabolism, signaling, and other vital functions. Proteomic measurements are thus integral to the study of development, disease, and other biological processes. Because transcript and protein expression levels can be weakly correlated[17,18] (especially at the single-cell level)[19], proteomics can complement and add to genomic characterization by revealing the current molecular state of the cell. Additionally, many different molecular forms of a protein – known as proteoforms – can arise from a single gene, due to alternative splicing of mRNA transcripts and post-translational modifications (e.g., phosphorylation, cleavage)[20]. Different proteoforms can have substantially different roles in cell signaling[21], drug response[22], and other processes[20]. Because genomic and transcriptomic characterizations do not indicate post-translational modifications, protein measurement techniques with proteoform specificity are especially valuable in studying the role of different proteoforms within the cell.

Few tools exist to characterize proteoforms with single-cell sensitivity. Assays which rely solely on antibody binding to detect proteins with single-cell resolution – such as immunohistochemistry[23,24], flow[25,26] and mass[27] cytometry, and antibody barcode chips[28] – often lack proteoform specificity due to antibody cross-reactivity and the lack of commercially available proteoform-specific antibodies[29,30]. Alternatively, fluorescent protein tagging can be used to visualize protein distribution within individual cells[31]. However, because fluorescent fusion proteins are typically made by introducing a fluorescent tag sequence at the DNA level, this approach also cannot distinguish post-transcriptional and post-translational modifications. Mass spectrometry is one of the most robust approaches for proteoform analysis, and has recently been demonstrated at the single-cell level[32]. However, the enzymatic digestion involved in bottom-up mass spectrometry limits analysis of intact proteoforms; for example, the molecular origin of peptide fragments cannot be traced back to understand whether multiple post-translational modifications are expressed together on one protein or expressed separately on several different proteins. Top-down mass spectrometry overcomes this challenge, but has limited ability to detect low-abundance targets and high molecular mass proteoforms[33].

Electrophoretic approaches offer improved proteoform specificity by using an electrophoretic separation to separate proteoforms based on mass or charge prior to antibody-based detection. Because mass or charge variants are spatially resolved, electrophoretic separation allows both nonspecific antibody binding and specific proteoforms to be distinguished. While isoelectric focusing[34] and western blotting[35] typically require bulk lysate of at least 10s or 100s of cells, respectively, microscale approaches have been developed to achieve single-cell sensitivity[36,37]. By achieving proteoform specificity at the single-cell level, electrophoretic cytometry facilitates study of how different protein variants contribute to cellular heterogeneity, improving our understanding of development, disease progression, and other biological processes.

1.3 Critical enabling features of electrophoretic cytometry

Here, we overview fundamental aspects of electrophoretic cytometry assay design which contribute to assay throughput and sensitivity. An overview of a typical electrophoretic cytometry workflow is shown in **Figure 1.1**.

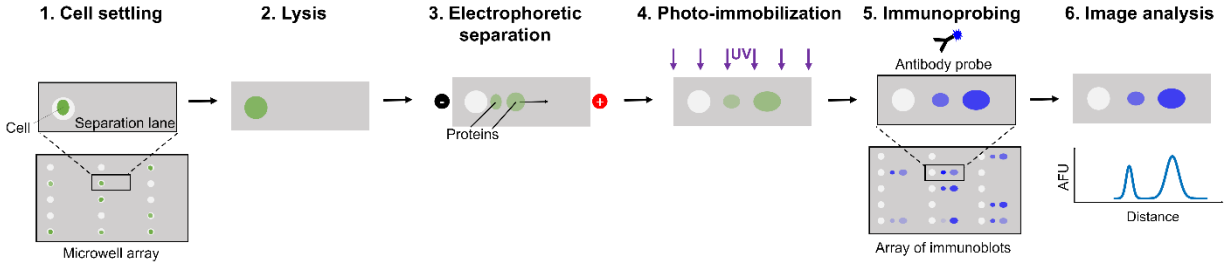

Figure 1.1. Overview of electrophoretic cytometry process. Assays contain 100s–1000s of separation lanes; microwell and immunoblot array schematics show a limited number of separation lanes for simplicity.**Open microwell array supports single-cell isolation and massively parallel cell lysis.** Microwell arrays have been used to isolate and measure a variety of parameters from single cells, including DNA damage[38] and oxygen consumption[39] levels. An electrophoretic cytometry chip consists of a ~40 µm-thick polyacrylamide hydrogel with 100s – 1000s of arrayed microwells (~32 µm-diameter) cast on a glass microscope slide. The dimensions of the microfabricated mold on which the gel is cast can be adjusted to generate microwells of different sizes, accommodating different cell types. Passive gravity settling achieves stochastic cell settling with ~40% of microwells containing a single cell[36], while active settling approaches such as centrifugal settling[40] or droplet dispensing systems[41] can achieve higher single-cell settling efficiency.

The open microwell array format facilitates rapid and massively parallel cell lysis without the need for complex valving or other instrumentation to access each microwell. Lysis buffer is either poured over the microwell array[36] or introduced via a gel lid[42] to lyse all cells simultaneously. Despite some diffusive loss from the microwell, cell lysate remains relatively concentrated within the microwell due to multiple factors. First, there is minimal convection within the microwell, preventing advective protein loss[36]. Additionally, protein diffusion across the sides and bottom of the microwell is reduced due to ~10× lower protein diffusivity in gel as compared to free solution[43]. Overall, the open microwell assay format facilitates rapid cell lysis and protein solubilization, while keeping protein from individual cells compartmentalized to support single-cell analysis.

In-gel protein immobilization minimizes protein loss and allows for long-term archiving. Because the electrophoretic cytometry hydrogel is substantially thinner than standard bulk western blotting gels (~40 µm vs. ~1 mm), proteins will diffuse out of the electrophoretic cytometry gel more quickly. Thus, after electrophoretic separation, electrophoretic cytometry utilizes in-gel protein immobilization, rather than transferring proteins to a blotting membrane as is standard for bulk immunoblotting. Upon UV (350-360 nm) exposure, proteins are covalently linked to benzophenone moieties in the hydrogel via hydrogen abstraction of the C – H bonds in proteins[44]. Photo-immobilization minimizes protein losses and eliminates confounding effects of protein- and buffer-dependent transfer efficiency[45]. Additionally, because proteins are covalently bound within the gel, electrophoretic cytometry chips can be stored and probed for targets months later, if new research questions or proteoforms are of interest[46].

Thin hydrogel requires increased antibody probe concentration but decreases immunoprobing time. Proteins immobilized within the electrophoretic cytometry hydrogel are detected via antibody binding. The timescale of diffusive antibody transport ($\tau_{transport}$) scales with

the square of gel thickness (z) and is inversely proportional to the diffusivity of antibody in the gel (D_{gel}) (**Eq. 1.1**).

$$\tau_{transport} = \frac{z^2}{2D_{gel}} \quad \textbf{Eq. 1.1}$$

The timescale of the antibody-antigen binding reaction ($\tau_{reaction}$) depends on the kinetics (k_{on}, k_{off}) and local concentration ([Ab]) of the antibody (**Eq. 1.2**).

$$\tau_{reaction} = \frac{1}{k_{on}[Ab] + k_{off}} \quad \textbf{Eq. 1.2}$$

Damköhler analysis can be used to determine whether the system is transport- or reaction-limited. A previous analysis found that electrophoretic cytometry immunoprobing is primarily transport-limited[47], though the antibody diffusivity, concentration, and affinity will vary from system to system depending on the gel density and specific antibody used. Though immunoprobing is mass-transport limited, antibody incubation times are feasible (on the order of ~1-2 h) due to the thin electrophoretic cytometry gel (~40 μm thickness).

While in-gel protein immobilization minimizes protein losses, one tradeoff is that protein detection in-gel requires incubation with a higher concentration of antibody as compared to detection on a blotting membrane. In-gel antibody concentration is limited by size-exclusion partitioning, which depends on gel density and antibody hydrodynamic radius[48]. The partition coefficient (K) is defined as the ratio between solute concentration in-gel (C_{gel}) and in free solution ($C_{solution}$) (**Eq. 1.3**).

$$K = \frac{C_{gel}}{C_{solution}} \quad \textbf{Eq. 1.3}$$

For a typical polyacrylamide gel density required for size separation (~6%T), $K < 0.10$, as measured using confocal microscopy[49]. Thus, to achieve sufficient in-gel antibody concentration, the electrophoretic cytometry chip must be incubated with highly concentrated antibody solution.

1.4 Challenges in characterizing technical variation of single-cell assays

Measurements consist of two equally necessary components: a value of the measured quantity (i.e., the measurand), and the uncertainty of the measurement[50]. Quantitative comparisons and tests for statistical differences between groups depend on quantification of measurement uncertainty. Measurement error is typically quantified based on the variation of measurements of replicate samples (i.e., technical replicates). However, destructive single-cell assays (i.e., assays in which the cell is lysed) lack true technical replicates because each cell can only be measured once. Thus, characterization of technical variation of single-cell assays often poses unique challenges.

Approaches to characterize single-cell assay technical variation have involved modifications to both assay and post-processing workflows. In terms of assay design, replicate measurements have been made from a single cell by dividing the cell lysate into separate measurement paths[28]; however, this approach drives more targets below the limit of detection and may not be feasible for all systems and/or targets. Alternatively, single-cell RNA sequencing techniques often employ a 'pool/split' approach to quantify technical variation, in which technical replicates are obtained from the pooled lysate of many cells[51,52]. However, replicate measurements of pooled cell lysate do not reflect technical variation of the cell lysis step of the assay, and the

differences in loading cell lysate into an assay as compared to whole-cell loading may yield different sources of technical variation. Assays can also be run with internal standards or spike-in controls[53–55] – these controls are materials with known properties, so that any deviation from the expected control readout indicates technical variation. However, spike-in controls may be subject to some of the same limitations as the pool/split approach, in that it can be difficult to design a control which is subject to the same sources of technical variation as the cellular target itself due to the dependence of technical variation on molecular target, cell lysis, and other factors. Assay measurements can also be normalized to either a spike-in or endogenous control (e.g., a housekeeping gene or protein), or to total cellular content. However, traditional housekeeping genes have been shown to be variably expressed at the single cell level[56]. Normalization to an additional target and/or total cellular content also requires additional multiplexing capability.

In electrophoretic cytometry, numerous sources of intra- and inter-assay technical variation in both protein abundance and protein migration (used to determine molecular mass or charge) exist. Technical variation in protein abundance measurements can arise from variation in protein diffusion out of the microwell, protein photoimmobilization efficiency, and immunoprobing efficiency, among other factors. Additionally, variation in gel pore size, electric field strength, and protein denaturation state can contribute to technical variation in protein migration. Quantifying and reducing technical variation in electrophoretic cytometry is critical to leverage the high-throughput nature of electrophoretic cytometry to make accurate quantitative comparisons among single cells, and will be further discussed in Chapters 2-4.

1.5 Motivation for UV-C dosimetry

As further discussed in Chapters 8-9, germicidal UV-C (200–280 nm) irradiation has broad applications to decontamination of air[57,58], water[59], healthcare surfaces[60], and has recently been applied to decontaminate N95 respirators to mitigate shortages induced by the COVID-19 pandemic[61–63]. The efficacy and safety of UV-C decontamination depends critically on received UV-C dose, which must be sufficient for pathogen inactivation yet not so high as to cause material degradation. The minimum and cumulative maximum safe UV-C dose thresholds are material- and pathogen-dependent and can span many orders of magnitude[64,65]. Because UV-C radiation is distance- and angle-dependent, UV-C dose delivered across a decontamination system – especially across nonplanar surfaces on which UV-C strikes at a range of angles of incidence – can also vary by several-fold, as shown in Chapters 10 and 12. Thus, dynamic range is an important consideration for sensors used to validate UV-C decontamination systems.

Wavelength specificity is also a key consideration for accurate measurement and reporting of germicidal UV-C decontamination. Germicidal UV-C sources have differing UV-C emission spectra, and pathogens and UV-C sensors have differing sensitivity to different wavelengths. While some UV-C sources are monochromatic (e.g., ~95% of low pressure mercury lamps emission is 253.7 nm), others are polychromatic (e.g., medium pressure mercury lamps emit at multiple wavelengths between 200–400 nm, pulsed xenon sources emit broadly across both the UV and visible range)[65–67]. LEDs, which typically emit a narrow bandwidth of wavelengths, have also been implemented for both UV-C (~265 nm) and far-UV-C (~222 nm) irradiation[68,69]. Because materials have variable transmission spectra, any materials which UV-C radiation passes through will also alter the range of wavelengths reaching the item to be decontaminated. For example, many types of plastics and glass transmit limited or no UV-C[70,71]. Understanding the emission spectrum of a given UV-C source is important because pathogen susceptibility is wavelength-dependent, as described by a pathogen's action spectrum[72]. Similarly, radiometers,

photodiodes, photochromic indicators, and other radiation sensors have differing spectral responsivities[73], which impacts the irradiance or dose readout.

Overall, validating delivery of a safe and effective UV-C dose is challenging due to the spatial and temporal variations[74,75] in dose distribution and the lack of standards for evaluating germicidal UV device efficacy[76]. Quantitative UV-C dose measurement tools with sufficient wavelength specificity and dynamic range for the pathogen and material of interest are critical for validation of UV-C decontamination protocols, and will be the focus of Chapters 10-12.

1.6 Conclusions

Biological research and clinical practices depend on a variety of measurement techniques. Here, we have described measurement gaps in two fields: single-cell proteomics and germicidal UV-C decontamination. In particular, to understand the role that different proteoforms play in development, metastasis, and other biological events involving rare cell subpopulations, there is a need for proteomic assays with single-cell sensitivity and proteoform specificity. To characterize and relate UV-C dose distribution across complex geometries to resulting pathogen inactivation, there is a need for UV-C dose measurement techniques with relatively high throughput, small footprint, ideal angular response, and low cost. To meet these measurement gaps, in this dissertation we will describe work to develop and improve electrophoretic cytometry and quantitative UV-C dosimetry workflows, advancing quantitative single-cell biology and pathogen inactivation research.

1.7 References

1. Method of the Year 2014. *Nat Methods* **12**, 1–1 (2015).
2. Girkin, J. M. & Carvalho, M. T. The light-sheet microscopy revolution. *J. Opt.* **20**, 053002 (2018).
3. Hood, L. & Rowen, L. The Human Genome Project: big science transforms biology and medicine. *Genome Medicine* **5**, 79 (2013).
4. Koboldt, D. C., Steinberg, K. M., Larson, D. E., Wilson, R. K. & Mardis, E. The Next-Generation Sequencing Revolution and Its Impact on Genomics. *Cell* **155**, 27–38 (2013).
5. Method of the Year 2013. *Nat Methods* **11**, 1–1 (2014).
6. Ting, D. T. *et al.* Single-Cell RNA Sequencing Identifies Extracellular Matrix Gene Expression by Pancreatic Circulating Tumor Cells. *Cell Reports* **8**, 1905–1918 (2014).
7. Ramsköld, D. *et al.* Full-length mRNA-Seq from single-cell levels of RNA and individual circulating tumor cells. *Nat Biotechnol* **30**, 777–782 (2012).
8. Lan, F., Demaree, B., Ahmed, N. & Abate, A. R. Single-cell genome sequencing at ultra-high-throughput with microfluidic droplet barcoding. *Nat Biotechnol* **35**, 640–646 (2017).
9. Coxon, C. H., Longstaff, C. & Burns, C. Applying the science of measurement to biology: Why bother? *PLoS Biol* **17**, e3000338 (2019).
10. Plant, A. L. *et al.* How measurement science can improve confidence in research results. *PLOS Biology* **16**, e2004299 (2018).
11. Karaböce, B. Challenges for medical metrology. *IEEE Instrumentation Measurement Magazine* **23**, 48–55 (2020).
12. Myers, G. L. *et al.* A Reference Method Laboratory Network for Cholesterol: A Model for Standardization and Improvement of Clinical Laboratory Measurements. *Clinical Chemistry* **46**, 1762–1772 (2000).

13. Leech, D. P. & Belmont, P. A. *The economic impacts of NIST cholesterol standards program*. https://www.nist.gov/system/files/documents/tpo/No-13-PR-00-4-Cholesterol.pdf (2000).
14. Current status of blood cholesterol measurement in clinical laboratories in the United States: a report from the Laboratory Standardization Panel of the National Cholesterol Education Program. *Clinical Chemistry* **34**, 193–201 (1988).
15. Altschuler, S. J. & Wu, L. F. Cellular Heterogeneity: Do Differences Make a Difference? *Cell* **141**, 559–563 (2010).
16. Crick, F. Central Dogma of Molecular Biology. *Nature* **227**, 561–563 (1970).
17. Guo, Y. *et al.* How is mRNA expression predictive for protein expression? A correlation study on human circulating monocytes. *Acta Biochimica et Biophysica Sinica* **40**, 426–436 (2008).
18. Schwanhäusser, B. *et al.* Global quantification of mammalian gene expression control. *Nature* **473**, 337–342 (2011).
19. Darmanis, S. *et al.* Simultaneous Multiplexed Measurement of RNA and Proteins in Single Cells. *Cell Reports* **14**, 380–389 (2016).
20. Aebersold, R. *et al.* How many human proteoforms are there? *Nat Chem Biol* **14**, 206–214 (2018).
21. Edwards, A. V. G., Schwämmle, V. & Larsen, M. R. Neuronal process structure and growth proteins are targets of heavy PTM regulation during brain development. *Journal of Proteomics* **101**, 77–87 (2014).
22. Arribas, J., Baselga, J., Pedersen, K. & Parra-Palau, J. L. p95HER2 and Breast Cancer. *Cancer Res* **71**, 1515–1519 (2011).
23. Magaki, S., Hojat, S. A., Wei, B., So, A. & Yong, W. H. An Introduction to the Performance of Immunohistochemistry. in *Biobanking: Methods and Protocols* (ed. Yong, W. H.) 289–298 (Springer, 2019). doi:10.1007/978-1-4939-8935-5_25.
24. Johnson, C. W. Issues in Immunohistochemistry. *Toxicol Pathol* **27**, 246–248 (1999).
25. Moldavan, A. PHOTO-ELECTRIC TECHNIQUE FOR THE COUNTING OF MICROSCOPICAL CELLS. *Science* **80**, 188–189 (1934).
26. Picot, J., Guerin, C. L., Le Van Kim, C. & Boulanger, C. M. Flow cytometry: retrospective, fundamentals and recent instrumentation. *Cytotechnology* **64**, 109–130 (2012).
27. Bandura, D. R. *et al.* Mass Cytometry: Technique for Real Time Single Cell Multitarget Immunoassay Based on Inductively Coupled Plasma Time-of-Flight Mass Spectrometry. *Anal. Chem.* **81**, 6813–6822 (2009).
28. Shi, Q. *et al.* Single-cell proteomic chip for profiling intracellular signaling pathways in single tumor cells. *PNAS* **109**, 419–424 (2012).
29. James, L. C., Roversi, P. & Tawfik, D. S. Antibody Multispecificity Mediated by Conformational Diversity. *Science* **299**, 1362–1367 (2003).
30. Trenchevska, O., Nelson, R. W. & Nedelkov, D. Mass spectrometric immunoassays for discovery, screening and quantification of clinically relevant proteoforms. *Bioanalysis* **8**, 1623–1633 (2016).
31. Taniguchi, Y. *et al.* Quantifying E. coli Proteome and Transcriptome with Single-Molecule Sensitivity in Single Cells. *Science* **329**, 533–538 (2010).
32. Zhu, Y. *et al.* Proteomic Analysis of Single Mammalian Cells Enabled by Microfluidic Nanodroplet Sample Preparation and Ultrasensitive NanoLC-MS. *Angewandte Chemie International Edition* **57**, 12370–12374 (2018).
33. Smith, L. M. & Kelleher, N. L. Proteoforms as the next proteomics currency. *Science* **359**, 1106–1107 (2018).

34. O'Neill, R. A. *et al.* Isoelectric focusing technology quantifies protein signaling in 25 cells. *PNAS* **103**, 16153–16158 (2006).
35. Cai, X., Zheng, Y. & Speck, N. A. A western blotting protocol for small numbers of hematopoietic stem cells. *Journal of Visualized Experiments* **2018**, 6–9 (2018).
36. Hughes, A. J. *et al.* Single-cell western blotting. *Nature Methods* **11**, 749–755 (2014).
37. Tentori, A. M., Yamauchi, K. A. & Herr, A. E. Detection of Isoforms Differing by a Single Charge Unit in Individual Cells. *Angewandte Chemie International Edition* **55**, 12431–12435 (2016).
38. Wood, D. K., Weingeist, D. M., Bhatia, S. N. & Engelward, B. P. Single cell trapping and DNA damage analysis using microwell arrays. *PNAS* **107**, 10008–10013 (2010).
39. Molter, T. W. *et al.* A microwell array device capable of measuring single-cell oxygen consumption rates. *Sensors and Actuators B: Chemical* **135**, 678–686 (2009).
40. Kim, J. J., Sinkala, E. & Herr, A. E. High-selectivity cytology via lab-on-a-disc western blotting of individual cells. *Lab Chip* **17**, 855–863 (2017).
41. Rosàs-Canyelles, E. *et al.* Multimodal detection of protein isoforms and nucleic acids from low starting cell numbers. *Lab on a Chip* **21**, 2427–2436 (2021).
42. Yamauchi, K. A. & Herr, A. E. Subcellular western blotting of single cells. *Microsystems and Nanoengineering* **3**, (2017).
43. Hughes, A. J., Lin, R. K. C., Peehl, D. M. & Herr, A. E. Microfluidic integration for automated targeted proteomic assays. *PNAS* **109**, 5972–5977 (2012).
44. Dorman, G. & Prestwich, G. D. Benzophenone Photophores in Biochemistry. *Biochemistry* **33**, 5661–5673 (1994).
45. Bass, J. *et al.* An overview of technical considerations for Western blotting applications to physiological research. *Scand J Med Sci Sports* **27**, 4–25 (2017).
46. Kang, C.-C. *et al.* Single cell–resolution western blotting. *Nature Protocols* **11**, 1508–1530 (2016).
47. Vlassakis, J. & Herr, A. E. Effect of Polymer Hydration State on In-Gel Immunoassays. *Anal. Chem.* **87**, 11030–11038 (2015).
48. Ogston, A. G. The spaces in a uniform random suspension of fibres. *Trans. Faraday Soc.* **54**, 1754–1757 (1958).
49. Su, A., Smith, B. E. & Herr, A. E. In situ measurement of thermodynamic partitioning in open hydrogels. *Anal. Chem.* (2019) doi:10.1021/acs.analchem.9b03582.
50. Possolo, A. & Iyer, H. K. Invited Article: Concepts and tools for the evaluation of measurement uncertainty. *Review of Scientific Instruments* **88**, 011301 (2017).
51. Marinov, G. K. *et al.* From single-cell to cell-pool transcriptomes: Stochasticity in gene expression and RNA splicing. *Genome Res.* **24**, 496–510 (2014).
52. Streets, A. M. *et al.* Microfluidic single-cell whole-transcriptome sequencing. *PNAS* **111**, 7048–7053 (2014).
53. Candia, J. *et al.* Assessment of Variability in the SOMAscan Assay. *Scientific Reports* **7**, (2017).
54. Zainol, M. *et al.* Introducing a true internal standard for the Comet assay to minimize intra- and inter-experiment variability in measures of DNA damage and repair. *Nucleic Acids Res* **37**, e150 (2009).
55. Brennecke, P. *et al.* Accounting for technical noise in single-cell RNA-seq experiments. *Nat Methods* **10**, 1093–1095 (2013).
56. Lin, Y. *et al.* Evaluating stably expressed genes in single cells. *GigaScience* **8**, (2019).

57. Tseng, C.-C. & Li, C.-S. Inactivation of Virus-Containing Aerosols by Ultraviolet Germicidal Irradiation. *Aerosol Science and Technology* **39**, 1136–1142 (2005).
58. Nardell, E., Vincent, R. & Sliney, D. H. Upper-Room Ultraviolet Germicidal Irradiation (UVGI) for Air Disinfection: A Symposium in Print. *Photochemistry and Photobiology* **89**, 764–769 (2013).
59. EPA. *Ultraviolet Disinfection Guidance Manual for the Final Long Term 2 Enhanced Surface Water Treatment Rule*. (2006).
60. Jelden, K. C. *et al.* Ultraviolet (UV)-reflective paint with ultraviolet germicidal irradiation (UVGI) improves decontamination of nosocomial bacteria on hospital room surfaces. *Journal of Occupational and Environmental Hygiene* **14**, 456–460 (2017).
61. CDC. *Recommended Guidance for Extended Use and Limited Reuse of N95 Filtering Facepiece Respirators in Healthcare Settings*. (2020).
62. Zunner-Keating, B. P. *et al.* Rapid implementation of ultraviolet germicidal irradiation and reuse processes for N95 respirators at a health system during the coronavirus disease 2019 (COVID-19) pandemic. *Infect Control Hosp Epidemiol* 1–3 doi:10.1017/ice.2020.1386.
63. Lowe, J. J. *et al. N95 Filtering Facepiece Respirator Ultraviolet Germicidal Irradiation (UVGI) Process for Decontamination and Reuse*. https://www.nebraskamed.com/sites/default/files/documents/covid-19/n-95-decon-process.pdf (2020).
64. Grist, S. M. *et al.* Current Understanding of Ultraviolet-C Decontamination of N95 Filtering Facepiece Respirators. *Applied Biosafety* apb.20.0051 (2021) doi:10.1089/apb.20.0051.
65. Kowalski, W. *Ultraviolet Germicidal Irradiation Handbook: UVGI for Air and Surface Disinfection*. (Springer Berlin Heidelberg, 2009). doi:10.1007/978-3-642-01999-9.
66. Risović, D., Maver-Bišćanin, M., Mravak-Stipetić, M., Bukovski, S. & Bišćanin, A. Quantitative Investigation of Efficiency of Ultraviolet and Visible Light in Eradication of Candida albicans In Vitro. *Photomedicine and Laser Surgery* **32**, 232–239 (2014).
67. Nerandzic, M. M. *et al.* Evaluation of a Pulsed Xenon Ultraviolet Disinfection System for Reduction of Healthcare-Associated Pathogens in Hospital Rooms. *Infection Control & Hospital Epidemiology* **36**, 192–197 (2015).
68. Bui, H. Q. T., Velpula, R. T., Jain, B. & Nguyen, H. P. T. III-Nitride Based Narrow Band Far-UVC LEDs for Airborne and Surface Disinfection. *ECS Trans.* **98**, 83 (2020).
69. Shen, L. *et al.* Efficacy of UVC-LED in water disinfection on Bacillus species with consideration of antibiotic resistance issue. *Journal of Hazardous Materials* **386**, 121968 (2020).
70. Rubin, M. Optical properties of soda lime silica glasses. *Solar Energy Materials* **12**, 275–288 (1985).
71. Ha, J.-W., Back, K.-H., Kim, Y.-H. & Kang, D.-H. Efficacy of UV-C irradiation for inactivation of food-borne pathogens on sliced cheese packaged with different types and thicknesses of plastic films. *Food Microbiology* **57**, 172–177 (2016).
72. Beck, S. E., Wright, H. B., Hargy, T. M., Larason, T. C. & Linden, K. G. Action spectra for validation of pathogen disinfection in medium-pressure ultraviolet (UV) systems. *Water Research* **70**, 27–37 (2015).
73. Corróns, A. C. *et al.* Ultraviolet calibration of detectors with respect to a cryogenic radiometer. *Metrologia* **37**, 555–558 (2000).
74. Schmalwieser, A. W. *et al.* Aging of low-pressure amalgam lamps and UV dose delivery. *Journal of Environmental Engineering and Science* **9**, 113–124 (2014).

75. Su, A., Grist, S. M., Geldert, A., Gopal, A. & Herr, A. E. Quantitative UV-C dose validation with photochromic indicators for informed N95 emergency decontamination. *PLOS ONE* **16**, e0243554 (2021).
76. Poster, D. L. *et al.* Innovative Approaches to Combat Healthcare-Associated Infections Using Efficacy Standards Developed Through Industry and Federal Collaboration. *Proc SPIE Int Soc Opt Eng* **10730**, (2018).

Chapter 2

Characterizing technical variation in protein loss and fluorescence imaging in electrophoretic cytometry

2.1 Abstract

Electrophoretic cytometry enables measurement of proteoform expression in single cells, which provides insight on cell signaling and regulation during key biological processes such as development and disease progression. However, biological differences are only detectable if they are greater than the technical variability of the assay used to measure them. Technical variability of single cell assays is challenging to quantify due to the lack of true technical replicates. Here, we aim to understand and control for sources of technical variability in single cell protein abundance measurements made by electrophoretic cytometry. To do so, we develop methods to robustly quantify fluorescent protein abundance from single cells at different stages of the electrophoretic cytometry assay, to quantify the amount of intra-assay technical variation introduced by different assay stages. First, we develop and optimize a method to quantify whole-cell fluorescent protein abundance from widefield fluorescence microscopy images while minimizing imaging artifacts. Next, we characterize the spatial uniformity of ultraviolet irradiance applied to photoimmobilize proteins in the gel, and develop a method to quantify captured protein from photoimmobilized protein fluorescence. Finally, we compare corresponding whole-cell, photoimmobilized, and immunoprobed fluorescent protein abundance measurements from ~100 of the same single cells assayed per device to quantify the amount of intra-assay technical variation in both protein capture and protein detection. Identifying and controlling for sources of technical variability in protein abundance measurements will enable true biological variation to be distinguished from measurement error to a finer degree.

2.2 Introduction

Single cell measurements are crucial to identifying and understanding rare cell subpopulations, bimodal expression, and other cases where an ensemble measurement does not represent the behavior of some, or all, individual cells.[1] Cell-to-cell differences can be manifested in different types of measurements, including RNA or protein expression levels. On the single cell level, RNA and protein expression are often poorly correlated due to differing rates of transcription, translation, and degradation.[2] Thus, protein expression levels often cannot be predicted from RNA expression levels. Additionally, a single messenger RNA molecule can encode multiple protein structures (proteoforms) due to post-translational modifications such as phosphorylation and glycosylation.[3] Thus, single cell protein expression measurements provide unique information about the state of individual cells which cannot be inferred from RNA measurements.

Numerous techniques enable measurement of single cell protein expression, but these approaches generally lack proteoform specificity. Many techniques, such as immunocytochemistry, flow cytometry, mass cytometry[4], and antibody barcode chips[5], all rely on

antibody binding to detect proteins. However, antibodies often lack target specificity and cannot be used to distinguish different proteoforms with the same epitope.[6,7] Alternatively, proteins can be labeled with genetically encoded fluorescent fusion tags so that single cell protein expression can be measured using fluorescence microscopy.[8] However, the addition of a fluorescent protein tag or other labels substantially increases the size of the protein of interest, which can alter its function or localization within a cell. Because the protein tags are genetically encoded, they also will not distinguish between proteoforms. Lastly, mass spectrometry of single cells has recently been demonstrated[9]; however, proteins must first be digested into peptides, and thus it is not possible to reconstruct individual protein identities from the pooled digest to understand which post-translational modifications were associated with which individual proteins and/or proteoforms. Thus, there is a need for a tool which can measure proteoform expression on a single-cell level.

Electrophoretic cytometry tools fill this measurement gap by enabling high-throughput measurement of proteoforms in single cells. In electrophoretic cytometry, proteins are first separated by a physical property such as mass or charge prior to antibody-based detection (immunoprobing) (**Figure 2.1**). The prepended separation step enables proteoforms which bind the same antibody to be distinguished because they are spatially resolved based on mass or charge. Additionally, each electrophoretic cytometry assay makes use of a microwell array to enable tens to hundreds of single cells to be measured simultaneously. Electrophoretic cytometry assays have been applied to quantify HER2 isoform expression in single breast tumor cells[10] and to study expression of multiple proteins from single circulating tumor cells[11].

However, a key limitation of any quantitative assay is technical variability; in electrophoretic cytometry, there are several process steps which can introduce technical variability into the system. Technical variability of single cell assays is challenging to quantify due to the lack of true technical replicates. Here, we aim to understand and control for sources of technical variation in single cell protein abundance measurements made by electrophoretic cytometry. Because electrophoretic cytometry involves both a protein separation and immunoblot, technical variability from multiple stages of the assay contribute to variation in the final readout. There are two overarching ways in which technical variability can arise – either as variation in the amount of protein captured in the gel, or variation in the amount of protein detected during the immunoprobing step. First, intra-assay variation can arise from different amounts of protein loss prior to photoimmobilization. Electrophoretic cytometry is an open microfluidic assay in which lysis buffer is poured over the top of the microwell array to initiate simultaneous lysis of all cells. Thus, variation in microwell depth as well as variation in lysis buffer flow profile across the microwell array can lead to variation in the amount of diffusive and/or convective loss of cell lysate from the open microwells prior to electrophoresis. Additionally, variation in ultraviolet (UV) intensity across the gel during the photoimmobilization step can lead to differences in protein capture efficiency. Second, technical variation can arise from the protein detection step, for instance due to variation in local antibody concentration.

While previous studies have measured variation in isolated aspects of the assay, such as intra-assay variation in microwell height and protein diffusion out of the microwell[12], the cumulative amount of technical variability in the amount of protein captured and detected via immunoprobing has not been quantified. To assess intra-assay technical variation arising from different assay stages, here we develop a method to quantify protein abundance at multiple upstream assay stages in addition to the traditional immunoprobing readout, using imaging techniques to quantify fluorescent protein abundance (**Figure 2.1**). After optimizing the upstream

assay readouts to minimize confounding factors in relating measured fluorescence to protein abundance, we characterize intra-assay technical variation at different assay stages by comparing protein abundance measured at different stages. Additionally, we quantify the total assay technical variability to understand the precision of protein abundance measurements made by electrophoretic cytometry.

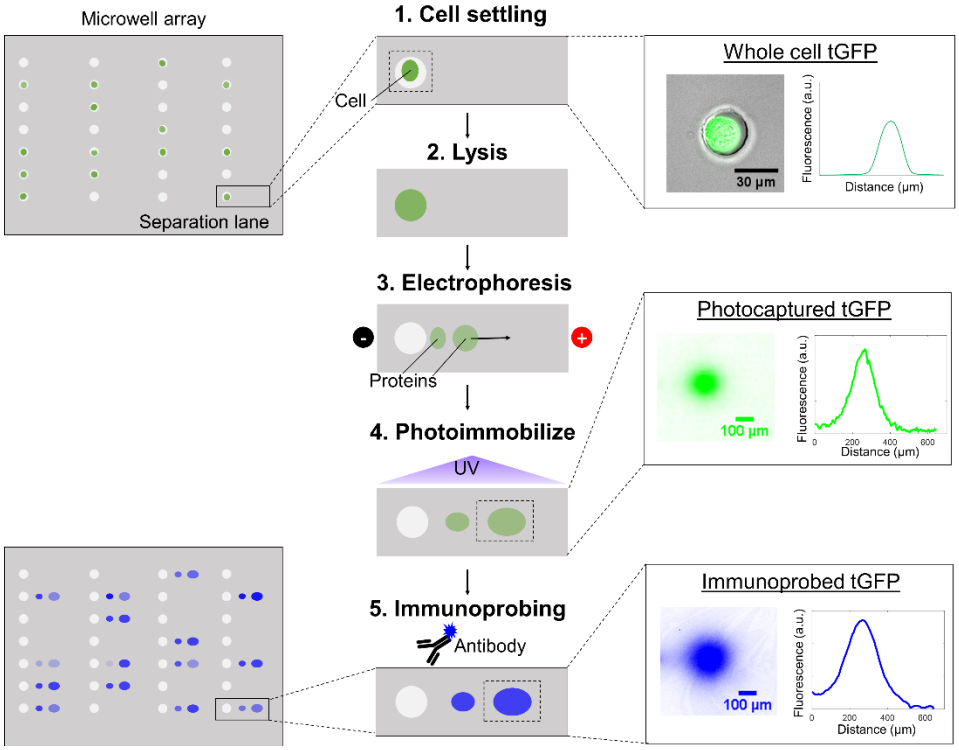

Figure 2.1. Method to quantify protein abundance at different stages of electrophoretic cytometry. By running the assay with cells expressing a fluorescent protein (Turbo GFP; tGFP), tGFP abundance can be measured not only from immunoprobed area under the curve (AUC; the standard assay readout), but also at upstream steps (whole-cell and photoimmobilized abundance) via tGFP fluorescence.

2.3 Materials & Methods

Materials and equipment. Alexa Fluor 647-labeled beads used for microscopy optimization were generated by conjugating Alexa Fluor 647-labeled His-tagged Protein G to PureProteome nickel magnetic microparticles with 10 µm diameter obtained from Millipore Sigma (LSKMAGH02), as previously described[13]. Uniformly fluorescent reference slides for microscopy optimization are from Ted Pella (#2273). All microscopy was performed on an Olympus IX71 inverted epifluorescence microscope with a Lumen Dynamics X-cite exacte fluorescence illumination source coupled to a liquid light guide (Lumatec, 805-00038), an Andor iXon+ EMCCD camera (DU-885K-C00-#VP), and MetaMorph image acquisition software. All photoimmobilized and immunoprobed protein bands were imaged with a fluorescence microarray scanner (Genepix 4300A, Molecular Devices). Electrophoretic cytometry reagents are the same as reported previously[14].

Characterization of the impact of sample height variation on fluorescent image quantification. 160 images were acquired across a uniform fluorescent reference slide (Ted Pella #2273), with ~2.5 mm spacing between each image. Automated stage control (Metamorph Multi-Dimensional Acquisition) was used to program acquisition of images in an arrayed pattern. The uniform reference slide was placed either on a custom-made 3D-printed stage adapter, or on a

commercial metal stage adapter with a petri dish and slide insert (Applied Scientific Instrumentation).

Characterization of technical variation in photoimmobilized protein quantification. 8%T, 40 µm-thick polyacrylamide gels were cast with 200 nM purified turbo GFP (tGFP; Evrogen FP552) evenly mixed into the precursor. After chemical polymerization, the gels were exposed to collimated UV light (~20 mW/cm^2, OAI Model 30 Collimated UV Light Source) for 300 s to photoimmobilize the tGFP uniformly within the gel. Gels were washed in 1× Tris buffered saline with Tween 20 (TBST) for at least 30 min, then rinsed in deionized (dI) water, dried with a nitrogen stream, and imaged with Genepix to confirm a uniform initial protein distribution. Gels were subsequently rehydrated, and different mock assay procedures (application of lysis buffer, electric field, and/or uncollimated UV exposure with a Lightningcure LC8 for photoimmobilization) were performed, depending on the experiment. Gels were then washed, rinsed, dried, and imaged with Genepix again to quantify fluorescence uniformity after the experiment.

Polyacrylamide gel fabrication. 8%T polyacrylamide gels with microwell arrays were cast from micropost molds microfabricated by SU-8 photolithography. Microposts were 40 µm tall and 32 µm in diameter, with 600 µm axial spacing and 800 µm spacing along the separation lane. Microposts (and corresponding microwells) were patterned in 10 × 18 micropost/well blocks, with larger spacing in between each block, for ease of subsequent mapping of whole-cell images to corresponding photoimmobilized and immunoprobed protein images.

Whole-cell imaging and quantification. tGFP-expressing U251 glioblastoma cells were settled in 32 µm-diameter, 40 µm-deep microwells as described previously.[14] After cell settling, ~1 mL of 1× phosphate-buffer saline (PBS) was pipetted on top of the gel to keep it hydrated during whole-cell imaging. The gel was placed in a petri dish lid on a metal stage adapter (Applied Scientific Instrumentation) on the microscope. Brightfield and fluorescence images of each well were taken with a 20×/0.45 numerical aperture (NA) objective with a correction collar set to correct for the ~1 mm-thick petri dish lid and ~1 mm-thick glass slide under the gel. Automated stage control was used to program stage movement to each microwell in the array, and image location was saved with each image to facilitate mapping of whole-cell fluorescence to downstream protein abundance measurements from the same corresponding cell.

All whole cell images were flat-field corrected to correct for nonuniform illumination across the field of view. Dark and flat-field images were obtained as described previously[15], except that a uniformly fluorescent reference slide (Ted Pella #2273) was used as a uniformly fluorescent sample for flat-field images. Flat-field correction was performed by subtracting each fluorescence image by the dark image, and then dividing by the flat-field image of a uniformly fluorescent sample. After flat-field correction, an intensity profile was generated from each fluorescence image by calculating the mean of each column of pixels in the image, subtracted by the median of each column (because the cell diameter was substantially less than half the width and height of the field of view, the median of each column served as a measure of the background intensity in the image). Whole-cell fluorescence was quantified by area-under-the-curve (AUC) analysis from a Gaussian fit, as described previously[16]. Whole-cell fluorescence was only quantified from wells containing a single cell, and microwell indices for each whole-cell AUC were used to match whole-cell AUC to photoimmobilized and immunoprobed AUC from the same cell.

Electrophoretic cytometry. Immediately after whole-cell imaging, electrophoretic cytometry was performed using a modified protocol optimized for photoimmobilized tGFP quantification, as described previously[14]. Briefly, the gel was adhered in a custom-built electrophoresis chamber with Vaseline, and subjected to cell lysis (30 s at 4 ^{o}C) and then electrophoresis (20 s at 40 V/cm).

Immediately after electrophoresis, the electric field was turned off and leads unclipped from the chamber for safety, Vaseline was wiped off the back of the glass slide, and the gel was moved to a 4-well dish with 1× TBST, with gel side facing up. The gel was then exposed to collimated UV (365 nm, 300 s at ~20 mW/cm^2) for photoimmobilization.

Immunoprobing. Immunoprobing was performed as reported previously[16,17], using rabbit anti-TurboGFP primary antibody (ThermoFisher PA5-22688) at a concentration and donkey anti-rabbit Alexa Fluor 647 secondary antibody (ThermoFisher A31573), both diluted to a concentration of 0.1 mg/mL in 1× TBST with 2% bovine serum albumin (BSA).

Linear range determination. We focused on technical variation of protein abundance measurements within the linear range of the immunoassay, where starting and measured protein abundance are proportional. The linear range of the whole-cell and immunoprobed measurements was identified using the approach developed by Kroll et al.[18] Briefly, data points are determined to be in the linear range if there is less than a 10% improvement (as defined by the root mean square error, RMSE) in a 4-parameter logistic model fit over a linear fit for the data points (**Figure 2.2).** In electrophoretic cytometry, we expect the plot of starting vs. measured protein abundance will be linear at low protein levels and plateau at high protein levels due to antibody saturation. To determine the upper bound of the linear range, linear and 4-parameter logistic models were both fit to increasingly wide subsets of the data. The maximum whole-cell tGFP abundance increased so that one new cellular measurement was included with each round of fitting. The upper bound of the linear range is the maximum whole-cell tGFP abundance level that can be included in the dataset before the RMSE of the 4-parameter logistic model fit is >10% lower than the RMSE of the linear fit. The linear ranges of whole-cell AUC vs. photoimmobilized AUC and photoimmobilized AUC vs. immunoprobed AUC were determined with the same method. Only data from separation lanes in which all 3 measurements (whole-cell, photoimmobilized, and immunoprobed AUC) were within the linear range were used for subsequent analysis.

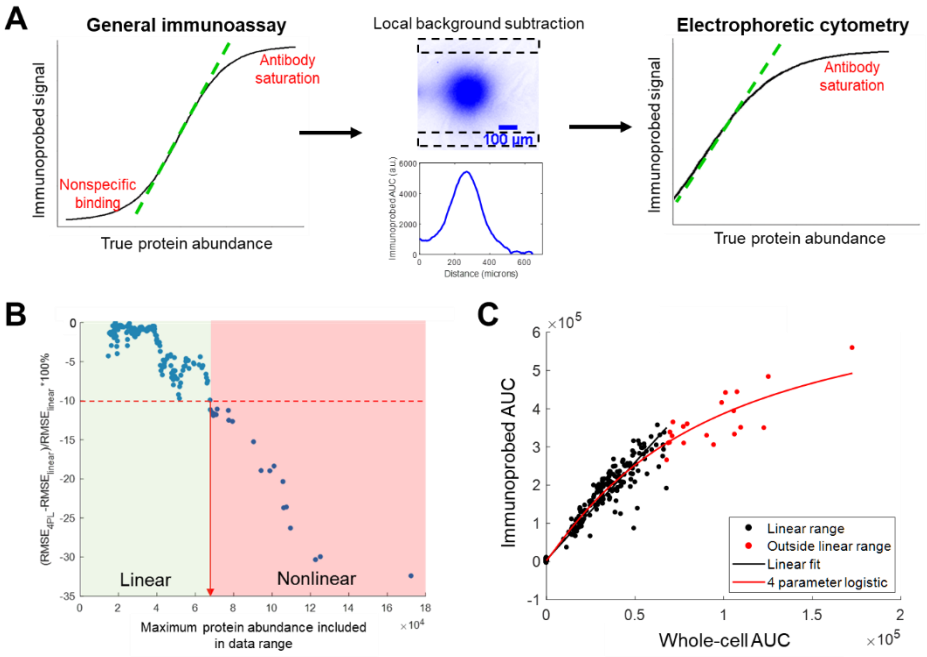

Figure 2.2. Determination of the linear range of electrophoretic cytometry data. (A) Many immunoassays exhibit a sigmoidal dose-response curve, with a plateau at low analyte levels due to nonspecific antibody binding, and a plateau at high analyte levels due to antibody saturation. However, the local background subtraction implemented in electrophoretic cytometry analysis eliminates the lower plateau from the dose response curve. (B) The percent

difference of the root-mean-square error (RMSE) for a linear vs. 4 parameter logistic fit to electrophoretic cytometry dose response data as a function of the maximum protein abundance included in the fitted data. The linear range is defined as the data for which the linear fit has a similar goodness of fit as a 4 parameter logistic fit (RMSE difference of <10%). (C) Electrophoretic cytometry dose response data, with the linear data and fit indicated in black, and the nonlinear data and fit indicated in red.

2.4 Results & Discussion

Minimizing technical variation of whole-cell quantitative fluorescence imaging. To accurately compare the fluorescence of whole suspended U251-tGFP cells isolated in microwells across a ~37 mm × 25 mm electrophoretic cytometry chip, we first sought to develop a robust whole-cell quantitative fluorescence imaging workflow. In particular, we aimed to eliminate vertical smearing, minimize spatial variation in chip height, and correct for uneven illumination across each field of view.

Vertical smearing is dependent on the ratio of exposure time to image transfer time on frame-transfer CCD sensors. We optimized image acquisition settings to eliminate vertical smearing artifacts, which appear as vertical fluorescent lines above and below fluorescent objects such as whole cells (**Figure 2.3**). These vertical lines have greater fluorescence intensity than the surrounding background (**Figure 2.3B-C**), which introduces error in background subtraction and whole cell fluorescence quantification.

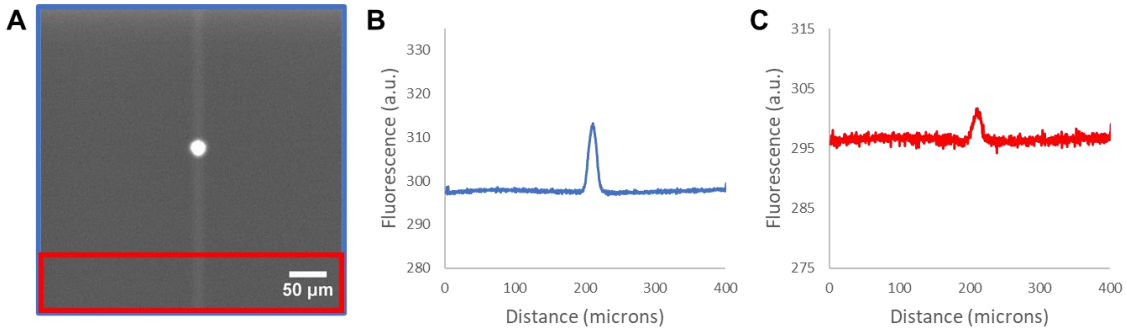

Figure 2.3. Vertical smearing in whole U251-tGFP cell fluorescence image impacts fluorescence quantification. (A) Widefield fluorescence microscopy image (2 ms exposure, 1.02 µs/pixel vertical shift speed) of a single U251-tGFP cell settled in a microwell. (B) Average fluorescence intensity profile of the whole image. (C) Average fluorescence intensity profile of a background region in the image. For B-C, the average fluorescence of each column of pixels is plotted as a function of horizontal distance across the image.

We hypothesized that vertical smearing arises from the frame transfer process of the CCD sensor. The camera used here has a frame-transfer EMCCD sensor, in which photons collected in the top half of the chip are rapidly shifted to the bottom shielded half ('storage region') of the chip prior to readout. We hypothesize there is a slight delay between the time when image acquisition begins and the time when the light guide (excitation source) shutter closes. Because the camera model used here does not have a shutter, the CCD chip may still be exposed to incident light as the pixels are being vertically shifted down during the frame transfer process; this explains the vertical line above the fluorescent point. There is also a vertical line below each fluorescent point because the camera "recycles" each row of pixels, so after each row is read out the bottom of the image, it is cycled back up to the top. Because the camera does not have a shutter, we hypothesize that the camera reads the current frame prior to reading the actual image data in order to clear the array and set all the pixels to zero. Thus, the lower streak is from the pre-acquisition "zeroing" image, and the upper streak is from the acquired image exposure. If the exposure time is short (so

it is on the same order as the duration of frame transfer), the vertical lines will be more significant[19,20].

To test this hypothesis, we acquired images of fluorescent beads with different ratios of exposure time to transfer time. Transfer time is equal to the product of the vertical dimension of the image and the vertical shift speed. In agreement with our hypothesis, we find that vertical smearing is eliminated when exposure time is substantially longer than transfer time (**Figure 2.4**). Thus, vertical smearing in whole-cell fluorescent imaging was eliminated by a combination of increasing vertical shift speed and/or increasing exposure time. While faster vertical shift speeds can reduce charge transfer efficiency, effectively decreasing pixel full-well depth and dynamic range, we found that dynamic range remained sufficient to quantify whole-cell fluorescence.

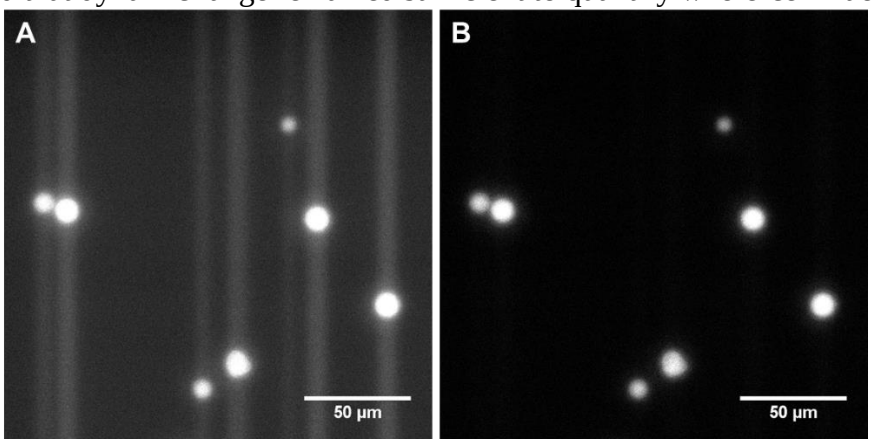

Figure 2.4. Increasing exposure time relative to transfer time reduces vertical smearing in images acquired with frame-transfer CCD cameras. 1002 (height) × 1004 (width) pixel images of AF647-labeled beads acquired with 2 ms exposure with either (A) the slowest possible vertical shift speed (3.73 µs/pixel), corresponding to 3.74 ms transfer time, or (B) the fastest possible vertical shift speed (0.56 µs/pixel), corresponding to 0.56 ms transfer time. All other imaging and image contrast settings are the same in both images.

Uniform sample height is critical for quantitative fluorescence imaging across large-area chips. To quantify whole-cell fluorescence, we aimed to image each cell settled in microwells across a 37 mm × 25 mm electrophoretic cytometry chip. The vertical position of the sample relative to the microscope objective's depth of focus influences the image fluorescence. To verify that variation in measured whole-cell fluorescence is due to biological variation and not variation in sample height, we characterized the measured fluorescence of 160 images taken across a 25 mm × 75 mm uniformly fluorescent reference slide. We find that the stage adapter used to hold the slide introduces spatial variation in measured fluorescence. The fluorescence of images of a uniformly fluorescent slide placed on a 3D-printed stage adapter had substantial spatial variation, with a coefficient of variation (CV) among all images of 10.2% (**Figure 2.5A**). In contrast, the fluorescence of images of the same slide placed in a petri dish on a metal stage adapter exhibited no strong spatial pattern, with a CV of 1.0% (**Figure 2.5B**). We hypothesize that the metal stage adapter is more level than the 3D printed adapter, leading to less variation in sample height and resulting image fluorescence.

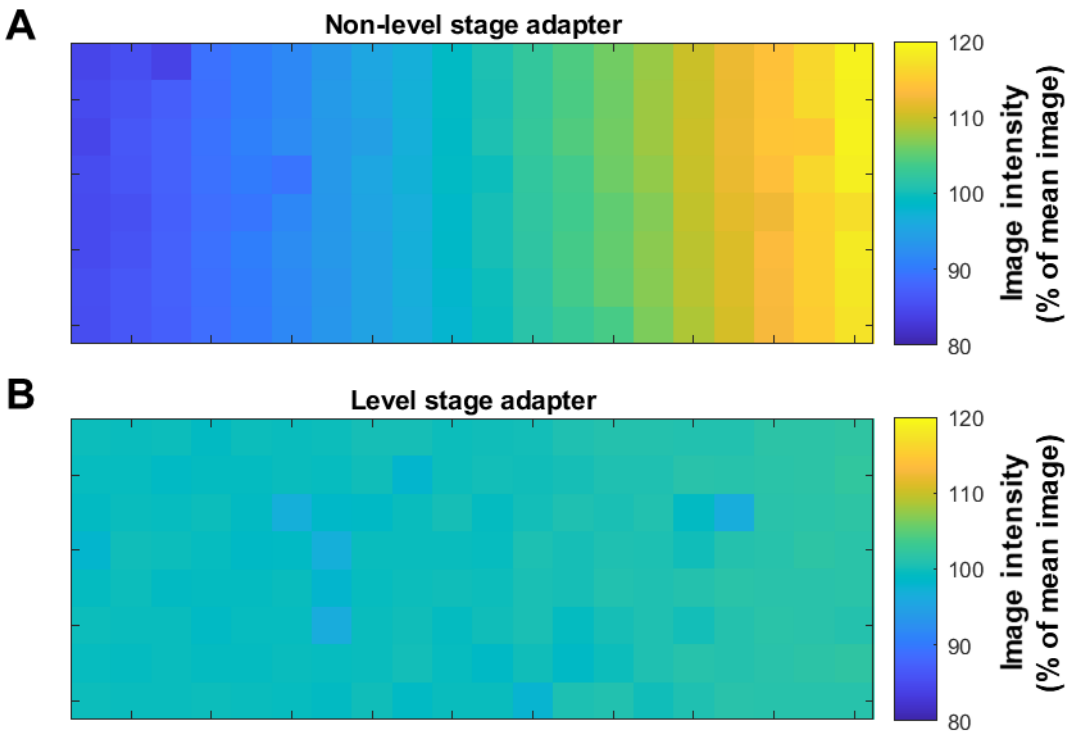

Figure 2.5. Sample tilt introduces spatial technical variation in fluorescence imaging. Heatmap of mean image intensity of 160 images (normalized to the mean of all images) taken at even spacing across a 25 mm × 75 mm uniformly fluorescent reference slide placed on (A) a non-level stage adapter, and (B) a level stage adapter.

Flat-field correction reduces error introduced by nonuniform illumination within a field of view. Because fluorescence illumination is often nonuniform across the field of view, flat-field correction should be performed to correct for uneven illumination[21]. To characterize the effect of flat-field correction, we quantified the intra-image variation in fluorescence intensity of a uniformly fluorescent reference slide before and after flat-field correction (n = 220 images). We find that flat-field correction decreases the mean intra-image standard deviation in fluorescence from 6.37% to 1.70% (**Figure 2.6**). Thus, we have confirmed that flat-field correction post-processing reduces technical variation in widefield fluorescence images by reducing the effect of nonuniform illumination.

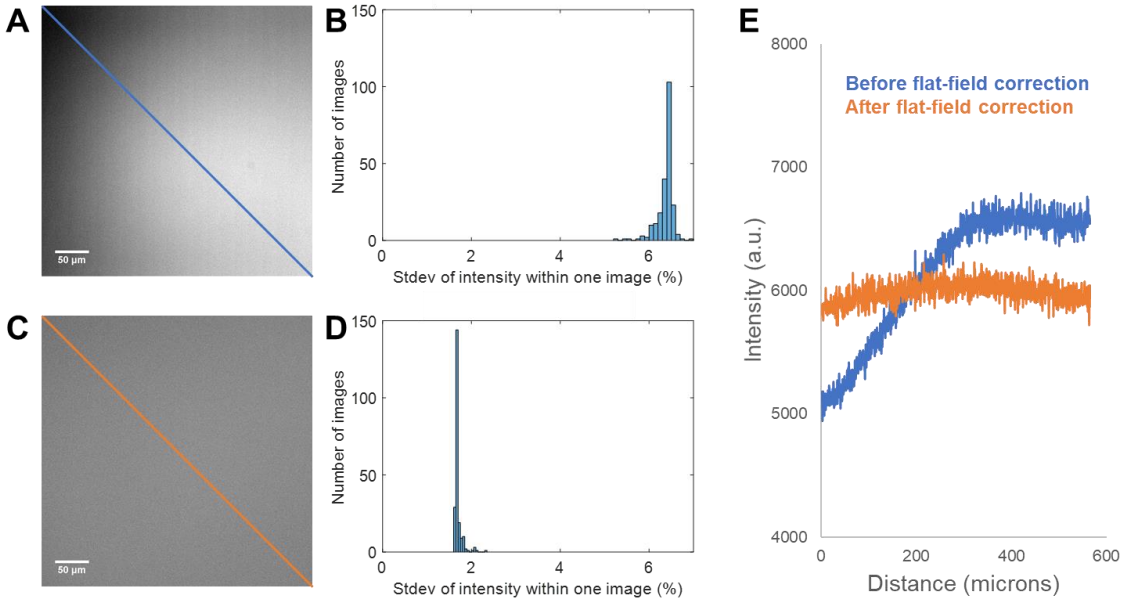

Figure 2.6. Flat-field correction reduces error introduced by nonuniform fluorescence excitation. Representative widefield fluorescence image of a uniformly fluorescent reference slide and histogram of the intra-image standard deviation in fluorescence intensity for multiple images before (A,B) and after (C,D) flat-field correction. (E) Intensity line profile across the diagonal of one representative image before and after flat-field correction.

Overall, we have reduced technical variation in whole-cell quantitative widefield fluorescence imaging over an array of microwells spanning 10s of mm through optimization of both acquisition parameters and post-processing. At the image acquisition stage, we have eliminated vertical smearing artifacts associated with slow frame transfer times relative to exposure times, and we have minimized variation due to sample tilt. At the post-processing stage, we implemented flat-field correction to correct for uneven illumination.

Minimizing technical variation of protein photoimmobilization. To quantify the amount of protein captured within the gel after electrophoresis and photoimmobilization, we aimed to perform electrophoretic cytometry on U251-tGFP cells and quantify the fluorescence of photoimmobilized tGFP. However, the 365 nm UV light used to initiate the photoimmobilization reaction causes tGFP photobleaching and has been shown to increase autofluorescence of electrophoretic cytometry gels[22]. In order for gel fluorescence to correspond to tGFP abundance, the amount of tGFP photobleaching and gel autofluorescence must be uniform across the gel area. To assess whether photobleaching and autofluorescence are uniform, we characterized the intra-chip variation in fluorescence of gels with uniformly distributed tGFP before and after performing a mock electrophoretic cytometry run (i.e., incubation in lysis buffer, electric field application, and UV photoimmobilization). To distribute tGFP uniformly within the gel, tGFP was mixed into the gel precursor. After gel polymerization, tGFP was photoimmobilized in the gel with a collimated UV source (which we hypothesized would have a more uniform UV distribution than the uncollimated, but higher-intensity, UV source typically used for electrophoretic cytometry photoimmobilization).

We characterized the intra-gel variation in fluorescence before and after running a mock electrophoretic cytometry assay on the gel. To mimic standard analysis of electrophoretic cytometry separation lanes, the gel image was divided into ~1500 separation lanes (1000 µm × 400 µm) (**Figure 2.7A-B**). We calculated the CV of the mean intensities of all separation lanes

before and after UV exposure from the uncollimated UV source used for photoimmobilization (Hamamatsu LC8). Before the mock assay, the intra-gel variability in fluorescence was relatively low (CV of lane intensities = 5.5% ± 2.2%) (**Figure 2.7C**). After the mock assay, intra-gel variability in fluorescence was significantly higher (2-tailed paired T test), with a CV of 19.2% ± 2.7% (**Figure 2.7D-E**).

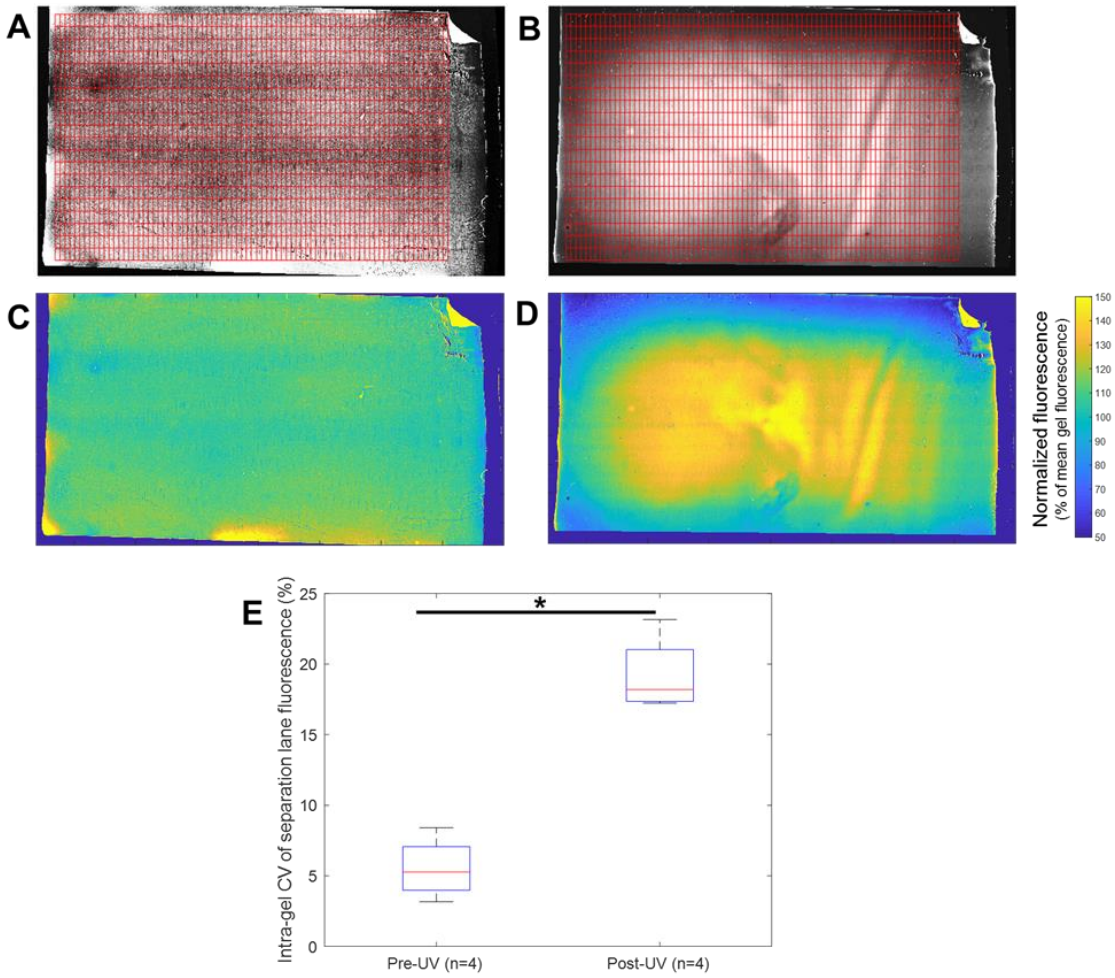

Figure 2.7. Intra-gel variability in fluorescence increases after mock electrophoretic cytometry. CV was calculated among mean fluorescence intensities of over 1000 separation lanes chosen from the images of the gel (A) pre-UV and (B) post-UV. Heatmaps of gel fluorescence (C) pre-UV and (D) post-UV demonstrate the increased variation in intra-gel fluorescence after UV exposure, which was quantified through (E) a box plot of intra-gel CV before and after UV exposure (2-tailed paired T test, $p<0.05$).

We observed that after the mock electrophoretic cytometry process, the gels often displayed streaky fluorescence patterns (**Figure 2.7D**). Because bubbles have been found to alter the path and intensity of incident light (i.e., lensing)[23], we hypothesized that bubbles formed by electrolysis during application of an electric field increase spatial variation in UV irradiance, contributing to the nonuniform gel fluorescence observed. To test this hypothesis, we compared the spatial variation in tGFP gel fluorescence after UV exposure in gels either with or without a preceding electrophoresis step. We found that intra-gel variation in fluorescence was significantly higher in gels in which an electric field was applied than in gels without electrophoresis, as seen both qualitatively from heatmaps of gel fluorescence (**Figure 2.8**) and box plots of intra-gel CV

in fluorescence (**Figure 2.9**). The results support our hypothesis that bubbles generated during electrophoresis increase spatial variation in UV irradiance during the photoimmobilization step. We have demonstrated that the spatial variation in UV irradiance yields spatial variation in tGFP photobleaching and/or gel autofluorescence; it remains unclear whether variation in UV irradiance also yields spatial variation in protein photoimmobilization efficiency. When comparing whole cell and photoimmobilized tGFP abundance to characterize intra-assay technical variation, we thus chose to use an alternate electrophoretic cytometry workflow in which the gel was moved into a different buffer bath (containing no bubbles) after electrophoresis, and a collimated UV source was used to immobilize proteins within the gel[14]. In this workflow, we assumed in-gel tGFP fluorescence corresponds to photoimmobilized protein abundance because UV irradiance is more uniform across the gel.

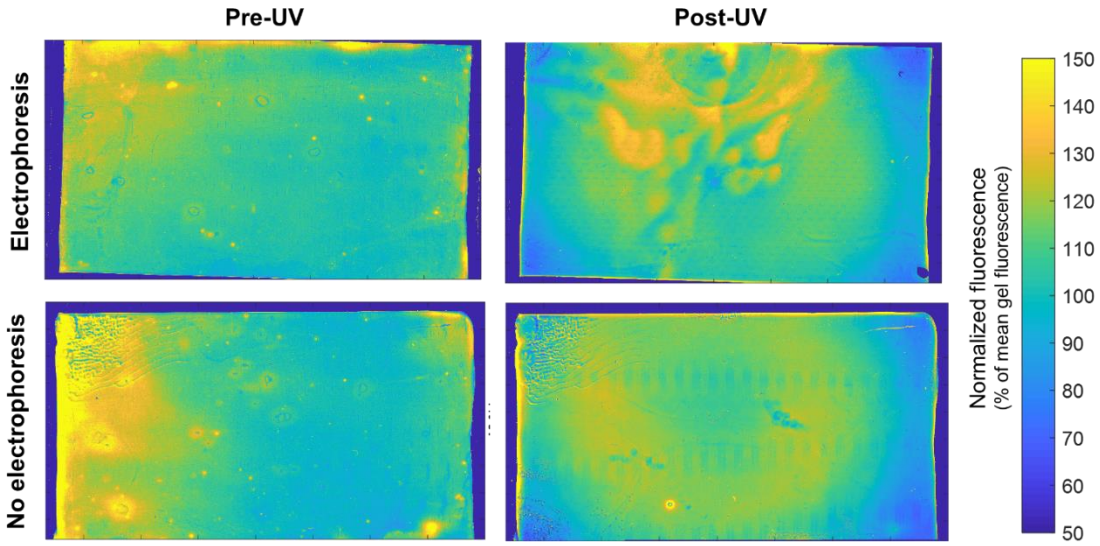

Figure 2.8. Electric field application followed by UV exposure using the uncollimated UV source results in streaky in-gel fluorescence patterns, whereas UV exposure alone does not. Heatmaps of fluorescence distribution in representative gels containing uniformly distributed tGFP before and after UV exposure. A lysis buffer and electric field were applied to gels in the top row prior to UV exposure, to mimic the electrophoretic cytometry process. Only lysis buffer (no electric field) was applied to gels in the bottom row prior to UV exposure.

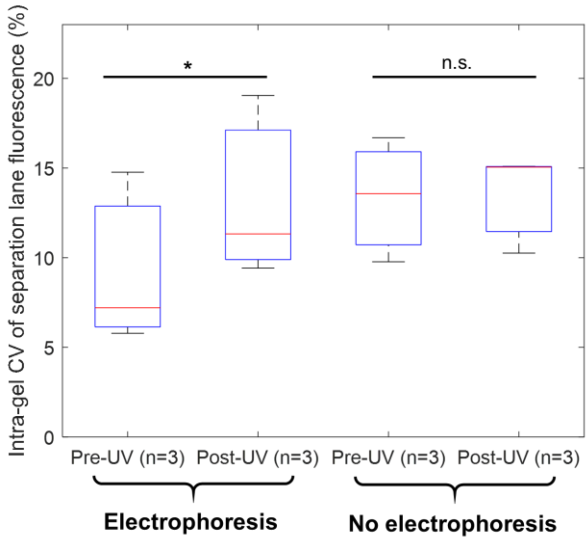

Figure 2.9. Intra-gel variability in fluorescence is significantly higher after electric field application (i.e., an electrophoresis step) and UV exposure, but not after UV exposure alone. Box plots of intra-gel variation in fluorescence for gels with uniformly distributed tGFP, subjected to different assay conditions. Two-tailed paired t-test, p = 0.0023 (comparison of pre- and post-UV gels with electrophoresis) and 0.967 (comparison of pre- and post-UV gels with no electrophoresis).

Characterizing technical variation at different assay stages from corresponding whole-cell, photoimmobilized, and immunoprobed protein measurements.

After optimizing the approach to imaging whole cells and photoimmobilized protein to minimize technical variation which would confound the relationship between fluorescence and protein abundance, we performed electrophoretic cytometry assays in which tGFP abundance was quantified from each whole cell, photoimmobilized protein band, and immunoprobed protein band. Measurements were spatially indexed so that protein abundance from the same cell could be compared across different assay stages.

To visualize the amount of technical variation in different assay stages, we plotted tGFP abundance measured at two different stages against each other (**Figure 2.10**). In the absence of technical variation, the tGFP abundance at one assay stage would be directly proportional to tGFP abundance at another assay stage, so the data points from all cells would form a straight line (r^2 = 1). However, we observe dispersion in all assay stage comparisons. The relationship between whole-cell and photoimmobilized tGFP abundance (**Figure 2.10A, Table 2.1**) indicates the amount of technical variation in protein capture; comparison of photoimmobilized and immunoprobed tGFP abundance (**Figure 2.10B, Table 2.1**) indicates the amount of technical variation in protein detection; comparison of whole-cell and immunoprobed tGFP abundance indicates the amount of technical variation in the entire electrophoretic cytometry assay (**Figure 2.10C, Table 2.1**). Overall, the correlation coefficients for corresponding stages were similar in magnitude to previously reported correlations between photoimmobilized and immunoprobed tGFP[24], and whole-cell and immunoprobed GFP[25]. In 2 out of 3 replicate gels, the correlation between whole-cell and immunoprobed tGFP abundance (indicating total assay technical variation) is lower than the correlation between intermediate stages, as would be expected. It is unclear why the r^2 value between photoimmobilized tGFP and immunoprobed tGFP abundance is lower than the total assay r^2 for Gel 1, but we hypothesize that some remaining technical variation

in the photoimmobilized tGFP abundance measurement (e.g., nonuniform tGFP photobleaching) may contribute by confounding exact measurement of photoimmobilized tGFP abundance.

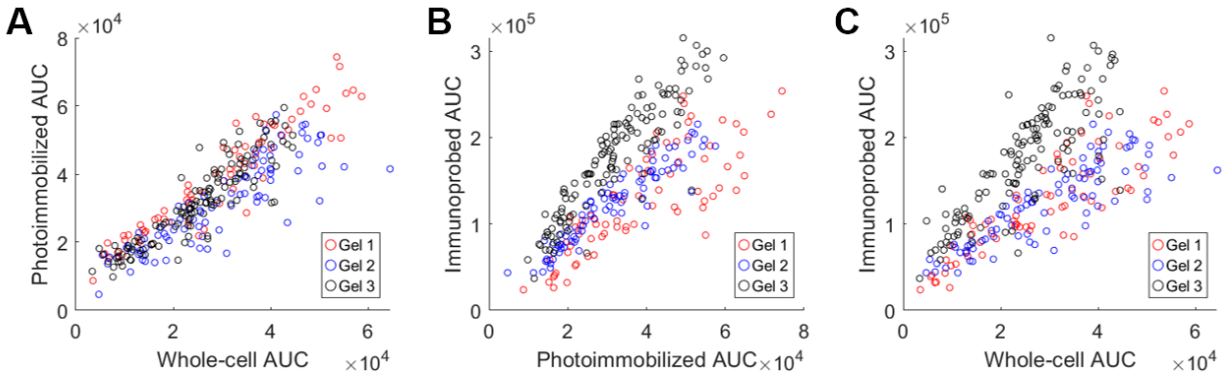

Figure 2.10. Correlation between tGFP abundance at different assay stages. (A) Scatterplot of whole-cell vs. photoimmobilized tGFP AUC, indicating the amount of technical variation in protein immobilization. (B) Scatterplot of photoimmobilized vs. immunoprobed tGFP AUC, indicating the amount of technical variation in protein detection (via antibody binding). (C) Scatterplot of whole-cell vs. immunoprobed tGFP AUC, indicating total amount of technical variation in electrophoretic cytometry. N = 73, 87, and 127 cells for Gels 1, 2, and 3, respectively.

Table 2.1. Correlation coefficients (r^2) between tGFP abundance measurements at different assay stages.

	r^2, Whole-cell vs. photoimmobilized	**r^2, Photoimmobilized vs. immunoprobed**	**r^2, Whole-cell vs. immunoprobed**
Gel 1	0.8896	0.6649	0.7444
Gel 2	0.7462	0.8838	0.7152
Gel 3	0.8158	0.8306	0.6764

While the correlation coefficient (r^2) provides a measure of the overall intra-assay variation, we also sought to quantify the expected measurement error of any individual photoimmobilized or immunoprobed protein band. To do so, we applied Bland-Altman analysis[26] to quantify the limits of agreement between each pair of datasets, as described previously[14]. The limits of agreement (marked in red in **Figure 2.11**) indicate the range of expected y values for a given x, based on the distribution of differences between the two datasets and a chosen threshold (e.g., ±2σ from the mean difference). From the limits of agreement, we can determine the expected fold difference between replicates (**Figure 2.12**). For example, from Bland-Altman analysis of the whole-cell and immunoprobed datasets, we find that two cells with equal whole-cell tGFP abundance may have immunoprobed tGFP abundance measurements that differ by up to 2.40 ± 0.22-fold (N = 3 replicate assays), due to intra-assay technical variation.

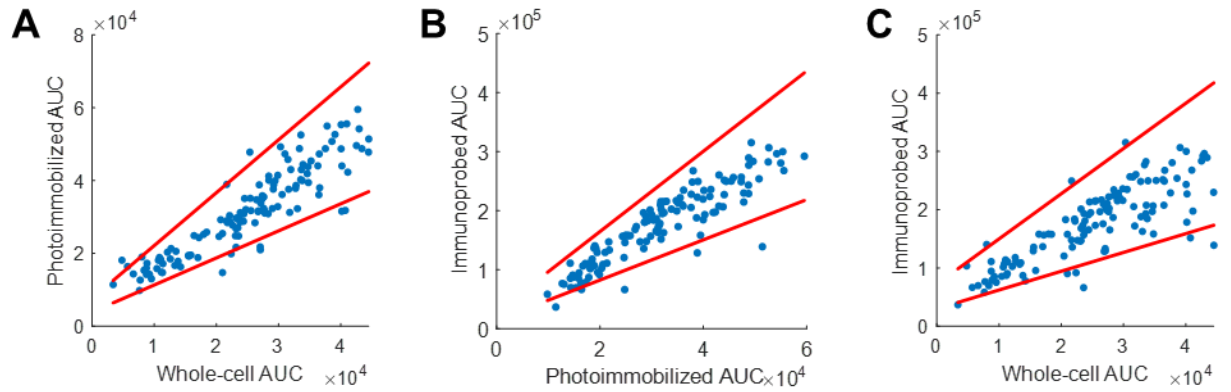

Figure 2.11. Quantifying the degree of agreement between tGFP abundance at different assay stages with Bland-Altman analysis. Scatterplot of tGFP abundance measured at different assay stages for one representative assay (N = 127 cells). Red lines indicate the Bland-Altman limits of agreement between each pair of datasets. (A) Whole-cell vs. photoimmobilized tGFP AUC, indicating the amount of technical variation in protein immobilization. (B) Photoimmobilized vs. immunoprobed tGFP AUC, indicating the amount of technical variation in protein detection (via antibody binding). (C) Whole-cell vs. immunoprobed tGFP AUC, indicating total amount of technical variation in electrophoretic cytometry.

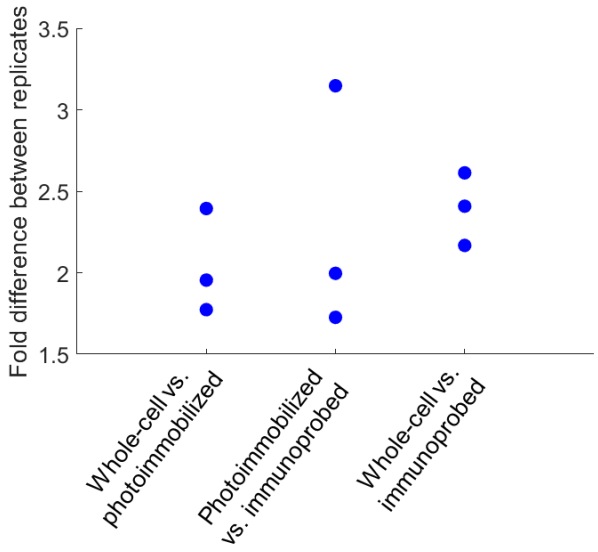

Figure 2.12. Fold difference in downstream tGFP abundance measurements which may arise from two replicate starting tGFP abundance measurements. For each pair of tGFP abundance measurements, fold differences are calculated from Bland-Altman analysis for N = 3 gels (each containing 73 – 127 cells).

2.5 Conclusions

Quantifying technical variation in single-cell destructive assays such as electrophoretic cytometry is challenging due to the lack to true technical replicates. Here, we have developed a workflow to track the abundance of a fluorescent protein throughout the electrophoretic cytometry process, to quantify not only overall intra-assay technical variation, but also the technical variation arising from different stages of the assay. We find similar levels of correlation between whole-cell and photoimmobilized protein abundance, and between photoimmobilized and immunoprobed protein abundance, suggesting that there are similar levels of technical variation in protein capture and detection. However, to avoid nonuniform UV photobleaching of photoimmobilized tGFP, the assay characterized here used a more uniform (collimated) UV source for photoimmobilization;

further studies are needed to investigate whether the uncollimated, higher-irradiance UV source traditionally used for electrophoretic cytometry introduces additional technical variation. While here we used a relatively small cytoplasmic protein (tGFP), future work could use fluorescent fusion proteins of different molecular masses and/or subcellular localizations to understand how the amount of technical variation differs depending on molecular mass, protein structure, or solubilization rate and location within the cell. The fluorescent imaging and analysis frameworks established in this study support robust characterization of fluorescent protein abundance through the electrophoretic cytometry process to facilitate further studies to understand and minimize sources of technical variation in single-cell protein abundance measurements, improving assay precision. The next chapter will build upon these findings to further investigate and minimize technical variation in the immunoprobing stage of the assay.

2.6 References

1. Altschuler, S. J. & Wu, L. F. Cellular heterogeneity: do differences make a difference? *Cell* **141**, 559–563 (2010).
2. Darmanis, S. *et al.* Simultaneous Multiplexed Measurement of RNA and Proteins in Single Cells. *Cell Reports* **14**, 380–389 (2016).
3. Aebersold, R. *et al.* How many human proteoforms are there? *Nature Chemical Biology* **14**, 206–214 (2018).
4. Spitzer, M. H. & Nolan, G. P. Mass Cytometry: Single Cells, Many Features. *Cell* **165**, 780–791 (2016).
5. Shi, Q. *et al.* Single-cell proteomic chip for profiling intracellular signaling pathways in single tumor cells. *PNAS* **109**, 419–424 (2012).
6. Bordeaux, J. *et al.* Antibody validation. *Biotechniques* **48**, 197–209 (2010).
7. Michel, M. C., Wieland, T. & Tsujimoto, G. How reliable are G-protein-coupled receptor antibodies? *Naunyn-Schmied Arch Pharmacol* **379**, 385–388 (2009).
8. Crivat, G. & Taraska, J. W. Imaging proteins inside cells with fluorescent tags. *Trends Biotechnol* **30**, 8–16 (2012).
9. Zhu, Y. *et al.* Proteomic Analysis of Single Mammalian Cells Enabled by Microfluidic Nanodroplet Sample Preparation and Ultrasensitive NanoLC-MS. *Angewandte Chemie* **130**, 12550–12554 (2018).
10. Kang, C.-C. *et al.* Electrophoretic cytopathology resolves ERBB2 forms with single-cell resolution. *NPJ Precis Oncol* **2**, (2018).
11. Sinkala, E. *et al.* Profiling protein expression in circulating tumour cells using microfluidic western blotting. *Nature Communications* **8**, 14622 (2017).
12. Hughes, A. J. *et al.* Single-cell western blotting. *Nat Meth* **11**, 749–755 (2014).
13. Kim, J. J., Chan, P. P. Y., Vlassakis, J., Geldert, A. & Herr, A. E. Microparticle Delivery of Protein Markers for Single-Cell Western Blotting from Microwells. *Small* **14**, 1802865 (2018).
14. Geldert, A., Huang, H. & Herr, A. E. Probe-target hybridization depends on spatial uniformity of initial concentration condition across large-format chips. *Scientific Reports* **10**, 8768 (2020).
15. UCSF Center for Advanced Light Microscopy. How to acquire flat-field correction images. https://calm.ucsf.edu/how-acquire-flat-field-correction-images.
16. Kang, C.-C. *et al.* Single cell–resolution western blotting. *Nature Protocols* **11**, 1508–1530 (2016).
17. Hughes, A. J. *et al.* Single-cell western blotting. *Nature Methods* **11**, 749–755 (2014).

18. Kroll, M. H., Emancipator, K., Floering, D. & Tholen, D. An algorithm for finding the linear region in a nonlinear data set. *Comput. Biol. Med.* **29**, 289–301 (1999).
19. Olson, G. G. Image motion compensation with frame transfer CCDs. in *Machine Vision and Three-Dimensional Imaging Systems for Inspection and Metrology II* vol. 4567 153–160 (International Society for Optics and Photonics, 2002).
20. *Andor iXon3 hardware guide*. https://andor.oxinst.com/downloads/uploads/iXon3_Hardware_Guide.pdf (2011).
21. Waters, J. C. Accuracy and precision in quantitative fluorescence microscopy. *Journal of Cell Biology* **185**, 1135–1148 (2009).
22. Jeeawoody, S. Microscale devices for quantitative characterizations of human biology. (UC Berkeley, 2019).
23. Sinton, D., Erickson, D. & Li, D. Microbubble lensing-induced photobleaching (μ-BLIP) with application to microflow visualization. *Exp Fluids* **35**, 178–187 (2003).
24. Vlassakis, J. & Herr, A. E. Effect of Polymer Hydration State on In-Gel Immunoassays. *Anal. Chem.* **87**, 11030–11038 (2015).
25. Sinkala, E. *et al.* Profiling protein expression in circulating tumour cells using microfluidic western blotting. *Nature Communications* **8**, 14622 (2017).
26. Martin Bland, J. & Altman, DouglasG. Statistical methods for assessing agreement between two methods of clinical measurement. *The Lancet* **327**, 307–310 (1986).

Chapter 3

Probe-target hybridization depends on spatial uniformity of initial concentration condition across large-format chips

Adapted with permission from A. Geldert, H. Huang, & A. E. Herr, "Probe-target hybridization depends on spatial uniformity of initial concentration condition across large-format chips", *Scientific Reports*, 2020.

3.1 Abstract

Diverse assays spanning from immunohistochemistry (IHC), to microarrays (protein, DNA), to high-throughput screens rely on probe-target hybridization to detect analytes. These large-format 'chips' array numerous hybridization sites across centimeter-scale areas. However, the reactions are prone to intra-assay spatial variation in hybridization efficiency. The mechanism of spatial bias in hybridization efficiency is poorly understood, particularly in IHC and in-gel immunoassays, where immobilized targets are heterogeneously distributed throughout a tissue or hydrogel network. In these systems, antibody probe hybridization to a target protein antigen depends on the interplay of dilution, thermodynamic partitioning, diffusion, and reaction. Here, we investigate parameters governing antibody probe transport and reaction (i.e., immunoprobing) in a large-format hydrogel immunoassay. Using transport and bimolecular binding theory, we identify a regime in which immunoprobing efficiency (η) is sensitive to the local concentration of applied antibody probe solution, despite the antibody probe being in excess compared to antigen. Sandwiching antibody probe solution against the hydrogel surface yields spatially-nonuniform dilution. Using photopatterned fluorescent protein targets and a single-cell immunoassay, we identify regimes in which nonuniformly-distributed antibody probe solution causes intra-assay variation in background and η. Understanding the physicochemical factors affecting probe-target hybridization reduces technical variation in large-format chips, improving measurement precision.

3.2 Introduction

Probe-target hybridization over centimeter length scales underpins diverse workhorse assays, including DNA and protein microarrays, immunohistochemistry (IHC), in situ hybridization (ISH), and in-gel immunoassays. In such large-format chips, fluorescently labeled probes or targets bind to species immobilized across an area approximating a microscope slide in size (~25 mm x ~75 mm). Large-format chips facilitate either concurrent measurement of 100s to 1000s of samples arrayed as spots, or study of the tissue microenvironment over centimeter distances. Although the large format increases throughput via concurrent measurements, intra-assay spatial variability is often observed, which increases measurement error.[1–4]

The mechanism of spatial bias in probe-target reactions in large-format chips is platform-dependent. When immobilized probes are incubated with a solution containing limited amounts of targets (e.g., DNA microarrays), spatial variation is attributable to diffusive transport limitations

and target depletion.[1] In contrast, in other assays (e.g., reverse phase protein arrays, IHC, ISH, and single-cell immunoblots) immobilized targets are incubated with a more concentrated probe solution. The mechanism of spatial technical variation in these immobilized-target, probe-in-excess formats is poorly understood. Hypothesized mechanisms of spatial bias in probe-target hybridization include intra-assay variation in substrate density and permeability[3] as well as nonuniform reagent distribution due to warped coverslips or evaporation near the edges of the fluid layer[5]; however, few studies have validated or addressed the mechanism of spatial bias. While strategies to reduce spatial bias using internal standards[6], normalization[3,4], and other post-processing approaches have been developed – particularly for arrayed systems – these approaches can be challenging to integrate in all assay formats. Understanding the mechanism of spatial variation in probe-target hybridization is crucial to eliminate the root cause of intra-assay technical variation in immobilized-target, probe-in-excess assays.

The amount and mechanism of spatial variability in IHC and in-gel immunoassays (e.g., single-cell immunoblotting[7]) is especially unclear, as complex phenomena impact probe-target binding in these assays. In both IHC and in-gel immunoassays, the target antigen is distributed throughout a sample matrix (e.g., tissue slice or hydrogel) with non-negligible thickness (~10s of μm), rather than being printed on a planar substrate as in microarrays. Local antibody probe concentration within the sample matrix may vary both depth-wise and laterally. Thermodynamic partitioning,[8,9] unknown diffusive timescales into tissue[10], and variable tissue permeability[11] reduce probe concentration in the sample matrix and may add variability to Z-directional probe penetration in tissue sections. The fluid layer on a hydrated hydrogel surface or rinsed IHC tissue slice increases variation in the degree of probe dilution.[12] To minimize technical variation due to probe depletion, probe concentrations should be in excess of target[13]; thus, probe concentration must be especially high to overcome thermodynamic partitioning and dilution effects. The necessary high concentration of probe increases the importance of minimizing probe volume to conserve reagents and cost. However, unlike in microarrays, the location of target molecules in tissue sections and single-cell immunoblot chips is unknown; thus, probe must be distributed across the entire surface of the chip and cannot be precision-spotted at defined locations. Additionally, both IHC and single-cell immunoblotting (as well as other immunoassays) rely on antibodies as probes, which exhibit a wide range of binding affinities (probe-to-probe, and lot-to-lot for the same probe).[14–18] Overall, the complex and variable interplay of thermodynamic partitioning effects, nonuniform probe dilution, and concentration-dependent reaction phenomena raise important considerations for making semi-quantitative protein measurements across large-format chips.

Here, we characterize antibody probe uniformity across centimeter distances in an in-gel immunoassay and determine the impact of initially nonuniform probe concentration on immunoprobing efficiency (η). Hydrogels are an excellent model system in which to study spatial variation in immunoprobing because hydrogels can be fabricated with controlled porosities, measurable partition coefficients[9], and specific concentrations of immobilized target. We demonstrate that sandwiching a hydrated gel against a thin layer of probe solution (a commonly-used method of probe introduction[5,19,20]) distributes antibody nonuniformly across the chip. We apply bimolecular binding theory to identify a regime within standard IHC and in-gel immunoassay conditions in which η is highly sensitive to local antibody probe concentration, even when the antibody is in excess compared to the antigen. For experimental validation, we develop a stirring strategy which homogenizes antibody probe concentration across the area of the chip without requiring any increase in antibody concentration or volume. This stirring strategy allows

us to test controlled boundary conditions while maintaining the same assay format, to compare intra-assay spatial variation in η in chips probed with uniform and nonuniform antibody fluid layers. Using polyacrylamide gels with photopatterned protein spots as well as single-cell immunoblots[7], we demonstrate significant intra-assay spatial variation in η and background fluorescence when antibody probe is distributed nonuniformly across the assay, despite the antibody being in excess. We establish for the first time, to our knowledge, that probe is nonuniformly distributed across large-format chips immediately after probe is interfaced with the chip (before any spatial variation in partitioning, depletion, or other factors could have an effect). Using both a bimolecular binding model and a controlled hydrogel system, we identify the regime in which this nonuniformity impacts η.

3.3 Materials & Methods

Chemicals/Reagents. Acrylamide/bis-acrylamide 30% solution (37.5:1, A3699), sodium deoxycholate (D6750), sodium dodecyl sulfate (SDS; L3771), and Triton X-100 (X100) for cell lysis buffer, ammonium persulfate (A3678) and N,N,N′,N′-Tetramethylethylenediamine (T9281) for gel polymerization, dichlorodimethylsilane (440272) and 3-(trimethoxysilyl)propyl methacrylate (440159) for wafer and glass silanization, respectively, and bovine serum albumin (BSA, A7030) were all purchased from Sigma-Aldrich. N-(3-((3-benzoylphenyl)formamido)propyl) methacrylamide (BPMAC) was custom-synthesized by PharmAgra Labs. Gels were cast on wafers (WaferPro C04009) microfabricated with SU-8 3050 photoresist (Kayaku Advanced Materials Y311075), coated with dichlorodimethylsilane and gel slick solution (Lonza 50640). 1.5 M Tris-HCl, pH 8.8 (T1588) was purchased from Teknova, 10× tris-glycine buffer (1610734) was purchased from Biorad, and 10× Tris buffered saline with Tween 20 (TBST, 9997S) was purchased from Cell Signaling Technologies. Purified Turbo GFP (tGFP) protein (FP552) was purchased from Evrogen. Rabbit anti-TurboGFP primary antibody (PA5-22688, lots UC2733591 and UD2749791) and donkey anti-rabbit Alexa Fluor 647 secondary antibody (A31573, lot 1964354) were purchased from ThermoFisher.

Cell culture. U251 glioblastoma cells were lentivirally infected (multiplicity of 10) to express tGFP. These cells were transfected by and generously provided by Dr. Ching-Wei Chang in Prof. S. Kumar's Laboratory at UC Berkeley. U251-tGFP cells were cultured in a humidified 37 ºC incubator kept at 5% CO_2 with DMEM + Glutamax - I medium (ThermoFisher 10566-016) supplemented with 10% fetal bovine serum (Gemini Bio-Products 100-106), 1× non-essential amino acids (ThermoFisher 11140-050), 1 mM sodium pyruvate (ThermoFisher 11360-070), and 100 U/ml penicillin/streptomycin (ThermoFisher 15140-122). Cells were detached with 0.05% Trypsin-EDTA (ThermoFisher 25300-120) and resuspended in 4 °C 1× phosphate-buffered saline to generate cell suspensions used for single-cell immunoblots.

Single-cell immunoblotting. Single-cell immunoblotting was performed as previously described[20], with the following modifications. 8%T polyacrylamide gels were chemically polymerized using APS and TEMED on an SU-8 3050 microfabricated mold with microposts (32 μm diameter, ~40 μm height; 800 μm spacing along electrophoretic separation axis, 600 μm spacing between separation lanes). 300 μL of a U251-tGFP cell suspension was pipetted onto a polyacrylamide gel microwell array cast on half a microscope slide (~25 mm x 37.5 mm) and passively settled into microwells.

After cell settling, excess cells were rinsed off the gel, the device was adhered with Vaseline inside a custom-built electrophoresis chamber, and cell lysis (30 s at 4 ºC), electrophoresis (20 s at 40 V/cm), and photo-immobilization (300 s at ~20 mW/cm^2) were performed.

Lysis/electrophoresis buffer (1× RIPA: 0.5% SDS, 0.25% sodium deoxycholate, 0.1% Triton X-100, 0.5× Tris-glycine, as previously reported[20]) at 4 ºC was used, as this was found to maximize the number of detectable photo-immobilized tGFP bands. We hypothesize that keeping the proteins at 4 ºC (rather than the previously-reported 50 ºC[20]) minimizes tGFP denaturation and diffusive losses. Immediately after electrophoresis, the device was removed from the electrophoresis chamber and placed gel side up in a 4-well dish with 4 ºC 1× TBST and photo-immobilized (OAI Model 30 Collimated Ultraviolet [UV] Light Source). Proteins were photo-immobilized using a collimated UV source to ensure that UV intensity, and thus tGFP photobleaching rate, is spatially-uniform. It is important to wipe Vaseline off the back of the slide prior to photo-immobilization and ensure no bubbles are trapped between the UV source and the gel, as these will make the UV illumination nonuniform by inducing scattering and/or lensing artifacts. After photo-immobilization, the gels were washed for ≥30 min in 1× TBST on a rotator, rinsed with dI water, dried with a nitrogen stream, and imaged with the 488 nm laser channel of a fluorescence microarray scanner (Genepix 4300A, Molecular Devices) to image photo-immobilized tGFP bands.

After collecting images of the photo-immobilized tGFP, gels were rehydrated in 1× TBST and immunoprobed for tGFP. The immunoprobing sequence consisted of primary antibody probe incubation (2 h), wash (2 × 30 min in 1× TBST), secondary antibody probe incubation (1 h), wash (2 × 30 min in 1× TBST). Afterward, gels were rinsed with dI water, dried, and imaged again using the 635 nm laser channel to detect immunoprobed signal.

Antibody probe introduction methods and imaging. A 40 μL droplet of antibody probe solution was pipetted onto a clean glass plate and a half slide gel (hydrated in 1× TBST) was placed gel side down on top of the droplet, spreading the droplet across the area of the gel. In some experiments, the antibody fluid layer was stirred by laterally shifting the gel across the antibody solution a distance of ~3 cm in multiple directions 3-4 times. When immunoprobing with an antibody bath, 5 half slides were placed in a slide mailer (Globe Scientific, 513062) with enough antibody solution to cover the top of the slides (10 mL). 0.05 mg/ml primary and secondary antibody solutions (diluted in 1× TBST with 2% wt/vol BSA) were used in all experiments.

To image antibody probe distribution across a half slide, fluorescently-labeled secondary antibody incubations were set up against a 50 mm x 75 mm glass slide using polyacrylamide gels with the same composition and dimensions as were used for single-cell immunoblotting separations, except without microwells. The polyacrylamide gels did not contain any photo-immobilized protein. Widefield fluorescence (Cy5 filter cube, Chroma 49009) images of the gel were taken with an Olympus 4x/0.13 NA objective on an Olympus IX71 inverted epifluorescence microscope, with a Lumen Dynamics X-cite exacte fluorescence illumination source coupled to a liquid light guide (Lumatec, 805-00038). Images were stitched in ImageJ.

Creating and immunoprobing photopatterned protein spots. 0.005 mg/ml purified tGFP protein was diffused into an 8%T polyacrylamide gel using the same 'sandwich' introduction method as described above for antibodies. After incubating for 1 h, the gel was briefly dipped in dI water to remove excess tGFP pooled on the surface of the gel, and then placed gel side down against a #1.5H glass coverslip (Ibidi 10812). The gel was laterally shifted against the coverslip to remove any bubbles which would scatter or lens UV. The coverslip-gel assembly was placed on top of a mylar mask (coverslip side down) and exposed to collimated UV light for 300 s at ~20 mW/cm^2 (**Figure 3.1a**). tGFP is only photo-immobilized in regions of the gel exposed to UV (i.e., regions of the gel which are over clear parts of the mask)[21] (**Figure 3.1b-e**). Thus, the size, spacing, and number of protein spots is highly tunable, as has been shown with other hydrogel

photopatterning methods.[22,23] After photo-immobilization, gels were washed in 1× TBST for 2 × 30 min to remove non-immobilized protein from the gel.

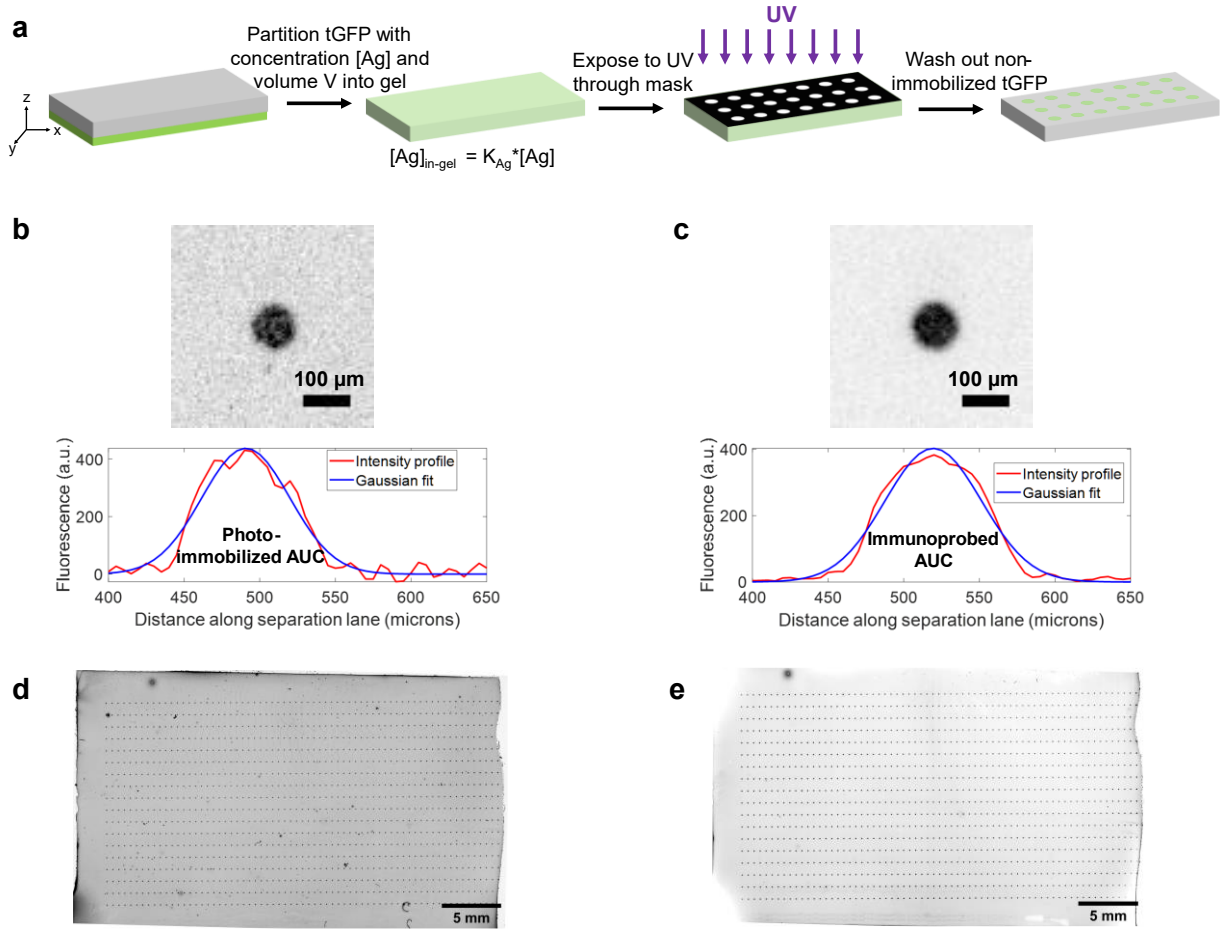

Figure 3.1. Protein photopatterning in polyacrylamide gels. (a) Workflow for generating photopatterned protein spots in a polyacrylamide hydrogel. The number of spots in the schematic is reduced for simplicity. Inverted fluorescence micrographs of a single (b) photo-immobilized Turbo GFP (tGFP) and (c) immunoprobed tGFP spot, with corresponding Gaussian intensity profiles. Inverted fluorescence micrographs demonstrate that ~1100 (d) photo-immobilized and (e) immunoprobed tGFP spots can be patterned and measured on a single array.

Estimation of partition coefficients and antibody/antigen stoichiometry in photopatterned protein system. We can estimate the concentration of target antigen and antibody probe within the gel based on the partition coefficients of antigen and antibody into the gel, as well as the antigen photo-immobilization efficiency. The total number of antigen molecules in the gel can be estimated by **Eq. 3.1**:

$$\text{Antigen molecules in gel} = [Ag]*V*K_{Ag}*A*\gamma \qquad \textbf{Eq. 3.1}$$

where [Ag] and V are the concentration and volume of antigen solution the gel is incubated with, respectively, K_{Ag} is the partition coefficient of the antigen in the gel, A is the fractional open area on the photomask, and γ is the photo-immobilization efficiency. A can be easily tuned via mask design, by altering the spacing and size of the UV-exposed areas.

Similarly, the total number of antibody molecules in the gel can be estimated by **Eq. 3.2**. Because antibodies are distributed across the entire half slide and not photo-immobilized in place, the A and γ terms do not play a role:

$$\text{Antibody molecules in gel} = [Ab]*V*K_{Ab} \quad \textbf{Eq. 3.2}$$

To ensure antibody was in excess of tGFP for immunoprobing experiments, we calculated the necessary concentration of tGFP and antibody with which to incubate the gels to ensure the antibody/tGFP ratio was >>1. In our system, we determine the antibody/tGFP ratio is 23.5:1, based on a photo-immobilized spot diameter of 100 microns and spacing of dx = 500 microns and dy = 1000 microns, as well as the previously-published[7] value of $\gamma_{tGFP\ in\ 8\%T} = 0.275$.

The partition coefficient of tGFP in an 8%T polyacrylamide gel was calculated from Ogston's ideal size-exclusion model[24], which relates the partition coefficient (K) of a solute to its hydrodynamic radius (R_h), as well as to the polymer volume fraction (Φ) and polymer fiber radius (a_f) of the matrix according to **Eq. 3.3:**

$$K = \exp\left[-\Phi\left(1+\frac{R_h}{a_f}\right)^2\right] \quad \textbf{Eq. 3.3}$$

Φ can be calculated from the gel density (%T) according to **Eq. 3.4**[9,25]:

$$\Phi = 0.0093 \times \%T - 0.03151 \quad \textbf{Eq. 3.4}$$

We assume R_h of tGFP is similar to the R_h of enhanced GFP, which was previously reported[26] to be 2.4 nm. K of an Alexa Fluor 647-labeled antibody ($R_h \approx 6.11$ nm) was experimentally measured to be 0.085 in 6%T polyacrylamide gel; using these values and the adjusted Ogston model as previously described[9], we can back-calculate a_f to be 0.647 nm. Thus, we estimate the partition coefficient of tGFP in an 8%T gel to be 0.386.

Because antibodies were diluted in a solution containing 2% wt/vol BSA, the partition coefficient of an unlabeled antibody in an 8%T gel was calculated as 0.0282 using the adjusted Ogston model[27] to account for the interactions between antibody and BSA. Adjusted Ogston model calculations were performed as previously-reported[9], except that in the case of this experiment, Φ was calculated for an 8%T gel and R_h of an unlabeled antibody[28] (5.41 nm) was used.

Impact of higher temperature on antibody probe diffusive timescale. To determine whether increasing the temperature of the antibody fluid layer could increase antibody diffusivity enough to sufficiently reduce the timescale of lateral antibody probe diffusion across the fluid layer, we estimated the diffusive timescale of antibody probe across the fluid layer at 37 °C. The diffusivity of antibody probe at 37 °C was calculated to be 6.02×10^{-11} m^2/s, based on the Stokes-Einstein equation (**Eq. 3.5**) and parameters in **Table 3.1**:

$$D = \frac{k_B T}{6\pi\mu r_H} \quad \textbf{Eq. 3.5}$$

Table 3.1. Parameters used to estimate antibody probe diffusivity

Symbol	Name	Value
k_B	Boltzmann constant	1.38×10^{-23} J/K
T	Temperature	310 K
μ	Dynamic viscosity of water at given temperature[29]	6.97×10^{-4} Pa s
r_H	Hydrodynamic radius of antibody probe[28]	5.41 nm

Using the estimated antibody probe diffusivity at 37 °C and the relationship between antibody diffusivity in free solution (D_{soln}) and the lateral length scale of the fluid layer (L)

according to **Eq. 3.6**, we estimate that the timescale of antibody probe diffusion across a 45 mm distance in free solution is 98 days.

$$\tau_{\text{across fluid layer}} = \frac{L^2}{4D_{soln}} \qquad \textbf{Eq. 3.6}$$

Thus, increased temperature will not sufficiently enhance antibody diffusion to achieve uniform antibody probe distribution across the sample-fluid layer interface. Raising the temperature may also alter antibody-antigen binding affinity[30], increase the rate of sample drying, and (at higher temperatures) induce protein denaturation.

Estimation of cost of immunoprobing with concentrated probe. We estimate the amount and cost of antibody required to ensure the local antibody concentration in the sample ($[Ab]_{sample}$) > antibody dissociation constant (K_D) (so that η does not substantially depend on intra-assay variation in antibody probe concentration). Because K_D of commercial antibodies is rarely reported but can be as high as μM, we assume that $[Ab]_{sample}$ must be 10 μM to ensure $[Ab]_{sample} > K_D$. In the case of single-cell immunoblotting, where target antigens are immobilized within an ~8%T polyacrylamide sieving gel, thermodynamic partitioning limits in-gel antibody concentration. We estimate $\frac{[Ab]_{sample}}{[Ab]_{solution}} = 0.0282$, and thus the gel must be incubated with an even higher concentration of antibody probe (354 μM). Each single-cell immunoblot is incubated with 40 μL of probe solution. 40 uL of 354 μM antibody equates to 2.13 mg antibody. Assuming primary antibody costs $4/μg (the approximate cost of primary antibodies used in this study), 2.13 mg primary antibody would cost $8520. Secondary antibodies are generally cheaper (~$0.24/μg for the secondary antibodies used in this study), but would cost an additional $509). Thus, the total cost to probe a single immunoblot with concentrated antibody probe to ensure $[Ab]_{sample} > K_D$ would be >$9,000.

Image and statistical analysis. Fiji (ImageJ version 1.52p, https://imagej.net/Fiji)[31,32] was used to generate all fluorescence micrographs (i.e., separation lanes and photopatterned protein images); the Grid/Collection stitching plugin[33] in Fiji was also used to stitch widefield fluorescence microscopy images. All other image analysis and plot generation were performed with MATLAB R2018b (https://www.mathworks.com/products/matlab.html). Area under the curve (AUC) fluorescence of photo-immobilized tGFP bands and immunoprobed protein bands was calculated using custom MATLAB scripts, as previously described.[20] Briefly, regions of interest were defined around each protein band, and a Gaussian function was fit to the background-subtracted intensity profile of each region of interest. AUC values were calculated by summing the intensity profile values within the peak center ± 2 standard deviations. As quality control, AUCs of intensity profiles with a signal-to-noise ratio <3 or a Gaussian fit r^2 <0.7 were disregarded. Only separation lanes with AUC values which passed quality control standards for both measurements (photo-immobilized AUC and immunoprobed AUC) were considered for calculation of η and Bland-Altman analysis. Heatmaps were generated using the *imagesc* function in MATLAB, and beeswarm plots were generated using the *plotspread* function[34].

Statistical analysis was performed using the nonparametric test functions *kruskalwallis* (Kruskal-Wallis test), *multcompare* (post-hoc Tukey test), and *ranksum* (2-tailed Mann-Whitney U test) in MATLAB R2018b. Nonparametric tests were chosen because the sample sizes of data being compared were too small to make distribution assumptions. All error values reported following a ± sign are standard deviations (not standard errors of the mean). Results were determined to be statistically significant if the statistical test yielded a p-value of less than 0.05.

Microsoft Powerpoint version 16.0 (https://products.office.com/en-us/powerpoint) was used to generate all schematics and compile figures.

3.4 Results & Discussion

η depends on local antibody probe concentration and affinity. We sought to apply bimolecular binding theory to understand the sensitivity of η to two key immunoprobing parameters: antibody probe concentration and affinity. We consider an example system in which a chip with ~cm lateral dimensions and ~μm thickness is sandwiched against a thin layer of antibody solution (**Figure 3.2a-b**). These lateral and/or axial dimensions are characteristic of DNA microarrays[1], reverse-phase protein microarrays[3,35], single-cell immunoblots[7], IHC/ISH/imaging mass cytometry staining[36], and other high-throughput assays[37]. We focus our study on IHC, in-gel immunoassays, and other large-format chips in which antibody probes (in excess concentration) bind to targets (in limited concentration) immobilized within a hydrogel, tissue slice, or other 3D matrix which we call the 'sample'. In these systems, three primary phenomena influence antibody probe binding: dilution, partitioning, and reaction. First of all, samples are typically incubated with a small (10s of μL) volume of antibody to conserve reagents; as a result, however, the fluid layer on the hydrated samples may non-negligibly dilute the antibody (**Figure 3.2b**).[12] The concentration of antibody reaching targets within the sample is further limited by partitioning, the phenomenon in which solute concentration in a material may be lower than in free solution due to size-exclusion from pores or other factors (**Figure 3.2c**).[38] Ultimately, η depends on antibody-antigen reaction (**Figure 3.2d**). To study the interplay of these factors, we chose hydrogels as a model system because we can precisely pattern target antigen within the gel, as well as control hydrogel density, which governs antibody probe partitioning into the gel. Hydrogels are also a valuable biosensing platform, as hydrogels offer unique advantages as compared to planar substrates, such as minimal fouling, facile functionalization, and higher-capacity molecular capture within a 3D volume.[39–42]

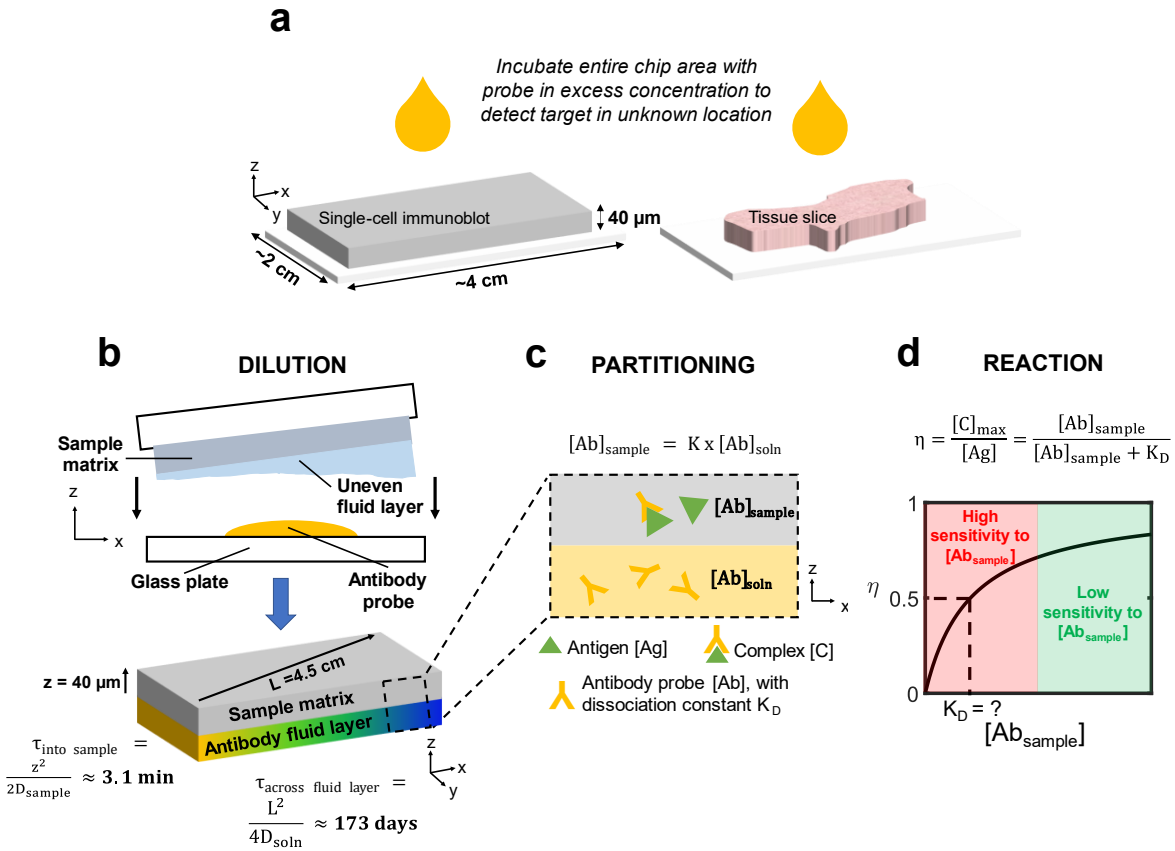

Figure 3.2. Critical parameters influencing and affected by local antibody probe concentration in large-format chips. (a) Two examples of large-format chips: single-cell immunoblot and immunohistochemistry. In both systems, target molecules are immobilized in unknown locations withing a sample matrix (10s of µm thick, centimeters long) and must be incubated with concentrated probe solution for detection. (b-d) Physicochemical phenomena which influence immunoprobing efficiency in these assays. (b) Method of distributing a thin antibody fluid layer across a hydrated sample surface may nonuniformly dilute the antibody. Lateral spatial variation in antibody concentration will not equilibrate over assay immunoprobing timescales because the diffusive timescale of antibody across the lateral length scale (L) of the assay ($\tau_{across\ fluid\ layer}$) is much greater than the diffusive timescale of antibody into the sample matrix ($\tau_{into\ sample}$). Here, $\tau_{into\ sample}$ is calculated using the diffusivity of antibody in an 8%T polyacrylamide gel. (c) Equilibrium antibody concentration in a porous sample ($[Ab]_{sample}$) is governed by the partition coefficient (K) of antibody into the sample and the antibody concentration at the free solution-sample boundary ($[Ab]_{soln}$). (d) η is strongly dependent on the concentration of antibody in the sample when the concentration is near the antibody dissociation constant (K_D), even when antibody is in excess compared to antigen.

Immunoprobing time is governed by the sum of the characteristic timescales of antibody transport into the sample ($\tau_{into\ sample}$) and antibody binding (τ_{rxn}). Antibody transport into the sample is dependent on the thickness of the sample (z) and diffusivity of the antibody in the sample (D_{sample}), according to **Eq. 3.7:**

$$\tau_{into\ sample} = \frac{z^2}{2D_{sample}} \qquad \textbf{Eq. 3.7}$$

In the case of a model 40 µm thick, 8%T polyacrylamide gel with D_{gel} of 4.3×10^{-12} $m^2\ s^{-1}$ as previously reported[7], $\tau_{into\ gel} \approx 3.1$ min. Antibody reaction time is dependent on the kinetics of the antibody (k_{on} and k_{off} rates) as well as the local antibody concentration in the sample, according to **Eq. 3.8:**

$$\tau_{rxn} = \frac{1}{k_{on}[Ab]_{sample} + k_{off}} \quad \textbf{Eq. 3.8}$$

For an intermediate-affinity antibody ($k_{on} = 10^5$ $M^{-1}s^{-1}$, $k_{off} = 10^{-4}$ s^{-1}) and $[Ab]_{gel}$ of 10 nM, $\tau_{rxn} \approx$ 15 min. Thus, taking into consideration both antibody transport and reaction times (4 τ each), immunoprobing protein captured in a gel tens of μm thick takes ~1.2 h.

To understand whether antibodies in the fluid layer would equilibrate laterally over standard immunoprobing timescales, we also estimated the timescale of antibody transport across the fluid layer. This timescale is dependent on the diffusivity of the antibody in free solution (D_{soln}) and the lateral length scale of the fluid layer (L), according to **Eq. 3.6**. For L = 45 mm and D_{soln} of 3.4×10^{-11} m^2 s^{-1} as previously reported[43], $\tau_{across\ fluid\ layer}$ = 173 days, suggesting that the lateral concentration profile of antibody in the fluid layer (and thus, in the gel) will not reach equilibrium during immunoprobing. Increasing the temperature of the fluid layer to increase antibody diffusivity does not sufficiently reduce the diffusive timescale; for example, at 37 ºC, $\tau_{across\ fluid\ layer}$ is still 98 days. Thus, any initial lateral spatial variation in antibody concentration across large-format chips such as IHC and single-cell immunoblots will not equilibrate, introducing spatial variation in η in certain regimes of antibody affinity and concentration. η depends on $[Ab]_{sample}$ and the antibody dissociation constant (K_D) according to **Eq. 3.9**[16]**:**

$$\eta = \frac{[C]_{max}}{[Ag]} = \frac{[Ab]_{sample}}{[Ab]_{sample} + K_D} \quad \textbf{Eq. 3.9}$$

where $[C]_{max}$ is the maximum concentration of immunocomplex formed and [Ag] is the antigen concentration in the sample. From this relationship, it is evident that η is highly sensitive to variation in $[Ab]_{sample}$ when $K_D \approx [Ab]_{sample}$, even when the antibody is in excess compared to antigen (**Figure 3.2d**).

$[Ab]_{sample}$ in IHC and in-gel immunoassays falls within the same range as reported antibody K_D values, making it likely that assays operate in the regime where η is highly sensitive to variation in $[Ab]_{sample.}$ In IHC, tissue slices are typically incubated with antibody probe concentrations of ~10s of nM.[44,45] In single-cell immunoblotting, hydrogels are incubated with ~67-333 nM antibody probe[20], but in-gel antibody concentrations are much lower (~10 nM) due to thermodynamic partitioning[9]. K_D of commercial antibodies span many orders of magnitude, from fM to μM[14,15,18], thus encompassing typical $[Ab]_{sample}$ levels. However, it is typically impossible to determine whether an assay is operating in the $K_D \approx [Ab]_{sample}$ regime without substantial additional characterization. K_D of commercial antibodies is not typically reported and can vary from lot to lot.[17,46] While K_D can be measured using techniques such as surface plasmon resonance, enzyme linked immunosorbent assay, and kinetic polyacrylamide gel electrophoresis[47], K_D values measured by these techniques can vary by orders of magnitude due to run-to-run variability and differences in measurement conditions which may not match the system of interest (e.g., binding in solution vs. on a surface).[47,48] $[Ab]_{sample}$ may also be unknown, as antibody penetration into tissue sections for IHC has been found to be nonuniform and variable.[10] Increasing probe concentration to try to avoid the $K_D \approx [Ab]_{sample}$ regime is often cost-prohibitive, as thermodynamic partitioning limits the proportion of antibody which will diffuse into nanoporous samples such as hydrogels. For example, to ensure $[Ab]_{sample} > K_D$ (and thus, η is relatively insensitive $[Ab]_{sample}$) in the case where K_D = 1 μM, we estimate that one single-cell immunoblot would need to be incubated with >2 mg each of primary and secondary antibody (>US$9,000 total, based on prices in 2020). Thus, because it is challenging to avoid a regime in which η is sensitive to spatial variation in $[Ab]_{sample}$, we instead sought to investigate strategies to minimize spatial variation in $[Ab]_{sample}$.

Characterizing and controlling antibody probe distribution at the sample-fluid layer interface. We hypothesize that spatial variation in local antibody probe concentration can arise when sandwiching a hydrated large-format chip with a droplet of antibody solution, via nonuniform local dilution of antibody due to an uneven fluid layer on the hydrated gel, tissue slice, or other sample containing immobilized target (**Figure 3.3a**). Because these samples are only ~10s of μm thick and are often incubated with small volumes (~10s of μL) of probe solution[5,12,20], any fluid layer on the sample can substantially impact local antibody probe concentration. For example, excess buffer remaining on an IHC sample prior to primary antibody incubation has been observed to add variation to antibody dilution, although the effect on lateral uniformity was not characterized.[12] Nonuniform local antibody dilution would lead to differences in antibody concentration boundary conditions (at the sample-fluid layer boundary) in different regions of the immunoassay, which can result in intra-assay technical variation in η.

To determine whether local antibody concentration varies across a large-format chip, we characterized intra-assay variation in antibody concentration in a model system in which a hydrated ~22 x 35 mm polyacrylamide gel was sandwiched against a 40 μL droplet of fluorescently-labeled antibody solution (i.e., 'stationary' configuration). To do so, we used widefield fluorescence microscopy to image the antibody fluid layer sandwiched against the gel. Median fluorescence intensity varied by 60% ± 24% along the x axis and 77% ± 13% along the y axis (n = 3 gels). To estimate the degree to which antibody concentration would differ between individual target spots on a large-format chip, we also divided the antibody fluorescence micrograph into 500 μm x 1000 μm 'analysis regions'. In the stationary configuration, mean fluorescence of individual analysis regions within a single chip differed by up to 2.88-fold (± 0.13-fold). Thus, we observed substantial variation in antibody fluorescence (a proxy for antibody concentration) across the gel (**Figure 3.3b**).

To determine the impact of the observed nonuniform antibody probe distribution, we sought to develop a method to control the boundary condition at the gel-antibody solution interface. By controlling the boundary condition, we could compare intra-assay variation in η in configurations where antibody was either uniformly or nonuniformly distributed. Numerous microscale fluid mixers based on heating[49], oscillation[50], pneumatics[5] and electrokinetics[51] have been developed and applied to probe solutions in microarray[5], immunoassay[51], and automated immunohistochemistry platforms[52] to speed up reactions and increase staining uniformity. However, the improvement in uniformity has not been substantially characterized. Additionally, we sought a method to control the initial boundary condition that minimally altered assay format, to facilitate comparison of nonuniform and uniform antibody concentration boundary conditions. With these considerations in mind, we hypothesize that stirring the antibody fluid layer by laterally shifting the gel over the antibody fluid layer will homogenize the concentration of the antibody fluid layer (i.e., 'stirred' configuration). By imaging the antibody fluid layer after each successive stirring movement, we find that the antibody fluid layer becomes well-mixed after moving the gel ~2-3 cm once in each of 4 different directions (**Figure 3.4**). Indeed, in the stirred configuration, intra-assay fluorescence varied by 35% ± 10% in the x axis and 15 ± 4.1% in the y axis (n = 3 gels), which is substantially lower variation than in the stationary configuration (**Figure 3.3b**). Likewise, mean fluorescence (i.e., antibody concentration) of analysis regions within a stirred gel exhibited smaller region-to-region fold-change differences of up to 1.50 ± 0.19 for the stirred configuration as compared to almost 3-fold in the stationary configuration.

As a positive control for a homogeneous boundary condition, we also characterized antibody distribution across a gel immersed in an antibody bath. We expect that bath immersion

will yield a uniform antibody concentration boundary condition, as any fluid layer (volume of μLs) on the sample is now negligible as compared to the antibody bath solution (volume of mL) and will not induce substantial antibody dilution. Additionally, the thickness of the antibody fluid layer bordering the gel is on the order of mm in the bath, rather than on the order of μm in the stationary or stirred configurations, which facilitates concentration equilibration. In an antibody bath, lateral variation in antibody concentration at the gel boundary is quickly homogenized by diffusion of antibodies from the thicker antibody fluid layer (length scale ~ μm, diffusive τ ~ min) to the gel boundary, rather than by lateral diffusion of antibodies across the fluid layer (length scale ~ mm, diffusive τ ~ days). As expected, we found that antibody concentration variation across the hydrogel was low in the bath configuration (**Figure 3.3b**); median fluorescence varied by 13% ± 2.0% in the x axis, 8.8% ± 1.5% in the y axis (n = 3 gels). Mean fluorescence of analysis regions within the bath configuration differed by up to 1.20-fold (± 0.04-fold), the smallest difference among the three immunoprobing configurations characterized. However, the bath configuration requires a ~50× larger volume of antibody probe solution than the stationary and stirred configurations. Due to the high antibody concentrations typically required due to thermodynamic partitioning of antibody into nanoporous hydrogels, routine bath immunoprobing would be extremely costly. For example, in the model system described here, the stationary or stirred configurations require ~ $8 of primary anti-tGFP antibody per gel while the bath configuration requires ~$400 of the same antibody. Overall, we have observed substantial spatial variation in antibody probe concentration when a large-format hydrogel is sandwiched against antibody solution, a phenomenon we hypothesize is due to uneven antibody dilution by a nonuniform fluid layer on the hydrogel. We have also demonstrated methods to control the concentration boundary condition to investigate the relationship between intra-assay variation in antibody concentration and η in a precise manner.

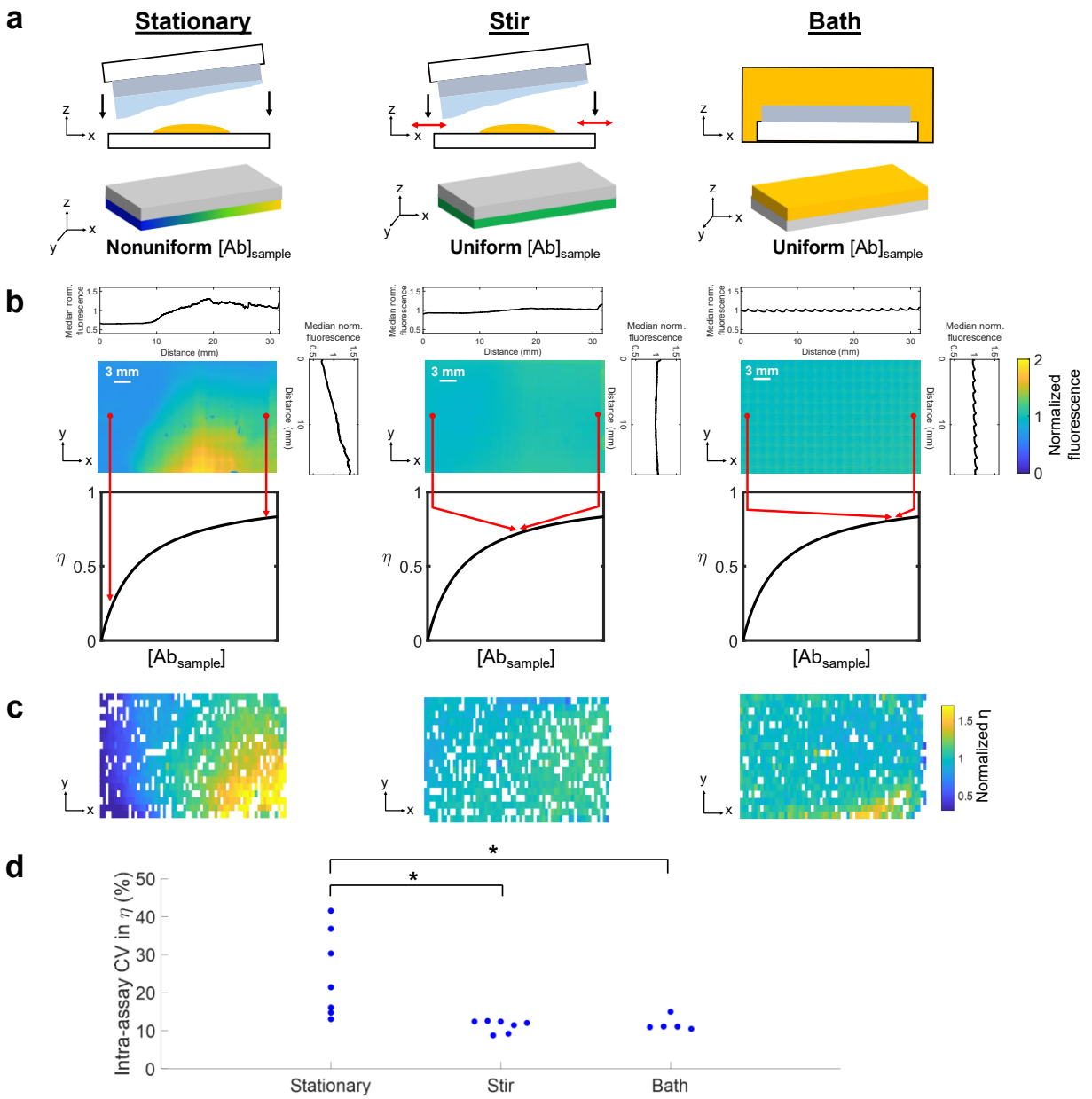

Figure 3.3. Intra-assay spatial variation in antibody probe distribution and η in three immunoprobing configurations yielding different concentration boundary conditions: a stationary antibody fluid layer, a stirred antibody fluid layer, or an antibody bath. (a) We hypothesize that a stationary antibody fluid layer will have lateral spatial variation in antibody concentration due to nonuniform dilution by an uneven fluid layer on the gel. We also hypothesize that stirring the antibody fluid layer by shifting the gel laterally will homogenize the fluid layer to a similar extent as an antibody bath (positive control). (b) Representative heatmaps of antibody fluorescence across the fluid layer, normalized to the mean fluorescence intensity within each image. Median intensity profiles in the x- and y- directions demonstrate that spatial nonuniformity in antibody concentration is greatest in the stationary antibody fluid layer. Bimolecular binding modeling shows that if $K_D \approx [Ab_{sample}]$, spatial variation in antibody distribution yields variation in η. (c) Representative heatmaps of η of photopatterned tGFP spots immunoprobed with a stationary antibody fluid layer, stirred antibody fluid layer, or antibody bath (chips in Fig. 2c were *not* probed with the antibody fluid layers shown in Fig. 2b; the spatial patterns are not directly comparable). Each rectangle in the heatmap represents one tGFP spot; white rectangles are spots which did not pass quality control standards and thus do not have quantifiable η. (d) Beeswarm plot of intra-assay CV in η (Kruskal-Wallis test, $p = 0.0033$; post-hoc Tukey test, $p_{\text{stationary vs. stir}} = 0.0091$, $p_{\text{stationary vs. bath}} = 0.0131$).

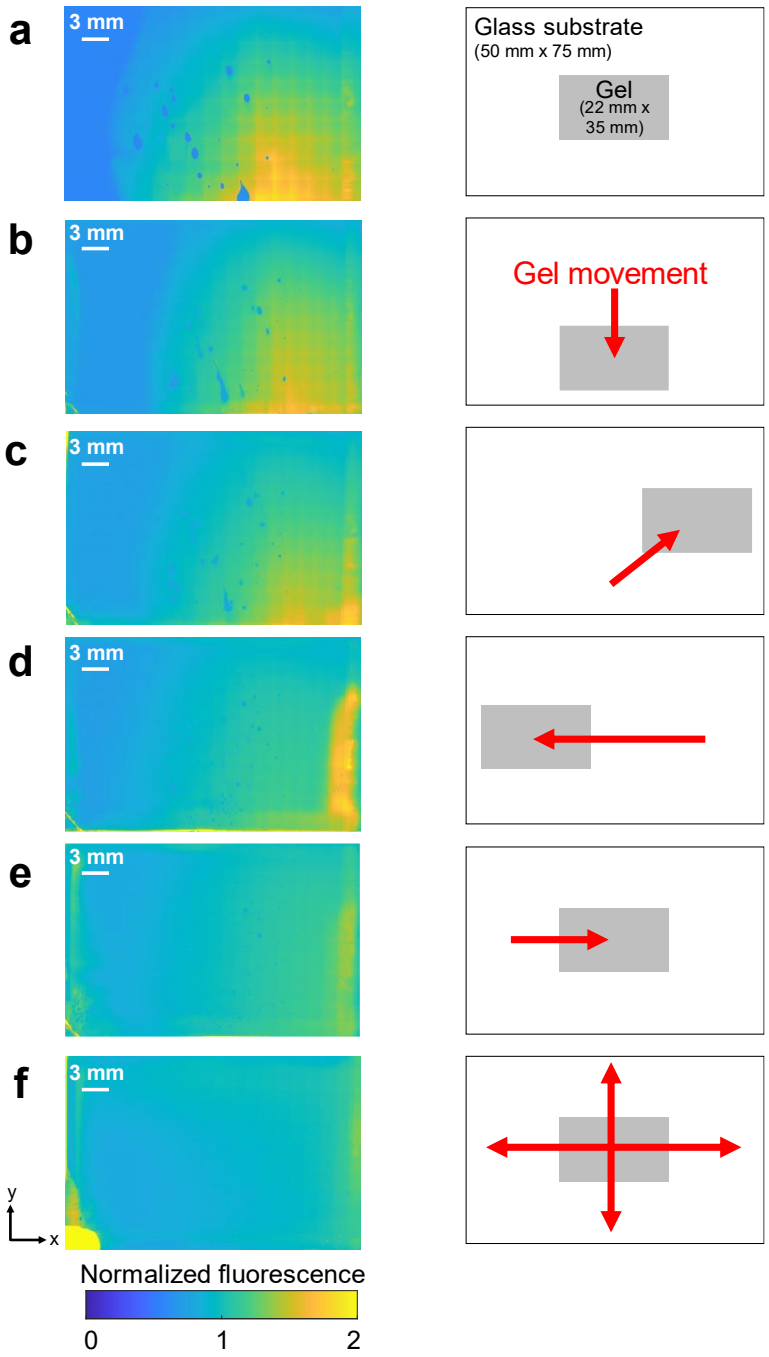

Figure 3.4. Stirring homogenizes antibody probe concentration across centimeter length scales. Widefield fluorescence microscopy images of a fluorescently-labeled secondary antibody fluid layer between a polyacrylamide gel (~22 mm x 35 mm) and glass substrate (50 mm x 75 mm) are displayed as heatmaps of fluorescence intensity (normalized by the mean fluorescence within each image). (a) Intra-assay CV in antibody fluorescence (a proxy for concentration) is 32.8% in the stationary antibody fluid layer (immediately after sandwiching the gel with the antibody). (b-e) Spatial variation in the antibody fluid layer is reduced by stirring the fluid layer by sliding the gel ~2-3 cm laterally across the glass substrate. Heatmaps show antibody distribution after each successive movement. After 4 movements (e), intra-assay CV in antibody fluorescence has dropped to 14.0% and antibody is homogenized to a similar degree as a gel which has been thoroughly stirred (with ~20 movements) (f). Stirring the fluid layer does increase the risk of gel tearing off the glass slide, as is seen in the bottom left corner of (f).

Spatial variation in antibody probe concentration yields variation in η even when antibody is in excess. After observing intra-assay variation in antibody concentration across a stationary antibody fluid layer, we next sought to test our hypothesis that intra-assay variation in η is greater in the stationary configuration (with nonuniform boundary condition) than in the stirred configuration (with a more uniform boundary condition). Variable antibody concentration at the boundary will cause intra-assay variation in η if $K_D \approx [Ab_{sample}]$, yielding intra-assay technical variation in protein abundance measurements. To investigate whether intra-assay variation in η is higher in the stationary configuration, we photopatterned ~1100 tGFP spots on a ~22 mm x 35 mm gel and immunoprobed using an excess of antibody probe and measured η based on the ratio of the AUCs of immunoprobed and photo-immobilized spots (**Figure 3.1**). Because tGFP is fluorescent, photo-immobilized tGFP spots (prior to immunoprobing) can be detected via fluorescence imaging. The relative photo-immobilized and immunoprobed tGFP signal is quantified as the AUC of the fluorescence intensity profile. Experimentally, η is defined as **Eq. 3.10**:

$$\eta = \frac{\text{Immunoprobed AUC}}{\text{Photo-immobilized AUC}} \qquad \textbf{Eq. 3.10}$$

We observed the largest intra-assay spatial variation in η in the gels immunoprobed with a stationary antibody fluid layer (**Figure 3.3c**). To quantify the level of intra-assay variation, we calculated the coefficient of variation (CV) in η within each gel and found that the CV was significantly higher in the stationary immunoprobing configuration (n = 7 gels) as compared to the stirred (n = 7 gels) and bath (n = 5 gels) immunoprobing configurations (Kruskal-Wallis test, p = 0.0033; post-hoc Tukey test, $p_{\text{stationary vs. stir}} = 0.0091$, $p_{\text{stationary vs. bath}} = 0.0131$), supporting our hypothesis (**Figure 3.3d**).

Bland-Altman analysis quantifies degree of agreement between replicates. We sought to quantify intra-assay technical variation in terms of the expected measurement error of immunoprobed AUC. While CV of η provides a measure of overall intra-assay variation, it does not quantify the expected measurement error of any individual spot. We apply Bland-Altman analysis to quantify the degree of agreement between photo-immobilized and immunoprobed measurements. Bland-Altman analysis defines limits of agreement between two paired datasets based on the distribution of differences in the datasets.[53] Photo-immobilized AUC is a measure of the true amount of protein in the gel, while the immunoprobed AUC is convolved with technical variation in η. Because photo-immobilized and immunoprobed AUCs were measured in different fluorescence channels and thus have different scales, we used a linear fit between photo-immobilized and immunoprobed data to map each photo-immobilized AUC to the immunoprobed AUC scale. We consider the immunoprobed AUC predicted by the linear fit from each photo-immobilized data point as the *true* immunoprobed AUC; we consider the AUC measured from immunoprobed signal intensity as the *measured* immunoprobed AUC (**Figure 3.5a**). True and measured immunoprobed AUCs were then log transformed (**Figure 3.5b**) and limits of agreement were calculated as described previously (**Figure 3.5c**).[53] Due to the logarithm quotient rule, the difference in logarithms (i.e., limits of agreement of log-transformed data) equals the logarithm of a quotient (i.e., the ratio between measured and true immunoprobed AUC). Thus, we can back-transform the limits of agreement to determine the minimum and maximum percentage difference between true and measured immunoprobed AUC (**Figure 3.5d**). The ratio of the maximum and minimum percentage difference yields the possible measured fold difference between replicates. For example, a fold difference of 3 means that the immunoprobed AUC of two replicate protein spots with identical photo-immobilized AUC would differ by up to 3-fold.

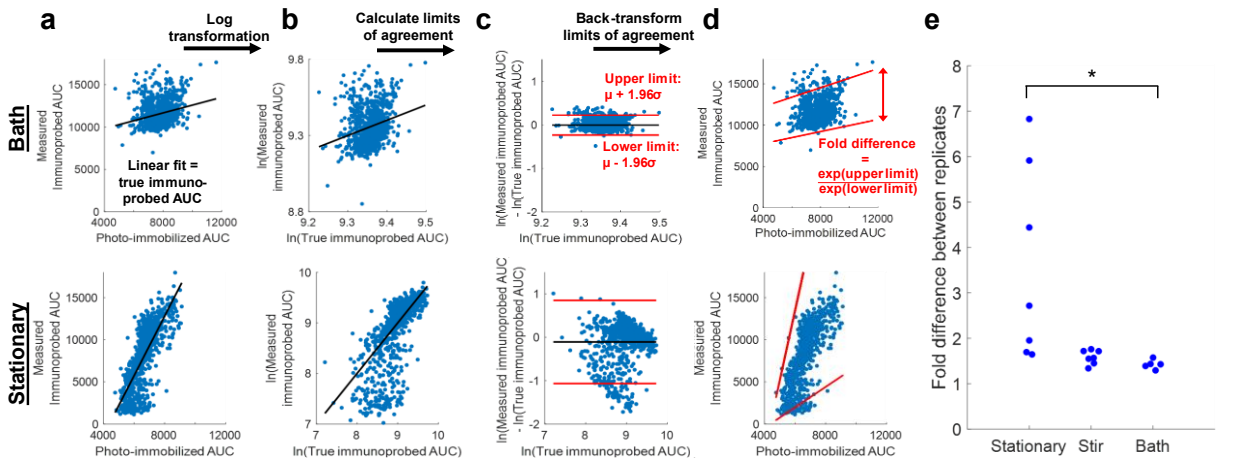

Figure 3.5. Quantifying the degree of agreement between photo-immobilized and immunoprobed AUC of photopatterned tGFP spots as a measure of intra-assay technical variation. Bland-Altman analysis is used to obtain a measure of technical variation in the stationary, stirred, and bath immunoprobing conditions. (a) Photo-immobilized AUC values are mapped to the immunoprobed AUC scale using the linear fit of photo-immobilized and immunoprobed data. (b) True immunoprobed AUCs (based on the linear fit mapping of photo-immobilized AUC) and measured immunoprobed AUCs are log-transformed to facilitate subsequent data analysis and interpretation. The line of equality (y = x) is also shown to indicate what the data would look like in the absence of technical variation. (c) The differences between the log-transformed measured and true immunoprobed AUCs are plotted against protein abundance. The limits of agreement are calculated based on the mean (μ) and standard deviation (σ) of these differences. (d) Data and limits of agreement are back-transformed by taking the anti-log of each value. (e) Fold difference in measured immunoprobed signal which arises from two replicate photo-immobilized protein spots, based on Bland-Altman analysis. Each point on the beeswarm plot is a replicate assay; each assay contains ~1100 photopatterned tGFP bands. Gels immunoprobed with a stationary antibody fluid layer have significantly greater technical variation as compared to the bath immunoprobing configurations (Kruskal-Wallis test, $p = 0.0039$; post-hoc Tukey test, $p_{\text{stationary vs. bath}} = 0.0032$).

Here, we do not aim to evaluate whether true and measured immunoprobed AUCs are equivalent (as Bland-Altman analysis has traditionally been used for). Instead, we use Bland-Altman analysis to quantify the intra-assay technical variation, in order to compare amount of error introduced with stationary, stir, and bath immunoprobing. Applying Bland-Altman analysis to the photopatterned immunoprobing data in **Figure 3.3**, we find that the measured fold difference between replicates is significantly higher when photopatterned tGFP spots are immunoprobed with a stationary antibody fluid layer (fold difference = 3.60 ± 2.14, n = 7 gels) as compared to an antibody bath (fold difference = 1.42 ± 0.10, n = 5 gels) (Kruskal-Wallis test, $p = 0.0039$; post-hoc Tukey test, $p_{\text{stationary vs. bath}} = 0.0032$) (**Figure 3.5e**). This result supports our hypothesis that immunoprobing with a stationary antibody fluid layer increases technical variation in immunoprobing measurements due to greater intra-assay variation in antibody concentration. While the stirred configuration (fold difference = 1.59 ± 0.16, n = 7 gels) did not have significantly lower fold differences than the stationary configuration, stirring lowers and narrows the range of fold differences as compared to the stationary immunoprobing configuration. Given that protein fold changes of ≤ 3 have been implicated in differential chemotherapeutic response[54,55], reducing the measured fold difference between technical replicates is key to studying important biological variation[56].

Application to single-cell immunoblotting. We sought to confirm that the dependence of η on local antibody probe concentration observed when immunoprobing photopatterned protein spots also held true in the single-cell immunoblot, an array of in-gel immunoassays across a large-format

chip. This large-format chip is designed to measure single-cell protein abundance (**Figure 3.6a**). Individual U251-tGFP cells were settled into microwells and lysed, and proteins were electrophoresed through the gel and photo-immobilized as previously-reported.[20] Lysis and electrophoresis temperature were tuned to reduce diffusive losses and tGFP denaturation to maximize photo-immobilized tGFP intensity. Gels were subsequently immunoprobed and η was measured for each separation lane containing a cell.

We first investigated whether background intensity of immunoprobed separation lanes was spatially dependent in the different immunoprobing configurations. We hypothesized that the amount of antibody probe retained in the gel after the wash step (due to chemical interactions with hydrogel components[9] or entropic trapping[57]) would be proportional to the local in-gel antibody concentration, and thus background intensity could provide insight on the antibody concentration distribution across the assay during immunoprobing. Indeed, we observed that background intensity of the immunoprobed separation lanes had a similar spatial pattern as η (**Figure 3.6b-c**), suggesting that background intensity after probe washout is proportional to local antibody concentration at the gel-fluid boundary during probe incubation (i.e., antibody is proportionally partitioning into the gel and not fully washing out). Intra-assay variation in background intensity is significantly greater in gels probed with a stationary antibody fluid layer (n = 5 gels), as compared to a stirred fluid layer (n = 4 gels) (Mann-Whitney U test, p = 0.0159) (**Figure 3.6d**). Thus, immunoprobing with a stationary antibody fluid layer yields larger intra-assay variation in antibody concentration both in the fluid layer and in the gel after washout.

The implications of the finding that background intensity is proportional to local antibody concentration differ depending on the immunoprobing regime in which the assay is operating. If $K_D \approx [Ab]_{sample}$, areas with higher local antibody probe concentration will have higher η, but our results suggest these areas will also have higher background after probe washout, creating two opposing effects on the limit of detection. In contrast, if $[Ab]_{sample} >> K_D$, areas of the sample incubated with higher antibody probe concentration will not have substantially higher η (as in this regime, η is insensitive to $[Ab]_{sample}$). However, areas incubated with higher probe concentrations will retain more antibody after washout, leading to higher background and thus a higher limit of detection. It is important to minimize intra-assay variation in limit of detection so that expression of low-abundance proteins in single cells can be accurately compared. Thus, nonuniform antibody distribution can have multiple detrimental effects on assay performance, by increasing intra-assay technical variation in η and/or increasing the limit of detection, depending on the K_D and $[Ab]_{sample}$ regime.

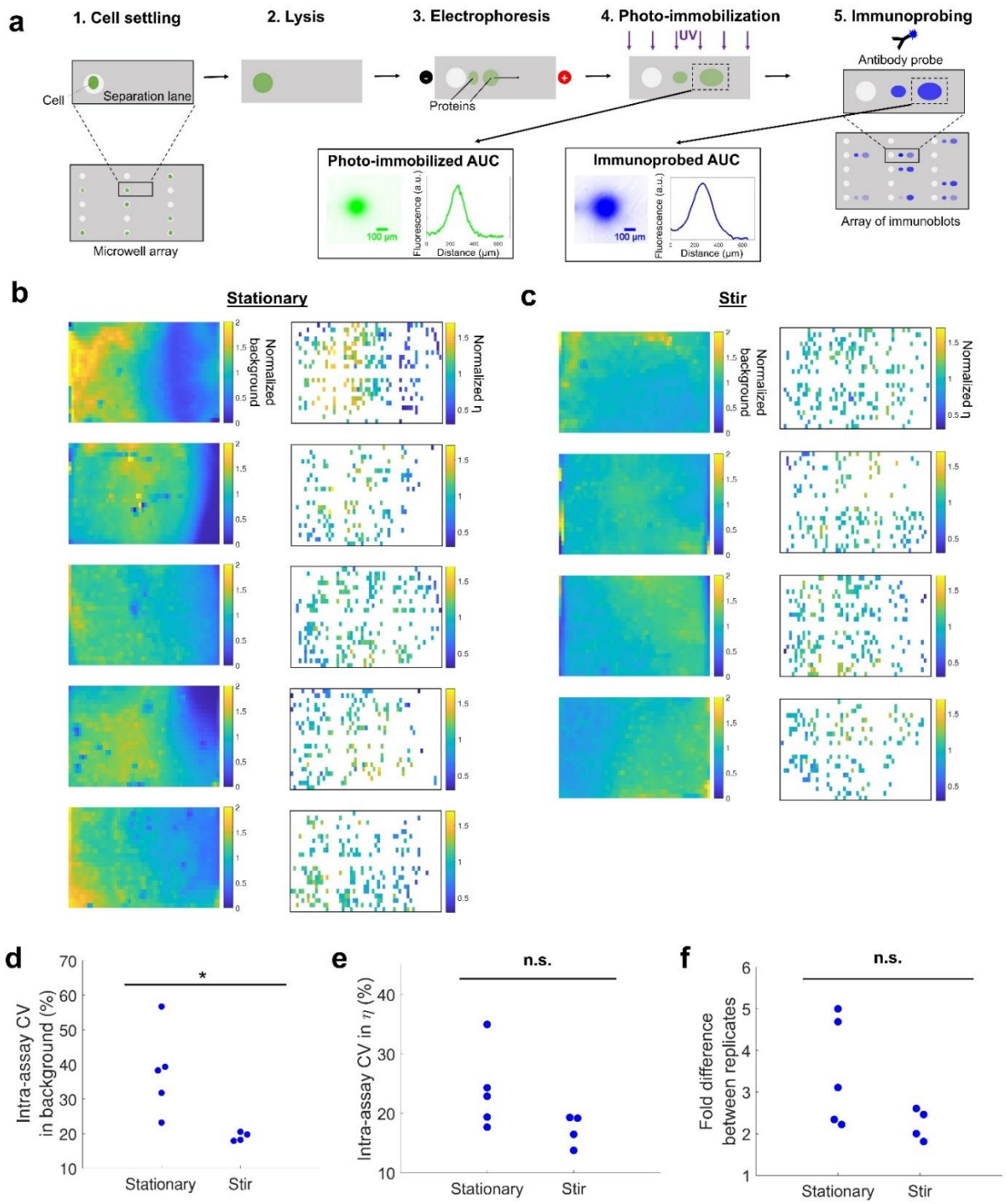

Figure 3.6. Spatial distribution of background fluorescence and η in a large-format in-gel immunoassay to measure single-cell protein abundance. (a) Single-cell immunoblotting workflow. When run with tGFP-expressing cells, upstream measurement of photo-immobilized tGFP abundance can be measured in addition to immunoprobed tGFP abundance, the standard assay readout. (b-c) Heatmaps of background fluorescence and η in each assay (normalized to the mean within each assay); background was measured in each separation lane, but η is only measured in lanes with a settled cell. Spatial variation in background fluorescence and η is greater when immunoprobing with a (b) stationary antibody fluid layer than with a (c) stirred antibody fluid layer. (d) Intra-assay CV in background fluorescence is significantly higher in assays immunoprobed with a stationary antibody fluid layer than a stirred layer, supporting the hypothesis that in-gel antibody concentration does not diffusively homogenize over immunoprobing

timescales (Mann-Whitney U test, p = 0.0159). (e) Intra-assay CV in η in assays immunoprobed with a stationary (n=5) and stirred (n=4) fluid layer. (f) Fold difference in measured immunoprobed signal which arises from two replicate photo-immobilized protein spots, based on Bland-Altman analysis. The fold difference is generally greater for assays immunoprobed with a stationary antibody fluid layer, indicating higher technical variation in η.

Subsequently, we investigated whether the stationary antibody fluid layer would yield larger intra-assay variation in η in the single-cell immunoblot, as was observed in the photopatterned protein system. While there was no significant difference in intra-assay variation in η between the stationary and stirred immunoprobing configurations, stirring narrows and lowers the range of CVs in η (**Figure 3.6e**). Similarly, the fold difference in expected immunoprobed AUC from replicate protein spots narrowed and lowered in the stirred system as compared to the stationary system, although not significantly (**Figure 3.6f**). We hypothesize that the smaller sample size (~100 cells/assay, due to stochastic settling, rather than ~1100 photopatterned protein spots/assay as in **Figure 3.3**) may reduce the statistical power of the single-cell immunoblotting system to detect differences in the immunoprobing methods. Additionally, the exact mechanics of the fluid layer on the hydrated gel are not fully understood. It is likely that some replicate assays had a more uniform fluid layer to begin with, resulting in a more homogeneous local antibody concentration; thus, some stationary immunoprobing replicates may match the more uniform antibody concentration boundary conditions of the stirred fluid layers.

3.5 Conclusions

Here, we pose and investigate a physicochemical mechanism of intra-assay spatial variation for immunoassays performed across large-format chips, specifically focusing on configurations where target is immobilized at unknown locations within a sample matrix, such as in single-cell immunoblotting and tissue section-analysis by IHC. Using fluorescence microscopy, we have characterized the uniformity of antibody probe distribution across a model polyacrylamide gel sample, observing substantial intra-assay spatial variation in antibody concentration which is reduced by laterally shifting the gel to stir the antibody fluid layer. Based on bimolecular binding theory, we hypothesized that for antibody probe concentrations near K_D, η is highly sensitive to local antibody probe concentration, despite the antibody being in excess as compared to the antigen. Both in photopatterned gels and single-cell immunoblot samples, we find that intra-assay variation in η is generally higher when the antibody fluid layer is not stirred (and thus more nonuniform), supporting our hypothesis. We also apply Bland-Altman analysis to rigorously quantify intra-assay technical variation based on the degree of agreement between photo-immobilized and immunoprobed AUC values. Overall, this research demonstrates that uniform intra-assay probe distribution can be critical to reducing technical variation in large-format chips. This is especially true for in-gel immunoassays and IHC, where it can be difficult to know or adjust the regime one is operating in due to limited antibody probe partitioning into the porous sample and the fact that the binding kinetics of commercial antibodies are rarely reported. If a researcher has a choice of antibodies with known K_D values, we recommend selecting an antibody with K_D at least an order of magnitude lower than the expected local antibody probe concentration at the position of the target antigen, to avoid being in a regime where η is sensitive to variation in probe concentration. Regardless of whether K_D is known or not, we recommend ensuring that antibody probe concentration is spatially uniform via stirring or other microscale mixing techniques, as we have demonstrated here that uniform probe distribution reduces intra-assay technical variation in η and background. By reducing intra-assay technical variation, finer biological differences can be distinguished, facilitating discoveries in a variety of spatially-arrayed assays.

3.6 References

1. Steger, D. *et al.* Systematic Spatial Bias in DNA Microarray Hybridization Is Caused by Probe Spot Position-Dependent Variability in Lateral Diffusion. *PLoS One* **6**, (2011).
2. Mazoure, B., Nadon, R. & Makarenkov, V. Identification and correction of spatial bias are essential for obtaining quality data in high-throughput screening technologies. *Scientific Reports* **7**, 11921 (2017).
3. Anderson, T., Wulfkuhle, J., Liotta, L., Winslow, R. L. & Petricoin, E. Improved reproducibility of reverse-phase protein microarrays using array microenvironment normalization. *Proteomics* **9**, 5562–5566 (2009).
4. Kaushik, P. *et al.* Spatial Normalization of Reverse Phase Protein Array Data. *PLOS ONE* **9**, e97213 (2014).
5. Adey, N. B. *et al.* Gains in Sensitivity with a Device that Mixes Microarray Hybridization Solution in a 25-μm-Thick Chamber. *Anal. Chem.* **74**, 6413–6417 (2002).
6. Zainol, M. *et al.* Introducing a true internal standard for the Comet assay to minimize intra- and inter-experiment variability in measures of DNA damage and repair. *Nucleic Acids Res* **37**, e150 (2009).
7. Hughes, A. J. *et al.* Single-cell western blotting. *Nature Methods* **11**, 749–755 (2014).
8. Tong, J. & Anderson, J. L. Partitioning and diffusion of proteins and linear polymers in polyacrylamide gels. *Biophysical Journal* **70**, 1505–1513 (1996).
9. Su, A., Smith, B. E. & Herr, A. E. In situ measurement of thermodynamic partitioning in open hydrogels. *Anal. Chem.* (2019) doi:10.1021/acs.analchem.9b03582.
10. Melvin, N. R. & Sutherland, R. J. Quantitative Caveats of Standard Immunohistochemical Procedures: Implications for Optical Disector–based Designs. *J Histochem Cytochem* **58**, 577–584 (2010).
11. Torres, E. M., Meldrum, A., Kirik, D. & Dunnett, S. B. An investigation of the problem of two-layered immunohistochemical staining in paraformaldehyde fixed sections. *Journal of Neuroscience Methods* **158**, 64–74 (2006).
12. Grube, D. Constants and variables in immunohistochemistry. *Archives of Histology and Cytology* **67**, 115–134 (2004).
13. Sjørup, A. H. Education Guide Immunohistochemical Staining Methods Sixth Edition. 218.
14. Nishikori, S. *et al.* Broad Ranges of Affinity and Specificity of Anti-Histone Antibodies Revealed by a Quantitative Peptide Immunoprecipitation Assay. *Journal of Molecular Biology* **424**, 391–399 (2012).
15. Landry, J. P., Ke, Y., Yu, G.-L. & Zhu, X. D. Measuring Affinity Constants of 1,450 Monoclonal Antibodies to Peptide Targets with a Microarray-based Label-Free Assay Platform. *J Immunol Methods* **417**, 86–96 (2015).
16. Goodrich, J. A. & Kugel, J. F. Binding and Kinetics for Molecular Biologists. in (2006).
17. Kim, H. S. *et al.* Analysis of Reagent Lot-to-Lot Comparability Tests in Five Immunoassay Items. *Ann Clin Lab Sci* **42**, 165–173 (2012).
18. Liu, S. *et al.* Characterization of monoclonal antibody's binding kinetics using oblique-incidence reflectivity difference approach. *mAbs* **7**, 110–119 (2015).
19. Donaldson, J. G. UNIT 4.3 Immunofluorescence Staining. *Curr Protoc Cell Biol* **0 4**, Unit-4.3 (2001).
20. Kang, C.-C. *et al.* Single cell–resolution western blotting. *Nature Protocols* **11**, 1508–1530 (2016).
21. Hughes, A. J. & Herr, A. E. Microfluidic Western blotting. *PNAS* **109**, 21450–21455 (2012).

22. Shin, D.-S. *et al.* Photodegradable Hydrogels for Capture, Detection, and Release of Live Cells. *Angewandte Chemie International Edition* **53**, 8221–8224 (2014).
23. Liu, V. A. & Bhatia, S. N. Three-Dimensional Photopatterning of Hydrogels Containing Living Cells. *Biomedical Microdevices* **4**, 257–266 (2002).
24. Ogston, A. G. The spaces in a uniform random suspension of fibres. *Trans. Faraday Soc.* **54**, 1754–1757 (1958).
25. Baselga, J., Hernández-Fuentes, I., Masegosa, R. M. & Llorente, M. A. Effect of Crosslinker on Swelling and Thermodynamic Properties of Polyacrylamide Gels. *Polymer Journal* **21**, 467–474 (1989).
26. Bhunia, D., Chowdhury, R., Bhattacharyya, K. & Ghosh, S. Fluorescence fluctuation of an antigen–antibody complex: circular dichroism, FCS and smFRET of enhanced GFP and its antibody. *Phys. Chem. Chem. Phys.* **17**, 25250–25259 (2015).
27. Lazzara, M. J., Blankschtein, D. & Deen, W. M. Effects of Multisolute Steric Interactions on Membrane Partition Coefficients. *Journal of Colloid and Interface Science* **226**, 112–122 (2000).
28. Armstrong, J. K., Wenby, R. B., Meiselman, H. J. & Fisher, T. C. The Hydrodynamic Radii of Macromolecules and Their Effect on Red Blood Cell Aggregation. *Biophysical Journal* **87**, 4259–4270 (2004).
29. Appendix C: Physical Properties of Water. in *MWH's Water Treatment: Principles and Design, Third Edition* 1861–1862 (John Wiley & Sons, Ltd, 2012). doi:10.1002/9781118131473.app3.
30. Reverberi, R. & Reverberi, L. Factors affecting the antigen-antibody reaction. *Blood Transfus* **5**, 227–240 (2007).
31. Schneider, C. A., Rasband, W. S. & Eliceiri, K. W. NIH Image to ImageJ: 25 years of image analysis. *Nature Methods* **9**, 671–675 (2012).
32. Schindelin, J. *et al.* Fiji: an open-source platform for biological-image analysis. *Nature Methods* **9**, 676–682 (2012).
33. Preibisch, S., Saalfeld, S. & Tomancak, P. Globally optimal stitching of tiled 3D microscopic image acquisitions. *J. Bioinform.* **25**, 1463–1465 (2009).
34. Jonas. *plot spread points (beeswarm plot) (https://www.mathworks.com/matlabcentral/fileexchange/37105-plot-spread-points-beeswarm-plot), MATLAB Central File Exchange.* (2020).
35. Delehanty, J. B. & Ligler, F. S. A Microarray Immunoassay for Simultaneous Detection of Proteins and Bacteria. *Anal. Chem.* **74**, 5681–5687 (2002).
36. Giesen, C. *et al.* Highly multiplexed imaging of tumor tissues with subcellular resolution by mass cytometry. *Nature Methods* **11**, 417–422 (2014).
37. Candia, J. *et al.* Assessment of Variability in the SOMAscan Assay. *Scientific Reports* **7**, (2017).
38. Gehrke, S. H., Fisher, J. P., Palasis, M. & Lund, M. E. Factors Determining Hydrogel Permeability. *Annals of the New York Academy of Sciences* **831**, 179–184 (1997).
39. Le Goff, G. C., Srinivas, R. L., Hill, W. A. & Doyle, P. S. Hydrogel microparticles for biosensing. *European Polymer Journal* **72**, 386–412 (2015).
40. Arenkov, P. *et al.* Protein Microchips: Use for Immunoassay and Enzymatic Reactions. *Analytical Biochemistry* **278**, 123–131 (2000).
41. Zubtsov, D. A. *et al.* Comparison of surface and hydrogel-based protein microchips. *Analytical Biochemistry* **368**, 205–213 (2007).

42. Pedrosa, V. A., Yan, J., Simonian, A. L. & Revzin, A. Micropatterned Nanocomposite Hydrogels for Biosensing Applications. *Electroanalysis* **23**, 1142–1149 (2011).
43. Hughes, A. J., Lin, R. K. C., Peehl, D. M. & Herr, A. E. Microfluidic integration for automated targeted proteomic assays. *PNAS* **109**, 5972–5977 (2012).
44. Dubois, L., Andersson, K., Asplund, A. & Björkelund, H. Evaluating real-time immunohistochemistry on multiple tissue samples, multiple targets and multiple antibody labeling methods. *BMC Res Notes* **6**, 542 (2013).
45. *IHC/ICC Protocol Guide*. (R&D Systems).
46. Bordeaux, J. *et al.* Antibody validation. *BioTechniques* **48**, 197–209 (2010).
47. Kapil, M. A. & Herr, A. E. Binding Kinetic Rates Measured via Electrophoretic Band Crossing in a Pseudohomogeneous Format. *Anal. Chem.* **86**, 2601–2609 (2014).
48. Heinrich, L., Tissot, N., Hartmann, D. J. & Cohen, R. Comparison of the results obtained by ELISA and surface plasmon resonance for the determination of antibody affinity. *Journal of Immunological Methods* **352**, 13–22 (2010).
49. Kim, S.-J., Wang, F., Burns, M. A. & Kurabayashi, K. Temperature-Programmed Natural Convection for Micromixing and Biochemical Reaction in a Single Microfluidic Chamber. *Anal. Chem.* **81**, 4510–4516 (2009).
50. Liu, Y. & Rauch, C. B. DNA probe attachment on plastic surfaces and microfluidic hybridization array channel devices with sample oscillation. *Analytical Biochemistry* **317**, 76–84 (2003).
51. Yasun, E., Trusty, T., Abolhosn, R. W., Clarke, N. J. & Mezić, I. Electrokinetic Mixing for Improving the Kinetics of an HbA1c Immunoassay. *Scientific Reports* **9**, 1–10 (2019).
52. Prichard, J., Bitting, A. & Myers, J. Overview of Automated Immunohistochemistry. in *Handbook of Practical Immunohistochemistry: Frequently Asked Questions* (eds. Lin, F. & Prichard, J.) 23–30 (Springer New York, 2011). doi:10.1007/978-1-4419-8062-5_3.
53. Martin Bland, J. & Altman, DouglasG. Statistical methods for assessing agreement between two methods of clinical measurement. *The Lancet* **327**, 307–310 (1986).
54. Cohen, A. A. *et al.* Dynamic Proteomics of Individual Cancer Cells in Response to a Drug. *Science* **322**, 1511–1516 (2008).
55. Kang, C.-C. *et al.* Electrophoretic cytopathology resolves ERBB2 forms with single-cell resolution. *npj Precision Oncology* **2**, 10 (2018).
56. Shi, Q. *et al.* Single-cell proteomic chip for profiling intracellular signaling pathways in single tumor cells. *PNAS* **109**, 419–424 (2012).
57. Liu, L., Li, P. & Asher, S. A. Entropic trapping of macromolecules by mesoscopic periodic voids in a polymer hydrogel. *Nature* **397**, 141–144 (1999).

Chapter 4

Protein-loaded microparticles as internal controls for single-cell immunoblotting

Portions of this chapter are adapted with permission from J. J. Kim, P. P. Y. Chan, J. Vlassakis, A. Geldert, & A. E. Herr, "Microparticle delivery of protein markers for single-cell western blotting from microwells", *Small*, 2018.

4.1 Abstract

Immunoblotting confers protein identification specificity beyond that of immunoassays by prepending protein electrophoresis (sizing) to immunoprobing. To accurately size protein targets, sample analysis includes concurrent analysis of protein markers with known molecular masses. To incorporate protein markers in single-cell western blotting, microwells are used to isolate individual cells and protein marker-coated microparticles. A magnetic field directs protein-coated microparticles to >75% of microwells, so as to 1) deliver a quantum of protein marker to each cell-laden microwell and 2) synchronize protein marker solubilization with cell lysis. Nickel-coated microparticles are designed, fabricated, and characterized, each conjugated with a mixture of histidine-tagged proteins (42.3–100 kDa). Imidazole in the cell lysis buffer solubilizes protein markers during a 30 s cell lysis step, with an observed protein marker release half-life of 4.46 s. Across hundreds of individual microwells and different microdevices, robust log-linear regression fits ($R^2 > 0.97$) of protein molecular mass and electrophoretic mobility are observed. The protein marker and microparticle system is applied to determine the molecular masses of five endogenous proteins in breast cancer cells (GAPDH, β-TUB, CK8, STAT3, ER-α), with <20% mass error. To evaluate the potential of protein-loaded microparticles to serve as protein abundance standards to control for technical variation in protein expression measurements, microparticle heterogeneity in protein loading was also characterized. Microparticle-delivered protein standards underpin robust, reproducible electrophoretic cytometry that complements single-cell genomics and transcriptomics.

4.2 Introduction

Single-cell analysis tools report biomolecular heterogeneity that drives processes from immune-cell response to cancer progression.[1–4] A key component of many single-cell analysis tools are microwell arrays, which facilitate isolation of single cells.[5–8] Microwell arrays have been used for high throughput and automatic analysis of DNA[8–10] and protein[11,12] from hundreds to thousands of cells. Gravity is commonly used to sediment single cells into open microwells, followed by *in situ* cytometry. Physically isolated inside microwells, intact individual cells are readily monitored for cell morphology[13,14] and lysed to measure DNA damage and repair,[8,15] transcriptional levels,[9,10] and protein expression.[16,17] To conduct electrophoresis of single-cell lysate, an external electric field is applied across cell-laden microwells (fabricated in agarose or polyacrylamide) to initiate and drive electrophoretic separation.

To characterize proteoforms from single cells, an "open" microfluidic single-cell western blotting device comprising an array of microwells cast in a thin layer of polyacrylamide gel can be used to perform electrophoretic analyses of isolated mammalian cells, including circulating tumor cells and breast cancer cells.[11,18–22] In addition to cell isolation, each microwell acts as a reactor for cell preparation (e.g., imaging, staining, chemical lysis), with each cell lysate then subjected to electrophoretic analysis (e.g., protein polyacrylamide gel electrophoresis [PAGE], isoelectric focusing) in the surrounding polyacrylamide gel layer. When photosensitive benzophenone methacrylamide monomer has been cross-linked into the polyacrylamide molecular sieving matrix, protein electrophoresis can be followed by UV-activated protein blotting in the gel (photoblotting, 1 min) and subsequent immunoprobing also in the gel. UV activation of benzophenone changes the polyacrylamide gel from a molecular sieving matrix for electrophoresis into a blotting membrane for the subsequent immunoassay probing steps. The molecular sieving gel rapidly toggles to a blotting membrane, thus eliminating the lossy blotting transfer step used in traditional bulk western blotting. Because proteoforms are spatially resolved based on size, single-cell western blotting measures targets that may not be discernable using an immunoassay alone.[19] Single-cell western blotting facilitates analysis of protein isoforms, which are involved in pathological processes including cancer,[19] autoimmune diseases,[23] diabetes,[24] heart hypertrophy,[25] and other conditions.[26]

While single-cell western blotting facilitates massively parallel characterization of single cells, the accuracy and precision of either protein abundance or protein molecular mass (i.e., size) measurements depends critically on the amount of technical variation in the assay. Quantifying and minimizing technical variation in protein abundance is critical to protein expression measurements; for example, assay precision sufficient to distinguish protein abundance changes of $\leq$ 3-fold is valuable to distinguish between protein levels associated with different chemotherapeutic responses.[27] Technical variation in electromigration is also key to characterizing and distinguishing between proteoforms of different molecular mass. Analysis of cell lysate by electrophoretic separations typically uses protein size markers to estimate the molecular mass of a target from the known masses of the markers. In order to accurately size and identify targets, protein markers control for technical variation in the uniformity of the electric field, sieving matrix structure, and buffer composition—all of which influence protein electromigration.[28–30] Well-validated protein standards are also crucial in identifying and understanding "gel shifting," a phenomenon in which a protein does not electromigrate proportionally with its molecular mass due to amino acid substitutions, post-translational modifications, or other unknown factors.[31,32] Consequently, protein markers and ladders find utility in slab-gel, capillary, and microchannel electrophoresis formats.[33–37] In slab-gel protein PAGE, the first or last separation lanes of the slab gel are used for analysis of protein markers.[38–41] In western blotting, protein markers not only estimate the molecular mass of a target, but also indicate the quality of protein transfer from the PAGE slab gel to the immunoblotting membrane.[42–45] Run-to-run reproducibility in electromigration is monitored using protein markers, providing a quality control indicator.[37] Such protein markers to assess technical variation in electromigration would be invaluable for quantifying proteoform expression that drives drug resistance in single cancer cells.[19]

Molecular standards play an important role in deconvolving biological variation from technical variation arising from a measurement tool.[18,46] In single-cell sequencing, synthetic spike-ins and unique molecular identifiers (e.g., short-random DNA sequences) directly measure error rates, analytical sensitivity, and biases stemming from sample preparation.[47–49] In flow cytometry, lasers are calibrated before cell sorting using fluorescent microparticles.[50,51] In microfluidic protein

assays of a single cell lysate (e.g., single-cell barcode assay), estimates of technical variation are inferred from multiple measurements of each lysate.[52]

Here, we introduce microparticle-based standards to facilitate characterization of technical variation in single-cell western blotting. We design a vehicle to deliver discrete quanta of purified protein standards selectively into each microwell. We design to meet two key performance metrics: quantized delivery to cell-laden microwells and triggered release of fluorescent protein markers in each microwell. The microparticle-delivery maintains locally high protein standard concentrations by eliminating diffusion of proteins into both the gel network and the microwells prior to cell lysis. In this study, we consider 10 μm-diameter magnetic microparticles coated with nickel (Ni^{2+}). To meet the particle-loading metric, we choose magnetic particles so that we might use an applied, external magnetic field for directed loading of the microparticles into cell-laden microwells.[23,53,54] To meet the more stringent triggered release metric, we utilize microparticles coated with Ni^{2+} for reversible binding of histidine(His)-tagged proteins, which can then be chemically released from the microparticle concurrently with a 30 s cell lysis step.[53,55] We investigate the performance of the "solid phase" protein-loaded microparticle standard to serve as a standard for either protein abundance or protein sizing measurements.

4.3 Materials & Methods

Chemicals/Reagents. Acrylamide/bis-acrylamide (40% wt/wt) solution (A7802), N,N,N′,N′-tetramethylethylenediamine (TEMED, T9281), ammonium persulfate (APS, A3678), sodium deoxycholate (D6750), β-Mercaptoethanol (M3148), imidazole (792 527), and SDS (L3771), were obtained from Sigma-Aldrich. Triton X-100 was purchased from Fisher Scientific (BP-151). 10× Tris/glycine buffer was obtained from Bio-Rad (161-0734). Phosphate buffered saline (PBS), pH 7.4 was obtained from Gibco (10 010-023). Tris-HCl, pH 6.8 was purchased from Teknova (T1568). PureProteome nickel magnetic microparticles with 10 μm diameter were obtained from Millipore Sigma (LSKMAGH02). A 6-tube magnetic separation rack was obtained from New England BioLabs (S1506S). N-[3-[(3-Benzoylphenyl)-formamido]propyl] methacrylamide (BPMAC) was custom synthesized by PharmAgra Laboratories. SU-8 developer (Y020100) and photoresist SU-8 2025 (Y111069) were obtained from MicroChem. Deionized water (ddH2O, 18.2 mΩ) was obtained using ultrapure water system (Millipore). Unless stated otherwise, chemicals and reagents were obtained from Sigma-Aldrich.

Proteins. Recombinant protein A His Tag (Protein A, ab52953) and recombinant human EpH receptor B4 protein His Tag (EpH, ab167746) were obtained from Abcam. Protein A and EpH were fused with 6× polyhistidine domains on N- and C-terminus, respectively. VEGFR2 (KDR) recombinant human protein, His Tag (KDR, 10012H08H50), ICAM1 recombinant human protein, hIgG1-Fc. His Tag (ICAM1, 10346H03H5) and CHI3L1 recombinant mouse protein His Tag (CHI3L1, 50929M08H50) were purchased from ThermoFisher Scientific. KDR, ICAM1, and CHI3L1 were expressed from a DNA sequence from the extracellular domains fused to a C-terminal polyhistidine tags. Unless stated otherwise, His Tag proteins were fluorescently labeled using Alexa Fluor 647 NHS ester succinimidyl ester (Life Technologies, A20006). Fluorescently labeled His Tag proteins were purified using dye removal columns (ThermoFisher Scientific, 22858) according to the manufacturer protocol. Details of the recombinant proteins used for protein markers are listed in **Table 4.1**.

Table 4.1. List of proteins carried by nickel-conjugated magnetic microparticles.

Protein	Species	Molecular mass (kDa)	Company (catalog #)
Recombinant protein A, His tag	E. coli	39	Abcam (ab52953)

CHI3L1 recombinant mouse protein, His tag	Mouse	42.3	Thermofisher (50929M08H50)
Recombinant protein A + protein G, His tag	E. coli	59.7	Abcam (ab52213)
PDGFRA recombinant human protein (without catalytic activity), His tag	Human	57.7	Abcam (ab52213)
Recombinant human EpH receptor B4 protein	Human	58	Abcam (ab167746)
KDR (VEGFR2) Recombinant human protein, His tag	Human	84.6	Abcam (ab167746)
ICAM1 Recombinant human protein, hIgG1-Fc. His tag	Human	100	ThermoFisher (10346H03H25)

Primary antibodies to recognize endogenous proteins include rabbit anti-β-tubulin (ab6046, Abcam), goat anti-GAPDH (SAB2500450, Sigma), mouse anti-cytokeratin 8 (C5301, Sigma), rabbit anti-estrogen receptor α (ab16660, Abcam), and rabbit anti-STAT3 (79D7, Cell Signaling). For the primary antibody host species, secondary antibodies with Alexa Fluor were purchased from ThermoFisher Scientific: anti-mouse secondary antibody with Alexa Fluor 555 (A31570), anti-rabbit secondary antibody with Alexa Fluor 488 (A21206), anti-goat secondary antibody with Alexa Fluor 555 (A21432).

Protein loading on nickel microparticles. Magnetic microparticles (5 μL) were equilibrated with buffer (50×10^{-3} M sodium phosphate, 300×10^{-3} M sodium chloride, 10×10^{-3} M imidazole, pH 8). A protein solution (500 μL) containing a mixture of His Tag proteins in (30% v/v) ethanol/PBS was loaded with the microparticles and mixed gently for 2 h at 4 °C using a rotator. Unbound proteins were washed 3 times using wash buffer (50×10^{-3} M sodium phosphate, 300×10^{-3} M sodium chloride, 20×10^{-3} M imidazole, pH 8). Residual liquid was separated from the microparticle using a magnetic rack and removed after each of the above steps. The protein bound microparticles were resuspended in 1× PBS.

In order to determine protein release kinetics, microparticles (5 μL) were loaded with Protein A (4.1 μg). For electrophoretic separations, microparticles (5 μL) were loaded with either one of two protein mixtures containing: 1) Protein A (2 μg), or 2) CHI3L1 (14.8 μg), EpH (54.5 μg), KDR (21.9 μg), and HIgG1-F (7.4 μg). The bound His Tag protein was eluted from the microparticles using lysis/electrophoresis buffer prepared with imidazole (0 or 1 M), SDS (2.5 g), sodium deoxycholate (1.25 g), Triton X-100 (500 μL), Tris/glycine buffer (25 mL, 10×), and ddH2O (474.5 mL).

Measurement of microparticle loading efficiency via flow cytometry. The percentage of microparticles loaded with AF647-labeled proteins was determined by flow cytometry. The fluorescence (RL1-A, with PMT gain 180) of microparticles with and without the protein ladder was measured using an Attune NxT acoustic focusing flow cytometer (ThermoFisher Scientific). Microparticles were drawn from a solution (333,333 microparticles mL^{-1}), and a threshold of FSC-A > 25,000 was applied to avoid detection of debris. Results were analyzed using FlowJo analysis software (FlowJo).

Cell culture. The MCF-7 breast cancer cell line was purchased from ATCC and maintained in RPMI 1640 (ThermoFisher Scientific) containing fetal bovine serum (10%) and penicillin/streptomycin (1%) in a humidified incubator held at 37 °C under 5% CO_2. MCF-7 was tested mycoplasma negative and authenticated with short tandem repeat analysis.

Fabrication of single-cell western blot chip. The master mold comprised a silicon wafer with SU-8 features that was fabricated according to standard photolithography procedure.[21] Single-cell western blot devices containing an array of microwells (250 μm well-to-well spacing and 1 mm

long separation lane) with feature heights and diameters of 35 and 30 μm, respectively, were fabricated by casting a polyacrylamide gel against the mold.[21] The polyacrylamide gel layer was chemically polymerized (7 %T, 3.45 %C, 3×10^{-3} M BPMAC, 0.08% APS, and 0.08% TEMED).

Single-cell western blot buffer exchange. After settling cells in microwells by gravity, a chemical lysis buffer (0.5× Tris glycine, 0.5% SDS, 0.25% sodium deoxycholate, 0.1%Triton X-100, 1 M imidazole, pH 9.2, 55 °C) was poured into the single-cell western blot for 30 s to release protein markers from microparticles and solubilize endogenous proteins from mammalian cells. Then, a 2 s electrophoresis at 40 V cm^{-1} was applied immediately for protein injection. For protein separation, an electrophoretic buffer (0.5× Tris glycine, 0.5% SDS, 0.25% sodium deoxycholate, 0.1%Triton X-100, pH 8.7, 22 °C) was introduced, followed by immediate electrophoresis at 40 V cm^{-1} for 23 s.

Fluorescence imaging. An Olympus IX71 inverted fluorescence microscope equipped with Applied Scientific Instrumentation (ASI) motorized stage, X-cite mercury lamp light source (Lumen Dynamics), standard Cy5 filter cube, and iXon+ EMCCD camera (Andor Technology Ltd.), controlled by MetaMorph software (Molecular Devices) was used for all widefield fluorescence microscopy imaging of microparticles. To characterize protein release kinetics, microparticles with Protein A bound were prepared and settled into microwells with a magnetic field. After application of lysis buffer, fluorescent protein release was imaged with 60 ms exposure time and 2 s time intervals using a 40× objective.

To characterize microparticle-to-microparticle variation in size and protein loading, a 15 μL suspension of microparticles loaded with AlexaFluor 647-labeled Protein G or Protein A/G (with concentrations between $1.4 – 3.6 \times 10^6$ microparticles/mL, as counted by a hemocytometer) was pipetted onto a glass microscope slide and covered with a 25 × 25 mm coverslip. Microparticles were imaged through the coverslip with a 40×, 0.60 numerical aperture objective (50 ms exposure, 100% X-Cite illumination intensity, no EM gain, 13 MHz readout rate, 1× pre-amplification gain, 0.56 μs/pixel vertical shift speed), using MetaMorph's *scan slide* module.

Image analysis and quality control. For the release kinetics measurement, image processing was performed using a Python script (Anaconda Python 3.5.3). Circular region of interest (ROI) was manually selected via a Graphical User Interface provided using the cv2 Python package (OpenCV 3.1.0). Image pixel statistics were estimated using the numpy Python package (numpy 1.13.1). Mean fluorescence intensity from a ROI covering the whole microparticle with AF647-labeled Protein A was obtained using the widefield fluorescence microscope, which includes the out-of-focus fluorescence along the z-axis. Background signal was designated as the mean fluorescence intensity measured from an adjacent empty microwell. Each mean fluorescence intensity of the microwell was background subtracted and then normalized to the value at the start of the release process (t = 0).

To characterize microparticle-to-microparticle variation in size and protein loading, we measured the size and fluorescence of protein-loaded microparticles segmented from widefield fluorescence microscopy images. First, images were flat-field corrected to correct for nonuniform illumination across the field of view, as described in Chapter 2. Then, microparticles were segmented according to the process outlined in **Figure 4.1** (see Supplement for full MATLAB script). Microparticle segmentation performance was evaluated by comparing the results of segmentation analysis of fluorescence images to manual identification of microparticles from corresponding brightfield images (n = 20 images with 142 microparticles total). From this comparison, we found that the segmentation script had a false negative rate of 12.7% (the proportion of microparticles undetected by the script) and a false positive rate of 2.1% (the

proportion of segmented objects that are not microparticles, or are clustered or cut off microparticles).

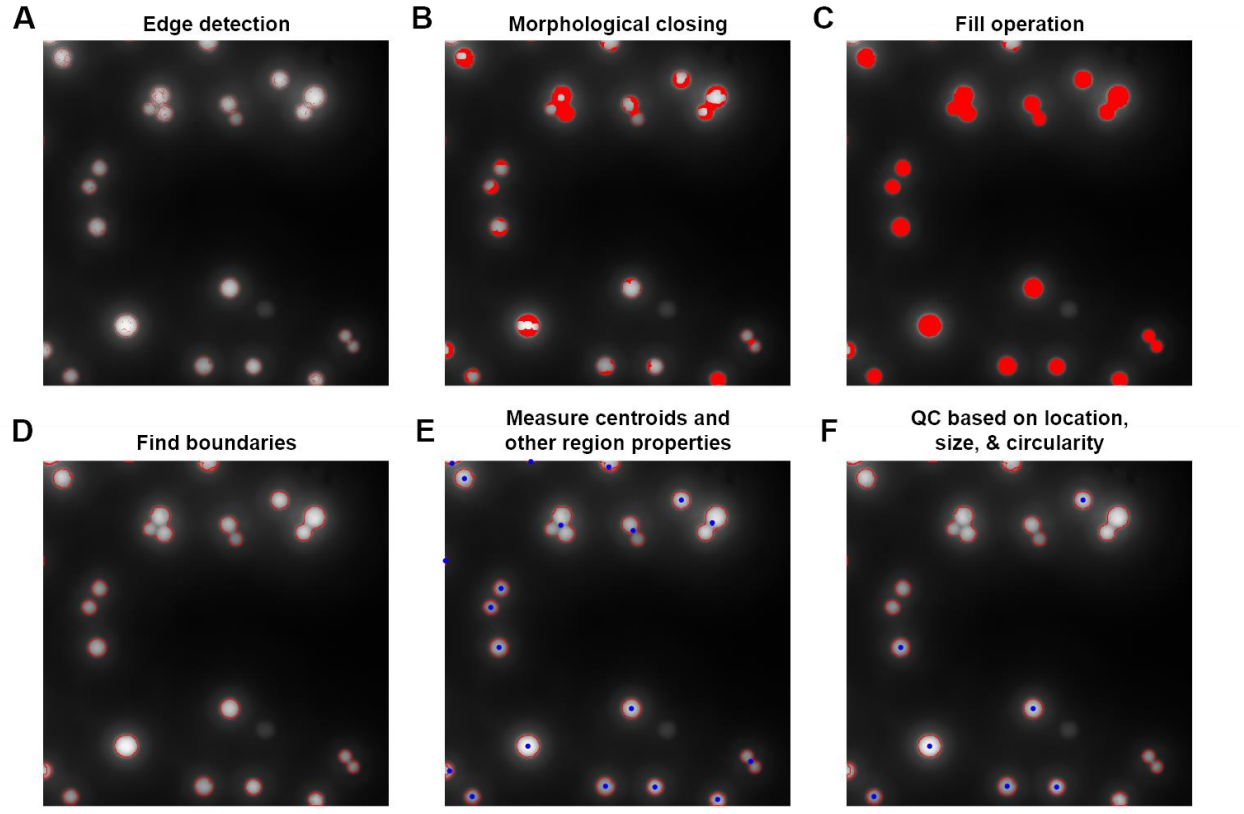

Figure 4.1. Microparticle segmentation workflow. Microparticles are segmented from flat-field corrected widefield fluorescence microscopy images with the following steps, in order: (A) Canny edge detection, (B) Morphological closing to connect edge segments, (C) Fill holes in the image, (D) Boundary detection, (E) Measurement of region properties (red outlines indicate all detected boundaries; blue points indicate centroids), and (F) Quality control (QC) to remove clustered and cut-off microparticles (red outlines indicate all detected boundaries; blue points indicate centroids of segmented regions which pass QC).

For the single-cell western blot analysis, images of proteins were collected by scanning the single-cell western blot devices with a fluorescence microarray scanner (Genepix 4300A, Molecular Devices). The images were processed by applying a median filter with a 2-pixel radius and a threshold value of 50 (ImageJ). Quantitation of proteins from the images was processed by in-house MATLAB (R2016b) scripts.[21] Protein peaks were fitted with Gaussian functions. For quality control protocol, the protein peaks with Gaussian fitting $R^2 \geq 0.7$ and SNR ≥ 3 were analyzed.[21] From the curve fitting, protein peak width and location were extracted from the Gaussian fit parameters to determine protein molecular mass from Ferguson analysis.[36,43] Separation resolution (SR) between adjacent protein peaks is defined according to **Eq. 4.1**, where Δx is the center-to-center distance between protein peaks and σ is the peak width:

$$\mathrm{SR} = \frac{\Delta \mathrm{x}}{2(\sigma_1 + \sigma_2)} \qquad \textbf{Eq. 4.1}$$

To characterize spatial variation in electromigration, we applied semi-variogram analysis.[56,57] The semi-variance (γ) of the slope or y-intercept values (Z) from the log-linear

regressions of protein ladder markers from N pairs of microwells with variable microwell-to-microwell spacing (h) was calculated according to **Eq. 4.2**:

$$\gamma = \frac{1}{2N}\sum_{i=1}^{N}(Z_i - Z_{i+h})^2 \qquad \textbf{Eq. 4.2}$$

4.4 Results & Discussion

Design of the rapid-release protein marker delivery vehicle. A magnetic microparticle delivery system was selected for delivery of protein markers to each microwell of the multistage, single-cell western blot (**Figure 4.2A**). We employed i) an applied magnetic field to actively seat marker-coated microparticles in microwells (i.e., in contrast to gravity-based cell settling; **Figure 4.2B**) and ii) a flexible coordination chemistry on the microparticle surface for protein marker immobilization and triggered solubilization/release (**Figure 4.2C**). We utilized two key microparticle characteristics to achieve the desired functionality and performance: i) magnetic cores for active microparticle seeding in microwells directed via magnetic field and ii) a Ni^{2+} coating that supports high-efficiency protein immobilization with rapid protein release (<30 s) when exposed to imidazole.

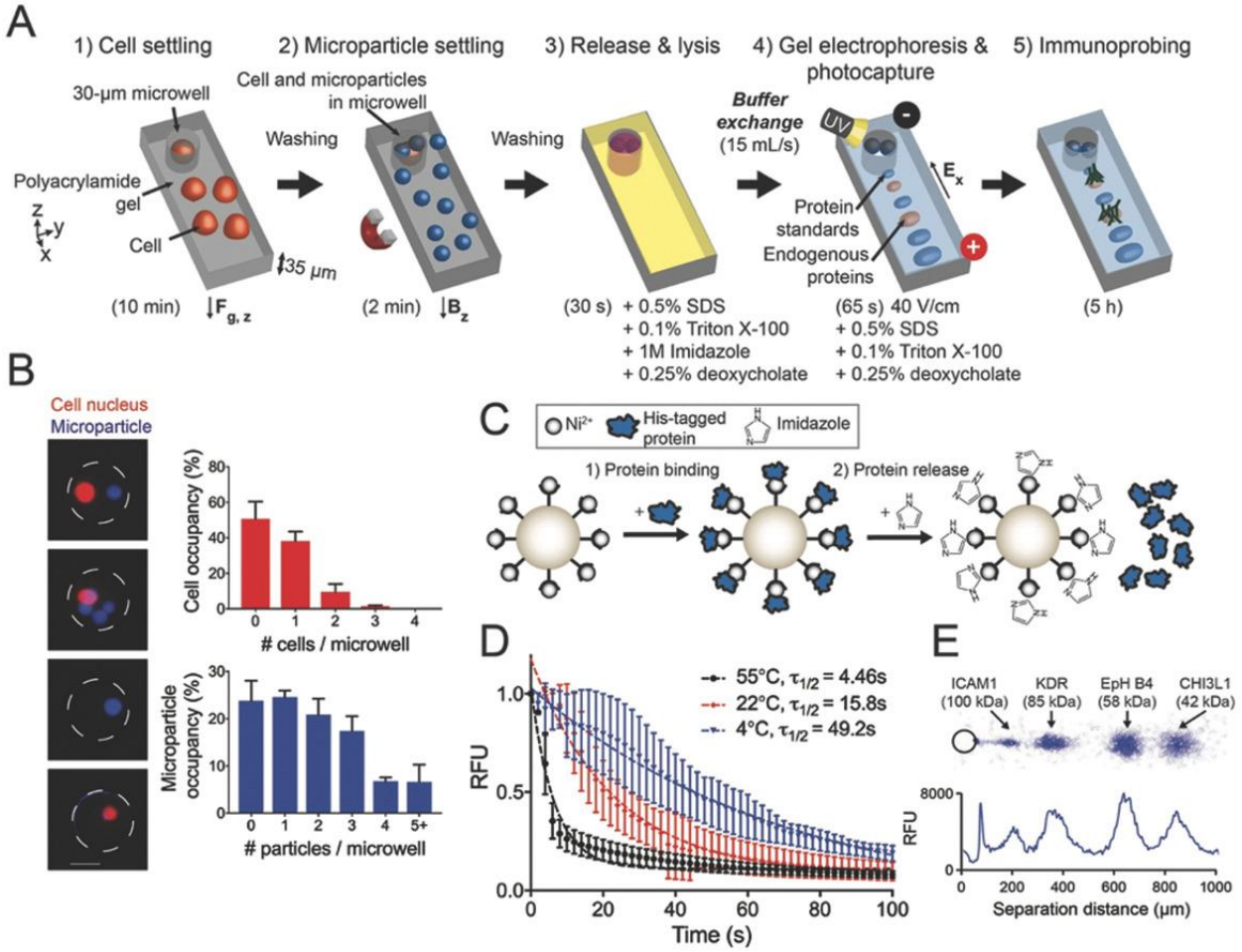

Figure 4.2. Microparticles delivery protein markers for mass sizing in single-cell western blotting. A) Schematic of the single-cell western blot workflow that incorporates microparticles to deliver protein markers (blue peaks) for molecular mass determination of endogenous proteins from mammalian cells (orange peaks). The single-cell western

blot comprises five stages: 1) Cell settling into microwells by gravity ($F_{g,z}$), 2) Microparticle settling into microwells by an applied magnetic field (z-axis) (B_z), 3) In-microwell protein marker release (imidazole) and chemical cell lysis, 4) Concurrent polyacrylamide gel electrophoresis and photo-activated immobilization (photoblotting) of protein markers and single-cell lysate, and 5) In-gel immunoprobing. B) Microwell occupancy of MCF-7 cells and protein-coated microparticles. False-color micrographs of microwells housing a cell (red, nucleus) and/or microparticles (blue). Scale bar is 15 μm. Distributions of microwell occupancy for cells and microparticles. Error bars are standard deviations (n = 3 chips). C) Schematic of His-tagged protein marker delivery and release from Ni^{2+}-coated microparticles. D) Time-lapse fluorescence signal during 1 M imidazole-trigged release of a fluorescent protein marker from a single protein-loaded microparticle in a microwell (n = 3 microwells, error bars are standard deviation). Colored dashed lines represent exponential curve fitting. The marker release half-life for each condition is listed. Black: $y = 1.04 \times \exp(-0.16t) + 0.11$, $R^2 = 0.91$. Red: $y = 1.18 \times \exp(-0.04t) + 0.08$, $R^2 = 0.90$; Blue: $y = 1.03 \times \exp(-0.01t) - 0.09$, $R^2 = 0.87$. E) False-color micrograph and intensity profile of four standard proteins (ICAM1, 100 kDa; KDR, 85 kDa; EpH B4, 58 kDa; CHI3L1, 42 kDa) after electrophoresis separation and photoblotting in the polyacrylamide gel. The 30 μm diameter microwell is at the left of the micrograph.

We first sought to assess the efficiency of a two-step microwell loading process. First, we seated MCF-7 breast cancer cells in each microwell by applying a suspension of the cells (≈25 μm diameter) onto the polyacrylamide gel layer stippled with 1300 microwells. Cells were sedimented via gravity for 10 min (**Figure 4.2A**, step 1). Gentle washing removed cells that settled onto the surface of the polyacrylamide gel, with cells that settled into the microwells retained on the chip. Next, to deliver microparticles coated with the 4 protein markers into each cell-laden microwell, we applied a solution of the microparticles (10^6 microparticles mL^{-1}) onto the single-cell western blot device and applied a magnetic field to the device for 2 min to direct microparticles into microwells (**Figure 4.2A**, step 2). A circular magnet (4 cm diameter × 1.53 cm height) was located under the 2.5 cm × 3.75 cm device and was moved across the device to expose all microwells to the applied magnetic field. Gentle washing was used to remove microparticles from the surface of the polyacrylamide gel, with microparticles that settled into the microwells retained on the chip.

At the completion of the two-stage microwell loading process, we used brightfield microscopy and selected a random region of interest (≈300 microwells) from each chip to analyze both microparticle and cell occupancies. We observed ≈75% of microwells sampled housed ≥1 microparticle (n = 3 chips, standard deviation σ = 4%, **Figure 4.2B**). Microwells were designed to house MCF-7 cells (30 μm diameter and 35 μm deep microwells), so we opted for 10 μm diameter microparticles so as not to interfere with cell loading. We observed 38.3% of microwells contained a single MCF-7 cell (**Figure 4.2B**), corroborating our previous studies that also utilized gravity for cell settling.[12] In addition to passive cell sedimentation, we have reported on alternate approaches for cell loading including, for example, precision transfer of rare cells[18] and two-step centrifugation by utilizing a second layer of polyacrylamide gel as raised and crescent-shaped dam structures on the perimeter of each microwell.[20] A centrifugal force directed cells to the dams. Upon removal of the centrifugal force, each cell localized to the dam then settles into the proximal microwell.[20] For the two-step loading process, we observed that 35.3% of microwells contained both a single cell and ≥1 microparticle (n = 3 chips, ≈300 microwells sampled per chip, standard deviation σ = 8.1%), as desired for concurrent electrophoretic analysis of protein markers and cell lysate from each microwell.

We next sought to quantitatively assess i) the Ni^{2+} chelation for solid phase immobilization of protein markers on the microparticle surface and ii) the subsequent rapid triggered solubilization of protein markers into the PAGE separation stage (**Figure 4.2C,D**). We aimed to trigger release of protein markers from the microparticle surface with a <30 s release duration and a "pulse" release profile.[21] The <30 s duration was sought to match the time frame of the rapid, in-microwell cell lysis, and endogenous protein solubilization step. A pulse profile was sought to minimize

injection dispersion (i.e., sample tailing) arising from marker release during electroinjection of microwell contents into the PAGE lane.

To immobilize the protein markers on the microparticle surface, the microparticles were incubated (2 h) in a cocktail of fluorescently labeled His-tagged marker proteins (KDR, 21.9 ng μL^{-1}; ICAM1, 7.40 ng μL^{-1}; EpH B4, 54.5 ng μL^{-1}; CHI3L1, 14.8 ng μL^{-1}). After incubation with proteins, the microparticles were washed three times with a washing buffer containing mild imidazole (20×10^{-3} M). Via flow cytometry, we observed 98% of microparticles (≈2000 particles) were coated with the fluorescent protein markers (**Figure 4.2C, Figure 4.3**).

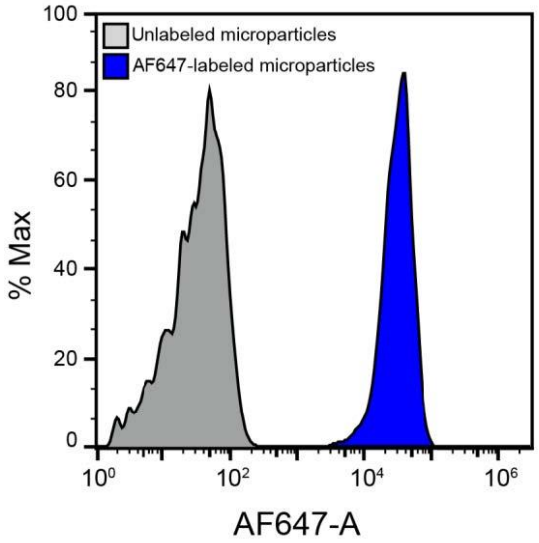

Figure 4.3. Percent of microparticles labelled with AF647-tagged proteins (ICAM1, KDR, EpH B4, CHI3L1) is analyzed by flow cytometry. Blue histogram represents fluorescence variation and % maximum population of microparticles labelled with AF647-tagged proteins ($n_{labelled}$ = 2587). The blue peak between 10^3 and 10^5 indicates 98% of microparticles are tagged with AF647-proteins. Grey histogram represents fluorescence variation and % maximum population of microparticles without AF647-tagged proteins ($n_{unlabelled}$ = 2201).

After preparing the microparticle-based protein marker delivery system, we examined the release kinetics of His-tagged recombinant Protein A labeled with Alexa Fluor 647 (AF647), as a representative protein marker. To displace the His-tagged proteins from the microparticle surface, imidazole was used as a competitive binding ligand. Imidazole has a similar structure to His and serves as an electron donor.[58] Release of His-tagged Protein A from the microparticles was modeled according to one-state ligand–receptor kinetics (an exponential decay).

In a negative control, lysis buffer without imidazole resulted in release of Protein A with a half-life of 63.4 s and a dissociation rate constant of 0.011 s^{-1} (**Figure 4.4**). The observed dissociation rate constant was 10× greater than that previously reported,[59] a difference we attributed to the elevated (55 °C) buffer temperature employed here.

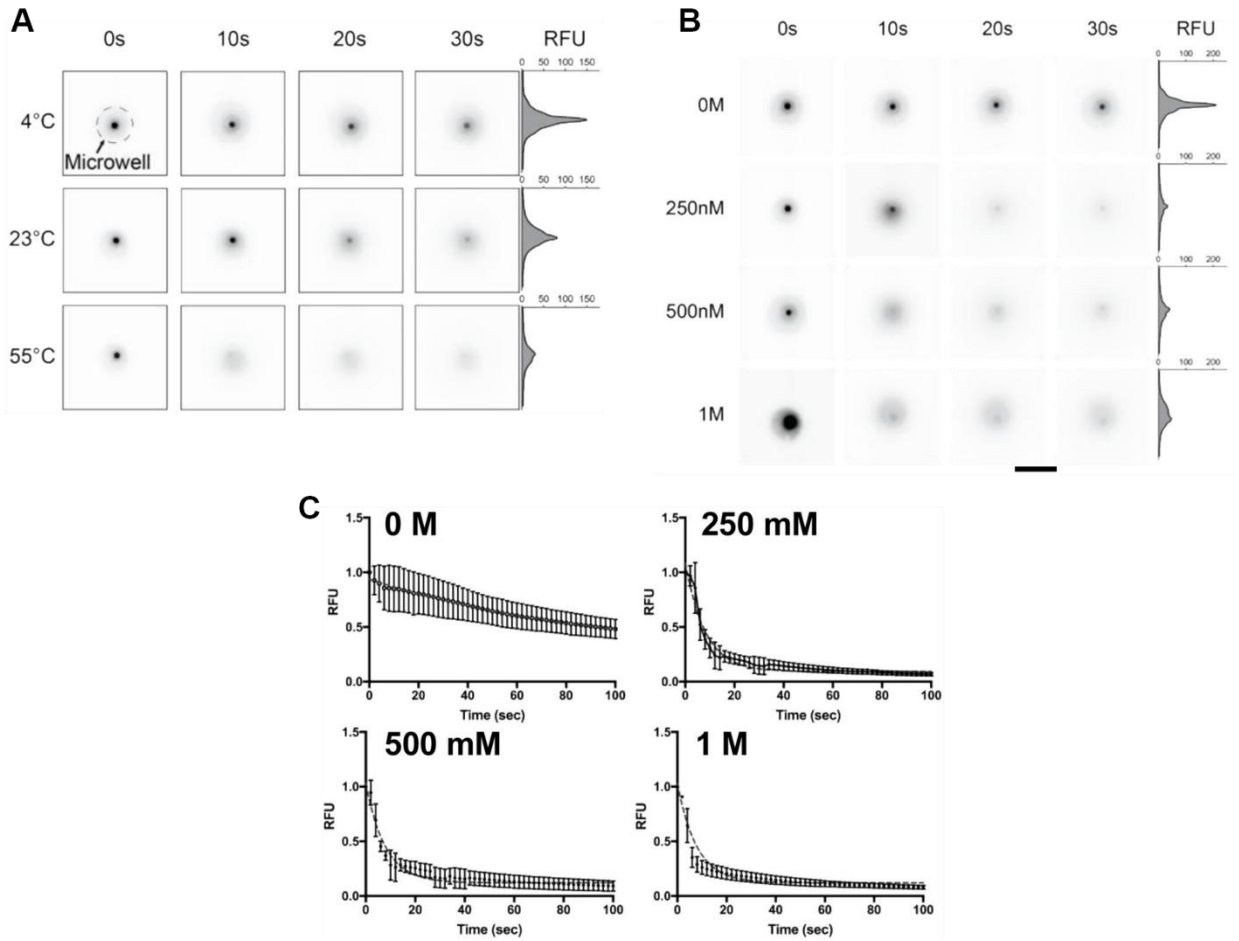

Figure 4.4. The effect of temperature and imidazole concentration on AF647-tagged Protein A release kinetics from microparticles. Representative fluorescence false-color micrographs showing protein release from a microparticle in a microwell at different lysis (A) temperatures (4 °C, 23 °C, 55 °C) and (B) imidazole concentrations (0 M, 250 mM, 500 mM, 1 M). Scale bar, 30 μm length. (C) Time-lapse plots of the fluorescence intensity from microwell in buffer with different Imidazole concentrations. Dashed lines represent exponential curve fitting. 0 M: $y = 0.94*\exp(-0.01t) + 0.25$, $R^2 = 0.64$, 250 mM: $y = 1.09*\exp(-0.12t) + 0.09$, $R^2 = 0.90$, 500 mM: $y = 1.03*\exp(-0.13t) + 0.12$, $R^2 = 0.85$, 1 M: $y = 1.04*\exp(-0.16t) + 0.11$, $R^2 = 0.91$.

Next, we investigated the impact of imidazole concentration on protein marker release from the microparticles using a series of different imidazole concentrations in the cell lysis buffer. During the protein marker release from the Ni–His linkage we assume that the competitive binding of imidazole to the Ni^{2+} is not affected by the molecular size of protein markers conjugated to the His tag, given that the molecular mass of imidazole is 68 Da. The lowest imidazole concentration studied was 15 mmol imidazole per 15 mL, which was in excess as compared to the concentration of the His-tagged Protein A (0.12 nmol per 15 mL). Given the orders-of-magnitude excess of imidazole, we assume that the imidazole concentration in the buffer is not significantly reduced over the 30 s time course of protein marker release and cell lysis, even for this lowest imidazole concentration condition. We opt to study Protein A as a model marker protein for the release because Protein A is a low-molecular mass marker (39 kDa) that enables measurement of the protein fraction bound on microparticles using wide-field fluorescence microscopy—the unbound protein diffuses away quickly from the region of interest (estimated diffusion coefficients, 36.1 $\mu m^2\ s^{-1}$ at 4 °C to 158 $\mu m^2\ s^{-1}$ at 55 °C).[60,61] The Protein A release kinetics at the 1 M imidazole

concentration and at 4 °C yield a protein marker release half-life of 49.2 s (95% confidence interval, CI = 39.0–65.9 s) and a dissociation rate constant of 0.014 s^{-1} (n = 3 particles, coefficient of variation, CV = 123.7%; **Figure 4.2D**). For the same imidazole concentration, we elevated the temperature of the cell lysis buffer and observed dissociation rate constants of 0.044 s^{-1} (at 23 °C; n = 3 particles, CV = 51.5%) and 0.16 s^{-1} (at 55 °C; n = 3 particles, CV = 40.6%), with the latter condition yielding a protein release half-life of 4.46 s (95% CI = 4.01–4.97 s). Within 30 s, more than 80% of the His-tagged Protein A was released from the microparticles at 55 °C (**Figure 4.2D**). We scrutinized the dissociation rate constant for a range of higher imidazole concentrations at the most elevated temperature condition. We observed the shortest release half-life (4.46 s) with a 1 M imidazole concentration at 55 °C (**Figure 4.4**). Because the estimated time scale of the His-tagged Protein A (39 kDa) diffusing out of a microwell is similar to the protein release half-life in 55 °C 1 M imidazole, the release reaction is rapid compared to diffusion of protein out of the well.[60,61] Any protein markers with ≥39 kDa would remain at higher concentrations in the microwell prior to single-cell protein PAGE. As the protein marker delivery would be concurrent with the rapid cell lysis step, we selected the 1 M imidazole at 55 °C as the condition to trigger release of His-tagged protein markers.

Investigating the use of protein-loaded microparticles as a protein abundance standard. We first sought to investigate whether protein-loaded microparticles could be used to load a replicate amount of protein into each microwell to serve as a protein abundance standard. We hypothesized that protein-loaded microparticles could be used to deposit an equal amount of fluorescently labeled standard protein into each well, so that technical variation in protein capture and detection could be determined based on variations in the amount of photo-immobilized and immunoprobed standard protein, respectively (**Figure 4.5**). While the mechanism of protein release from microparticles differs from the mechanism of protein release from mammalian cells, proteins from a microparticle-based abundance standard would be subject to and could indicate many of the same sources of technical variation (i.e., variable diffusive protein loss, variable photo-immobilization and immunoprobing efficiency) that impact the measured abundance of cellular proteins.

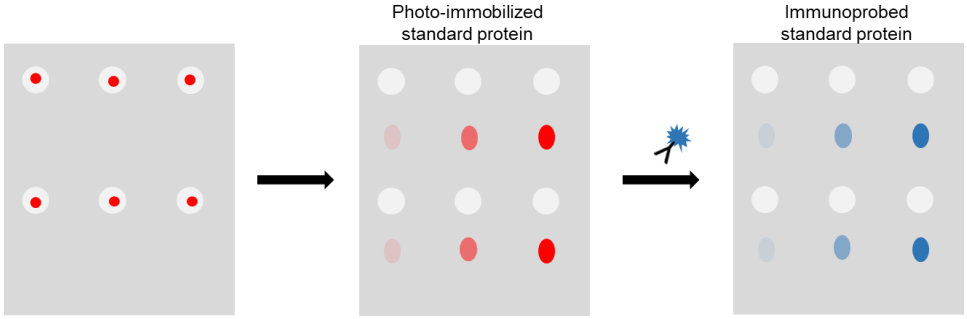

Figure 4.5. Microparticles loaded with equal amounts of protein may serve as a protein abundance standard to identify technical variation in protein capture and detection efficiency. Protein-loaded microparticles would be used to deposit equal amounts of protein into each microwell (left). After lysis, electrophoresis, and photo-immobilization, the abundance of the fluorescently-labeled photo-immobilized standard protein in each separation lane indicates technical variation protein capture (center), while abundance of immunoprobed standard protein indicates technical variation in protein detection (right).

To use protein-loaded microparticles as an abundance standard without the need for additional pre-immunoblot imaging steps, the microparticles must be able to deposit an equal amount of protein into each microwell. Thus, we sought to characterize the amount of microparticle-to-microparticle variation in protein loading, to assess whether protein-loaded microparticles could serve an abundance standard. We characterized microparticle protein loading

with two different proteins, using either the previously optimized incubation concentration (termed 1× concentration) or 2× concentration, and using either 2 h (previously optimized) or 4 h incubation times (**Table 4.2**). After incubation with protein, all microparticles underwent the standard wash steps (see Materials & Methods). The nickel magnetic microparticles used in this study have a binding capacity of 1–5.5 mg protein per mL of microparticle suspension, according to manufacturer specifications.[62] A previous study of His-tagged protein loading on nickel microspheres found that microspheres saturated with protein had less variation in protein loading (coefficient of variation [CV] of protein loading was 11-18%) than unsaturated microspheres (CV 30-40%).[63] Thus, to minimize variation in protein loading, all of the protein incubation concentrations used to load microparticles are within or above the manufacturer-specified range of protein binding capacity.

After protein loading and standard wash steps, the size and fluorescence of 100s–1000s of microparticles were quantified from widefield fluorescence microscopy images (see Materials & Methods). Despite incubating the microparticles with saturating concentrations of protein, we observed substantial variation in microparticle protein loading – summed microparticle fluorescence (a proxy for total loaded protein) among microparticles of each loading condition had CVs of 49.1–66.9%. To evaluate whether the variation in the amount of protein loaded arises from variation in microparticle size or variation in protein loading density, we also quantified the variation in mean microparticle fluorescence (a proxy for protein loading density, which is independent of microparticle size) (**Table 4.2**, **Figure 4.6**). The CVs of mean microparticle fluorescence (23.2–39.8%) were approximately half the CVs of total microparticle fluorescence, indicating that variation in both microparticle size and protein loading density contribute to the variation in the total amount of protein loaded per microparticle. Increasing protein incubation time or concentration (beyond manufacturer-specified protein binding capacity of the microparticles) both significantly increase mean microparticle fluorescence (**Figure 4.7**), which suggests that microparticles are not saturated with protein. We hypothesize that the increased protein loading at concentrations above the manufacturer-specified binding capacity may be due to nonspecific protein adsorption to the microparticle, and would propose that future studies investigate the impact of increasing the imidazole concentration of the wash buffer to minimize nonspecific protein adsorption and identify the protein incubation concentration which saturates the microparticle binding capacity.

Table 4.2. Microparticle-to-microparticle variation in protein loading.

Protein	Concentration (mg protein/mL microparticle suspension), relative to optimized loading concentration	Incubation time (h)	Number of microparticles analyzed	CV, mean fluorescence	CV, total fluorescence
Protein G	11 (1×)	2	4193	23.2%	49.1%
	11 (1×)	4	3409	24.9%	51.5%
	22 (2×)	2	462	26.7%	51.8%
	22 (2×)	4	2079	30.1%	56.6%
Protein A/G	3.2 (1×)	2	2389	30.0%	57.8%
	6.4 (2×)	2	174	39.8%	66.9%

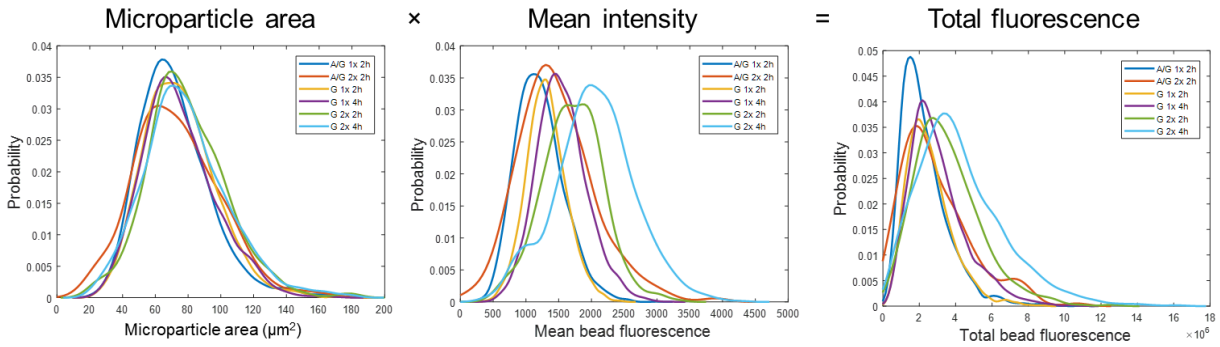

Figure 4.6. Histograms of microparticle area, mean intensity, and summed intensity distributions for different proteins and loading protocols. The total microparticle fluorescence from a 2D fluorescence micrograph is the product of the microparticle area and mean fluorescence intensity in the image.

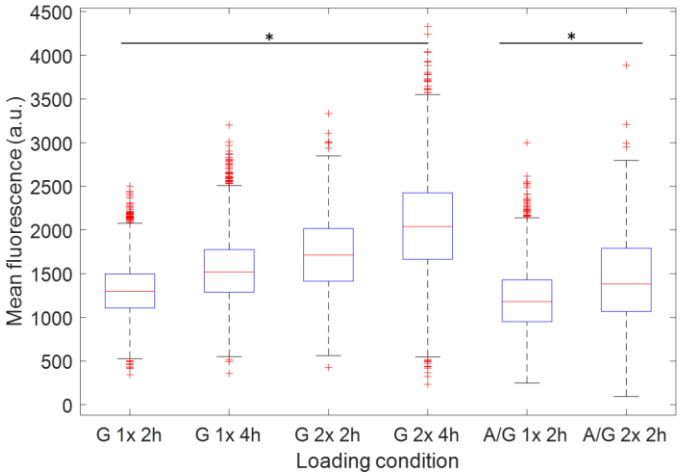

Figure 4.7. Protein loading density on microparticles increases significantly with greater incubation concentration and incubation time. Boxplots of mean fluorescence of microparticles incubated with Protein G or Protein A/G with the concentrations and durations as specified in **Table 4.2**. Increased concentration (1×, 2×) or incubation time (2 h, 4 h) yields a significant increase in mean microparticle fluorescence (i.e., protein loading density). Kruskal-Wallis test with post-hoc Tukey test, $p<0.05$.

Overall, we observe substantial heterogeneity in the amount of protein loaded per microparticle, due to both variation in microparticle size and protein loading density. Though the protein:microparticle ratios used here are within or above the manufacturer-specified protein binding capacity of the microparticles, we find that protein loading density increases with incubation concentration, as well as incubation time. The microparticle protein loading variation is greater than previously reported variation in both saturated and unsaturated protein loading on nickel microspheres[63], which we hypothesize may be due to variable nonspecific protein adsorption and other factors unique to the surface properties and polydispersity of the nickel microparticles used in this study. Based on the observed heterogeneity in protein loading, we find that further optimization is required to develop more uniformly-loaded microparticles suitable for use as protein abundance standards in single-cell immunoblotting. However, we hypothesized that protein-loaded microparticles can serve as a molecular mass standard, which does not require homogenous protein loading.

Validating the protein marker as a molecular mass standard. After rapid release of the protein markers in the microwell, we scrutinized the protein marker electromigration during single-cell

protein PAGE (**Figure 4.2E** and **Figure 4.8**). At 30 s of cell lysis and protein marker release, protein PAGE was initiated by applying an electric field (E = 40 V cm^{-1}) for 25 s. Separated protein peaks were immobilized with a 45 s UV exposure of the benzophenone in the polyacrylamide gel. After photoblotting, Ferguson analysis of the protein electromigration was performed.[36,43] In protein sizing (gel electrophoresis with sodium dodecyl sulfate (SDS)), we expect a log-linear relationship between the molecular mass and observed electrophoretic mobility of each target. Log-linear fitting of the protein markers yielded $R^2 > 0.97$ for >300 PAGE separation lanes (**Figure 4.8A**), which is comparable to the log-linearity of many other slab gel and capillary electrophoresis systems.[64–66] The final protein peak location had CV ranging from 2.2% to 11.0% depending on the protein marker considered ($\mu \pm \sigma$ of CV across 3 chips: ICAM1, 9.41 ± 2.06; KDR, 6.29 ± 2.03; EpH B4, 5.00 ± 2.30; CHI3L1, 5.07 ± 2.53; n_{chip1} = 147, n_{chip2} = 104, n_{chip3} = 340; **Table 4.3**).

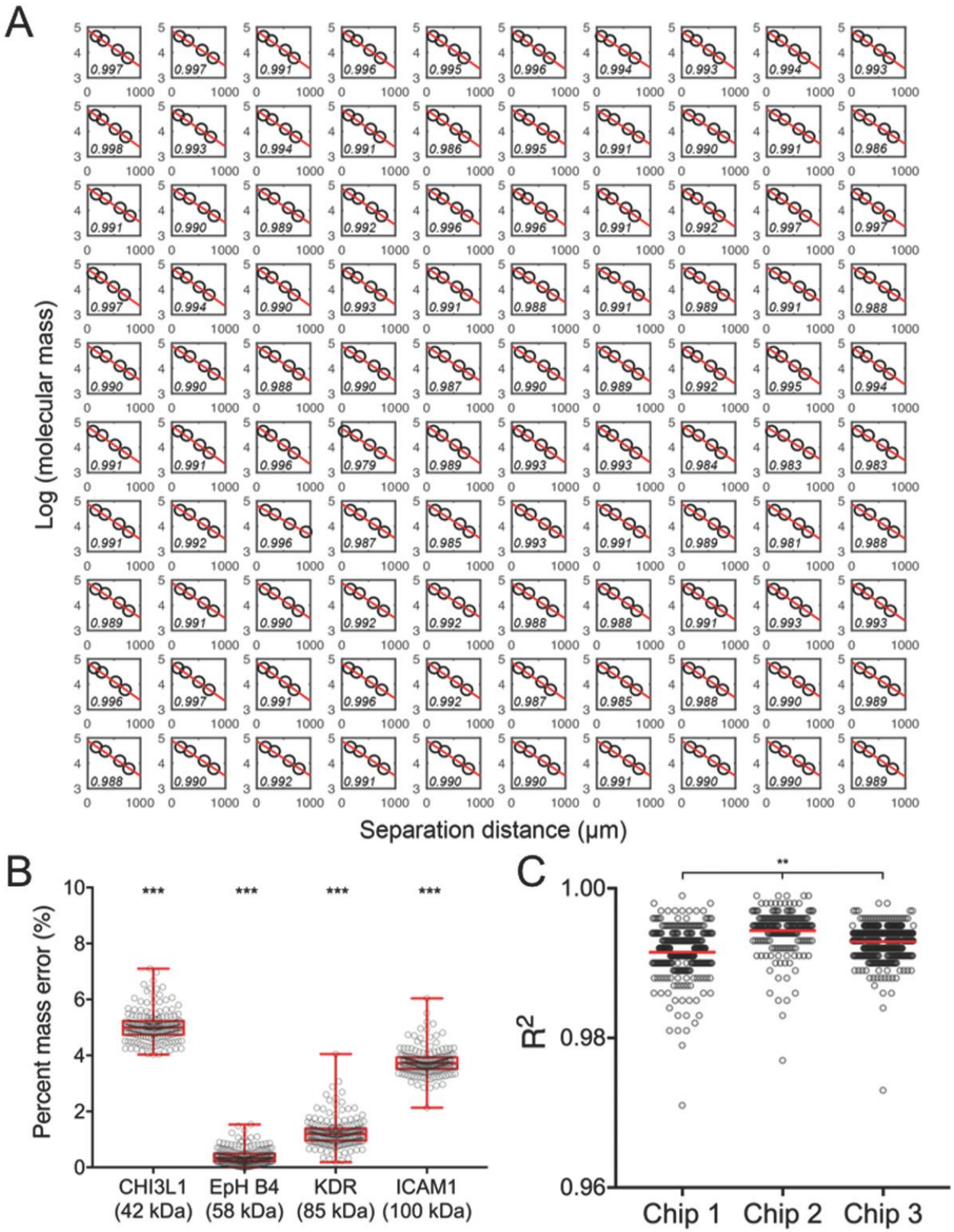

Figure 4.8. Ferguson analyses of protein markers support their utility as an estimator of molecular mass for endogenous protein targets. (A) Log-linear regression fitting of protein markers (ICAM1, KDR, EpH B4, CHI3L1) in 100 representative single-cell PAGE protein separations. R^2 value for each linear fit is shown in lower left of each

plot. Black circles, protein markers; red lines, linear regression fits. B) Box and scatter plots of percent mass errors between expected and estimated (from the log-linear regression fits) molecular masses of protein markers in a single-cell western blot chip. Each black circle represents percent mass error for each PAGE separation lane. Box extents indicate 25th and 75th quantiles; black line at box midpoint indicates median value; whiskers extend to minimum and maximum values. Kruskal–Wallis test with Dunn's multiple comparisons test, ***$p < 0.0001$, $n = 168$ PAGE separation lanes. C) Scatter plots indicate chip-to-chip R^2 values for linear regression fits. Black circles indicate R^2 values for PAGE separation lanes; red line indicates mean value for each chip ($\mu_1 = 0.991$, $\mu_2 = 0.994$, $\mu_3 = 0.993$); $n_1 = 327$, $n_2 = 204$, $n_3 = 516$; one-way ANOVA test, $p < 0.001$, Cohen's $d < 0.2$.

Table 4.3. Quantitation of peak location for microparticle-delivered protein ladder markers from 3 chips.

	Chip 1			Chip 2			Chip 3		
Protein	Mean (μm)	Standard deviation (μm)	CV (%)	Mean (μm)	Standard deviation (μm)	CV (%)	Mean (μm)	Standard deviation (μm)	CV (%)
ICAM1	180.74	13.85	11.0	125.72	12.75	10.14	175.78	12.44	7.08
KDR	349.37	22.30	7.91	281.76	19.59	6.95	339.42	13.61	4.01
EpH B4	624.28	35.35	6.50	544.14	33.40	6.14	616.48	14.48	2.35
CHI3L1	817.90	49.34	6.65	741.44	47.43	6.40	809.54	17.40	2.15

Across each device, we found no observable spatial dependence on the *y*-intercept values of the log-linear regression but did observe a decrease in the slope across the width of the chip (**Figure 4.9**). Recognizing that a $\Delta E = \approx 1$ V cm^{-1} across the width of the chip (left to right) would result in the observed slope variation, we hypothesized that the apparatus has a slight offset in electrode pair spacing from one end of the chip to the other (**Figure 4.9**).

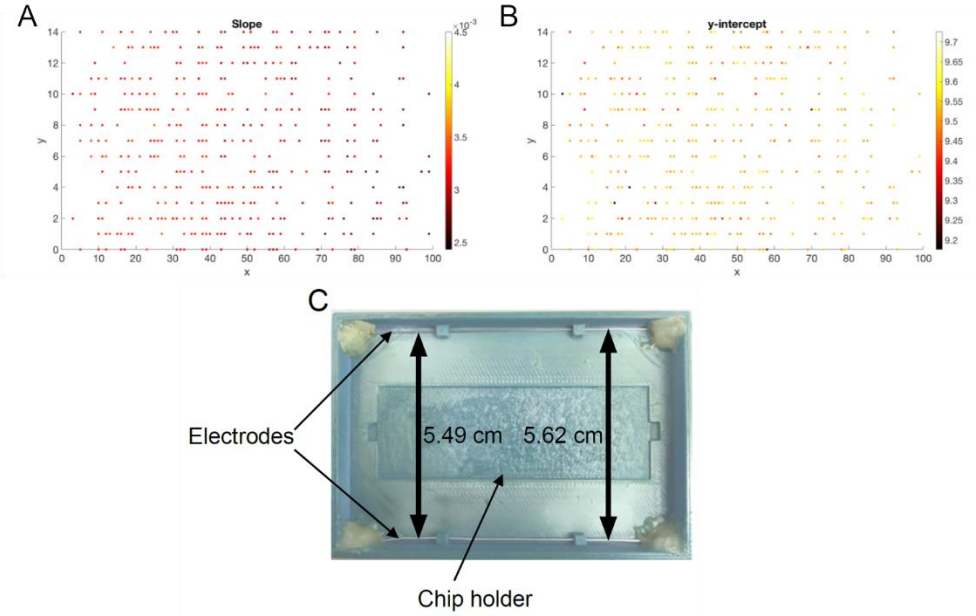

Figure 4.9. Variation of protein ladder electromigration in a single-cell immunoblot chip. (A) Heat map displaying variance of log-linear regression slope values from microwells with protein ladder markers. (B) Heat map displaying variance of log-linear regression y-intercept values from microwells with protein ladder markers. (C) A top view of the electrophoretic chamber. The chamber is composed of two electrodes and a holder for the single-cell western blot chip. Distance difference between the electrodes, measured at the ends of the holder in x-axis, leads to $\Delta E = \sim 1$ V/cm from left to right across the chip.

For each protein marker, we compared the expected molecular mass to the measured molecular mass. An analysis of 168 single-cell PAGE lanes gave a difference between the two values of <5%, with an interquartile range <1% (**Figure 4.8B**), for all protein markers that passed

quality control (see Materials & Methods). Although peak location CV values are not significantly different among all four markers (**Table 4.3**, $n = 3$ chips with 147, 104, and 340 peaks, respectively; one-way ANOVA test, $p > 0.5$), the percent mass errors of the smallest ladder component (CHI3L1, 42 kDa) and the largest ladder component (ICAM1, 100 kDa) were significantly higher than those of EpH B4 (58 kDa) and KDR (85 kDa) ($\mu \pm \sigma$ of percent mass error: ICAM1, 3.77 ± 0.49; KDR, 1.24 ± 0.53; EpH B4, 0.39 ± 0.30; CHI3L1, 5.05 ± 0.57; Kruskal–Wallis test with Dunn's multiple comparisons test, $^{***}p < 0.0001$, $n = 168$ PAGE separation lanes; **Figure 4.8B**). The slightly higher mass errors in CHI3L1 and ICAM1 were ascribable to CHI3L1 and ICAM1 peaks electromigrating less than what the log-linear regression fitting expected, resulting in estimated masses lower than the expected masses. High and low molecular mass proteins should be included in each set of protein marker standards for most accurate estimation of molecular mass, which agrees with previous work demonstrating that the use of a pair of high and low molecular mass protein standards controlled for technical variation in migration rate in a capillary gel electrophoresis platform.[65]

Next, we examined chip-to-chip variation in molecular mass estimation to assess reproducibility of the protein marker as a size standard (**Figure 4.8C**, **Figure 4.10**). Regarding the goodness of the log-linear regression fit, we observed $R^2 > 0.97$ ($n = 3$ chips; **Figure 4.8C**). One-way ANOVA tests indicate that the distributions of the R^2 values are significantly different among the chips. However, the magnitude of the chip-to-chip difference in R^2 values is minimal, with a Cohen's $d < 0.2$ (**Figure 4.8C**). We further investigated technical variation across the chips by analyzing percent mass errors of the protein markers. Although the slight run-to-run difference in the gel electrophoresis duration might contribute to the fact that distributions of percent mass errors are significantly different across chips (**Figure 4.10**), we observed consistent protein electromigration (CV of peak locations <12%) and <10% mass errors in sizing of the protein markers (42–100 kDa protein masses; **Figure 4.10** and **Table 4.3**).

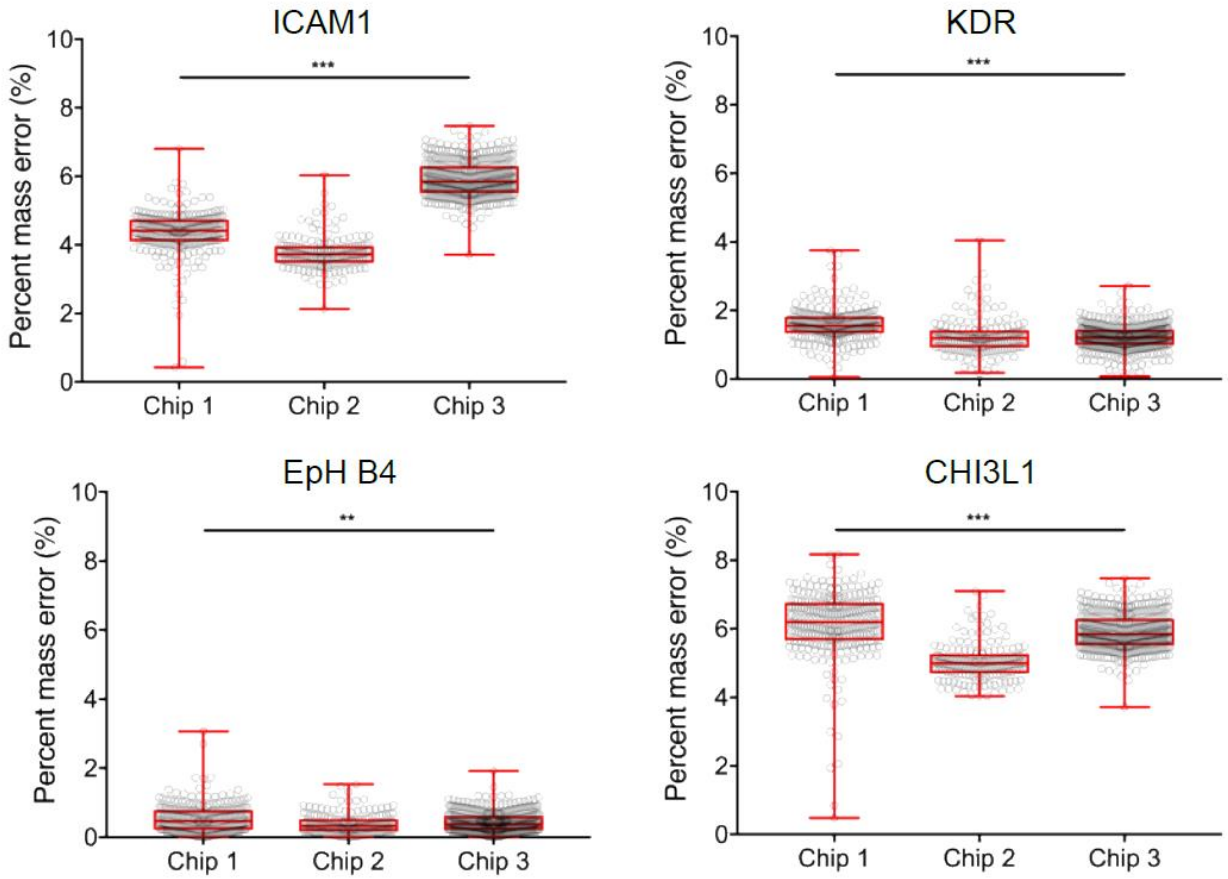

Figure 4.10. Scatter plots of percent mass error between expected and estimated molecular weight of protein markers across 3 chips. Each black circle represents percent mass error per separation lane. Red box ends indicate 25th and 75th quantiles; middle red line at box indicates median value; whiskers extend to minimum and maximum values. Kruskal-Wallis test, ***p < 0.0001, **p < 0.001; n_{chip1} = 257, n_{chip2} = 168, n_{chip3} = 415.

Given that not all cell-containing microwells were populated with microparticles, we sought to assess the impact of protein marker performance when employing protein markers proximal to single-cell PAGE separations lanes as size standards. We used a semi-variogram analysis of the log-linear fitting coefficients and determined that molecular mass estimates of protein targets are accurate using proximal protein marker electromigration, if the protein markers are released in a microwell that is located ≤2.5 mm (center-to-center pitch) from the microwell containing the cell of interest (**Eq. 4.2**, **Figure 4.11**).[56,57] We observed no significant difference (Kruskal–Wallis test with Dunn's multiple comparisons test, $p > 0.05$) in molecular mass error when protein sizing of endogenous targets was performed either using the protein markers from the same PAGE separation lane or in "proximal" separation lanes (i.e., located ≤2.5 mm from the PAGE separation lane containing the proteins targets; **Figure 4.12**).

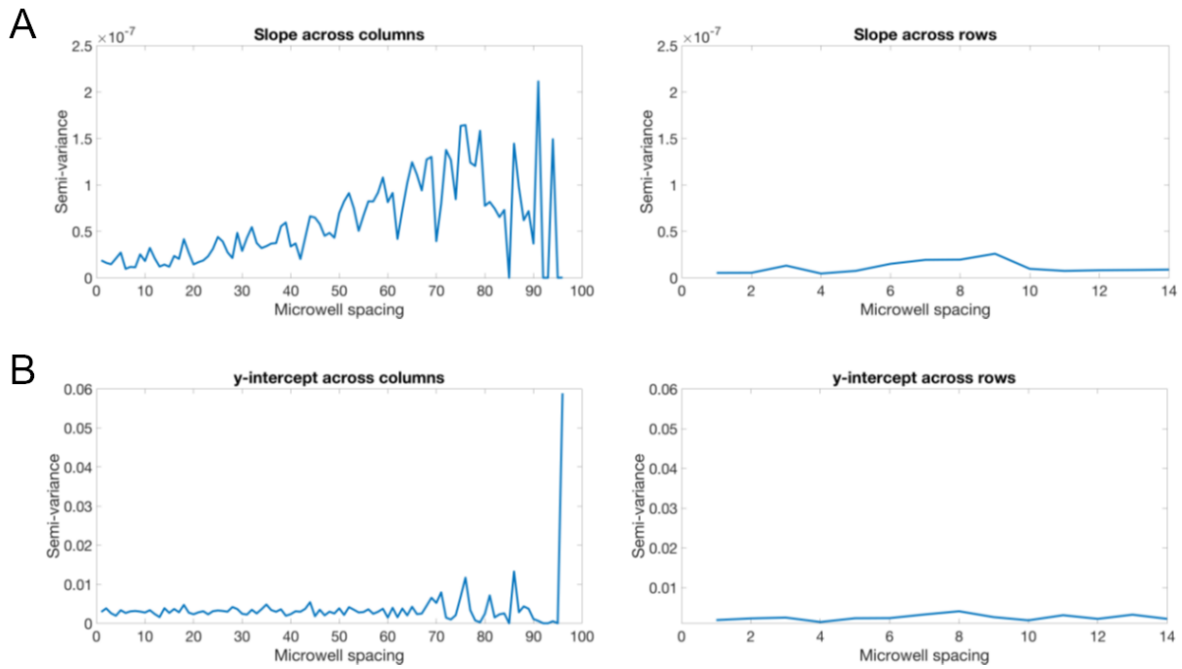

Figure 4.11. Spatial analysis of protein ladder electromigration. (A) Semi-variogram of the slope values at different microwell spacing across the single-cell western blot array columns (left) and rows (right). Across the columns, slope variance begins to increase when microwell spacing > 10. The slope variance does not vary across rows. Microwell spacing (center-to-center pitch) across columns, 250 µm and across rows, 1 mm. (B) Semi-variogram of the y-intercept values at different microwell spacing across the single-cell western blot array columns (left) and rows (right). The y-intercept semi-variograms indicate that variance does not dependent on microwell locations across the device.

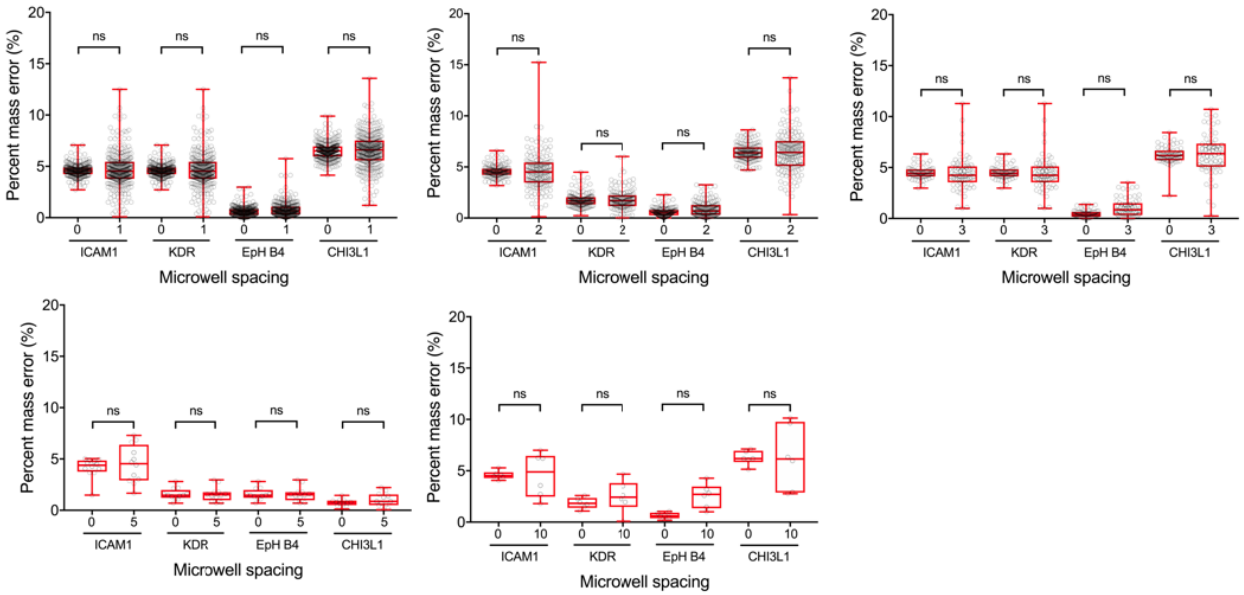

Figure 4.12. Scatter plots indicating percent mass error distribution of protein markers at different microwell spacing (A) 1, (B) 2, (C) 3, (D) 5, (E) 10. Each microwell spacing (center-to-center pitch) is 250 µm. After the log-linear fitting, mass of protein ladder markers at proximal microwells are measured with the log-linear regression. Each black circle represents percent mass error per separation lane. Box ends indicate 25th and 75th quantiles; middle black line at box indicates median value; whiskers extend to minimum and maximum values. Kruskal-Wallis test with Dunn's multiple comparisons test, ns: $p > 0.05$, $n_A = 318$; $n_B = 152$; $n_C = 67$; $n_D = 12$; $n_E = 6$.**Imidazole interferes**

with protein photoblotting. After protein PAGE, efficient photoblotting is critical for protein detection and immunoprobing readout of the single-cell western. During photoblotting, we expected interference between the imidazole (1 M) and the UV-activated benzophenone group, as benzophenone can abstract hydrogen from a secondary amine group on the imidazole, thus allowing benzophenone to form a covalent bond with the high concentration imidazole (**Figure 4.13**).[67] In some sense, the imidazole would act to "block" the benzophenone from forming covalent bonds with protein targets. When photoblotting was performed in the presence of 1 M imidazole, we observed just 3.7% of separation lanes with protein marker signals that exceeded the minimum signal to noise ratio (SNR), as described in the quality control protocol (**Figure 4.14A,F**, see Materials & Methods).

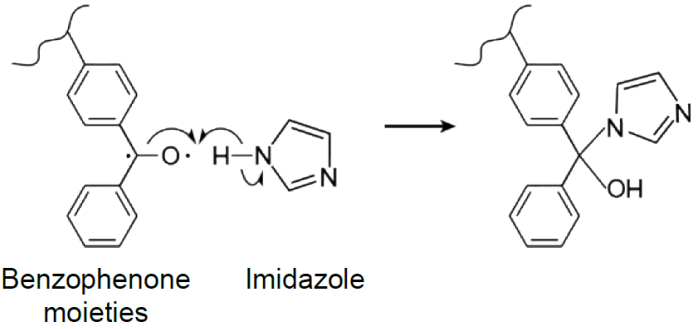

Figure 4.13. Mechanism for imidazole reaction with UV-activated benzophenone moieties incorporated in a polyacrylamide gel.

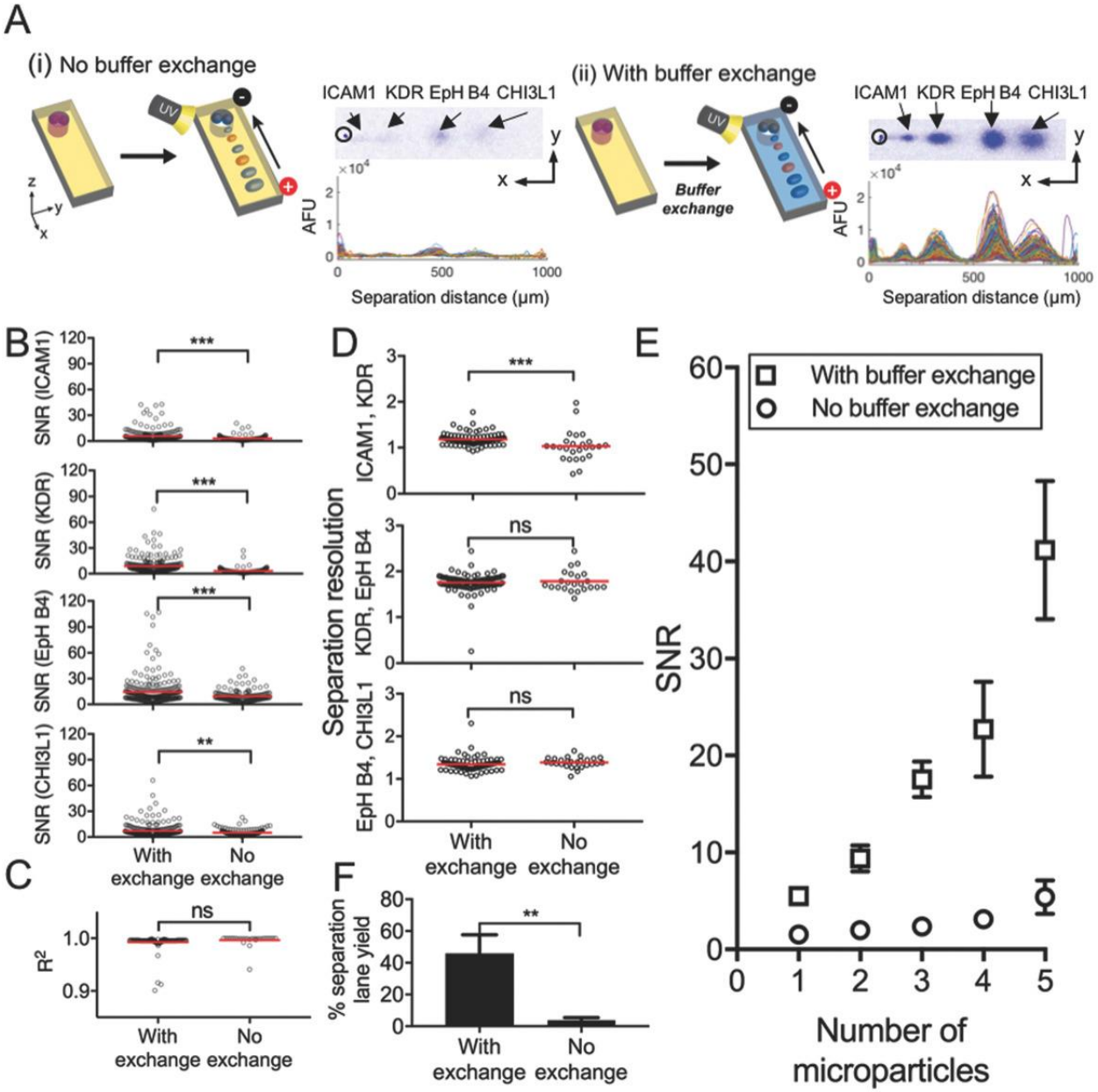

Figure 4.14. Imidazole interferes with protein blotting efficiency thus necessitating buffer exchange prior to UV exposure. (A) False-color micrographs of single-cell protein PAGE with 1 M imidazole present during photoblotting (left) and with buffer exchange to dilute imidazole prior to photoblotting (right). Each intensity plot represents the protein markers along one PAGE separation lane. B) Scatter plots of signal-to-noise ratio (SNR) of protein marker peaks with and without buffer exchange ($n_{with\_exchange}$ = 249, $n_{no\_exchange}$ = 149). C) Scatter plot indicating R^2 values with and without buffer exchange ($n_{with\_exchange}$ = 107, $n_{no\_exchange}$ = 27). D) Scatter plots of separation resolution between two protein markers with or without buffer exchange ($n_{with\_exchange}$ = 107, $n_{no\_exchange}$ = 27). E) Scatter plot of KDR peak SNR as a function of the number of microparticles in the microwell (n = 4 microwells, error bar is standard deviation). Each square represents a mean SNR value of KDR with buffer exchange. Each circle represents a mean SNR value of KDR without buffer exchange. With buffer exchange, one microparticle per microwell is sufficient to detect all protein markers with SNR ≥ 3. F) Bar graph representing fraction of protein markers that passed quality control (SNR ≥ 3, R^2 for Gaussian curve fitting ≥ 0.7). Error bars represent standard deviations, n = 3 chips with exchange and without exchange. Black circles represent data per PAGE separation lane; red lines represent mean values; unpaired t test, ***p < 0.0001, **p < 0.002, ns = no significance (p > 0.05).

To enhance the photoblotting efficiency of the protein markers, we modified the standard single-cell western blot workflow to include a buffer-exchange step between the chemical cell lysis step and the protein PAGE step (see Materials & Methods). This buffer exchange step reduces the imidazole concentration in the polyacrylamide gel matrix prior to the UV photoblotting step. A similar approach to buffer exchange has been employed to reduce Joule heating during single-cell electrophoresis.[68] Comparing mean SNR values for the protein markers, the SNR with the buffer exchange step was >20% greater than the SNR without the buffer exchange step (**Figure 4.14B**). For endogenous proteins in each MCF-7 cell lysate, the buffer exchange increased immunoprobing signal from β-tubulin (β-TUB), cytokeratin 8 (CK8), and GAPDH to levels observed with no imidazole included in the chemical lysis step (**Figure 4.15**).

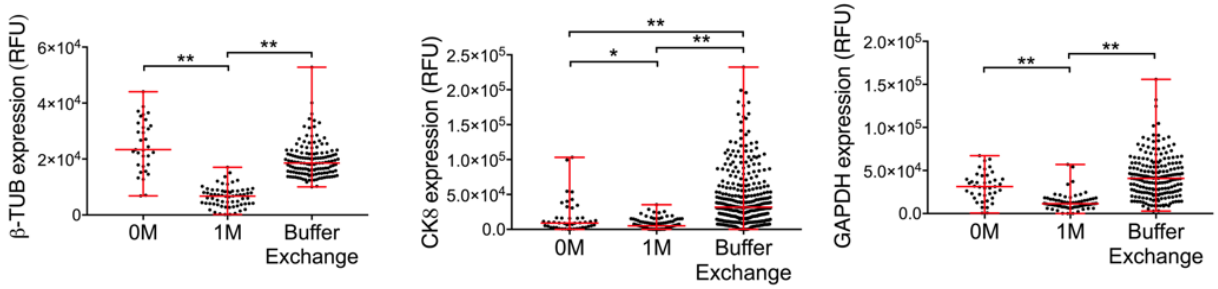

Figure 4.15. Scatter plots of measured β-TUB, CK8, GAPDH abundance under different lysis buffer conditions. After protein lysis and release, buffer exchange eliminates imidazole that interferes with UV-activated protein photocapture. Each black dot represents an endogenous protein from individual cells per microwell. Red lines indicate median with range from maximum to minimum expression values. Kruskal Wallis test, Dunn–Šidák corrections, *p < 0.05, **p < 0.0001. β-TUB: $n_{0M} = 33$, $n_{1M} = 66$, $n_{buffer\_exchange} = 141$; CK8: $n_{0M} = 46$, $n_{1M} = 116$, $n_{buffer\_exchange} = 328$; GAPDH: $n_{0M} = 41$, $n_{1M} = 69$, $n_{buffer\_exchange} = 201$.

Considering total assay performance, we next asked whether the buffer exchange might affect the goodness of fit in the log-linear regression and separation resolution (SR) of the protein markers (**Figure 4.14C,D**, **Eq. 4.1**). The goodness of fit distribution of R^2 values with the buffer exchange was not significantly different from that without the buffer exchange (unpaired *t*-test, $p = 0.20$, $n_{with\_exchange} = 107$, $n_{no\_exchange} = 27$; **Figure 4.14C**). Furthermore, no decrease in SR between the protein markers was detectable (unpaired *t*-test; $SR_{ICAM1\&KDR}$, $p = 0.0003$; $SR_{KDR\&EpH\ B4}$, $p = 0.55$; $SR_{EpH\ B4\&CHI3L1}$, $p = 0.19$; **Figure 4.14D**). For each adjacent protein pair in a four-protein ladder spanning ~40-100 kDa, SR>1 was achieved. The buffer exchange here utilized room temperature lysis buffer that simply omits imidazole, while still containing high concentrations of conductive ionic detergents that result in Joule heating-induced peak dispersion during electrophoresis. Joule heating may be reduced with further optimization of the exchanged buffer (e.g., by reducing the concentration of conductive components).[68]

Detection threshold: Minimum number of microparticles per microwell. We sought to assess the number of microparticles per microwell required to detect protein markers with an SNR ≥ 3. We used the KDR protein to assess the relationship between SNR of protein peaks ($E = 40$ V cm^{-1}; $\Delta t = 25$ s) and the number of microparticles per microwell. As expected, the SNR increased with an increasing number of microparticles per microwell (**Figure 4.14E**). Without buffer exchange, >3 microparticles per microwell were required to achieve an SNR ≥ 3 (**Figure 4.14E**). By contrast, the buffer exchange and dilution of imidazole yielded SNR > 5 with a single microparticle in a microwell (**Figure 4.14E**). As compared to just 3.7% of separation lanes yielding suitable detection signal without the buffer exchange, under these conditions we observed 55% of lanes yielding an acceptable signal (**Figure 4.14F**).

In formulating "design rules" for protein sizing markers based on these findings, one microparticle per microwell was sufficient for detection of the protein markers in single-cell western blotting. In cases where no microparticles are loaded into a cell-laden microwell, proximal microwells containing protein markers may be used for cellular protein sizing. In cases where protein targets are >100 kDa, microparticle loading of the cell-laden microwell should not exceed 3 microparticles, as we observed nonspecific signal proximal to each microwell—that may interfere with detection of large protein markers—when ≥4 microparticles were seated in a single microwell (**Figure 4.16**).

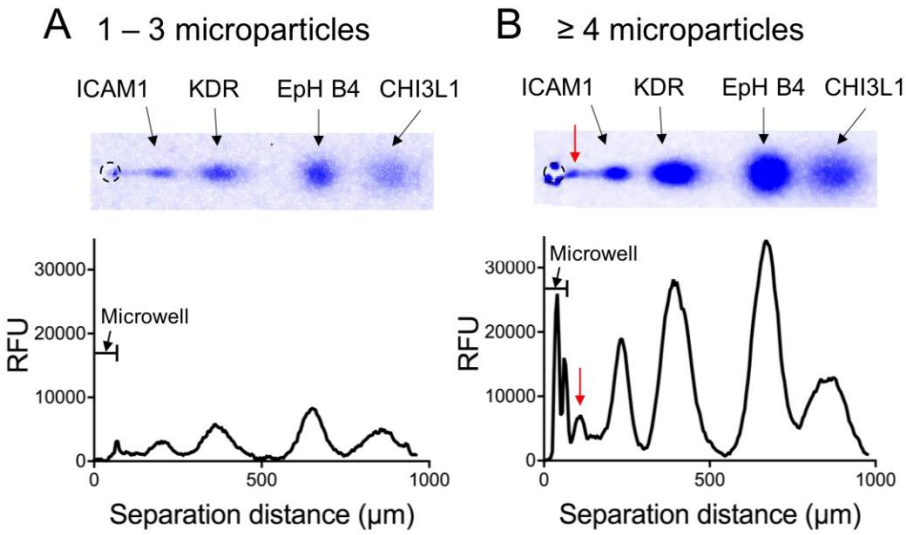

Figure 4.16. Protein marker design rule for sizing larger protein targets (> 100 kDa) from microwells populated with multiple microparticles. (A) False-color micrograph reports protein sizing from a microwell seeded with 1 microparticle. (B) False-color micrograph reports protein sizing from a microwell seeded with ≥ 4 microparticles. Red arrow indicates marker-derived background signal near the microwell, which may interfere with detection of large molecular mass protein targets if analyzed from cell lysate injected from the same microwell.

Determining molecular mass of endogenous protein targets in MCF-7 cells. Next, we applied the protein markers to estimate the molecular masses of endogenous proteins from single MCF-7 breast cancer cells (**Figure 4.17**). For microwells containing both individual MCF-7 cells and ≥1 microparticles, we performed single-cell western blotting and concurrently resolved protein markers and endogenous proteins in all PAGE separation lanes (**Figure 4.17A**).

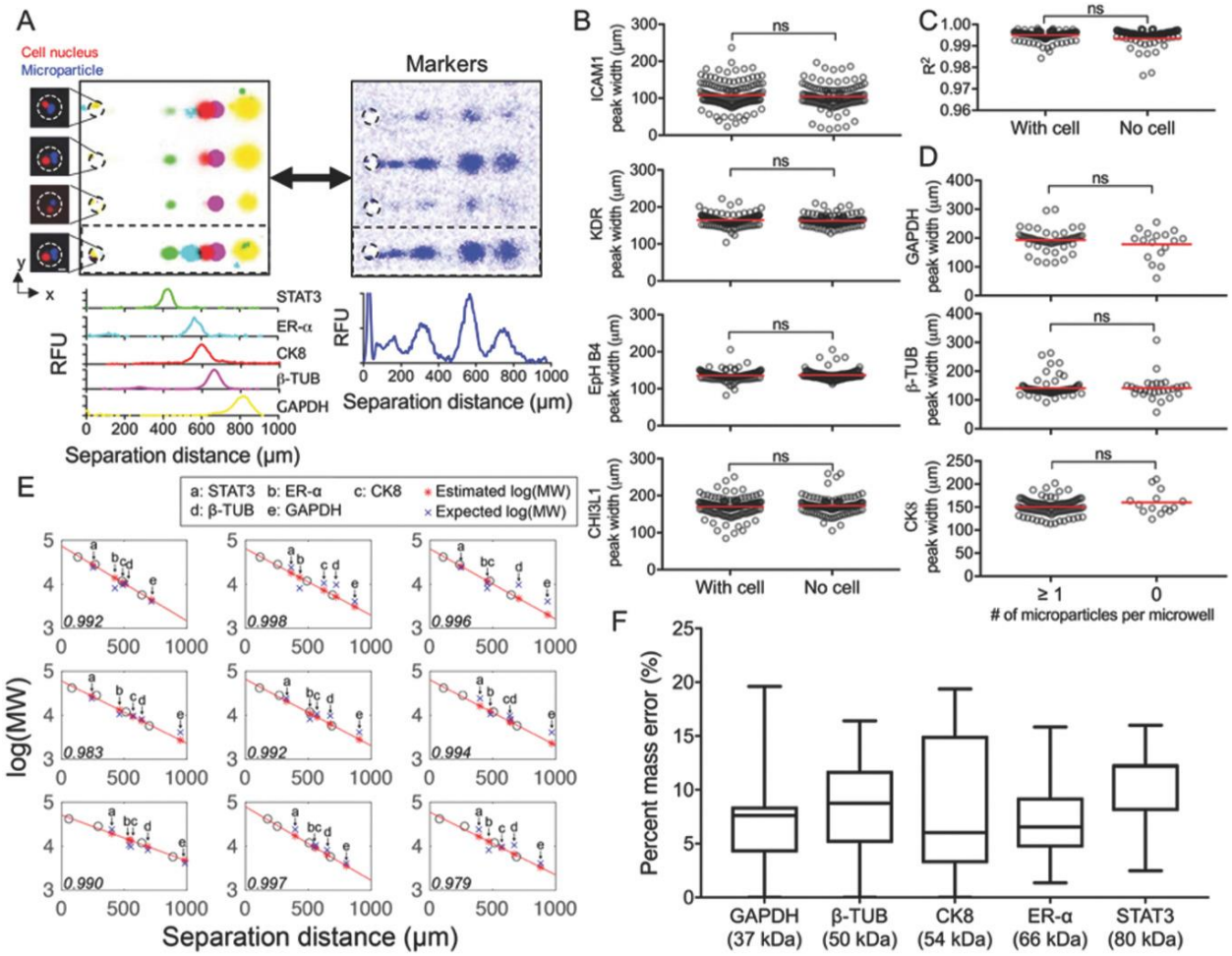

Figure 4.17. Protein markers estimate protein target molecular mass in single-cell western blotting. (A) Top: false-color micrographs display microwells containing an MCF-7 cell (red) and microparticles (blue). Scale bar, 10 μm. Bottom: intensity profiles and false-color micrographs of four representative PAGE lanes containing both endogenous proteins (STAT3, 80 kDa; ER-α, 66 kDa; CK8, 54 kDa; β-TUB, 50 kDa; GAPDH, 37 kDa) and protein markers (blue). B) Scatter plots indicate no significant difference in peak widths of protein markers with and without cells in microwells. Black circles represent peak width of each protein marker; red lines represent mean values; unpaired t-test and F-test, ns = no significance ($p > 0.05$); $n_{with\_cell} = 141$, $n_{no\_cell} = 127$. C) Scatter plot indicates no significant difference in R^2 values from linear regression with and without a cell in the microwell. Black circles indicate R^2 values per separation lane; red lines represent mean values; unpaired t-test and F-test, ns = no significance ($p > 0.05$); $n_{with\_cell} = 141$, $n_{no\_cell} = 127$. D) Scatter plot representing no significance difference in GAPDH ($n_{\geq 1} = 55$, $n_0 = 17$), β-TUB ($n_{\geq 1} = 77$, $n_0 = 28$), and CK8 ($n_{\geq 1} = 97$, $n_0 = 14$) peak widths in microwells with or without microparticles. Black circles indicate endogenous protein peak width per separation lane; red lines represent mean values; Mann–Whitney test, ns = no significance ($p > 0.05$). E) Representative log-linear regression plots display estimated (*) and expected (x) molecular masses of endogenous proteins extracted from linear regression of the protein marker. R^2 value for each log-linear fit is in the lower left of each plot. Black circles, protein marker; red lines, log-linear regression fitting. F) Box plots depict % error between estimated and expected molecular masses of STAT3 (n = 95 cells), ER-α (n = 7 cells), CK8 (n = 794 cells), β-TUB (n = 551 cells), and GAPDH (n = 430 cells) from the Ferguson analysis plots. Box extents indicate 25th and 75th quantiles; black line at box midpoint indicates median value; whiskers extend to minimum and maximum values.

We sought to identify any confounding interactions when running protein PAGE on the protein marker and single-cell lysate from the same microwell. We found no significant difference in the distribution of the peak widths of the protein markers in the presence of MCF-7 cells ($\mu \pm \sigma$; ICAM1: 108.5 ± 34.5 μm, KDR: 165.6 ± 22.8 μm, EpH B4: 135.8 ± 12.5 μm, CHI3L1: 170.4

± 24.2 μm), as compared to the same protein marker analysis without cells present (μ ± σ; ICAM1: 118.1 ± 27.1 μm, KDR: 160.3 ± 25.8 μm, EpH B4: 137.3 ± 12.1 μm, CHI3L1: 176.5 ± 21.9 μm). The comparison suggests that negligible interference arises from coloading, cell lysis concurrent with protein marker solubilization, and concurrent sample injection (**Figure 4.17B**; unpaired *t*-test and F-test, $p > 0.05$, $n_{with\_cell} = 141$, $n_{no\_cell} = 127$). The goodness of the log-linear fit to the protein markers remained $R^2 > 0.97$ and was not significantly different from conditions in which no cells were loaded into the microwells (**Figure 4.17C**; unpaired *t*-test and F-test, $p > 0.05$, $n_{with\_cell} = 141$, $n_{no\_cell} = 127$).

Reciprocally, for microwells with and without microparticles, we analyzed the immunoprobed endogenous proteins to identify any confounding effects. We probed for endogenous proteins expressed at median or higher copy numbers of the mammalian proteome.[69] GAPDH, β-TUB, CK8, ER-α, and STAT3 have copy numbers above the limit of detection for the single-cell western blot (≈27 000 copies of protein immobilized in the gel).[12,18,21] We analyzed GAPDH, β-TUB, CK8 and found that the protein peak widths were not notably affected by the presence of protein-loaded microparticles in the same microwells ([$\text{median}_{\geq 1\ \text{microparticle}}$, $\text{median}_{0\ \text{microparticle}}$]; GAPDH [193.4, 192.5 μm], β-TUB [134.3, 136.9 μm], CK8 [151.3, 151.9 μm]; Mann–Whitney test, $p > 0.05$; **Figure 4.17D**).

Next, we applied the protein markers to estimate the molecular masses of endogenous proteins from single MCF-7 cells (**Figure 4.17**). For microwells containing both individual MCF-7 cells and ≥1 microparticles, we performed single-cell western blotting and concurrently resolved protein markers and endogenous proteins in all PAGE separation lanes (**Figure 4.17A**).

Here, we utilized the log-linear regression equation developed from the protein markers and the measured peak location for each target (for ladders and single-cell western blots performed within the ≤2.5 mm mentioned earlier). We analyzed >100 single-cell western blots with protein markers that passed quality control (see Materials & Methods) and a $R^2 \geq 0.97$ for the log-linear regression. In these cases, the observed molecular masses of GAPDH (39.6 kDa), β-TUB (47.0 kDa), CK8 (54.3 kDa), and ER-α (66 kDa) and the reported molecular masses (determined by conventional slab-gel western blots) agreed with both median and mean mass errors of <10% (**Figure 4.17E,F**). Out of all endogenous protein targets, STAT3 had the highest mean (10.3%) and median (12.2%) mass error values (**Figure 4.17F**, **Table 4.4**). Conventional slab-gel western blotting reports three protein peaks within the 70–100 kDa range when probing with the STAT3 antibody (**Figure 4.18**), possibly slightly reducing the accuracy of target sizing in the single-cell western blot, which has lower resolving power than the 4 cm long separation lengths utilized for pooled cell lysate analysis in slab gels. Overall, single-cell western blotting incorporating the protein markers resulted in mean and median mass errors <12% for all endogenous protein targets from the MCF-7 cells (**Figure 4.17F**). This observed performance is comparable to the mass sizing performance of both slab-gel PAGE and microfluidic sizing chips (Agilent Bioanalyzer), which reports mass errors ≈10%.[37,64] Perhaps not surprisingly, we found lower protein target mass errors estimating mass using the microparticle-delivered protein markers as compared to using endogenous proteins from cell lysate as markers (**Figure 4.8B** and **Figure 4.17F**). For example, the mean and median mass errors for CK8 were 40% lower when determined by the microparticle-delivered protein markers, as compared to using endogenous cellular protein targets (**Figure 4.19**). We anticipate the microparticle protein marker vehicle will find utility in assigning molecular masses to proteoforms, including truncated isoforms with >20% molecular mass differences from the full-length protein (**Figure 4.17F**).[70–72] In the future, the protein marker microparticles may find application in microfluidic isoelectric focusing,[73,74] co-immunoprecipitation,[75] and to the

delivery of DNA/RNA markers for single-cell comet assays to accurately measure DNA damage and modifications.[8,15]

Table 4.4. Statistics of percent mass errors for endogenous cellular protein targets from MCF-7 cells.

Endogenous protein	Percent mass error (%)				n
	Minimum	Median	Maximum	Mean	
GAPDH	0.01	7.61	19.61	7.50	430
β-TUB	0.01	8.75	16.40	8.46	551
CK8	0.003	6.01	19.30	8.37	794
ER-α	1.35	6.54	15.82	7.18	7
STAT3	2.47	12.2	15.99	10.3	95

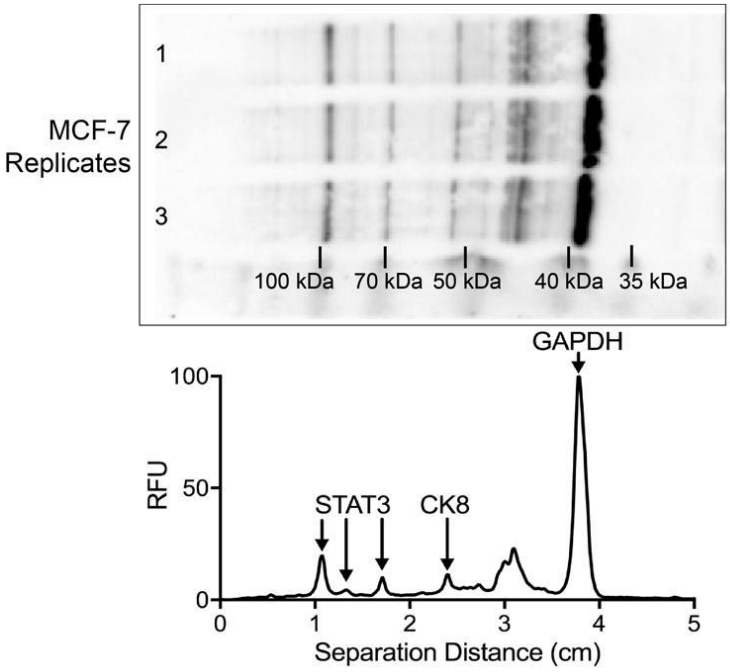

Figure 4.18. Slab-gel western blots of STAT3, CK8, and GAPDH from MCF-7 cells.

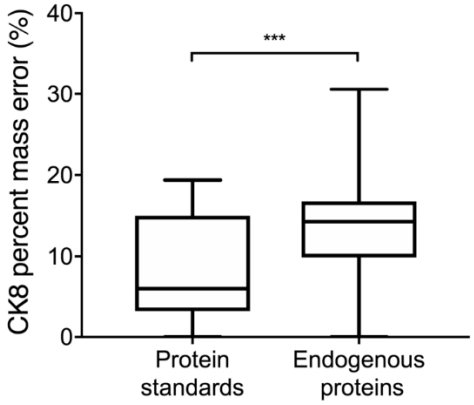

Figure 4.19. Scatter plots indicating percent mass error distribution of CK8, estimated by performing log-linear regression with protein markers or four cellular proteins (GAPDH, β-TUB, ER-α, STAT3). For protein sizing with the protein markers (n = 794), the protein markers located ≤ 10 microwell spacing apart from CK8 protein peaks

are used. For protein sizing with the endogenous proteins (n = 8820), every combination of GAPDH, β-TUB, ER-α, STAT3, and CK8 peaks within ≤ 2.5 mm is computed and evaluated. Mann Whitney test, *** $p < 0.0001$.

4.5 Conclusions

As single-cell resolution assays emerge and mature, emphasis on accuracy and reproducibility is increasing. This emphasis is relevant for single-cell resolution genomics and transcriptomics, as well as for complementary single-cell protein assays (flow cytometry, immunofluorescence, immunohistochemistry, mass cytometry/CyTOF). For multistep assays, measuring variation from each assay step isolates biological variation from technical variation imparted by the measurement itself. Standardized tools allow robust quality control and enhanced accuracy to ensure meaningful and reproducible biological insights.

To establish a molecular mass standard for single-cell western blotting, we design, characterize, and apply protein markers delivered to microwells in "solid-phase" as a coating on a magnetic microparticle vehicle. Magnetically directed microparticle delivery and chemical triggering of protein marker release allow concurrent analysis of the protein marker with each electrophoretic separation of single-cell lysate. To assess intra- and inter-assay variability, we utilize His-tagged ligands, which allows customization of the protein markers to match the single-cell western target needs. Endogenous protein targets are identifiable with selectivity greater than immunoassays alone, owing to dual measurements of molecular mass and reactivity with an immunoprobe.

Protein markers promise to aid in identification of unknown protein targets from single cells, as well as very importantly aiding in the identification and subsequent measurement of sources of technical variation in single-cell western blotting. Inclusion of protein markers allows a user to understand the variation arising from each stage of their custom assay—from cell lysis to immunoprobing—which allows adjustment of assay conditions to modulate the dominant contributors to variation (e.g., peak location, area-under-the-curve, dispersion).

Design and development of protein markers that are compatible with other single-cell immunoblotting modalities—including immunoprobed isoelectric focusing and immunoblotting of native species—are underway. With further optimization to deliver controlled (and known) quantities of standard proteins to each microwell, protein markers have the potential to aid in absolute protein quantitation of targets from each single-cell lysate and possibly even from sub-cellular compartments.[18,76]

4.6 References

1. Amir, E. D. *et al.* viSNE enables visualization of high dimensional single-cell data and reveals phenotypic heterogeneity of leukemia. *Nat Biotechnol* **31**, 545–552 (2013).
2. Powell, A. A. *et al.* Single cell profiling of circulating tumor cells: transcriptional heterogeneity and diversity from breast cancer cell lines. *PLoS One* **7**, e33788 (2012).
3. Werner, M., Palankar, R., Arm, L., Hovius, R. & Vogel, H. Microfluidic Single-Cell Analysis with Affinity Beads. *Small* **11**, 2607–2613 (2015).
4. Zhang, X. *et al.* Quantitative Analysis of Multiple Proteins of Different Invasive Tumor Cell Lines at the Same Single-Cell Level. *Small* **14**, e1703684 (2018).
5. Rettig, J. R. & Folch, A. Large-scale single-cell trapping and imaging using microwell arrays. *Anal Chem* **77**, 5628–5634 (2005).

6. Revzin, A., Sekine, K., Sin, A., Tompkins, R. G. & Toner, M. Development of a microfabricated cytometry platform for characterization and sorting of individual leukocytes. *Lab Chip* **5**, 30–37 (2005).
7. Di Carlo, D., Aghdam, N. & Lee, L. P. Single-cell enzyme concentrations, kinetics, and inhibition analysis using high-density hydrodynamic cell isolation arrays. *Anal Chem* **78**, 4925–4930 (2006).
8. Wood, D. K., Weingeist, D. M., Bhatia, S. N. & Engelward, B. P. Single cell trapping and DNA damage analysis using microwell arrays. *PNAS* **107**, 10008–10013 (2010).
9. Gierahn, T. M. *et al.* Seq-Well: portable, low-cost RNA sequencing of single cells at high throughput. *Nat Methods* **14**, 395–398 (2017).
10. Yuan, J. & Sims, P. A. An Automated Microwell Platform for Large-Scale Single Cell RNA-Seq. *Sci Rep* **6**, 33883 (2016).
11. Duncombe, T. A. *et al.* Hydrogel Pore-Size Modulation for Enhanced Single-Cell Western Blotting. *Adv Mater* **28**, 327–334 (2016).
12. Hughes, A. J. *et al.* Single-cell western blotting. *Nature Methods* **11**, 749–755 (2014).
13. Rosenthal, A., Macdonald, A. & Voldman, J. Cell patterning chip for controlling the stem cell microenvironment. *Biomaterials* **28**, 3208–3216 (2007).
14. Doh, J., Kim, M. & Krummel, M. F. Cell-laden microwells for the study of multicellularity in lymphocyte fate decisions. *Biomaterials* **31**, 3422–3428 (2010).
15. Collins, A. R. The comet assay for DNA damage and repair: principles, applications, and limitations. *Mol Biotechnol* **26**, 249–261 (2004).
16. Varadarajan, N. *et al.* A high-throughput single-cell analysis of human $CD8^+$ T cell functions reveals discordance for cytokine secretion and cytolysis. *J Clin Invest* **121**, 4322–4331 (2011).
17. Yang, L. *et al.* Single-Cell, Multiplexed Protein Detection of Rare Tumor Cells Based on a Beads-on-Barcode Antibody Microarray. *Anal Chem* **88**, 11077–11083 (2016).
18. Sinkala, E. *et al.* Profiling protein expression in circulating tumour cells using microfluidic western blotting. *Nature Communications* **8**, 14622 (2017).
19. Kang, C.-C. *et al.* Electrophoretic cytopathology resolves ERBB2 forms with single-cell resolution. *NPJ Precis Oncol* **2**, 10 (2018).
20. J. Kim, J., Sinkala, E. & E. Herr, A. High-selectivity cytology via lab-on-a-disc western blotting of individual cells. *Lab on a Chip* **17**, 855–863 (2017).
21. Kang, C.-C. *et al.* Single cell–resolution western blotting. *Nature Protocols* **11**, 1508–1530 (2016).
22. Kang, C. C., Lin, J. M. G., Xu, Z., Kumar, S. & Herr, A. E. Single-cell western blotting after whole-cell imaging to assess cancer chemotherapeutic response. *Analytical Chemistry* **86**, 10429–10436 (2014).
23. Ohyama, K. *et al.* Immune complexome analysis of serum and its application in screening for immune complex antigens in rheumatoid arthritis. *Clin Chem* **57**, 905–909 (2011).
24. Geraldes, P. & King, G. L. Activation of protein kinase C isoforms and its impact on diabetic complications. *Circ Res* **106**, 1319–1331 (2010).
25. Yin, Z., Ren, J. & Guo, W. Sarcomeric protein isoform transitions in cardiac muscle: a journey to heart failure. *Biochim Biophys Acta* **1852**, 47–52 (2015).
26. Stastna, M. & Van Eyk, J. E. Analysis of protein isoforms: can we do it better? *Proteomics* **12**, 2937–2948 (2012).
27. Cohen, A. A. *et al.* Dynamic Proteomics of Individual Cancer Cells in Response to a Drug. *Science* **322**, 1511–1516 (2008).

28. Sargiacomo, M. *et al.* Oligomeric structure of caveolin: implications for caveolae membrane organization. *Proc Natl Acad Sci U S A* **92**, 9407–9411 (1995).
29. Cleasby, M. E., Reinten, T. A., Cooney, G. J., James, D. E. & Kraegen, E. W. Functional studies of Akt isoform specificity in skeletal muscle in vivo; maintained insulin sensitivity despite reduced insulin receptor substrate-1 expression. *Mol Endocrinol* **21**, 215–228 (2007).
30. Bass, J. *et al.* An overview of technical considerations for Western blotting applications to physiological research. *Scand J Med Sci Sports* **27**, 4–25 (2017).
31. Rath, A., Glibowicka, M., Nadeau, V. G., Chen, G. & Deber, C. M. Detergent binding explains anomalous SDS-PAGE migration of membrane proteins. *PNAS* **106**, 1760–1765 (2009).
32. Shi, Y. *et al.* Abnormal SDS-PAGE migration of cytosolic proteins can identify domains and mechanisms that control surfactant binding. *Protein Sci* **21**, 1197–1209 (2012).
33. Hu, S., Zhang, L., Cook, L. M. & Dovichi, N. J. Capillary sodium dodecyl sulfate-DALT electrophoresis of proteins in a single human cancer cell. *Electrophoresis* **22**, 3677–3682 (2001).
34. Chen, X., Kapil, M. A., Hughes, A. J. & Herr, A. E. Single-microchannel, multistep assay reports protein size and immunoaffinity. *Anal Chem* **83**, 6573–6579 (2011).
35. Hughes, A. J. & Herr, A. E. Microfluidic Western blotting. *PNAS* **109**, 21450–21455 (2012).
36. Herr, A. E. & Singh, A. K. Photopolymerized cross-linked polyacrylamide gels for on-chip protein sizing. *Anal Chem* **76**, 4727–4733 (2004).
37. Goetz, H. *et al.* Comparison of selected analytical techniques for protein sizing, quantitation and molecular weight determination. *J Biochem Biophys Methods* **60**, 281–293 (2004).
38. Gomis, D. B., Junco, S., Expósito, Y. & Gutiérrez, M. D. Size-based separations of proteins by capillary electrophoresis using linear polyacrylamide as a sieving medium: model studies and analysis of cider proteins. *Electrophoresis* **24**, 1391–1396 (2003).
39. Kyhse-Andersen, J. Electroblotting of multiple gels: a simple apparatus without buffer tank for rapid transfer of proteins from polyacrylamide to nitrocellulose. *J Biochem Biophys Methods* **10**, 203–209 (1984).
40. Uliana, C. V., Peverari, C. R., Afonso, A. S., Cominetti, M. R. & Faria, R. C. Fully disposable microfluidic electrochemical device for detection of estrogen receptor alpha breast cancer biomarker. *Biosens Bioelectron* **99**, 156–162 (2018).
41. Mahmood, T. & Yang, P.-C. Western Blot: Technique, Theory, and Trouble Shooting. *N Am J Med Sci* **4**, 429–434 (2012).
42. Shapiro, A. L., Viñuela, E. & Maizel, J. V. Molecular weight estimation of polypeptide chains by electrophoresis in SDS-polyacrylamide gels. *Biochem Biophys Res Commun* **28**, 815–820 (1967).
43. Ferguson, K. A. Starch-gel electrophoresis -- Application to the classification of pituitary proteins and polypeptides. *Metabolism* **13**, SUPPL:985-1002 (1964).
44. Burnette, W. N. 'Western blotting': electrophoretic transfer of proteins from sodium dodecyl sulfate--polyacrylamide gels to unmodified nitrocellulose and radiographic detection with antibody and radioiodinated protein A. *Anal Biochem* **112**, 195–203 (1981).
45. Bowen, B., Steinberg, J., Laemmli, U. K. & Weintraub, H. The detection of DNA-binding proteins by protein blotting. *Nucleic Acids Res* **8**, 1–20 (1980).
46. Streets, A. M. *et al.* Microfluidic single-cell whole-transcriptome sequencing. *PNAS* **111**, 7048–7053 (2014).
47. Arzalluz-Luque, Á., Devailly, G., Mantsoki, A. & Joshi, A. Delineating biological and technical variance in single cell expression data. *Int J Biochem Cell Biol* **90**, 161–166 (2017).

48. Jiang, L. *et al.* Synthetic spike-in standards for RNA-seq experiments. *Genome Res* **21**, 1543–1551 (2011).
49. Islam, S. *et al.* Quantitative single-cell RNA-seq with unique molecular identifiers. *Nat Methods* **11**, 163–166 (2014).
50. Perfetto, S. P., Ambrozak, D., Nguyen, R., Chattopadhyay, P. K. & Roederer, M. Quality assurance for polychromatic flow cytometry using a suite of calibration beads. *Nat Protoc* **7**, 2067–2079 (2012).
51. Schwartz, A., Marti, G. E., Poon, R., Gratama, J. W. & Fernández-Repollet, E. Standardizing flow cytometry: a classification system of fluorescence standards used for flow cytometry. *Cytometry* **33**, 106–114 (1998).
52. Shi, Q. *et al.* Single-cell proteomic chip for profiling intracellular signaling pathways in single tumor cells. *PNAS* **109**, 419–424 (2012).
53. McFadden, M. J., Junop, M. S. & Brennan, J. D. Magnetic 'fishing' assay to screen small-molecule mixtures for modulators of protein-protein interactions. *Anal Chem* **82**, 9850–9857 (2010).
54. Carrick, B. H., Hao, L., Smaldino, P. J. & Engelke, D. R. A Novel Recombinant DNA System for High Efficiency Affinity Purification of Proteins in Saccharomyces cerevisiae. *G3 (Bethesda)* **6**, 573–578 (2015).
55. Ananth, A. *et al.* Reversible Immobilization of Proteins in Sensors and Solid-State Nanopores. *Small* **14**, 1703357 (2018).
56. Matheron, G. Principles of geostatistics. *Economic Geology* **58**, 1246–1266 (1963).
57. Cressie, N. Fitting variogram models by weighted least squares. *Mathematical Geology* **17**, 563–586 (1985).
58. Porath, J. Immobilized metal ion affinity chromatography. *Protein Expr Purif* **3**, 263–281 (1992).
59. Khan, F., He, M. & Taussig, M. J. Double-hexahistidine tag with high-affinity binding for protein immobilization, purification, and detection on ni-nitrilotriacetic acid surfaces. *Anal Chem* **78**, 3072–3079 (2006).
60. Evans, R., Dal Poggetto, G., Nilsson, M. & Morris, G. A. Improving the Interpretation of Small Molecule Diffusion Coefficients. *Anal Chem* **90**, 3987–3994 (2018).
61. Young, M. E., Carroad, P. A. & Bell, R. L. Estimation of diffusion coefficients of proteins. *Biotechnology and Bioengineering* **22**, 947–955 (1980).
62. *PureProteome™ Nickel Magnetic Bead System specifications*. https://www.emdmillipore.com/US/en/product/PureProteome-Nickel-Magnetic-Bead-System,MM_NF-LSKMAGH02#overview.
63. Lauer, S. A. & Nolan, J. P. Development and characterization of Ni-NTA-bearing microspheres. *Cytometry* **48**, 136–145 (2002).
64. Guttman, A. & Nolan, J. Comparison of the separation of proteins by sodium dodecyl sulfate-slab gel electrophoresis and capillary sodium dodecyl sulfate-gel electrophoresis. *Anal Biochem* **221**, 285–289 (1994).
65. Luo, S., Feng, J. & Pang, H.-M. High-throughput protein analysis by multiplexed sodium dodecyl sulfate capillary gel electrophoresis with UV absorption detection. *J Chromatogr A* **1051**, 131–134 (2004).
66. Dolnik, V. & Gurske, W. A. Size separation of proteins by capillary zone electrophoresis with cationic hitchhiking. *Electrophoresis* **32**, 2884–2892 (2011).

67. Becker, G. *et al.* Surface-attached poly(phosphoester)-hydrogels with benzophenone groups. *Polymer Chemistry* **9**, 315–326 (2018).
68. Vlassakis, J. & Herr, A. E. Joule Heating-Induced Dispersion in Open Microfluidic Electrophoretic Cytometry. *Anal. Chem.* **89**, 12787–12796 (2017).
69. Li, J. J., Bickel, P. J. & Biggin, M. D. System wide analyses have underestimated protein abundances and the importance of transcription in mammals. *PeerJ* **2**, e270 (2014).
70. Martegani, M. P., Del Prete, F., Gasbarri, A., Natali, P. G. & Bartolazzi, A. Structural variability of CD44v molecules and reliability of immunodetection of CD44 isoforms using mAbs specific for CD44 variant exon products. *Am J Pathol* **154**, 291–300 (1999).
71. Figtree, G. A., McDonald, D., Watkins, H. & Channon, K. M. Truncated estrogen receptor alpha 46-kDa isoform in human endothelial cells: relationship to acute activation of nitric oxide synthase. *Circulation* **107**, 120–126 (2003).
72. Inoue, K. & Fry, E. A. Aberrant Splicing of Estrogen Receptor, HER2, and CD44 Genes in Breast Cancer. *Genet Epigenet* **7**, GEG.S35500 (2015).
73. Tentori, A. M., Yamauchi, K. A. & Herr, A. E. Detection of Isoforms Differing by a Single Charge Unit in Individual Cells. *Angewandte Chemie International Edition* **55**, 12431–12435 (2016).
74. Yamauchi, K. A., Tentori, A. M. & Herr, A. E. Arrayed isoelectric focusing using photopatterned multi-domain hydrogels. *Electrophoresis* **39**, 1040–1047 (2018).
75. Hillion, J. *et al.* Coaggregation, cointernalization, and codesensitization of adenosine A2A receptors and dopamine D2 receptors. *J Biol Chem* **277**, 18091–18097 (2002).
76. Yamauchi, K. A. & Herr, A. E. Subcellular western blotting of single cells. *Microsyst Nanoeng* **3**, 16079 (2017).

4.7 Supplement: Microparticle segmentation script

```
% Ensure all old variables and windows are cleared
clear all
close all
clc

% Inputs (change these for each image set)
addpath('C:\Desktop\Test image set');
dark = imread('dark.tif');
flat = imread('flat.tif');
filename_start = 'test';
filename_end = '.tif';
numImages = 20;
showFigures = 0; %Boolean determining whether image segmentation
results (for each image) are displayed or not

for i = 1:numImages %for each image...

    %READ IMAGE
    filename_mid = num2str(i);
    filename = strcat(filename_start, filename_mid, filename_end);
    try
        img = imread(filename);
    catch
```

```
        continue; %If there isn't a file with the specified filename,
move on to the next image index
    end

    %FLAT-FIELD CORRECTION, and normalize to the max image intensity
to improve contrast
    corrected = flatfield(img, dark, flat);
    Imax = max(max(corrected));
    corrected_contrast = double(corrected)./Imax; %only used if
displaying the image

    %GENERATE OUTLINES
    img_edge = edge(corrected, 'Canny', [0.05 0.25]); %Canny edge
detection
    se = strel('disk', 10); %Create morphological structuring element
    img_close = imclose(img_edge, se); %Connect edge segments using
disk with a radius of 10 pixels (microscopy image scale is 5
pixels/micron)
    img_fill = imfill(img_close,'holes'); %Fill the outlines. This
means that smaller outlines within one microparticle will be
encapsulated within the larger microparticle edge.
    mask = boundarymask(img_fill); %Find boundaries of the filled
regions
    boundaryOverlay = imoverlay(corrected_contrast,mask,'red');
%Overlay boundary outlines on original image

    %MEASURE PROPERTIES
    stats = regionprops(img_fill, corrected, 'Area', 'Centroid',
'Perimeter', 'MeanIntensity', 'PixelValues', 'MajorAxisLength',
'MinorAxisLength');

    %Get stats for all segmented objects, in pixel units
    area = cat(1, stats.Area);
    perim = cat(1, stats.Perimeter);
    circularity = (4*pi.*area)./perim.^2;
    centroid = cat(1, stats.Centroid);
    major = cat(1,stats.MajorAxisLength);
    minor = cat(1,stats.MinorAxisLength);
    diameters = (major+minor)/2;
    radii = diameters/2;
    meanInt = cat(1,stats.MeanIntensity);
    x = centroid(:,1);
    y = centroid(:,2);

    %{
    Select objects based on location (i.e., exclude microparticles
that are cut off at the edge of image), area, and circularity
    Reject if x is <25 or >1004-25=979. reject if y is <25 or >1002-
25=981. (pixel units, based on image size of 1002 x 1004 pixels)
    %}
    acceptLoc = find((x>25&x<979)&(y>25&y<977)); %Only accept
microparticles with centroids more than 25 pixels (5 microns, the
```

```
radius of the microparticle) from the edge to avoid quantifying cut-
off microparticles
    acceptArea = find(area>491&area<4418); %Only use microparticles
with area between 491 and 4418 pixels (corresponds to about 5-15
micron diameter microparticles)
    acceptCirc = find(circularity>0.86); %Only use microparticles with
circularity above 0.86
    accept = intersect(acceptLoc, acceptArea);
    accept = intersect(accept, acceptCirc);

    %{
    Accept only microparticles that don't overlap with other
microparticles' halos (the fluorescent ring around the microparticle,
    which may confound measurement of true microparticle fluorescence
(i.e., protein loading).
    %}
    goodCenters = centroid(accept,:); %Centers with proper area,
location, circularity (but BEFORE halo overlap selection)
    reject = zeros();
    if size(centroid,1)==1   %If there is only one microparticle in
the image, don't need to check if it overlaps with halos
    else %If there are multiple microparticles in the image, remove
ones that overlap with halo
        for m = 1:length(accept) %For each microparticle that passed
area, location, circularity thresholds...
            microparticleIndex = accept(m);
            x1 = centroid(microparticleIndex,1);
            y1 = centroid(microparticleIndex,2);
            neighbors = 1:size(centroid,1);  %Neighbors are ALL
segmented objects, not just the accepted ones! Because halos from non-
accepted objects would still confound intensity measurement of given
microparticle
            neighbors(microparticleIndex) = [];    %The microparticle
being analyzed is not a neighbor to itself
            distances = zeros(length(neighbors));
            for n = 1:length(neighbors) %For each neighbor of a single
microparticle
                neighborIndex = neighbors(n);
                x2 = centroid(neighborIndex,1);
                y2 = centroid(neighborIndex,2);
                dist = sqrt((x2-x1)^2+(y2-y1)^2);
                if dist<100 %if the centroids are less than 100 pixels
apart (25 pixels per radius*2 microparticles + 50 pixels is halo
width)
                    reject = [reject; microparticleIndex]; %this
microparticle gets added to reject list
                    break %stop calculating distance between
microparticle and neighbors if we reject the microparticle
                end
            end
        end
    end
```

```
    acceptFinal = setdiff(accept, reject); %remove rejects from the
original accept list

    %{
    Label the accepted segmented components with their indices.
    Generates a figure with all identified boundaries (whether they
pass QC or not) outlined in red, and
    microparticles which pass all segmentation QC labeled with an
index number.
    %}
    if showFigures
        figure;
        imshow(boundaryOverlay) %Plot all segmented regions identified
prior to QC
        hold on
        for k = 1:numel(stats)
            c = stats(k).Centroid;
            if ismember(k,acceptFinal)  %If it is a selected object,
label the microparticle with the index number
                text(c(1), c(2), sprintf('%d', k), ...
                    'HorizontalAlignment', 'center', ...
                    'VerticalAlignment', 'middle');
            end

        end
        hold off
    end

    %Add microparticle stats to table
    imageTable = zeros(length(acceptFinal),8);
    imageTable(:,1) = i; %Fill first column with image index
    imageTable(:,2) = acceptFinal; %2nd column is microparticle index
    imageTable(:,3) = area(acceptFinal); %3rd column is area
    imageTable(:,4) = radii(acceptFinal); %4th column is radius
    imageTable(:,5) = perim(acceptFinal); %5th column is perimeter
    imageTable(:,6) = circularity(acceptFinal); %6th column is
circularity
    imageTable(:,7) = meanInt(acceptFinal); %7th column is mean
intensity
    imageTable(:,8) = imageTable(:,3).*imageTable(:,7); %8th column is
summed intensity

    %Add the statistics from the i'th image to the statistics of all
images already processed.
    if i==1
        microparticles = imageTable;
    else
        microparticles = [microparticles; imageTable];
    end

end
```

```
function corrected = flatfield(raw, dark, flat)

subtracted = imsubtract(raw, dark);

flatMed = median(median(flat));
flatMed = cast(flatMed,'double');
flatNorm = double(flat)./flatMed;
%Note: Using double to keep image in the 14 bit range, rather than
im2double (which converts everything to a 0 to 1 scale)
corrected = imdivide(double(subtracted),flatNorm);

end
```

Chapter 5

Open microfluidic tools for multimodal analysis of single embryos to single blastomeres

Adapted with permission from E. Rosàs-Canyelles, A. J. Modzelewski, A. Geldert, L. He, & A. E. Herr, "Assessing heterogeneity among single embryos and single blastomeres using open microfluidic design", *Science Advances*, 2020, and E. Rosàs-Canyelles, A. J. Modzelewski, A. Geldert, L. He, & A. E. Herr, "Multimodal detection of protein isoforms and nucleic acids from mouse preimplantation embryos", *Nature Protocols*, 2021.

5.1 Abstract

The process by which a zygote develops from a single cell into a multicellular organism is poorly understood. Advances are hindered by detection specificity and sensitivity limitations of single-cell protein tools and by challenges in integrating multimodal data. While mammalian embryo development depends on critical protein isoforms that arise from embryo-specific nucleic acid modifications, the role of these isoforms is not yet clear. We introduce an open microfluidic tool expressly designed for same-embryo phenotypic, protein, and mRNA profiling. We examine difficult-to-study—yet critically important—murine preimplantation embryo stages. In blastomeres dissociated from less well-studied two-cell embryos, we observe no significant GADD45a protein expression heterogeneity, apparent at the four-cell stage. In oocytes, we detect differences in full-length versus truncated DICER-1 mRNA and protein, which are insignificant by the two-cell stage. Single-embryo analyses reveal intraembryonic heterogeneity, differences between embryos of the same fertilization event and between donors, and reductions in the burden of animal sacrifice. Open microfluidic design integrates with existing workflows and opens new avenues for assessing the cellular-to-molecular heterogeneity inherent to preimplantation embryo development.

5.2 Introduction

The events that initiate cell fate commitment in preimplantation blastomeres remain open questions in developmental biology. While functional studies and embryonic plasticity suggest that blastomeres remain equivalent until the compacted morula[1,2], growing evidence of interblastomeric differences in early-stage embryos points to heterogeneity even at the earliest multicellular stages[3–10]. Although transcriptional profiling of single embryos and single blastomeres has greatly advanced our knowledge of key developmental steps[4], there is a disconnect between transcription and translation; this disconnect is especially apparent in the preimplantation embryo[11]. Holistic understanding of transcript-based predictions demands companion phenotypic and protein-profiling analyses of the same embryo.

Same-cell mRNA and protein profiling capacities are emerging, yet the study of mammalian preimplantation embryos presents novel and long-standing challenges. At the protein level, immunofluorescence (IF) does report protein abundance and localization in embryos. Nevertheless, IF is stymied in three critical aspects. First, IF is unsuitable for detecting small

variations in protein expression and multiplexing beyond ~5 targets[12] owing to cross-reactivity, a ubiquitous problem with immunoreagents. Second, even when immunoreagents with a measure of selectivity do exist, proteoforms remain "blind spots" because isoform-specific immunoreagents have limited availability[13]. Third, chemical fixation artifacts confound measurement of endogenous intracellular protein targets (i.e., epitope masking, cell morphology modifications, and perturbation of protein localization by diffusional gradients in fixation)[14,15]. Given dependence on immunoreagents, flow cytometry and mass cytometry also suffer from specificity and fixation issues[16]. While recent advances in bottom-up mass spectrometry afford single-cell sensitivity[17,18], proteoforms remain a blind spot here as well. Bottom-up mass spectrometry requires protein digestion, which obscures proteoform stoichiometry. Top-down mass spectrometry of intact proteins has insufficient sensitivity, multiplexing, and protein identification to fill the gap[19]. Further, benchtop approaches that complement wide-coverage discovery tools are lacking[17,18]. Although recently developed single-cell electrophoretic tools offer higher specificity by separating proteins by mass or charge before immunoreagent-based detection, they have primarily been designed to handle suspensions of cultured cell lines[20–24]. For developmental biology questions, fundamental inconsistencies exist between cell lines and mammalian embryos. Critical differences include cell composition and size (i.e., oocyte volume is ~100× HeLa cell volume), membrane structure, embryo handling, and low cell availability (~10 to 20 embryos per mouse, depending on strain)[25–28].

Same-cell mRNA and protein analysis of single cells[3,29] shows that mRNA measurements very often do not correlate with protein measurements[30]. In the preimplantation embryo, transcription and translation can be asynchronous for up to 15 hours[11]. Current same-cell mRNA and protein analysis methods can be categorized into three main assay strategies; imaging, division of lysate, and conversion to common molecular format (**Table 5.1**)[31]. Imaging-based assays combine either fluorescence-activated cell sorting (FACS)[32], mass cytometry[33], or imaging mass cytometry[34] to measure protein targets, with fluorescence in situ hybridization (FISH)[32,34,35] or proximity ligation assay for RNA (PLAYR)[33] to quantify mRNA. However, cytometry-based methods typically require large starting sample sizes (100s to 1000s of cells), and thus are difficult to implement when studying embryos. An average of ~20 embryos are collected from a single super ovulated C57BL/6J female mouse. Therefore, obtaining a lower estimate of 100s to 1000s of embryos would require sacrificing dozens of mice for estimate single experiment, which is unrealistic for the average laboratory. A second class of methods divide single cell lysates into fractions for protein or mRNA analysis, applying RT-qPCR to the mRNA fraction and proximity extension assay (PEA)[30] or digital proximity ligation assay (dPLA)[36] to the protein fraction. However, dividing the cell lysate may reduce assay sensitivity, particularly for detection of mRNA which can exist in low copy numbers in a single cell.

Finally, a third category of techniques map protein information to nucleic acid information using oligonucleotide-labeled antibodies[37,38] or a PEA[39]. Thus, the assay converts both DNA/RNA and protein measurements to a common molecular format: nucleic acids which can be amplified and read out using RT-qPCR[39] or single-cell RNA sequencing[37,38]. While techniques combining single-cell RNA sequencing and oligo-labeled antibody staining can be very powerful in terms of multiplexing (10,000s of RNA targets, 10s-100s of protein targets)[37,38], these methods are predominantly designed for the detection of surface proteins[37,38]. The methods can only be extended to intracellular targets using reversible chemical cross-linking[40], which was found to reduce the number of genes detected by ~10%[40] and can lead to common fixation artifacts such as epitope masking[15,41,42]. Additionally, antibody-based detection is limited by

cross-reactivity and the limited specificity of immunoreagents. While PLA, dPLA and PEA-based methods[36,39,43] increase specificity by requiring two antibodies to the same target for amplification to occur, it may be difficult to identify two isoform-specific antibodies which can bind a certain isoform at the same time (i.e., antibodies which bind to different epitopes)[44].

Table 5.1. Benchmarking same-cell, single-cell RNA and protein measurement approaches

Assay strategy	RNA method	Protein method	Multiplexing (per cell)	Throughput	Protein selectivity
Single-cell nucleic acid profiling and immunoblotting (our approach)	RT-qPCR *Only detects nuclear mRNA*	Immunoblotting *Only detects cytoplasmic and surface proteins*	RNA: 10s of targets Protein: ~11 targets[20]	10s of cells	Immunoaffinity and protein sizing
Imaging	*In situ* hybridization[32,34,35] or proximity ligation assay for RNA (PLAYR)[33]	Fluorescence-activated cell sorting (FACS)[32], mass cytometry[45], imaging mass cytometry[34]	~8-17 targets total if using fluorescence[32,46] ~50 targets total if using metal isotopes[47]	100s[34] - 10000s of cells[32,45]	Immunoaffinity
Division of lysate[30,36]	RT-qPCR	Proximity extension assay (PEA)[30] or digital proximity ligation assay (dPLA)[36]	RNA: 10s of targets[30] Proteins: 10s of targets[30]	~100 cells	Immunoaffinity* **Increased specificity due to 2 antibodies required for PEA/dPLA*
Conversion to common molecular format	RT-qPCR[39]	PEA[39]	RNA: 10s-100 targets Proteins: 10s of targets	~100 cells	Immunoaffinity **Increased specificity due to 2 antibodies required for PEA*
	Single-cell RNA sequencing[38,48]	Oligonucleotide-labeled antibody labeling[38,48] *Only detects surface proteins, unless using reversible fixation*[40]	RNA: 10,000s of targets Proteins: 10s-100s of targets	1000s of cells	Immunoaffinity

Our approach to provide developmental biologists with multimodal profiles of preimplantation embryos is an open microfluidic tool that reports embryo phenotype (whole-embryo imaging), protein and protein isoform expression (single-embryo immunoblotting), and mRNA expression [reverse transcription qPCR (RT-qPCR)] for the same single embryo. Open microfluidic design is key, as the unenclosed devices integrate seamlessly with workhorse developmental biology approaches, including embryo preparation tools (pipettes) and whole-embryo bright-field and fluorescence microscopy, as well as integrate with unique approaches introduced here, including release and retrieval of microscale gel pallets that shuttle nuclei off-chip for mRNA analysis after immunoblotting of that same embryo. Precision microfluidic design maps the molecular composition of each component blastomere back to the originating murine

embryo, providing datasets that are suitable for quantitative examination of cellular and molecular relationships. To generate robust, quantitative relationships, we establish and validate technical variation thresholds and expression normalization approaches. We then examine relationships by subjecting blastomeres from two-cell and four-cell embryos to protein analysis of GADD45a, a protein involved in DNA damage repair reported to show bimodal transcription levels at the two-cell and four-cell stages. Within oocytes, but not two-cell embryos, we find significant expression differences between truncated and full-length isoforms of DICER-1 (Dicer 1, ribonuclease type III) by both mRNA and direct alternate protein isoform detection. In the more mature blastocysts, we scrutinize dissociated blastomeres and—by integrating fluorescence imaging of intact blastomeres for internalized fluorescent beads—we corroborate mutually exclusive expression of CDX-2 versus SOX-2 in cells acquiring trophectoderm (TE) versus inner cell mass (ICM) state, respectively. Together, we see the study of preimplantation development as uniquely well positioned to benefit from multimodal molecular analysis tools offering single-blastomere resolution.

5.3 Materials & Methods

Animals and ethics statement. As a matter of caution and compliance, all appropriate authorizations have been acquired from institutional and/or federal regulatory bodies before performing this protocol. All mouse use, including but not limited to housing, breeding, production, sample collection for genotyping, and euthanasia, is in accordance with the Animal Welfare Act, the American Veterinary Medical Association (AVMA) Guidelines on Euthanasia and are in compliance with the Institute of Laboratory Animal Resources (ILAR) Guide for Care and Use of Laboratory Animals, and the University of California Berkeley Institutional Animal Care and Use Committee (IACUC) guidelines and policies. Our animal care and use protocol has been reviewed and approved by our IACUC for this project.

Chemical reagents. Tetramethylethylenediamine (TEMED; T9281), ammonium persulfate (APS; A3678), β-mercaptoethanol (M3148), 30%T/2.7%C acrylamide/bis-acrylamide (37.5:1) (A3699), bovine serum albumin (BSA; A9418), Tyrode's solution (T1788), trypsin 10× (59427C), Accutase (A6964), and 3-(trimethoxylsilyl)propyl methacrylate (440159) were purchased from Sigma-Aldrich. Triton X-100 (BP-151) and phosphate-buffered saline (PBS; pH 7.4; 10010023) were purchased from Thermo Fisher Scientific. Premixed 10× tris-glycine EP (electrophoresis) buffer [25 mM tris (pH 8.3), 192 mM glycine] was purchased from Bio-Rad. Tris-buffered saline with Tween-20 (TBST) was prepared from 20× TBST (sc-24953, Santa Cruz Biotechnology). Deionized water (18.2 megohms) was obtained using an ultrapure water system from Millipore. Alexa 555–labeled BSA (A34786) was purchased from Invitrogen. N-[3-[(3-benzoylphenyl)formamido]propyl] methacrylamide (BPMAC) was custom synthesized by Pharm-Agra Laboratories (Brevard, NC). GelSlick (50640) and Lonza GelBond PAG Film for Acrylamide Gels (BMA54746) were purchased from Lonza.

Device fabrication. Devices for protein immunoblotting were fabricated using SU-8 microposts patterned on silicon wafers to mold the PA gel microwells, as previously reported[49]. Briefly, polyacrylamide precursor solution including acrylamide/bis-acrylamide (7 to 12%T) and 3 mM BPMAC was degassed with sonication for 9 min. APS (0.08%) and TEMED (0.08%) were added to the precursor solution, and the solution was pipetted between the SU-8 wafer (rendered hydrophobic with Gel Slick solution) and either (i) a glass microscope slide functionalized with 3-(trimethoxylsilyl)propyl methacrylate (to ensure covalent grafting of PA gel to glass surface) for immunoblotting alone, or (ii) a GelBond polymer cut to the size of a standard glass slide for same-

embryo immunoblotting and mRNA measurement devices. After chemical polymerization (20 min), devices (glass or GelBond polymer with grafted PA gel layer) were lifted from the wafer, rinsed with deionized water, and stored dry until use.

Microwell diameter and height were optimized for each sample, where microwell diameter approximates the average blastomere or embryo diameter (from 20 to 30 μm for dissociated blastocyst blastomeres to 150 μm for whole embryos), and the diameter-to-height ratio was kept at approximately 3:4 to prevent convection streamlines from dislodging settled cells during the pouring of lysis buffer[21]. In devices for same-embryo immunoblotting and mRNA measurements, microwell diameter and height were 200 μm, to allow alignment of laser over the area containing the microwells.

Mouse embryo isolation and culture. Three to five-week-old female C57BL/6J mice (000664, the Jackson laboratory) were superovulated by intraperitoneal (IP) injection of 5 IU of pregnant mare serum gonadotropin (PMSG; Calbiochem, 367222, Millipore), and 46 to 48 hours later, IP injection of 5 IU human chorion gonadotropin (hCG; Calbiochem, 230734, Millipore). Superovulated females were housed at a 1:1 ratio with 3to 8-monthold C57BL/6J males to generate one-cell zygotes at 0.5 day after coitum. Using forceps under a stereomicroscope (Nikon SMZ-U or equivalent), the ampulla of the oviduct was nicked, releasing fertilized zygotes and oocytes associated with surrounding cumulus cells into 50 μl of M2 + BSA medium [M2 medium (MR-015-D, Millipore) supplemented with BSA (4 mg/ml; A3311, Sigma-Aldrich)]. Using a handheld pipette set to 50 μl, zygotes were dissociated from cumulus cells after the cumulus oocyte complexes were transferred into a 200-μl droplet of hyaluronidase/M2 solution (MR-051-F, Millipore), incubated for up to 2 min, and passed through five washes in the M2 + BSA medium to remove cumulus cells.

From this point on, embryos were manipulated using a mouth-controlled assembly consisting of a capillary pulled from glass capillary tubes (P0674, Sigma-Aldrich) over an open flame attached to a 15-inch aspirator tube (A5177, Sigma-Aldrich). Embryos were passed through five washes of M2 + BSA to remove cumulus cells. Embryos were then transferred to KSOM + BSA medium (KCl-enriched simplex optimization medium with amino acid supplement, ZEKS-050, Zenith Biotech) that was equilibrated to final culturing conditions at least 3 to 4 hours before incubation. Embryos were cultured in 20-μl droplets of KSOM + BSA overlaid with mineral oil (ES-005-C, Millipore) in 35 × 10–mm culture dishes (627160, CellStar Greiner Bio-One) in a water-jacketed CO_2 incubator (5% CO_2, 37°C, and 95% humidity).

Single-embryo RT-qPCR for DICER-1. All single-embryo cDNA was prepared using a modified version of the single cell–to–Ct RT-qPCR kit (4458236, Life Technologies). Whole embryos were isolated at the desired developmental stage. Using a mouth pipette, embryos were then passed through three washes of PBS. With a handheld pipette set to 1 μl, a single embryo was collected and transferred to one tube of an 8-well PCR strip. Presence of embryo was visually confirmed in each tube before complementary DNA (cDNA) synthesis. To account for the larger sample input, twice the protocol-recommended volume of lysis buffer/ deoxyribonuclease (20 μl) was added to each embryo and allowed to incubate at room temperature (RT) for 15 min. Then, 2 μl of Stop Solution was added and incubated for 2 min. At this point, half of the reaction was stored in −80°C conditions as a technical replicate, and the remaining sample (11 μl) continued through the original single cell–to–Ct protocol. All RT-qPCRs were performed using SSO Universal SYBR Green SuperMix, as per the manufacturer's instructions (1725275, Bio-Rad). Primer sequences used were Rfx1 (5′AGT GAG GCT CCA CCA CTG GCC G, 5′TGG GCA GCC GCT TCT C), Dicer-1 (5′GGA TGC GAT GTG CTA TCT GGA, 5′GCA CTG CTC CGT GTG

CAA), and DICER-1 (5′CTC TTT CCT TTG AAT GTA CAG CTA C, 5′CAG TAA GCA GCG CCC CTC). All RT-qPCR analyses were performed on the StepOnePlus RealTime PCR System (437660, Thermo Fisher Scientific).

Single-embryo and single-blastomere microfluidic immunoblotting. Once the desired developmental stage was reached, embryos were transferred to a ~50-µl droplet of acid Tyrode's solution (T1788, Sigma-Aldrich) and incubated at 37°C for up to 2 min to remove the zona pellucida. If dissociation into blastomeres was required, embryos were incubated with a 1:1 solution of Accutase and 10× trypsin (15090046, Thermo Fisher Scientific) at 37°C (time varied with development stage, ranging from 5 min for two-cell embryos to up to 5 hours for blastocysts). Embryos were then mechanically disrupted by passing each embryo through a capillary repeatedly until dissociation. Single embryos or blastomeres were washed with PBS and deposited into microwells of the PA gel. Microwells were imaged by bright-field microscopy to collect data on size, morphology, and ensure occupancies of one embryo or blastomere per microwell.

Once isolated in each microwell, cell samples were chemically lysed. Lysis conditions, including buffer composition, temperature, and treatment time, were optimized for each developmental stage (**Table 5.2**). To minimize diffusive losses during lysis, cylindrical microwells are designed to approximate the volume of our samples and, thus, maintain the high local protein concentrations that exist inside cells. Thus, as described previously, for each stage, we designed microwells with diameters that approximate the diameter of the individual embryo or blastomere we wish to isolate (20 to 150 µm). After lysis, an electric field (E = 40 V/cm) was applied to drive PAGE in a 3-mm-long separation lane abutting each lysate containing microwell. Electrophoresis was performed at 40 V/cm for varying times (from 20 s to 2:17 min, depending on developmental stage and protein targets; **Table 5.2**).

Table 5.2. Conditions for assaying embryos and blastomeres of murine preimplantation stages.

Sample Type (zona-free)	Lysis Buffer Composition	Lysis temperature & time	EP time	Electric field	PA Gel %T
Oocyte, two-cell & four-cell (whole or disaggregated)	*	55ºC, 60-75 s	75 s	40 V/cm	7, 10
Whole morula	*	55ºC, 60 s	50 s	40 V/cm	7
Disaggregated morula blastomeres	*	55ºC, 60 s	45 s	40 V/cm	7
Disaggregated blastocyst blastomeres	**	55ºC, 35 s	20 s	40 V/cm	10
Dual mRNA and immunoblotting, all stages	***	RT, 60 s	2 min 17 s	40 V/cm	10

* "Harsh lysis buffer": 25 mM Tris-glycine buffer at pH 8.3 with 1% SDS, 0.5% sodium deoxycholate, and 1% Triton X-100

** "RIPA-like lysis buffer": 25 mM Tris-glycine buffer at pH 8.3 with 0.5% SDS, 0.25% sodium deoxycholate, and 0.1% Triton X-100

*** Fractionation lysis buffer: 0.125 mg/mL digitonin, 1% v/v Triton X-100 and 0.5 X Tris-glycine

Immobilization of proteins by photoblotting was carried out by illumination with an ultraviolet (UV) light source (100% power, 45 s; Lightningcure LC5, Hamamatsu). Gels were washed in 1× TBST for at least 1 hour before probing with antibodies. Primary antibodies were incubated at 1:10 or 1:5 dilution (40 µl per gel, in 2% BSA in 1× TBST), while fluorophore-conjugated secondary antibodies were incubated at 1:10 or 1:20 dilution (40 µl per gel, in 2% BSA in TBST). To strip bound antibodies and reprobe for new targets, gels were treated with 2% SDS,

0.8% β-mercaptoethanol, and 62.5 mM tris base at 55°C for 1 to 3 hours, washed in TBST (1 hour) twice, and then reprobed.

In terms of throughput, we concurrently assay up to 40 samples (blastomeres or embryos) on one device, with the possibility of up to 100 samples per device if all microwells are used. Primary limitations to throughput include (i) sample availability, with ~20 embryos collected per mouse[25–27], (ii) and sample preparation, including serial microtransfer of one cell to each microwell.

Optimization of lysis and electrophoresis times depends on (i) target markers and (ii) starting sample. The molecular mass range of the target markers determines how long the lysate must be separated to resolve protein markers in a given gel composition (%T, or acrylamide monomer concentration). For the protein targets, the design of single-embryo PAGE aims to achieve needed separation resolution while maintaining sufficient analytical sensitivity. Here, these two critical performance metrics depend on (i) target marker characteristics and (ii) starting sample type. The molecular masses of the target markers determine the electrophoresis duration needed to resolve protein targets using a given gel composition (%T, or acrylamide monomer concentration). The starting sample type dictates available mass of protein available for analysis, where small-volume samples (e.g., blastocyst blastomeres) have lower starting mass than samples with larger volumes (e.g., oocytes). In the open microfluidic geometries used here, proteins diffuse out of the gel during the lysis and electrophoresis steps, thus diluting the lysate sample until the limit of detection is, eventually, passed (~27,000 copies of protein target)[21]. Migration distances for the same protein may therefore also vary between different starting samples.

Same-embryo mRNA analysis and immunoblotting. Embryos were prepared as described above and transferred to same-embryo mRNA and immunoblotting devices (GelBond^{TM}-grafted PA devices). Embryos were chemically lysed with fractionation lysis buffer [digitonin (0.125 mg/ml), 1% v/v Triton X-100, and 0.5× tris-glycine) at room temperature for 60 s. An electric field (E = 40 V/cm) was applied for 2 min and 17 s, followed by UV light illumination (100% power, 45 s; Lightningcure LC5, Hamamatsu). Devices were immediately placed in nuclei wash buffer (320 mM sucrose, 5 mM MgCl2, and 10 mM Hepes) at 4°C and kept over ice, with buffer exchanged three times.

A CO_2 laser cutter (HL40-5G-110, Full Spectrum Laser) was used to excise 2 × 3–mm sections of the PA-polymer device encompassing single microwells, called gel pallets. Gel pallets containing the fractionated nuclei were placed in PCR tubes containing 20 μl of DNA/RNA shield buffer (R1100-50, Zymo Research) and stored at −80°C. Devices were washed with TBST and probed following the same protocol as described under the previous section.

The mRNA was isolated from gel pallets using Quick-DNA/RNA, Microprep Plus (D7005, Zymo Research). All of the extracted mRNA was used for cDNA synthesis (SuperScript4, 18091050, Thermo Fisher Scientific). cDNA was amplified with PerfeCTa PreAmp SuperMix (95146, QuantaBio), and RT-qPCRs were performed using SSO Universal SYBR Green SuperMix, as per the manufacturer's instructions (1725275, Bio-Rad). Primer sequences used were as follows: β-actin F: GGCTGTATTCCCCTCCATCG, β-actin R: CCAGTTGGTAACAATGCCATGT. All RT-qPCR analyses were performed on the StepOnePlus Real-Time PCR System (437660, Thermo Fisher Scientific).

Antibody probes for immunoblotting. Antibodies used for analysis of embryos include rabbit anti–β-tubulin (Abcam, ab6046, polyclonal, lot: GR31927-5), mouse anti–DICER-1 (Santa Cruz Biotechnology, sc-136981, A-2, lot: I1817), mouse anti– CDX-2 (Abcam, ab157524, CDX2-88, lot: GR300552-6), anti-rabbit anti-CDX2 antibody (Abcam, ab76541, lot #GR300552-18), rabbit

anti-SOX-2 (EMD Millipore, AB5603, polyclonal, lot: NG1863962 and 3254559), goat anti–glyceraldehyde-3-phosphate dehydrogenase (GAPDH) (Sigma-Aldrich, SAB2500450, polyclonal, lot: 6377C2), rabbit anti-GADD45a (Invitrogen, MA5-17014, D.81.E, lot: R12274975), Alexa Fluor 647 anti-mouse/human CD324 (E-cadherin) antibody (BioLegend catalog no. 147307, lot no. B254794), Alexa Fluor 594 FGFR-1 antibody (Santa Cruz Biotechnology, catalog no. sc-57132 AF594, lot no. J0218), Rhodamine anti-β-actin immunoglobulin G (Bio-Rad, 12004163, lot: 64219909), hFAB Rhodamine anti-tubulin primary antibody (Bio-Rad, 12004165, lot no. 64210670). Donkey secondary antibodies Alexa Fluor 647–conjugated anti-mouse (A31571, lot #1903516), Alexa Fluor 594–conjugated anti-mouse (A21203, lot #2066086), and Alexa Fluor 488-conjugated anti-rabbit (A21206) were purchased from Thermo Fisher Scientific, CA, USA. All bands migrated to approximate molecular masses stated by manufacturers or previously published studies (**Table 5.3**).

Table 5.3. Previously reported immunoblots using the same antibodies as in this study show corresponding non-specific protein bands

Protein	Location	Reference
DICER-1	**Figure 5.8**, multiple bands at < 100 kDa	Santa Cruz Biotechnologies. Dicer Antibody (A-2): sc-136981. (2019). Available at: https://www.scbt.com/scbt/product/dicer-antibody-a-2.
GADD45a	**Figure 5.7**, bands at > 50 kDa	Abcam. Anti-GADD45A antibody (ab180768). (2019).
SOX-2	**Figure 5.9** and **Figure 5.1**, bands at > 50 kDa	Que, J. *et al.* Multiple dose-dependent roles for Sox2 in the patterning and differentiation of anterior foregut endoderm. *Development* 134**,** 2521–2531 (2007).
GAPDH	**Figure 5.1**, high molecular mass bands attributed to dimers at ~70 kDa	Qvit, N., Joshi, A. U., Cunningham, A. D., Ferreira, J. C. B. & Mochly-rosen, D. Glyceraldehyde-3-Phosphate Dehydrogenase (GAPDH) Protein-Protein Interaction Inhibitor Reveals a Non-catalytic Role for GAPDH Oligomerization in Cell Death. 291**,** 13608–13621 (2016).

Validation of SOX-2/CDX-2 expression by dissociated blastocyst blastomeres. Fluorescent microspheres (0.2 μm) (Polysciences cat. no. 17151, lot #671952) were provided by D. Fletcher's laboratory at UC Berkeley. Selective fluorescence labeling of outer (TE) blastomeres was performed as previously described[50]. Briefly, blastocysts (3.5 to 4 dpc) were incubated with a 1:100 dilution of 0.2 μm of fluorescently labeled microspheres for 1 min and then rinsed in medium before dissociation. Cells were then settled into microwells, imaged (bright-field and 488 nm), and assayed for β-tubulin, CDX-2, and SOX-2.

Conventional western blotting of pooled oocytes. Oocytes (N = 85) collected from five super ovulated C57BL/6J female mice were isolated and placed into 16 μl of harsh lysis buffer (**Table 5.2**), heated to 55°C for 60 s to mimic immunoblotting lysis conditions, and stored at −80°C until required. To this sample, 4 ul of 5× Laemmli buffer was added and mixed by brief vortexing and centrifugation. The sample was loaded onto a 10% polyacrylamide gel and electrophoresed for 30 min at 50 V and 1 hour at 150 V. After transfer, the membrane was blocked with 5% milk in 1× TBST, and then probed overnight at 4°C with an antibody against DICER-1 (Santa Cruz Biotechnology, sc-136981; 1:500 dilution in blocking buffer). The membrane was washed three times with 1× TBST and then probed with goat–anti-mouse secondary antibody (Rockland, 18-8817-33; 1:5000 dilution) for 1 hour at room temperature. Three additional washes were made before detection using enhanced chemiluminescence (Millipore WBKLS0100) and imaged on a

Bio-Rad GelDoc XR+. Given that sample preparation for single embryo PAGE is not equivalent to that of bulk, slab-gel SDS-PAGE (i.e., amount of protein in both cases varies considerably), we do not expect equivalent protein sizing for all targets between the methods.

Determination of immunoblotting detection range, multiplexing, and separation resolution. We first sought to directly measure protein expression in cells ranging from single oocytes (~80 μm in diameter) to single blastomeres from dissociated blastocysts (<20 μm in diameter at 3.5 to 4.0 days after coitus, dpc) (**Figure 5.1A**). Single oocytes and single blastomeres from dissociated blastocysts were immunoblotted for the protein loading control β -tubulin (**Figure 5.1A**). By detecting β-tubulin band passing the quality control metrics of signal-to-noise (SNR) ratios above the threshold of 3 and Gaussian fit with $R^2 > 0.8$ for both samples, we determined a dynamic detection range spanning femtomoles (10^{-15}) to tens of attomoles (10^{-17}), with the assumed starting protein target concentration in the micromolar range[51].

We next assayed single morula (3.0 dpc) for the loading control GAPDH and two transcription factors that are key regulators of pluripotency and differentiation[52,53], SOX-2 and CDX-2. Multiplexing is granted by the four spectral channels available with our current microarray imaging system (Genepix 400A, Molecular Devices) in combination with availability of antibodies raised in four different species. With stripping and reprobing, up to nine rounds have been reported[21]. By using a combination of (i) primary antibodies raised in different animals (goat–anti-GAPDH, rabbit–antiSOX-2, and mouse–anti-CDX-2) and (ii) secondary antibodies conjugated to different fluorophores (donkey–anti-goat, rabbit, and mouse conjugated to Alexa Fluor 555, 488, and 594, respectively), the microfluidic immunoblot resolved the three targets, with molecular masses of 37, 38, and 39 kDa, from intact morula without chemical stripping and reprobing of the gel (**Figure 5.1B**). The observed log-linear relationship between molecular mass and migration distance distinguishes target protein bands from nonspecific antibody signal and demonstrates that single-morula PAGE resolves protein targets with molecular mass as close as 1 to 2 kDa. Electromigration of protein targets with known molecular mass displays an expected log-linear relationship across a wide molecular mass range (from 50 to 100 kDa; **Figure 5.2**). As with slab-gel SDS-PAGE, membrane proteins are known to be difficult to size accurately, and the same behavior is expected with single-cell protein electrophoresis[54].

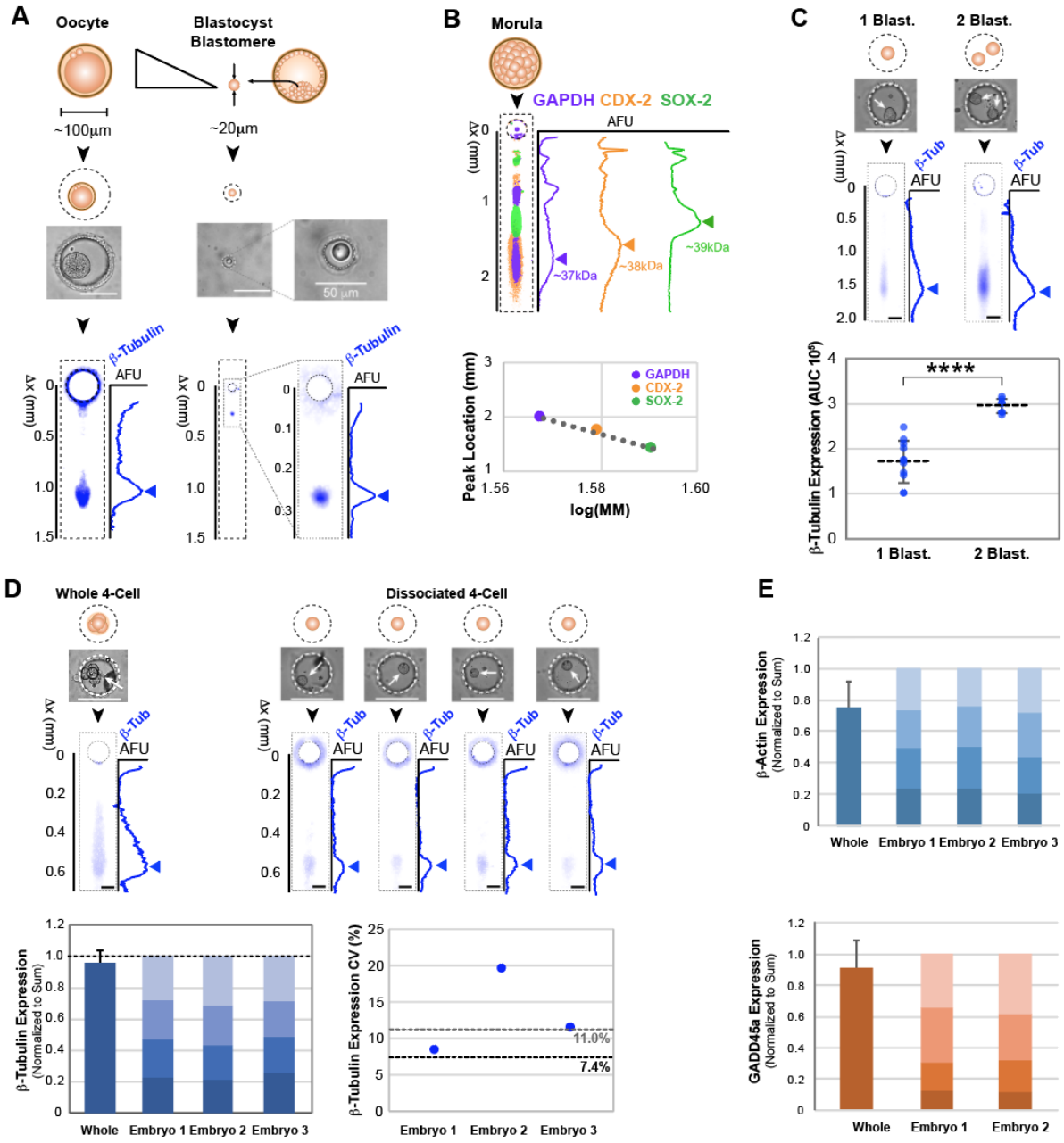

Figure 5.1. Microfluidic immunoblotting detects intra-embryonic biological variation. (**a**) β-tubulin was measured from single oocytes down to single blastocyst blastomeres. Bright-field micrographs of a settled oocyte and blastocyst blastomere are shown above false-color micrographs of resulting β-tubulin immunoblots and fluorescence intensity profiles. Arrows mark position of protein bands. Scale bars are 100 µm, unless specified. (**b**) Single morula assayed for multiple targets that differ by 1-2 kDa (GAPDH, CDX-2 and SOX-2) show a strong log-linear relationship between migration distance and molecular mass (R^2 = 0.984). (**c**) β-tubulin titration experiment. One or two blastomeres of dissociated four-cell embryos are sampled into microwells and assayed for β-tubulin. Bright-field images show blastomeres settled into microwells prior to lysis. Under these, false-color fluorescence micrographs of immunoblots and corresponding β-tubulin intensity profiles. Arrows mark the position of protein bands. Dot plot of β-tubulin signal for immunoblots of one and two blastomeres demonstrates an increase in β-tubulin detection for two blastomeres over one blastomere (horizontal bars indicate mean ± S.D., Mann Whitney U test, p value < 0.001, N = 11 and 7 for microwells with one and two blastomeres, respectively). (**d**) Reconstruction of a whole embryo from dissociated blastomeres. Bright-field micrographs of whole and dissociated four-cell embryos settled into microwells

above corresponding false-color fluorescence micrographs of immunoblots and fluorescence intensity profiles. Arrows mark position of protein bands. Stacked bar graphs of individual blastomere contributions to total β-tubulin expression of four-cell embryos, where whole embryos assayed alongside dissociated blastomeres show similar levels of total β-tubulin expression (error bar indicates S.D., Wilcoxon matched-pairs signed rank test, p value = 0.5, N = 3 independent experiments), indicating sum of individually assayed blastomeres is equivalent to a whole embryo. Dot plot of β-tubulin expression coefficient of variation (CV) for blastomeres of three dissociated four-cell embryos. All CV values are above the technical $CV_{threshold}$ of 7.4% (**Figure 5.3**) with the blastomeres from one of the three embryos exhibiting variation that is below the conservative $CV_{Average\_with\_lysis}$ of 11%[62]. Scale bars are 200 µm. (**e**) β-actin and GADD45a expression from disaggregated and whole four-cell embryos. Stacked bar graphs show individual blastomere contributions to total β-actin or GADD45a expression of four-cell embryos. Whole and disaggregated embryos show similar levels of total expression (error bars indicate S.D., Mann-Whitney test, p values for β-actin and GADD45a are 0.400 and 0.333, for *N* = 3 and 2 independent experiments, respectively).

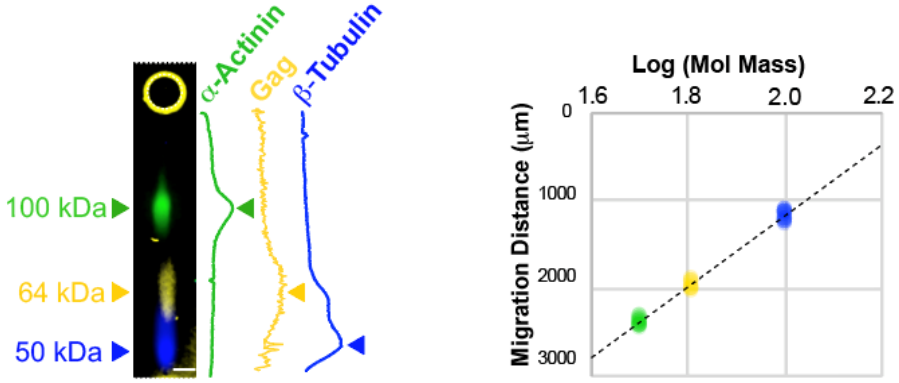

Figure 5.2. Validation of electromigration behavior for a wide (50 to 100 kDa) protein mass range. On the left, false-color fluorescence micrograph of a two-cell embryo immunoblotted for α-actinin (green), Gag (yellow) and β-tubulin (blue). Corresponding intensity profiles are shown to the right, with arrows marking position of protein peaks. On the right, bivariate plot of migration distance and log of molecular mass, showing a linear correlation with R^2 of 0.904 for N = 16.

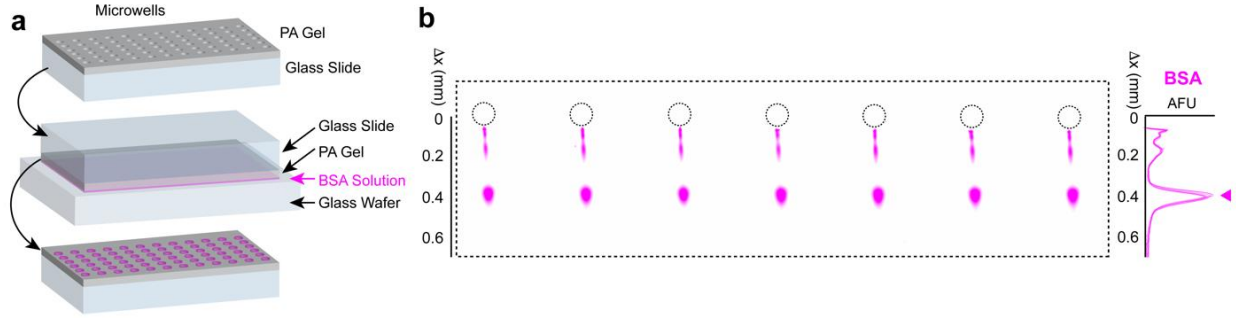

Figure 5.3. Determination of the technical variation threshold of the microfluidic immunoblot. (a) Schematic of purified protein immunoblotting assay. The polyacrylamide (PA) gel of the microfluidic immunoblotting device is incubated with a solution of fluorescently labeled bovine serum albumin (BSA) for 30 min for BSA to partition into microwells. Assay is then run as described in main text. (b) False-color fluorescence micrograph of resulting BSA immunoblots (left) and corresponding fluorescence intensity profiles used to perform area-under-the-curve (AUC) quantification (right). The coefficient of variation (CV%) was calculated as S.D./mean x 100 for N = 9 replicates. The technical variation threshold was computed as the mean CV (4.7%) plus three standard deviations for a 99% confidence interval (S.D. = 0.9%) yielding a CV threshold of 7.4%.

Validation of biological variation detection in dissociated versus intact embryo immunoblotting. Given our ability to immunoblot dissociated blastomeres, we examined (i) if embryo dissociation artificially alters the protein abundance of the whole embryo and (ii) if we can reconstruct the expression profile of the whole embryo, even when constituent blastomeres are

individually assayed. We first inquired if loading a predetermined increase in protein in the microfluidic immunoblot would yield a concomitant increase in protein signal. We, thus, performed titrations where we controlled loaded protein by using individual blastomeres from dissociated four-cell embryos (2.0 dpc) as discrete and easily manipulable loads of protein. We loaded either one or two blastomeres into microwells and assayed the microwell lysate for β-tubulin (**Figure 5.1C**). We observed an increase in β-tubulin expression [area under the curve signal (AUC)] from microwells loaded with two blastomeres as compared with microwells loaded with one blastomere (Mann-Whitney U Test, $P = 6.28 \times 10^{-5}$, with n = 7 and 11 microwells, respectively; **Figure 5.1C**). The observation corroborates the supposition that two blastomeres would contain twofold more protein than a single blastomere.

To assess if the protein profile of a whole embryo could be reconstructed from immunoblots of individual, dissociated blastomeres, to rule out the concern of material loss during disaggregation, lysis, or electrophoresis. To do so, we simultaneously assayed (i) intact four-cell embryos and (ii) blastomeres from dissociated four-cell embryos (each blastomere contained in a separate microwell) (**Figure 5.1D**). We observed that protein bands for whole embryos had larger peak dispersion than protein bands for dissociated blastomeres, where we attribute the larger peak dispersion from whole embryos to the four-fold larger starting sample mass than in dissociated blastomeres. All protein peaks passed the quality control metrics of SNRs above the threshold of 3 and Gaussian fit with $R^2 > 0.8$ (**Figure 5.1D**). The resulting AUCs for β -tubulin were normalized to the summed immunoblot signal from the four dissociated blastomeres (**Figure 5.1D**). While the interembryonic variation showed an average embryo-to-embryo variation in total β-tubulin of 8%, we observed no significant difference between the sum of the contributions of dissociated blastomeres and signal obtained from a four-cell embryo (Wilcoxon matched-pairs signed rank test, P = 0.5, n = 3 independent experiments) (**Figure 5.1D**). For all dissociated four-cell embryos studied, the interblastomeric β -tubulin expression CV exceeded the technical variation threshold (CVs = 8.3, 19.6, and 11.3% for embryos; **Figure 5.1D**). We observed similar results with additional protein markers β -actin and GADD45a (**Figure 5.1E**). These results suggest that immunoblotting of individual blastomeres can reconstruct the protein profile of the originating intact four-cell embryo.

Determination of immunoblotting technical variation. To assess if the source of the observed interblastomeric variation in β-tubulin AUC was attributable to biological variation or confounding technical variation, we first sought to deconvolve sources of variation arising from preparatory steps (e.g., cell lysis) from those arising from analytical steps (e.g., PAGE, photoblotting, and immunoprobing). Variation in measured protein expression levels originates from biological sources, technical sources, or a combination. In the analytical steps, the sources of variation are predominantly technical. Consequently, to estimate the technical variation threshold for these downstream analytical steps, we used a well characterized method using purified proteins[21,22] (bead-based delivery of protein ladders is also possible[55]) that allows us to establish a technical variation threshold by quantifying immunoblots of microwells uniformly loaded with purified protein. Given that endogenous loading control protein targets (i) show significant cell-to-cell variation[56] or (ii) form dimers that are difficult to solubilize[57], we utilize purified protein to estimate technical variation as we have previously reported[58]. Briefly, we partitioned a solution of purified bovine serum albumin (BSA) (1 μM in PBS) into the microwells by incubating PA gels in BSA solution for 30 min. We then performed the immunoblotting assay and quantified the AUC for each BSA protein band. We calculated the coefficient of variation in BSA AUC based on the standard deviation (SD) and mean of the AUC ($CV_{AUC}\% = SD_{AUC}/mean_{AUC} \times 100$) and computed

a technical variation threshold defined as >3 × SD of the mean CV_{AUC} ($CV_{threshold}$ = mean CV_{AUC} + 3 SD = 7.4%, where mean CV_{AUC} = 4.69% and SD = 0.92%; **Figure 5.3**)[58] .

In single-cell resolution assays, sources of variation in cell preparatory steps become nuanced. Cell lysis is the dominant preparatory step for the single-cell immunoblot, and lysis behavior is influenced by the biochemical (e.g., fluidity or membrane composition[59]) and biomechanical (e.g., changes in viscoelasticity[60]) properties of each cell, which can vary extensively in embryos[60]. Consequently, given the established link between cellular properties and cellular lysis behavior, we primarily attribute variation in cell lysis behavior to biological sources. As such, including cell lysis variability in estimates of the technical variation threshold is likely to be overly conservative. Nevertheless, a more conservative technical variation threshold, at 11%, can be estimated when the impact of variable lysis behavior is included in protein expression variation of an enhanced green fluorescent protein–expressing cell line[58]. When comparing the intraembryonic variation in β-tubulin expression to the conservative average coefficient of variation of 11% (includes variation from cell lysis, which is arguably biological in origin), we observe a majority of embryos having variation larger than the threshold value (two of three embryos, n = 4 blastomeres per embryo; **Figure 5.1D**).

Determination of mRNA technical variation threshold. mRNA was extracted from mouse embryonic stem (ES) cells using TRIzol reagent, as per the manufacturer's instruction. mRNA was titrated to the expected mRNA content of embryos with low, medium, and high mRNA content (0.05, 0.4, and 1 ng per reaction, corresponding to two-cell embryos, oocytes, and blastocysts, respectively). Samples were processed as described and analyzed by RT-qPCR for β-actin, with 24 replicates per concentration. C_T values were calculated from amplification curves. The technical variation threshold $CV_{CT\ tech\ threshold}$ was computed as the average CV_{CT} plus three SDs for a 99% confidence interval ($CV_{CT\ tech\ threshold}$ = 0.77%; **Figure 5.4**).

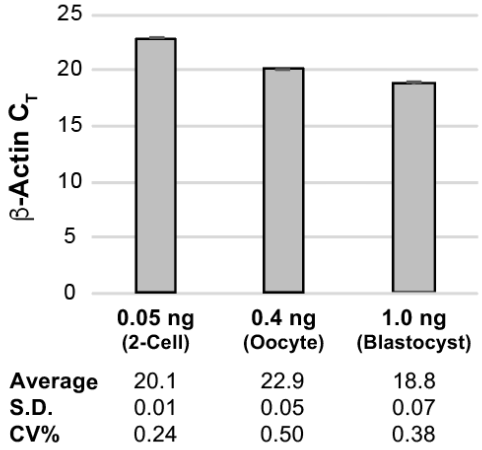

Figure 5.4. Determination of the mRNA technical variation threshold. mRNA was isolated from mouse embryonic stems cells and diluted to three concentrations of total mRNA (0.05 ng, 0.4 ng and 1 ng) corresponding to three embryonic stages with low, medium and high mRNA content (two-cell embryos, oocytes and blastocysts, respectively). 24 replicates of each concentration were analyzed for β-actin transcript abundance by RT-qPCR and C_T values were obtained from amplification curves. The C_T coefficient of variation (CV%) was calculated as the S.D./mean x 100 (N = 24 replicates per concentration). A technical variation threshold was computed as the mean CV across the three stages (0.37%) plus three standard deviations for a 99% confidence interval (S.D. = 0.13%) yielding $CV_{CT\ tech\ threshold}$ = 0.77%.

Image processing, signal quantification, and statistical analysis. The datasets generated and analyzed during this study are available from the corresponding author on reasonable request. Statistical tests were performed using GraphPad Prism 7.0b and MATLAB (R2017a, MathWorks). Quantification of fluorescence signal of protein immunoblots used in-house scripts written in MATLAB (R2017a, MathWorks)[58]. Briefly, Gaussian curves were fit to protein band fluorescence intensity profiles using MATLAB's Curve Fitting Toolbox. Gaussian fit parameters of protein peak location and σ were used to compute AUC by integrating the fluorescence intensity profile for the peak width, defined as 4 σ. We applied quality control metrics during quantification and identification of protein target peaks: (i) SNRs above the threshold of 3 and (ii) Gaussian fit with $R^2 > 0.7$. For assays exhibiting immunoreactivity on the perimeter of the microwell, we classified lysis as sufficient, if we observed that (i) all antibodies probed showed the same immunoreactivity and that (ii) all protein peaks passed the aforementioned quality control metrics. Fiji (ImageJ) was used to false color fluorescence micrographs and overlay channels to create composite images. ImageJ was used to compute cell volume[61]. Briefly, cell boundaries were traced using the freehand selection tool. We first computed cell diameter (ϕ) from traced area, followed by cell volume from cell diameter. For figures requiring stringent single-cell microwell occupancies, given the spherical shape of dissociated blastomeres[8], we excluded area traces with circularity factor of <0.8.

5.4 Results

Early-and late-stage embryos exhibit differences in mRNA-to-protein correlation. We sought to examine the transition from maternally deposited transcripts and proteins to postzygotically activated blastocysts[62,63]. In early-stage preimplantation embryos, transcripts are maternally inherited. In late-stage preimplantation embryos (i.e., blastocysts), the zygotic genome is fully activated and maternal transcripts are largely cleared by active and passive mechanisms[62,63]. With maturation, we anticipate a strengthening correlation between mRNA and protein levels. Consequently, we assessed two-cell embryos, four-cell embryos and blastocysts by same-embryo immunoblotting and mRNA analysis (**Figure 5.5A**). The same-embryo, multimodal analysis uses an open microfluidic device designed for (i) precision cell isolation, imaging, and fractionation of the cytoplasm from nucleus; (ii) single-embryo immunoblotting; and (iii) subsequent release and retrieval of nuclei-laden gel pallets for RT-qPCR. Suitable for analysis of intact embryos down to dissociated single blastomeres (100 to <5 pl), precision microfluidic handling indexes molecular and cellular information back to the originating intact embryo, allowing for measurements across multiple modalities to be compared. Given the wide range of cellular volumes among the preimplantation specimens under study (**Figure 5.5B**)[25], at the protein level, we first established a dynamic protein detection range spanning femtomoles (10^{-15}) to tens of attomoles (10^{-17}), with an assumed starting protein concentration in the micromolar range (**Figure 5.1**)[51]. At the mRNA level, nuclei derived from single blastocysts and analyzed by gel pallets subjected to RT-qPCR showed significantly lower cycle threshold (C_T) values for β-actin than negative controls. Negative controls included blanks, gel pallets with empty microwells, and samples lacking reverse transcriptase (Mann-Whitney *U* Test, $P = 0.0238$, with $n = 3$ replicates per sample; **Figure 5.6**).

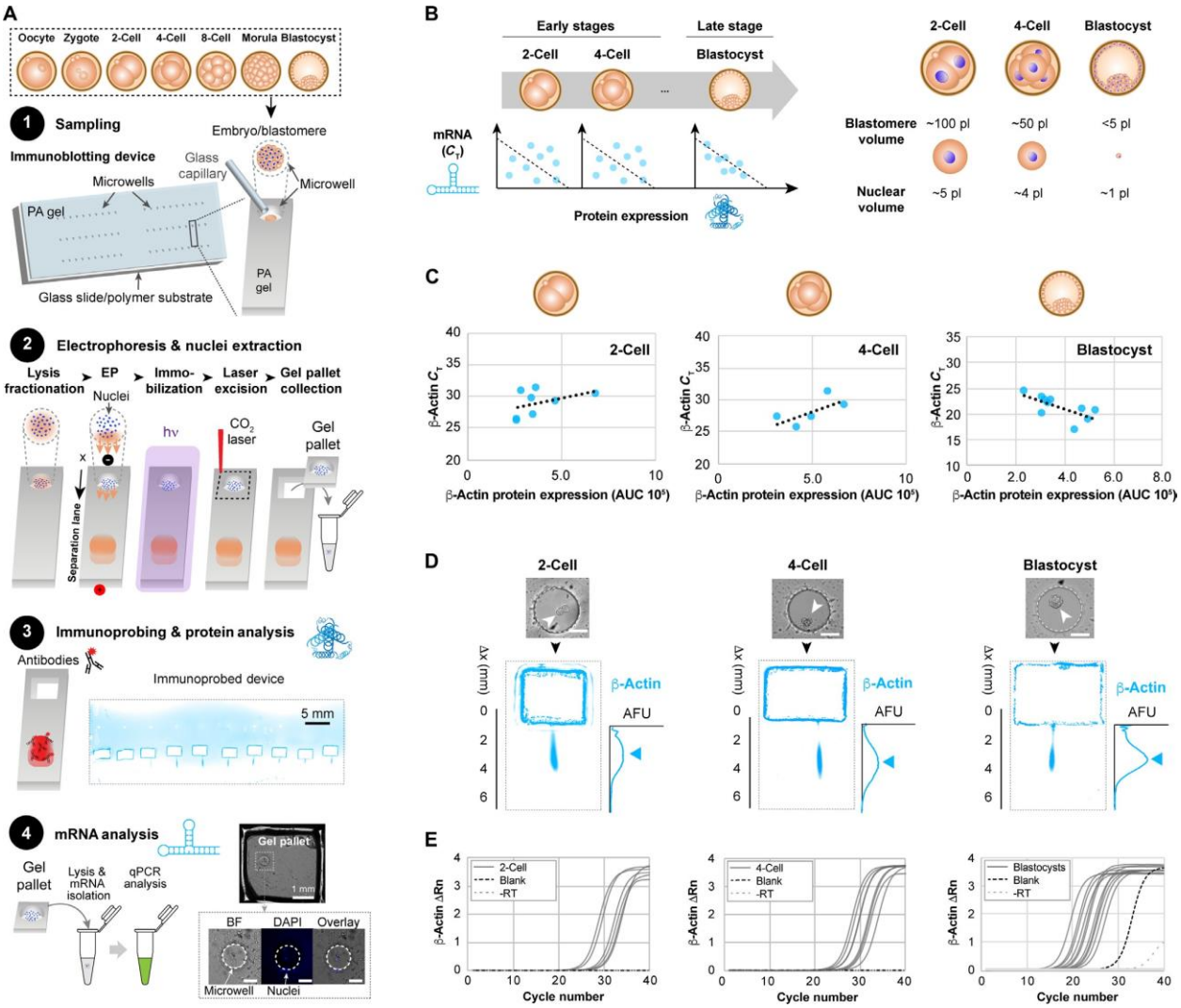

Figure 5.5 Same-embryo mRNA and protein expression analyses show positive correlation for late-stage murine preimplantation embryos, but not two-cell and four-cell embryos. (A) The same-embryo mRNA and microfluidic immunoblotting workflow begins with (1) sampling a single embryo or single blastomere into a microwell patterned on a polyacrylamide (PA) gel. (2) The cytoplasmic fraction of embryos sampled into wells is first lysed and electrophoresed across the PA layer, achieving separation of proteins by molecular mass. EP, electrophoresis. Proteins are photoblotted, or immobilized to the PA by UV-activated benzophenone chemistry, while a CO_2 laser cutter is used to extract sections of the PA-polymer film device, termed "gel pallets," that contain nuclei retained in the microwells. (3) The cytoplasmic proteins are probed with fluorophore-conjugated antibodies. False-color fluorescence micrograph shows a device immunoprobed for β-actin. (4) mRNA is isolated from gel pallets and analyzed for targets by RT-qPCR. Micrograph of a gel pallet housing Hoechst-stained nuclei. DAPI, 4′,6-diamidino-2-phenylindole. Scale bars, 50 μm unless specified. (B) Schematic illustrations of the expected correlations between mRNA and protein for early-stage versus late-stage preimplantation embryos (left), and relative dimensions of embryos and blastomeres for the stages studied (right). (C) β-Actin mRNA CT values and protein expression levels (AUC) for two-cell, four-cell, and blastocyst-stage embryos. Dashed lines show best linear fits (Pearson correlation coefficients for two-cell embryos, four-cell embryos, and blastocysts: 0.437, 0.674, and −0.668; with P = 0.279, 0.212, and 0.0348, for n = 8, 5, and 10 embryos, respectively). AFU, arbitrary fluorescence units. (D) Bright-field micrographs show intact two-cell–, four-cell–, and blastocyst- laden microwells. False-color fluorescence micrographs show resulting β-actin immunoblots, with rectangular perimeter of excised gel pallets visible in micrographs and corresponding intensity profiles shown to the right. (E) RT-qPCR β-actin amplification curves for two-cell–, four-cell–, and blastocyst-stage embryos and corresponding negative controls (−RT and blank controls consisting of empty gel pallets).

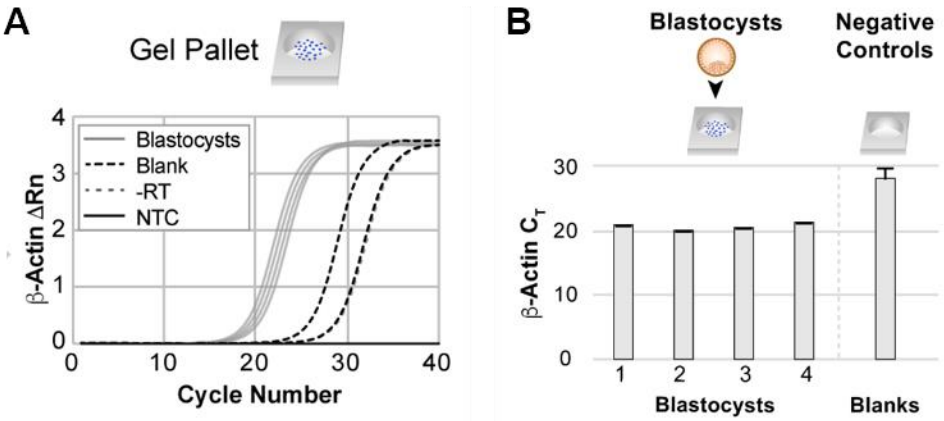

Figure 5.6. Validation of mRNA isolation and analysis from gel pallets. (a) RT-qPCR amplification curves reveal successful amplification of β-actin from mRNA isolated from gel pallets resulting from assayed blastocysts. Negative controls include blanks (empty gel pallets), –RT and NTC. (b) Bar graph of β-actin CT results after performing RT-qPCR on gel pallets containing single blastocyst nuclei and blanks (N = 3 replicates, 2 blanks).

We next examined protein and mRNA expression of β-actin in two-and four-cell embryos, where we observed no significant correlation between protein expression and β-actin C_T (Pearson correlation coefficients of 0.437 and 0.674 with P = 0.279 and 0.212, n = 8 two-cell embryos and n = 5 four-cell embryos) (**Figure 5.5C**). At the blastocyst stage, on the other hand, β-actin C_T and protein expression showed a significant, negative correlation (Pearson correlation coefficient = −0.668, P = 0.0348, for n = 10 embryos), indicating that mRNA and protein expression are positively correlated (**Figure 5.5C-D**). For two-cell and four-cell embryos, negative controls did not amplify. For blastocysts, all β-actin C_T values were significantly lower than the negative controls (**Figure 5.5E**). For all murine embryo stages assayed, interembryonic mRNA variation was higher than the C_T technical variation threshold ($CV_{CT\ tech\ threshold}$ = 0.77%; **Figure 5.4**), suggesting that biological and not technical variation was detected (CV_{CT} = 7.2, 7.8, and 10.8% for two-cell embryos, four-cell embryos, and blastocysts, respectively).

These results are in line with the transitioning status of the embryo from maternally deposited transcripts and proteins (actively and passively degraded at different rates), to the more stable environment of the postzygotically activated blastocyst at which point maternal clearance is largely or totally complete[62]. Given the unpredictable relationship between transcripts and protein at very early and unstable developmental stages, complementing transcriptional profiling with protein profiling from the same individual embryo provides a more comprehensive window into the biology governing preimplantation development.

Sister-blastomere GADD45a expression uniformity disappears between the two-cell and four-cell stages. The exact stage and circumstances by which blastomeres first acquire certain fates remain unknown. On the one hand, embryonic plasticity points to blastomere symmetry up to the eight-cell embryo, where embryos can compensate for the loss of one blastomere as early as the two-cell stage[64]. On the other hand, studies showing consistent bimodal expression of genes related to differentiation in early-stage sister blastomeres suggest that the involved factors may not be inherited equally by all blastomeres[8]. Whether this heterogeneity is transcriptional noise or leads to functional heterogeneity in the subsequent protein products remains an open question.

Consequently, we sought to inspect early-stage embryos for lineage biases by dissociating two-cell and four-cell embryos and measuring cell fate–related protein markers among the blastomeres of each embryo stage. We assayed early-stage blastomeres for a protein involved in DNA damage repair (GADD45a) that has been reported to show bimodal transcription levels at the two-cell and four-cell stages (**Figure 5.7A**)[3]. We controlled for variation arising from stochastic factors, such as asymmetrical partitioning of proteins and mRNA during cell division[10]. To do this, we concurrently probed for intracellular structural proteins expressed proportionally to cell volume (β-tubulin and β-actin; **Figure 5.7B**)[3] and compared protein expression variation among the protein markers.

In four-cell embryos, where sister blastomeres were assayed in parallel, we observed intraembryonic GADD45a expression variation that was significantly higher than both β-actin and β-tubulin expression variation ($CV_{GADD45a}$ = 29.9 ± 12.7%; $CV_{β\text{-}tub}$ = 11.1 ± 3.1%; $CV_{β\text{-}actin}$ = 10.5 ± 4.6%; mean $CV_{expression}$ ± SD, Mann-Whitney *U* test, *P* = 0.0012 for $CV_{GADD45a}$ versus $CV_{β\text{-}tub}$ and $CV_{GADD45a}$ versus $CV_{β\text{-}actin}$, and *P* = 0.805 for $CV_{β\text{-}tub}$ versus $CV_{β\text{-}actin}$, for *n* = 6 dissociated four-cell embryos, where all CVs > $CV_{threshold}$ of 7.4%) (**Figure 5.7C**). Furthermore, normalization by β-tubulin expression did not decrease the GADD45a CVs (Wilcoxon match-paired rank test, *P* = 0.156, *n* = 6). These findings suggest that blastomeres of four-cell embryos show heterogeneous expression of GADD45a, as corroborated by mRNA and IF-based findings[3]. Given that *Gadd45a* transcript levels have been shown to differ between sister two-cell blastomeres[3], we next determined if this heterogeneity in mRNA levels manifests as differential GADD45a protein expression in the two-cell embryo (**Figure 5.7D**). In contrast to the four-cell stage, dissociated two-cell sister blastomeres showed a statistically significant increase in GADD45a protein expression CV over β-tubulin, but not β-actin ($CV_{GADD45a}$ = 16 ± 6.0%; $CV_{β\text{-}tubulin}$ = 10 ± 6.5%; $CV_{β\text{-}actin}$ = 11 ± 7.0%; mean ± SD, Mann-Whitney *U* test, *P* = 0.0323 for $CV_{GADD45a}$ versus $CV_{β\text{-}tubulin}$ and *P* = 0.130 for $CV_{GADD45a}$ versus $CV_{β\text{-}actin}$, for *n* = 11 dissociated two-cell embryos) (**Figure 5.7E**). Thus, while the expression of GADD45a at the four-cell stage shows higher heterogeneity than both β-tubulin and β-actin, the same cannot be said about sister blastomeres from the two-cell stage.

Given the unique nature of the two-cell embryo, which is the only "multicellular" stage of development undergoing both zygotic genome activation (ZGA) and maternal clearance[63], single-blastomere protein analysis complements our understanding of heterogeneity observed at the mRNA level[3]. While the exact nature of the transcriptional, translational, and degradation events occurring within the two-cell embryos are not completely clear, deeper scrutiny of the early two-cell state is essential.

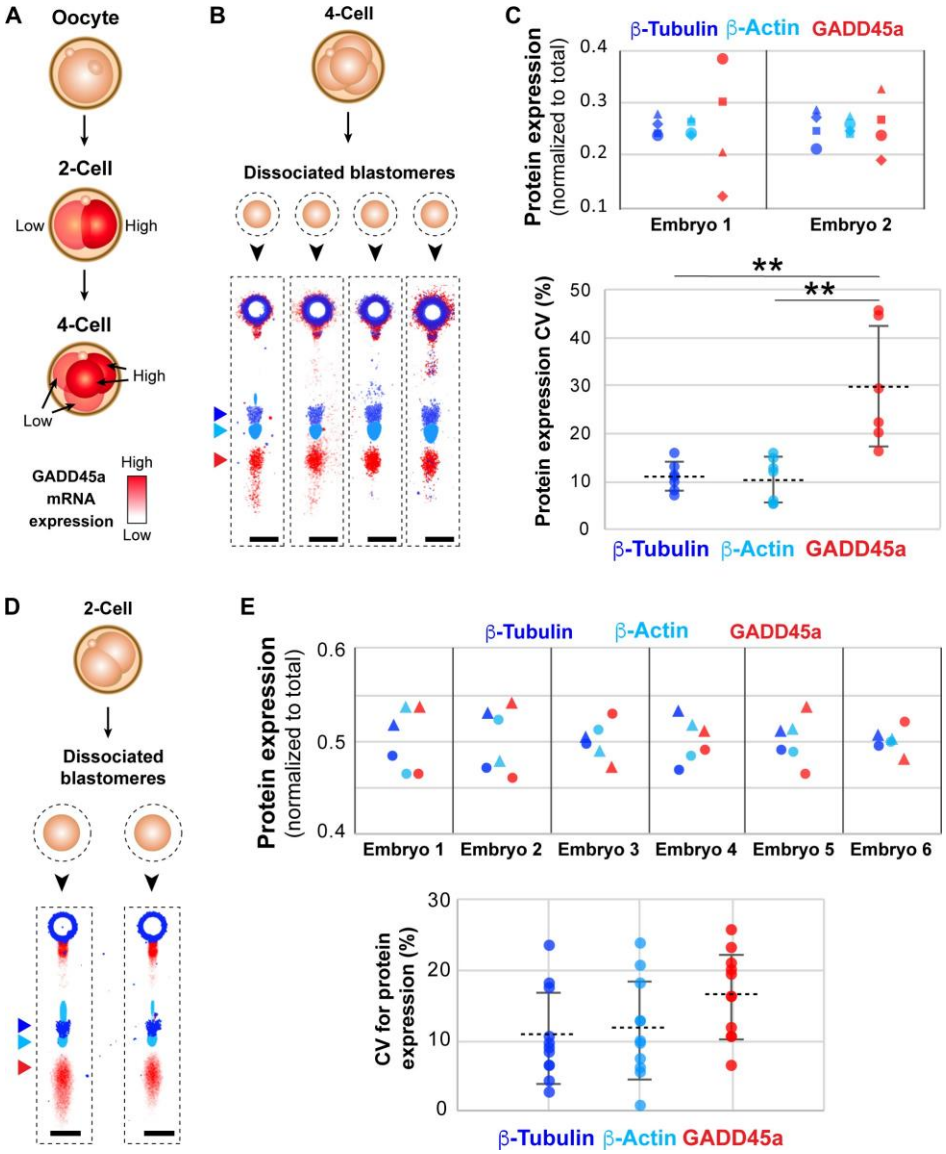

Figure 5.7. Microfluidic immunoblotting measures intraembryonic heterogeneity in GADD45a expression in murine four-cell and two-cell embryos. (A) GADD45a transcript levels have been shown to exhibit bimodality at the two- and four-cell stages. (B) Four-cell embryos are dissociated into individual blastomeres and immuno- blotted for protein expression of β-tubulin, β-actin, and GADD45a, as shown in false-color fluorescence micrographs. (C) Dot plot of expression of β-tubulin (blue), β-actin (cyan), and GADD45a (red) normalized to total expression by individual blastomeres from two representative four-cell embryos (top). Dot plot of intraembryonic coefficient of variation (CV) in protein expression for β-tubulin, β-actin, and GADD45a (bottom, Mann-Whitney *U* test, P = 0.0012 for $CV_{GADD45a}$ versus $CV_{β\text{-}tubulin}$ and $CV_{GADD45a}$ versus $CV_{β\text{-}actin}$, and P = 0.805 $CV_{β\text{-}tub}$ versus $CV_{β\text{-}actin}$, for n = 6 dissociated embryos). **P < 0.01. (D) Two-cell embryos are dissociated into individual blastomeres and assayed for protein expression of β-tubulin, β-actin, and GADD45a, as shown in false-color fluorescence micrographs. (E) Dot plots of β-tubulin, β-actin, and GADD45a expression by sister blastomeres, normalized to sum of expression of sister blastomeres, for six representative two-cell embryos (top). Dot plot of interblastomeric CV% in expression of β-tubulin, β-actin, and GADD45a (bottom, Mann-Whitney U test, P = 0.0323 for $CV_{GADD45a}$ versus $CV_{β\text{-}tubulin}$, P = 0.130 for $CV_{GADD45a}$ versus $CV_{β\text{-}actin}$, and P = 0.598 for $CV_{β\text{-}tubulin}$ versus $CV_{β\text{-}actin}$, for n = 11 dissociated two-cell embryos). Same marker for a given embryo in (C) and (E) indicates same blastomere. Horizontal bars in (C) and (E) indicate mean ± SD. Scale bars, 200 μm.

Truncated DICER-1 isoform expression decreases from the oocyte to the two-cell stage. Alternative splicing occurs frequently during early embryonic development in mouse and human[65]. However, efforts to investigate whether the corresponding alternate protein isoforms are ultimately and stably generated require pooling hundreds of collected embryos from each stage, losing interblastomeric information[66]. The role of alternative isoform usage between sister blastomeres and what role this has on cell fate specification are still unclear. Thus, resolving proteoforms generated by alternative splicing would benefit from precision tools with single-embryo resolution.

To this end, we examined one of the earliest known examples of a protein isoform that exists in mouse development: DICER-1. DICER-1 is essential for small RNA–mediated gene expression regulation. By processing small RNAs into their mature form, DICER-1 generates sequence-specific guides required by effector complexes to target cognate mRNAs and regulate their translation[67]. Bulk analyses of mouse oocytes by others have found high expression of an N-terminally truncated isoform, denoted $DICER^{O}$ (**Figure 5.8A**)[67], which demonstrates higher catalytic activity than its full-length version and is believed to drive the high activity of endogenous small interfering RNAs (endo-siRNAs) in mouse oocytes, but not in somatic cells[67]. The $DICER^{O}$ transcript persists until the fertilized zygote stage, but whether the $DICER^{O}$ protein isoform is exclusive to oogenesis or is maternally inherited by the preimplantation embryo remains unknown.

We asked if $DICER^{O}$ is specific to the oocyte stage by assaying oocytes and two-cell embryos for isoforms of DICER-1 at the protein and mRNA level. We collected oocytes and two-cell embryos and divided each sample for analysis of either protein or mRNA. Samples destined for protein analysis were processed by single-embryo immunoblotting, while samples analyzed for mRNA were individually lysed and processed by single-embryo RT-qPCR. Using a pan-specific DICER-1 antibody probe, single-embryo polyacrylamide gel electrophoresis (PAGE) resolved multiple DICER-1 isoforms by relative order of electromigration, detecting both the full-length DICER-1 form (larger molecular mass band) and the truncated form (smaller molecular mass band; **Figure 5.8B**). We observed that both oocytes and two-cell embryos expressed truncated isoforms of DICER-1 (**Figure 5.8B-C**). Nonreducing slab-gel Western blotting of 85 pooled oocytes also reported two DICER-1 protein bands, with a smaller molecular mass peak of higher intensity, corroborating single-oocyte immunoblotting results regarding the truncated DICER-1 isoform (**Figure 5.8D**).

Within oocytes, we observed significantly higher expression of the truncated isoform over the full-length DICER-1 for both normalized mRNA and protein (for $mRNA/Rfx1_{DICER\text{-}1}$ versus $mRNA/Rfx1_{DICER^{O}}$: Mann-Whitney *U* test, $P = 0.0052$ for $n = 18$; for protein band $AUC_{DICER\text{-}1}$ versus $AUC_{DICER^{O}}$: Mann-Whitney *U* test, $P = 0.0079$ for $n = 5$; **Figure 5.8B**). For whole two-cell embryos, we found no significant difference between expression of truncated and full-length isoforms of DICER-1 (for $mRNA/Rfx1_{DICER\text{-}1}$ versus $mRNA/Rfx1_{DICER^{O}}$: Mann-Whitney *U* test, $P = 0.9551$ for $n = 7$ for DICER-1 and $n = 8$ for DICER; for $AUC_{DICER\text{-}1}$ versus $AUC_{DICER^{O}}$: Mann-Whitney *U* test, $P = 0.20$ for $n = 4$) (**Figure 5.8C**).

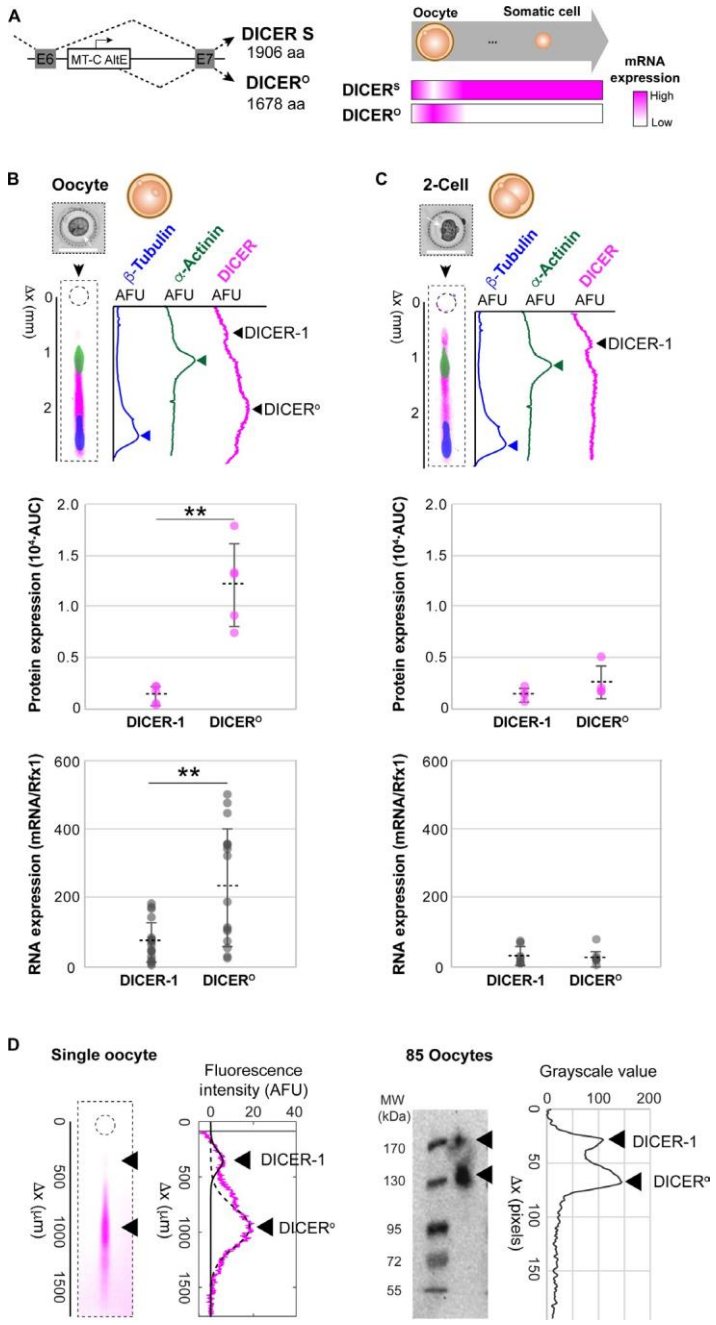

Figure 5.8. Higher DICER-1 isoform expression in murine oocytes than in two-cell embryos correlates with mRNA levels. (A) DICER^{O}, a truncated isoform of DICER-1, appears at the oocyte stage and is a product of alternative promoter usage. aa, amino acid. Bright-field micrographs of (B) a settled oocyte, **P < 0.01 and (C) a settled two-cell embryo, with corresponding overlaid false-color fluorescence micrographs and intensity profiles showing protein bands for loading controls (α-actinin and β-tubulin) and DICER-1. Oocyte immunoblot demonstrates presence of a full-length DICER-1 (top arrow) and a lower molecular mass isoform (bottom arrow). Under these, dot plots of DICER isoform mRNA levels normalized by endogenous control Rfx1 (top) and protein expression (AUC, bottom). Expression of the truncated isoform is higher than the full-length DICER-1 for both mRNA and protein in oocytes (mRNA/Rfx1$_{DICER\text{-}1}$ versus mRNA/Rfx1$_{DICER}{}^{O}$: Mann-Whitney U test, P = 0.0052 for n = 18; for AUC$_{DICER\text{-}1}$ versus AUC$_{DICER}{}^{O}$: Mann-Whitney U test, P = 0.0079 for n = 5), but not in two-cell embryos (for mRNA/Rfx1$_{DICER\text{-}1}$ versus mRNA/Rfx1$_{DICER}{}^{O}$: Mann-Whitney U test, P = 0.9551 for n = 7 for DICER-1 and n = 8 for DICER^{O}; for AUC$_{DICER\text{-}1}$ versus AUC$_{DICER}{}^{O}$: Mann-Whitney U test, P = 0.20 for n = 4). Oocytes show higher mRNA and protein expression than two cells for the truncated isoform mRNA/Rfx1$_{DICER}{}^{O}$: Mann Whitney U test, P = 0.0004 for n = 18

oocytes and 8 two cells; AUC_{DICER}^{O}: Mann Whitney U test, P = 0.0159 for n = 5 oocytes and 4 two-cell embryos), but not the full-length DICER-1 (mRNA/$Rfx1_{DICER-1}$: Mann Whitney U test, P = 0.084 for n = 18 oocytes and 7 two-cell embryos; $AUC_{DICER-1}$: Mann Whitney U test, P = 0.9048 for n = 5 oocytes and 4 two-cell embryos). Horizontal bars indicate mean ± SD. Scale bars, 200 μm. (D) Fluorescence micrograph of a single oocyte immunoblotted for DICER-1 with corresponding fluorescence intensity profiles and Gaussian curve fits to the $DICER^{O}$ isoform (low molecular mass, R^2= 0.83, solid black line) and DICER-1 full-length isoform (R^2 = 0.89, dotted black line). To the right, slab-gel Western blot analysis of pooled oocytes (n = 85 oocytes) and corresponding grayscale value profile show two DICER-1 protein bands. Oocytes were pooled, lysed, and assayed by nonreducing SDS-PAGE followed by immunoprobing. Buffers and immunoprobing reagents matched the single-embryo protocol. Black arrowheads mark the position of the DICER-1 bands.

When comparing full-length DICER-1 expression levels between the oocyte and two-cell stages, expression was not significantly different by mRNA or by protein expression (mRNA/$Rfx1_{DICER-1}$: Mann Whitney *U* test, $P = 0.084$ for $n = 18$ oocytes and 7 whole two-cell embryos; $AUC_{DICER-1}$: Mann-Whitney *U* test, $P = 0.9048$ for $n = 5$ oocytes and 4 two-cell embryos). When comparing the truncated DICER-1 isoform expression levels, however, we observed a significant decrease from the oocyte to the two-cell stage in both mRNA and protein levels (mRNA/$Rfx1_{DICER}^{O}$: Mann-Whitney *U* test, P = 0.0004 for $n = 18$ oocytes and 8 two cells; AUC_{DICER}^{O}: Mann-Whitney *U* test, $P = 0.0159$ for $n = 5$ oocytes and 4 two-cell embryos).

Precision analyses of oocytes and two-cell embryos report a notable decrease in the truncated DICER-1 protein isoform and mRNA expression between the stages, but no notable decrease in full-length DICER-1 across the same development stages. Our results support a role for $Dicer^{O}$ being maternally generated and available at the time of fertilization. In line with previous studies[67], $Dicer^{O}$ appears to have a critical role in oocyte maturation and spindle assembly before fertilization. The observed clearance of the truncated isoforms after fertilization suggests a role limited to the oocyte that does not extend into the preimplantation embryo.

Integrating phenotypic information with precision molecular profiling of cell lineage. We sought to achieve a more comprehensive understanding of cell state by integrating phenotype profiling of intact cells with subsequent single-cell analyses of mRNA and protein. First, we asked whether the TE or ICM state could be determined among blastomeres dissociated from blastocysts using a multimodal assay that integrates intact cell imaging with relative expression of protein markers understood to be specific to TE versus ICM (i.e., CDX-2 versus SOX-2, respectively) (**Figure 5.9A**). Here, internalization of fluorescent beads acted as a proxy for TE or ICM cell type within a blastocyst[50], on the basis of the originating location of the blastomere.

To obtain phenotypic information, we selectively stained the outer TE cells by incubating blastocysts (3.5 to 4 dpc) with a solution of fluorescent microspheres[50]. With bead-based staining, ICM cells (inner cells) do not fluoresce, while TE cells (outer cells) do fluoresce, indicating internalization of fluorescent microspheres[50]. Blastocysts were then dissociated into single cells, settled into microwells, and imaged for the presence of microspheres (**Figure 5.9A**). Subsequent immunoblotting for β-tubulin, SOX-2, and CDX-2 revealed negligible levels of SOX-2 and high levels of CDX-2 in blastomeres that were positive for microsphere signal, indicating TE cell type (**Figure 5.9A**). Blastomeres with no detectable microsphere signal, suggesting ICM cell type, expressed high levels of SOX-2 and negligible levels of CDX-2 (**Figure 5.9A**).

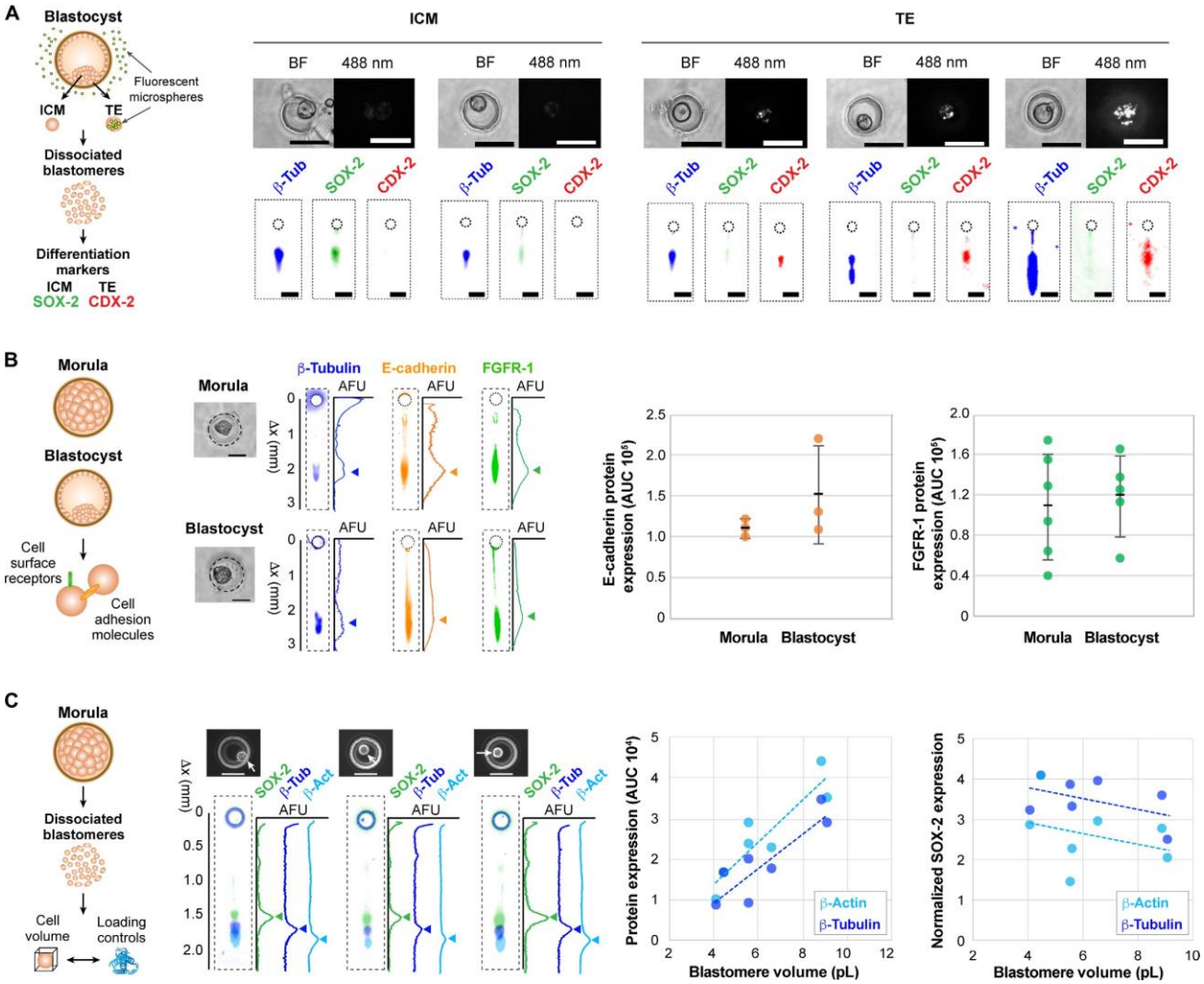

Figure 5.9. Whole-cell imaging adds phenotypic content to protein analysis of single embryos and blastomeres. (A) Cell type-graded expression of CDX-2 and SOX-2 in blastomeres from dissociated blastocysts. Bright-field and fluorescence micrographs of dissociated blastocysts after incubation with fluorescent microspheres and corresponding micrographs of blastocysts immunoblotted for β-tubulin, CDX-2, and SOX-2. Scale bars, 50 μm. (B) Detection of membrane proteins in morula and blastocysts. Bright-field micrographs showing embryos settled into microwells before lysis, with resulting false-color micrographs immunoblots for β-tubulin, E-cadherin, and FGFR-1, with corresponding fluorescence intensity profiles shown to the right. Scale bars, 100 μm. Dot plots of E-cadherin (left) and FGFR-1 (right) expression for morula and blastocysts (for E-cadherin: n = 3 and 3 morula and blastocysts, for FGFR-1: n = 6 and 5 morula and blastocysts). Horizontal bars represent mean ± SD. (C) Microscopy and single-blastomere immunoblotting identifies correlations between cell volume and marker expression in dissociated morula blastomeres. False-color fluorescence micro- graphs show β-tubulin, β-actin, and SOX-2 protein bands, with intensity profiles adjacent to micrographs. Arrows mark the position of protein bands. Scale bars, 100 μm. To the right, bivariate plot of blastomere cell volume and loading control expression (β -tubulin and β-actin) shows significant positive linear correlation (Pearson correlation, n = 8, ρ = 0.883 and 0.908, P = 0.00366 and 0.00018, respectively). Bivariate plot of cell volume versus SOX-2 expression normalized by β-tubulin and β-actin expression show a negative, but nonsignificant, association (Pearson correlation, n = 8, ρ = −0.487 and −0.315, P = 0.221 and 0.447, respectively).

In a corollary study, we considered modulation of preimplantation development through membrane proteins[68]. In both morula and blastocysts, we profiled the cell adhesion protein E-cadherin and the cell surface receptor fibroblast growth factor receptor 1 (FGFR-1; **Figure 5.9B**). For both proteins, expression did not significantly differ between the morula and blastocyst

stages (Mann-Whitney *U* test, $n = 3$, $P = 0.400$ for E-cadherin; $n = 6$ and 5 for morula and blastocysts, respectively, $P = 0.465$ for FGFR-1; **Figure 5.9B**).

Second, we sought to integrate knowledge that cellular concentration is understood to be a more accurate indicator of cell phenotype than total abundance[69]. The transcriptional profile of housekeeping genes (e.g., β-actin and β-tubulin) is often not stably and homogeneously expressed across different cell samples, experimental conditions, or treatments[70]. To understand if this observed variability prevails at the protein level, we scrutinized the assertion that—at the protein level—both β-tubulin and β-actin can be used as proxies for cell volume. Dissociated morula blastomeres were first interrogated by whole-cell bright-field imaging and subsequently by single-cell immunoblotting (**Figure 5.9C**). We observed a significant, positive correlation between cell volume and protein expression of both β-tubulin and β-actin (**Figure 5.9C**; Pearson correlation, $\rho = 0.883$ and 0.908, $P = 0.00366$ and 0.00018, respectively, for $n = 8$ blastomeres).

We further scrutinized dissociated blastocysts to establish if smaller blastomeres express higher levels of SOX-2, the transcription factor involved in pluripotency gene expression[71]. We dissociated blastocysts into single blastomeres, measured the diameter of each by bright-field microscopy, and then assayed each for SOX-2 by single-blastomere immunoblot. For blastomeres expressing SOX-2, we compared SOX-2 expression to the measured cell volume and found a significant, negative correlation (Pearson correlation, $\rho = -0.899$, $P = 0.00589$ for $n = 7$ single blastomeres; **Figure 5.10**), as expected at the blastocyst stage[71,72]. We then performed the same analysis for morula and again observed an expected negative correlation[72] between SOX-2 expression and volume of morula blastomeres for both β-tubulin and β-actin normalization (**Figure 5.9C**; Pearson correlation, $n = 8$, $\rho = -0.487$ and -0.315, $P = 0.221$ and 0.447, respectively).

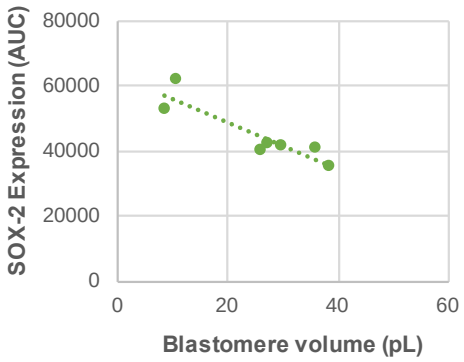

Figure 5.10. Validating an expected inverse correlation between cell volume and SOX-2 expression for single blastomeres disaggregated from blastocysts. SOX-2 expression was measured by single-blastomere immunoblot and blastomere volume was computed from bright field images of each blastomere seated in a microwell prior to immunoblot. SOX-2 expression shows a significant negative correlation with blastomere volume (Pearson correlation, $\rho = -0.899$, p value = 0.00589 for N = 7 single blastomeres).

5.5 Discussion & Conclusions

The exact timing and mechanism by which the first cell fate decisions occur during mammalian preimplantation development remain unknown. Pivotal open questions include whether developing blastomeres remain homogeneous and functionally equivalent until the compacted morula stage[1] or if blastomeres exhibit symmetry-breaking configurations, perhaps as early as the two-cell stage[5,7,9]. Yet, transcript abundance is not an accurate determinant of protein abundance. The asynchrony observed between mRNA and protein expression may reflect

the uncoupled relationship between transcription and translation in the early embryo (up to 15 hours between transcription and translation), synchronizing more tightly in later cleavage stages[11].With both the now-understood loose correlation between mRNA and protein expression levels and critical shortcomings of the de facto standard for direct measurement of endogenous, unmodified proteins (i.e., immunoassays), we describe a multimodal microfluidic platform optimized for the study of murine preimplantation embryo development.

During cell fate determination, we scrutinized two-cell and four-cell embryos for GADD45a heterogeneity at protein level; *GADD45a* is a gene shown to be bimodally transcribed in early embryonic stages. By scrutinizing the blastomeres that comprise four-cell embryos, we detected higher heterogeneity in GADD45a protein expression than loading controls β-tubulin and β-actin, providing the protein-based validation of recent single-cell RNA sequencing (RNA-Seq) predictions. At the oocyte and two-cell embryo stages, we observed a truncated DICER-1 protein isoform as dominant in the oocyte stage with significantly lower truncated *DICER-1* mRNA and isoform levels at the two-cell stage. The observation suggests inheritance from the oocyte stage and corroborates studies suggesting that the higher-activity truncated DICER-1 isoform is oocyte-specific.

Simultaneous measurement of mRNA and protein from embryos of the same donor enhances the biological accuracy of correlations between mRNA levels and protein expression at different stages of the preimplantation embryo. Such insight into the expression dynamics would clarify how modulation in transcription dictates cellular phenotype. Our findings more accurately characterize the discrepancy between transcript abundance and protein presence in the early preimplantation embryo, a phenomenon that is ameliorated by the blastocyst stage, which coincides precisely with the maternal-to-zygotic transition experienced by all preimplantation embryos of all studied species. Companion functional competency measurements guided by the ever-increasing resolution of single-cell transcript approaches will help in determining the proteins and isoforms involved in key cell fate decisions. Further, given the importance of secreted proteins in lineage segregation[68], a study is underway to advance same-cell microfluidic tools to assess both intraembryonic proteins and secreted proteins.

As detailed here, the ~10 to 20 embryos harvested from a single mouse donor are sufficient not just for one immunoblot but for multiple single-embryo and single-blastomere immunoblots. The precision in sample handling and enhanced sensitivity notably reduces the conventional PAGE sample requirements of several hundreds or thousands of embryos[66,67]. The implications are multifold. First, as single-embryo immunoblots inherently and markedly lower sample requirements, the burden of animal sacrifice is likewise reduced. Current gold standard protein measurements consist of conventional western blotting, which, depending on expected protein abundance, requires combination of 50 to 100 embryos to ensure a detectable signal[73]. These issues are made further dismal in cases involving subfertility or when a specific genotype is required. For wild-type mouse conditions, conventional western blotting would require the sacrifice of 5 to 10 mice per lane (or measurement). If a specific genotype is needed, then this value is multiplied by the difficulty in procuring the needed samples. With the strategy described here, a single mouse could provide sufficient material for up to 10 to 20 individual measurements. Second, statistical interpretation of single-embryo and single-blastomere immunoblot results is feasible, revealing intraembryonic heterogeneity, as well as significant differences between embryos of the same fertilization event and between donors. Last, immunoblots can be stored and reprobed for additional proteins as previously unidentified, important targets emerge in the rapidly advancing field of developmental biology.

Open questions remain; although nuclear mRNA and whole-cell mRNA are strongly correlated[74], specific exceptions do exist, including genes involved in splicing[74,75]. Biological interpretation of correlation (or lack thereof) between mRNA and protein expression levels should include consideration of whether nuclear mRNA levels (measured here) reflect whole-embryo mRNA levels. Understanding of nuclear versus whole-cell mRNA distributions in the preimplantation embryo is currently lacking. Reports on ZGA and maternal clearance suggest that, as maternal transcripts are degraded[76], the whole-cell mRNA, thus, comprises a mixture of old (cytoplasmic) transcripts and new (nuclear) transcripts. After fertilization, nuclear transcripts should largely represent the total and zygotically active transcriptome, while most of cytoplasmic transcripts are inherited and no longer actively contribute to the newly active zygotic proteome; however, the kinetics of this transition have been difficult to study. Using approaches like that described here, we seek to boost understanding of questions such as if and when the nuclear mRNA fraction constitutes an accurate representation of the embryo's emerging proteome.

In mice, ZGA occurs shortly after fertilization and is not fully realized until the two-cell stage, at which point nascent mRNA populates the embryonic transcriptome[76]. At the same time, maternally inherited transcripts and proteins are being actively and passively cleared and degraded at different rates, further confounding results and interpretations of early preimplantation studies[62]. While recent single-cell RNA-Seq experiments reveal sister blastomere transcriptome heterogeneity as early as the two-cell embryo in both humans and mice[3], functional studies suggest these differences may not be relevant until the four-cell stage or later (if at all)[2,6]. Therefore, careful assessment of exact fertilization times is needed to compare early embryos (pronucleus and two-cell), while sister blastomere comparisons are ideal for later stages. Biological variation such as the exact timing of fertilization can potentially be more tightly controlled using in vitro fertilization, at the risk of introducing technical artifacts. The use of in vitro culture could additionally complicate analysis as sibling embryos can spontaneously respond poorly to identical culturing conditions[77].

Last, with the advent of new gene editing technologies (e.g., CRISPR, genomic screening methods including targeted, exome, or whole-genome sequencing), screening for on-target and off-target activity has become critical, as unintended editing events can lead to exon skipping, alternative splicing, and deletions that occasionally lead to active versions of supposedly "knocked out" targets[78]. Protein assays that can complement genomic screening, such as the one described in this study, will be crucial for screening embryos for protein-level effects of both on-target and off-target mutations, even when the latter occur in noncoding regions.

5.6 References

1. Motosugi, N., Bauer, T., Polanski, Z., Solter, D. & Hiiragi, T. Polarity of the mouse embryo is established at blastocyst and is not prepatterned. *Genes and Development* **19**, 1081–1092 (2005).
2. Fujimori, T. Analysis of cell lineage in two- and four-cell mouse embryos. *Development* **130**, 5113–5122 (2003).
3. Biase, F. H., Cao, X. & Zhong, S. Cell fate inclination within 2-cell and 4-cell mouse embryos revealed by single-cell RNA sequencing. *Genome Research* **24**, 1787–1796 (2014).
4. Brown, C. E. *et al.* Genetic programs in human and mouse early embryos revealed by single-cell RNA sequencing. *Nature* **500**, 4062–4072 (2016).

5. Torres-Padilla, M. E., Parfitt, D. E., Kouzarides, T. & Zernicka-Goetz, M. Histone arginine methylation regulates pluripotency in the early mouse embryo. *Nature* **445**, 214–218 (2007).
6. Bischoff, M., Parfitt, D.-E. & Zernicka-Goetz, M. Formation of the embryonic-abembryonic axis of the mouse blastocyst: relationships between orientation of early cleavage divisions and pattern of symmetric/asymmetric divisions. *Development* **135**, 953–962 (2008).
7. White, M. D. *et al.* Long-Lived Binding of Sox2 to DNA Predicts Cell Fate in the Four-Cell Mouse Embryo. *Cell* **165**, 75–87 (2016).
8. Casser, E. *et al.* Totipotency segregates between the sister blastomeres of two-cell stage mouse embryos. *Scientific Reports* **7**, 1–15 (2017).
9. Plachta, N., Bollenbach, T., Pease, S., Fraser, S. E. & Pantazis, P. Oct4 kinetics predict cell lineage patterning in the early mammalian embryo. *Nature Cell Biology* **13**, 117–123 (2011).
10. Shi, J. *et al.* Dynamic transcriptional symmetry-breaking in pre-implantation mammalian embryo development revealed by single-cell RNA-seq. *Development* **142**, 3468–3477 (2015).
11. Nothias, J. Y., Miranda, M. & DePamphilis, M. L. Uncoupling of transcription and translation during zygotic gene activation in the mouse. *The EMBO journal* **15**, 5715–25 (1996).
12. Bordeaux, J. *et al.* Antibody validation. *BioTechniques* **48**, 197–209 (2010).
13. Trenchevska, O., Nelson, R. W. & Nedelkov, D. Mass spectrometric immunoassays for discovery, screening and quantification of clinically relevant proteoforms. *Bioanalysis* **8**, 1623–1633 (2016).
14. Schnell, U., Dijk, F., Sjollema, K. A. & Giepmans, B. N. G. Immunolabeling artifacts and the need for live-cell imaging. *Nature Methods* **9**, 152–158 (2012).
15. Teves, S. S. *et al.* A dynamic mode of mitotic bookmarking by transcription factors. *Elife* **5**, (2016).
16. Zhu, Y. *et al.* Nanodroplet processing platform for deep and quantitative proteome profiling of 10-100 mammalian cells. *Nature Communications* **9**, 1–10 (2018).
17. Zhu, Y. *et al.* Proteomic Analysis of Single Mammalian Cells Enabled by Microfluidic Nanodroplet Sample Preparation and Ultrasensitive NanoLC-MS. *Angewandte Chemie International Edition* **14642**, 12370–12374 (2018).
18. Budnik, B., Levy, E. & Slavov, N. SCoPE-MS: Mass-spectrometry of single mammalian cells quantifies proteome heterogeneity during cell differentiation. *Genome Biology* 1–16 (2017) doi:10.1101/102681.
19. Specht, H. & Slavov, N. Transformative Opportunities for Single-Cell Proteomics. *J Proteome Res.* **17**, 2562–2571 (2018).
20. Kang, C. C., Lin, J. M. G., Xu, Z., Kumar, S. & Herr, A. E. Single-cell western blotting after whole-cell imaging to assess cancer chemotherapeutic response. *Analytical Chemistry* **86**, 10429–10436 (2014).
21. Hughes, A. J. *et al.* Single-cell western blotting. *Nature Methods* **11**, 749–755 (2014).
22. Kang, C.-C. *et al.* Single cell–resolution western blotting. *Nature Protocols* **11**, 1508–1530 (2016).
23. Kim, J. J., Sinkala, E. & Herr, A. E. High-selectivity cytology via lab-on-a-disc western blotting of individual cells. *Lab Chip* **17**, 855–863 (2017).
24. Yamauchi, K. A. & Herr, A. E. Subcellular western blotting of single cells. *Microsystems and Nanoengineering* **3**, (2017).
25. Tsichlaki, E. & Fitzharris, G. Nucleus downscaling in mouse embryos is regulated by cooperative developmental and geometric programs. *Scientific Reports* **6**, 1–7 (2016).

26. Epifano, O., Liang, L. F., Familari, M., Moos, M. C. & Dean, J. Coordinate expression of the three zona pellucida genes during mouse oogenesis. *Development (Cambridge, England)* **121**, 1947–56 (1995).
27. Martín-Coello, J., González, R., Crespo, C., Gomendio, M. & Roldan, E. R. S. Superovulation and in vitro oocyte maturation in three species of mice (Mus musculus, Mus spretus and Mus spicilegus). *Theriogenology* **70**, 1004–1013 (2008).
28. Marangos, P. Preparation of Cell Lysate from Mouse Oocytes for Western Blotting Analysis. in *Oogenesis: Methods and Protocols* (ed. Nezis, I. P.) 209–215 (Springer New York, 2016). doi:10.1007/978-1-4939-3795-0_15.
29. Tang, F. *et al.* RNA-Seq analysis to capture the transcriptome landscape of a single cell. *Nature Protocols* **5**, 516–535 (2010).
30. Darmanis, S. *et al.* Simultaneous Multiplexed Measurement of RNA and Proteins in Single Cells. *Cell Reports* **14**, 380–389 (2016).
31. Stuart, T. & Satija, R. Integrative single-cell analysis. *Nature Reviews Genetics* **20**, 257–272 (2019).
32. Nicolet, B. P., Guislain, A. & Wolkers, M. C. Combined single-cell measurement of cytokine mRNA and protein identifies T cells with persistent effector function. *J. Immunol.* **198**, 962–970 (2017).
33. Frei, A. *et al.* Highly multiplexed simultaneous detection of RNAs and proteins in single cells. *Nat Methods* **3**, (2016).
34. Schulz, D. *et al.* Simultaneous multiplexed imaging of mRNA and proteins with subcellular resolution in breast cancer tissue samples by mass cytometry. *Cell Systems* **6**, 25-36.e5 (2018).
35. Eliscovich, C., Shenoy, S. & Singer, R. Imaging mRNA and protein interactions within neurons. *Proceedings of the National Academy of Sciences* **114**, E1875–E1884 (2017).
36. Albayrak, C. *et al.* Digital Quantification of Proteins and mRNA in Single Mammalian Cells. *Molecular Cell* **61**, 914–924 (2016).
37. Peterson, V. M. *et al.* Multiplexed quantification of proteins and transcripts in single cells. *Nature Biotechnology* **35**, 936–939 (2017).
38. Stoeckius, M. *et al.* Simultaneous epitope and transcriptome measurement in single cells. *Nature Methods* **14**, 865–868 (2017).
39. Genshaft, A. S. *et al.* Multiplexed, targeted profiling of single-cell proteomes and transcriptomes in a single reaction. *Genome Biology* **17**, 1–15 (2016).
40. Gerlach, J. P. *et al.* Combined quantification of intracellular (phospho-)proteins and transcriptomics from fixed single cells. *Scientific Reports* **9**, 1–10 (2019).
41. Gosselin, E. J., Cate, C. C., Pettengill, O. S. & Sorenson, G. D. Immunocytochemistry: Its evolution and criteria for its application in the study of epon-embedded cells and tissue. *American Journal of Anatomy* **175**, 135–160 (1986).
42. Burry, R. W. Controls for immunocytochemistry: an update. *J Histochem Cytochem* **59**, 6–12 (2011).
43. Darmanis, S. *et al.* Simultaneous Multiplexed Measurement of RNA and Proteins in Single Cells. *Cell Reports* **14**, 380–389 (2016).
44. Albayrak, C. *et al.* Digital Quantification of Proteins and mRNA in Single Mammalian Cells. *Molecular Cell* **61**, 914–924 (2016).
45. Frei, A. P. *et al.* Highly multiplexed simultaneous detection of RNAs and proteins in single cells. *Nature Methods* **13**, 269–275 (2016).

46. Perfetto, S. P., Chattopadhyay, P. K. & Roederer, M. Seventeen-colour flow cytometry: unravelling the immune system. *Nature Reviews Immunology* **4**, 648–655 (2004).
47. Han, G., Spitzer, M. H., Bendall, S. C., Fantl, W. J. & Nolan, G. P. Metal-isotope-tagged monoclonal antibodies for high-dimensional mass cytometry. *Nature Protocols* **13**, 2121–2148 (2018).
48. Peterson, V. *et al.* Multiplexed quantification of proteins and transcripts in single cells. *Nat Biotechnol* **35**, 936–939 (2017).
49. Hughes, A. J., Lin, R. K. C., Peehl, D. M. & Herr, A. E. Microfluidic integration for automated targeted proteomic assays. *PNAS* **109**, 5972–5977 (2012).
50. Suwińska, A., Czołowska, R., Ozdzeński, W. & Tarkowski, A. K. Blastomeres of the mouse embryo lose totipotency after the fifth cleavage division: Expression of Cdx2 and Oct4 and developmental potential of inner and outer blastomeres of 16- and 32-cell embryos. *Developmental Biology* **322**, 133–144 (2008).
51. Mozziconacci, J., Sandblad, L., Wachsmuth, M., Brunner, D. & Karsenti, E. Tubulin dimers oligomerize before their incorporation into microtubules. *PLoS ONE* **3**, 1–8 (2008).
52. Strumpf, D. Cdx2 is required for correct cell fate specification and differentiation of trophectoderm in the mouse blastocyst. *Development* **132**, 2093–2102 (2005).
53. Zhang, S. Sox2, a key factor in the regulation of pluripotency and neural differentiation. *World Journal of Stem Cells* **6**, 305 (2014).
54. Rath, A., Glibowicka, M., Nadeau, V. G., Chen, G. & Deber, C. M. Detergent binding explains anomalous SDS-PAGE migration of membrane proteins. *PNAS* **106**, 1760–1765 (2009).
55. Kim, J. J., Chan, P. P. Y., Vlassakis, J., Geldert, A. & Herr, A. E. Microparticle Delivery of Protein Markers for Single-Cell Western Blotting from Microwells. *Small* **14**, 1802865 (2018).
56. Eaton, S. L. *et al.* Total Protein Analysis as a Reliable Loading Control for Quantitative Fluorescent Western Blotting. *PLoS ONE* **8**, 1–9 (2013).
57. Qvit, N., Joshi, A. U., Cunningham, A. D., Ferreira, J. C. B. & Mochly-Rosen, D. Glyceraldehyde-3-Phosphate Dehydrogenase (GAPDH) protein-protein interaction inhibitor reveals a non-catalytic role for GAPDH oligomerization in cell death. *Journal of Biological Chemistry* **291**, 13608–13621 (2016).
58. Sinkala, E. *et al.* Profiling protein expression in circulating tumour cells using microfluidic western blotting. *Nature Communications* **8**, 14622 (2017).
59. Brown, R. B. & Audet, J. Current techniques for single-cell lysis. *Journal of the Royal Society Interface* **5**, S131–S138 (2008).
60. Kort, J. & Behr, B. Biomechanics and developmental potential of oocytes and embryos. *Fertility and Sterility* **108**, 738–741 (2017).
61. Johnson, D. E., Ostrowski, P., Jaumouillé, V. & Grinstein, S. The position of lysosomes within the cell determines their luminal pH. *Journal of Cell Biology* **212**, 677–692 (2016).
62. Tadros, W. & Lipshitz, H. D. The maternal-to-zygotic transition: a play in two acts. *Development* **136**, 3033–3042 (2009).
63. Lee, M. T., Bonneau, A. R. & Giraldez, A. J. Zygotic Genome Activation During the Maternal-to-Zygotic Transition. *Annual Review of Cell and Developmental Biology* **30**, 581–613 (2014).
64. Morris, S. A., Guo, Y. & Zernicka-Goetz, M. Developmental Plasticity Is Bound by Pluripotency and the Fgf and Wnt Signaling Pathways. *Cell Reports* **2**, 756–765 (2012).
65. Wang, E. T. *et al.* Alternative isoform regulation in human tissue transcriptomes. *Nature* **456**, 470–6 (2008).

66. Gao, Y. *et al.* Protein Expression Landscape of Mouse Embryos during Pre-implantation Development. *Cell Reports* **21**, 3957–3969 (2017).
67. Flemr, M. *et al.* A retrotransposon-driven dicer isoform directs endogenous small interfering rna production in mouse oocytes. *Cell* **155**, 807 (2013).
68. Chazaud, C. & Yamanaka, Y. Lineage specification in the mouse preimplantation embryo. *Development* **143**, 1063–1074 (2016).
69. Padovan-Merhar, O. *et al.* Single Mammalian Cells Compensate for Differences in Cellular Volume and DNA Copy Number through Independent Global Transcriptional Mechanisms. *Molecular Cell* **58**, 339–352 (2015).
70. Jeong, J. K. *et al.* Evaluation of reference genes in mouse preimplantation embryos for gene expression studies using real-time quantitative RT-PCR (RT-qPCR). *BMC Research Notes* **7**, 1–12 (2014).
71. Wicklow, E. *et al.* HIPPO Pathway Members Restrict SOX2 to the Inner Cell Mass Where It Promotes ICM Fates in the Mouse Blastocyst. *PLoS Genetics* **10**, (2014).
72. Ziomek, C. A., Johnson, M. H. & Handyside, A. H. The developmental potential of mouse 16-cell blastomeres. *Journal of Experimental Zoology* **221**, (1982).
73. Zhang, J. Y., Diao, Y. F., Kim, H. R. & Jin, I. D. Inhibition of endoplasmic reticulum stress improves mouse embryo development. *PLoS ONE* **7**, (2012).
74. Grindberg, V. R. *et al.* RNA-sequencing from single nuclei. *Proceedings of the National Academy of Sciences* **110**, 19802–19807 (2013).
75. Abdelmoez, M. N. *et al.* SINC-seq: Correlation of transient gene expressions between nucleus and cytoplasm reflects single-cell physiology. *Genome Biology* **19**, 1–11 (2018).
76. Schultz, R. M. Regulation of zygotic gene activation in the mouse. *BioEssays* **15**, 531–538 (1993).
77. Simon, A. & Laufer, N. Assessment and treatment of repeated implantation failure (RIF). *Journal of Assisted Reproduction and Genetics* **29**, 1227–1239 (2012).
78. Lee, H. & Kim, J.-S. Unexpected CRISPR on-target effects. *Nature Biotechnology* **36**, 703–704 (2018).

Chapter 6

Multimodal detection of protein isoforms and nucleic acids from low starting cell numbers

Adapted with permission from E. Rosàs-Canyelles, A. J. Modzelewski, A. E. Gomez Martinez, A. Geldert, A. Gopal, L. He, & A. E. Herr, "Multimodal detection of protein isoforms and nucleic acids from low starting cell numbers", *Lab on a Chip*, 2021.

6.1 Abstract

Protein isoforms play a key role in disease progression and arise from mechanisms involving multiple molecular subtypes, including DNA, mRNA and protein. Recently introduced multimodal assays successfully link genomes and transcriptomes to protein expression landscapes. However, the specificity of the protein measurement relies on antibodies alone, leading to major challenges when measuring different isoforms of the same protein. Here we utilize microfluidic design to perform same-cell profiling of DNA, mRNA and protein isoforms (triBlot) on low starting cell numbers (1–100s of cells). After fractionation lysis, cytoplasmic proteins are resolved by molecular mass during polyacrylamide gel electrophoresis (PAGE), adding a degree of specificity to the protein measurement, while nuclei are excised from the device in sections termed "*gel pallets*" for subsequent off-chip nucleic acid analysis. By assaying TurboGFP-transduced glioblastoma cells, we observe a strong correlation between protein expression prior to lysis and immunoprobed protein. We measure both mRNA and DNA from retrieved nuclei, and find that mRNA levels correlate with protein abundance in TurboGFP-expressing cells. Furthermore, we detect the presence of TurboGFP isoforms differing by an estimated <1 kDa in molecular mass, demonstrating the ability to discern different proteoforms with the same antibody probe. By directly relating nucleic acid modifications to protein isoform expression in 1–100s of cells, the triBlot assay holds potential as a screening tool for novel biomarkers in diseases driven by protein isoform expression.

6.2 Introduction

The discovery of biomarkers for early detection, diagnosis, and therapy remains a persistent challenge across all fields of medicine.[1–4] Protein isoforms are prevalent disease-specific markers and can arise from a variety of events that involve DNA, mRNA and protein, including single nucleotide polymorphisms (SNPs), alternative splicing, or post-translational modifications (PTMs).[5–9] Many studies have focused on identifying novel potential protein targets by inferring proteoforms from disease-specific modifications to DNA or mRNA.[1,7] However, confirming if DNA or mRNA modifications encode protein isoforms that can become potential diagnostic or therapeutic targets requires multimodal assays that measure all molecules that are produced.

Because DNA, RNA, and protein molecules are the conduit for cellular-level information flow via the "central dogma", simultaneous, same-sample detection of multiple molecular species can provide new insight.[10,11] At the protein level, multimodal analysis is key to understanding gene regulatory networks and the source of variations in both the abundance and molecular forms of

proteins expressed. For example, to understand mechanisms of over- or under-expression, multimodal measurements can ascertain the impact of DNA copy number variations on mRNA and protein expression levels.[12–14] In another example, combining proteoform measurements with upstream DNA and RNA measurements can indicate whether proteoforms arise from DNA modifications, alternative RNA splicing, or PTMs. In addition to informing study of gene regulatory networks, multimodal measurements can facilitate more accurate cell subtype classification and lineage tracing.[15–17]

Recently introduced technologies allow interrogation of the genome, epigenome, transcriptome, metabolome and proteome at single-cell resolution.[18–27] Multimodal tools that measure proteins and DNA and/or RNA from single cells allow us to link genome, transcriptome and proteome in challenging cell types with low availability, such as rare cell populations (e.g., circulating tumor cells, or CTCs) or stem cells[28], or other cells that cannot be expanded by culture (e.g., cells from biopsies).[18] Measurements with single- or few-cell resolution are also essential to studying cell-to-cell heterogeneity and distinguishing different population distributions (e.g., bimodal vs. normally-distributed expression) which may have the same population mean expression level.[29] However, the specificity of the protein measurement in such assays typically relies on antibody probes alone, which are subject to nonspecific cross-reactivity and cannot detect isoforms without isoform-specific antibody probes. Thus, selective detection of specific protein isoforms is problematic when isoform-specific antibody probes are not available.[30] While Western blotting adds specificity by separating protein isoforms by mass prior to antibody-based detection, conventional Western blotting requires 10,000s of cells.[28] As a result, identifying different proteoforms arising from modifications to DNA or mRNA at the single- or few-cell scale remains extremely challenging. Recently introduced multimodal assays that perform protein isoform and nucleic acid detection were specifically designed for murine embryos, which are ~100 times larger in volume than somatic cells, and only demonstrated detection of mRNA and not DNA.[31,32] We sought to build upon the previously developed assays by incorporating DNA measurements and improving sensitivity to demonstrate multimodal measurements from as small a sample as a single mammalian cell.

Here, we perform same-cell DNA, mRNA and protein isoform immunoblotting measurements (triBlot) on low starting cell numbers (i.e., 1 to 100s of cells); a clinically relevant range that includes single CTCs and CTC clusters,[33] as well as cells recovered from needle biopsies (100s of cells).[34,35] Our technique first fractionates cells into nuclear and cytoplasmic compartments. The cytoplasmic fraction undergoes polyacrylamide gel electrophoresis (PAGE), while the nuclei are excised from the triBlot device and analysed for mRNA and/or DNA. We measure expression of protein isoforms from the cytoplasmic fraction of 1–100s of cells, while achieving same-sample analysis of DNA and of mRNA retained in the nuclei, where nuclear mRNA has been demonstrated to generally correlate well with whole-cell mRNA expression.[36–38]

6.3 Materials & Methods

Chemical reagents. Tetramethylethylenediamine (TEMED, T9281), ammonium persulfate (APS, A3678), β-mercaptoethanol (M3148), 30% T/2.7% C acrylamide/bis-acrylamide (37.5 : 1) (A3699), bovine serum albumin (BSA, A9418), trypsin 10× (59427C), digitonin (D141), sucrose (S0389-500G), magnesium chloride (M8266) and HEPES (90909C) were purchased from Sigma-Aldrich. Triton X-100 (BP-151), phosphate-buffered saline (PBS, pH 7.4, 10 010 023), SYBR Gold (S11494), agarose (BP-1356-500) were purchased from Thermo Fisher Scientific. Premixed 10× Tris-glycine electrophoresis buffer (25 mM Tris, pH 8.3; 192 mM glycine; 0.1% SDS) was

purchased from Bio-Rad. Tris buffered saline with Tween-20 (TBST) was prepared from 20× TBST (sc-24 953, Santa Cruz Biotechnology, Dallas, TX). Deionized water (18.2 MΩ) was obtained using an Ultrapure water system from Millipore. N-[3-[(3-Benzoylphenyl)formamido]propyl] methacrylamide (BPMAC) was custom synthesized by Pharm-Agra Laboratories (Brevard, NC). GelSlick™ (50640) and Lonza™ GelBond™ PAG film for acrylamide gels (BMA54746) was purchased from Lonza. Taq PCR kit (E5000S), proteinase K (P8107S) were purchased from New England Biosciences.

Buffer compositions. Fractionation lysis buffer: 0.125 mg mL^{-1} digitonin, 1% v/v Triton X-100 and 0.5 X Tris-glycine. Nuclei wash buffer: 320 mM sucrose, 5 mM $MgCl_2$, 10 mM HEPES.

Cell culture. U251 human glioblastoma cells were obtained from the UC Berkeley Tissue Culture Facility *via* the American Type Culture Collection and stably transduced with TurboGFP *via* lentiviral infection (multiplicity of infection 10). Cells were cultured in high-glucose Dulbecco's modified eagle medium (DMEM) (11965, Life Technologies) supplemented with 1× MEM nonessential amino acids (11140050, Life Technologies), 100 U mL^{-1} penicillin–streptomycin (15140-122, Life Technologies), 1 mM sodium pyruvate (11360-070), and 10% fetal bovine serum (JR Scientific, Woodland) in an incubator at 37 °C with humidified 5% CO_2 air.

Device fabrication. SU-8 wafers, fabricated by photolithography as previously reported,[39] were used as molds to cast triBlot devices. SU-8 posts on wafers, which later translate into microwells in the PA gel, were 200 μm in diameter and 200 μm in height.[32] A modified wafer generating microwells 100 μm in diameter and 110 μm in height was used for triBlot assays of single cells. Briefly, PA precursor solution including acrylamide/bis-acrylamide (10% T) and 3 mM BPMAC was degassed with sonication for 9 min. 0.08% APS and 0.08% TEMED were added to precursor solution and solution was pipetted between the SU-8 wafer (rendered hydrophobic with Gel Slick™ solution) and a GelBond™ Film cut to the size of a standard glass microscope slide (25 mm × 75 mm). After chemical polymerization (20 min) the triBlot devices (thin PA gel layer covalently grafted onto the GelBond™ surface) were lifted from wafer, rinsed with deionized water and stored hydrated (DI water) at 4 °C until use.

Fractionation PAGE of 1-100s of U251-TurboGFP cells. TurboGFP-expressing U251 cells were harvested from tissue culture plates by incubation in trypsin/EDTA (15090046, Thermo) at 37 °C for 5 min. Trypsin was inactivated by addition of FBS and cells were pelleted by centrifugation at 100 rcf. After removal of supernatant, cells were resuspended in PBS at 1 × 10^6 cells per mL. For triBlot assays of single cells, cells were settled using the cellenONE single-cell dispenser as described below. For all other experiments, cells were gravity settled as follows: 1 mL of this cell suspension was pipetted over the triBlot device and cells were allowed to settle into microwells for 10 min. Excess cells not settled into microwells were then washed off the PA gel surface with PBS and microwells were imaged by brightfield and fluorescence microscopy (Olympus IX71 microscope, Lumen Dynamics X-cite fluorescence illumination source coupled to a liquid light guide (Lumatec, 805-00038), 10× (0.3 NA) objective (Olympus UPLANFL10X), DAPI (Omega XF02-2) and GFP (Chroma 49 011 ET) filter cubes, and an Andor iXon+ EMCCD camera (DU-885 K-C00-#VP)) to collect data on number of cells per microwell and TurboGFP expression. The device was placed into an electrophoresis (EP) chamber, and fractionation lysis buffer (room temperature, 12 mL) poured over the gel and incubated for 1 min. fPAGE was performed at 40 V cm^{-1} for 2–3 min (depending on the assay). Immobilization of proteins by photocapture was carried out by illumination with UV light source (100% power, 45 s, Lightningcure LC5, Hamamatsu). Gels were quickly placed in ice-cold nuclei wash buffer, and buffer was exchanged three times before proceeding to laser excision. Nuclei remaining in wells

can be laser-excised, while proteins immobilized in gel can be probed with fluorescently-labeled antibody probes.

Laser excision of triBlot device into gel pallets. Gel pallets were excised from the device as previously described.[32] Briefly, the PA gel was kept hydrated at all times with nuclei wash buffer and kept over ice between excision events. A CO_2 laser cutter (HL40-5G-110, Full Spectrum Laser) was used to excise gel pallets from triBlot devices. The device was placed with the PA gel face down onto a clear acrylic sheet (McMaster-Carr) engraved with a 5 × 5 mm grid. Using a brightfield microscope, microwells were aligned to be horizontally centered above a grid square and approximately 1 mm away from the top edge of each square. The laser was aligned over the left corner of a grid square and programmed to cut at 10% power, 20 speed and 1 pass.

Antibody probes. Rabbit anti-TurboGFP (PA5-22688) and AlexaFluor555-conjugated donkey anti-rabbit (A-31572) were purchased from Thermo Fisher Scientific.

Immunoprobing and fluorescence imaging of photo-blotted protein and immunoblots. After laser excision, devices were washed in deionized water and a 25 mm × 75 mm coverslip was placed over the hydrated PA gel. Devices were imaged in a microarray scanner (Genepix 4300A, Molecular Devices) for photo-blotted TurboGFP protein with the cover slip facing down. Devices were then washed in 1× TBST for at least 1 h before probing with antibody probes. Primary antibody probes were incubated at 1 : 10 dilution (80 μL per gel, in 2% BSA in 1× TBST), while fluorophore-conjugated secondary antibody probes were incubated at 1 : 20 dilution (80 μL per gel, in 2% BSA in TBST). Devices were scanned again for fluorescence immunoblot signal.

Protein band image analysis. Protein expression was quantified by area-under-the-curve analysis (AUC) of immunoblots as previously described. Briefly, custom MATLAB scripts were used to fit Gaussian curves to protein band intensity profiles. Gaussian fit parameters of peak location and σ were used to calculate the AUC for a peak width of 4σ. Protein bands passed quality control metrics if signal-to-noise ratio (SNR) was higher than 3 and the Gaussian fit R^2 was equal to or greater than 0.6.

Single-gel pallet PCR. After laser excision, gel pallets were placed into a 0.5 mL PCR tube containing 2.5 μL molecular grade water, 1 μL SDS (17 μM to final concentration of 3.4 μM) and 1.5 μL proteinase K. Tubes were incubated at 45 °C for 15 min followed by proteinase K inactivation by incubation at 95 °C for 20 min. Next, the following were added to each tube: 2.5 μL TurboGFP primers at 500 nM, purchased from Integrated DNA Technologies, sequences: (5′TGA TGG GCT ACG GCT TCT A, 5′GTG TTG CTG TGA TCC TCC TC), 1 μL dNTPs (at 200 μM, Taq PCR Kit), 0.25 μL Taq polymerase (Taq PCR kit), 5 μL of Standard Taq Reaction Buffer 10× (Taq PCR Kit) and water up to 50 μL. Template DNA (∼200 ng μL^{-1}) extracted TurboGFP-U251 lysate was added to positive control tubes. Negative controls did not contain DNA or gel pallets. For amplification of the TurboGFP gene, the following cycle steps were programmed using a thermal cycler (PTC-100™, MJ Research Inc): the first stage at 95 °C for 10 min, the second stage (annealing at 51 °C for 30 s, extension at 72 °C for 30 s, denaturation at 95 °C for 30 s) for 45 amplification cycles, and a final stage at 72 °C for 10 min. PCR products were analyzed on a 1% agarose gel by EP. SYBR Gold was used at 1× to stain agarose gels and a ChemiDoc™ XRS + gel imaging system (Bio-Rad) was used to image the DNA bands. Gels were analyzed by densitometry using ImageJ.[40]

Single-cell deposition with cellenONE system. Single cells were deposited into 100 μm diameter and 110 μm deep microwells in the triBlot device with the cellenONE X1 droplet printer (Scienion, Berlin, Germany) and a cellenONE PDC M piezo dispensing capillary (PDC-20-CM). TurboGFP-U251 cells were diluted to a concentration of 300 000 cells per mL in PBS. The triBlot PA gel was

briefly dried with a nitrogen stream before droplet deposition. Crosshair-shaped fiducial markers on the gel were used in conjunction with the "Find Target Reference Points" software function to align droplets to microwells. The target plate temperature was set to 4 °C to prevent the evaporation of deposited droplets. Single-cell occupancy in droplets was verified by imaging the interior of the PDC prior to droplet deposition. The PDC M deposits droplets of 350–400 pL in volume. After deposition, the single cells were immediately fractionally lysed.

Single-gel pallet quantitative reverse transcription polymerase chain reaction (RT-qPCR). Once excised, each gel pallet was transferred to one centrifuge tube, immediately followed by the addition of 20 μL of DNA/RNA Shield™ (R1100, Zymo). Sample were stored in −80 °C until RNA preparation. RNA and DNA were isolated following the manufacturer's protocol. Nucleic acids were eluted in 8 μL of water. Alternate mRNA and DNA isolation can be performed with Direct-zol™ RNA Miniprep Plus (Cat. R2070S, LOT: ZRC202000), RNA Clean & Concentrator™-5 Cat R1015S (10 preps), LOT: ZRC200969. All 8 μL of RNA sample was used for cDNA synthesis. Reverse transcription of mRNA to cDNA was accomplished with SuperScript IV First Strand Synthesis System (18091050, Thermo Fisher) as per manufacturer instructions. Pre-amplification was done on the resulting 20 μl cDNA sample using the Perfecta PreAmp SuperMix (95146 QuantaBio) as per the manufacturer's instructions, and using the 14 cycle option and a subsequent 20× dilution into nuclease free water (am9937, Fisher). All RT-qPCR reactions were performed using SSO Universal SYBR Green SuperMix, as per manufacturer instructions (1725275, BioRad). Primer sequences used were TurboGFP (5′TGA TGG GCT ACG GCT TCT A, 5′GTG TTG CTG TGA TCC TCC TC). All RT-qPCR analyses were performed on the StepOnePlus real time PCR system (437660, Thermo).

6.4 Results & Discussion

Design of same-cell protein and nucleic acid assay for low starting cell numbers. In order to perform multimodal measurements on the same mammalian cells, we developed an assay that integrates (i) electrophoretic separation of cytoplasmic proteins and (ii) extraction of nucleic acids from the nuclei. To do so, we designed the triBlot device, consisting of a 200 μm-thick polyacrylamide (PA) gel covalently bound to the treated surface of a flexible polyester film (Gelbond™ PAG Film). The PA layer is in turn patterned with an array of microwells (100 to 200 μm in diameter).[32]

Our assay begins with settling cells into the microwells of the triBlot device (**Figure 6.1a**). Cells can be passively settled into microwells by gravity,[39] or actively sampled using a micromanipulator[41,42] a liquid dispensing droplet printer (i.e., cellenONE), or a mouth-pipette assembly.[31] In terms of sample requirements, one microwell can hold from one single cell to ∼200 cells. Given that the triBlot device has 45 microwells, 45 separate samples can be analyzed simultaneously, each sample ranging from a single cell to ∼200 cells. Treatment of cells with fractionation lysis buffer[31,43] for 1 min achieves in situ lysis of the cytoplasmic fraction of cells (**Figure 6.1a**). An electric field is then applied for 2 to 3 min to (i) inject solubilized proteins through the microwell wall and into the PA gel layer and (ii) achieve fractionation PAGE (fPAGE), which separates cytoplasmic proteins by molecular mass along the separation lane, or region abutting the microwell. Proteins are then photo-blotted, or immobilized to the PA layer by 45 s long UV-light activation of benzophenone moieties incorporated in the PA gel matrix. After cytoplasmic fPAGE, the nuclei remain intact in the microwells. The polymer substrate of the triBlot device allows us to laser-excise areas of the gel, or gel pallets, containing the microwells with the fractionated nuclei. Nuclei-laden gel pallets are then placed into reaction vessels

(Eppendorf tubes) in order to perform extraction and off-chip analysis of either DNA or mRNA. The remaining triBlot device is then immunoprobed for proteins with fluorescently-labelled antibody probes, yielding protein immunoblots from the original settled cells.

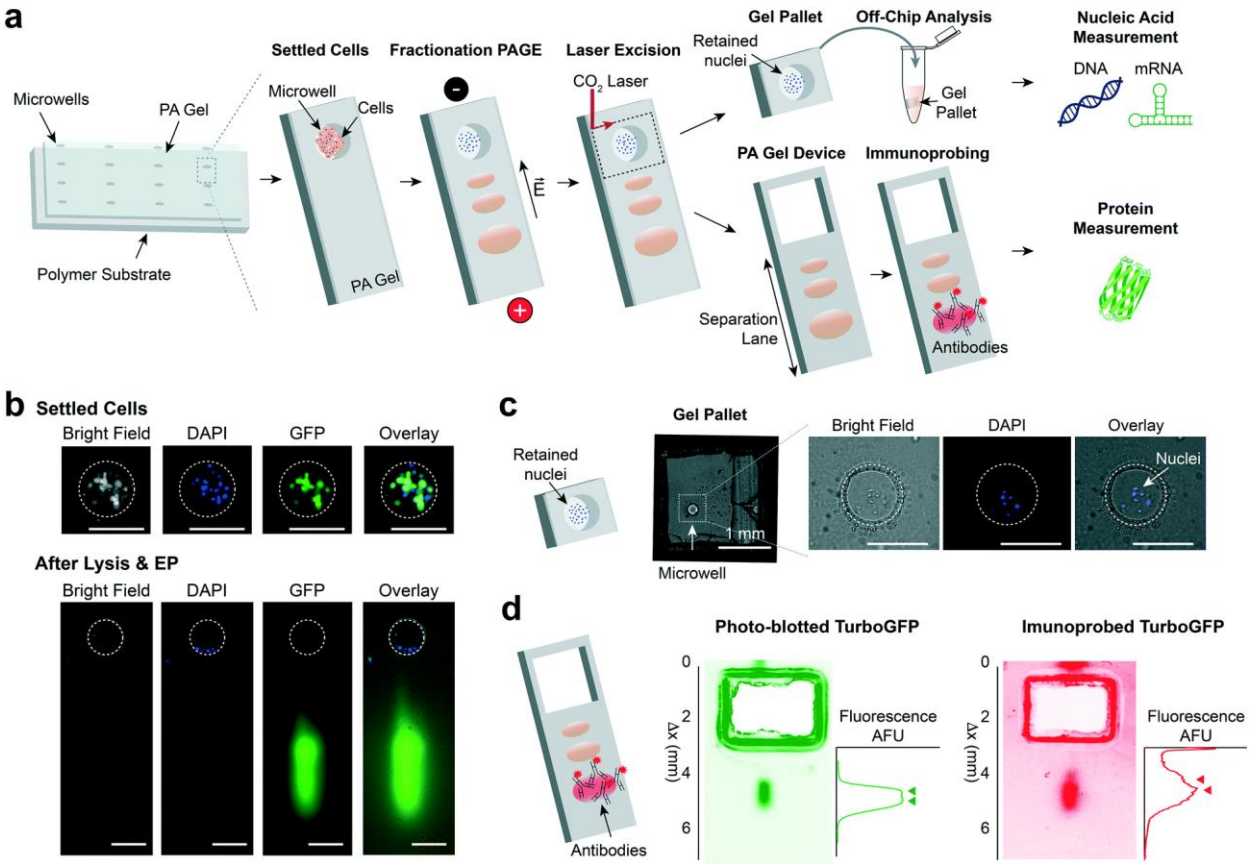

Figure 6.1. Multimodal measurements by fractionation PAGE coupled with laser excision of microwells into gel pallets for off-chip analysis of nucleic acids. (a) The same-cell nucleic acid and protein isoform immunoblotting device (triBlot) comprises a thin polyacrylamide (PA) gel covalently grafted to a polymer film and stippled with microwells. One to ~200 cells are settled into each microwell of the triBlot device and lysed with a fractionation lysis buffer. Application of an electric field injects the solubilized cytoplasmic proteins into the PA gel for separation by molecular mass. After protein sizing, the proteins are immobilized to the gel by UV-mediated activation of benzophenone that is polymerized into the PA gel matrix. A CO_2 laser excises 2 mm × 3 mm gel sections circumscribing each nuclei-laden microwell, creating gel pallets that are suitable for off-chip DNA or mRNA analysis. Each protein sizing lane of the planar triBlot device is immunoprobed with fluorescently labeled antibody probes, yielding protein immunoblots indexed to each excised gel pallet. (b) Fractionation PAGE retains nuclei in microwells. Top row displays brightfield, DAPI and GFP micrographs of TurboGFP-U251 cells settled into a microwell, prior to the cell lysis step. On bottom, brightfield, DAPI and GFP fluorescence micrographs of microwell and abutting PA gel (separation lane) after fPAGE, when cytoplasmic proteins have been electrophoresed into the PA gel while nuclei remain in the microwell. (c) Gel pallets allow extraction of nuclei for off-chip analysis of nucleic acids. Brightfield micrograph shows one gel pallet. Retention of nuclei can be verified by the fluorescence imaging of the Hoechst-stained nuclei, as displayed in the merged micrographs of a gel pallet microwell. (d) Immunoblots of photo-blotted and immunoprobed TurboGFP. On the left, a false-color micrograph of photo-blotted TurboGFP protein after electrophoretic separation, with a corresponding intensity profile. On the right, a false-color micrograph of the TurboGFP immunoblot, with corresponding intensity profile. Arrowheads mark the position of each protein peak. Scale bars are 200 μm, unless specified.

Questions surrounding rare cell types, such as CTCs and CTC clusters, may require simultaneous analysis of a wide range of cell numbers. To determine the dynamic range of our

assay, we utilized U251 human glioblastoma cells engineered to express the fluorescent protein TurboGFP in the cytoplasm, but not the nucleus.[43] Expression of fluorescent TurboGFP is a useful protein model for visualizing cell lysis, injection, fPAGE, and photo-blotting. We first settled TurboGFP-U251 cells stained with nuclear Hoechst dye into microwells (**Figure 6.1b**). After fractionation lysis, fPAGE and photo-blotting, we observed a TurboGFP band in the separation lane along with absence of TurboGFP fluorescence in the microwell, suggesting complete lysis and injection of the cytoplasmic proteins into the PA gel had been achieved (**Figure 6.1b**).

Next, to maintain the integrity of the nuclei we placed the gel device in nuclei wash buffer. We then excised gel pallets containing the microwells (**Figure 6.1c**). Fluorescence imaging of the Hoechst-stained nuclei confirmed the presence of the nuclei in the microwells (**Figure 6.1c**). The remaining gel device was imaged for native TurboGFP signal and then incubated with primary antibody probes against TurboGFP followed by AlexaFluor555-conjugated secondary antibody probes and imaged for resulting TurboGFP immunoblots (**Figure 6.1d**). The detection of two bands in both the photo-blotted and the immunoprobed protein bands (**Figure 6.1d**) indicates the ability to discern protein isoforms using the same antibody probe. Isoforms of GFP, which are estimated to differ by less than 1 kDa in molecular mass, have been attributed to differential C-terminal cleavage by non-specific proteases during bacterial expression of recombinant proteins.[44]

Extraction of gel pallets enables quantification of DNA from a single nucleus. We next sought to scrutinize the viability of nucleic acid analysis after gel pallet retrieval and determine detection limits. To do so, we performed amplification of the TurboGFP gene by polymerase chain reaction (PCR) from gel pallets containing a single nucleus (**Figure 6.2a**). We designed microwells to isolate single TurboGFP-expressing U251 cells (32 μm in diameter, 40 μm in height). After fPAGE of the cytoplasmic fraction, single nuclei retained in the microwells were excised into gel pallets. To verify retention of each nucleus, we used epifluorescence microscopy to inspect gel pallets for the Hoechst-stained nuclei. Gel pallets were then placed into separate reaction vessels (centrifuge tubes) for PCR amplification of the TurboGFP gene. PCR products were analysed on an agarose gel, revealing successful amplification of the TurboGFP from the gel pallet (**Figure 6.2b–c**). The presence of a PCR product of the same length as the positive control indicates amplification of the TurboGFP gene from the gel pallet sample, validating viability of DNA extraction from nuclei in gel pallets (**Figure 6.2b–c**). Densitometry analysis of the PCR product enables semi-quantitative analysis of the DNA present in the gel pallets (**Figure 6.2d**). Results indicate DNA can be retrieved from gel pallets from starting samples containing as few as a single nucleus per gel pallet.

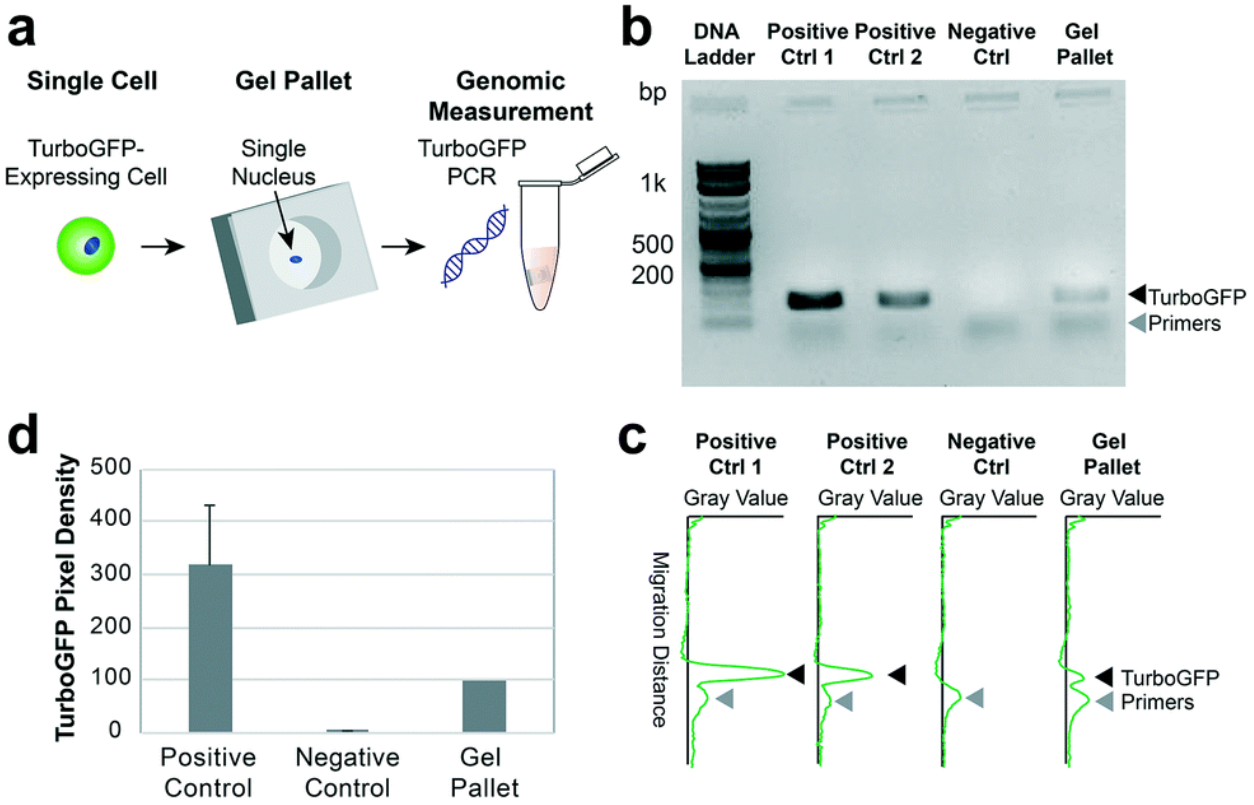

Figure 6.2. PCR amplification of TurboGFP DNA from a gel pallet containing a single TurboGFP-expressing U251 cell nucleus. (a) Schematic of gel pallets analyzed for TurboGFP DNA. (b) Agarose gel electrophoresis of DNA amplified for the TurboGFP gene by PCR from samples including: positive controls (10 ng DNA extracted from TurboGFP-U251 lysate), negative controls (no DNA) and gel pallet containing one TurboGFP-U251 nucleus. (c) Gray value intensity profiles for agarose gel lanes corresponding to positive controls, negative control and gel pallet containing a single TurboGFP-U251 nucleus. (d) Bar plots of densitometric quantitation of TurboGFP bands in agarose gel electrophoresis. Error bars indicate standard deviation for n = 3 replicates.

Photo-blotted and immunoblotted protein fluorescence signal correlates with protein expression prior to lysis. We next evaluated the performance of our assay in measuring protein targets, namely, whether protein measured after lysis, fPAGE and immunoblotting accurately measures protein abundance prior to lysis. We used the TurboGFP protein in TurboGFP-expressing U251 cells as a measure of protein abundance. We first loaded an increasing number of cells into microwells of a triBlot device, from a single cell to ~200 cells (**Figure 6.3a**). We imaged the TurboGFP-U251 cells settled into microwells for TurboGFP fluorescence prior to lysis and computed whole-cell fluorescence intensity by area-under-the-curve analysis (AUC). We then ran fPAGE and scanned the triBlot device for photo-blotted native TurboGFP fluorescence. Finally, we immunoprobed the triBlot devices with primary antibody probes against TurboGFP (rabbit-anti-TurboGFP), followed by fluorophore-conjugated secondary antibody probes (AlexaFluor555 donkey-anti-rabbit), and imaged the devices for immunoprobed TurboGFP signal. To quantify the photo-blotted and immunoprobed protein peaks, we performed Gaussian curve fitting on the protein peak intensity profiles and used the Gaussian fit parameters (peak center and σ) to calculate the AUC for a peak width of 4σ. Quality control metrics were defined as signal-to-noise ratio (SNR) greater than 3 and a Gaussian fit $R^2 > 0.6$.

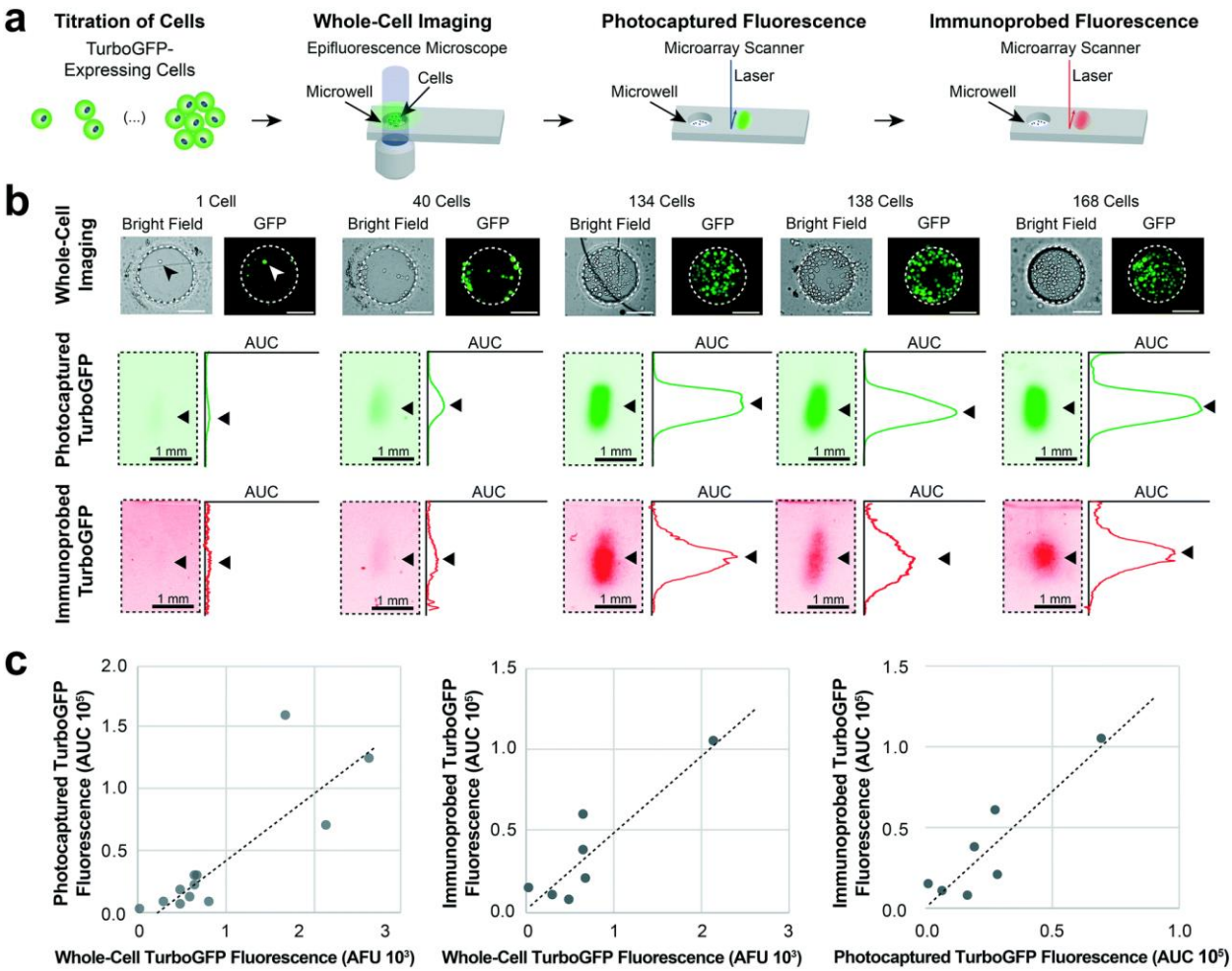

Figure 6.3. Photo-blotted and immunoprobed protein quantitation correlates with protein expression measured prior to lysis. (a) Schematic of experiment for quantifying TurboGFP protein at different stages of the same-cell nucleic acid and protein isoform measurement assay. (b) Brightfield and false color fluorescence micrographs of TurboGFP-expressing U251 cells settled into microwells. Cells were manually counted in ImageJ using overlay brightfield and GFP micrographs. Corresponding false color fluorescence micrographs of TurboGFP immunoblots imaged after photo-blotting and immunoprobing. Fluorescence intensity profiles are shown to the right of immunoblots. Black arrows mark the position of protein peaks. (c) Bivariate plots of whole-cell TurboGFP fluorescence prior to lysis, photo-blotted TurboGFP fluorescence (AUC) and immunoprobed TurboGFP fluorescence (AUC). Whole-cell TurboGFP fluorescence shows strong positive correlation with both photo-blotted and immunoprobed TurboGFP fluorescence (Pearson correlation, ρ = 0.839 and 0.902, for N = 9 and 7 microwells, respectively). Likewise, photo-blotted and immunoprobed TurboGFP fluorescence show a strong positive correlation (Pearson correlation, ρ = 0.909, N = 7 microwells).

When comparing (i) whole-cell TurboGFP prior to lysis, (ii) native signal from the photo-blotted TurboGFP and (iii) immunoprobed signal from fluorophore-conjugated antibody probes against TurboGFP (**Figure 6.3a–b**), we found that whole-cell TurboGFP fluorescence demonstrated a positive linear association with signal quantified from both photo-blotted TurboGFP fluorescence and immunoblotted TurboGFP fluorescence (Pearson correlation, ρ = 0.839 and 0.902, for N = 9 and 7 microwells, respectively) (**Figure 6.3c**). Photo-blotted and immunoprobed TurboGFP fluorescence also show a strong positive correlation (Pearson correlation, ρ = 0.909, N = 7 microwells, **Figure 6.3c**). These results suggest that endpoint immunoblots accurately estimate protein abundance in starting, intact cells. These results further

suggest that endpoint immunoblotting can accurately quantify endogenous protein targets (not tagged with fluorescent labels) for which pre-lysis quantification is impossible. Finally, the limit of detection (LOD) for proteins has been experimentally determined to be 27 000 copies,[45] corresponding to single-cell levels of a median-expressed protein.[46] As with any immunoassay, the LOD is dependent on antibody probe affinity for protein target epitope.

TurboGFP mRNA correlates with TurboGFP protein fluorescence measured prior to lysis, after fPAGE and after immunoprobing. We next examined whether mRNA collected from gel pallets correlates with protein expression. First, we examined if mRNA extracted from gel pallets containing single nuclei could be amplified. We used a single-cell droplet printer (cellenONE) to deposit single TurboGFP-expressing U251 cells into microwells of a triBlot device. After performing fPAGE with a 25 s lysis time, we excised gel pallets containing single nuclei and processed them for mRNA analysis (**Figure 6.4a**). We extracted and amplified mRNA from gel pallets and analysed amplified cDNA for TurboGFP by reverse transcription quantitative real-time PCR (RT-qPCR) (**Figure 6.4b**). To ensure the triBlot assay can support a single-cell LOD for mRNA, we used a kit that has been validated to detect transcripts from single cells by the manufacturer (Zymo). All samples prepared from gel pallets show higher expression (i.e., lower CT values) than all negative controls (high or absent CT values), including a sample containing TurboGFP-expressing U251 cDNA where the reverse transcriptase (RT) enzyme was left out (−RT), an RT mix only sample, a PreAmplification only sample and a sample containing primer but no cDNA sample to test for background primer dimer amplification (**Figure 6.4b–c**). Positive controls were cDNA from TurboGFP-U251 cell lysate (Pos Ctrl 1) and cDNA from a gel pallet containing multiple U251 nuclei (Pos Ctrl 2). Positive controls amplified either before or at similar CT values as samples from gel pallets containing a single TurboGFP-expressing U251 cell (**Figure 6.4b–c**). Companion TurboGFP immunoblots showed protein peaks that passed the quality control metrics of SNR > 3 and Gaussian fit $R^2 > 0.6$ (**Figure 6.4d**).

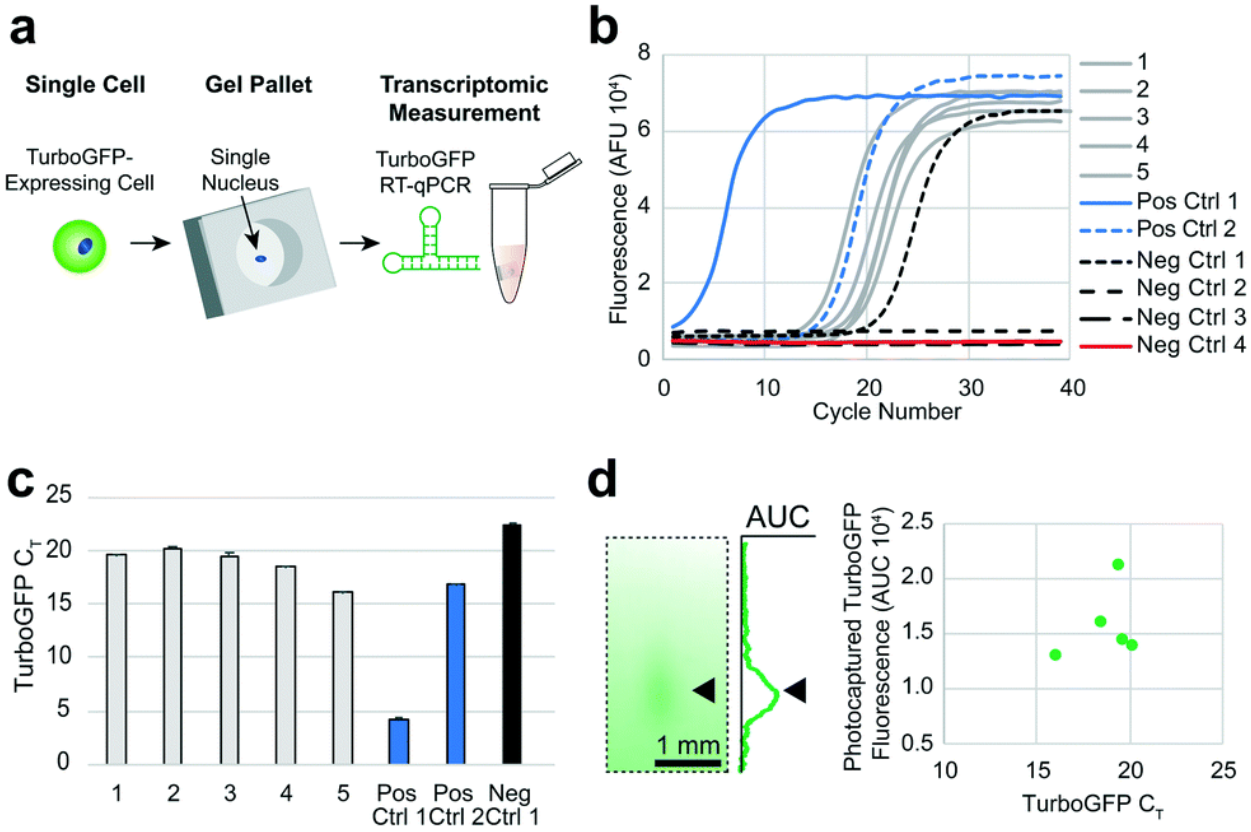

Figure 6.4. RT-qPCR amplification of mRNA from gel pallet containing single TurboGFP-expressing U251 cell nucleus. (a) Schematic of gel pallets analyzed for TurboGFP mRNA. (b) RT-qPCR amplification curves for TurboGFP from gel pallets containing a single nucleus (samples 1–5), positive controls (Pos Ctrl 1: cDNA amplified from TurboGFP-U251 lysate and Pos Ctrl2: gel pallet containing multiple TurboGFP-U251 nuclei) and negative controls (Neg Ctrl 1: cDNA from lysate without RT mix, Neg Ctrl 2: RT mix only, Neg Ctrl 3: PreAmplification mix only, Neg Ctrl 4: primers only with no cDNA to test for background from primer dimer amplification). (c) Bar graph of TurboGFP C_T values for all samples shown in panel (b) that amplified. Error bars indicate standard deviation for n = 3 replicates. (d) On left, false color fluorescence micrograph showing TurboGFP band from a single U251 cell with accompanying intensity profile to the right. Arrowheads mark the position of protein peak. On the right, bivariate plot of photocaptured TurboGFP fluorescence (AUC) and TurboGFP C_T values for samples containing a single U251 nucleus (n = 5 gel pallets containing a single U251 nucleus).

Finally, to examine correlations between mRNA and protein expression, we used passive gravity settling to load increasing numbers of cells into the microwells of a triBlot device. We loaded from 6 cells per microwell to 201 cells per microwell. After fPAGE and excision of the triBlot device into gel pallets, gel pallets were placed into separate reaction vessels containing DNA/RNA Shield™ solution (Zymo) to extract mRNA from retained nuclei (**Figure 6.5a**). While devices were immunoprobed with antibody probes against TurboGFP, isolated mRNA was first reverse transcribed and subsequent cDNA was analyzed for TurboGFP expression using semi-quantitative real-time PCR analysis (semi-RT-qPCR). Amplified cDNA was analyzed by agarose gel electrophoresis and bands were quantified by densitometry (**Figure 6.5b**). We observed an 85% yield for successful sample amplification, where 12 out of 15 samples had a detectable band at the correct TurboGFP amplicon length (**Figure 6.5b**, lanes 2–7, 9 and 11–15). To determine a failed amplification, we used the presence of a primer band and absence of a TurboGFP band (**Figure 6.5b**, lanes 8 and 10).

Results show that whole-cell fluorescence and photo-blotted protein signal are significantly correlated with mRNA levels (Pearson correlation, ρ = 0.849 and 0.843, N = 7 microwells, for whole-cell TurboGFP fluorescence and photo-blotted TurboGFP, respectively, **Figure 6.5c**. Failed PCR amplification samples or samples with protein peaks that did not pass QC metrics of SNR > 3 and R^2 > 0.6 were not considered). TurboGFP mRNA levels also show a strong positive association with immunoprobed TurboGFP signal (Pearson correlation, N = 5 microwells, ρ = 0.907, **Figure 6.5c**). These results validate the integrity of mRNA recovered from nuclei-laden gel pallets, and demonstrate that transcription levels can be quantified from the same-cell mRNA and immunoblotting assay.

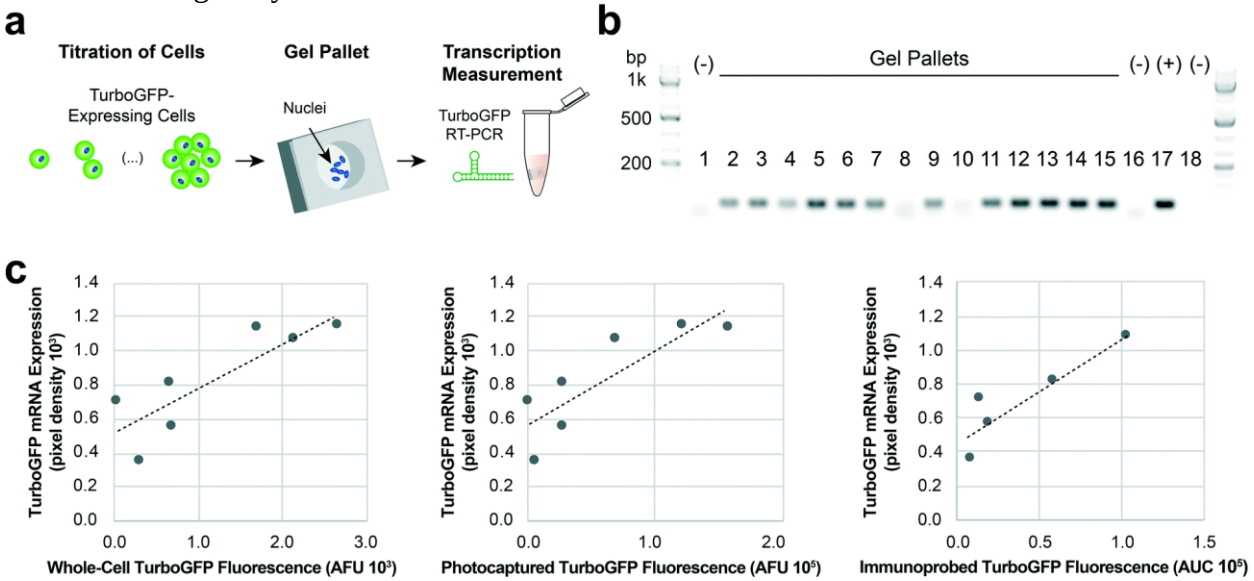

Figure 6.5. Semi-RT-qPCR amplification of TurboGFP mRNA from gel pallets correlates with same-cell protein expression measurement. (a) Schematic of analysis of gel pallets for TurboGFP mRNA. (b) Agarose gel electrophoresis of cDNA amplicons representing gel pallets with increasing number of cells (lanes 2–15). Negative controls include lanes 1 (no cells), lane 16 (–RT) and lane 18 (water). Positive control lane 17 containing TurboGFP plasmid (1 ng) was positive. DNA ladder used was Thermo 1 KB + DNA ladder. (c) Semi quantitative mRNA TurboGFP levels, measured from densitometry plots of cDNA agarose gel, demonstrate strong linear correlation with all protein measurements; whole-cell, photo-blotted and immunoprobed TurboGFP fluorescence (Pearson correlation, ρ = 0.849, 0.843 and 0.907, for N = 7, 7 and 5 microwells, respectively).

6.5 Conclusions

Assessing whether specific modifications at the nucleic acid level drive important mechanisms in disease progression requires measuring all molecular types involved, including proteins, DNA and mRNA. Here we design an assay for simultaneous measurement of protein isoforms and nucleic acids from low starting numbers of mammalian cells. We demonstrate that signal from immunoprobed protein correlates strongly with protein expression prior to lysis in TurboGFP-expressing cells. We also measure both mRNA and DNA from retrieved nuclei, with positive amplification of TurboGFP gene and TurboGFP transcripts, demonstrating our ability to recover, isolate and amplify nucleic acids from gel pallets. The cell number range over which we performed these measurements (from 1 to 100s of cells) includes the cell numbers relevant to tumor samples, including cells obtained from fine needle aspirates and CTC clusters.

Given the prevalence of protein isoforms across a wide range of diseases, tools that measure both nucleic acids and intracellular protein isoforms from the same cells are necessary to

(i) reveal the mechanisms by which the events at the nucleic acid level (including SNPs, alternative splicing or PTMs) regulate the production of pathogenic proteoforms, and (ii) identify new disease-specific biomarkers for early detection, diagnosis, and therapy.

Moreover, as more efficient gene editing tools continue to emerge, strict evaluation of how both on-target and off-target edits affect the transcriptional and protein expression landscapes will become critical for safely translating these gene editing tools into clinical applications.[47,48] Same-cell multimodal tools such as the one presented here will be instrumental in unequivocally linking modifications in protein expression profiles to on-target and off-target editing events.

6.6 References

1. Barrett, C. L. *et al.* Systematic transcriptome analysis reveals tumor-specific isoforms for ovarian cancer diagnosis and therapy. *Proceedings of the National Academy of Sciences of the United States of America* **112**, E3050–E3057 (2015).
2. Frankiw, L., Baltimore, D. & Li, G. Alternative mRNA splicing in cancer immunotherapy. *Nature Reviews Immunology* **19**, 675–687 (2019).
3. Martinez, B. I. & Stabenfeldt, S. E. Current trends in biomarker discovery and analysis tools for traumatic brain injury. *Journal of Biological Engineering* **13**, 1–12 (2019).
4. Ward, M. & Schofield, E. L. Biomarkers for brain disorders. *Therapy* **7**, 321–336 (2010).
5. Wei, J., Zaika, E. & Zaika, A. P53 family: Role of protein isoforms in human cancer. *Journal of Nucleic Acids* **2012**, (2012).
6. Bruikman, C. S., Zhang, H., Kemper, A. M., Van Gils, J. M. & Majerciak, V. Netrin Family: Role for Protein Isoforms in Cancer. *Journal of Nucleic Acids* **2019**, (2019).
7. Climente-González, H., Porta-Pardo, E., Godzik, A. & Eyras, E. The Functional Impact of Alternative Splicing in Cancer. *Cell Reports* **20**, 2215–2226 (2017).
8. Lorentzian, A., Uzozie, A. & Lange, P. F. Origins and clinical relevance of proteoforms in pediatric malignancies. *Expert Review of Proteomics* **16**, 185–200 (2019).
9. Jovanov-Milošević, N. *et al.* Human fetal tau protein isoform: Possibilities for Alzheimer's disease treatment. *International Journal of Biochemistry and Cell Biology* **44**, 1290–1294 (2012).
10. Stuart, T. & Satija, R. Integrative single-cell analysis. *Nature Reviews Genetics* **20**, 257–272 (2019).
11. Ståhlberg, A., Thomsen, C., Ruff, D. & Åman, P. Quantitative PCR Analysis of DNA, RNAs, and Proteins in the Same Single Cell. *Clin Chem* **58**, 1682–1691 (2012).
12. Ruggles, V. K. *et al.* Methods, tools and current perspectives in proteogenomics. *Molecular and Cellular Proteomics* **16**, 959–981 (2017).
13. Qui, S. *et al.* Analysis of plasma HER2 copy number in cell-free DNA of breast cancer patients: a comparison with HER2 extracellular domain protein level in serum. *Breast Cancer* (2021) doi:10.1007/s12282-020-01212-x.
14. Zhao, Y. *et al.* Nanoscale imaging of clinical specimens using pathology-optimized expansion microscopy. *Nature Biotechnology* 757–764 (2017).
15. Louie, R. H. & Luciani, F. Recent advances in single-cell multimodal analysis to study immune cells. *Immunology & Cell Biology* **99**, 157–167 (2021).
16. Nathan, A., Baglaenko, Y., Fonseka, C. Y., Beynor, J. I. & Raychaudhuri, S. Multimodal single-cell approaches shed light on T cell heterogeneity. *Current Opinion in Immunology* **61**, 17–25 (2019).

17. Stoeckius, M. *et al.* Simultaneous epitope and transcriptome measurement in single cells. *Nature Methods* **14**, 865–868 (2017).
18. Macaulay, I. C., Ponting, C. P. & Voet, T. Single-Cell Multiomics: Multiple Measurements from Single Cells. *Trends in Genetics* **33**, 155–168 (2017).
19. Gawad, C., Koh, W. & Quake, S. R. Single-cell genome sequencing: Current state of the science. *Nature Reviews Genetics* **17**, 175–188 (2016).
20. Schwartzman, O. & Tanay, A. Single-cell epigenomics: Techniques and emerging applications. *Nature Reviews Genetics* **16**, 716–726 (2015).
21. Wu, M. & Singh, A. K. Single-Cell Protein Analysis. *Current Opinion in Biotechnology* **23**, 83–88 (2012).
22. Stegle, O., Teichmann, S. A. & Marioni, J. C. Computational and analytical challenges in single-cell transcriptomics. *Nature Reviews Genetics* **16**, 133–145 (2015).
23. Xue, M. *et al.* Chemical methods for the simultaneous quantitation of metabolites and proteins from single cells. *Journal of the American Chemical Society* **137**, 4066–4069 (2015).
24. Peterson, V. M. *et al.* Multiplexed quantification of proteins and transcripts in single cells. *Nature Biotechnology* **35**, 936–939 (2017).
25. Frei, A. P. *et al.* Highly multiplexed simultaneous detection of RNAs and proteins in single cells. *Nature Methods* **13**, 269–275 (2016).
26. Albayrak, C. *et al.* Digital Quantification of Proteins and mRNA in Single Mammalian Cells. *Molecular Cell* **61**, 914–924 (2016).
27. Kawai, T. *et al.* Ultrasensitive Single Cell Metabolomics by Capillary Electrophoresis–Mass Spectrometry with a Thin-Walled Tapered Emitter and Large-Volume Dual Sample Preconcentration. *Analytical Chemistry* **91**, 10564–10572 (2019).
28. Cai, X., Zheng, Y. & Speck, N. A. A western blotting protocol for small numbers of hematopoietic stem cells. *Journal of Visualized Experiments* **2018**, 6–9 (2018).
29. Altschuler, S. J. & Wu, L. F. Cellular Heterogeneity: Do Differences Make a Difference? *Cell* **141**, 559–563 (2010).
30. Trenchevska, O., Nelson, R. W. & Nedelkov, D. Mass spectrometric immunoassays for discovery, screening and quantification of clinically relevant proteoforms. *Bioanalysis* **8**, 1623–1633 (2016).
31. Rosàs-Canyelles, E., Modzelewski, A. J., Geldert, A., He, L. & Herr, A. E. Assessing heterogeneity among single embryos and single blastomeres using open microfluidic design. *Science Advances* **6**, (2020).
32. Rosàs-Canyelles, E., Modzelewski, A., Geldert, A., He, L. & Herr, A. Multimodal detection of protein isoforms and nucleic acids from mouse pre-implantation embryos. *Nature Protocols* 1062–1088 (2021) doi:10.1038/s41596-020-00449-2.
33. Gkountela, S. *et al.* Circulating Tumor Cell Clustering Shapes DNA Methylation to Enable Metastasis Seeding. *Cell* **176**, 98-112.e14 (2019).
34. Pritzker, K. P. H. & Nieminen, H. J. Needle biopsy adequacy in the era of precision medicine and value-based health care. *Archives of Pathology and Laboratory Medicine* **143**, 1399–1415 (2019).
35. Lizotte, P. H. *et al.* Fine needle aspirate flow cytometric phenotyping characterizes immunosuppressive nature of the mesothelioma microenvironment. *Scientific Reports* **6**, 1–8 (2016).
36. Tang, F. *et al.* RNA-Seq analysis to capture the transcriptome landscape of a single cell. *Nature Protocols* **5**, 516–535 (2010).

37. Grindberg, V. R. *et al.* RNA-sequencing from single nuclei. *Proceedings of the National Academy of Sciences* **110**, 19802–19807 (2013).
38. Abdelmoez, M. N. *et al.* SINC-seq: Correlation of transient gene expressions between nucleus and cytoplasm reflects single-cell physiology. *Genome Biology* **19**, 1–11 (2018).
39. Kang, C.-C. *et al.* Single cell–resolution western blotting. *Nature Protocols* **11**, 1508–1530 (2016).
40. Schneider, C. A., Rasband, W. S. & Eliceiri, K. W. NIH Image to ImageJ: 25 years of image analysis. *Nature Methods* **9**, 671–675 (2012).
41. Sinkala, E. *et al.* Profiling protein expression in circulating tumour cells using microfluidic western blotting. *Nature Communications* **8**, 14622 (2017).
42. Rosàs-Canyelles, E., Dai, T., Lia, S. & Herr, A. E. Mouse-to-mouse variation in maturation heterogeneity of smooth muscle cells. *Lab on a Chip* **18**, 1875–1883 (2018).
43. Yamauchi, K. A. & Herr, A. E. Subcellular western blotting of single cells. *Microsystems and Nanoengineering* **3**, (2017).
44. Hughes, A. J., Tentori, A. M. & Herr, A. E. Bistable isoelectric point photoswitching in green fluorescent proteins observed by dynamic immunoprobed isoelectric focusing. *J Am Chem Soc.* **134**, 17582–17591 (2012).
45. Hughes, A. J. *et al.* Single-cell western blotting. *Nature Methods* **11**, 749–755 (2014).
46. Schwanhäusser, B. *et al.* Global quantification of mammalian gene expression control. *Nature* **473**, 337–342 (2011).
47. Lee, H. & Kim, J.-S. Unexpected CRISPR on-target effects. *Nature Biotechnology* **36**, 703–704 (2018).
48. Zischewski, J., Fischer, R. & Bortesi, L. Detection of on-target and off-target mutations generated by CRISPR/Cas9 and other sequence-specific nucleases. *Biotechnology Advances* **35**, 95–104 (2017).

Chapter 7

Proteoform analysis from adherent cells via 3D projection electrophoresis

Dr. Samantha M. Grist contributed to the literature review, experimental design, simulation setup, data collection, and data analysis in this chapter.

7.1 Abstract

Proteins play a critical role in controlling the cell-cell and cell-microenvironment interactions involved in differentiation, tissue remodeling, and cancer progression. *In situ* protein analysis from adherent (not detached) cells is key to studying these interactions. While immunocytochemistry can detect proteins *in situ* via antibody probing, distinguishing proteoforms (different molecular forms of a protein derived from the same gene) remains challenging, as antibodies often lack proteoform specificity. Here, we develop a platform for *in situ*, spatially resolved proteoform analysis from a layer of adherent cells via projection electrophoresis. Adherent cells on a microporous membrane are simultaneously lysed, and proteins rapidly electrophoretically separated by molecular mass through the depth of a ~1 mm-thick polyacrylamide sieving gel. Projection electrophoresis spatially resolves proteoforms in the Z dimension, conferring selectivity without proteoform-specific antibodies while preserving spatial context in the X-Y dimension. Using COMSOL simulations, we compare the sensitivity and lateral resolution of the adherent cell projection electrophoresis platform to a previously established microwell-based projection electrophoresis platform. Experimentally, we demonstrate size-based protein separation from a ~30% confluent layer of adherent BT474 breast cancer cells.

7.2 Introduction

Protein expression measurements are critical to understanding development, disease progression, and other important biological processes. In particular, it is often important to distinguish proteoforms – different molecular forms of a protein arising from the same gene[1] – as differential proteoform expression can yield different cellular phenotype. For example, expression of a truncated HER2 proteoform is associated with trastuzumab drug resistance in breast cancer, as the truncated proteoform lacks the extracellular domain to which trastuzumab binds[2,3]. Due to cell-to-cell heterogeneity[4] and spatial heterogeneity[5,6] in protein expression, proteoform measurements with single-cell sensitivity and which maintain spatial context information are particularly valuable to understand the role of proteoforms in influencing cell-microenvironment interactions, to evaluate the potential of proteoforms to serve as diagnostic biomarkers, and for other biological and clinical applications.

There is a need for proteomic measurement techniques with proteoform specificity, single-cell sensitivity, and spatial context preservation (**Figure 7.1**). Standard pathology techniques such as immunohistochemistry and imaging mass cytometry[7] detect proteins within tissue slices with single-cell resolution and spatial context preservation, but rely on antibodies, which can have non-specific, cross-reactive binding and often lack proteoform specificity[8,9]. Other techniques have

used electrophoresis[10] or mass spectrometry[11] to add proteoform specificity while maintaining spatial context information, but lack single-cell resolution. Microscale electrophoresis platforms have been developed to achieve single-cell proteoform-specific detection[12,13], but involve deposition of single-cell suspensions into microwells, eliminating spatial context information.

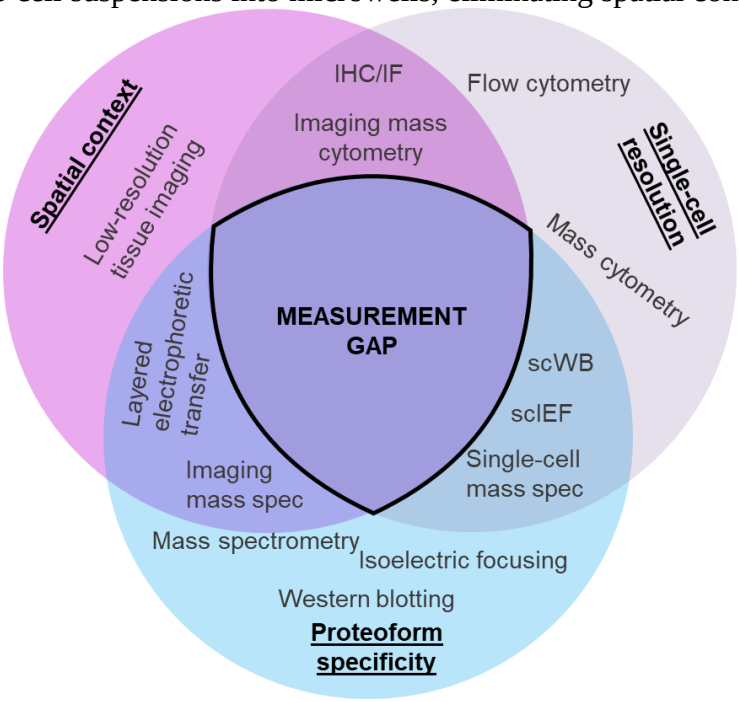

Figure 7.1. Measurement technologies with spatial context preservation, single-cell resolution, and proteoform specificity are lacking. IHC/IF = immunohistochemistry/immunofluorescence. scWB = single-cell western blotting. scIEF = single-cell isoelectric focusing.

Here, we investigate an approach to measure specific proteoforms from single cells while maintaining spatial context information, using projection electrophoresis. Recently, projection electrophoresis was developed to separate proteins in the Z dimension from an array of microwells loaded with single suspended cells[14]. We hypothesized that the projection electrophoresis platform could be adapted to electrophorese proteoforms from adherent cells cultured on a flat substrate, so that proteoforms are resolved in the Z dimension (e.g., thickness) of the separation gel, while maintaining information about the starting cell positions in the X-Y plane. We use COMSOL simulations and lysis monitoring experiments to characterize the impact of assay modifications on sensitivity and lateral resolution. Empirically, we demonstrate a proof-of-concept size-separation of proteins from adherent cells, providing a first-in-kind demonstration of an approach to fill a measurement gap in spatial proteomics.

7.3 Materials & Methods

Lysis and separation gel fabrication and buffers. Polyacrylamide lysis and separation gels were fabricated as described previously[14]. 1 mm-thick 6%T lysis gels were cut to ~14 × 14 mm and incubated overnight in 2× RIPA-like lysis buffer[14] containing 2× Tris-glycine and 0.2% Triton X-100; then, for a couple min prior to use of a lysis gel in an assay, the lysis gel was soaked in 55 ^{o}C 2× RIPA, 2× Tris-glycine, 0.2% Triton X-100 lysis buffer with 8 M urea. 1 mm-thick 7%T separation gels were cut to ~9 × 9 mm and incubated in 2× Tris-glycine overnight. To help

distinguish the orientation of the separation gel (i.e., which side is cell-side up), one corner of the separation gel was cut off, and a notch was cut into one side of the gel.

Lysis monitoring experiments and image analysis. Lysis monitoring was performed similar to previously reported experiments of microwell-based lysis monitoring[14], with some modifications to adapt the protocol to adherent cell lysis monitoring. Adherent U251 cells engineered to express Turbo GFP (tGFP) fluorescent protein were cultured either on polyacrylamide separation gels functionalized with fibronectin, similar to previously described[15], or on a microporous membrane (Millipore MCRP06H48 hanging cell culture insert with 1 μm-pore diameter PET). Substrates were seeded at ~25% confluency and cultured for ~12-24 h prior to lysis monitoring.

For lysis monitoring experiments without a microporous membrane, a fibronectin-functionalized 7%T polyacrylamide separation gel with adherent cells was adhered to a 60 mm petri dish with 5% agarose, as described previously[14]. A 20%T polyacrylamide lysis gel permeated with 2× RIPA-like, 1× Tris-glycine lysis buffer at room temperature was placed directly over the cells on the separation gel. Excess fluid on the separation and lysis gels was removed to different degrees ("less hydrated" vs. "more hydrated") either by using a Kim wipe at the corner of the gel to wick off fluid, patting the entire surface of the lysis gel dry with a Kim wipe, and/or letting the separation gels air dry for ~1 min prior to lysis.

For lysis monitoring experiments with a microporous membrane, the microporous membrane with adherent cells was cut out of the hanging cell culture insert and cut into sections which would fit on the ~9 × 9 mm separation gel using a scalpel and razor blade. The microporous membrane was placed cell-side-down on a 7%T polyacrylamide (without fibronectin) separation gel, which was adhered to a 60 mm petri dish with a small drop of superglue. A 6%T polyacrylamide lysis gel permeated with 2× RIPA-like, 2× Tris-glycine, 8 M urea lysis buffer at ~37 ^{o}C was placed on the microporous membrane (on the opposite side of the cells). The fluid volume on gels used in the microporous membrane lysis monitoring condition approximated the "more hydrated" state.

tGFP release from adherent cells during lysis was monitored by widefield fluorescence microscopy. Experiments without a microporous membrane were imaged with an Olympus 4× objective on an Olympus IX71 inverted epifluorescence microscope, with a Lumen Dynamics X-cite exacte fluorescence illumination source coupled to a liquid light guide (Lumatec, 805-00038) and an EM-CCD camera (Andor iXon). Experiments with a microporous membrane were imaged with an Olympus 2× objective on an Olympus IX51 inverted epifluorescence microscope, with a Lumen Dynamics X-cite exacte fluorescence illumination source coupled to a liquid light guide (Lumatec, 805-00038) and a CCD camera (Photometrics CoolSnap HQ2). Images were acquired every 1 s for at least 60 s, with an exposure time of 50 ms (no membrane – less hydrated and microporous membrane conditions) or 20 ms (no membrane – more hydrated condition). While the difference in exposure time may influence the proportion of protein spots which can be segmented from the image, we assumed that exposure time differences would not substantially alter quantification of the mean proportion of protein retained around cells.

tGFP protein release from cells was quantified from lysis monitoring timelapse images using custom MATLAB scripts[16], as reported previously[14]. Briefly, protein spots in each image were segmented with adapting thresholding and morphologic opening and closing operations, and centroids were determined using MATLAB's *regionprops* function. Centroids were tracked over time[17,18], and the fluorescence intensity summed within a 100 μm-diameter circle around each centroid was quantified from each image. Centroids present in <10 time points were discarded as noise or 'lost' tracked trajectories. Adaptive thresholding sensitivity was optimized to reduce the

rate of false positive protein spot detection and avoid combinatorics errors in centroid tracking; sensitivity was set to 0.5 for experiments without a membrane and 0.2 for experiments with a membrane. We hypothesize that lower sensitivity values (corresponding to thresholding fewer pixels as foreground, reducing the rate of false positive protein spot detection) are needed for the microporous membrane images to avoid identifying pores in the membrane as protein spots.

COMSOL simulations. Protein diffusion and electromigration was modeled with 2D axisymmetric COMSOL (version 5.6) models using the Transport of Diluted Species and Electric Currents physics, similar to described previously[14]. In contrast to the previously reported simulation[14], here, thermodynamic partitioning of protein into the hydrogel was modeled using the Partition boundary condition of the Transport of Diluted Species physics, rather than by setting flux boundary conditions. **Table 7.1** lists simulation parameters used.

Table 7.1. Parameters used for protein diffusion simulations.

Symbol	Parameter	Value	Notes
C_0	Starting protein concentration	2 µM	
r_H	Hydrodynamic radius of protein	2.4 nm (GFP) 5.4 nm (IgG)	Based on previously reported values[19,20]
$\%T_{sep}$	Separation gel density	7%T	To match experiments
$\%T_{lysis}$	Lysis gel density	6%T	To match experiments
D_{sep}	Protein diffusivity in separation gel	2.703E-11 m^2/s (GFP) 4.439E-12 m^2/s (IgG)	Calculated based on Park et al.[21]
D_{lysis}	Protein diffusivity in lysis gel	3.364E-11 m^2/s (GFP) 6.319E-12 m^2/s (IgG)	Calculated based on Park et al.[21]
D_{soln}	Protein diffusivity in free solution	1.369E-10 m^2/s (GFP) 6.085E-11 m^2/s (IgG)	Calculated from Stokes Einstein equation
K_{sep}	Partition coefficient of protein in separation gel	0.47732 (GFP) 0.05448 (IgG)	Calculated from Ogston model[22]
K_{lysis}	Partition coefficient of protein in lysis gel	0.58578 (GFP) 0.12193 (IgG)	Calculated from Ogston model[22]
T	Temperature	37 ºC	Estimated based on experimental protocol, in which lysis gel is taken from 55 ºC water bath and placed over a room-temperature separation gel
E	Electric field	60 V/cm	To match experiments
t_{lysis}	Duration of lysis step	20 s	
h_0_protein	Height of initial protein source	5 µm (adherent)[23] 15 µm (microwell)	Dimensions of protein source chosen based on approximate detached and adherent cell dimensions, while keeping the cell volume (and thus, protein amount) equal between the two assay formats.
w_0_protein	Width of initial protein source	26 µm (adherent) 15 µm (microwell)	
$h_{fluidLayer}$	Height of fluid layer	1.7 µm [24]	Height of fluid layer is measured from the lysis gel bottom to the top of either the adherent cell or separation gel. Thus, note the total distance between the two gels is greater in the adherent cell setup.

The center of the protein band was determined as the location with maximal protein concentration, determined using a Min/Max line through the axis of symmetry. Protein concentration profiles from r = 0 (the axis of symmetry) to the edge of the simulation were extracted using a 2D Cut Line. Lateral peak widths were determined by fitting a Gaussian function to the lateral concentration profile (the profile of half the band, from r = 0 to the edge of the simulation) extracted from the simulation using the fit function with fit type *gauss1* in MATLAB. Lower and upper limits on the Gaussian fit parameters (**Table 7.2**) were used to improve the goodness of fit to the data in some cases, though not in all cases. The fit function (bounded or unbounded) with the higher r^2 value was used to calculate peak width for a given concentration profile.

Table 7.2. Bounds on Gaussian fit parameters.

Parameter	Lower bound	Upper bound
a (amplitude)	0	Maximum concentration value
b (peak center)	-10E-6 m	10E-6 m
c (peak width)	The x coordinate at which concentration is half-maximum	$\sqrt{2}$ × the x coordinate at which concentration is half-maximum

Electrode system and determination of applied current. The electrode system is as described previously[14], with hot packs placed on the back sides of the electrodes to keep the electrodes at ~37 ^{o}C to aid in lysis and protein solubilization, and 3 mm-thick spacers placed between the electrodes to maintain uniform electrode spacing.

Electrophoretic separations were run by supplying a constant current with a DC power supply (Bio-Rad PowerPac Basic, #1645050). Constant current mode (as opposed to constant voltage mode) was used to maintain a more constant voltage drop (and thus, more constant electric field and electromigration) across the separation gel even if the resistance of the filter paper and other gel stack components changes over time due to joule heating and/or electrolysis. We aimed to apply an electric field of 40 – 60 V/cm (12 – 18 V across electrodes spaced 3 mm apart), as previously described[14]. To determine the appropriate current setting, we applied 18 V (constant voltage mode) across a dummy separation stack with all of the same components and buffers as are used for an actual projection electrophoretic separation, except cells, and recorded the measured current. This measured current was applied in constant current mode to adherent cell projection electrophoretic separations.

Adherent cell projection electrophoresis. BT474 cells were seeded at ~25% confluency on a hanging cell culture insert (Millipore MCRP06H48) and cultured for ~19 h, at which point the cells should remain subconfluent. After culturing, the microporous membrane of the cell culture insert was cut out with a scalpel, and cut into quarters (small enough to fit on a ~9 × 9 mm separation gel) using a scalpel and razor blade. To avoid detaching cells from the membrane, care was taken to place the scalpel and razor blade only along cut lines without scraping the rest of the membrane. Cells were stained with calcein in serum-free cell culture medium for ~1 h prior to projection electrophoresis.

To run projection electrophoresis, the microporous membrane with adherent cells was removed from the calcein-medium solution, dipped in 2× Tris-glycine, lightly dried by dabbing one side with a Kim wipe, and placed cell-side down on the separation gel. The starting cell locations were imaged using widefield fluorescence microscopy (Olympus IX51 microscope, described above). After imaging, the gel stack was set up in the electrode system as follows, from

bottom to top: a ~10 × 10 × 1 mm Western Blotting filter paper (Thermo Fisher 84783) permeated with lysis buffer at 55 ^{o}C, ~9 × 9 × 1 mm separation gel equilibrated in 2× Tris-glycine, microporous membrane with adherent BT474 cells (cell-side down), ~14 × 14 × 1 mm lysis gel permeated with lysis buffer at 55 ^{o}C. Care was taken to avoid introducing bubbles to the system during stack setup, as bubbles would alter or impede the electric field. Immediately after the stack setup was completed by adding the lysis gel, the lysis timer was started and the electrode system was closed. After 33 s of lysis, an electric field (57 mA constant current, typically yielding ~13 V initial voltage for an average electric field of 43 V/cm) was applied for 10 s to generate an electrophoretic separation. Immediately after the electrophoretic separation, the power supply was stopped, electrode system opened, gel stack disassembled and microporous membrane removed, and proteins were photo-immobilized by applying ultraviolet (UV) light (Lightningcure LC5, Hamamatsu) for 45 s to the separation gel. Because the microporous membrane may block UV light and/or get bonded to the gel upon UV exposure, the microporous membrane was removed from the separation gel prior to photo-immobilization. After photo-immobilization, separation gels were incubated in dI water for ~5 min and then stored in 1× TBST for at least 12 h prior to immunoprobing.

Electrophoretic immunoprobing of the separation gel was performed as described previously[14,25], with either a 0.5 or 1 mm-thick 1.5% agarose antibody delivery gel, depending on the replicate. Actinin was immunoprobed with rabbit anti-actinin primary antibody (Cell Signaling Technologies, CST6487) diluted 1:10 (final concentration 0.0121 mg/mL) and donkey anti-rabbit Alexa Fluor 488-labeled secondary antibody (Thermo Fisher A11055) diluted 1:20 (final concentration 0.1 mg/mL). GAPDH was immunoprobed with Rhodamine-labeled anti-GAPDH hFAB antibody fragment diluted 1:10 (Bio-Rad 12004167; injected during the secondary antibody injection step). All antibodies were electrophoretically injected into the separation gel for 13 min at 20 V constant voltage mode, and washed out for 25 min at 30 V constant voltage mode using a Bio-Rad PowerPacHV power supply (#1645056). Immunoprobed separation gels were imaged using a Zeiss LSM 880 laser-scanning confocal microscope with a 20× water immersion objective, as described previously[14].

Estimation of SDS delivered from lysis gel. Lysis gels are immersed in a lysis buffer composed of 1% wt/vol SDS, 0.5% wt/vol sodium deoxycholate, 0.2% Triton X-100, 2× Tris-glycine, and 8 M urea, at 55 ^{o}C. The 6%T gels are 1 mm thick and 14 mm × 14 mm laterally, but will be placed over a 9 mm × 9 mm separation gel. We assume that only SDS within a 1 mm × 9 mm × 9 mm volume of the lid gel can be delivered to the adherent cells (as timescales of SDS micelle diffusion across mm length scales are much longer than an average lysis duration of 30 s); the extra lateral size of the lysis gel makes it easier to ensure the lysis gel entirely covers the separation gel during lid placement.

SDS is delivered in two ways: either by diffusing through the free solution fluid layer on the lysis gel, or by diffusing out of the lysis lid gel and across the fluid layer to the adherent cells on the separation gel. We assume SDS exists as micelles, as the critical micelle concentration of SDS in tris-glycine buffer has been reported to be 3.4 mM,[26] and our lysis buffer (1% wt/vol SDS) contains 34.7 mM SDS.

SDS in fluid layer

We assume that the fluid layer on the lysis lid gel is 1.7 μm thick, based on Su et al.'s measurements of fluid layer thickness between two hydrogel slabs (30 μm thick 6%T microwell gel under a 500 μm thick 15%T lid gel).[24] Thus, the volume of the lysis buffer fluid layer is 9 mm × 9 mm × 1.7 μm = 0.137 μL. The lysis buffer is 1% wt/vol SDS, so the total mass of SDS in the

fluid layer is 1.377 µg. The diffusive timescale of SDS micelles through the 1.7 µm thick fluid layer is $\tau = \frac{x^2}{2D_{\text{free solution}}}$, where x = 1.7 µm and $D_{\text{free solution}}$ is estimated to be 5.75E-11 m^2/s from the Stokes-Einstein equation ($D = \frac{k_B T}{6\pi\eta r_h}$). We find that it takes a negligible amount of time (0.025 s) for SDS micelles to diffuse through the fluid layer, so we assume that all SDS in the fluid layer reaches the adherent cells and can be used to solubilize protein.

SDS delivered from lysis lid gel

The amount of SDS which can be loaded into the lid gel depends on the partition coefficient (K) of SDS micelles in a 6%T polyacrylamide gel, which can be estimated using the ideal Ogston model, which states that $K = \exp[-\Phi(1+\frac{R_h}{a_f})^2]$.[22] Polymer volume fraction (Φ) can be calculated from the gel density (%T) according to[27,28]: $\Phi = 0.0093 \times \%T - 0.03151$. The fiber radius ($a_f$) was estimated[29] as 6.47 Å (see Chapter 3). Thus, K of SDS micelles in a 6%T polyacrylamide gel is estimated to be 0.09635.

The diffusivity of SDS micelles in the 6%T lysis gel is calculated as $D_{6\%T} = D_{\text{free solution}}\exp(-3.03 r_h^{0.59} C^{0.94})$, where C is the polyacrylamide concentration (g/ml), according to Park et al.[21] The characteristic length scale of SDS micelle diffusion through a 6%T gel during a 30 s lysis period is $x = \sqrt{2D_{6\%T}t}$, where t = 30 s. We estimate that SDS micelles can only diffuse through a distance of 18.3 µm of gel. Thus, the majority of SDS which is loaded into the 1 mm thick lid gel is not able to be released during lysis; only SDS in a lid gel volume of 18.3 µm × 9 mm × 9 mm can diffuse out during a 30 s lysis period. The total mass of SDS in the lid gel which reaches the adherent cells is 1.42 µg (1% wt/vol SDS × K × (18.3 µm × 9 mm × 9 mm gel volume)). Thus, the total mass of SDS delivered from the fluid layer and lid gel is estimated to be 2.8 µg.

7.4 Results & Discussion

Strategies to reduce protein advection during lysis. To resolve proteoforms from adherent cells while maintaining spatial context information, we hypothesized that the microwell-based projection electrophoresis system for single-cell immunoblotting[14] could be adapted by culturing adherent cells on a flat separation gel. Upon placement of a lysis gel over the separation gel, adherent cells would lyse and release protein, which would then be electrophoretically separated into the thickness of the separation gel, while retaining protein localization information in the lateral dimension (**Figure 7.2**). While the use of a flat separation gel without microwells allows adherent cells to grow freely across the gel surface and eliminates the need for trypsinization or other cell detachment methods prior to projection electrophoresis, we hypothesized that there would be increased protein advection upon lysis because cells are no longer shielded from convective fluid flow[12] at the separation gel – lysis gel interface (**Figure 7.2B,C**). Upon placement of one polyacrylamide hydrogel on another, fluid velocity at the interface has been measured[24] to be 285 µm/s. Protein advection induced by this interfacial fluid flow would reduce assay sensitivity and hinder preservation of spatial context.

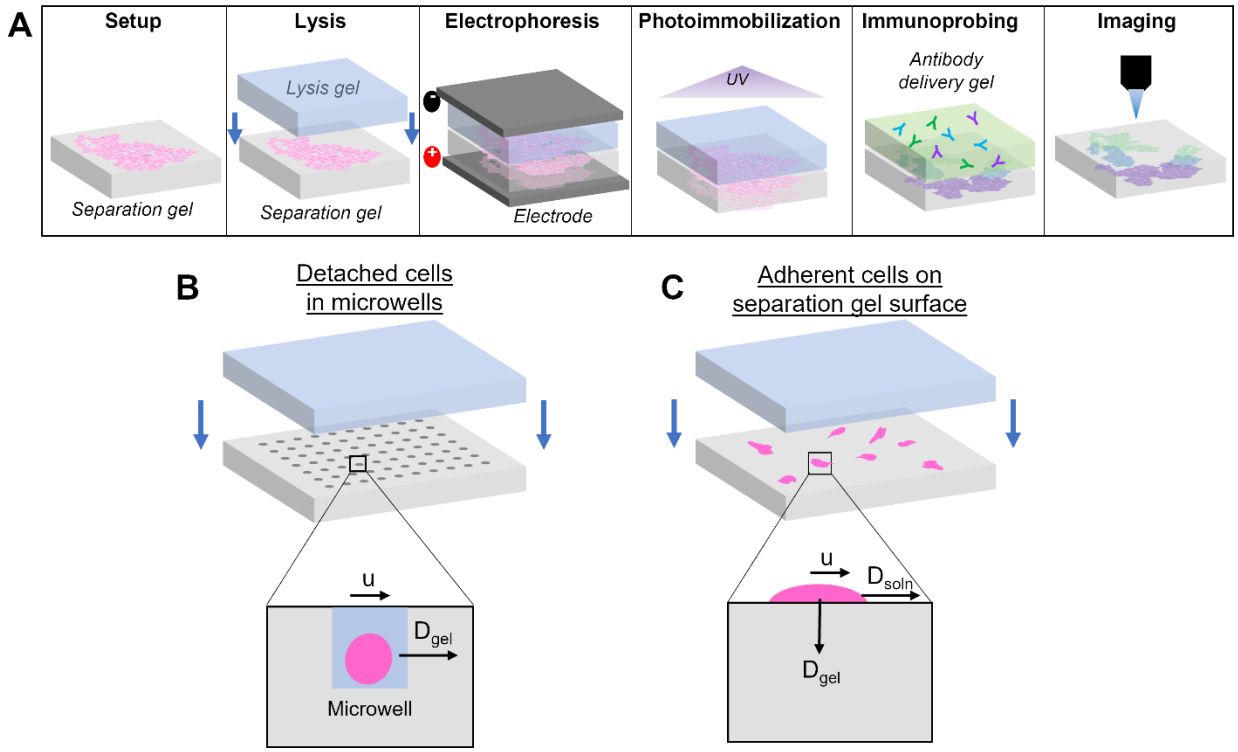

Figure 7.2. Sensitivity and spatial context preservation of adherent cell projection electrophoresis may differ from microwell-based separations due to differing physics at the lysis step. (A) Adherent cell projection electrophoresis workflow. The local geometry and associated physics at the lysis step differ between projection electrophoresis of (B) suspended single cells in microwells, and (C) adherent cells on a flat separation gel. u = convective fluid velocity at fluid interface; D_{gel} = diffusivity of protein in separation gel; D_{soln} = diffusivity of protein in free solution.

To characterize protein advection after lysis gel placement in the adherent cell projection electrophoresis system, we tracked the release of the fluorescent protein from adherent U251 cells engineered to express Turbo GFP (tGFP) over time using widefield fluorescence microscopy (**Figure 7.3**). Two approaches hypothesized to minimize protein advection were tested. First, we hypothesized that slight drying of the lysis and separation gels would reduce the volume and flow velocity of the fluid layer. Second, we hypothesized that the addition of a microporous membrane between the lysis gel and adherent cells would introduce a time delay between lysis gel placement and the start of lysis, so that protein is released after convection at the interface has subsided. We hypothesized that the microporous membrane would delay lysis buffer delivery by increasing the time required for lysis buffer components to diffuse across the membrane to reach the cells. We calculated the 4τ characteristic diffusion time of SDS micelles in the lysis buffer to travel across the membrane to be 4.2 s ($\tau = \frac{z^2}{2D}$, where the membrane thickness, z, is 11 µm and the SDS micelle diffusivity in free solution, D, is 5.75E-11 m^2/s, as calculated using the Stokes-Einstein equation and the reported hydrodynamic radius of an SDS micelle[30]).

To evaluate the effect of hydration state on protein advection, we quantified the proportion of tGFP remaining within a 100 µm-diameter region around the initial cell location over time after placement of the lysis gel that was dried to different extents with a Kim wipe (**Figure 7.3A-B, Figure 7.4**). While the lysis gel must remain hydrated enough to deliver lysis buffer to the cells and to avoid the formation of bubbles, which would impede the electric field, the gel was dried to different extents by either placing a Kim wipe over the entire lysis gel surface (i.e., gel is 'less

hydrated') or placing a Kim wipe at one corner of the lysis gel to wick away excess solution (i.e., gel is 'more hydrated'). We observed that the more hydrated gel had substantially greater protein loss, in agreement with our hypothesis (**Figure 7.4**). After 25 s of lysis, the more hydrated gel had 13% ± 6% of protein remaining, which is similar to the amount of protein retained in the microwell-based projection electrophoresis system[14]. After the start of lysis, fewer protein spots are visible and could be detected with image segmentation in the more hydrated gel as compared to the less hydrated gel, for a given lysis time (**Figure 7.3A-B**). In contrast, the less hydrated gel had 54% ± 12% of protein remaining after 25 s of lysis. Thus, our results suggest that reducing the hydration state of the lysis and separation gels minimize protein advection and protein loss, though further investigation is needed to determine the minimum hydration level needed for complete cell lysis and protein solubilization.

To evaluate whether a microporous membrane placed between the lysis gel and adherent cells reduced protein advection, we also compared the proportion of protein remaining from cells in systems with and without a microporous membrane. The proportion of protein remaining from cells in the microporous membrane system was similar to the level of protein retention in the less hydrated system (**Figure 7.4**). We hypothesize that the increase in the mean proportion of retained protein after ~14 s is due to the dropout of some quickly lysing cells as they become undetectable, thus raising the mean proportion of retained protein based on the remaining detectable cells. Additionally, in the microporous membrane system, we observe that some cells exhibit delayed lysis (blue arrows in **Figure 7.4**), which may also increase the measurement of retained protein if the fluorescent protein was self-quenched inside these cells and fluorescence increases upon cell lysis. The microporous membrane data is not directly comparable to the other lysis monitoring conditions, as the cells in the microporous membrane condition were lysed with a slightly different lysis buffer which more closely matches the buffer conditions needed for complete protein solubilization (buffer contains 8 M urea, and is at ~37 ^{o}C rather than room temperature). However, the similar or greater degree of protein retention in the microporous membrane system as compared to the other tested conditions, despite the higher temperature of the lysis buffer in the membrane system (which would lead to greater diffusional loss), suggests the microporous membrane may be a promising approach to minimize protein advection.

Further studies with exactly matching buffer conditions and imaging settings are needed to directly compare the performance of different strategies to minimize protein advection. Additionally, lysis monitoring experiments would benefit from strategies to better control hydration level and the force and directionality of lysis gel placement, which we hypothesize contribute to run-to-run variation.

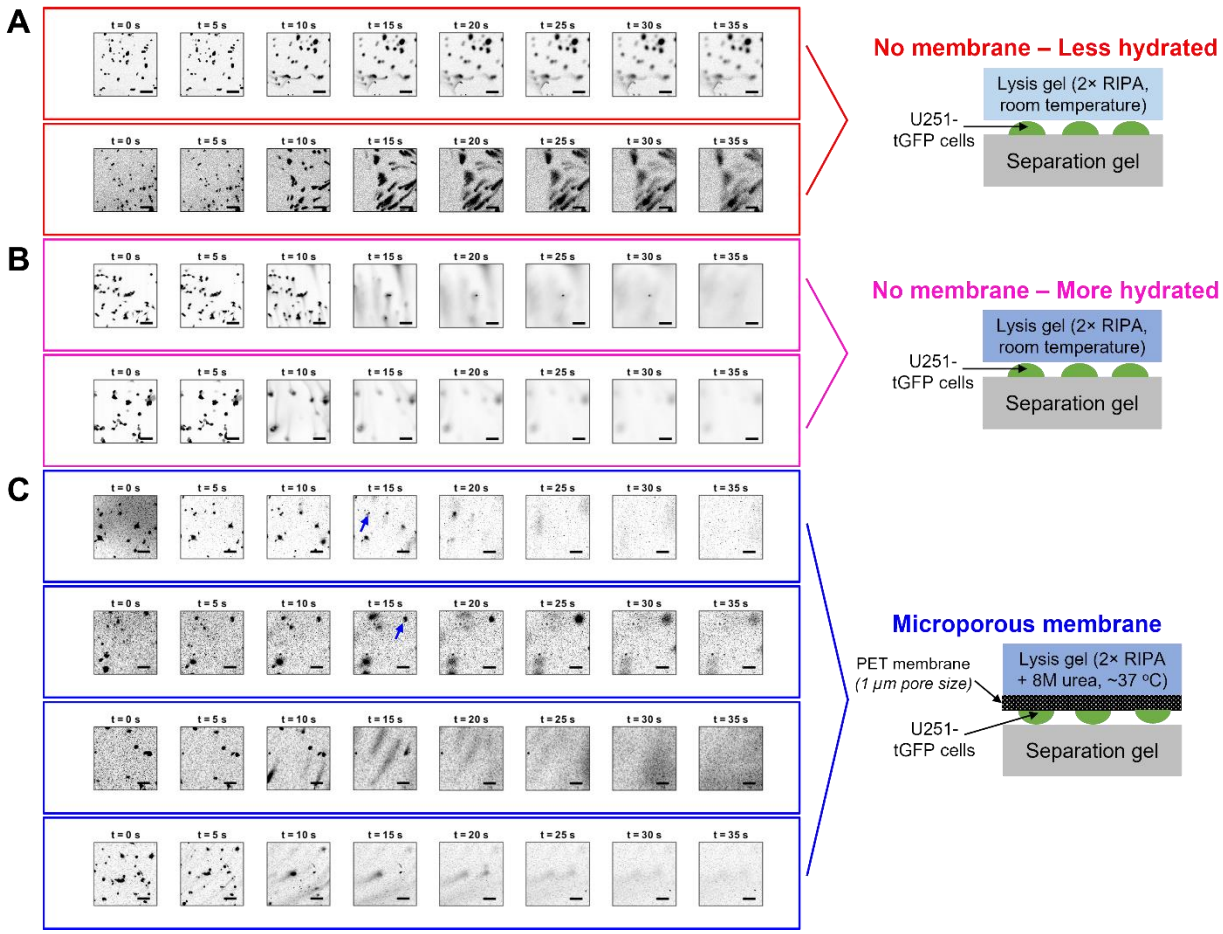

Figure 7.3. Timelapse images of adherent U251-tGFP cell lysis under different lysis conditions. Widefield fluorescent micrographs of tGFP release from adherent U251-tGFP cells as cells are lysed via lysis buffer delivered from a polyacrylamide lysis gel permeated with buffer. To evaluate whether the volume of the fluid interface impacted advective protein loss, lysis was monitored with either a (A) less hydrated or (B-C) more hydrated lysis gel. To evaluate whether a microporous membrane placed between the lysis gel and cells impacted advective protein loss, lysis was monitored with either (A-B) no membrane, or (C) a 1 µm-pore diameter, 11 µm-thick PET membrane present. The lysis gel was permeated with (A-B) room-temperature 2× RIPA-like lysis buffer, or (C) ~37 °C 2× RIPA-like buffer with 8 M urea. In the microporous membrane experimental condition, some cells exhibit delayed lysis (blue arrows in C). Each image within a timelapse series (i.e., within one row) has the same image contrast; contrast is set based on the minimum and maximum fluorescence intensity in the pre-lysis (t = 0 s) image. All scalebars are 300 µm.

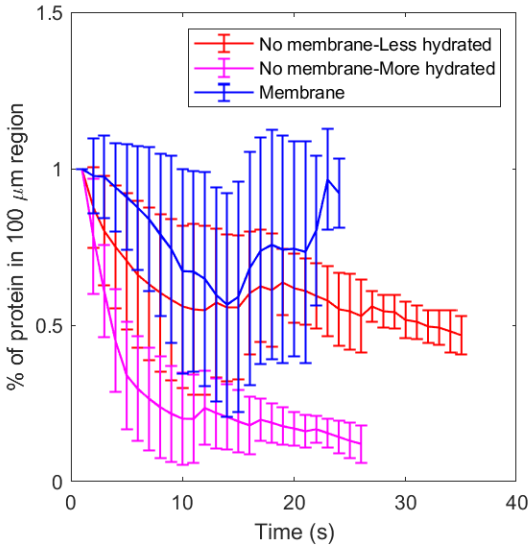

Figure 7.4. tGFP protein loss from adherent U251-tGFP cells depends on lysis conditions. The proportion of tGFP remaining within a 100 µm-diameter region during lysis was quantified from widefield fluorescence timelapse imaging. Plots indicate mean and standard deviation; plot extends to the time at which <3 protein spots were detected. N = 8 cells from 2 lysis experiments (no membrane – less hydrated), N = 30 cells from 2 lysis experiments (no membrane – more hydrated), N = 112 cells from 4 lysis experiments (membrane).

Comparing diffusional losses in the microwell-based and adherent cell platforms. Even if protein advection is eliminated in the adherent cell platform, we hypothesized that the adherent cell platform would have greater diffusional losses than a microwell-based system due to differing geometry and boundary conditions during the lysis and electrophoresis stages. In the microwell-based platform, cell lysate is bounded by polyacrylamide hydrogel on the bottom and sides of the microwell, which limit protein diffusion due to the decreased protein diffusivity in polyacrylamide as compared to in free solution[21]. In contrast, the adherent cell is bounded by free solution on three sides (**Figure 7.2B,C, Figure 7.5**). Additionally, we hypothesized that the differing aspect ratios of suspended and adherent cells contribute to differences in protein distribution during electrophoresis. Proteins which diffuse in the Z dimension will be re-stacked during Z-directional electrophoresis; because an adherent cell has a smaller Z dimension as compared to a rounded, detached cell of the same total volume, we hypothesized that electrophoresed protein bands in the adherent cell projection electrophoresis platform would have lower protein concentrations, spread over a larger lateral distance.

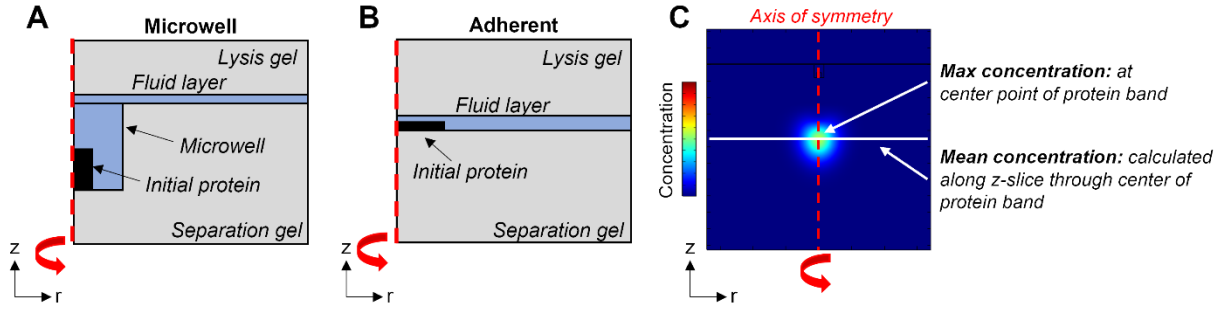

Figure 7.5. Components of simulated projection electrophoresis platforms. The 2D axisymmetric models are revolved around the z axis through the center of the initial protein region (axis of symmetry). (A) Detached cell-in-microwell projection electrophoresis. (B) Adherent cell projection electrophoresis. Schematics are not drawn to scale. (C) Heatmap of example protein concentration distribution. The maximum protein concentration is the concentration

at the center point of the protein band, while the mean protein concentration is calculated from the average concentration across all r at a single z plane, as would be used to generate intensity profiles of electrophoretic separations. Red dashed line indicates the axis of symmetry (not protein concentration).

To compare the sensitivity and protein band morphology of the adherent and microwell-based projection electrophoresis platforms, we used COMSOL to simulate protein diffusion and electromigration (**Figure 7.6**). To facilitate comparison, the volume and concentration of the initial protein region is the same between the two modeled platforms. Because protein diffusivity is dependent on protein size, we characterized the distribution of two proteins of differing hydrodynamic radii: GFP (2.4 nm radius, **Figure 7.6A**) and IgG (5.4 nm radius, **Figure 7.6B**). In agreement with our hypothesis, the simulations indicate that without convection (i.e., diffusive losses only), the local protein concentration is greater in the microwell-based platform (**Figure 7.6**, **Figure 7.7A**). To evaluate how the sensitivity of the two assay platforms compares, we calculated the ratio of protein concentration in the adherent and microwell systems ($\frac{C_{adherent}}{C_{microwell}}$; **Figure 7.7B**). As expected, $\frac{C_{adherent}}{C_{microwell}} < 1$ for both proteins for all simulated electrophoresis durations, indicating lower assay sensitivity in the adherent cell platform.

Protein concentration was determined as either the maximum concentration at the center of the protein band, or as the mean protein concentration at all lateral positions across a given Z position (**Figure 7.5C**). The mean protein concentration is representative of how an intensity profile of the electrophoretic separation is calculated. Due to the aspect ratio of adherent cells, the electrophoresed protein band is spread across a greater lateral distance, and thus we anticipate that the difference in the maximum protein concentration in the adherent and microwell-based platforms would be greater than the difference in mean protein concentration. In agreement with this hypothesis, $\frac{C_{adherent}}{C_{microwell}}$ is higher when using mean concentrations rather than maximum concentrations, for a given protein (**Figure 7.7B**).

By comparing simulations run with proteins of two different hydrodynamic radii representative of the sizes of GFP and IgG, we also find that the ratio of protein concentration between the two platforms is dependent on protein size. $\frac{C_{adherent}}{C_{microwell}}$ is closer to 1 for the smaller protein, indicating that the sensitivity of the adherent cell platform is more similar to the microwell-based platform for small proteins. In contrast, the microwell-based platform retains a relatively greater concentration of protein than the adherent cell platform as protein size increases. We hypothesize that the decreased in-gel diffusivity contributes more greatly to reduced diffusive losses in the microwell-based platform as protein size increases.

Overall, simulations indicate that the adherent cell platform has lower assay sensitivity than the microwell-based platform, as mean protein concentration in the adherent cell platform was 10.4% – 81.2% of the mean concentration in the microwell-based platform, depending on the protein size and electrophoresis time (**Figure 7.7B**). Whether these concentrations yield single-cell sensitivity depends on the protein size and EP time, as well as starting protein concentration, photo-immobilization and immunoprobing efficiency, and imaging performance.

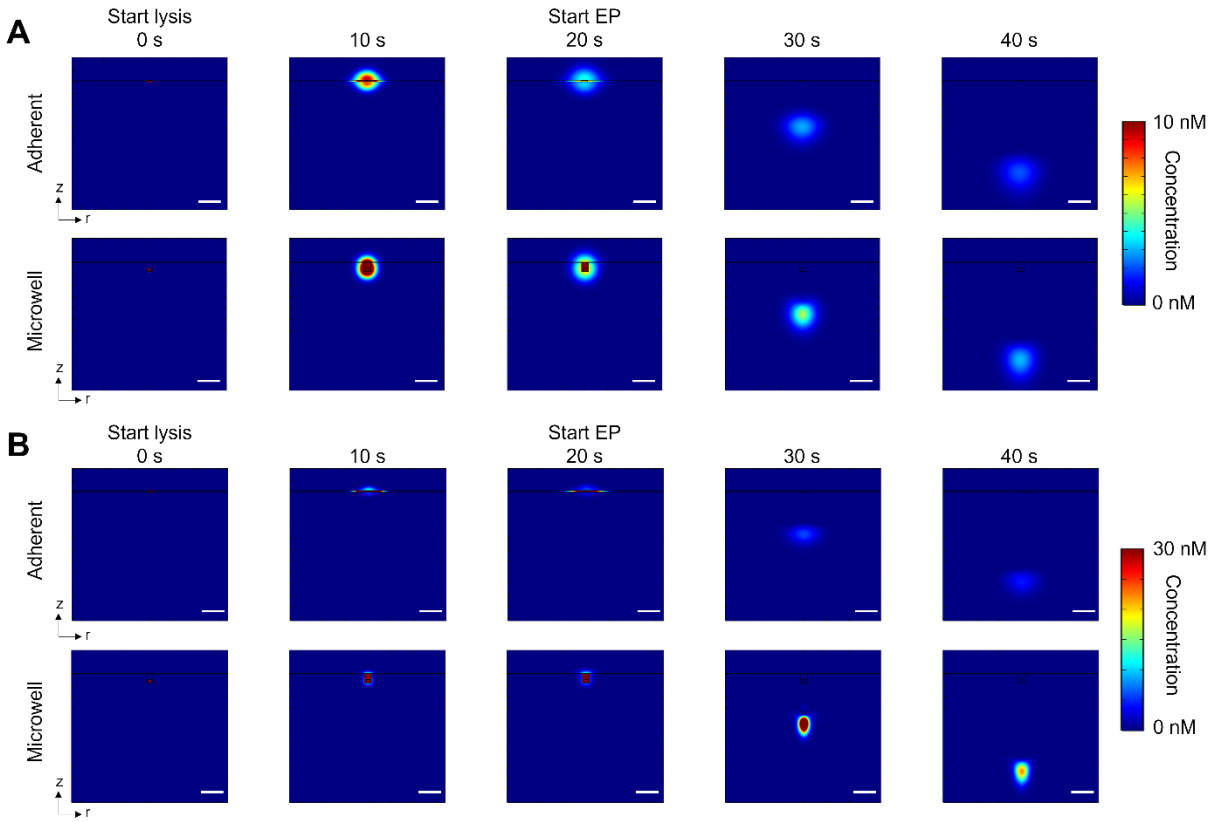

Figure 7.6. Assay sensitivity depends on projection electrophoresis platform and protein size. Side views of simulated distribution during lysis and electrophoresis (EP) of proteins with two different hydrodynamic radii: (A) 2.4 nm, representing GFP; (B) 5.4 nm, representing IgG. Scale bars are 100 µm. In some images, the maximum concentration exceeds the upper limit of the colorbar.

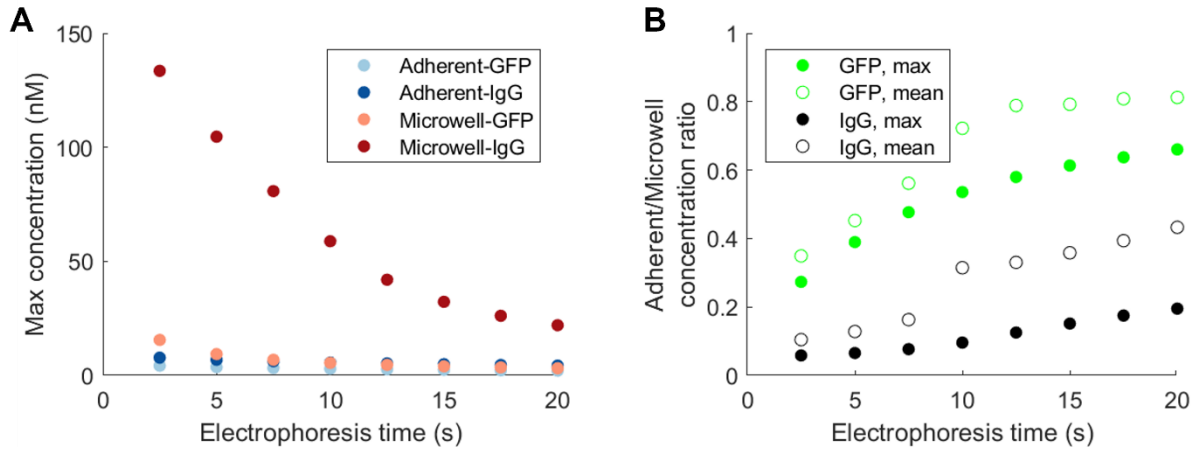

Figure 7.7. Microwell projection electrophoresis platform offers greater sensitivity benefit over adherent cell platform for analysis of larger proteins. (A) Simulated maximum concentration of electrophoresed protein band for proteins with hydrodynamic radii corresponding to the size of GFP (2.4 nm) and IgG (5.4 nm) in the adherent and microwell-based projection electrophoresis platforms. (B) The ratio of protein concentration in the adherent vs. microwell system ($\frac{C_{adherent}}{C_{microwell}}$) as a function of electrophoresis time and protein size. Both the maximum and mean protein concentrations across a z-slice are quantified.

Comparing lateral peak width in microwell-based and adherent cell platforms. To evaluate the lateral spatial resolution of the two platforms, we also quantified lateral peak width from simulated protein distributions. To evaluate the worst-case scenario, the smaller protein (GFP) peak width was characterized because the smaller protein would diffuse further. Lateral intensity profiles through the center of the protein band were extracted (**Figure 7.8A,B**) and fit to a Gaussian curve to extract the lateral peak width parameter (σ_{xy}). At a cell-to-cell spacing of $6\sigma_{xy}$, we anticipate <0.3% protein overlap based on Gaussian distributions, as described previously[14]. The minimum cell-to-cell spacing for single-cell lateral resolution is ~300 – 400 µm in the adherent cell platform and ~170 – 300 µm in the microwell platform, depending on electrophoresis time (**Figure 7.8C**).

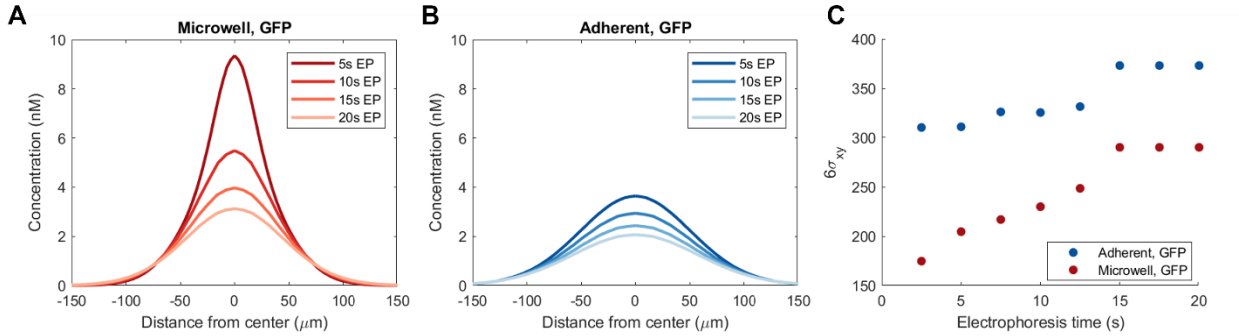

Figure 7.8. Simulated lateral protein peak width determines minimum cell-to-cell spacing for single-cell lateral resolution. Lateral concentration profiles of simulated GFP distribution in the (A) microwell, and (B) adherent cell projection electrophoresis platforms. (C) Minimum cell-to-cell spacing for <0.3% lateral signal overlap ($6\sigma_{xy}$), based on simulated GFP protein peak width, as a function of electrophoresis time and electrophoresis platform.

***In situ* size-based separation of proteins from subconfluent adherent cells.** Finally, we performed projection electrophoresis of subconfluent adherent BT474 cells. BT474 cells were grown on a microporous PET membrane, which facilitated transfer of the adherent cell layer to the separation gel, and may minimize protein advection by delaying diffusive lysis buffer delivery. Lysis time used (33 s) was longer than simulated lysis time (20 s) and previously reported lysis times for some applications of single-cell immunoblotting[12], based on the increased lysis time reported for BT474 cells[2] and to ensure full protein solubilization. After projection electrophoresis, the separation gel was immunoprobed for actinin (100 kDa) and GAPDH (36 kDa). GAPDH, the smaller protein, migrated further into the separation gel than actinin (**Figure 7.9A,B**), demonstrating protein size-dependent electromigration that is critical to resolve proteoforms. Immunoprobed protein signal is punctate, indicating that protein remains spatially localized in the XY-plane (**Figure 7.9C,D**). Because BT474 cells exhibit patchy growth, protein bands may arise from multilayered clusters of BT474 cells rather than a single cell. Future experiments with subconfluent cells which grow as a single layer are needed to empirically evaluate the sensitivity of adherent cell projection electrophoresis. However, these results are a promising proof-of-concept of size-based electrophoretic separation from adherent cells.

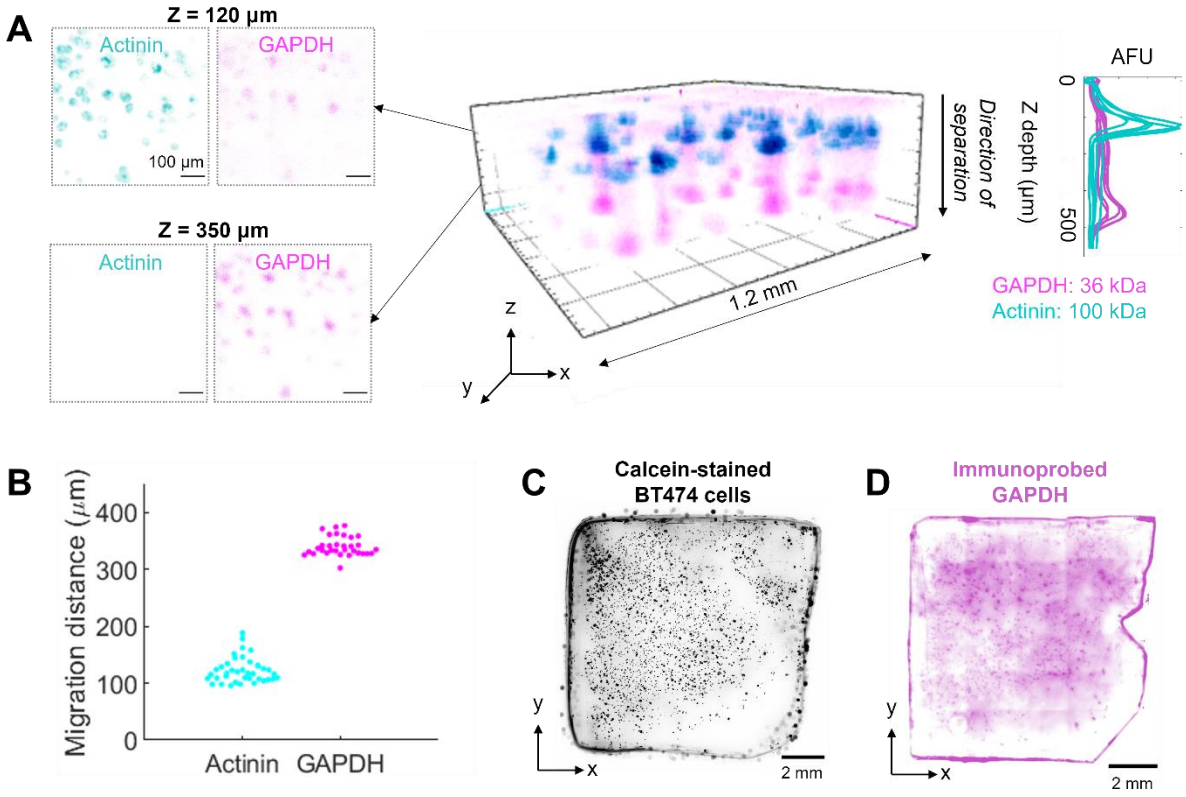

Figure 7.9. Projection electrophoresis of adherent BT474 cells separates proteins of different molecular mass in the Z dimension. (A) Confocal micrograph of actinin and GAPDH protein bands electrophoresed from subconfluent adherent BT474 cells (middle). Protein electromigration into the Z dimension of the separation gel is size-dependent, as indicated by micrographs of single Z-slices (left) and intensity profiles (right). (B) Beeswarm plot of migration distances of actinin (n = 39 protein bands from 2 gels) and GAPDH (n = 32 protein bands from 2 gels) into the separation gel. (C) Top-down widefield fluorescence micrograph of calcein-stained adherent cells on the separation gel prior to lysis and electrophoresis. (D) Top-down widefield fluorescence micrograph of GAPDH in the separation gel after lysis, electrophoresis, and immunoprobing.

Electrophoretic separation performance breaks down at high cell density. Having demonstrated effective protein size-separation in a projection electrophoresis assay of subconfluent BT474 cells, we next sought to evaluate assay performance with high cell densities. However, projection electrophoresis of confluent BT474 cells yielded little protein electromigration into the gel; the majority of protein remained at the top surface of the separation gel, with some skewed electromigration near the edges of the cell layer which appeared as ring-like features in the top-down widefield fluorescence microscopy image (**Figure 7.10**).

We hypothesize incomplete protein electromigration from confluent adherent cells may be due to a few different factors, which all relate to the fact that a confluent adherent cell layer contains orders of magnitude more protein than the microwell arrays of single cells spaced 100s of µm apart which are typically used for single-cell immunoblotting[12,14]. First, the lysis gel-based delivery of lysis buffer may deliver insufficient SDS to fully solubilize all protein. Based on the thickness of the fluid layer, SDS concentration in the lysis buffer, and diffusive timescales of SDS diffusion in free solution and polyacrylamide gel, we estimate that the total mass of SDS delivered from the fluid layer and lid gel is 2.8 µg (see Methods). Because 1.4 g of SDS associates with 1 g of protein at saturation[31], we estimate that the amount of SDS delivered by a 6%T lysis lid gel in

30 s can solubilize 2.0 µg of protein. Assuming a cell density at confluence of 130,000 cells/cm^2 (estimated from Thermo Fisher's Useful Numbers for Cell Culture guidelines[32]) and 250 pg protein per cell, a fully confluent monolayer spread over the 9 mm × 9 mm separation gel would have 26.3 µg of protein, which is an order of magnitude greater than the estimated amount of protein which can be solubilized by the amount of SDS delivered by the lysis gel.

Additionally, the lysis buffer composition may need to be optimized to handle the extracellular matrix and other components of confluent cell layers. Lastly, large amounts of other cellular material (lipids, nucleic acids) may impede electromigration by either clogging the polyacrylamide hydrogel pores, or by altering the local electric field. For example, the high lipid content of breast tissue has been found to impede electrophoresis[33]. Strategies to improve solubilization and electromigration of proteins from confluent layers of adherent cells have been briefly investigated, including the use of a nuclease to break down nucleic acid material during lysis, increased SDS concentration in the lysis buffer, use of filter paper rather than polyacrylamide gel to increase lysis buffer delivery, and application of a low electric field during cell lysis to electromigrate SDS into the cellular sample and minimize protein diffusion; however, further investigation and development is needed.

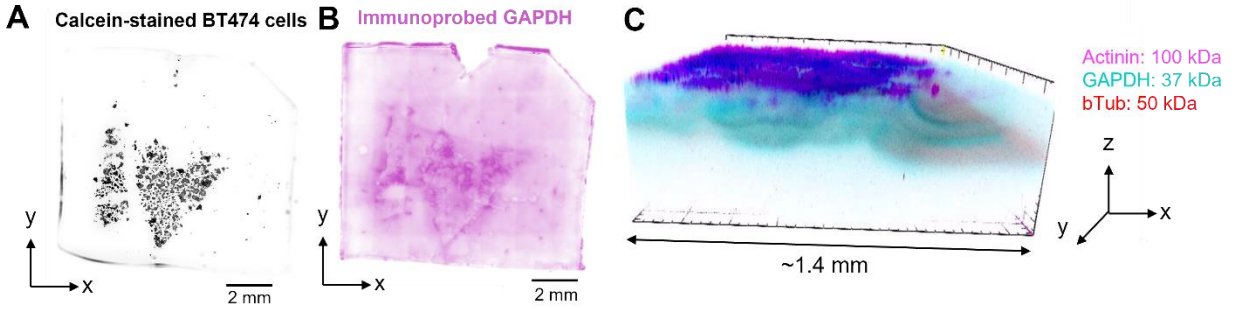

Figure 7.10. Protein fails to electromigrate into the separation gel in projection electrophoresis of confluent adherent BT474 cells. Top-down widefield fluorescence microscopy images of (A) confluent BT474 cells on the separation gel prior to projection electrophoresis, and (B) immunoprobed GAPDH after projection electrophoresis and immunoprobing. (C) Confocal micrograph of immunoprobed actinin, GAPDH, and beta tubulin.

7.5 Conclusions

Here, we have demonstrated a proof of concept projection electrophoretic separation of proteins from subconfluent adherent cells. Using simulation, we compared the performance of microwell-based and adherent cell projection electrophoresis in terms of assay sensitivity and lateral resolution. Adherent cell projection electrophoresis fulfills a measurement gap in single-cell, proteoform-specific characterization with preservation of spatial context, which has important applications to pathology and cell-microenvironment research. Ultimately, projection electrophoresis of tissue slices would prove valuable to facilitate new types of pathological analysis. However, further development of methods of lysis buffer delivery and sample preparation is needed to achieve complete cell lysis, protein solubilization, and electromigration from complex biological samples.

7.6 References

1. Aebersold, R. *et al.* How many human proteoforms are there? *Nat Chem Biol* **14**, 206–214 (2018).

2. Kang, C.-C. *et al.* Electrophoretic cytopathology resolves ERBB2 forms with single-cell resolution. *npj Precision Oncology* **2**, 10 (2018).
3. Ward, T. M. *et al.* Truncated p110 ERBB2 induces mammary epithelial cell migration, invasion and orthotopic xenograft formation, and is associated with loss of phosphorylated STAT5. *Oncogene* **32**, 2463–2474 (2013).
4. Altschuler, S. J. & Wu, L. F. Cellular Heterogeneity: Do Differences Make a Difference? *Cell* **141**, 559–563 (2010).
5. Buczak, K. *et al.* Spatial Tissue Proteomics Quantifies Inter- and Intratumor Heterogeneity in Hepatocellular Carcinoma (HCC). *Molecular & Cellular Proteomics* **17**, 810–825 (2018).
6. Guo, T. *et al.* Multi-region proteome analysis quantifies spatial heterogeneity of prostate tissue biomarkers. *Life Science Alliance* **1**, e201800042 (2018).
7. Giesen, C. *et al.* Highly multiplexed imaging of tumor tissues with subcellular resolution by mass cytometry. *Nature Methods* **11**, 417–422 (2014).
8. James, L. C., Roversi, P. & Tawfik, D. S. Antibody Multispecificity Mediated by Conformational Diversity. *Science* **299**, 1362–1367 (2003).
9. Trenchevska, O., Nelson, R. W. & Nedelkov, D. Mass spectrometric immunoassays for discovery, screening and quantification of clinically relevant proteoforms. *Bioanalysis* **8**, 1623–1633 (2016).
10. Zhu, L., Tangrea, M. A., Mukherjee, S. & Emmert-Buck, M. R. Layered electrophoretic transfer - A method for pre-analytic processing of histological sections. *Proteomics* **11**, 883–889 (2011).
11. Aichler, M. & Walch, A. MALDI Imaging mass spectrometry: current frontiers and perspectives in pathology research and practice. *Lab Invest* **95**, 422–431 (2015).
12. Hughes, A. J. *et al.* Single-cell western blotting. *Nature Methods* **11**, 749–755 (2014).
13. Tentori, A. M., Yamauchi, K. A. & Herr, A. E. Detection of Isoforms Differing by a Single Charge Unit in Individual Cells. *Angewandte Chemie International Edition* **55**, 12431–12435 (2016).
14. Grist, S. M., Mourdoukoutas, A. P. & Herr, A. E. 3D projection electrophoresis for single-cell immunoblotting. *Nat Commun* **11**, 6237 (2020).
15. Zhang, Y., Naguro, I. & Herr, A. E. In Situ Single-Cell Western Blot on Adherent Cell Culture. *Angewandte Chemie* **131**, 14067–14072 (2019).
16. Grist, S. M. *Lysis monitoring analysis*. (2020).
17. Blair, D. & Dufresne, E. *The Matlab Particle Tracking Code Repository*. (2008).
18. Crocker, J. C. & Grier, D. G. Methods of Digital Video Microscopy for Colloidal Studies. *Journal of Colloid and Interface Science* **179**, 298–310 (1996).
19. Bhunia, D., Chowdhury, R., Bhattacharyya, K. & Ghosh, S. Fluorescence fluctuation of an antigen–antibody complex: circular dichroism, FCS and smFRET of enhanced GFP and its antibody. *Phys. Chem. Chem. Phys.* **17**, 25250–25259 (2015).
20. Armstrong, J. K., Wenby, R. B., Meiselman, H. J. & Fisher, T. C. The Hydrodynamic Radii of Macromolecules and Their Effect on Red Blood Cell Aggregation. *Biophysical Journal* **87**, 4259–4270 (2004).
21. Park, I. H., Johnson, C. S. & Gabriel, D. A. Probe diffusion in polyacrylamide gels as observed by means of holographic relaxation methods: search for a universal equation. *Macromolecules* **23**, 1548–1553 (1990).
22. Ogston, A. G. The spaces in a uniform random suspension of fibres. *Trans. Faraday Soc.* **54**, 1754–1757 (1958).

23. Gregg, J. L., McGuire, K. M., Focht, D. C. & Model, M. A. Measurement of the thickness and volume of adherent cells using transmission-through-dye microscopy. *Pflugers Arch - Eur J Physiol* **460**, 1097–1104 (2010).
24. Su, E. J., Jeeawoody, S. & Herr, A. E. Protein diffusion from microwells with contrasting hydrogel domains. *APL Bioengineering* **3**, 026101 (2019).
25. Mourdoukoutas, A. P., M. Grist, S. & E. Herr, A. Rapid electrotransfer probing for improved detection sensitivity in in-gel immunoassays. *Analytical Methods* **12**, 4638–4648 (2020).
26. Schneider, G. F., Shaw, B. F., Lee, A., Carillho, E. & Whitesides, G. M. Pathway for Unfolding of Ubiquitin in Sodium Dodecyl Sulfate, Studied by Capillary Electrophoresis. *J Am Chem Soc* **130**, 17384–17393 (2008).
27. Baselga, J., Hernández-Fuentes, I., Masegosa, R. M. & Llorente, M. A. Effect of Crosslinker on Swelling and Thermodynamic Properties of Polyacrylamide Gels. *Polymer Journal* **21**, 467–474 (1989).
28. Su, A., Smith, B. E. & Herr, A. E. In situ measurement of thermodynamic partitioning in open hydrogels. *Anal. Chem.* (2019) doi:10.1021/acs.analchem.9b03582.
29. Geldert, A., Huang, H. & Herr, A. E. Probe-target hybridization depends on spatial uniformity of initial concentration condition across large-format chips. *Scientific Reports* **10**, 8768 (2020).
30. Samsó, M., Daban, J.-R., Hansen, S. & Jones, G. R. Evidence for Sodium Dodecyl Sulfate/Protein Complexes Adopting a Necklace Structure. *European Journal of Biochemistry* **232**, 818–824 (1995).
31. Pitt-Rivers, R. & Impiombato, F. S. A. The binding of sodium dodecyl sulphate to various proteins. *Biochem J* **109**, 825–830 (1968).
32. Useful Numbers for Cell Culture - US. https://www.thermofisher.com/us/en/home/references/gibco-cell-culture-basics/cell-culture-protocols/cell-culture-useful-numbers.html.
33. Zakharchenko, O., Greenwood, C., Alldridge, L. & Souchelnytskyi, S. Optimized Protocol for Protein Extraction from the Breast Tissue that is Compatible with Two-Dimensional Gel Electrophoresis. *Breast Cancer (Auckl)* **5**, 37–42 (2011).

Chapter 8

Current understanding of ultraviolet-C decontamination of N95 filtering facepiece respirators

Adapted with permission from S. M. Grist, A. Geldert, A. Gopal, A. Su, H. B. Balch, & A. E. Herr, "Current Understanding of Ultraviolet-C Decontamination of N95 Filtering Facepiece Respirators", *Applied Biosafety,* 2021.

8.1 Abstract

The COVID-19 pandemic has led to critical shortages of single-use N95 filtering facepiece respirators. The US Centers for Disease Control and Prevention has identified ultraviolet-C (UV-C) irradiation as one of the most promising decontamination methods during crisis-capacity surges; however, understanding the mechanism of pathogen inactivation and post-treatment respirator performance is central to effective UV-C decontamination. Here, we summarize the UV-C N95 decontamination evidence and identify key metrics. We evaluate the peer-reviewed literature on UV-C decontamination to inactivate SARS-CoV-2, viral analogues, and other microorganisms inoculated on N95s, as well as the resulting effect on respirator fit and filtration. Evidence supports that UV-C exposure of ≥1.0 J/cm^2 inactivates SARS-CoV-2 analogues (≥3log reduction) on the majority of tested N95 models. The literature cautions that (1) viral inactivation is N95 model-dependent and impeded by shadowing, (2) N95 straps require secondary decontamination, (3) higher doses may be necessary to inactivate other pathogens (e.g., some bacterial spores), and (4) while N95 fit and filtration appear to be preserved for 10–20 cycles of 1.0 J/cm^2, donning and doffing may degrade fit to unacceptable levels within fewer cycles. Effective N95 UV-C treatment for emergency reuse requires both (1) inactivation of the SARS-CoV-2 virus, achieved through application of UV-C irradiation at an appropriate wavelength and effective dose, and (2) maintenance of the fit and filtration efficiency of the N95. UV-C treatment is a risk-mitigation process that should be implemented only under crisis-capacity conditions and with proper engineering, industrial hygiene, and biosafety controls.

8.2 Background

The COVID-19 pandemic has led to severe shortages of single-use N95 filtering facepiece respirators (FFRs) worn by health care workers and first responders, and ultraviolet-C (UV-C) irradiation has been identified by the Centers for Disease Control and Prevention (CDC) as one of the most promising methods for N95 FFR decontamination under crisis-capacity conditions.[1] UV-C is already implemented for airborne pathogen inactivation and other applications in hospitals.[2] As per the recommendations of the CDC and the Healthcare Infection Control Practices Advisory Committee (HICPAC), UV-C light (254 nm peak) is widely used in US healthcare facilities for pathogen reduction in air,[2] and UV-C has found extensive use in water treatment.[3] In some settings, UV-C is also used for surface decontamination.[4] NIOSH offers guidelines for applying upper-room UVGI to kill or inactivate airborne tuberculosis bacteria in hospitals.[5] However, UV-C decontamination of N95 FFRs involves additional considerations. Access to consolidated

information on N95 FFR decontamination approaches is essential to maintaining a robust response to COVID-19. In this review, we examine the current understanding in the peer-reviewed literature regarding the use of UV-C irradiation for N95 FFR treatment.

In 2006, the US National Academies outlined that effective decontamination of personal protective equipment (PPE) like the N95 FFR requires (1) inactivation of pathogens (e.g., the SARS-CoV-2 virus), (2) maintenance of both the fit and filtration efficiency of the N95 FFR, and (3) harmlessness to the user (e.g., no toxic residues, minimal risk of cross-contamination).[6] Here, we review and summarize the ability of UV-C decontamination to meet these critical criteria, to help inform risk management decisions under crisis-capacity conditions.

In writing this review, we aimed to summarize the current evidence regarding UV-C treatment of N95 FFRs with respect to the critical criteria outlined by the US National Academies: (1) inactivation of pathogens (e.g., the SARS-CoV-2 virus), (2) maintenance of both the fit and filtration efficiency of the N95 FFR, and (3) harmlessness to the user (e.g., no toxic residues).[6] We searched PubMed, Google Scholar, Google, and library databases for keywords such as "UV-C," "N95," "filtering facepiece respirator," "decontamination," "UVGI," and "mask" to identify relevant primary research articles. Studies that are not yet peer-reviewed should be interpreted with particular caution, so we elected not to include academic or commercial studies posted to preprint serversin this review. We do, however, cite relevant hospital implementations and other work (e.g., federal guidance and summaries from professional societies) that do not normally go through peer review before public availability.

8.3 UV-C fundamentals and mode of action

UV-C inactivates pathogens primarily by introducing crosslinks between adjacent nucleic acid residues, thus damaging DNA and RNA and hindering reproduction.[7–10] UV-C decontamination is critically dependent on two factors: the wavelength applied and the dose (fluence).

First, energy must be applied at the appropriate ultraviolet (UV) wavelength (i.e., the germicidal UV-C region of the electromagnetic spectrum, with high efficacy near 260 nm[3]). UV sources emitting at wavelengths much beyond 260 nm, such as sunlight at the earth's surface (after UV-C has been absorbed by the earth's ozone layer[11]), tanning bed lamps, or other consumer products, have minimal or no germicidal efficacy.[10] UV light at 254 nm has >10× higher germicidal efficacy compared with UV light at 300 nm or longer wavelengths.[12]

Second, sufficient UV-C dose (fluence) must be delivered to the pathogens.[10] Fluence (J/cm^2) is defined as the integrated radiant (UV-C) power incident upon an infinitesimally small surface during the exposure period.[13] The term "UV-C dose" (J/cm^2) is widely used in the decontamination literature to denote UV-C fluence.[13] "Fluence" is the technically accurate term to describe the UV-C energy incident on the N95 surface, whereas "dose" refers to the fraction of incident energy absorbed at that surface. Nevertheless, to remain consistent with the cited literature and field, we use the term "dose" in this review when describing measured UV-C energy incident at the N95 surface.

The minimum dose required for pathogen inactivation depends on both the irradiation wavelength and the specific pathogen, with some pathogens requiring much higher UV-C doses for inactivation that others (e.g., certain bacterial spores compared to enveloped, single-stranded RNA viruses).[14] A pathogen's "action spectrum" describes relative inactivation efficacy as a function of wavelength, and action spectra typically have a peak near 260 nm (the maximum

absorption of nucleic acids).[3] The minimum dose required for inactivation also depends upon the material on or in which pathogens are present (e.g., air, surfaces, or aqueous media).[10]

Because biological validation of inactivation is often impractical or impossible to integrate into each and every treatment cycle, the UV-C dose measurement serves as the critical physical link between viral inactivation evidence and efficacy of each exposure. Dose (J/cm^2) is the product of irradiance (W/cm^2) and exposure time (s), assuming constant irradiance.[13] Because UV-C irradiance is dependent on the distance and angle from the UV-C source,[15] UV-C irradiance, and therefore dose, needs to be empirically measured at the precise location of the objects to be decontaminated, in the specific configuration used for UV-C treatment. These measurements must be performed using calibrated sensors (e.g., radiometers, dosimeters, or sensor strips) with specificity to the germicidal wavelength range output by the UV-C source, and appropriate sensitivity and dynamic range (range of measurable irradiances and doses).

The efficacy of N95 decontamination methods is typically evaluated by assessing the $\log_{10}$ reduction in active pathogens on N95 FFRs after decontamination treatment. For example, a 3-$\log_{10}$ reduction (subsequently referred to as "3-log reduction") corresponds to 99.9% inactivation of the pathogen under consideration compared to a positive control. As per US Food and Drug Administration (FDA) guidelines for N95 FFR decontamination Emergency Use Authorizations (EUAs), ≥3-log reduction in nonenveloped viral activity is required to achieve the minimally acceptable "Tier 3" level of bioburden reduction.[16] Therefore, in this review, we emphasize ≥3-log reduction of SARS-CoV-2 or its analogues, based on the minimally acceptable log reduction listed in the FDA EUA guidance and in accordance with previous studies of UV-C N95 FFR decontamination.[17,18] However, it is important to note that the UV-C dose required to achieve ≥3-log reduction is pathogen-dependent.[10] Thus, the UV-C dose required to achieve ≥3-log reduction of SARS-CoV-2 (an enveloped virus) may not necessarily yield ≥3-log reduction of nonenveloped virus, bacteria, or other pathogens required for various levels of FDA EUA approval.

8.4 Safety considerations

UV-C light is hazardous to human health, and as a result, sufficient skin and eye protection must be worn to protect processing personnel. According to the American Conference of Governmental Industrial Hygienists (ACGIH), the exposure dose limit per person per day is 0.003 J/cm^2 for UV radiation in the 200–315 nm region of the electromagnetic spectrum;[19] this same 0.003 J/cm^2 dose limit was identified by Directive 2006/25/EC of the European Parliament and of the Council for all UV radiation (180–400 nm).[20] Similarly, the National Institute for Occupational Safety and Health (NIOSH) recommends a total permissible 8-h dose of ~0.0046 J/cm^2 for 260 nm irradiation, for unprotected eyes or skin.[21]

Given the high UV-C irradiances emitted by sources typically used for UV-C decontamination, an unprotected user risks exposure to this dose in seconds under accidental illumination.[22,23] Thus, proper engineering controls for UV-C systems must ensure that all users are adequately protected before the UV-C light source is turned on, and full PPE must be worn for eye and skin protection. Furthermore, in addition to UV-C concerns, processing personnel should treat all respirators (including ones that have undergone UV-C treatment) as contaminated, and wear appropriate PPE to reduce pathogen exposure risk from respirator handling.[24]

8.5 Potential for SARS-CoV-2 inactivation

Several studies have demonstrated UV-C viral reduction of influenza and non-SARS-CoV-2 coronaviruses on N95 FFRs.[17,18,25] These viruses are hypothesized to be suitable SARS-CoV-2 analogues because they are also enveloped, single-stranded RNA viruses. A non-peer-reviewed report to the FDA by the contracting research laboratory Applied Research Associates (ARA)[18] found that UV-C treatment of 1.0 J/cm^2 at the surface of N95 FFR coupons from one FFR model yielded no detectable virus (≥3.95-log reduction) for six influenza and coronavirus strains considered, including MERS-CoV and SARS-CoV.

Even when viral inoculations were covered with artificial skin oil or saliva as soiling agents, N95 coupons yielded no detectable virus after UV-C treatment. Similar UV-C doses were effective for H5N1 and H1N1 in separate, peer-reviewed studies (**Table 8.1**).[25,26] At a UV-C dose of 0.5 J/cm^2, the viable virus remaining on N95 FFR coupons was 2–3 log lower than on positive control coupons, but detectable, indicating that a UV-C dose of 0.5 J/cm^2 may be insufficient for viral inactivation.[18]

Heimbuch and Harnish also studied the efficacy of UV-C viral inactivation across 15 different models (intact FFRs rather than coupons).[18] In 11 out of the 15 models tested, a UV-C dose of 1.0 J/cm^2 at the N95 surface was effective in inactivating H1N1 influenza by ≥3 log. The same study found that UV-C treatment was effective for the elastic straps of only 4 of 15 models; thus, straps may require a secondary decontamination method. N95 FFR models with a hydrophilic facepiece were less effectively decontaminated with UV-C than hydrophobic models.[18] Similarly, related studies measured ≥3-log reduction in H1N1 viability on the facepieces of 12 of 15 tested models and on the elastic straps of 7 of 15 tested models.[17]

In addition to the N95 FFR model, other factors may influence UV-C inactivation efficacy. High humidity decreases UV-C efficacy on generic surfaces[27] and on the surfaces of N95 FFRs,[28] suggesting that a drying step before N95 FFR treatment could be beneficial. Soiling agents (including from saliva and mucus) have been found to reduce UV-C inactivation efficacy of MS2 bacteriophage from N95 FFRs.[28] The effect of soiling agents on UV-C treatment efficacy likely depends on the exact concentration and composition of the soiling agent, and/or how the soiling agent is applied (e.g., mixed in with pathogens or applied on top of pathogen inoculation). In addition to fluids such as saliva and mucus,[28] sunscreen or other types of cosmetics may further attenuate UV-C irradiation during treatment.[29] Attenuation is dependent on the thickness and absorption coefficients of the applied materials.[30]

Pathogen inoculation mode may also impact UV-C treatment efficacy: N95 FFRs inoculated with larger MS2 droplets (9–10 µm) generally had lower UV-C bioburden reduction efficiencies in response to a 3.6 J/cm^2 dose compared with FFRs inoculated with smaller MS2 aerosols (1–2 µm).[28] Given that studies use a variety of methods to apply pathogens on an N95 FFR (aerosols, droplets, and/or pipetted solution), the question of whether the pathogen application method impacts UV-C treatment efficacy merits further study. It is also important to note that the impact of soiling agents and pathogen application method may differ depending on pathogen type, just as the minimally acceptable UV-C dose depends on pathogen type (as described in the Efficacy of UV-C on inactivation of other pathogens section). For example, MS2 is commonly used as a surrogate virus in inactivation studies due to its high culturability,[31] but as a nonenveloped virus, MS2 generally requires higher UV-C doses for inactivation compared with enveloped viruses like SARS-CoV-2 (**Table 8.1**).

Together, the studies reported in the ssRNA enveloped virus section of **Table 8.1** suggest a minimally acceptable UV-C dose of ~1.0 J/cm^2 for 3-log inactivation of viruses similar to SARS-

CoV-2 on N95 material. Research on UV-C inactivation of SARS-CoV-2 is ongoing. Smith et al. observed that 0.63 J/cm^2 of 254 nm UV-C light led to a substantial reduction of SARS-CoV-2 RNA infectivity in cell culture for only one out of three N95 models tested.[32] It should be noted that this RNA-based assessment of viral infectivity differs from the plaque or 50% tissue culture infectious dose ($TCID_{50}$) assays more commonly used for viral inactivity measurements. It remains unclear whether UV-C would more fully decontaminate SARS-CoV-2 from multiple N95 models if a dose above the minimally acceptable 1.0 J/cm^2 were applied, or if respirators were inoculated with a lower SARS-CoV-2 titer that more closely represents a realistic exposure expected for a health care worker.

Ozog et al. also characterized SARS-CoV-2 inactivation at multiple locations on intact N95 FFR facepieces and straps exposed to 254-nm UV-C. The authors report that ~1.5 J/cm^2 of 254-nm UV-C applied to both sides of the N95 yielded ≥3-log inactivation of SARS-CoV-2 in all studied locations on the facepieces of 1 out of 5 N95 models and on the straps of 2 out of 5 N95 models.[33] However, measurement of ≥3-log inactivation was not possible on many models in this study, because the difference between the limit of detection of the $TCID_{50}$ assay used to assess viral activity and the viral activity on the unexposed control N95 was often <3 log. In addition, Kohli et al. demonstrate (with a similar UV-C system) that the UV-C dose varies across the surface of the N95 FFR;[34] thus, as with many studies on decontamination of intact N95 respirators, the actual dose at each location studied may differ substantially from the 1.5 J/cm^2 nominal dose.

Other recent studies have investigated the impact of LED and pulsed UV sources on SARS-CoV-2 inactivation on N95s. One recent article reports SARS-CoV-2 inactivation in one N95 FFR model after UV-C treatment using an LED source.[35] However, caution should be exercised in interpretation or adoption of the reported approach, as the reported UV-C dose was calculated based on a single manufacturer-specified irradiance value, when irradiance may actually change over source lifetime due to slight changes in configuration and decay in LED output. As a result, even though the results suggest that UV-C LED sources could be promising, the study is difficult – perhaps even impossible – to accurately reproduce.

Similarly, another recent article reporting SARS-CoV-2 inactivation after UV treatment with a pulsed xenon source also shows significant viral inactivation (>4.79-log); however, the dose associated with this level of inactivation is not reported.[36] These data underscore the importance of accurate measurement and reporting of wavelength and UV-C dose for reproducible viral inactivation protocols. The National Institutes of Standards and Technology and the International Ultraviolet Association are actively collaborating to develop standards to assess the efficacy of UV devices for decontamination.[37] An American Society for Testing and Materials (ASTM) standard for evaluating UV-C efficacy for inactivating the influenza virus on textile surfaces such as N95 FFRs has been developed.[38] In addition to describing appropriate experimental steps, the standard stresses the importance of accurate, rigorous UV-C dose measurements.

Table 8.1. Efficacy of ultraviolet-C for inactivation of microorganisms

References	Organism, soiling agent, and method of application	Material	UV-C dose	Efficacy	Light source
Influenza and coronavirus strains: ssRNA enveloped virus					
Ozog et al.[33]	SARS-CoV-2; 10 µL drop pipetted on strap and multiple	5 N95 FFR models (3M 1860, 8210,	~1.5 J/cm^2	≥3-log reduction for 1/5 FFR model facepieces and 2/5 FFR	254-nm UV-C (Custom-manufactured by

	locations on N95 facepiece	8511, 9211; Moldex 1511)		model straps	Daavlin; Byron, OH, USA)
Fischer et al.[35]	SARS-CoV-2; 50 µL deposited by pipette	N95 FFR (AOSafety N9504C)	*1.98 J/cm^2 (estimated from manufacturer-specified irradiance)	*3-log reduction	LED high-power UV germicidal lamp (260–285 nm; LEDi2)
Smith et al.[32]	Pooled SARS-CoV-2 clinical samples; 100 µL deposited by pipette	N95 FFR (medical grade: 3M 1860, 3M 1870+; industrial grade: 3M 8511)	0.63 J/cm^2	Substantial reduction in infectivity (via SARS-CoV-2 RNA measurement) for only the3M1870+ FFR model	254-nm UV-C (General Electric 30W Germicidal T8 bulb)
Lore et al.[25]	H5N1 droplets	N95 FFR (3M 1860, 3M 1870)	1.8 J/cm^2	>4-log reduction	254-nm UV-C (Ultraviolet Products, Upland, CA, USA)
Mills et al.[17]	H1N1. 1 µL drops of suspension deposited by pipette. AS or ASO was placed on top of dried virus solution to study the effects of soiling.	N95 FFR (15 models)	1.0 J/cm^2	≥3-log reduction for 12/15 FFR model facepieces and 7/ 15 FFR model straps for all soiling conditions	254-nm UV-C (Fresh-Aire UV, Jupiter, FL, USA)
Heimbuch and Harnish[18] – Option Task B	Influenza strains (H1N1, H5N1, H7N9), MERS-CoV, SARS-CoV, all pipetted as 1 µL drops. AS or ASO was placed on top of dried virus solution to study the effects of soiling.	N95 FFR (3M 1870)	1.0 J/cm^2	No detectable virus (≥3.95-log reduction) for all organisms for all soiling conditions	254-nm UV-C (Mineralight_ XX-20S 20-W UV bench lamp)
Heimbuch and Harnish[18] – Base Task 4	H1N1, pipetted as 1 µL drops. AS or ASO was placed on top of dried virus solution to study the effects of soiling.	N95 FFR (15 models)	1.0 J/cm^2	≥3-log reduction for 11/15 FFR models and 4/15 FFR straps for all soiling conditions	254-nm UV-C (Fresh-Aire UV)
Walker and Ko[39]	Murine hepatitis virus (coronavirus)	Air	1.83×10^{-3} J/cm^2	3-log reduction[a]	254-nm UV-C (Lumalier, Memphis, TN, USA)

MS2: ssRNA nonenveloped virus					
Vo et al.[40]	MS2 droplets	N95 FFR (Willson N1105)	4.32 J/cm^2	3-log reduction	254-nm UV-C (5.5 mg Hg; lamp type TUV 36TS 4P SE; lamp voltage 94 V; lamp wattage, 40 W)
Fisher and Shaffer[41]	MS2 aerosol	N95 FFR (6 models)	0.32 – 40 J/cm^2 (equates to 0.1 J/cm^2 at the internal filtering medium due to model-dependent attenuation)	≥2.9-log reduction	254-nm UV-C (TUV 36T5 40 W Philips, Somerset, NJ, USA)
Woo et al.[28]	MS2 droplets (9–10 µm) and aerosol (1–2 µm), in water, BE, or AS	N95 FFR (3M 1870)	3.6 J/cm^2	Droplets: 4.8-, 2.7-, 2.5-log reduction in water, BE, AS Aerosols: 5.2-, 3.0-, 2.7-log reduction in water, BE, AS	254-nm UV-C (UVG-11, UV Products, Cambridge, United Kingdom)
Tseng and Li[27]	MS2	Non-porous surfaces	0.006 – 0.010 J/cm^2	>3-log reduction	254-nm UV-C (TUV 8W/G8 T5, Philips Electronic Instruments, Eindhoven, The Netherlands)
Vegetative bacteria and bacterial spores					
Lin et al.[42]	*Bacillus subtilis* spores, aerosolized	N95 FFR (3M 8210)	2.27 J/cm^2, 5.7 J/cm^2	2.27 J/cm^2 → ~2.7-log reduction 5.7 J/cm^2 → No detectable spores	254-nm UV-C (UVGL-58, VUP LLC, Upland, CA, USA)
Bentley et al.[43]	*E. coli, P. aeruginosa, S. aureus* (drug-sensitive and drug-resistant), *S. pseudintermedius* (drug-sensitive and drug-resistant). 1–2mL suspension deposited by pipette.	Microfiber, polyester, and cotton fabric swatches	0.27 J/cm^2	>2.5-log reduction for all bacteria on all fabrics. No detectable bacteria in 20/24 conditions	254-nm UV-C (American Ultraviolet, Inc., Lebanon, IN, USA)
Wallace et al.[44]	*Clostridium difficile* spores (with and without soiling agent)	Glass and plastic	0.17 – 0.63 J/cm^2	*C. difficile*: ~2.1-log reduction with soiling agent across all UV-C	254-nm UV-C (Lightbest Co., Ltd.,

	MRSA and MS2 (with and without 5% FBS)			doses; ~3.2-log reduction without soiling agent across upper three doses. MRSA: ~2.9-log reduction with FBS, ~3.4-log reduction without FBS. MS2: ~3.7-log reduction with FBS, ~2.9-log reduction without FBS	Changzhou, China)
Vegetative fungi					
Fu et al.[45]	5 *Candida* strains	Bed sheets	0.075 J/cm^2	>3-log reduction in all strains	254-nm UV-C (Thermo Fisher Scientific, Waltham, MA, USA)

[a] Estimate-based measured viral susceptibility to UV-C in air.
AS, artificial saliva; ASO, artificial skin oil; BE, beef extract; FBS, fetal bovine serum; FFR, filtering facepiece respirators; MRSA, methicillin-resistant *Staphylococcus aureus*; UV-C, ultraviolet-C.

8.6 Efficacy of UV-C on inactivation of other pathogens

UV-C susceptibility of different pathogens in air, water, and on surfaces. The UV-C dose required to inactivate pathogens in air, water, and on surfaces is organism-dependent, due to organism-to-organism differences in nucleic acid structure and nucleotide content, as well as varying amounts of UV-absorbing proteins and other photoprotective components.[14] Higher UV-C doses are generally required to inactivate bacterial and fungal spores, compared to viruses and vegetative bacteria.[10] Among viruses, ~3× higher UV-C doses are required to inactivate viruses with double-stranded RNA or DNA on surfaces, compared to single-stranded viruses; higher dose requirements in double-stranded viruses are attributable to more robust repair mechanisms, as the second strand can serve as a template for repair.[27]

While enveloped viruses are generally more susceptible to inactivation by mechanical and chemical agents,[46] it is unclear whether the UV-C susceptibility of enveloped and nonenveloped viruses differs. Blázquez et al. found that in water, enveloped viruses were inactivated with lower UV-C doses than nonenveloped viruses.[47] However, the mechanism for the observed difference between enveloped and nonenveloped virus susceptibility in water is not understood, nor is it clear whether the same pattern holds for viruses in air or on substrates.

UV-C susceptibility of different pathogens on N95 FFRs and textiles. The minimum UV-C dose required to inactivate both enveloped and nonenveloped viruses on N95 FFRs is several hundred-fold higher than doses typically used for decontamination of similar pathogens on nonporous surfaces,[14] in air, and in solution (**Table 8.1**), because UV-C light is attenuated upon passing through the N95 FFR layers. UV-C irradiances that reach the internal N95 filtering media are ~3–400× lower than the irradiance at the FFR surface, depending on the FFR model.[41] In addition, due to this limited and model-dependent UV-C transmission through N95 FFRs,[48] both sides of the FFR should be illuminated with the minimally acceptable UV-C dose, and this dose may not effectively decontaminate all layers of varying FFR models.

Different pathogens are also expected to have different UV-C susceptibility on N95 FFRs, although the study of UV-C inactivation of different pathogens on N95 FFRs is limited. MS2, a nonenveloped virus, has generally been reported to require higher UV-C doses to achieve 3-log reduction from N95 FFRs[40,41] compared with enveloped influenza and coronaviruses;[17,18] however, it is unclear whether other differences in study design (e.g., FFR model and method of virus application to the FFR) also contribute to the difference in required UV-C dose.

While UV-C has been demonstrated to inactivate several species of vegetative bacteria and bacterial spores on N95 FFRs and other textiles,[42,43,45,49–51] 3-log reduction was not always demonstrated and it is unclear how many bacterial pathogens would be inactivated by the 1.0 J/cm^2 UV-C dose required for SARS-CoV-2 analogue inactivation on most N95 FFR models. For example, UV-C inactivation of *Clostridium difficile* on N95 FFRs has not been studied. However, much higher UV-C doses are required to inactivate *C. difficile* spores on non-porous surfaces (~0.17–0.63 J/cm^2)[44] compared with MS2 on surfaces (~0.006–0.010 J/cm^2).[27] It has yet to be studied whether the same trend (higher UV-C doses required to inactivate *C. difficile* spores compared with MS2 on nonporous surfaces) would hold true in the case where these organisms are on N95 FFRs. In addition, Enterococcus faecium in polycotton swatches was inactivated to a lower degree (<1.97-log reduction) by UV-C[50] compared with laundering (3–4-log reduction),[52] although the applied UV-C dose was not specified, making it challenging to compare and reproduce results.

While UV-C treatment is expected to significantly reduce the risk of contamination, not every pathogen present on or within an FFR may be decontaminated by UV-C; and thus, health care personnel should continue to handle the respirator as if contaminated and reuse only their own FFR. Any UV-C treatment approach should be accompanied by an industrial hygiene workflow involving user training and sterile processing to minimize risk of cross-contamination.[24]

8.7 Sunlight is not likely to be an effective decontamination approach for N95 FFRs

The CDC does not list sunlight as an appropriate method of N95 FFR decontamination.[1] UV-C radiation from sunlight is absorbed by the top layer of the atmosphere and negligible UV-C radiation reaches the surface of the earth.[11] The UV component of sunlight at the earth's surface consists of UV-A (320–400 nm) and UV-B (280–320 nm) radiation. UV-A radiation is considered nongermicidal, while UV-B radiation has germicidal effects, which are much weaker than that of UV-C.[10] Theoretical calculations for the necessary sunlight exposure time needed to achieve UV-B germicidal effects in US cities (equivalent to a 1.0 J/cm^2 UV-C dose) suggest timescales of 57–5000 days, depending on season and geographic location.[12] Furthermore, studies with simulated sunlight showed minimal to no effect in inactivating MS2 and human adenovirus on the surface of fresh produce.[53]

UV-B radiation has some germicidal effects; studies of UV-B irradiation on MS2 bacteriophage and murine noroviruses in aqueous suspension demonstrated a 4-log reduction with UV-B doses of 0.909 and 0.367 J/cm^2, respectively.[54] To reach these doses, 0.34–4.2 h of sunlight exposure would be required, assuming UV-B irradiance from sunlight of ~60–300 μW/cm^2 (although UV irradiance from sunlight varies significantly depending on geographic location, season, and time of day).[55] For comparison, 4-log reduction of MS2 in phosphate-buffered saline solution[56] required ~0.07 J/cm^2 of UV-C – over an order of magnitude lower. UV-C dose required for viral inactivation in N95 FFRs is several hundred-fold higher than for viral inactivation in water, air, or on hard nonporous surfaces (**Table 8.1**).[10]

Sunlight reaching the earth's surface does not contain UV-C, but we would expect a similar trend for the longer wavelengths, with orders of magnitude higher UV-B doses being required for viral inactivation on N95s compared with water/air/nonporous surfaces. Thus, many days of sunlight exposure would be required to achieve a sufficient virucidal UV dose on N95 FFRs, in agreement with theoretical estimates.[12,57]

There is no evidence in the peer-reviewed literature of viral inactivation of SARS-CoV-2 on N95 FFRs by sunlight. Thus, extensive experimental verification and biological validation must be performed before considering sunlight as a decontamination method for N95 FFRs.

8.8 Integrity of N95 FFRs after UV-C treatment

Controlled laboratory studies have subjected 15 N95 FFR models to 10–20 donning/doffing cycles and UV-C treatment (1.0–1.2 J/cm^2 per cycle), then assessed: strap elasticity (with Imada force tester), particle penetration and breathing resistance (TSI 8130 automated filter tester to evaluate respirator function according to the CDC[58]), and fit factor (Static Advanced Headform StAH connected to TSI PortaCount 8038 automated breathing machine, subjected to a 240-s respiration test, testing for a fit factor >100).[18] Although donning and doffing yielded a statistically significant difference in fit factor for some models, minimal detrimental effects due to UV-C exposure specifically were observed for respirator fit, air flow resistance, or particle penetration from this dose (10 cycles, 1.0–1.2 J/cm^2 per cycle) of UV-C.[18]

Similarly, another study found that doses of 1–10 J/cm^2 of UV-C light (either at 254 or 265 nm) did not significantly affect filtration efficiency, material properties, pressure drop, or tensile strength of two N95 FFR models.[59] Other evaluations corroborated acceptable FFR performance after low-dose ultraviolet germicidal irradiation (UVGI) treatment,[60] although Ozog et al. did report (in a Letter to the Editor) that certain N95 FFR models failed qualitative fit testing either after one to two cycles (1.5 J/cm^2 per side, per cycle) or before any UV-C exposure at all, highlighting the importance of verifying N95 FFR fit regularly.[61] To approximate multiple decontamination cycles, application of 18.4 J/cm^2 (to the exterior convex surface) and 4.6 J/cm^2 (to the interior concave surface) 254-nm UV-C to three N95 respirator models was performed, and was found to significantly decrease the fit factor, but fit factors remained above the acceptable threshold of 100.[32]

At 100–1000× higher UV-C doses (120–950 J/cm^2), a substantial effect (>90% in some cases, but highly variable across N95 FFR models) on respirator material breaking strength was observed.[62] As variation in response to UV-C is to be expected from different N95 FFR models, the respirator must pass the ''user seal check'' as recommended by the CDC after decontamination to ensure that respirator fit integrity is maintained.[63]

As summarized in **Table 8.2**, the minimum 1.0 J/cm^2 UV-C dose necessary for SARS-CoV-2 analogue inactivation on most N95 FFR models has been found to minimally impact N95 fit and filtration performance over 10–20 treatment cycles. Aside from the effect of UV-C itself, it is possible that repeated donning and doffing may cause FFR fit to reach unacceptable levels within a lower number of cycles. One study found N95 FFR fit to decline with each donning and doffing without additional decontamination processes; for some N95 models, fit was found to fall below the US Occupational Health and Safety Administration (OSHA) standards after 5 donning/doffing cycles, while others maintained fit for >15 donning/doffing cycles.[64]

Table 8.2. Impact of ultraviolet-C on N95 filtering facepiece respirator integrity

Refs.	FFR model	UV-C dose (J/cm^2)	Particle penetration	Breathing resistance (mmH_2O) (max = 25)	Respirator material damage	Strap damage	UV-C source
Heimbuch and Harnish[18]	N95 FFRs (15 models)	1.0-1.2	0.18–3.29% (10 cycles) 0.12–2.74% (20 cycles)	4.53–14.93	No observable effect from UV-C. Some fit degradation from donning/doffing.	No significant difference from UVC alone. Some fit degradation from donning and doffing	254-nm UV-C (Fresh-Aire UV)
Lindsley et al.[62]	3M 1860 3M 9210 GE 1730 KC 46727	120-950 120-950 120-950 120-950	1 – 2.5% 1 – 2.5% 3 – 5% 3 – 5%	10 – 13 10 – 13 10 15 – 20	General decrease of strength 120 J/cm^2 dose = 2 layers significantly impacted 950 J/cm^2 = 10 layers significantly impacted	Statistically significant decrease in breaking strength for dose ≥590 J/cm^2 (≥10% decrease of mean strength)	254-nm UV-C
Zhao et al.[59]	3M 1860, Moldex 1500	1.0-10	<3% (no effect of UV-C)	No significant change after irradiation	No change in contact angle, no new peaks or decrease in peak height in FTIR spectra, no apparent change in material structure by electron or optical microscopy	No significant change after irradiation	254- and 265-nm UV-C
Smith et al.[32]	3M 1860, 1870+, 8511	18.4 at exterior surface, 4.6 at interior surface	Significantly reduced " FIT score," but average " FIT score" remains acceptable at ≥100 (2-log particle reduction threshold)	Not studied	Not studied	Not studied	254-nm UV-C (GE 30W Germicidal T8 bulb)
Ozog et al.[61]	3M 1860, 9210,8210; Cardinal Health N95 R/S; Moldex 1512	1.5 to each side of FFR	Passed saccharin solution aerosol qualitative fit test[65] for 20/25 cycles (3M 1860), 2/2 cycles (3M 9210), 1/2 cycles (3M 8210 and Cardinal Health N95 R/S), 2/3 cycles (Moldex 1512)	Not studied	Not studied	Not studied	254-nm UV-C (Daavlin Desktop UVC Germicidal Lamp)

FTIR, Fourier Transform Infrared

8.9 US federal guidelines: CDC, FDA, OSHA

Due to a limited supply of N95 FFRs in the unprecedented COVID-19 pandemic, the CDC has provided guidance that health care workers can practice extended use or limited reuse of N95 FFRs.[66] In addition, the CDC has provided guidance to hospitals on methods for decontaminating N95 FFRs during a crisis.[1] Consistent with all N95 FFR treatments for reuse, UV-C is viewed as risk mitigation for extraordinary circumstances rather than complete decontamination.[66]

As of January 2021, OSHA states that cosmetics or other barriers should not be present during regular respirator use.[29] EUAs that the FDA has granted for other methods of N95 FFR decontamination during the COVID-19 pandemic also stipulate that cosmetics not be present on respirators sent for decontamination.[67] After decontamination, the CDC recommends that a "user seal check" is performed when the respirator is donned to ensure an adequate seal.[1] A user seal check after every decontamination cycle is especially important because there is evidence that the fit factor of N95 respirators decreases with numerous donning/doffing cycles.[64]

Any new method for UV-C treatment should be verified through an institution's internal review processes before implementation, which may include applying for an FDA EUA[16] and referencing frequently updated CDC guidelines.

8.10 Implementation strategies

The University of Nebraska Medical Center (UNMC) published one of the first protocols[22] demonstrating implementation of UV-C treatment of N95s (including N95 FFR handling logistics and treatment), which has been the basis of additional research and discussion for UV-C treatment of N95 FFRs during the 2020 COVID-19 pandemic.[23,24] The UNMC protocol exposes each side of N95 FFRs to 0.9–1.2 J/cm^2, depending on FFR position within the treatment field.[22] This UNMC Process Flow is a 51-step process defined by role (health care worker, courier, UVGI associate) and covers the safe handling (intake, transport, processing, return), labeling (UV-C-decontaminated N95 FFRs should be returned to their specific original user as the process is not expected to be sterilizing),[24] and ancillary PPE and hygiene required for the protocol.

As with any decontamination strategy, an appropriate industrial hygiene workflow involving user training,[68] sterile processing, and other critical considerations must be implemented to avoid cross-contamination or damage to the N95. The Association for Professionals in Infection Control and Epidemiology (APIC) has recently disseminated guidance for infection prevention workflows for UV-C treatment of N95 FFRs during the COVID-19 crisis, in collaboration with N95DECON.[24] Additional implementation strategies are summarized in **Table 8.3**.

Table 8.3. Published implementation strategies for UV-C N95 treatment

Authoring group	Implementation type	UV-C source type
University of Nebraska Medical Center[22]	Hospital protocol for room-scale N95 UV-C treatment with full processing workflow (with personnel roles)	254 nm UV-C (ClorDiSys Torch)
University of Chicago Medical Center[23]	Hospital protocol for room-scale N95 UV-C treatment with full processing workflow	254 nm UV-C (Surfacide Helios)
APIC[24]	Implementation guidance for infection prevention workflows for N95 UV-C treatment	N/A
Carolina Ontiveros et al.[69]	Peer-reviewed study on characterization of a room-scale hospital UV-C treatment system for N95 processing	254 nm UV-C (Diversey MoonBeam3)

Purschke et al.[70]	Peer-reviewed study on design and characterization of cabinet-based N95 UV-C treatment system targeted at lower-resource settings	254 nm UV-C
Wilde et al.[71]	Peer-reviewed ray-trace modeling workflow for UV-C N95 treatment chamber design	254 nm UV-C
Bentancor and Vidal[72]	Peer-reviewed design of a room-scale UV-C treatment system (not designed for N95 UV-C treatment specifically)	254 nm UV-C

All but two surveyed studies demonstrating viral inactivation on N95 FFRs used low-pressure mercury UV-C sources with peak emission at 254 nm. Because both pathogen inactivation and light transmittance (through materials such as N95 layers) are wavelength-dependent,[10] sources with different emission spectra (e.g., LED sources, medium-pressure mercury sources, or pulsed xenon sources) could also be effective for viral inactivation but will have different minimum doses for viral inactivation. Implementation of these sources must specifically assess the minimally acceptable dose through viral inactivation studies with accurate dose measurements. Both research and validation dose measurements for any source must use appropriate, wavelength-matched detectors.

Validation of (1) UV-C viral inactivation and (2) subsequent N95 FFR reuse suitability (e.g., filtration efficiency, fit factor) is widely considered in the peer-reviewed literature and should be considered for all new processes.[17,18,25,64] Both of these critical features are dependent on UV-C dose, as summarized in Tables 1 and 2. From studies using SARS-CoV-2 viral analogues, UV-C treatment design must exceed a value of 1.0 J/cm^2 for all surfaces of each N95 FFR and the delivered dose should ideally be verified with every UV-C cycle, but periodically at a minimum (e.g., daily, after a set number of cycles).

Dose measurements should be performed with an accurately calibrated (e.g., traceable to standards such as those from the National Institute of Standards and Technology) UV-C-specific sensor to measure the irradiance or dose at each FFR position. Variation in irradiance is anticipated across the exposure area; the total exposure time should be chosen such that all N95 FFR surfaces are exposed to at least the minimally acceptable dose of 1.0 J/cm^2.

As is true with any form of light, shadowing reduces the dose of light that a target receives. Thus, shadows on the target N95 FFR(s) should be avoided by the following: (1) providing UV-C illumination to both sides of the FFR, and/or flipping the N95 FFRs mid-treatment to ensure all surfaces are exposed to the minimally acceptable UV-C dose, (2) lining walls, ceiling, and other surfaces with UV-C-reflective materials to increase delivered UV-C dose,[73] and (3) ensuring there are no obstructions or materials between the N95 FFRs and the UV-C source that could block the line-of-sight or attenuate the UV-C before reaching the N95. It is important to note that many standard types of glass block almost all UV-C light.[74]

In addition to shadowing, it is important to note that irradiance depends on the distance from the source as well as the incident angle of UV-C light on the N95 surface by Lambert's Cosine Law;[15] as such, the complex 3D morphology of the N95 surface impacts the dose delivered to various regions of the respirator and needs to be considered when designing UV-C treatments.

It is imperative to use caution and validate each source, as not all UV sources provide the required UV-C wavelength range, irradiance, or irradiance uniformity. Even more critically, there have been reports of UV sources falsely claiming to be germicidal, with emitted wavelength ranges not consistent with germicidal efficacy. In addition, UV-C sources emitting wavelengths below 210 nm can produce ozone,[10] which is hazardous to human health.

As a result, it is critical to measure the wavelength and irradiance of UV-C sources with sensors specific to UV-C to ensure sources emit radiation within the UV-C germicidal range (200–

280 nm with peak efficacy at ~260 nm). Viral inactivation efficacy has been reported to be ~10× lower at 300 nm (beyond UV-C range) compared with 254 nm,[3,57] highlighting the importance of using appropriate sources emitting in the UV-C range. The measured UV-C-specific irradiance values should then be used to calculate the time required to reach a minimum UV-C dose in excess of 1.0 J/cm^2 across all N95 FFR surfaces.

8.11 Summary and outstanding questions

Important points and open questions regarding UV-C treatment of N95 FFRs are summarized here:

1. N95 decontamination processes are only to be considered during crisis-capacity surges, after exhausting contingency-capacity and other crisis-capacity strategies.[1]
2. Direct exposure to UV-C light is harmful to humans. Proper engineering controls must be established before using UV-C systems to ensure that all users are protected from the UV-C light source before the light is turned on.[19,21]
3. UV-C only inactivates viruses subjected to at least the minimally acceptable UV-C dose. There remain open questions about UV-C penetration into the materials of the various N95 FFR models used in health care, as the amount of penetration varies widely across N95 FFR models.[41,70] Although the ARA report[18] and related peer-reviewed literature[17] demonstrate >3-log viral reduction (measured from fluid extraction from the N95 FFR materials as described in the ASTM standard for viral inactivation testing[38]), live virus could persist inside the N95 FFR after UV-C treatment. As such, UV-C and other deactivation approaches should be viewed as risk mitigation for extraordinary circumstances rather than complete decontamination. In addition, shadowed or highly angled regions of the N95 may be exposed to lower-than-expected UV-C doses, and thus, pathogens in these locations may be less effectively inactivated.
4. UV wavelengths of 175–210 nm can generate ozone, which is hazardous to human health. Some low-pressure UV lamps and most medium-pressure UV lamps emit some 185 nm UV and thus will generate ozone;[10] if there is the possibility of ozone generation, adequate ventilation should be confirmed within the working area to minimize ozone risk to operators. If possible, select UV-C sources with minimal or no ozone generation.
5. The configuration or orientation of UV-C light sources may generate shadows (as is the case for any type of light, not just UV-C), and the configuration of N95 FFRs should be designed to avoid or mitigate shadow generation on the FFR surface. For instance, UV-reflective materials may be used and/or N95 FFRs may be rotated and/or flipped to ensure that the adequate dose is applied across the entire surface area of the FFR (and this dose should be validated with a UV-C-specific sensor).
6. Reports have demonstrated residual virus on N95 FFR straps after UV-C exposure (likely due to the ability of N95 FFR attachment straps to twist and be shadowed from the UV-C light), suggesting a need for supplementary decontamination of the elastic straps.[17,18] Mills et al. suggest wiping N95 FFR straps with a compatible disinfectant.[17] If this additional step is used, extra caution should be used to avoid touching the N95 FFR facepiece as common disinfectant chemicals can degrade N95 FFR function.[75]
7. Although ≥1.0 J/cm^2 dose of UV-C resulted in ≥3-log reduction in viral activity of SARS-CoV-2 analogues on most N95 FFR models, such an observation does not imply sterility or full decontamination of the N95 FFR, as the N95 may still be contaminated with other pathogens that might not be similarly susceptible to UV-C irradiation (**Table 8.1**).

8.12 Conclusions

UV-C N95 treatment protocols should be implemented only if there is a dire shortage of N95 FFRs and appropriate federal and institutional approvals. While research on the UV-C dose necessary for SARSCoV-2 inactivation on N95 materials is ongoing, estimates can be drawn from the extensive body of literature evidence for similar viruses. Accurate measurements of dose and wavelength in forthcoming SARS-CoV-2 inactivation studies would outline effective and reproducible protocols for this virus.

Currently, the existing research suggests that, if implemented properly with validation of the delivered UV-C dose to the FFR, it is likely that UV-C applied at a minimum dose of $\geq$1.0 J/cm^2 inactivates SARS-CoV-2 on the outer layers of non-shadowed regions of N95s based on results from similar viruses.[17,18,25] As all but one of the dose measurements for viral inactivation reported here used 254 nm sources, there is an opportunity for future research to rigorously assess minimum doses required for viral inactivation with the diverse landscape of UV-C sources and matched detectors.

UV-C has shown promise as an effective method for inactivation of viruses and bacterial spores on N95 respirator material; however, UV-C cannot inactivate pathogens that are not irradiated with the minimum dose. For that reason, UV-C may not effectively decontaminate inner layers of the FFR and an auxiliary method of decontamination is suggested for elastic straps.

We note that as of January 2021, only one EUA[76] has been granted for UV-C decontamination of N95 FFRs (in fact, the EUA only allows one specific N95 respirator model to be decontaminated with UV-C, highlighting the substantial model-dependence of decontamination efficacy). Because UV-C processes to inactivate SARS-CoV-2 on N95 FFRs are not expected to result in sterilization (killing of all microorganisms), N95 FFRs treated with UV-C should be returned to the same user to avoid user-to-user cross-contamination. N95 FFR model-dependent viral inactivation efficacy has been reported. We stress that (1) after each round of irradiation, a user seal check should be performed, (2) extended cycles of doffing and redonning may affect FFR fit, and (3) that the FFR should not be considered fully decontaminated after UV-C treatment, as there may be other pathogens contaminating the FFR whose activity may not be fully reduced by UV-C. Thus, UV-C treatment should be viewed as risk management rather than complete decontamination or sterilization. Health care personnel should continue to handle the respirator as if the PPE is contaminated and reuse only their own N95 FFR.

8.13 References

1. Decontamination and Reuse of Filtering Facepiece Respirators using Contingency and Crisis Capacity Strategies. Centers for Disease Control. (2020).
2. Sehulster, L. M. et al. Guidelines for environmental infection control in health-care facilities. Recommendations from CDC and the Healthcare Infection Control Practices Advisory Committee (HICPAC). (American Society for Healthcare Engineering/American Hospital Association, 2004).
3. Pirnie, M., Linden, K. G., Malley, J. P., Schmelling, D. & of Water USA, O. Ultraviolet disinfection guidance manual for the final long term 2 enhanced surface water treatment rule: EPA 815-R-06-007. (EPA, 2006).
4. Marra, A. R., Schweizer, M. L. & Edmond, M. B. No-Touch Disinfection Methods to Decrease Multidrug-Resistant Organism Infections: A Systematic Review and Meta-analysis. Infect. Control Hosp. Epidemiol. **39**, 20–31 (2018).

5. CDC. Environmental Control for Tuberculosis: Basic Upper-Room Ultraviolet Germicidal Irradiation Guidelines for Healthcare Settings. (2014).
6. Institute of Medicine, Board on Health Sciences Policy, & Committee on the Development of Reusable Facemasks for Use During an Influenza Pandemic. Reusability of Facemasks During an Influenza Pandemic: Facing the Flu. (National Academies Press, 2006).
7. Anderson, J. G., Rowan, N. J., MacGregor, S. J., Fouracre, R. A. & Farish, O. Inactivation of food-borne enteropathogenic bacteria and spoilage fungi using pulsed-light. IEEE Trans. Plasma Sci. IEEE Nucl. Plasma Sci. Soc. **28**, 83–88 (2000).
8. Ito, A. & Ito, T. Absorption spectra of deoxyribose, ribosephosphate, ATP and DNA by direct transmission measurements in the vacuum-UV (150-190 nm) and far-UV (190-260 nm) regions using synchrotron radiation as a light source. Photochem. Photobiol. **44**, 355–358 (1986).
9. Jay, J. M. Modern Food Microbiology. (Springer, Boston, MA, 1995). doi:10.1007/978-1-4615-7476-7.
10. Kowalski, W. Ultraviolet Germicidal Irradiation Handbook: UVGI for Air and Surface Disinfection. (Springer Berlin Heidelberg, 2009). doi:10.1007/978-3-642-01999-9.
11. Epa, U. S. & OAR. UV Radiation. (2013).
12. Sagripanti, J.-L. & Lytle, C. D. Inactivation of Influenza Virus by Solar Radiation. Photochemistry and Photobiology **83**, 1278–1282 (2007).
13. Bolton, J. R. & Linden, K. G. Standardization of Methods for Fluence (UV Dose) Determination in Bench-Scale UV Experiments. J. Environ. Eng. **129**, 209–215 (2003).
14. Malayeri, A., Mohseni, M., Cairns, B. & Bolton, J. Fluence (UV Dose) Required to Achieve Incremental Log Inactivation of Bacteria, Protozoa, Viruses and Algae. IUVA News **18**, 4–6 (2016).
15. Reifsnyder, W. E. Radiation geometry in the measurement and interpretation of radiation balance. Agricultural Meteorology **4**, 255–265 (1967).
16. Center for Devices & Radiological Health. Decontamination Bioburden Reduction Systems for Face Masks Respirators. U.S. Food and Drug Administration (2020).
17. Mills, D., Harnish, D. A., Lawrence, C., Sandoval-Powers, M. & Heimbuch, B. K. Ultraviolet germicidal irradiation of influenza-contaminated N95 filtering facepiece respirators. American Journal of Infection Control **46**, e49–e55 (2018).
18. Heimbuch, B. & Harnish, D. Research to Mitigate a Shortage of Respiratory Protection Devices During Public Health Emergencies (Report to the FDA No. HHSF223201400158C). (2019).
19. Product: Ultraviolet Radiation: TLV(R) Physical Agents 8th Edition Documentation: ACGIH.
20. Directive 2006/25/EC - artificial optical radiation.
21. Criteria for a recommended standard... occupational exposure to ultraviolet radiation. (2018). doi:10.26616/NIOSHPUB7311009.
22. Lowe, J. J. et al. N95 Filtering Facepiece Respirator Ultraviolet Germicidal Irradiation (UVGI) Process for Decontamination and Reuse. https://www.nebraskamed.com/sites/default/files/documents/covid-19/n-95-decon-process.pdf (2020).
23. Brickman, J. et al. Optimization, Validation, and Implementation of a UV Disinfection Method for N95 Face Masks. (2020).
24. APIC and N95DECON suggested guidance for infection prevention and workflow for UV-C decontamination of N95 FFRs during COVID-19.

25. Lore, M. B., Heimbuch, B. K., Brown, T. L., Wander, J. D. & Hinrichs, S. H. Effectiveness of Three Decontamination Treatments against Influenza Virus Applied to Filtering Facepiece Respirators. The Annals of Occupational Hygiene **56**, 92–101 (2012).
26. Heimbuch, B. K. et al. A pandemic influenza preparedness study: use of energetic methods to decontaminate filtering facepiece respirators contaminated with H1N1 aerosols and droplets. Am. J. Infect. Control **39**, e1-9 (2011).
27. Tseng, C.-C. & Li, C.-S. Inactivation of Viruses on Surfaces by Ultraviolet Germicidal Irradiation. J. Occup. Environ. Hyg. **4**, 400–405 (2007).
28. Woo, M.-H. et al. Effects of Relative Humidity and Spraying Medium on UV Decontamination of Filters Loaded with Viral Aerosols. Applied and Environmental Microbiology **78**, 5781–5787 (2012).
29. OSHA. OSHA Technical Manual, Section VIII - Use of Respirators.
30. Mayerhöfer, T. G. & Popp, J. Beer's law derived from electromagnetic theory. Spectrochim. Acta A Mol. Biomol. Spectrosc. **215**, 345–347 (2019).
31. Tseng, C.-C. & Li, C.-S. Inactivation of Virus-Containing Aerosols by Ultraviolet Germicidal Irradiation. Aerosol Science and Technology **39**, 1136–1142 (2005).
32. Smith, J. S. et al. Effect of various decontamination procedures on disposable N95 mask integrity and SARS-CoV-2 infectivity. Journal of Clinical and Translational Science 1–5 (undefined/ed) doi:10.1017/cts.2020.494.
33. Ozog, D. M. et al. The effect of ultraviolet C radiation against different N95 respirators inoculated with SARS-CoV-2. Int. J. Infect. Dis. **100**, 224–229 (2020).
34. Kohli, I. et al. UVC Germicidal Units: Determination of Dose Received and Parameters to be Considered for N95 Respirator Decontamination and Reuse. Photochemistry and Photobiology **96**, 1083–1087 (2020).
35. Fischer, R. J. et al. Early Release - Effectiveness of N95 Respirator Decontamination and Reuse against SARS-CoV-2 Virus - Volume 26, Number 9—September 2020 - Emerging Infectious Diseases journal - CDC. doi:10.3201/eid2609.201524.
36. Simmons, S. et al. Deactivation of SARS-CoV-2 with Pulsed Xenon Ultraviolet: implications for environmental COVID-19 control. Infect. Control Hosp. Epidemiol. 1–19 (2020) doi:10.1017/ice.2020.399.
37. Poster, D. L. et al. Innovative Approaches to Combat Healthcare-Associated Infections Using Efficacy Standards Developed Through Industry and Federal Collaboration. Proc SPIE Int Soc Opt Eng **10730**, (2018).
38. ASTM International. Standard Test Method for Determining Antimicrobial Efficacy of Ultraviolet Germicidal Irradiation against Influenza Virus on Fabric Carriers with Simulated Soil. (2019).
39. Walker, C. M. & Ko, G. Effect of Ultraviolet Germicidal Irradiation on Viral Aerosols. Environmental Science & Technology **41**, 5460–5465 (2007).
40. Vo, E., Rengasamy, S. & Shaffer, R. Development of a Test System To Evaluate Procedures for Decontamination of Respirators Containing Viral Droplets. Appl Environ Microbiol **75**, 7303–7309 (2009).
41. Fisher, E. M. & Shaffer, R. E. A method to determine the available UV-C dose for the decontamination of filtering facepiece respirators. J. Appl. Microbiol. **110**, 287–295 (2011).
42. Lin, T.-H., Tang, F.-C., Hung, P.-C., Hua, Z.-C. & Lai, C.-Y. Relative survival of Bacillus subtilis spores loaded on filtering facepiece respirators after five decontamination methods. Indoor Air **28**, 754–762 (2018).

43. Bentley, J. J., Santoro, D., Gram, D. W., Dujowich, M. & Marsella, R. Can ultraviolet light C decrease the environmental burden of antimicrobial-resistant and -sensitive bacteria on textiles? Veterinary Dermatology **27**, 457-e121 (2016).
44. Wallace, R. L., Ouellette, M. & Jean, J. Effect of UV-C light or hydrogen peroxide wipes on the inactivation of methicillin-resistant Staphylococcus aureus, Clostridium difficile spores and norovirus surrogate. Journal of Applied Microbiology **127**, 586–597 (2019).
45. Fu, L. et al. Different efficacies of common disinfection methods against candida auris and other candida species. Journal of Infection and Public Health (2020) doi:10.1016/j.jiph.2020.01.008.
46. World Health Organization. Guidelines on viral inactivation and removal procedures intended to assure the viral safety of human blood plasma products. (2004).
47. Blázquez, E. et al. Evaluation of the effectiveness of the SurePure Turbulator ultraviolet-C irradiation equipment on inactivation of different enveloped and non-enveloped viruses inoculated in commercially collected liquid animal plasma. PLoS One **14**, (2019).
48. Fisher, E. M., Williams, J. L. & Shaffer, R. E. Evaluation of microwave steam bags for the decontamination of filtering facepiece respirators. PLoS One **6**, e18585 (2011).
49. Kenar, L., Ortatatli, M., Yaren, H., Karayilanoglu, T. & Aydogan, H. Comparative Sporicidal Effects of Disinfectants after Release of a Biological Agent. Military Medicine **172**, 616–621 (2007).
50. Smolle, C., Huss, F., Lindblad, M., Reischies, F. & Tano, E. Effectiveness of automated ultraviolet-C light for decontamination of textiles inoculated with Enterococcus faecium. Journal of Hospital Infection **98**, 102–104 (2018).
51. Tomas, M. E., Cadnum, J. L., Jencson, A. & Donskey, C. J. The Ebola Disinfection Booth: Evaluation of an Enclosed Ultraviolet Light Booth for Disinfection of Contaminated Personal Protective Equipment Prior to Removal. Infection Control & Hospital Epidemiology **36**, 1226–1228 (2015).
52. Tano, E. & Melhus, Å. Level of decontamination after washing textiles at 60°C or 70°C followed by tumble drying. Infect Ecol Epidemiol **4**, (2014).
53. Carratalà, A. et al. Effect of temperature and sunlight on the stability of human adenoviruses and MS2 as fecal contaminants on fresh produce surfaces. Int. J. Food Microbiol. **164**, 128–134 (2013).
54. Lee, J. E. & Ko, G. Norovirus and MS2 inactivation kinetics of UV-A and UV-B with and without TiO2. Water Research **47**, 5607–5613 (2013).
55. Heisler, G. M., Grant, R. H., Gao, W. & Slusser, J. R. Solar Ultraviolet-B Radiation in Urban Environments: The Case of Baltimore, Maryland¶†. Photochemistry and Photobiology **80**, 422–428 (2004).
56. Beck, S. E. et al. Comparison of UV-Induced Inactivation and RNA Damage in MS2 Phage across the Germicidal UV Spectrum. Appl. Environ. Microbiol. **82**, 1468–1474 (2016).
57. Lytle, C. D. & Sagripanti, J.-L. Predicted Inactivation of Viruses of Relevance to Biodefense by Solar Radiation. Journal of Virology **79**, 14244–14252 (2005).
58. CDC. 42 CFR Part 84 Respiratory Protective Devices. (1997).
59. Zhao, Z. et al. Germicidal Ultraviolet Light Does Not Damage or Impede Performance of N95 Masks Upon Multiple Uses. Environ. Sci. Technol. Lett. (2020) doi:10.1021/acs.estlett.0c00416.

60. Viscusi, D. J., Bergman, M. S., Eimer, B. C. & Shaffer, R. E. Evaluation of five decontamination methods for filtering facepiece respirators. Ann. Occup. Hyg. **53**, 815–827 (2009).
61. Ozog, D. et al. The importance of fit testing in decontamination of N95 respirators: A cautionary note. Journal of the American Academy of Dermatology **83**, 672–674 (2020).
62. Lindsley, W. G. et al. Effects of Ultraviolet Germicidal Irradiation (UVGI) on N95 Respirator Filtration Performance and Structural Integrity. Journal of Occupational and Environmental Hygiene **12**, 509–517 (2015).
63. CDC. Filtering out Confusion: Frequently Asked Questions about Respiratory Protection. (2018). doi:10.26616/NIOSHPUB2018130.
64. Bergman, M. S. et al. Impact of multiple consecutive donnings on filtering facepiece respirator fit. Am J Infect Control **40**, 375–380 (2012).
65. Occupational Safety and Health Standards: Appendix A to §1910.134 - Fit Testing Procedures (Mandatory). https://www.osha.gov/laws-regs/regulations/standardnumber/1910/1910.134AppA (2004).
66. CDC. Recommended Guidance for Extended Use and Limited Reuse of N95 Filtering Facepiece Respirators in Healthcare Settings. (2020).
67. Battelle. Instructions for Healthcare Personnel: Preparation of Compatible N95 Respirators for Decontamination by the Battelle Memorial Institute Using the Battelle Decontamination System. (2020).
68. Beam, B. L. & Hayes, K. A. N95 Respirator Limited Reuse - Healthcare Professionals Providing Clinical Care. (University of Nebraska Medical Center, 2020).
69. Carolina Ontiveros, C. et al. Characterization of a commercially-available, low-pressure UV lamp as a disinfection system for decontamination of common nosocomial pathogens on N95 filtering facepiece respirator (FFR) material. Environmental Science: Water Research & Technology **6**, 2089–2102 (2020).
70. Purschke, M. et al. Construction and validation of UV-C decontamination cabinets for filtering facepiece respirators. Appl. Opt., AO **59**, 7585–7595 (2020).
71. Wilde, J. P. et al. Modeling UV-C irradiation chambers for mask decontamination using Zemax OpticStudio. Appl. Opt., AO **59**, 7596–7605 (2020).
72. Bentancor, M. & Vidal, S. Programmable and low-cost ultraviolet room disinfection device. HardwareX **4**, e00046 (2018).
73. Rutala, W. A., Gergen, M. F., Tande, B. M. & Weber, D. J. Room Decontamination Using an Ultraviolet-C Device with Short Ultraviolet Exposure Time. Infection Control & Hospital Epidemiology **35**, 1070–1072 (2014).
74. International Ultraviolet Association. UV FAQS.
75. Viscusi, D. J., King, W. P. & Shaffer, R. E. Effect of Decontamination on the Filtration Efficiency of Two Filtering Facepiece Respirator Models. J Int Soc Resp Prot **24**, 15 (2007).
76. FDA. Lumin LM3000 for Bioburden Reduction of Compatible N95 Respirators - Letter of Authorization. (2020).

Chapter 9

Best practices for germicidal ultraviolet-C dose measurement for N95 respirator decontamination

Adapted with permission from A. Geldert*, H. B. Balch*, A. Gopal, A. Su, S. M. Grist, & A. E. Herr, "Best practices for germicidal ultraviolet-C dose measurement for N95 respirator decontamination", *J Res NIST,* 2021.

9.1 Abstract

Ultraviolet-C (UV-C) decontamination holds promise in combating the coronavirus disease 2019 pandemic, particularly with its potential to mitigate the N95 respirator shortage. Safe, effective, and reproducible decontamination depends critically on UV-C dose, yet dose is frequently measured and reported incorrectly, which results in misleading and potentially harmful protocols. Understanding best practices in UV-C dose measurement for N95 respirator decontamination is essential to the safety of medical professionals, researchers, and the public. Here, we outline the fundamental optical principles governing UV-C irradiation and detection, as well as the key metrics of UV-C wavelength and dose. In particular, we discuss the technical and regulatory distinctions between UV-C N95 decontamination and other applications of germicidal UV-C, and highlight the unique considerations required for UV-C N95 decontamination. Together, this discussion will inform best practices for UV-C dose measurement for N95 respirator decontamination during crisis-capacity conditions.

9.2 Introduction

The coronavirus disease 2019 (COVID-19) pandemic has led to severe shortages of N95 filtering facepiece respirators, which are essential personal protective equipment (PPE) for healthcare professionals worldwide. In response, the U.S. Centers for Disease Control and Prevention (CDC) have issued guidelines for decontamination and reuse of N95 respirators as a crisis capacity strategy and identified ultraviolet-C (UV-C) germicidal irradiation as one of the most promising methods for primary decontamination[1]. UV-C plays an important role in infection control across the medical industry but, due to the complex geometry and material properties of N95 respirators, the UV-C measurement considerations for N95 decontamination differ substantially from more established applications of germicidal UV-C. Safe and effective UV-C decontamination depends critically on (1) the spectral overlap between the emission spectrum of the light source and the wavelengths capable of inactivating the pathogen (i.e., the action spectrum), and (2) how much energy is delivered to the pathogen (fluence, often described as dose[1]). However, accurately measuring and reporting these characteristics for UV-C N95

[1] Not all the energy incident on a substrate is absorbed. While dose is almost always used in the germicidal UV-C literature to describe the energy incident on the material being decontaminated, dose can also refer to the total amount of absorbed (not incident) energy in other contexts. The most accurate technical term to describe the total incident UV-C energy (in units of J/cm^2) on a surface is fluence[2]. However, to align with the germicidal UV-C literature, here we choose to use the term "dose" to describe total incident energy on an N95. Similarly, while fluence rate is a more technically accurate term to describe the radiant power (in units of W/cm^2) irradiating a sample from all directions[2], here we use the term irradiance to align with the decontamination literature.

decontamination systems is complicated, and measurement standards targeting the unique challenges of complex, multi-material N95 respirators remain in development.

Accurate measurements of UV-C dose are central both for verifying that decontamination systems are operating within specification and for reproducible reporting. UV-C dose measurements provide a key link in the translation of effective and reproducible decontamination protocols across different communities: from UV-C device manufacturers and researchers, to infection control staff implementing UV-C N95 decontamination. In this paper, we highlight key measurement considerations for researchers, engineers, and clinical staff who are evaluating and implementing UV-C-based decontamination of N95 respirators. First, we highlight the technical and regulatory context for UV-C N95 decontamination; second, we discuss the science behind UV-C decontamination, highlighting the central importance of both wavelength and dose in viral inactivation; third, we examine techniques and common pitfalls in UV-C dose measurement; and finally, we outline best practices that help avoid these pitfalls.

9.3 UV-C for N95 decontamination

UV-C radiation is widely used as a secondary technique for decontamination of air[3], water[4], and non-porous surfaces[5]. Until April 2021, CDC guidance[1] and hospital protocols[6] indicated that UV-C was being used as a primary and standalone decontamination method for N95 respirators under crisis capacity conditions[7]. As a primary decontamination technique, the application of UV-C to N95 respirators requires specific consideration of the complex geometry, porous multi-material electret layers, and filtration central to N95 respirator function. For example, UV-C radiation is heavily attenuated through non-UV-C-transparent and scattering materials; dose received at interior layers may be orders of magnitude lower than the applied dose at the outer surface of the N95 (**Figure 9.1A**)[8]. UV-C attenuation through the porous layers requires special consideration to ensure that the dose received at all contaminated layers within the respirator is sufficient for decontamination[8]. Consequently, decontamination of porous materials can require 100× higher applied dose at the surface than that required for non-porous surfaces with low surface roughness[9,10], but excessive doses can reduce respirator function[11]. The electrostatic respirator filter material is also damaged by chemical disinfectants such as ethanol[12], limiting the use of some primary healthcare surface disinfectants. Furthermore, the complex 3D geometry of N95 respirators can result in the received dose varying several-fold across a single N95 respirator[13,14] and about twenty-fold across different N95 respirators within one decontamination system[14], with received dose strongly dependent on the incident angle of UV-C irradiation (**Figure 9.1A-B**)[15].

Due to the technical challenges and additional considerations required for implementing UV-C decontamination for N95 respirators, federal guidelines for UV-C decontamination of N95 respirators remain in development[16]. For example, the CDC has assessed the impact of several UV-C N95 decontamination systems on the fit and filtration of specific N95 respirator models, but the assessment "is not to determine the effectiveness of the decontamination procedure at killing the pathogenic microorganism"[17]. The U.S. Food and Drug Administration (FDA) guidelines emphasize that while the FDA regulates UV-C sources, the lack of clear and standardized manufacturer data on wavelength, duration and associated dose of UV-C radiation required to inactivate severe acute respiratory syndrome coronavirus 2 (SARS-CoV-2), the strain of coronavirus that causes COVID-19, presents an outstanding challenge[18]. In addition, the FDA allows previously approved disinfectant devices to be extended to SARS-CoV-2 inactivation[19]. However, the FDA requires any previously approved device to apply for an Emergency Use Authorization (EUA) and 510(k) when adapted to new applications including decontamination of

N95 respirators and other single-use PPE[16]. A 510(k) is a premarket submission made to the FDA to demonstrate that a device to be marketed is as safe and effective as a legally marketed device. For example, a steam sterilization device with prior 510(k) clearance for sterilization of materials in healthcare settings required an FDA-issued EUA before it was approved for N95 decontamination[20]. While the FDA has issued numerous EUAs for devices implementing the other two PPE decontamination methods (moist heat and vaporous hydrogen peroxide)[20,21] identified as promising by the CDC for crisis-capacity conditions, as of January 2021, only one limited EUA has been issued for the use of UV-C to reduce bioburden on one N95 model[22].

Despite this context, the accessibility and relatively low cost of UV-C sources has led to widespread implementation of UV-C for N95 decontamination in both research[12,23,24] and medical[6] environments. Decontamination system specifications depend on technical measurement factors, such as the wavelengths emitted, the wavelengths detected, the type and position of UV-C detector, and the method of analysis. Reports of UV-C-based decontamination of N95 respirators often fail to report parameters necessary to ensure validation and reproducibility despite using diverse types of UV-C sources and different measurement devices. To accurately describe, evaluate, and reproduce UV-C decontamination protocols, parameters such as type, number, and location of UV-C sources, orientation and position of both N95(s) and UV-C detector(s) relative to UV-C source(s), model of N95 and UV-C detector, decontamination chamber specifications (e.g., reflectivity), and other details of dose quantification (Appendix) are needed. Omitting these parameters for the source, target, or detector when reporting decontamination procedures substantially limits validation and reproducibility. In addition, standards for measurement are currently limited, which impedes comparison of UV-C sources and detectors[25]. In particular, minimum reporting standards for systems claiming UV-C decontamination of N95 respirators are urgently needed to facilitate comparison and critical evaluation. Here, we provide an overview of UV-C measurement fundamentals to inform the development of measurement and reporting standards for UV-C N95 decontamination systems.

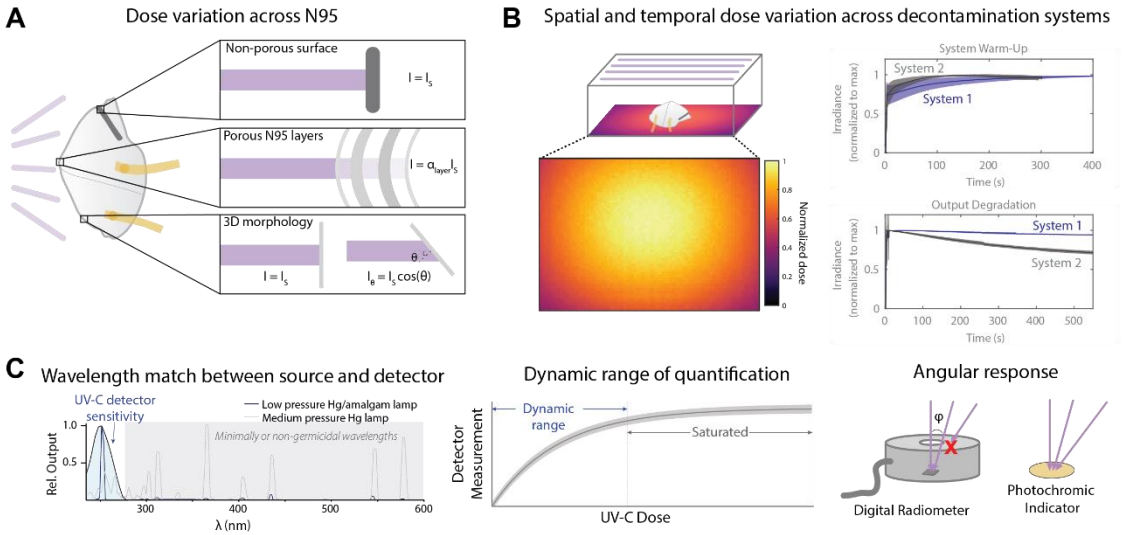

Figure 9.1. Factors affecting UV-C dose distribution and measurement for N95 decontamination. (A) Factors affecting UV-C dose applied to the N95 respirator. Sloped surfaces and attenuation by the N95 layers reduce received UV-C dose. (B) Factors affecting UV-C dose distribution within a decontamination system. UV-C irradiance can vary spatially and temporally. (C) Key specifications of UV-C detectors, including wavelength specificity, dynamic range, and angular response. Figure adapted with permission from Su & Grist, et al.[14]

9.4 Key germicidal UV-C specifications: Wavelength and dose

Not all wavelengths of UV radiation offer sufficient germicidal efficacy for N95 respirator decontamination. Absorbed germicidal UV-C radiation (200 nm - 280 nm) inactivates pathogens by promoting photochemical reactions that damage proteins and genomic material[26,27]. Distinct wavelengths have different microbe-specific germicidal efficacy, a relationship represented in what is known as the action spectrum of a microbe. The overlap between the action spectrum and the UV-C source emission spectrum will determine the efficiency of germicidal action, with higher efficiency when the overlap is greater. For many pathogens, there is a peak in the action spectrum at the absorption maximum of genomic material, around 260 nm. While research into the germicidal action spectrum of SARS-CoV-2 is ongoing, a working assumption is that the action spectrum will be similar to that of viral analogues with similar structure that exhibit a peak near 260 nm[27,28]. Germicidal UV-C radiation sources emit close to this maximum, such as the narrow emission around 254 nm from low-pressure mercury lamps commonly used as germicidal sources. The relative efficacy of emerging monochromatic and polychromatic UV-C sources is also an area of active research, highlighting the importance of rigorous measurement and reporting to facilitate accurate comparison of sources with different emission spectra. While shorter wavelengths within the UV-C range (~200 nm - 220 nm) can have higher germicidal efficacy[27], these wavelengths may be more strongly attenuated by the multiple N95 layers, requiring confirmation of dose and viral inactivation on interior layers. Longer-wavelength UV radiation (>280 nm), such as UV-B and UV-A in sunlight, has substantially lower germicidal activity[29] and has not been shown to decontaminate porous materials such as N95 respirators. While UV-B (280 nm - 320 nm) can photochemically damage nucleic acids, UV-B is orders of magnitude less efficient than UV-C wavelengths[29] due to reduced overlap with the absorption spectrum of nucleic acids. While UV-A (320 nm - 400 nm) can generate reactive oxygen species to contribute to pathogen inactivation (particularly in water)[30,31], UV-A is generally not considered germicidal[26]. Because absorption by the multiple porous N95 layers causes N95 decontamination to require about 100 times higher applied dose[8] as compared to more common applications (e.g., air, water, non-porous surface decontamination), UV-A and UV-B likely have insufficient germicidal efficacy to be feasible for N95 decontamination.

Efficacy of germicidal UV-C also depends critically on dose. Studies on other coronaviruses and influenzas indicate that 254 nm UV-C doses (from a low-pressure mercury UV-C source) of at least 1.0 J/cm^2 at the N95 respirator surface can lead to ≥ 99.9% viral inactivation on most N95 models[9,32]. Preliminary studies using both UV-C LEDs and mercury lamps have found that UV-C doses of at least 1.5 J/cm^2 are required to yield ≥ 99.9% inactivation of SARS-CoV-2 on some N95 respirator models[12,24], and research on SARS-CoV-2 inactivation on N95 respirators is ongoing. On the other hand, studies indicate that doses over 120 J/cm^2 can cause respirator degradation[11]. Because it is infeasible to measure UV-C dose delivered to viral particles embedded in the interior layers of the respirator during a decontamination cycle, the dose required for pathogen inactivation or degradation is typically reported in terms of dose applied at the respirator surface. However, because UV-C transmission through N95 respirator layers is N95 model-dependent[8], the minimum dose applied at the N95 surface for pathogen inactivation throughout all N95 layers will differ from model to model. These examples underscore that to use germicidal UV-C for effective and reproducible decontamination of N95 respirators, accurate measurement and reporting of UV-C wavelength and dose are paramount.

9.5 Critical UV-C source and detector metrics

Applying sufficient UV-C dose to N95 respirators can make – or break – effective decontamination[33]. While measurement of pathogen inactivation is the most direct way of verifying decontamination efficacy on N95 respirators, this approach is time- and resource-intensive. It is largely infeasible to perform pathogen inactivation assays at the frequency necessary to validate the ongoing efficacy of UV-C decontamination systems, especially in healthcare settings. UV-C decontamination systems must be regularly validated because the irradiance reaching an N95 can vary with UV-C light source age, environmental factors such as temperature, and setup-dependent shadowing or reflections. In particular, the material properties of nearby surfaces, such as UV-C reflectivity, have a substantial influence on the spatial pattern and magnitude of UV-C dose delivered to N95 respirators[34,35]. Thus, even if the UV-C output or pathogen inactivation efficacy of a particular UV-C lamp or decontamination system has been rigorously characterized by the manufacturer, frequent UV-C dose measurements are a more scalable, reliable, and cost-effective method (as compared to pathogen inactivation testing) for end users to ensure the system continues to operate within specification in the particular user environment.

Despite its critical role, UV-C dose is not always calculated or reported in a standardized way[25]. Dose (energy, in J/cm^2) is the integrated irradiance measured on a surface (W/cm^2) over the exposure time (s). Germicidal efficacy is wavelength dependent. Thus, to compare UV-C sources with different emission spectra and to evaluate overlap between a UV-C source and the pathogen action spectrum, dose reported from polychromatic sources should weight each wavelength by its respective, relative germicidal efficacy[2,36]. Unless a detector is omnidirectional, measured UV-C dose will depend on the location and orientation of the UV-C detector with respect to the source. As a result, to ensure reproducibility, it is critical to measure and report UV-C dose along with parameters such as UV-C source, distance from and position with respect to the source, measured irradiance, and exposure time (Appendix).

Accurate dose measurements depend on the selection of an appropriate UV-C sensor. Detectors such as radiometers, dosimeters, and dose indicator strips are all used to measure and/or calculate UV-C dose. Characteristics of UV-C sensors, such as the sensor wavelength sensitivity spectrum, dynamic range, and angular response strongly affect measured values[37]. As a result, it is important to consider the working principle of the sensor when matching a sensor to a given application. For example, radiometers can provide quantitative measurements appropriate for research or validation environments, but radiometers which do not have an ideal cosine response (e.g., those that are designed for collimated sources) will not accurately report UV-C doses from non-normal incident radiation. Additionally, angular response of UV-C sensors is often not characterized or provided. Spherical actinometric detectors relate the detector quantum yield to the dose on a surface, are widely used to calibrate physical sensors, and accurately measure dose on complex geometries. However, actinometry can be labor intensive, and the diversity of chemical transitions used in actinometry require careful reporting for accurate measurement and reproducibility[2,38]. Low-cost photochromic dose indicator strips can offer a straightforward colorimetric indicator of dose range, are commonly used in healthcare settings, and may facilitate implementation of UV-C decontamination across both low- and high-resource environments. However, these qualitative indicators are subject to potential pitfalls: dose indicator strips are commonly sensitive to both UV-B and UV-C, and those designed for non-porous or low-dose applications frequently have insufficient dynamic range, saturating below the 1.0 J/cm^2 dose required for decontamination of many N95 models[14,39]. Thus, even when the goal is simply to

verify that a decontamination system is operating within specification, understanding the specificity and dynamic range of qualitative UV-C dose indicators is critical. The ability to perform reproducible UV-C decontamination of N95 respirators, whether in the lab or the clinic, requires applied dose to be measured with a UV-C-specific sensor capable of measuring at least 1.0 J/cm^2 and with maximum sensitivity aligned with the pathogen action spectrum (e.g., 260 nm). If the detector has a non-ideal angular response, the beam divergence at the detector should be identical to the conditions under which the sensor was calibrated, without which measurement errors are common (**Figure 9.1C**).

9.6 Common measurement pitfalls

Several common pitfalls hinder accurate measurements of UV-C wavelength and dose, which are listed in **Table 9.1**. One common source of error is a mismatch between the light source and detector. For example, dose measurements with a broadband sensor will collect not only germicidal UV-C but also minimally- or non-germicidal wavelengths such as UV-A/B, visible, and infrared radiation – often with even greater sensitivity. Unless UV-C is specifically isolated at the sensor (e.g., with a bandpass filter), this mismatch will yield artificially high readings of UV-C dose. While different standards define different acceptable wavelength ranges of sensor sensitivity for different applications[2,40,41], sensors specifically used to measure UV-C should be responsive to wavelengths between 220-280 nm with peak response at the emission peak of the UV-C source (e.g., 254 nm for low-pressure mercury lamps)[41]. Methods to calculate a correction factor to account for the wavelength-dependence of a sensor are further described by Bolton & Linden[2]. Another common mistake is in mapping measurements of power or irradiance to dose. Since the irradiation of a UV-C source can vary over both space and time (**Figure 9.1B**), calculations of dose determined by multiplying a single irradiance measurement by exposure time can result in overestimates or underestimates of the dose applied (as shown in **Table 9.2**). Instead, applied dose is more accurately determined by integrating irradiance measured throughout the entire exposure time, to account for fluctuations in applied irradiance.

Many of the risks associated with over- or under-estimating applied dose can be managed with an understanding of the working principles of the UV-C source and detector and through adequate reporting. However, the implications of over- or under-reporting UV-C dose applied to N95 respirators are wide-ranging and user-dependent, as demonstrated in **Table 9.2**. For example, if researchers studying viral inactivation over-estimate the UV-C dose required to decontaminate N95 respirators (e.g., reported dose is higher than true delivered dose), this can provide a margin of safety; however, if clinical staff over-estimate the UV-C dose delivered to N95 respirators during a decontamination cycle, this could result in incomplete decontamination and create a transmission risk. Understanding the best practices in UV-C dose measurement can help users choose the most conservative UV-C measurement approach for their application.

Table 9.1. Common pitfalls in UV-C dose measurement for N95 decontamination.

Pitfall	Examples
Wavelength mismatch between UV-C source and sensor	▪ Sensor does not detect the UV-C germicidal wavelengths because sensor is specific for UV-A/UV-B wavelengths (280-400 nm). ▪ Sensor is broadband and measures a range of wavelengths across the UV, visible, or infrared spectrum, making it impossible to determine the UV-C-specific contribution to irradiance or dose without additional filters.
Dose indicators or sensors with insufficient dynamic range	▪ Photochromic dose indicator does not change color beyond 100 mJ/cm^2. ▪ Incident irradiance is not matched to the sensor dynamic range (e.g., irradiance is lower than the sensor noise floor or higher than the sensor saturation limit).
Calculating dose using a single measured irradiance value	▪ Irradiance is measured at a single time point but does not remain constant throughout the exposure period due to system-dependent variation in lamp output. ▪ Irradiance measured at a single N95 location does not represent irradiance received across all surfaces of N95s located closer/farther from the UV-C source or closer/farther from reflective surfaces.
Sensor with limited angular response	▪ Incident light is only partially collected by the radiometer (e.g., due to a sensor housing or sensor field of view that is narrower than the light source output).
Calculating dose using rated UV-C lamp power	▪ Identical UV-C lamp bulbs with identical make, model, and power ratings may have differing output efficiencies.

Table 9.2. Importance of considering over- and under-reporting of UV-C dose.

Problem		**Under-reporting** of UV-C dose *Measured or reported dose is lower than true delivered dose*	**Over-reporting** of UV-C dose *Measured or reported dose is higher than true delivered dose*
How? *Example case listed; see Table 1 for additional pitfalls*		Dose is calculated from a single irradiance measurement made at the start of the exposure period, but **lamp output increases throughout the exposure period as the lamp warms up.** The irradiance measurement underestimates the average irradiance over the exposure period, and thus reported (calculated) UV-C dose is lower than the true delivered dose.	Dose is calculated from a single irradiance measurement made at the start of the exposure period, but **lamp output decreases throughout the exposure period due to changes in air temperature.** The irradiance measurement overestimates the average irradiance over the exposure period, and thus reported (calculated) UV-C dose is higher than the true delivered dose.
Implications *User is a…*	Researcher studying the impact of UV-C on N95 viral inactivation	The researcher attributes measured viral inactivation to an artificially low UV-C dose. ► Protocols based on these reported results can yield insufficient decontamination.	The researcher attributes measured viral inactivation to an artificially high UV-C dose. ► Protocols based on these reported results may recommend unnecessarily high dose and unnecessarily increase decontamination time. ► If insufficient viral inactivation was observed, report may incorrectly claim that reported dose is ineffective for N95 decontamination, potentially conflicting with other publications in which UV-C dose was measured accurately.
	Researcher studying the impact of UV-C on N95 fit & filtration	The researcher attributes measured N95 respirator damage to an artificially low UV-C dose. ► The number of decontamination cycles an N95 can withstand prior to degradation is underestimated, leading to premature disposal of scarce resources.	The researcher attributes measured N95 respirator damage to an artificially high UV-C dose. ► The UV-C dose (and number of decontamination cycles) N95s can withstand prior to degradation is overestimated, which may lead to application of damaging levels of UV-C to N95 respirators.
	Clinical staff implementing UV-C decontamination of N95s	Clinical staff underestimate the delivered dose during N95 decontamination treatments, exceeding the target dose for decontamination. ► Inaccurate decontamination protocols are perpetuated. ► N95 respirator may be damaged (if reported UV-C dose is severely underestimated).	Clinical staff overestimate the UV-C dose delivered to N95 respirators during a decontamination cycle. ► Virus may persist due to insufficient UV-C dose delivery.

9.7 Best practices for UV-C measurements and methods

Because UV-C dose is the key metric used to link research to implementation, understanding the best practices for characterizing and reporting UV-C decontamination systems is critical for both the research and clinical communities. The measurement needs differ among communities (e.g., precise, quantitative UV-C dose readout may be valuable for researchers studying the effect of UV-C on pathogen inactivation or N95 function, while clinical staff may solely need to verify that the UV-C dose applied to N95 respirators is within a specified range). However, a shared understanding of the factors impacting UV-C dose measurements is critical to allow users to accurately evaluate and implement UV-C for N95 decontamination, in the context of current federal regulations. Here, we outline key considerations for multiple user groups when studying, evaluating, or implementing UV-C N95 decontamination.

In research. Researchers developing or studying UV-C N95 decontamination systems can support safe and effective UV-C N95 decontamination both in the way they perform and report UV-C measurements. In making UV-C measurements, consider the implications of over- and under-

estimating dose and choose the most conservative option (yellow cells in **Table 9.2**). For clinical staff to evaluate and reproducibly implement UV-C for N95 decontamination, researchers and device manufacturers also must report in sufficient detail the way in which UV-C measurements were made[25]. Best practices, or 'minimum reporting standards', are common across scientific disciplines[42,43]. These standards would be valuable for UV-C decontamination of N95 respirators. Standards should include physical specifications for both the UV source and the optical detector, along with necessary optical elements such as filters, diffusers, or cosine correctors. Data acquisition and analysis should also be explicitly reported, describing how dose was measured and calculated and how (or if) viral inactivation was verified. A list of suggested reporting parameters can be found in the Appendix. Thorough and standardized reporting provides a path to sidestep common pitfalls and realize the potential for UV-C to dramatically mitigate crisis capacity conditions.

In clinical implementation.

In evaluating UV-C decontamination systems: When reading and interpreting research, it is important for users to understand how UV-C dose was measured and to critically evaluate the accuracy of reported UV-C dose. To ensure N95 decontamination, data should establish UV-C-induced viral inactivation on the specific N95 model and in an enclosure that is comparable to that available at the workplace. To ensure that UV-C treatment does not reduce N95 respirator function, users should also assess whether preservation of respirator fit and filtration was evaluated, and consider how the applied UV-C dose compares to the maximum dose at which respirator integrity is expected to be maintained[11].

In implementing UV-C N95 decontamination protocols: UV-C decontamination should be used only during critical N95 shortages when in accordance with federal guidelines. UV-C dose should be regularly measured, particularly at locations receiving the highest and lowest dose, as the range of applied dose impacts decontamination efficacy and the number of times N95 respirators can be safely decontaminated prior to material degradation. The calibrated sensors used for these measurements should have narrow-band UV-C detection. Other factors that are important to consider when implementing N95 decontamination and reuse:

1. High UV-C exposure, whether through a single high dose treatment or many UV-C cycles, can degrade respirator materials and reduce filtration efficacy[11]. Due to differences in material construction, the maximum dose that an N95 can withstand may be model-dependent.
2. Decontamination and multiple donning and doffing cycles can affect fit[44].
3. Shadowing and irradiation of surfaces non-perpendicular to the incident UV-C decrease the received dose and increase dose non-uniformity. For example, the lower viral inactivation efficacy observed on N95 facepieces with ridges has been attributed to shadowing[9]. The irradiance reaching shadowed surfaces will depend on the absorbance of the material in the optical path between the UV-C source and shadowed surface. Additionally, because irradiance depends on the angle of incident radiation[15], N95 surfaces that are steeply-sloped with respect to the incident light will generally receive a lower UV-C dose (**Figure 9.1A**).
4. Soiling agents (saliva, oils) can modulate pathogen inactivation efficacy by reducing UV-C penetration into the respirator material[45,46].
5. Viral inactivation can be N95 model-dependent[9].

6. Other pathogens with lower UV-C susceptibility – especially bacterial spores – may remain active on N95 respirators even if the applied UV-C dose achieves viral inactivation[47–49].
7. Elastic straps may require a secondary decontamination method[9].

Applying the appropriate UV-C wavelength and dose are critical metrics for reproducible UV-C N95 decontamination protocols under crisis capacity conditions. Engaging vertically-integrated teams with engineering, infection control/sterile processing, and clinical expertise promotes technical validation and safe processing workflows. Full consideration of the technical and practical considerations of UV-C N95 decontamination is key to more safely weathering pandemic-induced crisis capacity conditions.

9.8 Appendix: Recommended UV-C author reporting summary

Recommended reporting summary for authors sharing research on UV-C decontamination of N95 respirators, to support dissemination of accurate and reproducible UV-C decontamination protocols.

UV-C Author Reporting Summary

This form provides structure for reproducibility and transparency in reporting on studies of viral inactivation by UV-C irradiation. Because equipment for UV-C based decontamination is not standardized and actual UV-C dose depends on numerous factors, it is important for accuracy and reproducibility to report the physical parameters as outlined below. There are additional factors that may affect the efficacy of this technique, such as N95 style, layout, and N95 model. This checklist also does not evaluate filtration efficiency or N95 degradation from the decontamination process.

Hardware

1. UV-C Source

if YES: specify where this information is in the text
if NO: explain why this information is not reported/not relevant

Make (brand) and model number
☐ Yes
☐ No

Type of source
For instance: mercury lamp, xenon lamp, LED, etc.
☐ Yes
☐ No

Dimensions of the source
Dimensions of emission source can be important for determining the angular variation in UV-C illumination. For instance: mercury lamp arc length (m) from electrode tip to electrode tip.
☐ Yes
☐ No

UV-C source layout
For instance: number, location, orientation, chamber specifications
☐ Yes
☐ No

Emission spectrum
State wavelengths emitted, and either show or reference the emission spectrum.
☐ Yes
☐ No

2. Optical Detector

Radiometer and sensor probe: make and model, wavelength range, calibration
☐ Yes
☐ No

For instance: "An ILT-1254 radiometer (International Light Technologies), which measures 254 nm wavelengths, was used to measure UV-C irradiance. The radiometer is calibrated annually according to manufacturer's instructions."

Any filters, diffusers, cosine correctors, or other optical elements attached to the sensor; brand and model number; **specifications (e.g., wavelength** range); purpose
☐ Yes
☐ No

For instance: "To specifically quantify UV-C irradiance, the spectroradiometer was fitted with a 254 nm shortpass filter (Newport HG-SC-OEM) to block out wavelengths above 254 nm."

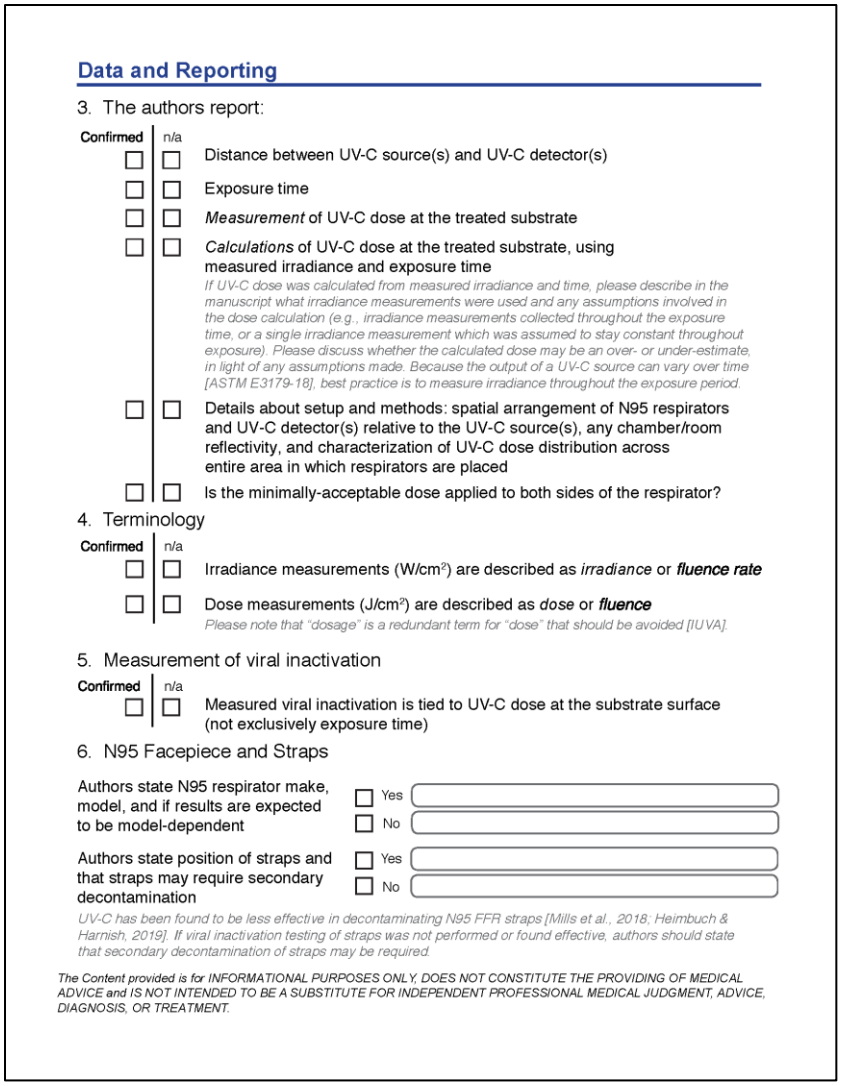

Data and Reporting

3. The authors report:

Confirmed	n/a	
☐	☐	Distance between UV-C source(s) and UV-C detector(s)
☐	☐	Exposure time
☐	☐	*Measurement* of UV-C dose at the treated substrate
☐	☐	*Calculations* of UV-C dose at the treated substrate, using measured irradiance and exposure time *If UV-C dose was calculated from measured irradiance and time, please describe in the manuscript what irradiance measurements were used and any assumptions involved in the dose calculation (e.g., irradiance measurements collected throughout the exposure time, or a single irradiance measurement which was assumed to stay constant throughout exposure). Please discuss whether the calculated dose may be an over- or under-estimate, in light of any assumptions made. Because the output of a UV-C source can vary over time [ASTM E3179-18], best practice is to measure irradiance throughout the exposure period.*
☐	☐	Details about setup and methods: spatial arrangement of N95 respirators and UV-C detector(s) relative to the UV-C source(s), any chamber/room reflectivity, and characterization of UV-C dose distribution across entire area in which respirators are placed
☐	☐	Is the minimally-acceptable dose applied to both sides of the respirator?

4. Terminology

Confirmed	n/a	
☐	☐	Irradiance measurements (W/cm²) are described as *irradiance* or ***fluence rate***
☐	☐	Dose measurements (J/cm²) are described as *dose* or ***fluence*** *Please note that "dosage" is a redundant term for "dose" that should be avoided [IUVA].*

5. Measurement of viral inactivation

Confirmed	n/a	
☐	☐	Measured viral inactivation is tied to UV-C dose at the substrate surface (not exclusively exposure time)

6. N95 Facepiece and Straps

Authors state N95 respirator make, model, and if results are expected to be model-dependent	☐ Yes	
	☐ No	
Authors state position of straps and that straps may require secondary decontamination	☐ Yes	
	☐ No	

UV-C has been found to be less effective in decontaminating N95 FFR straps [Mills et al., 2018; Heimbuch & Harnish, 2019]. If viral inactivation testing of straps was not performed or found effective, authors should state that secondary decontamination of straps may be required.

The Content provided is for INFORMATIONAL PURPOSES ONLY, DOES NOT CONSTITUTE THE PROVIDING OF MEDICAL ADVICE and IS NOT INTENDED TO BE A SUBSTITUTE FOR INDEPENDENT PROFESSIONAL MEDICAL JUDGMENT, ADVICE, DIAGNOSIS, OR TREATMENT.

9.9 References

1. *Decontamination and Reuse of Filtering Facepiece Respirators*. https://www.cdc.gov/coronavirus/2019-ncov/hcp/ppe-strategy/decontamination-reuse-respirators.html (2020).
2. Bolton, J. R. & Linden, K. G. Standardization of Methods for Fluence (UV Dose) Determination in Bench-Scale UV Experiments. *J. Environ. Eng.* **129**, 209–215 (2003).
3. Memarzadeh, F., Olmsted, R. N. & Bartley, J. M. Applications of ultraviolet germicidal irradiation disinfection in health care facilities: Effective adjunct, but not stand-alone technology. *American Journal of Infection Control* **38**, S13–S24 (2010).
4. Pirnie, M., Linden, K. G., Malley, J. P., Schmelling, D. & of Water USA, O. *Ultraviolet disinfection guidance manual for the final long term 2 enhanced surface water treatment rule: EPA 815-R-06-007*. (EPA, 2006).
5. FDA. *21CFR880.6600*. (2019).
6. Lowe, J. J. *et al. N95 Filtering Facepiece Respirator Ultraviolet Germicidal Irradiation (UVGI) Process for Decontamination and Reuse*.

https://www.nebraskamed.com/sites/default/files/documents/covid-19/n-95-decon-process.pdf (2020).
7. CDC. Strategies for Optimizing the Supply of N95 Respirators. *Centers for Disease Control and Prevention* https://www.cdc.gov/coronavirus/2019-ncov/hcp/respirators-strategy/index.html (2021).
8. Fisher, E. M. & Shaffer, R. E. A method to determine the available UV-C dose for the decontamination of filtering facepiece respirators. *J. Appl. Microbiol.* **110**, 287–295 (2011).
9. Mills, D., Harnish, D. A., Lawrence, C., Sandoval-Powers, M. & Heimbuch, B. K. Ultraviolet germicidal irradiation of influenza-contaminated N95 filtering facepiece respirators. *American Journal of Infection Control* **46**, e49–e55 (2018).
10. Tseng, C.-C. & Li, C.-S. Inactivation of Viruses on Surfaces by Ultraviolet Germicidal Irradiation. *J. Occup. Environ. Hyg.* **4**, 400–405 (2007).
11. Lindsley, W. G. *et al.* Effects of Ultraviolet Germicidal Irradiation (UVGI) on N95 Respirator Filtration Performance and Structural Integrity. *Journal of Occupational and Environmental Hygiene* **12**, 509–517 (2015).
12. Fischer, R. J. *et al.* Early Release - Effectiveness of N95 Respirator Decontamination and Reuse against SARS-CoV-2 Virus - Volume 26, Number 9—September 2020 - Emerging Infectious Diseases journal - CDC. doi:10.3201/eid2609.201524.
13. Kohli, I. *et al.* UVC Germicidal Units: Determination of Dose Received and Parameters to be Considered for N95 Respirator Decontamination and Reuse. *Photochemistry and Photobiology* **96**, 1083–1087 (2020).
14. Su, A., Grist, S. M., Geldert, A., Gopal, A. & Herr, A. E. Quantitative UV-C dose validation with photochromic indicators for informed N95 emergency decontamination. *PLOS ONE* **16**, e0243554 (2021).
15. Reifsnyder, W. E. Radiation geometry in the measurement and interpretation of radiation balance. *Agricultural Meteorology* **4**, 255–265 (1967).
16. *Recommendations for Sponsors Requesting EUAs for Decontamination and Bioburden Reduction Systems for Surgical Masks and Respirators During the Coronavirus Disease 2019 (COVID19) Public Health Emergency*. https://www.fda.gov/media/138362/download (2020).
17. CDC. NPPTL Respirator Assessments to Support the COVID-19 Response. https://www.cdc.gov/niosh/npptl/respirators/testing/DeconResults.html (2021).
18. FDA. UV Lights and Lamps: Ultraviolet-C Radiation, Disinfection, and Coronavirus. https://www.fda.gov/medical-devices/coronavirus-covid-19-and-medical-devices/uv-lights-and-lamps-ultraviolet-c-radiation-disinfection-and-coronavirus (2020).
19. *Enforcement Policy for Sterilizers, Disinfectant Devices, and Air Purifiers During the Coronavirus Disease 2019 (COVID-19) Public Health Emergency*. https://www.fda.gov/media/136533/download (2020).
20. FDA. STERIS STEAM Decon Cycle in AMSCO Medium Steam Sterilizers - Letter of Authorization (EUA). (2020).
21. FDA. Battelle Decontamination System - Letter of Authorization. (2020).
22. FDA. Lumin LM3000 for Bioburden Reduction of Compatible N95 Respirators - Letter of Authorization. (2020).
23. Smith, J. S. *et al.* Effect of various decontamination procedures on disposable N95 mask integrity and SARS-CoV-2 infectivity. *Journal of Clinical and Translational Science* 1–5 (undefined/ed) doi:10.1017/cts.2020.494.

24. Ozog, D. M. *et al.* The effect of ultraviolet C radiation against different N95 respirators inoculated with SARS-CoV-2. *Int. J. Infect. Dis.* **100**, 224–229 (2020).
25. Poster, D. L. *et al.* Innovative Approaches to Combat Healthcare-Associated Infections Using Efficacy Standards Developed Through Industry and Federal Collaboration. *Proc SPIE Int Soc Opt Eng* **10730**, (2018).
26. Kowalski, W. *Ultraviolet Germicidal Irradiation Handbook: UVGI for Air and Surface Disinfection*. (Springer Berlin Heidelberg, 2009). doi:10.1007/978-3-642-01999-9.
27. Beck, S. E., Wright, H. B., Hargy, T. M., Larason, T. C. & Linden, K. G. Action spectra for validation of pathogen disinfection in medium-pressure ultraviolet (UV) systems. *Water Research* **70**, 27–37 (2015).
28. Iii, E. R. B., Petri, B. & Sun, W. SARS-CoV-2 UV Dose-Response Behavior. 6.
29. Lytle, C. D. & Sagripanti, J.-L. Predicted Inactivation of Viruses of Relevance to Biodefense by Solar Radiation. *Journal of Virology* **79**, 14244–14252 (2005).
30. McGuigan, K. G. *et al.* Solar water disinfection (SODIS): A review from bench-top to roof-top. *Journal of Hazardous Materials* **235–236**, 29–46 (2012).
31. Horton, L. *et al.* Spectrum of virucidal activity from ultraviolet to infrared radiation. *Photochemical & Photobiological Sciences* **19**, 1262–1270 (2020).
32. Lore, M. B., Heimbuch, B. K., Brown, T. L., Wander, J. D. & Hinrichs, S. H. Effectiveness of Three Decontamination Treatments against Influenza Virus Applied to Filtering Facepiece Respirators. *The Annals of Occupational Hygiene* **56**, 92–101 (2012).
33. Narla, S. *et al.* The importance of the minimum dosage necessary for UVC decontamination of N95 respirators during the COVID-19 pandemic. *Photodermatology, Photoimmunology & Photomedicine* **n/a**,.
34. Rutala, W. A., Gergen, M. F., Tande, B. M. & Weber, D. J. Room Decontamination Using an Ultraviolet-C Device with Short Ultraviolet Exposure Time. *Infection Control & Hospital Epidemiology* **35**, 1070–1072 (2014).
35. Rutala, W. A., Gergen, M. F., Tande, B. M. & Weber, D. J. Rapid Hospital Room Decontamination Using Ultraviolet (UV) Light with a Nanostructured UV-Reflective Wall Coating. *Infection Control & Hospital Epidemiology* **34**, 527–529 (2013).
36. Meulemans, C. C. E. The Basic Principles of UV–Disinfection of Water. *Ozone: Science & Engineering* **9**, 299–313 (1987).
37. Reed, N. G., Wengraitis, S. & Sliney, D. H. Intercomparison of instruments used for safety and performance measurements of ultraviolet germicidal irradiation lamps. *J Occup Environ Hyg* **6**, 289–297 (2009).
38. Rahn, R. O., Xu, P. & Miller, S. L. Dosimetry of room-air germicidal (254 nm) radiation using spherical actinometry. *Photochem Photobiol* **70**, 314–318 (1999).
39. *tesa 54140 UV strips: product information*. https://www.tesa.com/en-sg/industry/tesa-54140-uv-strips.html.
40. ASTM International. *Standard Test Method for Determining Antimicrobial Efficacy of Ultraviolet Germicidal Irradiation against Influenza Virus on Fabric Carriers with Simulated Soil*. (2019).
41. *Method of Testing Ultraviolet Lamps for Use in HVAC&R Units or Air Ducts to Inactivate Microorganisms on Irradiated Surfaces*. https://global.ihs.com/doc_detail.cfm?document_name=ASHRAE%20STD%20185%2E2&item_s_key=00634862 (2014).
42. Scrutinizing lasers. *Nature Photonics* **11**, 139–139 (2017).

43. A solar checklist. *Nature Photonics* **9**, 703–703 (2015).
44. Bergman, M. S. *et al.* Impact of multiple consecutive donnings on filtering facepiece respirator fit. *Am J Infect Control* **40**, 375–380 (2012).
45. Heimbuch, B. & Harnish, D. *Research to Mitigate a Shortage of Respiratory Protection Devices During Public Health Emergencies (Report to the FDA No. HHSF223201400158C)*. (2019).
46. Fisher, E. M., Williams, J. & Shaffer, R. E. The Effect of Soil Accumulation on Multiple Decontamination Processing of N95 Filtering Facepiece Respirator Coupons Using Physical Methods. *J Int Soc Respir Prot* **27**, 11 (2010).
47. Lin, T.-H., Tang, F.-C., Hung, P.-C., Hua, Z.-C. & Lai, C.-Y. Relative survival of Bacillus subtilis spores loaded on filtering facepiece respirators after five decontamination methods. *Indoor Air* **28**, 754–762 (2018).
48. Rutala, W. A., Weber, D. J. & HICPAC. Guideline for Disinfection and Sterilization in Healthcare Facilities. (2019).
49. Malayeri, A., Mohseni, M., Cairns, B. & Bolton, J. Fluence (UV Dose) Required to Achieve Incremental Log Inactivation of Bacteria, Protozoa, Viruses and Algae. *IUVA News* **18**, 4–6 (2016).

Chapter 10

Development of a quantitative UV-C dosimetry technique using photochromic indicators

Adapted with permission from A. Su*, S. M. Grist*, A. Geldert, A. Gopal, & A. E. Herr, "Quantitative UV-C dose validation with photochromic indicators for informed N95 emergency decontamination", *PLOS One*, 2021, and from A. Geldert*, A. Su*, A. W. Roberts, G. Golovkine, S. M. Grist, S. A. Stanley, & A. E. Herr, "Mapping of UV-C dose and SARS-CoV-2 viral inactivation across N95 respirators during decontamination," *MedRxiv and in revision*.

10.1 Abstract

N95 respirator shortages induced by the COVID-19 pandemic have led frontline medical personnel and first responders to reuse this disposable – but sophisticated – multilayer respirator. Widely used to decontaminate nonporous surfaces, ultraviolet-C (UV-C) light has demonstrated germicidal efficacy on porous, non-planar N95 respirators when all surfaces receive ≥1.0 J/cm^2 dose. Of utmost importance across disciplines, translation of empirical evidence to implementation relies upon UV-C measurements, which are frequently confounded by radiometer complexities. To enable rigorous on-respirator measurements, we introduce a photochromic indicator dose quantification technique for UV-C treatment design. While photochromic indicators traditionally have a qualitative readout, our methodology establishes that quantitative color-changing dosimetry can achieve the necessary accuracy (>90%), uncertainty (<10%), and UV-C specificity (>95%) required for UV-C dose measurements. Additionally, we demonstrate that numerous consumer electronics can be adapted for accessible quantitative readout. In a measurement infeasible with radiometers, we observe a striking ~20× dose variation over N95s within one decontamination system. By transforming photochromic indicators into quantitative dosimeters, we illuminate critical considerations for both photochromic indicators themselves and UV-C decontamination processes.

10.2 Introduction

Ultraviolet (UV) light in the UV-C wavelength range is one of three promising methods identified by the United States Centers for Disease Control and Prevention (CDC) for N95 respirator (N95) decontamination as a shortage mitigation strategy during the COVID-19 pandemic [1]. Building upon years of literature evidence demonstrating that specific UV-C doses inactivate viruses while preserving respirator fit and filtration [2–5], UV-C decontamination of N95 respirators has become a rapidly expanding area of interest for both research and implementation [6]. However, effective UV-C bioburden reduction (while appearing straightforward) requires exquisite attention to detail in both treatment design and validation of treatment parameters. Challenges and intricacies of UV-C measurements can stymie study translation when UV-C dose measurements reporting viral inactivation are not robustly characterized. Innovation is urgently needed to introduce new measurement workflows that are both quantitatively robust and translatable across UV-C systems and facilities.

UV-C pathogen inactivation critically depends on two physical properties: wavelength and dose (or fluence), where dose is defined as integrated irradiance over the exposure time. Longer UV-C wavelengths (240-280 nm) inactivate pathogens like SARS-CoV-2 by damaging their genetic material (absorption peak near 260 nm) [7] (**Figure 10.1a**); far (short-wavelength) UV-C also damages proteins [8]. Because UV-C decontamination relies upon pathogen interaction with electromagnetic radiation, efficacy depends on direct line-of-sight between the UV-C source and target surface. As is well established in the literature, UV-C irradiance, and therefore integrated dose, is attenuated throughout the thickness of an N95 respirator due to reflection, absorption, and scattering of UV-C photons as light passes through each porous N95 material layer (**Figure 10.1b**) [9]**.** Thus, in contrast to nonporous surfaces, effective decontamination of N95 respirators requires that the minimally acceptable UV-C dose is delivered not just to viral particles on the exterior surface, but also to those that may be embedded in interior N95 layers. Because integrating dosimeters into intact respirators is infeasible, decontamination efficacy throughout the N95 layers is typically measured in the peer-reviewed literature as a function of UV-C dose applied to the N95 surface. The established approach to quantify the minimum surface UV-C dose for N95 decontamination is to directly assess active virus recovered from throughout the N95 layers (e.g., using the $TCID_{50}$ assay) vs. surface dose [3,10,11]. On the majority of N95 models, studies (almost all of which used 254 nm low-pressure mercury light) support $\geq$1.0 J/cm^2 UV-C dose across the entire N95 surface for $\geq$3-log reduction of SARS-CoV-2 analogues [2,4,12]: a 100-1000× higher dose than that required for non-porous surface decontamination [13].

Researchers have also used an augmented approach to measure UV-C attenuation through the N95 layers, then used this attenuation to scale the surface dose and quantify the inner-layer UV-C dose delivered to embedded viral particles [9]. Critically, measured attenuation varied by a factor of >100 between N95 models [9]; furthermore, the wide variation in N95 morphology enhances inter-model differences in applied UV-C dose because irradiance depends on the incident angle following Lambert's cosine law (**Figure 10.1b**) [14]. Likely because of the impact of both model-dependent attenuation and morphology on UV-C dose reaching the N95's inner layers, UV-C viral inactivation efficacy on N95s varies between models [3,4,9].

UV-C measurement challenges are further exacerbated by radiometer complexities [15]. The accuracy and relative uncertainty of digital UV-C radiometers are established through calibration to a known standard (e.g., from the National Institute of Standards and Technology) [16]; however, accuracy is dependent on sensor linearity, spectral sensitivity, and angular response [15,17] (**Figure 10.1c**) . Though some countries have adopted standards for comparison between sensors [18], no universal standards exist [19]. Consequently, there is large variability between sensors in environments differing from the calibration setup, compromising replicability when detailed reporting is omitted. Furthermore, radiometers are costly, limited, low-throughput, and bulky, precluding measurements on complex 3D surfaces (which require fine spatial resolution and ideal angular response). As a result, UV-C dose is often not robustly characterized, and relative doses over a 3D N95 surface have not yet been empirically quantified using sensors rigorously validated for this application.

Photochromic, color-changing UV-C indicators (PCIs) for evaluating surface decontamination are commercially available and address challenges presented by digital sensors. Due to their low cost and small, flexible form factor, PCIs are ideal for characterizing UV-C uniformity and have been applied for this characterization in hospital rooms [20]. PCIs are intended for qualitative validation; however, there has been effort to quantify color change (a topic of broader interest [21–26]) to characterize water sterilization reactors [27].

In this work, we introduce a novel PCI-based dose quantification workflow (**Figure 10.1d**) for informed design and validation of UV-C N95 decontamination systems. We first demonstrate that PCI color quantification can yield UV-C-specific quantitative dose measurements with high accuracy (**Figure 10.1d, i**) and near-ideal angular response, using a variety of color measurement tools. We then use this relationship between color change and UV-C dose to show how PCIs can be implemented by end users: high throughput dose mapping within the treatment plane (**Figure 10.1d, ii**), combined with assessment of dose distribution across the N95 surface (**Figure 10.1d, iii**) allow PCIs to highlight critical locations to monitor (both on-respirator and on the treatment plane) for informed design. Relative dose measurements using PCIs can then be made on N95s positioned in the identified treatment locations (**Figure 10.1d, iii**) in order to identify the on-N95 locations receiving the lowest and highest UV-C dose. Overall, we show that quantitative PCI-based UV-C dosimetry is an accessible and versatile method to characterize UV-C dose distribution – within the dynamic range of the PCI-color reader pair – on both the treatment chamber floor and N95 surfaces.

10.3 Materials & Methods

UV-C sensors. A Model 308 data-logging UV radiometer equipped with a 254 nm sensor (Optical Associates, Inc., OAI) was used for irradiance measurements in **Figure 10.2**, **Figure 10.4a** and **Figure 10.4d** (all tools except Color Muse), **Figure 10.5**, and **Figure 10.6**. An ILT1254/TD UV-C (International Light Technologies, ILT) radiometer with a near-ideal cosine angular response was used for secondary validation of some OAI irradiance measurements, and was used in **Figure 10.3**, **Figure 10.4b-c** and the Color Muse data in **Figure 10.4d**, and **Figure 10.7**. Both radiometers are NIST-traceable and were calibrated within 2 months of data collection. Dose was calculated from irradiance data measured by the OAI radiometer and data logging software over the exposure time: $dose = \sum_{t_{exposure}}(Irradiance \cdot \Delta t)$.

UV-C sources. Two different Spectroline UV decontamination chamber models (of different sizes) were used as UV-C sources for all experiments other than the angular response measurements.

The larger model (referred to as the '1500 model') was either the XL-1500 Spectrolinker equipped with six low-pressure mercury bulbs (BLE-1T155, uvebay.com) or Spectroline HCL-1500 equipped with six low pressure amalgam bulbs (BLE-1T155, Spectroline); both have the same dimensions. In order to record the dose delivered in the XL-1500 enclosure using the radiometer, the OAI meter was wrapped in UV-C blocking material (PVC) and placed along the back wall of the chamber. This meter was plugged into a Microsoft Surface Pro tablet wrapped in multiple layers of UV-C blocking materials positioned on the left-hand side of the chamber floor. The tablet was controlled remotely using TeamViewer to record irradiance values over time. All PCI dose-response curves were measured near the center of the chamber, beside the Surface tablet. The HCL-1500 chamber had a custom-cut small notch in the door to accommodate a sensor cable. With this modified instrument, data logging could be performed with the meter and tablet outside of the UV-C chamber.

The smaller UV-C chamber model (referred to as the '1000 model') is a Spectronics XL-1000 chamber with BLE-8T254 low pressure amalgam bulbs and a custom-cut notch in the door for a radiometer sensor cable. The UV-C chamber model used for each experiment is stated in the corresponding figure caption.

UV-C dose-response of PCIs. Commercial PCIs marketed for UV-C detection from two different companies were assessed: UVC 100 Dosimeter Dots from Intellego ('PCI1') and Control-Cure® UV-C Intensity Labels (N010-004) from UV Process Supply ('PCI2'). Dose measurements were quantified by integrating irradiance measurements logged by the OAI radiometer over time using a custom Python script, or from measurement logged by the ILT radiometer using a custom MATLAB script. PCIs were placed on a plastic container of similar height to the sensor (16 mm [OAI] or 35 mm [ILT]). The irradiance at the PCI location was verified to be within 0.02 mW/cm^2 of the irradiance at the radiometer location prior to measurements. PCIs were cut into pieces and a single sample was placed on either the digital sensor or plastic container and exposed during bulb warm-up to serve as a saturated reference. D65/10º L*a*b* measurements of both saturated and unsaturated reference PCIs were recorded using an RM200QC spectrocolorimeter (X-Rite). After bulb warm-up, sample PCIs were irradiated for a set amount of time using the "time" operating mode of the UV-C treatment system. After UV-C exposure, the color of the exposed PCI was immediately (within 5 min) assessed using the RM200QC spectrocolorimeter (set to report the average of three measurements of each sample) or other color measurement tool.

Quantifying dose-response curves of PCIs. D65 L*a*b* measurements of PCI color assessed using the RM200QC spectrocolorimeter, along with UV-C doses (integrated from irradiance measurement logs of the radiometer readings: $dose = \sum_{t_{exposure}} Irradiance \cdot \Delta t$) were compiled into a spreadsheet format using custom Python scripts, and then analyzed in MATLAB® using scripts custom-written for this application. In order to minimize the impact of imaging/measurement conditions on the PCI color measurement, color difference from an unexposed PCI was assessed in all cases, rather than absolute PCI color. We computed the sets of equations for the CIEDE2000 ΔE color difference, as defined by Luo, Cui, and Rigg [28]. Our MATLAB implementation of CIEDE2000 was tested using the example color pairs presented by Luo, Cui, and Rigg [28], and found to yield the reported ΔE values for the 10 sample-reference pairs.

Quantifying unknown doses using PCIs. In order to quantify unknown UV-C doses (e.g. across the treatment plane of the UV-C exposure system, or across the surface of an N95 respirator), color measurements from the RM200QC were read in from a spreadsheet into a custom MATLAB® script. Previously generated calibration datasets (CIEDE2000 ΔE measured with the same instrument vs. known UV-C dose, as described in "Quantifying dose-response curves of PCIs" above) were read in and fitted with the calibration functions described in S3 File. For each measurement, the L*a*b* color values for the exposed PCI and unexposed PCI reference (measured on the same day with the same instrument) were read in and the CIEDE2000 ΔE between this pair was computed as previously described. The UV-C exposure dose was predicted from the CIEDE2000 ΔE using the calibration curve. First, the inverse of the fit function was used to predict the dose from the color change. **Eq. 10.1** describes the fit function corresponding to first-order reaction kinetics:

$$dose(\Delta E) = -b \cdot \ln\left(1 - {}^{\Delta E}/_{a}\right) \qquad \textbf{Eq. 10.1}$$

The fit function corresponding to second-order reaction kinetics was defined as **Eq. 10.2**:

$$dose(\Delta E) = \frac{\Delta E}{{}^{1}/_{2} \cdot a^2 \cdot b - a \cdot b \cdot \Delta E} \qquad \textbf{Eq. 10.2}$$

To estimate the uncertainty on the predicted dose measurement (u_{dose}), methods for estimating uncertainties of calibrated values via propagation of error, along with uncertainties on the fitted

parameters (standard deviations s_a and s_b) and ΔE measurement (standard deviation $s_{\Delta E}$), were used to estimate the variance of the measured value u_{dose}^2[29] according to **Eq. 10.3**:

$$u_{dose}^2 = \left(\frac{\delta dose}{\delta a}\right)^2 s_a^2 + \left(\frac{\delta dose}{\delta b}\right)^2 s_b^2 + \left(\frac{\delta dose}{\delta \Delta E}\right)^2 s_{\Delta E}^2 + 2\left(\frac{\delta dose}{\delta a}\right)\left(\frac{\delta dose}{\delta b}\right) s_{ab} \qquad \textbf{Eq. 10.3}$$

Where s_{ab} denotes the covariance between a and b. To complete this computation, s_a, s_b, and s_{ab} were computed from the curve fit covariance matrix, and the partial derivatives of the inverse fit functions used in the computation of are as described in **Table 10.1.**

Table 10.1. Fit functions, inverse fit functions, and partial derivatives used in uncertainty calculations for calibrated measurements.

Fit type	First-order	Second-order
Fit function	$\Delta E = a\left\{1 - e^{-\frac{dose}{b}}\right\}$	$\Delta E = \frac{\frac{1}{2}a^2 \cdot b \cdot dose}{1 + a \cdot b \cdot dose}$
Inverse fit function	$dose(\Delta E) = -b \cdot \ln\left(1 - {}^{\Delta E}/_{a}\right)$	$dose(\Delta E) = \frac{\Delta E}{{}^{1}/_{2} \cdot a^2 \cdot b - a \cdot b \cdot \Delta E}$
$\frac{\delta dose}{\delta a}$	$\frac{-b \cdot \Delta E}{a^2 - a \cdot \Delta E}$	$\frac{4\Delta E(\Delta E - a)}{b \cdot a^2 (a - 2 \cdot \Delta E)^2}$
$\frac{\delta dose}{\delta b}$	$-\ln\left(1 - {}^{\Delta E}/_{a}\right)$	$\frac{-2 \cdot \Delta E}{a \cdot b^2 \cdot (a - 2 \cdot \Delta E)}$
$\frac{\delta dose}{\delta \Delta E}$	$\frac{b}{a - \Delta E}$	$\frac{2}{b \cdot (a - 2 \cdot \Delta E)^2}$

The ΔE measurement uncertainty $s_{\Delta E}$ was measured from the standard deviation of 15 replicate measurements of unexposed PCI1 or PCI2 using the RM200QC, each compared to the same measurement of an exposed (saturated) PCI1 or PCI2, respectively.

Ninety-five percent confidence intervals for predicted doses from each curve fit ($\alpha = 0.05$) were predicted from the estimated variance (u_{dose}^2) using **Eq. 10.4**:[30]

$$CI = dose_{meas} \pm \sqrt{u_{dose}^2} \cdot t_{1-{}^{\alpha}/_{2},\upsilon} \qquad \textbf{Eq. 10.4}$$

where $t_{1-{}^{\alpha}/_{2},\upsilon}$ is the student's t-inverse cumulative distribution (tinv in MATLAB®), and υ is the degrees of freedom for the calibration curve fit. The relative widths of these 95% CIs (normalized to the measured dose) are defined by **Eq. 10.5**:

$$CI_{rel} = \frac{2\left(\sqrt{u_{dose}^2} \cdot t_{1-{}^{\alpha}/_{2},\upsilon}\right)}{dose_{meas}} \qquad \textbf{Eq. 10.5}$$

In experiments where triplicate PCI measurements of unknown doses were acquired and quantified using the calibration curve process described above, the measured doses were first equalized by correcting with a factor related to the dose logged by the radiometer during each exposure to correct for differences in the exposure time/dose between replicate measurements. To perform this correction, the doses measured from the PCI color change (as well as the confidence intervals and standard deviation of the measured value $\sqrt{u_{dose}^2}$) were multiplied by a target dose (constant across the replicate datasets) and divided by the logged OAI radiometer dose. After this correction

for differences in the dose to which the PCIs were exposed, the uncertainty estimated from the standard deviation of the replicate measurements was combined with the uncertainty from the calibration fit measurements by root sum of squares (**Eq. 10.6**):

$$u_{total} = \sqrt{u_{dose}^2 + u_{rep}^2} \quad \textbf{Eq. 10.6}$$

where u_{dose}^2 is as described above, and u_{rep}^2 is the squared standard deviation of replicate measurements. For several datasets, dose measurement data are presented as relative doses ($dose_{norm}$), normalized to measurements at a different location or in a different experimental setup (**Eq. 10.7**):

$$dose_{norm} = \frac{dose_{meas}}{dose_{ref}} \quad \textbf{Eq. 10.7}$$

For these normalized measurements, the uncertainty is calculated from the uncertainties on both the measured and reference estimated doses via propagation of error with **Eq. 10.8**:

$$u_{norm} = |dose_{norm}| \sqrt{\left(\frac{u_{total,meas}}{dose_{meas}}\right)^2 + \left(\frac{u_{total,ref}}{dose_{ref}}\right)^2} \quad \textbf{Eq. 10.8}$$

Measured doses were plotted as heatmaps and histograms using the 'inferno' perceptually uniform, colorblind-friendly colormap, which was created by Stéfan van der Walt and Nathaniel Smith and adapted from Python's *matplotlib* for use in MATLAB® by Ander Biguri [31].

Assessing alternative imaging systems and colorimeters. To compare to other imaging systems, after each PCI exposure, the exposed indicator was imaged between unexposed and saturated references with the iPhone and Nikon D5500 within a FotodioX LED Studio-in-a-Box (FOSIAB2424, B&H) with the grey background installed. A platform was frequently inserted underneath the grey background to raise the PCIs closer to the cameras. The included diffuser sheet was cut and installed to cover the LED lights but not the top hatch. Within the Studio-in-a-Box, raw images of the PCIs were acquired using a Nikon D5500 equipped with a 40 mm macro lens or using Halide on an iPhone X at 2× optical zoom. The settings for both cameras were set manually and kept consistent within each experiment. At the conclusion of each experiment, the PCIs were scanned using VueScan, set to acquire raw images, on a flatbed scanner (LiDE 400, Canon). A Color Muse colorimeter (Variable, Inc, with Variable color app) was also aligned over the PCI using a template to measure color.

In order to compare color quantification from the RM200QC spectrocolorimeter 'gold standard' tool with that from more widely available imaging devices, images of the PCIs acquired with multiple imaging devices were compared. For iPhone and DSLR images, a set of images (one for each exposed PCI) was acquired, each containing the exposed PCI between an unexposed and saturated PCI, with nearby white-balance region and Pantone® color match to the exposed PCI. For the flatbed scanner images, a single image of all of the exposed PCIs from a dose-response experiment, along with a single unexposed and single saturated PCI, was acquired on a white background. iPhone and DSLR images were acquired after each PCI exposure; scanner images were acquired once all PCI exposures in an experiment were complete. Raw images (.DNG for iPhone X, .NEF for DSLR, .TIF for flatbed scanner) were acquired and converted to .TIF format to be read into MATLAB® and analyzed using custom scripts.

In the image analysis script, each image was read in sequentially and the user prompted to draw rectangular areas over (a) the exposed PCI, (b) the Pantone® match to the PCI, (c) the white region proximal to the PCI(s), (d) the unexposed PCI, and (e) the saturated PCI. In all cases, care

was taken to draw a region encompassing only the region of interest (i.e., not edges, dust, or shadowed regions). For the camera images (an image for each PCI), all 5 regions were denoted on each image (for each exposed PCI). For the scanner images (a single image for all PCIs), a single region was denoted for the white, unexposed, and saturated regions, respectively, and used in the analysis for all exposed PCIs in one experiment, with only the PCI region denoted for each exposure dose (Pantone® matches were not scanned). After all regions on each image were selected, the average RGB value for the white region was used to white-balance and exposure-correct the image before computing the average RGB values for the other region types. The RGB value for each region was then converted to the L*a*b* color space using MATLAB®'s built-in rgb2lab function. RGB and L*a*b* values from the processed images were then subjected to the same processing for color difference calculations as described above for the measured RM200QC L*a*b* values in "Quantifying dose-response curves of PCIs".

CIEDE2000 color differences from an unexposed PCI, computed from each image type as well as the RM200QC measurements of the same set of PCIs, were fitted to the appropriate calibration function and plotted (along with 95% prediction intervals) as a function of exposure dose, in order to compare the relative dose-responses and calibration uncertainties measured with each tool.

Characterizing variability across the treatment plane. A 279.4 mm x 431.8 mm paper grid with 63.5 mm markings was centered on the floor of the treatment plane in the 1500 model chamber. After bulb warm-up, the digital UV-C radiometer was placed at specified grid locations and peak irradiance was recorded over 15-20 s. The irradiance at the center of the treatment plane was verified to remain constant every 3-6 measurements to minimize variability caused by bulb output changes. The irradiances at all designated spatial locations were measured in triplicate. For PCI measurements (performed in duplicate), indicators were secured to the spatial locations on a copy of the 63.5 mm grid using double-sided tape. The grid was then inserted into the treatment system atop the master grid. The digital radiometer was placed in its designated location for data logging. After exposure, PCIs were transferred to a consolidated layout for RM200QC analysis and measured within ~15 min.

PCI response to non-germicidal light. A 300 nm longpass filter (#46-417, Edmund Optics) was used to assess the reactivity of the PCIs to wavelengths longer than the germicidal (200-280 nm) UV-C range. For each experiment, one PCI was placed beneath the longpass filter on top of the plastic container and one PCI was placed on the digital sensor as an unfiltered control. Post-exposure color was measured using the RM200QC. In order to assess the reactivity of the PCIs to sunlight, both models of commercial PCI were taped to the same white background using double-sided tape and covered with black cardstock during transport outside. The exposure to sunlight began at 17:50 on May 30th, 2020 in Berkeley, CA, USA, when the UV index [32] was reported as 1 by Apple Weather. The color change was recorded over 5 min via iPhone 8 video. Both pre- and post-exposure PCIs were imaged using the Nikon D5500 and quantified using the RM200QC.

Angular response measurements. PCI angular response was characterized by measuring the RM200QC-measured dose quantified from PCIs exposed to a UV-C point source (Spectroline E-Series handheld UV lamp with a BLE-2537S bulb and custom-built 2.54 cm diameter aperture) at different angles of incidence. To ensure the UV-C source was point-like (i.e., near-normally incident to a PCI perpendicular to the optical axis), we first determined the distance at which UV-C output power is independent of distance by measuring the irradiance at several distances from the UV-C source using a radiometer[16]. UV-C output power at each distance was calculated from the Keitz equation using average (N = 3) irradiance measured at different distances from the UV-

C source. The distance from the UV-C source at which output power changes by <5% between measurements (determined here to be ≥10.2 cm) was considered to be the point at which UV-C output power is independent of distance, which indicates that UV-C light is near-normally incident to a PCI perpendicular to the optical axis.

To measure PCI angular response, UV-C dose measured by a PCI with differing incident light angles from a UV-C point source, normalized to the measured dose at 0^o. Angular response was measured between 0^o-90^o in 15^o increments, in accordance with the range of angles used to characterize the angular response of other dosimeters.[33] Each PCI was affixed with double-sided tape to a glass microscope slide in a filter holder (Thorlabs FH2) mounted on a rotation platform (Thorlabs QRP02). PCIs were placed 10.2 cm away from a UV-C lamp (Spectroline E-Series handheld UV lamp with a BLE-2537S bulb and custom-built 2.54 cm diameter aperture). At this spacing, UV-C is near-normally incident to a PCI perpendicular to the optical axis based on UV-C output power measurements collected at different distances. To ensure consistent UV-C output between exposures, a radiometer was used to monitor dose during each exposure; all PCIs within an experiment were exposed to the same dose, as measured by the radiometer. To avoid shadowing, the radiometer was placed behind the PCI and at an offset such that the PCI/glass slide did not shadow the radiometer.

Measuring dose received by N95 respirator surface. PCIs were affixed to the appropriate location on the surface of a NIOSH-approved Gerson 1730 N95 respirator using double-sided tape. Due to the limited dose range of the PCIs, preliminary experiments were conducted to determine an exposure time that caused all PCIs to change color within the dynamic range of the color calibration curves. For all but one condition, the exposure time was set for 8 s. For two exposures using PCI2 to quantify dose on a peripheral N95, the time was set for 19 s to take advantage of more of the PCI2 indicators' range. These differences in exposure were compensated for in the analysis workflow described in "Quantifying unknown doses using PCIs" above. The respirator was positioned in its marked location within the UV-C source (either center or periphery). In the center, the straps were spread away from the respirator to minimize shadowing. For measurements of the respirator on the periphery of the treatment plane, the straps were taped together and tucked under the respirator. The OAI radiometer, with a corresponding PCI on top, was placed in its designated location for irradiance logging. The color of all PCIs after exposure was recorded using the RM200QC.

Visualizing reduced UV-C transmission through permanent marker ink. To demonstrate spatially resolved measurement, we visualized the UV-C shadowing abilities of permanent marker ink. The "Cal" university logo was drawn with Sharpie® permanent marker on a UV-C-transmissive (~82% transmittance) plastic plate sealer adhesive film. The plastic film with permanent marker logo was then placed atop a PCI1 indicator within the UV-C treatment plane and exposed to UV-C for ~10s (applied UV-C not precisely controlled for this qualitative test). After exposure, the film and exposed PCI were imaged using the flatbed scanner.

10.4 Results & Discussion

Specifications for quantitative PCI-based UV-C dosimetry. UV-C dose measurements are frequently the only link between viral inactivation studies and implementation of each decontamination cycle. Decontamination efficacy and safety consequently depend on robust UV-C measurements, defined by several critical metrics (**Figure 10.1e**) for which we have defined marginal and ideal values (**Table 10.2**).

First, we considered the dynamic range of measurement. The marginal dose measurement dynamic range for *in situ* validation of an N95 decontamination process (≥1.0 J/cm^2) is based upon the marginally-acceptable dose to be delivered to each and every N95 surface for ≥3-log inactivation of enveloped viruses (based on peer-reviewed evidence in the scientific literature [2,4,12]). The measurement method needs to be able to discern whether this dose has been exceeded. Ideally, the measurement range would be higher (>3.0 J/cm^2) as the location of the reference sensor during decontamination will likely receive a higher dose than the N95 surface receiving the lowest dose due to shadowing and the model-dependent angles of the N95 surfaces. While the dynamic range of PCIs alone did not meet the design specification for in-process validation (**Figure 10.2**), we investigate strategies to extend PCI dynamic range in Chapter 11. However, because informed design of N95 decontamination systems and processes can use relative dose measurements, the necessary dose measurement dynamic range for informed design can be lower than that for in-process validation. >0.1 J/cm^2 was chosen as the marginal value for this application to ensure that the UV-C exposure times for informed design were no less than 1/10th those for in-process validation. As informed design uses the same exact UV-C exposure system as that used for the actual decontamination process, low dynamic range PCIs would require very short exposure times because the systems are designed to deliver ≥1.0 J/cm^2 during a reasonable exposure time. These short exposure times during informed design may (1) not be feasible or (2) introduce unacceptable degrees of run-to-run variability.

Next, we considered the allowable uncertainty of dose quantification. The calibration uncertainty for very well characterized UV-C radiometers is ~5% [34] (although many radiometers will not reach this level due to sources of error in UV-C measurements [35]). As measurement solutions like PCIs have advantages over even the best calibrated radiometers (e.g., form factor), we identified a marginal target for PCIs of 4 times the value for radiometers, and an ideal target as twice the radiometer value. These values (20% and 10%, respectively) allow reasonable 'safety factors' of <50% to be implemented to ensure minimally-acceptable doses are reached. Safety factors are multipliers on the target dose to take into account uncertainty on the measurements (e.g., for 20% total propagated uncertainty, one may want to use a safety factor of 1.5 and ensure at least ≥1.5 J/cm^2 was delivered to all N95 surfaces). Similarly, accuracy values (how well measurements align with a calibrated, NIST-traceable reference measurement) were chosen to align with target relative uncertainty.

Finally, UV-C measurements for decontamination characterization and validation should only report irradiance or dose within the germicidal range (UV-C extends to 280 nm; germicidal efficacy at 300 nm is <10% of that at 254 nm [36]). For wavelength specificity, we selected marginal and ideal values such that the measurement response to >300 nm was 1-2 orders of magnitude less than that to <300 nm light from a commonly employed low-pressure mercury/amalgam source.

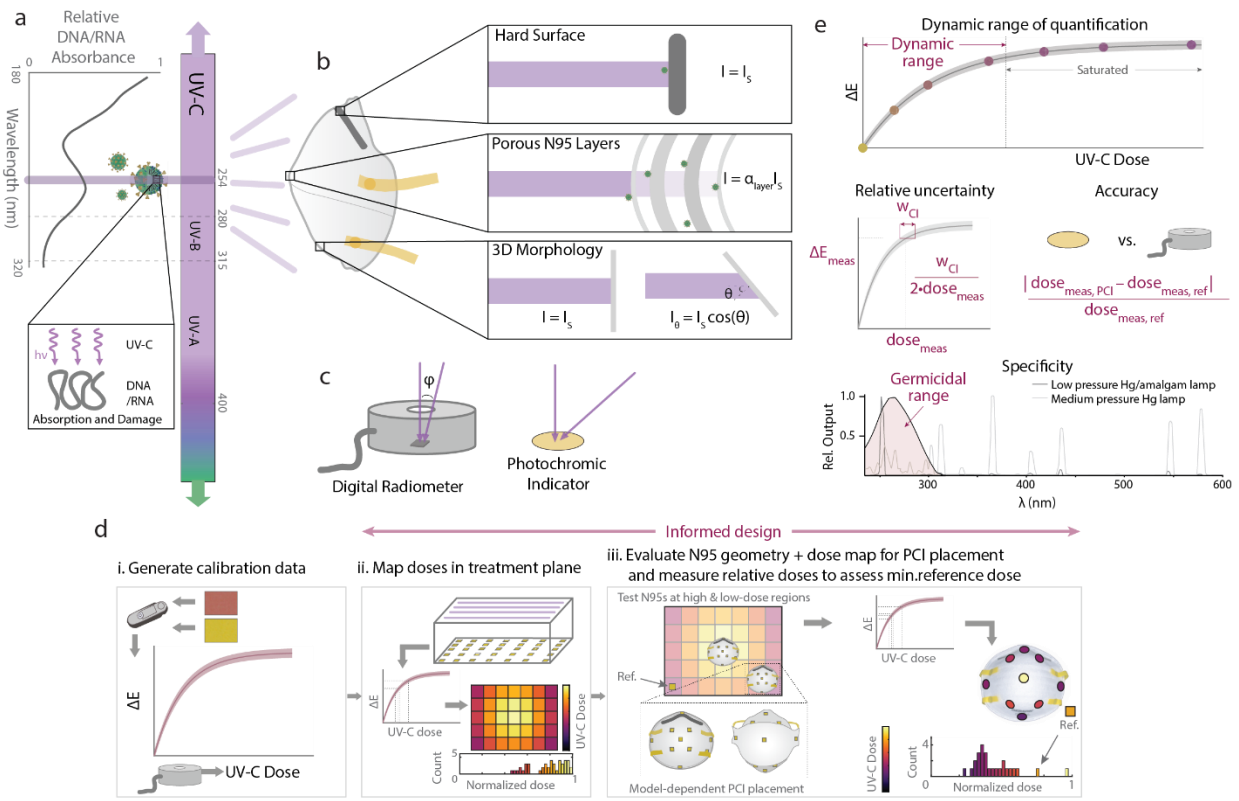

Figure 10.1. Mechanism and challenges of UV-C for N95 decontamination. (a) UV-C at 254 nm primarily inactivates pathogens by damaging genomic material (absorption peak near 260 nm). (b) The multilayer porous N95 materials and 3D morphology reduce the irradiance (and thus dose) available for pathogen inactivation compared to the irradiance that reaches nonporous surfaces (I_S), like the metal nosepiece (α_{layer} represents the layer-dependent attenuation factor). (c) UV-C detectors often have angle-dependent responses that differ from the ideal cosine response expected from a surface such as flat PCIs. (d) The introduced workflow allows end users to both design and validate their UV-C systems, reducing source- and sensor-specific inaccuracies. Critically, assessment of treatment area dose nonuniformity informs N95 placement during on-N95 measurements; on-N95 measurements in turn determine the parts of the N95 receiving the lowest and highest dose. On-N95 measurements are designed to specifically measure steep-angled or potentially shadowed N95 regions. (e) Robust UV-C measurements must meet key specifications, including dynamic range of quantification (before the indicator saturates), relative measurement uncertainty (determined from error propagation from the confidence intervals on the calibration curve fit), accuracy of the measurement compared to a calibrated standard sensor, and specificity of the PCI response to the germicidal wavelength range (in order to accurately report germicidal activity). Nucleic acid absorbance spectrum modified from Voet et al. [37]. SARS-CoV-2 diagrams adapted from an image by Maya Peters Kostman for the Innovative Genomics Institute.

Table 10.2. Specifications for robust UV-C measurements.

Number	Metric	Units	Marginal value	Ideal value
1	Dose measurement range (in-process validation)	J/cm^2	≥ 1.0	> 3.0
2	Dose measurement range (informed design)	J/cm^2	> 0.1	> 0.3
3	Relative uncertainty on dose measurement (CI)	%	< 20	< 10
4	Accuracy	%	> 80	> 90
5	Sensitivity to non-germicidal longer wavelengths	%	< 5	< 1

UV-C dose can be quantified from PCI color change. PCIs have the potential to fill three urgent gaps in UV-C dose validation; however, a quantitative rather than qualitative readout strategy is required. To assess the indicators' suitability for contributing to informed design of UV-C treatment processes, we introduce a novel quantification workflow and demonstrate the capability to measure spatial heterogeneity within a UV-C treatment system from a single exposure. We first assessed whether UV-C dose could be quantified from the color change of commercially available PCIs; quantification relies upon distinct, reproducible color change that follows a known, predictable relationship. Measurement of color differences between the sample and a reference (rather than absolute colors) improves quantification robustness as the difference between two colors measured under the same conditions is less sensitive to many confounding effects [21,22]. To test whether two models of commercial PCIs (Intellego UVC 100 Dosimeter Dots: 'PCI1', and UV Process Supply UV-C Intensity Labels: 'PCI2') could meet the specifications of S1 Table, we exposed them to UV-C doses measured with a calibrated radiometer, quantified their endpoint color using an RM200QC spectrocolorimeter (outputting a single L*a*b* color per PCI), and computed the CIEDE2000 [28] industry-standard color difference (ΔE) from an unexposed indicator as a function of UV-C dose (**Figure 10.2a**). Both PCI models showed visually discernable color change up to ~0.15 J/cm^2. PCI1 has a higher maximum ΔE of ~45 compared to ~25 for PCI2 (**Figure 10.2a**). Higher maximum ΔE will lead to lower relative uncertainty for a constant color difference measurement uncertainty. We observe some batch-to-batch variation among calibration curves for PCI1 (**Figure 10.3**), although overall shape of the curves is similar.

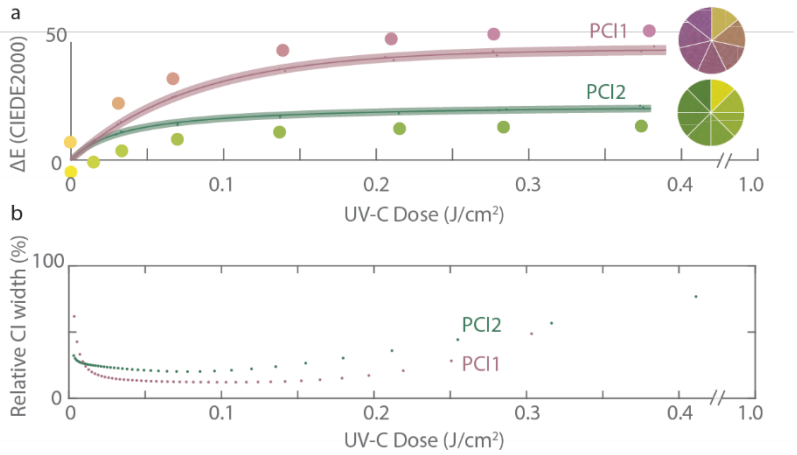

Figure 10.2. Robust color measurement facilitates UV-C dose quantification from two models of PCIs. (a) CIEDE2000 color difference between exposed and unexposed Intellego UVC Dosimeter Dot (PCI1, pink) and UV Process Supply UVC Intensity Label (PCI2, green) as a function of UV-C dose. Dose-responses for PCI1 were fit with a calibration function corresponding to first-order reaction kinetics (**Eq. 10.9**: R^2 = 0.998; a = 47.1 (46.1, 48.1); b = 80.4 (74.6, 86.3); 95% confidence interval on fit parameters reported in parentheses). Dose responses for PCI2 were fit with a calibration curve corresponding to second-order reaction kinetics (**Eq. 10.10**: R^2 = 0.992; a = 47.7 (45.9, 49.5); b = 0.00060 (0.00049, 0.00072)). PCI color is depicted by the RM200QC-measured color values (circles) and digital SLR camera (DSLR) image swatches in the comparison wheels. For each PCI type, the datapoints within the shaded region denote individual PCI measurements, line denotes best fit, and shaded region denotes 95% prediction interval on prediction of color change from observation of UV-C dose. (b) Relative quantification uncertainties using the PCI calibration workflow. Plots depict quantified 95% confidence intervals on measurements of UV-C dose from CIEDE2000 color difference between exposed and unexposed PCIs, normalized to and as a function of UV-C dose. All measurements were made in the 1500 chamber model.

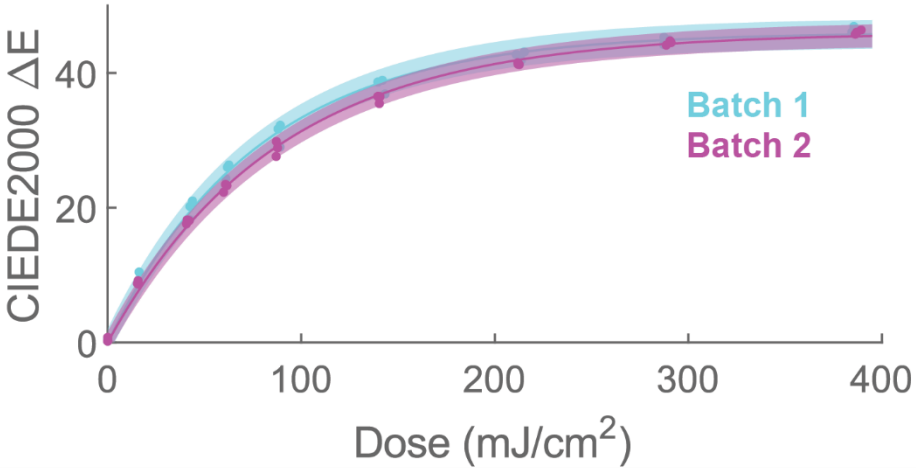

Figure 10.3. PCI calibration curve is batch-dependent. Each curve consists of 3 replicate datasets using PCI1 in the 1000 chamber model, and was fit to the function based on first-order reaction kinetics defined by Su & Grist, et al.[38] For batch 1, R^2 = 0.9964, a = 46.0 (45.2, 46.8), b = 77.6 (73.5, 81.6). For batch 2, R^2 = 0.9976, a = 46.0 (45.3, 46.7), b = 87.4 (83.6, 91.2). Batch to batch variation may be due to changes in PCI starting color or variation in indicator reaction kinetics.

We next scrutinized whether fitting the ΔE vs. dose data to a calibration function could predict UV-C dose from ΔE with relative dose measurement uncertainty below the 10-20% thresholds of **Table 10.2**. We fit the data to calibration functions based upon first- and second-order reaction kinetics. For PCI1, we used a fit function corresponding to first-order reaction kinetics (a, b are fit parameters) (**Eq. 10.9**):

$$\Delta E = a\left\{1 - e^{-\frac{dose}{b}}\right\} \qquad \textbf{Eq. 10.9}$$

while for PCI2 we observed better goodness-of-fit with a fit function corresponding to second-order reaction kinetics (**Eq. 10.10**):

$$\Delta E = \frac{\frac{1}{2}a^2 \cdot b \cdot dose}{1 + a \cdot b \cdot dose} \qquad \textbf{Eq. 10.10}$$

We note that although these fit functions serve as effective calibration functions with high goodness-of-fit, the current implementation does not facilitate extraction of reaction parameters (e.g., reaction order, reaction rate) from the curve fit because the relationship between CIEDE2000 and colored reaction product concentration is not known. The unknown chemical composition of the commercial PCIs confounds determination of reaction parameters. Colorimetric absorbance of dye on paper has been found to deviate from Beer's Law [24], so careful calibration of colorimetric absorbance over a range of known dye concentrations is required to quantify concentrations or reaction kinetics from colorimetric absorbance on paper [39]. Nevertheless, adoption of colorimetric absorbance approaches will be useful to inform design of new optimized chemistries for PCI materials.

We assessed the precision of the measurement by comparing the width of the dose measurement confidence intervals (CIs) to the respective dose values (**Figure 10.2b**). The relative 95% CIs on UV-C doses measured with the calibration function from known CIEDE2000 color differences were considerably larger for PCI2 than for PCI1, suggesting that PCI1 is better-suited to robust UV-C quantification using CIEDE2000. Dose quantification uncertainties are dependent

on the ΔE uncertainty, encompassing both the uncertainty of the measurement tool and the variability in PCI coating color. Using an experimentally determined ΔE uncertainty of 0.273 for PCI1 and 0.083 for PCI2 (see Methods), we find that the two PCI models yield disparate relative uncertainties on the dose measurements. At a dose of ~0.1 J/cm^2, the relative CI width (width of the CI divided by the measured dose) of PCI1 is 12.1%, equivalent to 6.05% relative uncertainty and meeting the <10% ideal relative uncertainty target. At the same dose, the relative CI width of PCI2 is 21.2%, equivalent to 10.6% relative uncertainty. PCI2 thus does not meet the ideal relative uncertainty target but does meet the marginally acceptable 20% relative uncertainty target. PCI1 relative uncertainty remains <10% up to ~0.20 J/cm^2. The relative quantification uncertainty of PCI1, while higher than that established for calibration of UV-C radiometers under ideal conditions [34], should still facilitate dose quantification as long as appropriate safety factors on applied dose (i.e., a multiplier >1) are included in the N95 treatment protocol to account for the propagated relative uncertainty in the dose measurement and ensure minimum doses are met.

We note that the PCI color changes are governed by reaction kinetics; thus, environmental factors (e.g., temperature and humidity) are expected to affect the rate of color change with dose [40,41]. Additionally, we have observed PCI color instability after exposure; thus, PCIs should be quantified immediately (within 10-20 min of exposure for these models). Although the PCI1 quantifiable dynamic range of <0.2 J/cm^2 is not sufficient for in-process validation (≥1.0 J/cm^2 to all N95 surfaces [2–4]), it meets the ≥0.1 J/cm^2 marginal threshold to assess relative doses for informed design of UV-C treatment systems.

To overcome spectrocolorimeter limitations (e.g., cost, availability, and throughput) as well as work towards capturing spatial information already recorded in the PCIs, we generated and assessed device-specific calibration curves using widely available imaging tools under controlled lighting conditions. The calibration curves were generated from images of PCI1 acquired using a flatbed scanner (Canon LiDE-400), a digital SLR camera (DSLR, Nikon D5500), and a smartphone (iPhone X) (DSLR and iPhone images were acquired in a light box to minimize the impact of ambient illumination). All tools captured raw images of the entire surface of both the exposed PCI as well as an unexposed reference PCI. The resulting calibration curves were then compared to those generated with data from the RM200QC (**Figure 10.4a**). Additionally, we compared PCI quantification using two different colorimeters – the RM200QC spectrocolorimeter and substantially lower-cost alternative, the Color Muse colorimeter (**Figure 10.4b**). The relative uncertainty of each color reader was also characterized as a function of dose (**Figure 10.4c,d**). We observe the highest CIEDE2000 ΔE values from measurement with the cameras. Though the flatbed scanner measures the lowest ΔE values, its measurements trend with those of the RM200QC and conveniently do not require a light box. Color measurement literature stresses that careful control of lighting conditions (e.g., using an enclosed light box or contact measurement) is critical in order to minimize variation induced by changes in ambient lighting [22,42]. Even under identical lighting conditions with tight control of acquisition parameters, different imaging devices have different spectral sensitivities and color processing. For this reason, device-specific calibration (using a stringent color reference chart with a range of known colors) has been proposed as an essential step for image-based color quantification for several applications [23,24,42,43]. A smartphone algorithm has been generated for this purpose [26], and flatbed scanners may be a promising, accessible approach provided raw images are acquired (e.g., with third-party software). Overall, these results suggest that with rigorous characterization and proper implementation, widely available imaging tools are appealing for spatially resolved and/or lower-cost PCI quantification.

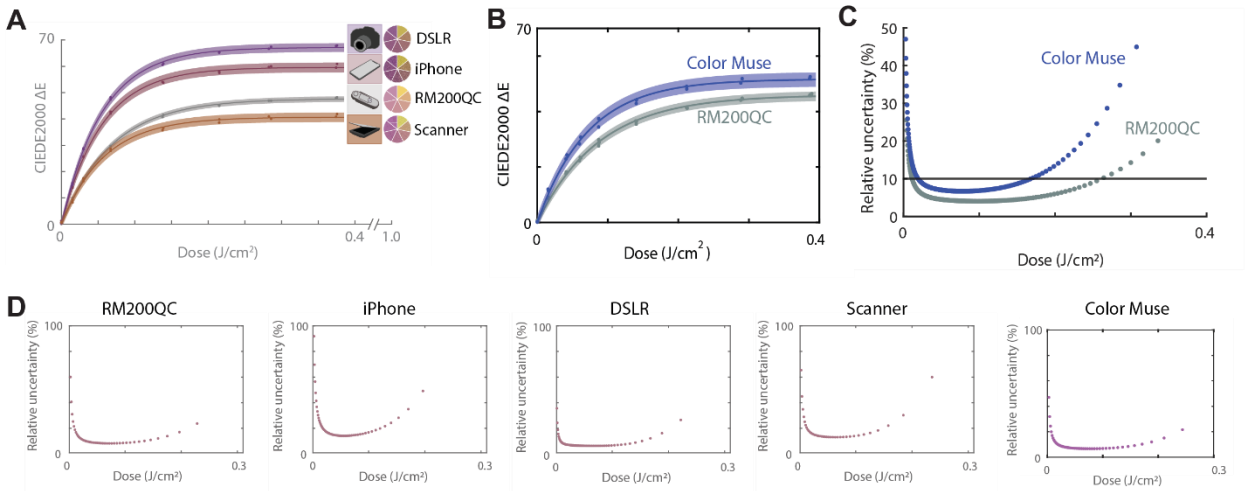

Figure 10.4. UV-C dose quantification from PCIs is feasible with numerous different color measurement tools. PCI1 was used for all calibration curves. (a) Comparison of calibration curve fits of CIEDE2000 ΔE from an unexposed PCI vs. UV-C dose, where PCI color is quantified using the digital SLR and iPhone X in a light box, RM200QC spectrocolorimeter, and flatbed scanner. Datapoints within the shaded region denote individual PCI measurements, line denotes best fit, and shaded region denotes 95% prediction interval on prediction of color change from observation of UV-C dose. PCI color is depicted by swatches indicating either the RM200QC-measured color values or image swatches (for the iPhone, DSLR, and scanner) in the comparison wheels. All calibration curves were measured in the 1500 model UV-C chamber. (b) Comparison of calibration curve fits for two colorimeters: the RM200QC spectrocolorimeter (N = 3 replicate datasets) and the Color Muse (N = 2 replicate datasets) colorimeter. Datapoints within the shaded region denote individual PCI measurements, line denotes best fit, and shaded region denotes 95% prediction interval on prediction of color change from observation of UV-C dose. Calibration curves were measured in the 1000 model UV-C chamber. (c) Relative uncertainty of dose measurements made in the 1000 model chamber. Relative uncertainty is defined as half the width of the 95% confidence interval on UV-C dose measurements, divided by measured dose. UV-C dose measurements have <10% relative uncertainty from 11.3 – 261.4 mJ/cm^2 (RM200QC) or 19.2 – 168.1 mJ/cm^2 (Color Muse). (d) Relative uncertainty of dose measurements made with all color measurement tools. All measurements were made in the 1500 model chamber except for the Color Muse measurements, which were made in the 1000 model chamber.

We also used the quantification workflow to start to investigate PCI specificity to UV-C wavelengths (**Figure 10.5**). Specificity of the measurement tool to UV-C light is important because many UV-C sources (e.g., medium-pressure mercury or xenon arc lamps) emit wavelengths outside of the germicidal UV-C range [7]. Even near-monochromatic UV-C sources such as low-pressure mercury and amalgam lamps emit wavelengths >300 nm (**Figure 10.1e**) [44]. We asked two questions: (1) how much of the PCI color change from low-pressure amalgam bulbs is due to non-germicidal wavelengths, and (2) how susceptible are PCIs to perturbation by spurious solar exposure during transport or storage. When exposed to filtered (>300 nm) low-pressure amalgam illumination, one PCI (PCI1) showed negligible color change, thus meeting the <5% specification. In another PCI model (PCI2), the same longer-wavelength, non-germicidal components of the emission generated ~19% of the total color change resulting from 280 mJ/cm^2 measured from the unfiltered source, highlighting how specificity to the germicidal range is PCI model-dependent. Similar results were observed when the two PCI models were exposed to natural sunlight (**Figure 10.5**). These results demonstrate the importance of UV-C specificity characterization when assessing PCIs. We see quantitative assessment and reporting of PCI color change in response to well-controlled, known non-germicidal wavelengths as beneficial to PCI development. Specifically, PCI color change arising from exposure to common UV sources including low,

medium, and high-pressure mercury lamps, xenon arc lamps, and solar simulators would inform both end users and future PCI design iterations.

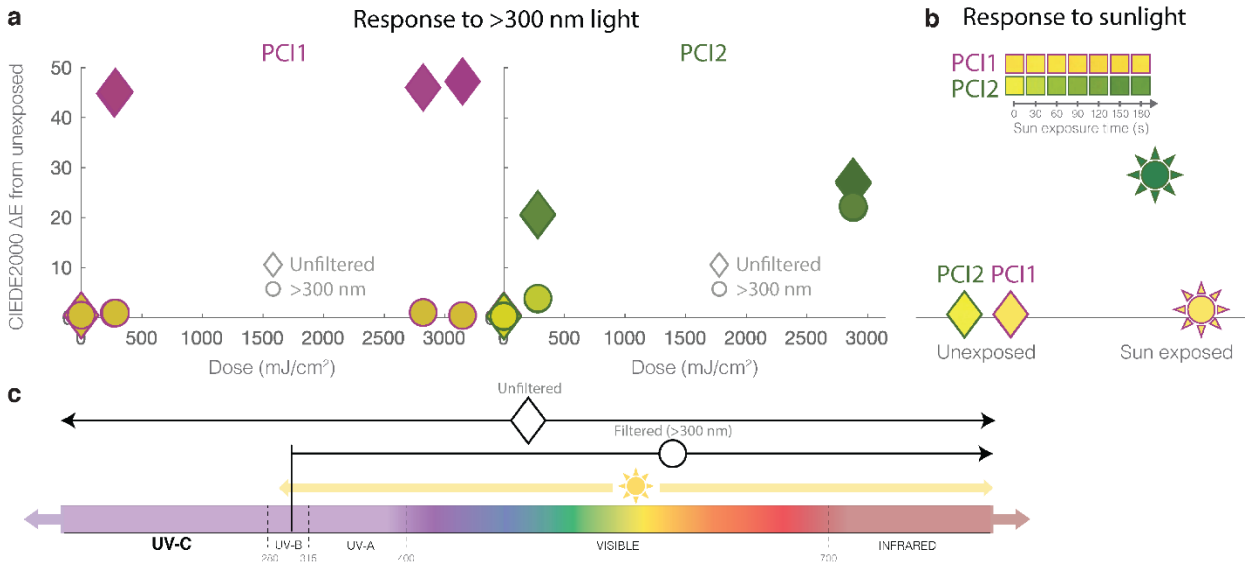

Figure 10.5. Assessing PCI specificity to germicidal UV-C wavelengths. PCI quantification workflow reveals model-dependent indicator specificity to germicidal UV-C. (a) Comparing responses from bare, unfiltered indicators (diamonds) to those underneath a longpass filter (circles; blocking light below 300 nm) quantifies the sensitivity of PCIs to >300 nm light. Dose axis denotes unfiltered 254 nm UV-C dose measured with the OAI radiometer, and measurements were made in the 1500 model chamber. N = 2 replicates are plotted. (b) Quantified color change after sun exposure of the indicators outdoors assesses indicator sensitivity to sunlight. Pink symbol outlines correspond to PCI1, green symbol outlines refer to PCI2. Symbol fill color depicts the sensor color of each measurement (yellow shows minimal color change; pink or green shows color change). Inset shows the white-balanced PCI color recorded over time using iPhone 8 video (not raw). Plot shows a representative replicate of N = 2 PCIs. (c) Schematic showing the relevant portion of the electromagnetic spectrum and the relevant wavelengths associated with the filtered and unfiltered measurements and sunlight.

Characterizing UV-C dose distribution across UV-C chamber floor using PCIs. Having established a novel PCI quantification workflow, we next asked whether PCI measurements could scrutinize spatial dose uniformity within a UV-C treatment system as the first step towards informed design of N95 decontamination (**Figure 10.1d, ii**). Guiding principles of optics dictate that irradiance nonuniformities will be present in nearly any UV-C treatment system; however, the accuracy and reproducibility of UV-C measurements is hindered by a lack of standardization of critical sensor properties such as angular response, which can drastically impact readings [17,35] (with system-dependent impact). We first mapped UV-C dose within a Spectroline HCL-1500 UV-C source using simulation (**Figure 10.6a**) and 23 individual OAI 308 radiometer measurements (**Figure 10.6b**). We observed that the radiometer under-reports irradiance and dose due to its nonideal angular response[38]; the reported readings (**Figure 10.6b**) are post-correction. After correction, the irradiance measured near the corners of the treatment plane is ~40% of that measured at the center.

We leveraged the nonuniform treatment plane irradiance to validate our quantification workflow by comparing PCI-measured doses (**Figure 10.6c-d**), quantified using the appropriate calibration curve depicted in **Figure 10.2a**) to corrected radiometer measurements (**Figure 10.6b**). The relative quantification error ($|dose_{PCI} - dose_{radiometer}|/dose_{radiometer}$) for PCI1 is 7% ± 7% (mean ± standard deviation of N = 23 spatial measurements averaged across N = 2 replicates),

meeting the >90% accuracy target. In contrast, the relative quantification error for PCI2 is 28% ± 10%, failing to meet the marginal >80% accuracy target. While it is unclear why PCI2 performs so discordantly in this test, the good agreement between PCI1 and the radiometer suggests not only that our PCI quantification workflow can capture nonuniformities in a single UV-C exposure (compared with 23 radiometer exposures), but also that color difference quantification should facilitate new classes of measurements not feasible with radiometers.

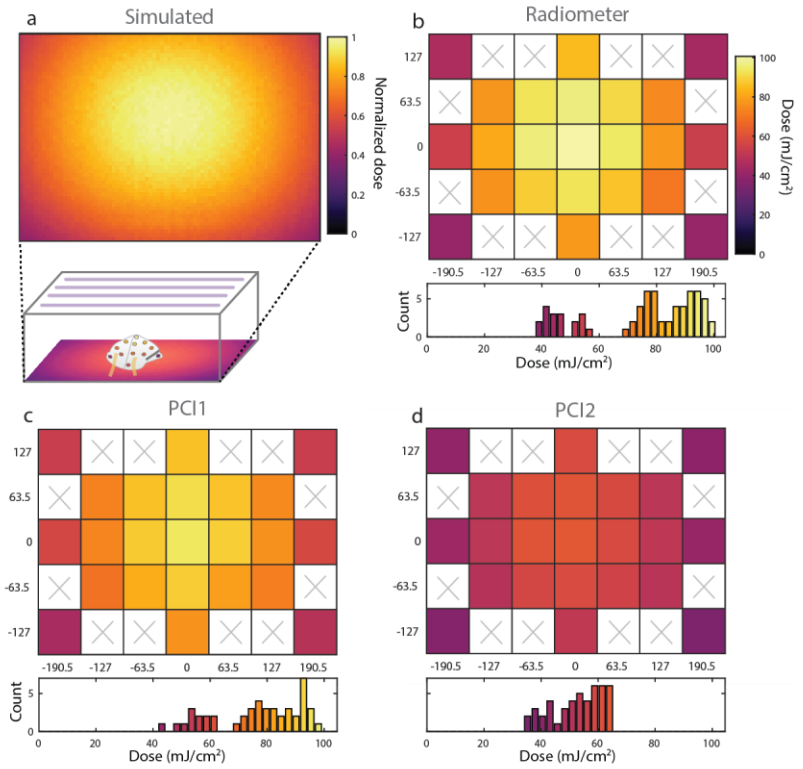

Figure 10.6. Spatial variation in UV-C dose across the UV-C chamber floor. Heatmaps and histograms of delivered UV-C dose to locations across the treatment plane, quantified with (a) Zemax OpticStudio simulations (plot depicts relative dose), (b) digital radiometer (with correction factor, mean of N = 3 measurements at each location), (c) PCI1 (mean of N = 2 measurements at each location), and (d) PCI2 (mean of N = 2 measurements at each location). The PCI2 model appears to underestimate both dose and nonuniformity. Heatmaps in (b-d) are plotted on the same color scale (up to the radiometer maximum measured dose), while heatmap in (a) depicts dose normalized to the highest value observed. White regions with '×'s in (b-d) were not measured. All measurements were made in the 1500 model chamber.

PCI-based UV-C dose quantification on non-planar surfaces. Next, we sought to investigate whether PCIs could be used to quantify UV-C dose across complex 3D morphologies, where measurement with bulky radiometers is not possible. For accurate measurement on non-planar surfaces and/or in systems with uncollimated light, PCIs must have an ideal angular response (i.e., the dose measured by the PCI should vary as the cosine of the angle of incidence of radiation, according to Lambert's cosine law[14]). We measured the angular response of PCIs by characterizing the dose measured by PCIs at a range of angles of incidence, as described previously[16], and verified a near-ideal response (**Figure 10.7**), confirming that PCIs are suitable to measure UV-C dose on non-planar surfaces.

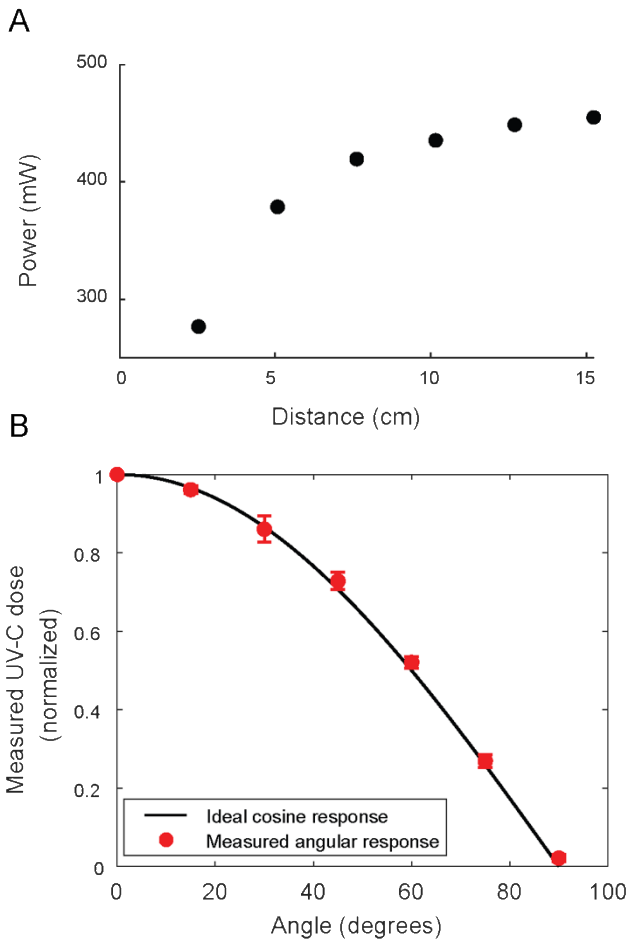

Figure 10.7. Measuring PCI angular response. (A) UV-C output power is independent of distance (i.e., output differs by <5% between distances) at ≥10.2 cm from the UV-C source. For angular response measurements, the PCI should be placed at a distance such that UV-C output power is independent of distance. (B) UV-C dose measured by a PCI with differing incident light angles from a point-like UV-C source, normalized to the measured dose at 0°, indicates that PCIs have near-ideal cosine angular response. The mean of 3 replicates is plotted (error bars are the standard deviation of the replicates).

To highlight the impact of our workflow, we mapped relative UV-C doses across the 3D morphology of a Gerson 1730 N95 respirator in three orientations (**Figure 10.8a**) informed by the treatment area dose mapping (**Figure 10.6**). We exposed PCI1 indicators located on exterior and interior N95 surfaces to sub-saturating UV-C treatments (**Figure 10.8b-d**). Limited by PCI dynamic range, the exposure times were insufficient for N95 decontamination, but did measure relative dose delivered to different respirator regions (informed design, **Figure 10.1d,iii**). We observe that while nonuniformities in the system alone suggest ~2.5× irradiance nonuniformity across the treatment plane (**Figure 10.6**), on-N95 measurements show that nearly 20× disparity exists across multiple N95s in the same treatment system (**Figure 10.8b-d**).

The respirator morphology has a striking impact on delivered dose: even in the center of the treatment plane there are regions on the exterior (convex) N95 surface that receive only ~25% of the dose at the apex (**Figure 10.8b**). There is similar but less dramatic nonuniformity present on the respirator interior (exposed concave side-up) (**Figure 10.8c**). Perhaps most strikingly, there are regions of a respirator in the treatment plane periphery (**Figure 10.8d**) that receive only 6% of the dose at the apex of the central N95 (**Figure 10.8b**). Due to the angular dependence of

irradiance [14] as well as respirator self-shadowing stemming from the 3D morphology with respect to the UV-C source, the entire N95 surface must be considered when estimating UV-C dose for decontamination; measuring the irradiance in an empty system does not sufficiently predict irradiance on the N95 surface. Scientific evidence suggests that all N95 surfaces must receive ≥1.0 J/cm^2 UV-C dose for 3-log bioburden reduction of several enveloped viruses [2–4]; however, our results show that 1.0 J/cm^2 delivered to the apex of the central N95 in this system would result in only 0.06 J/cm^2 applied to the side of an N95 placed in the periphery of the treatment plane. While this dose heterogeneity is certainly system- and N95 model-specific, it underscores the challenges of N95 decontamination and the critical importance of considering complex 3D geometries when designing and validating UV-C decontamination workflows.

In contrast with single-point radiometers, each PCI also records spatially resolved doses (**Figure 10.8e**). As many N95 decontamination implementations track N95s using permanent marker labelling, we assessed whether such labels might shadow underlying respirator layers by positioning a pattern ('Cal') drawn on UV-C-transmitting film overtop a PCI1 indicator during exposure. We observe pattern transfer onto the indicator (**Figure 10.8e**), suggesting that material underneath marker labels may not be as effectively decontaminated as unmarked regions. These examples of on-respirator dose quantification and spatially resolved measurement illustrate the novel, robust measurements PCIs can provide when combined with suitable, spatially resolved readout tools (vs. the single-measurement spectrocolorimeter), better informing UV-C treatment design.

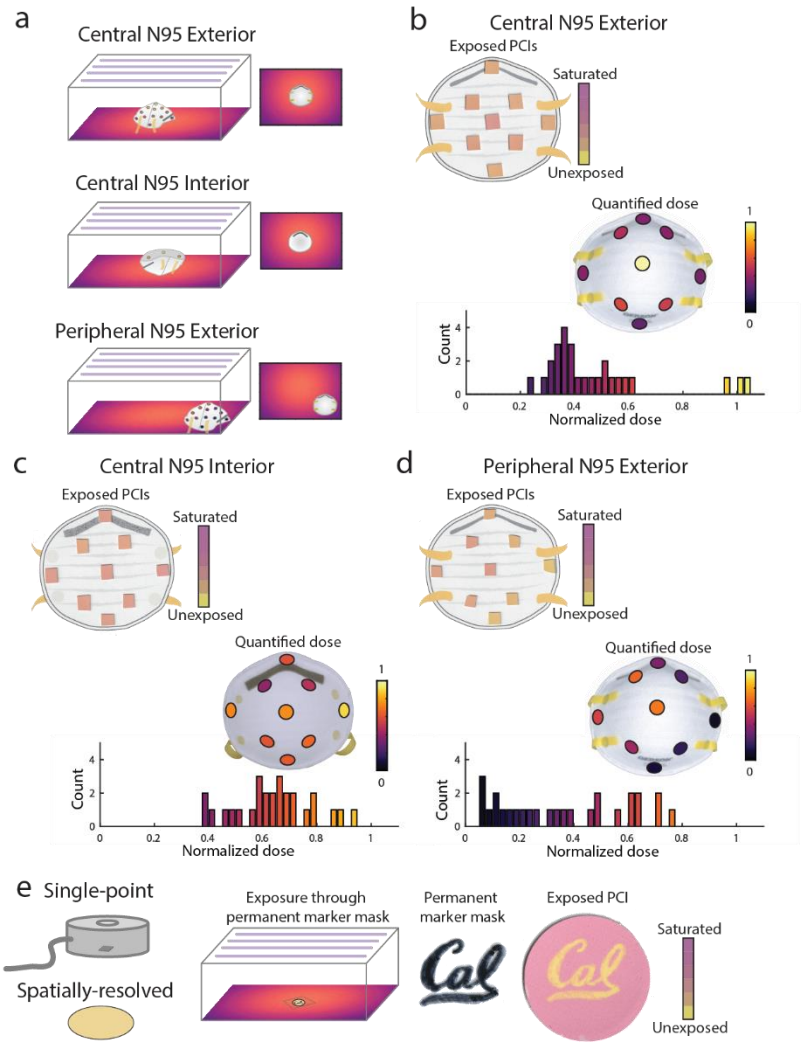

Figure 10.8. Quantifying PCIs elucidates UV-C treatment questions not measurable with radiometers. (a) Illustration of the three sets of on-N95 measurements, mapping dose across: (1) the exterior of an N95 placed in the treatment plane center (highest-dose region), (2) the interior of an N95 placed in the treatment plane center, (3) the exterior of an N95 placed in the treatment plane periphery (lowest-dose region). (b-d) Scanned PCI1 images and corresponding UV-C dose quantified from PCI1 at various respirator surface locations. Although PCI color differences can appear subtle, quantification reveals substantial dose variation. Each relative dose measurement is normalized to the measurement at the apex of the central 'convex-up'-oriented (exterior) respirator. Scanned images show a representative replicate, on-N95 heatmaps plot the mean of N = 3 measurements, while the histograms below each measurement plot all individual measurements. (b) Exterior of central respirator; ~3-4× dose difference is measured across the respirator surface. (c) Interior of central respirator. (d) Exterior of peripheral respirator. The corner-facing side of the N95 at the peripheral location is only exposed to 6.3 ± 1.1% of the dose delivered to the apex of the central respirator. (e) PCIs are 2-dimensional surface-like sensors that facilitate spatially resolved measurements. We leveraged this characteristic to show that permanent marker ('Cal' pattern) on a UV-C-transparent film placed atop PCI1 can mask UV-C exposure, suggesting that markings on respirators should be minimized. PCI1 changes from yellow to pink as it is exposed to higher UV-C doses; yellow regions correspond to areas shadowed by the marker. All measurements were made in the 1500 model chamber.

10.5 Conclusions

Quantifying color from PCIs addresses urgent needs in UV-C dose measurement for (and beyond) N95 respirator decontamination. By tailoring established color measurement protocols to PCIs, we designed and validated a photochromic quantification workflow and then applied it to conduct measurements not robustly quantifiable with existing tools. Novel aspects of our workflow include quantifying CIEDE2000 color difference metrics for PCIs, implementing calibration informed by chemical kinetics, and quantifying PCI dose measurement uncertainty. Our workflow quantified performance specifications and revealed that while performance was highly PCI model-dependent, one indicator model met all specifications for informed design of UV-C N95 treatment systems: UV-C dose measurement range up to 0.2 J/cm^2 with relative measurement uncertainty of 6.05% at 0.1 J/cm^2, <5% response to UV-A/UV-B, and >90% accuracy compared to a calibrated digital radiometer. Our workflow enabled on-respirator dose quantification using PCIs, identifying nearly 20× dose nonuniformity across different N95 surface regions within a treatment system. As a result, the target dose delivered to the treatment plane within the UV-C system may need to be much higher than 1.0 J/cm^2 to ensure that all N95 surfaces are exposed to ≥1.0 J/cm^2. Because these dose nonuniformities across the N95 surface are model- and configuration-dependent, each treatment system should be characterized with the N95 models *in situ* for informed design of UV-C N95 treatment processes. PCI calibration curves for widely available imaging and colorimeter tools like flatbed scanners, iPhones, and DSLRs also meet minimum performance specifications and facilitate accessible and/or spatially resolved dose measurements.

Subsequent chapters extend the PCI dosimetry technique established here. A key limitation of most commercial PCIs, including the models studied here, is that they were designed for non-porous surface decontamination, and thus saturate at substantially lower doses (< 1.0 J/cm^2) than necessary for N95 decontamination. In Chapter 11, we investigate the use of optical attenuators of known UV-C transmittance to extend the dynamic range of PCIs; importantly, we characterize the relationship between attenuator material properties and angular response. In Chapter 12, we use the novel PCI dosimetry technique to make paired measurements of UV-C dose and SARS-CoV-2 inactivation on N95 respirators, a measurement not possible with radiometers. We anticipate that the PCI quantification workflow will be widely applied to meet the current urgent validation need, facilitating (1) informed design of UV-C treatment protocols to ensure that all N95 surfaces are exposed to the minimum dose, (2) in-process dose validation of each cycle, and (3) characterization of the robustness of new PCI materials.

10.6 References

1. CDC. Decontamination and Reuse of Filtering Facepiece Respirators. *Centers for Disease Control and Prevention* https://www.cdc.gov/coronavirus/2019-ncov/hcp/ppe-strategy/decontamination-reuse-respirators.html (2020).
2. Lore, M. B., Heimbuch, B. K., Brown, T. L., Wander, J. D. & Hinrichs, S. H. Effectiveness of Three Decontamination Treatments against Influenza Virus Applied to Filtering Facepiece Respirators. *The Annals of Occupational Hygiene* **56**, 92–101 (2011).
3. Mills, D., Harnish, D. A., Lawrence, C., Sandoval-Powers, M. & Heimbuch, B. K. Ultraviolet germicidal irradiation of influenza-contaminated N95 filtering facepiece respirators. *American Journal of Infection Control* **46**, e49–e55 (2018).

4. Heimbuch, B. & Harnish, D. *Research to Mitigate a Shortage of Respiratory Protection Devices During Public Health Emergencies.* https://www.ara.com/wp-content/uploads/MitigateShortageofRespiratoryProtectionDevices_3.pdf (2019).
5. Lindsley, W. G. *et al.* Effects of Ultraviolet Germicidal Irradiation (UVGI) on N95 Respirator Filtration Performance and Structural Integrity. *Journal of Occupational and Environmental Hygiene* **12**, 509–517 (2015).
6. John J. Lowe *et al. N95 Filtering Facemask Respirator Ultraviolet Germicidal Irradiation (UVGI) Process for Decontamination and Reuse*. https://www.nebraskamed.com/sites/default/files/documents/covid-19/n-95-decon-process.pdf (2020).
7. Kowalski, W. *Ultraviolet Germicidal Irradiation Handbook: UVGI for Air and Surface Disinfection*. (Springer Berlin Heidelberg, 2009). doi:10.1007/978-3-642-01999-9.
8. Beck, S. E., Hull, N. M., Poepping, C. & Linden, K. G. Wavelength-Dependent Damage to Adenoviral Proteins Across the Germicidal UV Spectrum. *Environ. Sci. Technol.* **52**, 223–229 (2018).
9. Fisher, E. M. & Shaffer, R. E. A method to determine the available UV-C dose for the decontamination of filtering facepiece respirators: UV-C decontamination of respirators. *Journal of Applied Microbiology* **110**, 287–295 (2011).
10. Ozog, D. M. *et al.* The Effect of Ultraviolet C Radiation Against Different N95 Respirators Inoculated with SARS-CoV-2. *International Journal of Infectious Diseases* 224–229 (2020) doi:10.1016/j.ijid.2020.08.077.
11. Cadnum, J. L. *et al.* Effectiveness of Ultraviolet-C Light and a High-Level Disinfection Cabinet for Decontamination of N95 Respirators. *Pathogens and Immunity* **5**, 52–67 (2020).
12. Heimbuch, B. K. *et al.* A pandemic influenza preparedness study: Use of energetic methods to decontaminate filtering facepiece respirators contaminated with H1N1 aerosols and droplets. *American Journal of Infection Control* **39**, e1–e9 (2011).
13. Tseng, C.-C. & Li, C.-S. Inactivation of Viruses on Surfaces by Ultraviolet Germicidal Irradiation. *Journal of Occupational and Environmental Hygiene* **4**, 400–405 (2007).
14. Reifsnyder, W. E. Radiation geometry in the measurement and interpretation of radiation balance. *Agricultural Meteorology* **4**, 255–265 (1967).
15. Bolton, J. R. & Linden, K. G. Standardization of Methods for Fluence (UV Dose) Determination in Bench-Scale UV Experiments. *J. Environ. Eng.* **129**, 209–215 (2003).
16. Lawal, O. *et al.* Method for the Measurement of the Output of Monochromatic (254 nm) Low-Pressure UV Lamps. *IUVA News* **19**, 9–16.
17. Reed, N. G., Wengraitis, S. & Sliney, D. H. Intercomparison of Instruments Used for Safety and Performance Measurements of Ultraviolet Germicidal Irradiation Lamps. *Journal of Occupational and Environmental Hygiene* **6**, 289–297 (2009).
18. Schmalwieser, A. W. Fifteen years of experience with standardized reference radiometers for controlling low-pressure UV disinfection plants for drinking water. *Water Supply* **17**, 975–984 (2017).
19. Poster, D. L. *et al.* Innovative approaches to combat healthcare-associated infections using efficacy standards developed through industry and federal collaboration. in *Nanoengineering: Fabrication, Properties, Optics, and Devices XV* (eds. Sakdinawat, A. E., Attias, A.-J., Panchapakesan, B. & Dobisz, E. A.) 55 (SPIE, 2018). doi:10.1117/12.2500431.
20. Lindblad, M., Tano, E., Lindahl, C. & Huss, F. Ultraviolet-C decontamination of a hospital room: Amount of UV light needed. *Burns* **46**, 842–849 (2020).

21. ASTM International. Standard Practice for Calculation of Color Tolerances and Color Differences from Instrumentally Measured Color Coordinates. *ASTM Standard D2244-16* https://www.astm.org/Standards/D2244.htm (2016).
22. Cui, G., Luo, M. R., Rhodes, P. A., Rigg, B. & Dakin, J. Grading textile fastness. Part 1: Using a digital camera system. *Coloration Technol* **119**, 212–218 (2003).
23. Carpenter, K. & Farnand, S. Assessing the use of smartphones to determine crop ripeness. *Electronic Imaging* (2020) doi:10.2352/ISSN.2470-1173.2020.12.FAIS-173.
24. Soda, Y. & Bakker, E. Quantification of Colorimetric Data for Paper-Based Analytical Devices. *ACS Sens.* **4**, 3093–3101 (2019).
25. Singh, G., Raj, P., Singh, H. & Singh, N. Colorimetric detection and ratiometric quantification of mercury using azophenol dye: 'dip & read' based handheld prototype device development. *J. Mater. Chem. C* **6**, 12728–12738 (2018).
26. Yetisen, A. K., Martinez-Hurtado, J. L., Garcia-Melendrez, A., da Cruz Vasconcellos, F. & Lowe, C. R. A smartphone algorithm with inter-phone repeatability for the analysis of colorimetric tests. *Sensors and Actuators B: Chemical* **196**, 156–160 (2014).
27. Solari, F., Girolimetti, G., Montanari, R. & Vignali, G. A New Method for the Validation of Ultraviolet Reactors by Means of Photochromic Materials. *Food Bioprocess Technol* **8**, 2192–2211 (2015).
28. Luo, M. R., Cui, G. & Rigg, B. The development of the CIE 2000 colour-difference formula: CIEDE2000. *Color Res. Appl.* **26**, 340–350 (2001).
29. NIST/SEMATECH. 2.3.6.7.1. Uncertainty for quadratic calibration using propagation of error. *NIST/SEMATECH e-Handbook of Statistical Methods* https://www.itl.nist.gov/div898/handbook/mpc/section3/mpc3671.htm DOI: 10.18434/M32189 (2020).
30. NIST/SEMATECH. 4.5.2.1. Single-Use Calibration Intervals. *NIST/SEMATECH e-Handbook of Statistical Methods* https://www.itl.nist.gov/div898/handbook/pmd/section5/pmd521.htm#:~:text=Although%20calibration%20confidence%20intervals%20have,for%20the%20true%20average%20response. DOI: 10.18434/M32189 (2020).
31. Biguri, A. Perceptually uniform colormaps. *MATLAB Central File Exchange* https://www.mathworks.com/matlabcentral/fileexchange/51986-perceptually-uniform-colormaps (2020).
32. Rehfuess, E. & World Health Organization. *Global solar UV index: a practical guide.* (World Health Organization, 2002).
33. Quintern, L. E., Horneck, G., Eschweiler, U. & Bücker, H. A Biofilm Used as Ultraviolet-Dosimeter. *Photochemistry and Photobiology* **55**, 389–395 (1992).
34. Larason, T. & Ohno, Y. Calibration and characterization of UV sensors for water disinfection. *Metrologia* **43**, S151–S156 (2006).
35. Larason, T. C. & Cromer, C. L. Sources of error in UV radiation measurements. *J. Res. Natl. Inst. Stand. Technol.* **106**, 649 (2001).
36. Lytle, C. D. & Sagripanti, J.-L. Predicted Inactivation of Viruses of Relevance to Biodefense by Solar Radiation. *Journal of Virology* **79**, 14244–14252 (2005).
37. Voet, D., Gratzer, W. B., Cox, R. A. & Doty, P. Absorption spectra of nucleotides, polynucleotides, and nucleic acids in the far ultraviolet. *Biopolymers* **1**, 193–208 (1963).

38. Su, A., Grist, S. M., Geldert, A., Gopal, A. & Herr, A. E. Quantitative UV-C dose validation with photochromic indicators for informed N95 emergency decontamination. *PLOS ONE* **16**, e0243554 (2021).
39. Soda, Y., Robinson, K. J., Cherubini, T. J. & Bakker, E. Colorimetric absorbance mapping and quantitation on paper-based analytical devices. *Lab Chip* **20**, 1441–1448 (2020).
40. Abdel-Fattah, A. A., El-Kelany, M. & Abdel-Rehim, F. Development of a radiation-sensitive indicator. *Radiation Physics and Chemistry* **48**, 497–503 (1996).
41. El Seoud, O. A., Baader, W. J. & Bastos, E. L. Practical Chemical Kinetics in Solution. in *Encyclopedia of Physical Organic Chemistry, 5 Volume Set* (ed. Wang, Z.) 1–68 (John Wiley & Sons, Inc., 2016). doi:10.1002/9781118468586.epoc1012.
42. Nixon, M., Outlaw, F., MacDonald, L. W. & Leung, T. S. The importance of a device specific calibration for smartphone colorimetry. *color imaging conf* **2019**, 49–54 (2019).
43. Martinez, A. W. *et al.* Simple Telemedicine for Developing Regions: Camera Phones and Paper-Based Microfluidic Devices for Real-Time, Off-Site Diagnosis. *Anal. Chem.* **80**, 3699–3707 (2008).
44. Schmid, J., Hoenes, K., Rath, M., Vatter, P. & Hessling, M. UV-C inactivation of Legionella rubrilucens. *GMS Hyg Infect Control* **12**, 1–6 (2017).

Chapter 11

Optical attenuators extend dynamic range but alter angular response of planar ultraviolet-C dosimeters

Adapted with permission from A. Su*, S. M. Grist*, A. Geldert, A. Gopal, & A. E. Herr, "Quantitative UV-C dose validation with photochromic indicators for informed N95 emergency decontamination", *PLOS One*, 2021, and from A. Su*, A. Geldert*, S. M. Grist, & A. E. Herr, "Optical attenuators extend dynamic range but alter angular response of planar ultraviolet-C dosimeters", *arXiv and in revision*.

11.1 Abstract

A challenge for sensors used in ultraviolet-C (UV-C) decontamination protocols of N95 respirators is validation that the entire N95 surface receives the minimum acceptable dose. Photochromic indicators (PCIs) can accurately measure UV-C dose on nonplanar surfaces, but often saturate below doses required to decontaminate porous, multilayered textiles such as N95s. Here, we investigate the use of optical attenuators to extend PCI dynamic range while maintaining a near-ideal angular response – critical for accurate measurements when UV-C is uncollimated. Through an analytical model, we show that tuning attenuator refractive index, attenuation coefficient, and thickness can extend dynamic range, but compromises ideal angular response unless the attenuator is an ideal diffuser. To demonstrate this tradeoff empirically, we pair PCIs with model specular (floated borosilicate) and diffuse (polytetrafluoroethylene) attenuators, characterize the angular response, and evaluate on-N95 UV-C dose measurement accuracy of each PCI-attenuator stack in a UV-C decontamination system. While both borosilicate and polytetrafluoroethylene increase PCI dynamic range >4×, both attenuators introduce angle-dependent transmittance, which causes location-dependent underestimation of UV-C dose. The PCI-borosilicate and PCI-polytetrafluoroethylene stacks underreport true on-N95 dose by 1) 14.7% and 3.6%, respectively, on a surface near-normal to the array of source lamps, and 2) 40.8% and 19.8%, respectively, on a steeply sloped location. Overall, we demonstrate that while planar optical attenuators can increase PCI dynamic range, verification of near-ideal angular response is critical for accurate UV-C dose measurement.

11.2 Introduction

Ultraviolet-C (UV-C) radiation is a key germicidal technique regularly applied in healthcare settings to decontaminate air[1], surfaces[2], and recently, N95 respirators to address the COVID-19 pandemic-induced shortages[3,4]. UV-C photons catalyze protein and nucleic acid photodegradation; after sufficient cumulative photon absorption (UV-C dose), compromised pathogens are inactivated. The UV-C dose needed for decontamination depends on the pathogen, substrate, and other factors[5]. In particular, porous and multilayered textiles such as N95 respirators and surgical masks and gowns require higher applied outer surface doses as compared to nonporous materials, to offset attenuation of UV-C reaching pathogens embedded in the inner material layers[6,7]. Decontamination efficacy is directly related to UV-C dose, and UV-C dose

measurements are frequently the only metric bridging laboratory viral inactivation studies and clinical implementation; thus, accurate UV-C dose measurements are critical for protocol validation.

Validation of decontamination of N95s and other porous and/or nonplanar substrates poses unique UV-C measurement challenges. The ~100× higher UV-C dose required to decontaminate porous materials as compared to nonporous surfaces[2,6,8] require UV-C sensors with sufficiently high dynamic range. UV-C systems often deliver system-dependent nonlinear doses over time[9,10] (**Figure 11.1**), precluding extrapolation from short exposures. Additionally, the complex N95 geometry complicates measurement accuracy, as the UV-C dose received by a surface at a given angle of incidence θ is reduced by a factor of $\cos(\theta)$ from the dose received at normal incidence (Lambert's cosine law[11]). Thus, UV-C dose measurement accuracy depends on how proportional the sensor readout over angles of incidence $0° \leq \theta \leq 90°$ (termed "angular response") is to $\cos(\theta)$ (termed "ideal response"). A sensor with an ideal response is critical for applications such as N95 decontamination, which involves both nonplanar targets and uncollimated UV-C. However, sensor housing, spectral filters, and other elements in the optical path often alter angular response[12] and sensor angular response is often non-ideal[13,14], uncharacterized, or unreported.

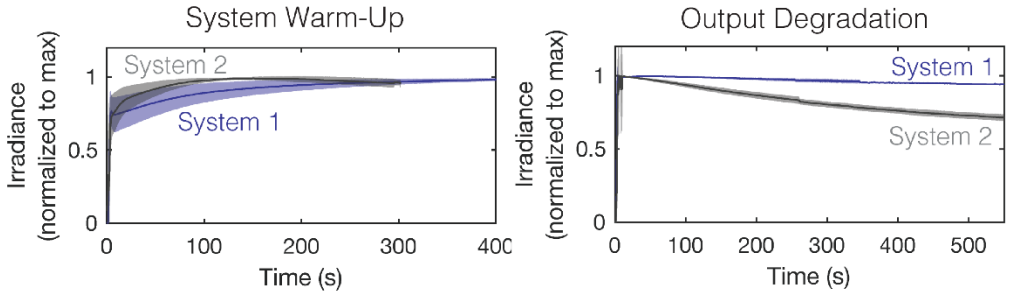

Figure 11.1. Irradiance variability over time and between UV-C systems. Two near-identical UV-C exposure systems have significantly different output profiles over time, both during warm-up (left), and during long exposures (right). Plots depict mean (line) and standard deviation (shaded region) of the replicate measurements: N = 16 (System 1 warm-up); N = 10 (System 2 warm-up); N = 19 (System 1 long exposure); N = 11 (System 2 long exposure).

UV-C photochromic indicators (PCIs), which change color in response to UV-C dose, overcome many challenges associated with on-N95 measurements. PCIs can have an ideal angular response[15] because PCI dose response and specificity are governed by chemistry[16] rather than additional physical elements within the optical path. Though PCI readout is traditionally qualitative or at-best semi-quantitative (if a color swatch to dose reference is provided), a recent study developed a robust workflow to quantify UV-C dose from PCI color change to map UV-C dose across N95 facepieces[9]. However, because PCIs were originally designed to validate nonporous surface decontamination, UV-C doses required for porous material decontamination typically exceed the PCI dynamic range. Thus, an extended PCI dynamic range spanning higher UV-C doses is urgently needed to validate decontamination of porous materials like N95s.

There are two approaches to extend the PCI dynamic range: (1) altering the chemistry governing the PCI color change, (e.g., adding reagents to modify the reaction kinetics or equilibrium[16,17]), or (2) attenuating UV-C incident on the PCI[18]. As a PCI-agnostic approach, attenuation lends itself to widespread adoption across diverse settings. However, objects within the optical path may alter the PCI angular response due to angle-dependent refraction, reflection, scattering, and absorption[12,19]. A non-ideal angular response will cause angle-dependent dose measurement errors. If the angle of incidence is known or constant, an angle-dependent correction factor can be determined[9,20,21]. However, the deformable N95 facepiece shape combined with

significant UV-C scattering and reflection render this correction-factor approach infeasible for N95 UV-C decontamination systems.

Here, we employ theoretical and empirical approaches to investigate whether readily available materials can serve as optical attenuators to extend PCI dynamic range while maintaining measurement accuracy for N95 decontamination protocol validation. We develop an analytical model based on fundamental optics principles and attenuator properties to predict attenuator transmittance as a function of angle of incidence. Analytically and empirically with a point-like UV-C source, we characterize the angular response of PCIs stacked directly behind (with respect to the optical axis) each of two model attenuator materials: one non-diffuse and one diffuse. Finally, to mimic implementation in an N95 decontamination protocol, we evaluate the measurement accuracy of each PCI-attenuator stack on two differently sloped N95 facepiece locations in a decontamination chamber, where UV-C angles of incidence are unknown. We demonstrate that although attenuators with diffuse properties improve angular response as compared to non-diffuse attenuators, a model planar diffuse attenuator still alters angular response, which compromises measurement accuracy. In total, we develop frameworks to relate key material properties of optical attenuators to the dynamic range and angular response of the PCI-attenuator stack and assess model PCI-attenuator stacks in an example end-use case to highlight critical considerations when modifying planar dosimeters for measurements on nonplanar surfaces.

11.3 Materials & Methods

Materials. The attenuators used were floated borosilicate (Borofloat®, 25.4 mm width × 25.4 mm length × 1.1 mm ± 0.1 mm thickness, 80/50 scratch/dig quality, Precision Glass & Optics 0025-0025-0011-GE-CA), referred to as "borosilicate", polytetrafluoroethylene film (Teflon®, 0.51 mm thickness, cut into 25.4 mm squares, McMaster-Carr 8569K23), referred to as "PTFE", and a mounted 1.3 OD neutral density filter (NDUV13A, Thorlabs). Irradiance measurements recorded in **Figure 11.1** and dose measurements made in **Figure 11.7** were made with a Model 308 data-logging UV radiometer equipped with a 254 nm sensor (Optical Associates, Inc., OAI). All other radiometer measurements were collected using a calibrated ILT1254 UV-C radiometer with a Teflon dome diffuser (International Light Technologies). PCIs were UVC 100 Dosimeter dots (American Ultraviolet).

For transmittance and angular response measurements, a modified handheld UV-C lamp (EF-140) with one BLE-2537S amalgam bulb (254 nm emission) and a UV-C-blocking plate with a 25.4 mm-diameter aperture installed was used as a point-like UV-C source (Spectronics). Irradiance variation over time and between systems (**Figure 11.1**) was characterized with two different Spectroline commercial UV-C decontamination chambers (same dimensions): a Spectroline HCL-1500 ('System 1') equipped with six low-pressure amalgam bulbs (BLE-1T155, Spectroline) and an XL-1500 Spectrolinker ('System 2') equipped with six low-pressure mercury bulbs (BLE-1T155, uvebay.com). PCI and PCI-attenuator stack calibration curves shown in **Figure 11.7** were made in System 1 or System 2. All other calibration curves, as well as all on-N95 measurements, were made in a commercial UV-C decontamination chamber (Spectronics XL-1000 UV-C with an array of 5 BLE-8T254 254 nm low-pressure amalgam bulbs along the top). All decontamination chambers either had a small custom notch in the door for the radiometer cord to pass through, or irradiance measurements were made by placing both the radiometer and a Microsoft Surface Pro tablet (equipped with TeamViewer for remote control) wrapped in UV-C blocking materials inside the chamber. All on-N95 measurements were made on one 3M 1860 N95

respirator. All analytical modelling and analyses were performed in Python or MATLAB® R2020b.

Assessing temporal fluctuations in irradiance. Irradiances over time logged using the OAI radiometer either during system warm-up or during long-exposures after warm-up were parsed from the output .txt files using a custom Python script and read into MATLAB. Warm-up datasets approximated the variance that would be present in applied conditions because the time since previous use was not controlled (the datasets began with the lamps in varying states of warm-cool). Each dataset was analyzed to automatically detect the iteration (i_{end}) at which lamp shutoff occurred (from the change from the previous measurement). The irradiance data were plotted until 2 measurements prior to that measurement iteration (i_{end-2}). For the system warm-up datasets, warm-up rise time was computed as the time for the irradiance to rise from 10% of the maximum recorded value to 90% of the maximum recorded value. For the long exposure datasets, the output degradation was assessed by extracting the irradiance degradation slope from linear least-squares curve fitting.

Borosilicate transmittance measurement. To measure total transmittance through borosilicate (T_{total}), a radiometer placed normal to the point-like UV-C source at a distance of 127 mm recorded the irradiance with and without borosilicate in the optical path (**Figure 11.2A**). To ensure borosilicate is placed normal to the optical path and radiometer, borosilicate is mounted on a custom-made acrylic (McMaster-Carr 85635K421) platform with a 20 mm-diameter aperture centered over the radiometer sensor (borosilicate is placed ~9 mm in front of the top of the radiometer diffuser dome). The acrylic blocks all UV-C, so UV-C is incident only through the 20 mm aperture. For homogeneous materials, the attenuation coefficient (α) can be calculated from the measured T_{total} and modeled T_{int} at 0°, and the attenuator thickness (d), according to **Eq. 11.1**:

$$\alpha = \frac{-ln(T_{total}(0°)/(T_{int1}(0°)T_{int2}(0°)))}{d} = \frac{-ln(T_{mat}(0°))}{d} \qquad \textbf{Eq. 11.1}$$

Analytical model. The attenuation coefficient (α) of borosilicate was calculated from the total transmittance measured at near-normal angles of incidence (**Figure 11.2A**). We estimated the refractive index $n_{att} \approx 1.50$ at 254 nm for borosilicate based on linear extrapolation of n for the two shortest wavelengths reported[22] (~365 nm and 405 nm). We estimated $n_{att} \approx 1.38$ for PTFE, as reported by a manufacturer[23]. Integrated cosine error was calculated in MATLAB using the "cumtrapz" function.

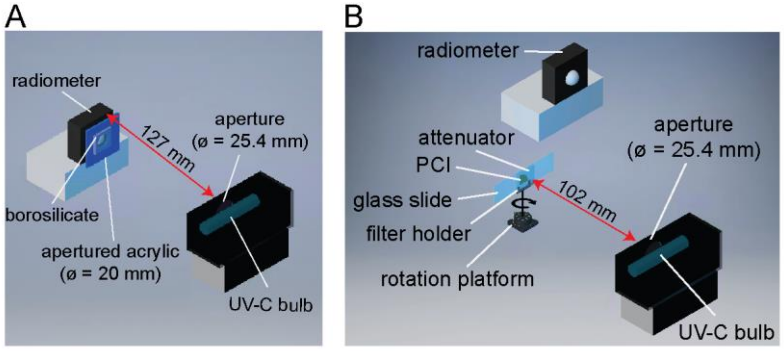

Figure 11.2. Schematics of measurement setups to characterize borosilicate transmittance and PCI-attenuator stack angular response. (A) Borosilicate transmittance (T_{total}) at near-normal angles of incidence is measured by comparing irradiance measurements with and without borosilicate in the optical path. (B) Angular response of PCI-

attenuator stacks is measured by exposing the PCI-attenuator stack to UV-C from a point-like source at different angles of incidence. Arrow around optical post denotes axis of rotation.

PCI quantification. PCIs were quantified as previously described[9]. Briefly, D65/10° L*a*b* values of PCIs were measured using an RM200QC spectrocolorimeter (X-rite®). Color change with respect to an unexposed PCI was quantified using the CIEDE2000 ΔE formula[9,24]. To generate calibration curves, a radiometer and PCI were positioned within the UV-C chamber at planar locations of equal irradiance (**Figure 11.3**) to measure UV-C dose and CIEDE2000 ΔE, respectively. CIEDE2000 ΔE values and corresponding UV-C doses were fit to a function based on first-order reaction kinetics[9]. Unless otherwise noted, reported errors are the root-sum-square of standard deviations corresponding to both replicate variation and PCI quantification uncertainty.

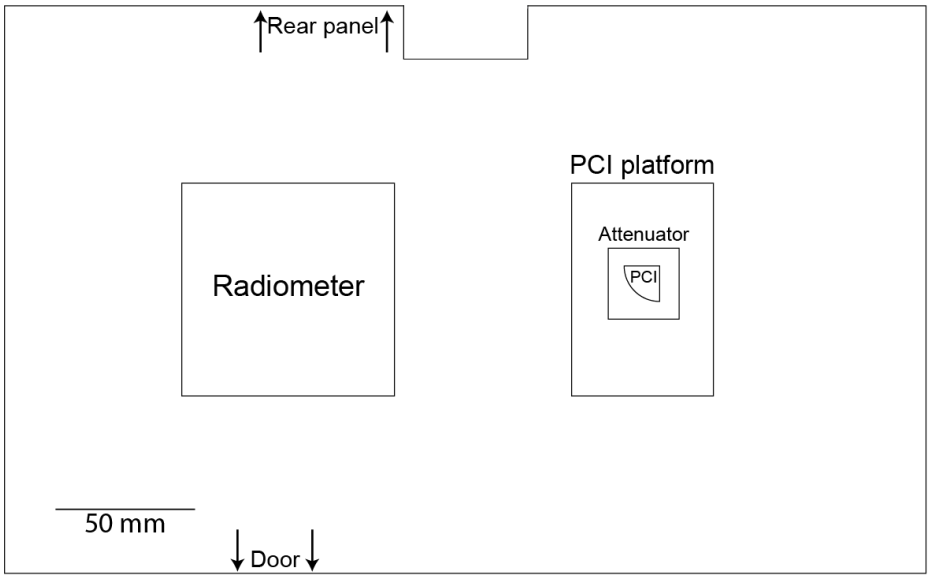

Figure 11.3. UV-C chamber floor map for calibration curve measurements. The PCI was placed on a custom acrylic platform to raise the PCI to the same height as the base of the Teflon dome on the radiometer. For PCI-attenuator stack calibration curves, the attenuator was placed directly on top of the PCI on the platform. Irradiances at the radiometer and PCI locations were verified to be equivalent. Rectangular cut-out near the rear panel allows the floor map to fit around a raised component built into the UV-C chamber.**Angular response measurements with apertured UV-C source.** The angular responses of PCI-attenuator stacks were determined from the dose measured by PCIs rotated around an optical post to expose the PCIs to quasi-parallel UV-C rays at different angles of incidence (0°-90° in 15° increments)[25] from a point-like source (**Figure 11.2B**). PCI-attenuator stacks were affixed to a glass microscope slide (VWR 48300-026) with double-sided tape (3M MMM137). The glass slide was held in a filter holder (Thorlabs FH2) on an optical post attached to a rotation platform (Thorlabs QRP02). To ensure the UV-C source was point-like, we placed the PCI-attenuator stack ~102 mm from the UV-C source aperture, where source power (calculated from the Keitz formula from radiometer-measured irradiance) was independent of distance (i.e., varied by <5% between distances)[10,15]. We assumed the borosilicate and PCI-attenuator stacks received negligible reflected and scattered UV-C, as no enclosure was used and wall paint is minimally UV-C-reflective.[26] Dose was monitored using a radiometer at an offset, non-shadowed location; all PCIs within an angular response set were exposed to the same radiometer-measured dose. After UV-C exposure, the PCI-attenuator stack was disassembled and dose received by the PCI was immediately determined ("PCI quantification").

On-N95 dose measurements with PCI-attenuator pairs. On-N95 dose measurements were made at two N95 facepiece locations: near the apex where the N95 surface is nearly normal to the UV-C bulb array ("low-angle"), and near the base where the N95 surface is steeply sloped ("high-angle"). For consistent placement, high- and low-angle locations were marked on the N95, and facepiece deformation was minimized. During each exposure, the N95 was centered in the UV-C chamber, and a radiometer at a fixed location in the chamber recorded irradiance. A chamber floor map reduced positioning error (**Figure 11.4**).

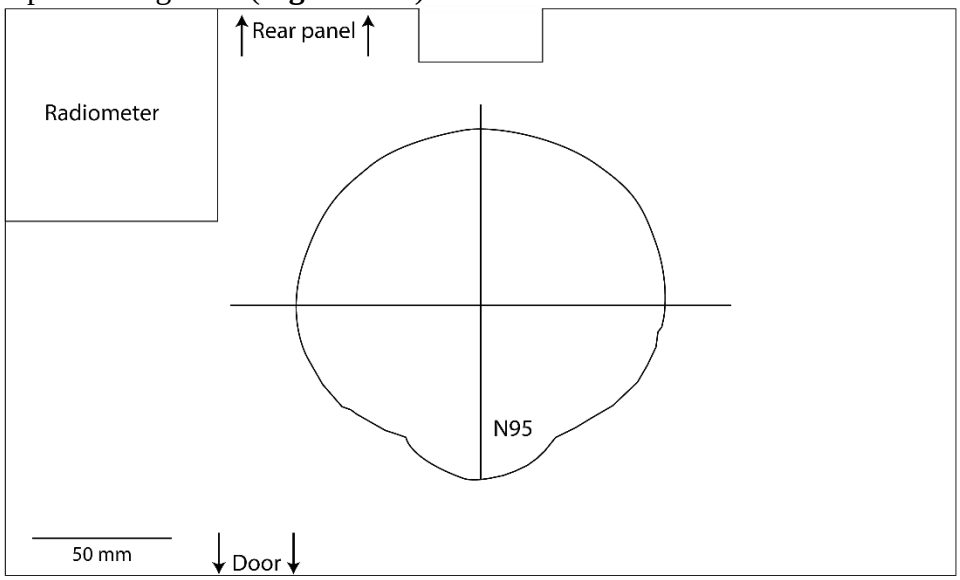

Figure 11.4. UV-C chamber floor map for on-N95 measurements. Dose measurements from the radiometer were used to determine the true dose applied to the N95 surface based on the predetermined irradiance ratio between the radiometer and each on-N95 location.

To measure on-N95 dose with PCI-attenuator stacks, PCIs were taped with the sensor side flush against the attenuator. The PCI-attenuator stack was then attached to the N95 facepiece using double-sided tape. Measured on-N95 dose was determined from PCI-attenuator calibration curves generated within the UV-C chamber. To compare to the bare PCI results, PCI-attenuator calibration curves were generated from the same locations in-chamber. To calculate the true applied on-N95 dose for measurements made by PCI-attenuator stacks and PCIs exposed to UV-C doses that exceeded the bare PCI dynamic range, we multiplied the *in-situ* radiometer measurement by the ratio of irradiance at each on-N95 location to the radiometer location. Irradiance ratios were predetermined from 3 replicate measurements of dose measured by a radiometer and bare PCIs at each on-N95 location which were concurrently exposed to lower doses within the bare PCI dynamic range. Bare PCI dose measurement at doses within the PCI dynamic range are accurate because unmodified PCIs have an ideal angular response[15]. We assumed the irradiance ratio between locations is independent of dose, as exposure times ($\leq$ 6 min) were substantially shorter than the timescales over which spatial variation in bulb output has been observed.[27] PCI dose was quantified as described above, and dose at the radiometer was quantified by integrating the recorded irradiance.

11.4 Results & Discussion

Design specifications relevant to pathogen inactivation. In this study, we sought to characterize the performance of PCIs stacked behind optical attenuators in measuring UV-C surface doses

required for viral inactivation throughout porous materials on nonplanar N95 facepieces. Because planar materials are accessible and scalable (can be cut to size from bulk material), we chose to study planar attenuators. We identified key performance specifications relevant to measurement accuracy: dynamic range and angular response (**Figure 11.5A**). We define the PCI dynamic range[9] as the UV-C doses between a lower and upper limit of quantification (LLOQ and ULOQ, respectively) where the relative PCI quantification uncertainty is <10% (**Figure 11.6**). As studies support ≥1.0 J/cm^2 for ≥99.9% inactivation of non-enveloped viruses on most N95 models[28–30], the PCI-attenuator stack ULOQ must exceed 1.0 J/cm^2 for N95 decontamination protocol validation. However, pathogen- and model-specific UV-C efficacy may require higher ULOQ, and should be determined on a case-by-case basis. Additionally, on-N95 dose has been found to vary by ~20× within a decontamination system[9]. To maximize the continuous measurement range in order to characterize the full range of nonuniform doses within a system, the PCI-attenuator stack LLOQ must remain below the bare PCI ULOQ (0.261 J/cm^2 for the PCI model and color-readout method used here[9]; **Figure 11.6**).

UV-C dose measurement accuracy on nonplanar surfaces depends on the angular response of the detector. Depending on attenuator material properties, transmittance may change with angle of incidence due to angle-dependent reflection, absorption, and degree of scattering (i.e., specular or diffuse reflectance and transmittance), leading to a non-ideal angular response. Because non-ideal angular response is infeasible to correct for without prior knowledge of the angle(s) of incidence, we sought to identify a PCI-attenuator stack with near-ideal angular response. At a given angle of incidence θ, deviation from the ideal angular response is defined as the cosine error[31] (**Eq. 11.2**). Integration of the cosine error between 0° and 80° (integrated cosine error, **Eq. 11.3**, defined[31] in ISO/CIE 19476) quantifies the overall deviation from the ideal angular response[32]:

$$Cosine\ error = f_2(\theta) = \left(\frac{response(\theta)}{response(0^o) \cdot \cos(\theta)} - 1\right) \times 100\% \qquad \textbf{Eq. 11.2}$$

$$Integrated\ cosine\ error\ = \int_0^{80^\circ} |f_2(\theta)| \cdot sin(2\theta) d\theta \qquad \textbf{Eq. 11.3}$$

To match the order of magnitude of bare PCI measurement error[9,10] (average error of 7%), PCI-attenuator stack cosine error magnitude must remain ≤10% over all angles of incidence (0-90°).

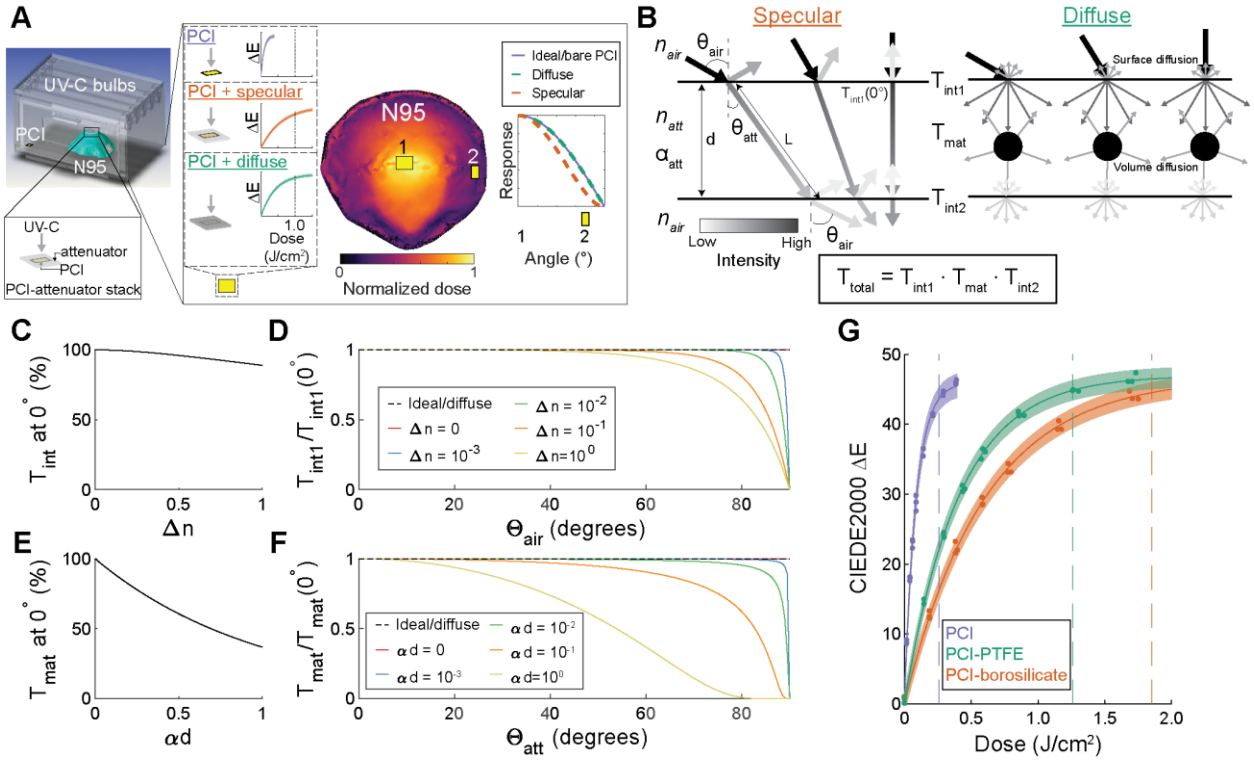

Figure 11.5. Attenuator material properties govern dynamic range and angular response of PCI-attenuator stacks. (A) 3D rendering of N95 UV-C decontamination system with 2D top-down view of chamber floor. Attenuators stacked in front of PCIs can extend the PCI dynamic range to measure on-N95 dose variation (shown as heatmap), but measurement accuracy on non-planar surfaces like N95s requires an ideal PCI-attenuator angular response. (B) Schematic representation of UV-C transmittance through ideal specular and diffuse attenuators at varying angles of incidence: UV-C enters through the air-attenuator interface (T_{int1}), traverses the attenuator (T_{mat}), and exits via the attenuator-air interface (T_{int2}). Arrow shade represents irradiance magnitude. In non-diffuse materials, reflection and attenuation increase with angle of incidence. In ideal diffusely transmitting materials, transmittance is independent of angle of incidence due to surface and volume diffuser behavior. (C-D) Non-zero Δn yields both decreased (C) and angle-dependent transmittance (D) at a specular interface. (E-F) Material thickness and attenuation coefficient yield both decreased (E) and angle-dependent (F) transmittance in a non-diffuse material. (G) Two attenuator materials, borosilicate (specular) and PTFE (diffuse) extend the PCI upper limit of quantification (dashed vertical lines) beyond 1.0 J/cm^2.

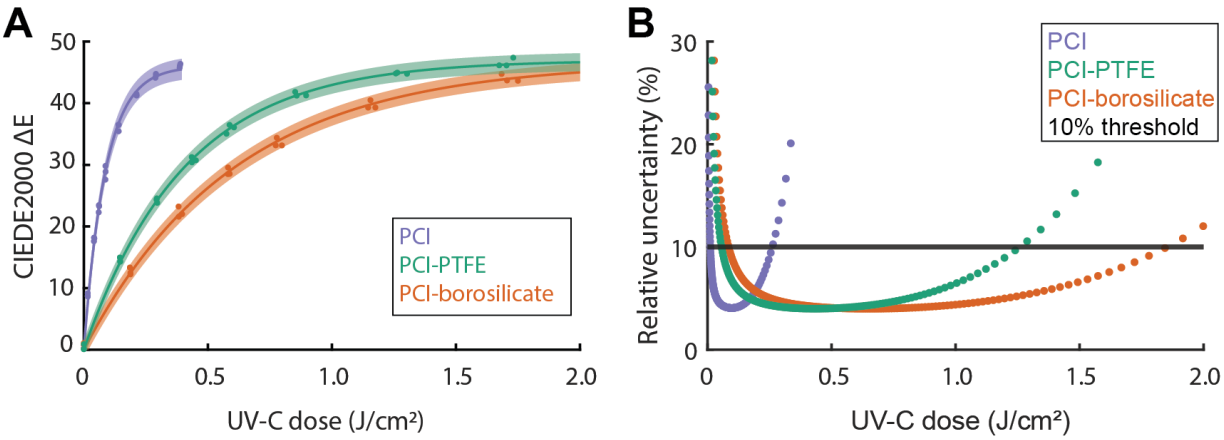

Figure 11.6. Dynamic range of PCI-attenuator pairs is determined from the relative uncertainty of calibration curves. (A) Calibration curves relating UV-C dose to PCI color change (CIEDE2000 ΔE). UV-C was applied to either bare PCIs or PCIs stacked directly underneath an attenuator (0.51 mm-thick PTFE or 1.1 mm-thick borosilicate).

Based on first-order reaction kinetics, a fit function ($\Delta \boldsymbol{E} = \boldsymbol{a}\{\mathbf{1} - \boldsymbol{e}^{-\frac{\boldsymbol{dose}}{\boldsymbol{b}}}\}$) is defined for each calibration curve, as described previously[9]. Shaded regions indicate the 95% prediction interval on prediction of PCI color change from measured UV-C dose. For bare PCIs, R^2 = 0.9976, a = 46.0 (45.3, 46.7), b = 87.4 (83.6, 91.2). For PCI-PTFE, R^2 = 0.9982, a = 47.0 (46.5, 47.5), b = 407.3 (393.2, 421.4). For PCI-borosilicate, R^2 = 0.9982, a = 46.7 (46.2, 47.3), b = 605.9 (584.3, 627.5). For each calibration curve, N = 3 replicates were measured at each target dose. (B) The dynamic range (LLOQ to ULOQ) is defined as the dose range over which relative uncertainty in dose measurement is <10%. Relative uncertainty is defined as half the width of the 95% confidence interval on UV-C dose measurements, divided by measured dose. UV-C dose measurements have <10% relative uncertainty from 0.011 – 0.261 J/cm^2 (bare PCI), 0.057 – 1.259 J/cm^2 (PCI-PTFE), and 0.085 – 1.853 J/cm^2 (PCI-borosilicate).

Optical properties governing attenuator design for measurements on non-planar surfaces. To inform design of an attenuator that meets the required specifications, we first sought to identify and relate optical properties that affect attenuator transmittance through a planar material. Transmittance will affect both the dynamic range and angular response of a PCI-attenuator stack. Attenuators may exhibit entirely specular reflection and transmission (i.e., no scattering effects, 'non-diffuse'), or diffuse scattering at the interface ('surface diffusers'), within the material ('volume diffusers'), or at both the interface and throughout the material. We developed an analytical model for total transmittance (T_{total}) through materials based on two main interactions (**Eq. 11.4**): (1) reflection and refraction at air-attenuator interfaces, which govern the transmittance across the interfaces (T_{int1} and T_{int2}) and (2) attenuation throughout the attenuator thickness, which governs the transmittance through the attenuator volume (T_{mat}).

$$T_{total} = T_{int1} \cdot T_{mat} \cdot T_{int2} \qquad \textbf{Eq. 11.4}$$

At each air-attenuator interface, the Fresnel equations[12] (**Eq. 11.5**) for randomly polarized radiation describe T_{int} based on the air and attenuator refractive indices (n_{air} and n_{att}, respectively) and angle of incidence with respect to the surface normal (θ_{air}). Snell's law[33] (**Eq. 11.6**) governs the angle of refraction within the attenuator (θ_{att}) (**Figure 11.5B**).

$$T_{int} = 1 - \left\{\frac{1}{2} \cdot \left[\left(\frac{n_{air}cos(\theta_{air}) - n_{att}cos(\theta_{att})}{n_{air}cos(\theta_{air}) + n_{att}cos(\theta_{att})}\right)^2 + \left(\frac{n_{air}cos(\theta_{att}) - n_{att}cos(\theta_{air})}{n_{air}cos(\theta_{att}) + n_{att}cos(\theta_{air})}\right)^2\right]\right\} \qquad \textbf{Eq. 11.5}$$

$$n_{air}sin(\theta_{air}) = n_{att}sin(\theta_{att}) \qquad \textbf{Eq. 11.6}$$

Note that the attenuator-to-air interface transmittance (T_{int2}) calculation requires interchanging n_{air} and n_{att} as well as θ_{att} and θ_{air} in **Eq. 11.5**. Specular reflectors have a microscopically flat interface, such that a collimated UV-C beam will strike the material at a single θ_{air} that governs T_{int}. In contrast, due to interface roughness on surface diffusers, the surface normal varies randomly over distances much smaller than the length scale of interest (e.g., dimensions of the PCI)[12]. Thus, the textured interface causes collimated UV-C at any angle to actually strike the microscopically textured interface over a range of θ_{air}. As a result, the proportion of UV-C transmitted across a surface diffuser interface does not depend on the angle of incidence (**Figure 11.5B**).

Using this analytical framework, we modeled specular and diffuse interface transmittance as a function of both refractive index difference (Δn, **Figure 11.5C**) and the angle of incidence (θ_{air}, **Figure 11.5D**). Increasing Δn decreases T_{int1}, thus extending the dynamic range of the PCI-attenuator stack (**Eq. 11.5**; **Figure 11.5C**). To characterize the effect of Δn on angular response, we evaluated T_{int1} normalized to $T_{int1}(0°)$ as a function of θ_{air} over varying Δn values (**Figure 11.5D**). Because n of most materials[34] is ≤2 and n_{air} ≈1, we evaluated Δn ≤1. Surface diffusers

exhibit angle-independent transmittance at the interface regardless of Δn. However, interfaces with specular reflection and transmission have increasingly angle-dependent transmittance as both θ_{air} and Δn increase within the range of values modeled.

Internal transmittance through the attenuator thickness (d) depends on two parameters: the material attenuation coefficient (α) and the optical path length through the material (L). Bouguer's law[33] relates T_{mat} to α and L (**Eq. 11.7**):

$$T_{mat} = e^{(-\alpha L)} \quad \textbf{Eq. 11.7}$$

In non-diffuse materials and surface diffusers with no internal scattering, L is dependent on d and θ_{att} (**Eq. 11.8**):

$$L = \frac{d}{cos\,(\theta_{att})} \quad \textbf{Eq. 11.8}$$

In volume diffusers, microstructures within the material scatter rays in random directions[35], decoupling L from θ_{att}. Thus, in volume diffusers, T_{mat} is independent of angle of incidence (**Figure 11.5B**).

To elucidate contributions of attenuator properties (α and d) to the magnitude and angle-dependence of T_{mat}, we modeled T_{mat} as a function of a nondimensional parameter αd (**Figure 11.5E**) and θ_{att} (**Figure 11.5F**). Increasing αd decreases transmittance via increased material attenuation, thereby extending the PCI dynamic range (**Figure 11.5E**). For UV-C transmittance through volume diffusers at any angle, $T_{mat}/T_{mat}(0°)$ is independent of angle of incidence regardless of αd. However, increasing αd for non-diffuse materials increases angular dependence of transmittance because 1) increasing d expands the range of optical path lengths over which attenuation occurs, and 2) increasing α increases the sensitivity of T_{mat} on varying path lengths (**Figure 11.5F**).

Since the irradiance incident on the PCI-attenuator stack follows Lambert's cosine law[11], the irradiance ultimately incident on the PCI is proportional to $T_{total} \cdot cos(\theta_{air})$. Thus, PCIs stacked directly behind planar attenuators (relative to the optical path) will maintain an ideal response only if T_{total} remains constant over $0° \leq \theta_{air} < 90°$. However, the parameters (Δn, d, and α) required to reduce attenuator transmittance and thus increase the dynamic range of the PCI-attenuator stack concomitantly introduce angle-dependent transmittance. Thus, unless the attenuator diffuses UV-C sufficiently to transmit UV-C independent of angle, there is a fundamental tradeoff between reducing transmittance to extend dynamic range and maintaining an ideal cosine angular response.

Model diffuse and non-diffuse materials extend the PCI dynamic range beyond 1.0 J/cm^2. To investigate how attenuator material properties affect UV-C dose quantification accuracy, we chose to characterize the performance of PCIs stacked behind each of two widely accessible materials with different degrees of diffuse scattering. Floated borosilicate ("borosilicate") has been demonstrated[9] to extend PCI dynamic range on planar surfaces by ~5×, and thus was chosen as a model non-diffuse attenuator (i.e., exhibits specular reflection and transmission). Polytetrafluoroethylene ("PTFE") was chosen as a model volume diffuser[36], as PTFE is commonly used to improve angular response of radiometers within the ultraviolet range[37,38]. We generated calibration curves for PCIs and PCI-attenuator stacks to verify that chosen attenuator thicknesses extend the PCI dynamic range beyond 1.0 J/cm^2 (**Figure 11.5G**, **Figure 11.6**). The bare PCI ULOQ was 0.261 J/cm^2, below the 1.0 J/cm^2 design specification for on-N95 dose validation and in line with previous studies[9]. We found that 0.51 mm-thick PTFE and 1.1 mm-thick borosilicate

increased the ULOQ to 1.259 J/cm^2 and 1.853 J/cm^2, respectively, thus meeting the dynamic range specification. Other materials, such as neutral density filters, were found to extend PCI dynamic range even further (**Figure 11.7**). While we only studied one batch of each attenuator, transmittance may vary by batch and should be characterized prior to implementation.

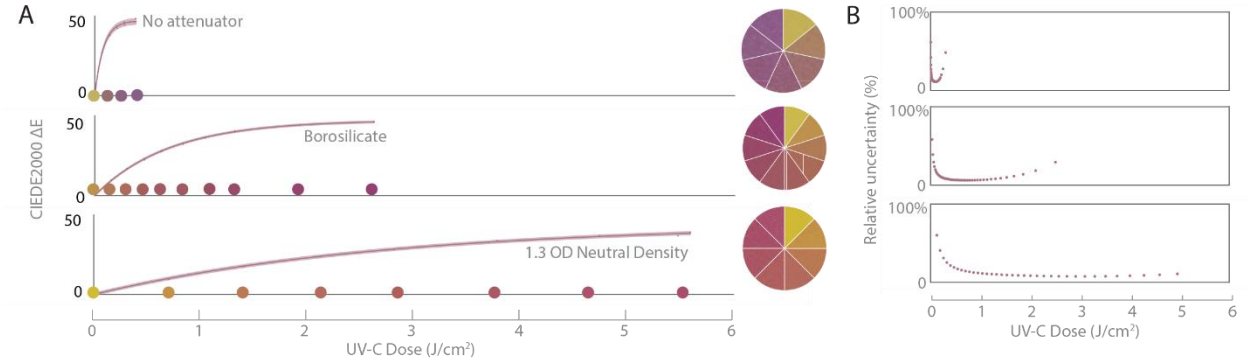

Figure 11.7. Attenuators extend PCI dynamic range several-fold. (A) Calibration curves relating UV-C dose to PCI color change when PCIs are bare, stacked with 1.1 mm-thick borosilicate, or stacked with a 1.3 OD neutral density filter. For bare PCIs, R^2 = 0.998, a = 47.1, b = 80.4. For PCI-borosilicate, R^2 = 0.999, a = 47.3, b = 699. For PCI-neutral density filter, R^2 = 0.998, a = 44.2, b = 2728. Color comparison wheels show PCI colors corresponding to doses marked along the x-axis, except in "No attenuator" case due to space constraints on the x-axis. Datapoints within the shaded region denote individual PCI measurements, line denotes best fit, and shaded region denotes 95% prediction interval on prediction of color change from observation of UV-C dose. (B) The relative uncertainty of UV-C dose measurements for a bare PCI, PCI-borosilicate stack, and PCI-1.3 OD neutral density filter stack (from top to bottom, corresponding to the calibration curves plotted in panel A).

Analytical and empirical characterization demonstrate non-ideal angular response of a model non-diffuse attenuator. To assess quantification accuracy of the PCI-borosilicate stack at different angles of incidence, we compared both the analytical and empirical angular response of a PCI stacked behind 1.1 mm-thick borosilicate to an ideal response. Using an apertured UV-C lamp to achieve near-normal angles of incidence (**Figure 11.8**), we measured a T_{total} of 15.63% ± 0.06% for 1.1 mm-thick borosilicate (standard deviation of 3 replicates). We used thickness and measured T_{total} to predict the PCI-borosilicate stack angular response analytically, and also measured angular response with the point-like UV-C source.

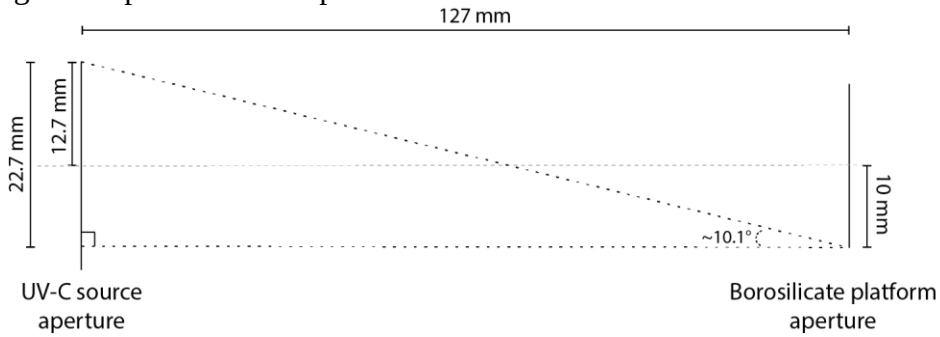

Figure 11.8. Borosilicate transmittance measurement involves a maximum angle of incidence of 10.1° from apertured UV-C source. To measure the total transmittance through borosilicate at near-normal incidence, the maximum angle incident on the borosilicate should be minimized. Borosilicate is placed on an apertured platform in front of the radiometer. In our setup, the maximum angle incident on the borosilicate from the apertured UV-C source is ~10.1°.

As a non-diffuse material, we hypothesized that the PCI-borosilicate stack would readout lower UV-C doses than expected from Lambert's cosine law, with deviations from ideal increasing

with angle of incidence due to angle-dependent reflection and absorption[19] (**Figure 11.9A**). We calculated the integrated cosine error (**Eq. 11.3**) using an upper limit of integration of 75º, the last angle measured <80º. For the PCI-borosilicate stack, we predicted analytically and measured an integrated cosine error of 12.7% and 14.5%, respectfully. Both analytically and empirically, we observed that the UV-C dose transmitted through borosilicate to the PCI underestimates an ideal angular response (**Figure 11.9B**). To quantify the deviation from the ideal response as a function of angle, we calculated the cosine error (**Eq. 11.2**, **Figure 11.9C**). At angles of incidence of 15º and 75º, our model predicted cosine errors of -2.7% and -64.8%, respectively, and we measured cosine errors of -8.2% ± 3.0% and -82.9% ± 5.7%, respectively. Thus, the PCI-borosilicate stack deviated more from an ideal response at higher angles of incidence (**Figure 11.9C**), as hypothesized. Importantly, PCI-borosilicate only meets the angular response design specification (i.e., magnitude of cosine error ≤10%) at near-normal angles of incidence: 0º (due to normalization) and 15º empirically, and up to ~29º analytically. While angle-specific correction factors have been determined and applied in tightly controlled systems[21], this approach is not feasible when the distribution of angles of incidence is not precisely known. For N95s in a UV-C chamber, both the 3D N95 facepiece morphology and uncollimated radiation confound application of an angle-specific correction factor to adjust inaccurate on-N95 UV-C dose measurements.

To evaluate the agreement between the analytical model and experiment, we compared the empirical angular response to model predictions. At 3 out of 6 non-normal angles measured, empirical angular response was within error (total propagated error of PCI quantification uncertainty and replicate variation) of model predictions (**Figure 11.10A-B**). The difference between empirical and analytical angular response was most substantial at 15° and 75° (**Figure 11.10B**), where the empirical normalized angular response was 0.0531 ± 0.0291 and 0.0469 ± 0.0147 below the model predictions, respectively. We hypothesize that the discrepancy between the empirical and analytical angular response arises from error in model parameters (e.g., refractive index, T_{total} at 0°), which will alter the predicted angular response (**Figure 11.5D,F**). Overall, however, analytical and empirical angular response measurements for the PCI-borosilicate stack correspond well. Both show a nonideal angular response with cosine error magnitude >10% for the majority of angles between 0°-90° and thus do not meet the angular response design specification. Negative cosine error at all non-normal angles of incidence means that the PCI-borosilicate stack underestimates UV-C dose, though to different amounts depending on angle.

Diffuse attenuators cause less deviation from ideal angular response. Materials like borosilicate that exhibit specular reflection and transmittance highlight a fundamental tradeoff between extending the PCI dynamic range and minimizing cosine error. In contrast, diffuse materials are predicted to overcome this tradeoff by reducing angle-dependent reflectance (surface diffusers) and/or optical path length (volume diffusers). Available in numerous thicknesses and sizes at relatively low cost as compared to glass diffusers, PTFE is a readily available attenuator material appropriate to a wide range of environments. As a volume diffuser[36], we hypothesized that bulk scattering within PTFE would reduce path length dependence on angle of incidence. Due to unspecified surface roughness, we could not assume ideal surface diffuser behavior; thus, we modeled PTFE analytically as a volume diffuser with specular reflection and transmission at the interfaces (**Figure 11.9D**).

To assess the accuracy of the volume diffuser analytical model and characterize the extent to which PTFE alters PCI angular response, we compared both the analytical and empirical angular response of a PCI-PTFE stack to an ideal response (**Figure 11.9E-F**). For UV-C angles of incidence ≤75°, we predicted analytically and measured an integrated cosine error of 2.7% and

0.97%, respectively. Both the analytical and empirical integrated cosine errors of the PCI-PTFE stack are smaller in magnitude than observed for the PCI-borosilicate stack, as anticipated, and are lower than others have measured for 0.5 mm-thick PTFE[32,39]. We hypothesize that the lower integrated cosine error observed here could arise from differing limits of integration. Due to the limited number of angles of incidence characterized empirically, we integrate through 75°, while others[32,39] integrate through 85° (past the ISO/CIE 19476 definition[31]), incorporating contributions from an additional 10° over which cosine error is typically large. At each rotation angle measured except 90°, PCI-PTFE angular response was within error of the ideal response (**Figure 11.9F**), suggesting a near-ideal angular response. Empirical angular response was within error of model predictions at <60º; at ≥60º, the empirical PCI-PTFE stack angular response was closer to an ideal response than model predictions (**Figure 11.10C-D**). We hypothesize that the empirical angular response of the PCI-PTFE stack was closer to ideal due to some surface diffuser behavior at the interface (not incorporated in the model), and/or slight curvature or non-negligible spacing between the deformable PTFE and PCI. Diffuser-sensor spacing and diffuser curvature have been shown to substantially alter the angular response of radiometers[39–41].

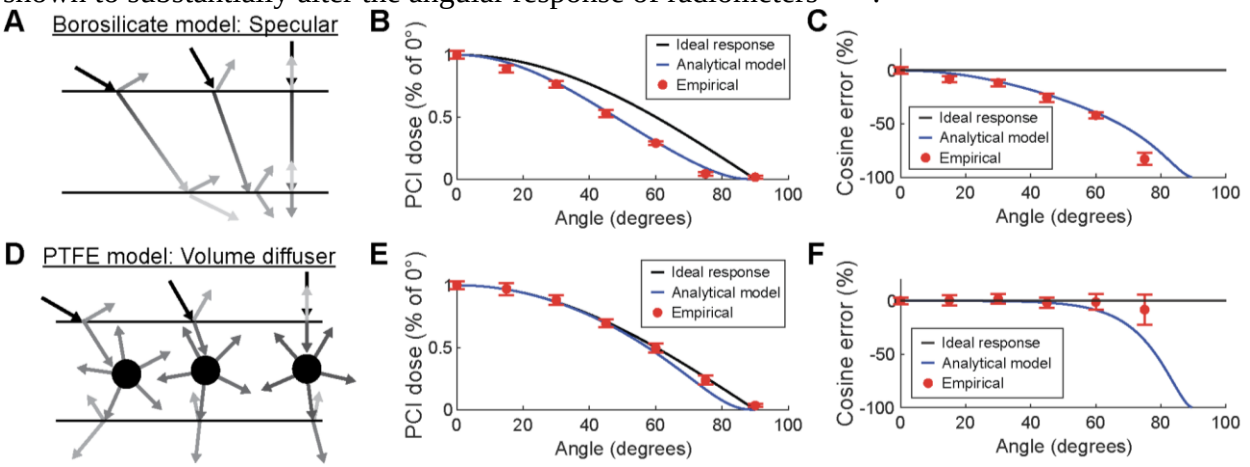

Figure 11.9. Concordance of analytical and empirical angular response of PCIs stacked with specular and diffuse attenuator materials. Analytical and empirical angular response and cosine error are compared for PCIs stacked behind (A-C) borosilicate, a model non-diffuse material, and (D-F) PTFE, a model volume diffuser. (A) Analytically, both reflection at the attenuator interfaces and path-length-dependent absorption through the material thickness contribute to the modeled angular response of non-diffuse materials. The (B) angular response and (C) cosine error of PCI-borosilicate stacks shows a non-ideal angular response at all angles of incidence. (D) The analytical model for PTFE as a volume diffuser includes specular reflection at interfaces, but assumes constant path length (and thus, absorption) through the material for all angles of incidence. The (E) angular response and (F) cosine error of PCI-PTFE stacks illustrate near-ideal response at low angles of incidence and non-ideal angular response at high angles of incidence. Error bars indicate total error, comprising both the standard deviation of replicates and the uncertainty of PCI measurements.

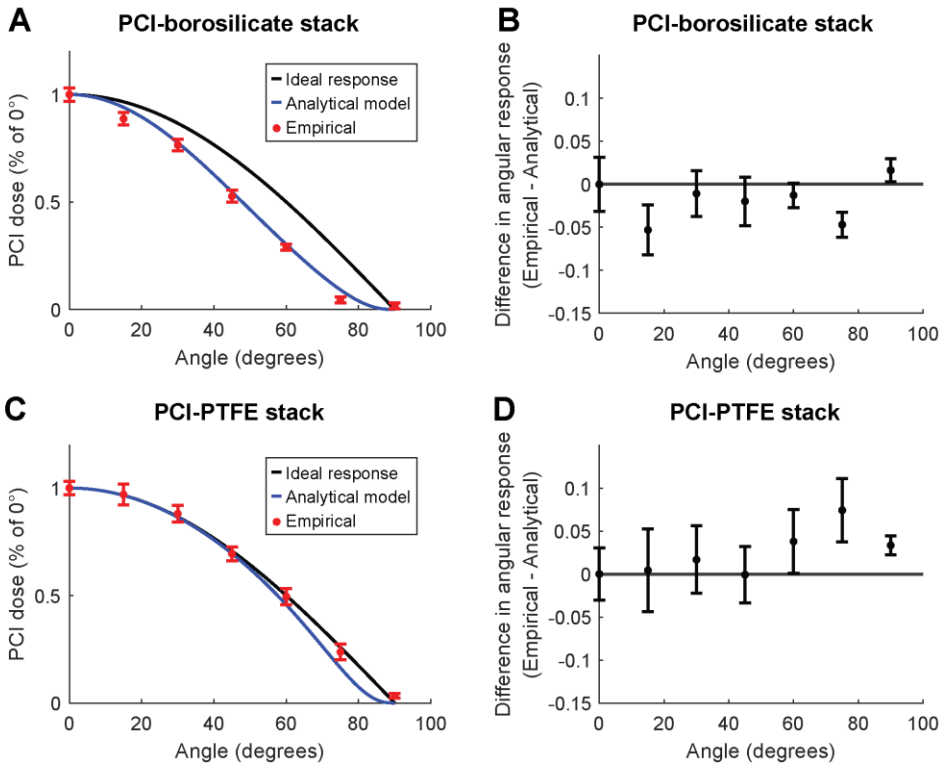

Figure 11.10. Analytical and empirical angular responses of PCI-attenuator pairs are concordant. (A) Analytical and empirical angular response of the PCI-borosilicate stack, along with ideal angular response (cos(θ)). Error bars on empirical measurements indicate total propagated error (the root-sum-square combination of both PCI quantification uncertainty and standard deviation of 3 replicate measurements, as described previously[9]). (B) The difference between empirical and analytical angular response of the PCI-borosilicate stack at each angle of incidence measured. (C) Analytical and empirical angular response of the PCI-PTFE stack, along with ideal angular response. (D) The difference between empirical and analytical angular response of the PCI-PTFE stack at each angle of incidence measured.

Quantifying error in on-N95 UV-C dose measurements by PCI-attenuator stacks. Based on the modeled and measured angular response measurements from the point-like UV-C source, we hypothesized that a PCI-PTFE stack would measure on-N95 dose more accurately than a PCI-borosilicate stack, particularly at on-N95 locations with high angles of incidence. To test this hypothesis, we compared UV-C dose measured with PCIs and PCI-attenuator stacks to true applied dose at two locations on an N95 centered in a chamber with 5 UV-C bulbs arrayed across the top. The presence of multiple UV-C bulbs, as well as scattering and reflection[42] in this and other commercial decontamination systems, stymie determination of angle of incidence distribution at any given location. We chose two on-N95 measurement locations which we hypothesized receive substantially different angles of incidence: (1) near the apex ("low-angle"; near-normal), and (2) near the base ("high-angle"; non-normal) (**Figure 11.11A**). Based on the analytical model and the point-like UV-C source measurements (**Figure 11.9**), we hypothesized that the PCI-borosilicate stack would underestimate UV-C dose at both N95 locations, with greater underestimation at the high angle location. In contrast, PCI-PTFE angular response had cosine error magnitudes <10% at all angles of incidence measured empirically and at angles $\leq 61^{o}$ analytically, so we hypothesized that the PCI-PTFE stack would measure on-N95 UV-C dose accurately, with some error introduced at the high-angle N95 location.

At both on-N95 locations, UV-C dose was measured from PCI color change using PCI-attenuator-specific calibration curves (**Figure 11.5G**). To evaluate the measurement accuracy, the true dose applied at each on-N95 location was determined by multiplying a radiometer measurement obtained in each exposure by the respective predetermined ratio of irradiances at each on-N95 location and at the radiometer ($\frac{Irr_{low-angle}}{Irr_{radiometer}}$= 2.27 ± 0.06; $\frac{Irr_{high-angle}}{Irr_{radiometer}}$= 0.93 ± 0.03). Based on the ULOQ of the two PCI-attenuator stacks, on-N95 UV-C dose measurements up to ~1.200 J/cm^2 were characterized and compared to the true dose to evaluate the on-N95 dynamic range and angular response of PCI, PCI-borosilicate, and PCI-PTFE (**Figure 11.11B-D**). In agreement with the dynamic ranges measured on a planar surface (**Figure 11.5G**), the measured UV-C dose of the PCI-attenuator stacks is linearly proportional to true dose throughout the entire dose range tested at each on-N95 location (~0.050 to ~1.200 J/cm^2, **Figure 11.11C-D**, top; **Table 11.1**). Thus, both borosilicate and PTFE meet the design specification of extending on-N95 PCI dynamic range to ≥1.0 J/cm^2. In contrast, UV-C dose measured by the bare PCI plateaus with measurement error greatly exceeding 10% at true doses above ~0.250 J/cm^2 (**Figure 11.11B**), in agreement with the PCI ULOQ (**Figure 11.5G**).

To evaluate overall measurement accuracy, we calculated the percent error of UV-C dose measurements (**Figure 11.11B-D**, bottom). Doses measured with the PCI-borosilicate stack underestimated the true dose by 14.7% ± 4.0% and 40.8% ± 3.0% at the low-angle and high-angle on-N95 locations, respectively (errors are the standard deviation of 18 total dose measurements at a given location). Thus, in agreement with our hypothesis, we found that dose measured with the PCI-borosilicate stack underestimated true UV-C dose to a greater extent at the more steeply sloped, high-angle on-N95 location. Inaccuracy in measured dose also arises due to differences in the distribution of angles of incidence between the calibration curve and on-N95 measurements. As discussed, it is infeasible to generate calibration curves or correction factors specific to each on-N95 location in the chamber. In contrast, doses measured with the PCI-PTFE stack only underestimated the true dose by 3.6% ± 6.7% and 19.8% ± 5.8% at the low-angle and high-angle on-N95 locations, respectively. UV-C dose measurements by the PCI-PTFE stack were more accurate than those by the PCI-borosilicate stack, supporting our hypothesis and model predictions that PCIs stacked behind diffuse materials have an angular response nearer to an ideal response than when stacked behind a non-diffuse material. Overall, PCI-PTFE dose measurements were within error of the true dose at the low-angle on-N95 location (measured dose underestimated true dose by 3.6% ± 6.7% over 18 measurements), in agreement with our hypothesis that PCI-PTFE has near-ideal angular response at low angles of incidence. We observe greater error in PCI-PTFE-measured dose at the high-angle on-N95 location than observed at all angles measured with the point-like UV-C source (**Figure 11.9F**). The larger error at the high-angle location on-N95 may indicate an average angle of incidence >75º at that location, yielding a greater cosine error than measured with the point-like UV-C source at angles ≤75º. As discussed previously, geometrical factors such as slight variations in PTFE curvature, as well as the use of calibration curves not specific to each experimental measurement location, may have also contributed to angular response differences measured in the two systems. Additionally, while guidance on the acceptable source-to-detector distance for accurate angular response measurements varies[10,43], insufficient distance can yield artificially high angular response[43]. This artifact may contribute to the near-ideal angular response measured with the point-like source, where the maximum source-to-detector distance was limited due to low source irradiance. On-N95, the PCI-PTFE attenuator stack underestimated dose to a greater extent with increasing dose, a phenomenon not observed with the PCI-borosilicate stack (**Figure 11.11C-D**). We hypothesize the dose-dependent error may arise

from an increasing difference between the true and applied calibration curve at higher doses (**Figure 11.12**), and/or temperature-induced changes in PTFE transmittance[44] not captured in the PCI-PTFE calibration curve (generated off-N95) due to differences in heat dissipation on-N95.

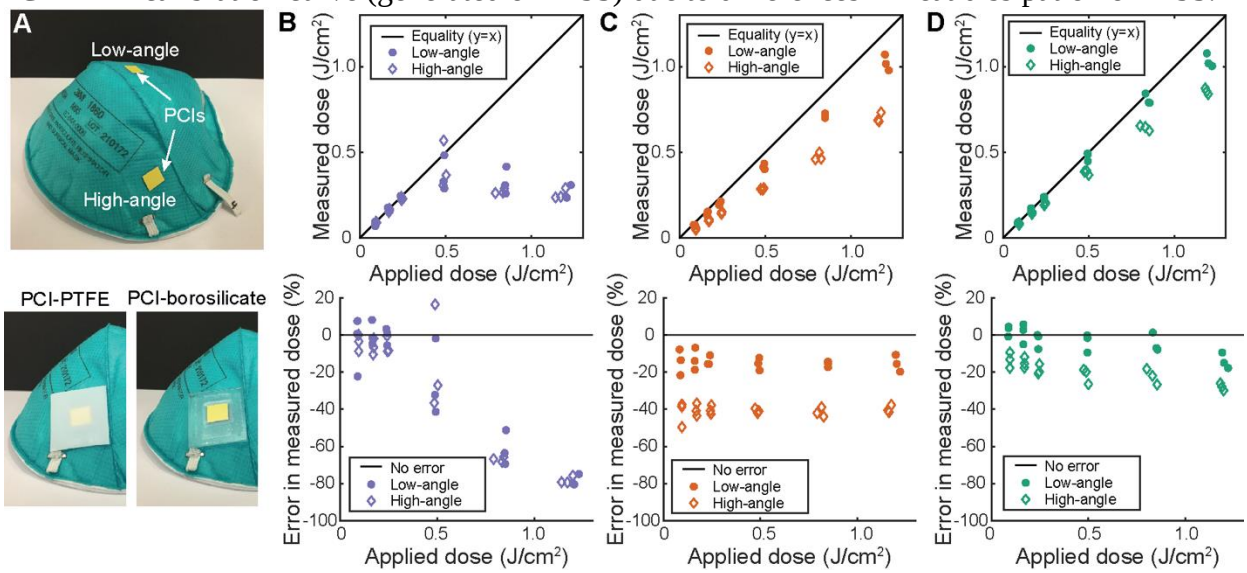

Figure 11.11. On-N95 UV-C dose measurement error depends on attenuator and on-N95 location. (A) UV-C dose was measured at two different on-N95 positions (top image): near the apex ("low-angle"), and on the steeply sloped side ("high-angle"). For PCI-attenuator stacks (PTFE or borosilicate), a PCI was placed directly underneath an attenuator (bottom image). On-N95 UV-C dose measurement accuracy of a (B) bare PCI, (C) PCI-borosilicate stack, or (D) PCI PTFE-stack was determined by comparing measured to true applied dose calculated from radiometer measurements and the predetermined ratio between the irradiance at the ratiometer and at each on-N95 location. Measured dose (top) and percent error in measured dose (bottom) were plotted against true applied dose. UV-C dose measurements underestimate true applied dose, particularly at the high-angle location.

Table 11.1. Significance of linear correlation between true and measured dose for each attenuator and on-N95 location tested.

Attenuator & on-N95 location	r^2	p
No attenuator, low-angle	0.282	0.024
No attenuator, high-angle	0.182	0.078
Borosilicate, low-angle	0.997	4.76e-21
Borosilicate, high-angle	0.997	8.21e-22
PTFE, low-angle	0.990	2.64e-17
PTFE, high-angle	0.995	1.68e-19

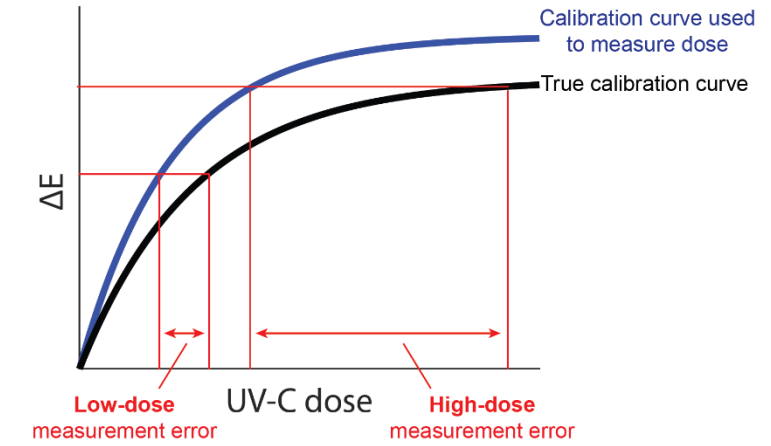

Figure 11.12. Use of incorrect calibration curve can yield dose-dependent measurement error. If the PCI-attenuator stack has a non-ideal angular response, and/or if PCI reaction kinetics are dependent on environmental conditions such as temperature or humidity, differences in UV-C angles of incidence and environmental factors may yield different calibration curve shapes. Because it is infeasible to generate calibration curves for every location and environmental condition within the UV-C chamber to exactly match the conditions of a given measurement, the calibration curve used to determine dose from a measured ΔE may not represent the true calibration curve for the exact chamber location and environmental conditions present at the time the PCI was exposed. Use of an incorrect calibration curve may lead to dose-dependent measurement error.

11.5 Conclusions

Overall, both modeling and measurements in two different UV-C systems demonstrate that diffuse attenuators such as PTFE alter the ideal angular response of PCIs less than non-diffuse materials such as borosilicate, but that both types of planar attenuators cause deviation from ideal at high angles of incidence. Unless the material is ideally diffuse, the factors which decrease attenuator transmittance (thus increasing PCI-attenuator ULOQ) also increase the angular dependence of transmittance, yielding a fundamental tradeoff between the two design requirements of increased dynamic range and minimal cosine error. Both attenuators increased the PCI ULOQ by >4×, but the non-ideal angular response of PCI-attenuator stacks led to underestimation of measured on-N95 dose at one or both locations. The on-N95 results highlight a critical consideration for designing optical attenuators: materials that lead to measurements within error of the ideal angular response in a controlled setting may not accurately translate to user environments. Additionally, cumulative UV-C exposure also affects the transmission properties of some attenuators (e.g., solarization of glass[45]), which limits reuse. Though relatively low-cost materials such as PTFE may be feasible for single-use applications, the stability of attenuator transmittance with increasing cumulative UV-C dose must be robustly characterized prior to implementation of any attenuator material. Future study could consider introducing surface roughness and/or curvature to volume diffusers to create PCI-attenuator stacks with smaller cosine error at higher angles of incidence. Alternative strategies to extend PCI dynamic range, such as the development of new PCI formulations, are also a promising approach that may be more robust than physically attenuating UV-C incident on the PCI.

11.6 References

1. Memarzadeh, F., Olmsted, R. N. & Bartley, J. M. Applications of ultraviolet germicidal irradiation disinfection in health care facilities: effective adjunct, but not stand-alone technology. *Am J Infect Control* **38**, S13-24 (2010).
2. Tseng, C.-C. & Li, C.-S. Inactivation of Viruses on Surfaces by Ultraviolet Germicidal Irradiation. *J. Occup. Environ. Hyg.* **4**, 400–405 (2007).
3. Lowe, J. J. *et al. N95 Filtering Facepiece Respirator Ultraviolet Germicidal Irradiation (UVGI) Process for Decontamination and Reuse*. https://www.nebraskamed.com/sites/default/files/documents/covid-19/n-95-decon-process.pdf (2020).
4. Ozog, D. M. *et al.* The Effect of Ultraviolet C Radiation Against Different N95 Respirators Inoculated with SARS-CoV-2. *Int. J. Infect. Dis.* 224–229 (2020) doi:10.1016/j.ijid.2020.08.077.
5. Kowalski, W. *Ultraviolet Germicidal Irradiation Handbook: UVGI for Air and Surface Disinfection*. (Springer, Berlin, Heidelberg, 2009). doi:10.1007/978-3-642-01999-9.
6. Fisher, E. M. & Shaffer, R. E. A method to determine the available UV-C dose for the decontamination of filtering facepiece respirators: UV-C decontamination of respirators. *J. Appl. Microbiol.* **110**, 287–295 (2011).
7. Huber, T., Goldman, O., Epstein, A. E., Stella, G. & Sakmar, T. P. Principles and practice for SARS-CoV-2 decontamination of N95 masks with UV-C. *Biophys. J.* S0006349521001971 (2021) doi:10.1016/j.bpj.2021.02.039.
8. Grist, S. M. *et al.* Current Understanding of Ultraviolet-C Decontamination of N95 Filtering Facepiece Respirators. *Applied Biosafety* (2021) doi:10.1089/apb.20.0051.
9. Su, A., Grist, S. M., Geldert, A., Gopal, A. & Herr, A. E. Quantitative UV-C dose validation with photochromic indicators for informed N95 emergency decontamination. *PLoS ONE* **16**, e0243554 (2021).
10. Lawal, O. *et al.* Method for the Measurement of the Output of Monochromatic (254 nm) Low-Pressure UV Lamps. *IUVA News* **19**, (2017).
11. Reifsnyder, W. E. Radiation geometry in the measurement and interpretation of radiation balance. *Agricultural Meteorology* **4**, 255–265 (1967).
12. McCluney, W. R. *Introduction to Radiometry and Photometry, Second Edition*. (Artech House, 2014).
13. Zorzano, M.-P., Martín-Soler, J. & Gómez-Elvira, J. UV Photodiodes Response to Non-Normal, Non-Colimated and Diffusive Sources of Irradiance. in *Photodiodes - Communications, Bio-Sensings, Measurements and High-Energy Physics* (IntechOpen, 2011).
14. Larason, T. & Ohno, Y. Calibration and characterization of UV sensors for water disinfection. *Metrologia* **43**, S151–S156 (2006).
15. Geldert, A. *et al.* Nonuniform UV-C dose across N95 facepieces can cause 2.9-log variation in SARS-CoV-2 inactivation. *medRxiv* (2021) doi:10.1101/2021.03.05.21253022.
16. Mills, A., McDiarmid, K., McFarlane, M. & Grosshans, P. Flagging up sunburn: a printable, multicomponent, UV-indicator that warns of the approach of erythema. *Chem. Commun.* 1345–1346 (2009) doi:10.1039/b900569b.
17. Smith, A. T. *et al.* Multi-color Reversible Photochromisms via Tunable Light-Dependent Responses. *Matter* **2**, 680–696 (2020).
18. Khiabani, P. S., Soeriyadi, A. H., Reece, P. J. & Gooding, J. J. Paper-Based Sensor for Monitoring Sun Exposure. *ACS Sens.* **1**, 775–780 (2016).

19. Furler, R. A. Angular Dependence of Optical Properties of Homogeneous Glasses. *ASHRAE Transactions* **97**, 1–9 (1991).
20. Seckmeyer, G. & Bernhard, G. Cosine error correction of spectral UV irradiance. *SPIE Proc.* **2049**, (1993).
21. Severin, B. F. & Roessler, P. F. Resolving UV photometer outputs with modeled intensity profiles. *Water Research* **32**, 1718–1724 (1998).
22. SCHOTT Technical Glass Solutions GmbH. BOROFLOAT® 33 – Optical Properties. https://www.schott.com/d/borofloat/bde16ad3-70e5-48a0-b8ac-9146fcd34511/1.0/borofloat33_opt_en_web.pdf.
23. Lake Photonics. Spectralex Optical Diffuser Films. https://www.lake-photonics.com/wp-content/uploads/Spectralex-Optical-Diffuser-Films.pdf.
24. Luo, M. R., Cui, G. & Rigg, B. The development of the CIE 2000 colour-difference formula: CIEDE2000. *Color Res. Appl.* **26**, 340–350 (2001).
25. Quintern, L. E., Horneck, G., Eschweiler, U. & Bücker, H. A Biofilm Used as Ultraviolet-Dosimeter. *Photochem. Photobiol.* **55**, 389–395 (1992).
26. Rutala, W. A., Gergen, M. F., Tande, B. M. & Weber, D. J. Rapid hospital room decontamination using ultraviolet (UV) light with a nanostructured UV-reflective wall coating. *Infect. Control Hosp. Epidemiol.* **34**, 527–529 (2013).
27. Schmalwieser, A. W. *et al.* Aging of low-pressure amalgam lamps and UV dose delivery. *J. Environ. Eng. Sci.* **9**, 113–124 (2014).
28. Lore, M. B., Heimbuch, B. K., Brown, T. L., Wander, J. D. & Hinrichs, S. H. Effectiveness of Three Decontamination Treatments against Influenza Virus Applied to Filtering Facepiece Respirators. *Ann. Occup. Hyg.* **56**, 92–101 (2011).
29. Mills, D., Harnish, D. A., Lawrence, C., Sandoval-Powers, M. & Heimbuch, B. K. Ultraviolet germicidal irradiation of influenza-contaminated N95 filtering facepiece respirators. *Am. J. Infect. Control* **46**, e49–e55 (2018).
30. Heimbuch, B. & Harnish, D. *Research to Mitigate a Shortage of Respiratory Protection Devices During Public Health Emergencies*. https://www.ara.com/wp-content/uploads/MitigateShortageofRespiratoryProtectionDevices_3.pdf (2019).
31. *Characterization of the performance of illuminance meters and luminance meters*. https://www.iso.org/cms/render/live/en/sites/isoorg/contents/data/standard/06/50/65048.html (2014).
32. Bernhard, G. & Seckmeyer, G. New Entrance Optics for Solar Spectral UV Measurements. *Photochem. Photobiol.* **65**, 923–930 (1997).
33. Allen, D. W., Early, E. A., Tsai, B. K. & Cooksey, C. C. *NIST measurement services: regular spectral transmittance*. https://nvlpubs.nist.gov/nistpubs/Legacy/SP/nistspecialpublication250-69.pdf (2011) doi:10.6028/NIST.SP.250-69.
34. Miller, D. C., Kempe, M. D., Kennedy, C. E. & Kurtz, S. R. Analysis of transmitted optical spectrum enabling accelerated testing of multijunction concentrating photovoltaic designs. *OE* **50**, 013003 (2011).
35. Li, Q., Lee, B. J., Zhang, Z. M. & Allen, D. W. Light scattering of semitransparent sintered polytetrafluoroethylene films. *J. Biomed. Opt.* **13**, 054064 (2008).
36. Lemaillet, P. *et al.* Goniometric and hemispherical reflectance and transmittance measurements of fused silica diffusers. in (ed. Hanssen, L. M.) 996109 (2016). doi:10.1117/12.2237975.

37. Pye, S. D. & Martin, C. J. A study of the directional response of ultraviolet radiometers: I. Practical evaluation and implications for ultraviolet measurement standards. *Phys. Med. Biol.* **45**, 2701–2712 (2000).
38. Sholtes, K. A. *et al.* Comparison of ultraviolet light-emitting diodes and low-pressure mercury-arc lamps for disinfection of water. *Environmental Technology* **37**, 2183–2188 (2016).
39. Pulli, T. *et al.* Improved diffusers for solar UV spectroradiometers. *AIP Conference Proceedings* **1531**, 813–816 (2013).
40. Martínez, M. A., Andújar, J. M. & Enrique, J. M. A New and Inexpensive Pyranometer for the Visible Spectral Range. *Sensors (Basel)* **9**, 4615–4634 (2009).
41. Cahuantzi, R. & Buckley, A. Geometric optimisation of an accurate cosine correcting optic fibre coupler for solar spectral measurement. *Rev. Sci. Instrum.* **88**, 095003 (2017).
42. Gostein, M. & Stueve, B. Accurate measurement of UV irradiance in module-scale UV exposure chambers, including spectral angular response of sensor. in *2016 IEEE 43rd Photovoltaic Specialists Conference (PVSC)* 0863–0866 (2016). doi:10.1109/PVSC.2016.7749731.
43. Schmalwieser, A. W. Fifteen years of experience with standardized reference radiometers for controlling low-pressure UV disinfection plants for drinking water. *Water Supply* **17**, 975–984 (2016).
44. Ylianttila, L. & Schreder, J. Temperature effects of PTFE diffusers. *Optical Materials* **27**, 1811–1814 (2005).
45. Gatto, A., Escoubas, L., Roche, P. & Commandré, M. Simulation of the degradation of optical glass substrates caused by UV irradiation while coating. *Opt. Commun.* **148**, 347–354 (1998).

Chapter 12

Mapping of UV-C dose and SARS-CoV-2 viral inactivation across N95 respirators during decontamination

Adapted with permission from A. Geldert*, A. Su*, A. W. Roberts, G. Golovkine, S. M. Grist, S. A. Stanley, & A. E. Herr, "Mapping of UV-C dose and SARS-CoV-2 viral inactivation across N95 respirators during decontamination", *MedRxiv and in revision.*

12.1 Abstract

During public health crises like the COVID-19 pandemic, ultraviolet-C (UV-C) decontamination of N95 respirators for emergency reuse has been implemented to mitigate shortages. Pathogen photoinactivation efficacy depends critically on UV-C dose, which is distance- and angle-dependent and thus varies substantially across N95 surfaces within a decontamination system. Due to nonuniform and system-dependent UV-C dose distributions, characterizing UV-C dose and resulting pathogen inactivation with sufficient spatial resolution on-N95 is key to designing and validating UV-C decontamination protocols. However, robust quantification of UV-C dose across N95 facepieces presents challenges, as few UV-C measurement tools have sufficient 1) small, flexible form factor, and 2) angular response. To address this gap, we combine optical modeling and quantitative photochromic indicator (PCI) dosimetry with viral inactivation assays to generate high-resolution maps of "on-N95" UV-C dose and concomitant SARS-CoV-2 viral inactivation across N95 facepieces within a commercial decontamination chamber. Using modeling to rapidly identify on-N95 locations of interest, in-situ measurements report a 17.4 ± 5.0-fold dose difference across N95 facepieces in the chamber, yielding 2.9 ± 0.2-log variation in SARS-CoV-2 inactivation. UV-C dose at several on-N95 locations was lower than the lowest-dose locations on the chamber floor, highlighting the importance of on-N95 dose validation. Overall, we integrate optical simulation with in-situ PCI dosimetry to relate UV-C dose and viral inactivation at specific on-N95 locations, establishing a versatile approach to characterize UV-C photoinactivation of pathogens contaminating complex substrates such as N95s.

12.2 Introduction

The global shortages of N95 respirators during the COVID-19 pandemic has required crisis capacity strategies for decontamination and reuse of these complex, multilayered, made-for-single-use protective textiles. With established applications in water[1,2], air[3,4], and non-porous surface[5] disinfection, ultraviolet-C (UV-C) germicidal (200-280 nm) irradiation was identified as a promising and accessible method for N95 decontamination[6]. Upon sufficient absorption by nucleic acids, UV-C inactivates pathogens by damaging their genetic material[5]; thus, UV-C decontamination efficacy is critically dependent on total received dose (integrated irradiance over time). The U.S. Food & Drug Administration (FDA) definition of tier 3 "bioburden reduction" requires sufficient UV-C dose to be applied across the N95 to yield ≥3-$\log_{10}$ inactivation of non-enveloped virus[7] ("$\log_{10}$" subsequently referred to as "log").

N95s present distinct challenges for UV-C decontamination: the applied surface dose required to decontaminate all N95 layers is orders of magnitude higher than the dose required on non-porous surfaces[8,9], and varies between N95 models[10,11] due to substantial differences in material composition. UV-C decontamination protocols must ensure that all N95 surfaces receive sufficient dose for pathogen inactivation, while also not exceeding the exposure threshold for material degradation, as high cumulative doses of UV-C degrade N95 material[12]. Additionally, UV-C dose is nonuniformly distributed across the complex, 3D N95 surface due to Lambert's cosine law[13] and self-shadowing. Thus, UV-C distribution across N95 surfaces is highly dependent on N95 morphology, as well as the decontamination system and N95 positioning. Together, these characteristics complicate determination of the UV-C dose applied to all N95 surfaces in a decontamination system, impacting both research and implementation[14,15].

Effective implementation requires translation of robust research studies linking on-N95 surface dose to viral inactivation for a given UV-C source emission spectrum and N95 model. However, coincident on-N95 dose and viral inactivation measurements are infeasible as the measurement sensor would shadow the pathogen. Furthermore, most UV-C dosimetry tools lack sufficient spatial resolution, throughput, and angular response for on-N95 measurements. As a result, UV-C dose for N95 decontamination is typically characterized indirectly. For example, to circumvent challenges associated with making UV-C dose measurements on non-planar surfaces, many studies, including a recent study of SARS-CoV-2[16], assess UV-C dose and viral inactivation on flat coupons of N95 material. N95 coupon studies determine the UV-C dose required for viral inactivation throughout the porous N95 material layers, but fail to capture the impact of the 3D facepiece shape on the received UV-C dose across the N95 surface. Other approaches use optical modeling to estimate the UV-C distribution across N95 surfaces from the UV-C dose measured in a single location, in order to relate approximate UV-C dose to SARS-CoV-2 inactivation[17]. Optical modeling is an attractive approach to study UV-C distribution, as it can recapitulate nearly any UV-C system to provide a high-resolution map of irradiance distribution[18] via entirely user-defined system parameters. However, optical models alone cannot capture non-idealities such as irradiance fluctuations, bulb-to-bulb differences in power output, and environmental and material changes over time[5,14,19,20]. Additionally, while the modularity of optical modeling is advantageous for broad applicability, the model accuracy depends on both the optics expertise of the user and the accuracy of user-defined parameters such as the reflective and scattering properties of all materials. Thus, the high resolution and rapid iteration capabilities of optical simulations would be most valuable when coupled with *in situ* validation measurements.

To this end, a promising *in situ* method has recently been developed to quantify on-N95 dose using UV-C photochromic indicators (PCIs)[14]. PCIs complement simulation results by providing absolute dose measurements and empirical validation. Planar, paper-like dosimeters similar to and including PCIs have been shown to have ideal angular detection response[21,22]. The low cost and small, flexible form factor of PCIs supports quantitative, spatially resolved and high-throughput on-N95 PCI dosimetry in the same exposure and in nearly the same on-N95 location as inoculated pathogens, minimizing confounding factors such as temporal or spatial variation[14] and angular dependence of UV-C irradiance[13]. Thus, PCIs may comprise a cornerstone to better inform safe and effective UV-C decontamination, especially when corroborated by further study to evaluate suitability for readout by diverse, lower-cost color readers.

Here, to investigate the impact of UV-C dose variation on SARS-CoV-2 inactivation on N95s, we introduce a method to simultaneously map UV-C dose and SARS-CoV-2 viral inactivation across N95 respirator facepieces. We integrate two approaches for high-spatial-

resolution on-N95 dosimetry: PCI quantification and optical modeling. We develop an optical modeling workflow to characterize UV-C dose distribution across N95s within a decontamination chamber to rapidly iterate on experimental design, and simultaneously inform and validate this model using *in-situ* PCI dose quantification. From the high-resolution simulated N95 dose maps, we identify pairs of proximal measurement sites receiving equivalent UV-C dose in order to measure UV-C dose at SARS-CoV-2 inoculation sites within the same UV-C exposure. For the first time, we apply quantitative *in-situ* PCI dosimetry to simultaneously quantify UV-C dose and SARS-CoV-2 inactivation across a model N95 facepiece (intra-N95) at multiple locations (intra-chamber), providing new, practical insight into how N95 facepiece shape impacts decontamination efficacy.

12.3 Materials & Methods

Inter-UV-C chamber and radiometer assessment. All UV-C decontamination experiments were performed with Spectronics XL-1000 UV-C chambers with BLE-8T254 low pressure amalgam bulbs. Irradiance was measured using calibrated, NIST-traceable ILT 1254/TD UV-C radiometers (International Light Technologies, ILT) and corresponding ILT DataLight III meter software. A custom notch in the UV-C chamber doors allowed a cable to pass through for *in-situ* radiometer measurements. One chamber and radiometer were used exclusively in a biosafety level 3 (BSL-3) laboratory for SARS-CoV-2 inactivation experiments, while another set was used for all experiments outside BSL-3. The UV-C irradiance over time and space within the two chambers were concordant (**Figure 12.1**), as were measurements from the two radiometers (**Figure 12.2**).

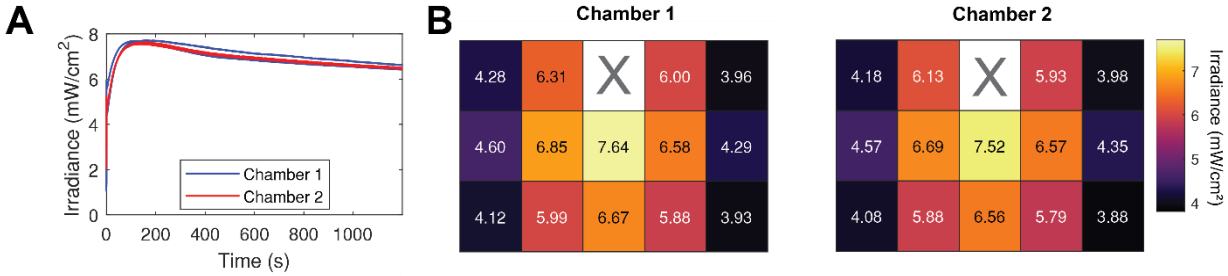

Figure 12.1. Two UV-C chambers have similar irradiance profiles over time and space. (A) Irradiance at the center of the chamber during the first 20 minutes of exposure after turning on the UV-C bulbs (N = 2 for each chamber). Note decrease in output over time after bulb warm-up. (B) Heatmaps of spatial irradiance distribution within each chamber (average of 3 replicate measurements at each location).

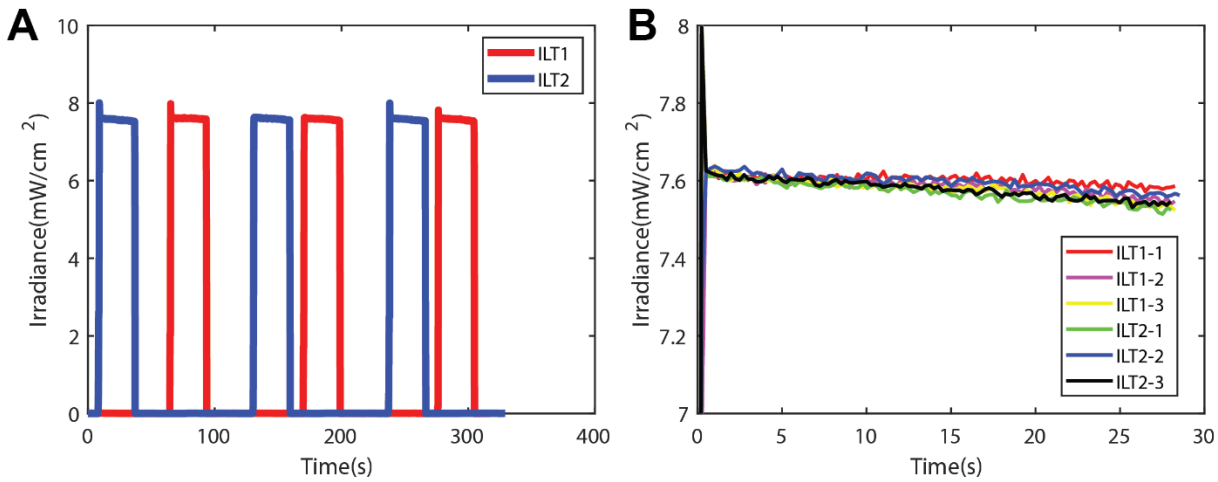

Figure 12.2. Equivalent performance of two ILT1254 radiometers. (A) Irradiance recorded by each radiometer (labeled ILT1, ILT2) when placed in the same location at the center of a UV-C chamber and exposed for 30 seconds in alternating fashion. (B) The irradiance data from (A) overlaid on top of one another, where t = 0 represents the start of each exposure.

PCI measurements. For UV-C dose measurements, PCIs (UVC 100 Dosimeter dots, American Ultraviolet; 25.4 mm diameter) were cut into quarters prior to use. D65/10° L*a*b* PCI color was measured using an RM200QC spectrocolorimeter (X-Rite, large aperture setting) and/or Color Muse colorimeter (Variable, Inc, with Variable color app). The Color Muse was aligned over the PCI using a template (**Figure 12.3**).

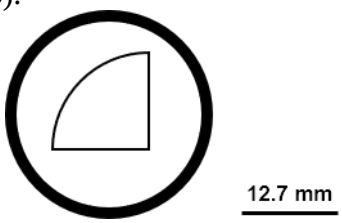

Figure 12.3. Template used to measure PCI color with Color Muse colorimeter. Because the Color Muse lacks a preview function, the template ensures that a quarter-circle PCI fills the Color Muse aperture.

PCI calibration curves, relative uncertainty, and dynamic range determination were performed as previously described[14]. Briefly, calibration curves relating PCI color change (CIEDE2000 ΔE) to received dose were established by placing a radiometer and a PCI at two locations of equal irradiance within the UV-C chamber. PCIs were placed on a platform of similar height to the radiometer sensor (34 mm). The dose (calculated by integrating recorded radiometer irradiance over time) and CIEDE2000 ΔE measured after 9 different exposure lengths were fit to a function based on first-order reaction kinetics, as reported previously (a and b are fit parameters)[14]: $\Delta E = a(1 - e^{\frac{-dose}{b}})$ (**Figure 12.4A,C**). 95% confidence intervals (CIs) on UV-C dose measurements were calculated via propagation of error from standard deviations of the fit parameters and the standard deviation of replicate ΔE measurements of unexposed PCIs (N = 10 and 11 for RM200QC measurement of PCI batches 1 and 2, respectively; N = 6 and 5 for Color Muse measurement of PCI batches 1 and 2, respectively). Relative uncertainty was defined as $\frac{CI\ width}{2*estimated\ dose}$ (**Figure 12.4B,D**). The dynamic range was quantified as the dose range over which the relative uncertainty was <10%. Batch-specific calibration curves were generated due to batch-to-batch variability

(**Figure 12.5**); calibration curves were also specific to the attenuator and colorimeter used. Custom MATLAB scripts performed PCI dosimetry analyses.

To measure doses beyond the PCI dynamic range on planar surfaces, a 1.1 mm-thick Borofloat borosilicate glass attenuator (25.4 mm width and length, 80/50 scratch/dig quality, Precision Glass & Optics 0025-0025-0011-GE-CA) with 12.4% ± 0.4% UV-C transmittance was placed over the PCI (**Figure 12.4**). For one batch of 1.1 mm-thick borosilicate glass, we measured a UV-C transmittance of 12.4% ± 0.4%, using a Spectroline XL-1500 chamber with BLE-1T155 bulbs and Model 308 data-logging UV radiometer with a 254 nm sensor (Optical Associates, Inc., OAI). While an ILT 1254 radiometer was used for all other experiments, the OAI Model 308 radiometer was used to measure borosilicate transmittance because the Model 308 radiometer sensor is flat, so transmittance measurements could be made by comparing the measured irradiance with and without borosilicate covering the sensor. Correspondingly, a different UV-C chamber (XL-1500) was used for transmittance measurement because the XL-1500 had a larger notch cut in the door to accommodate the Model 308 radiometer sensor cable. To generate calibration curves of the PCI-borosilicate attenuator pair, the borosilicate was placed over the PCI during exposure but removed prior to PCI color measurement. The exposure times were also multiplied by a factor of $\frac{1}{\%T}$, where %T is the UV-C transmittance of the borosilicate glass, to account for the lower proportion of UV-C light reaching the PCI. We generated calibration curves specific to the PCI batch, attenuator, and colorimeter to quantify UV-C dose from PCI color change (CIEDE2000 ΔE) with respect to an unexposed reference (**Figure 12.4**, **Figure 12.5**).

For all ratios of two PCI measurements (e.g., fold difference in on-N95 dose), other than cases where PCI measurements are normalized to a maximum PCI reading, we report total error: the root sum square of standard deviations associated with both replicate variation and propagated uncertainty in PCI dose estimation. All other error values report the standard deviation of replicate measurements.

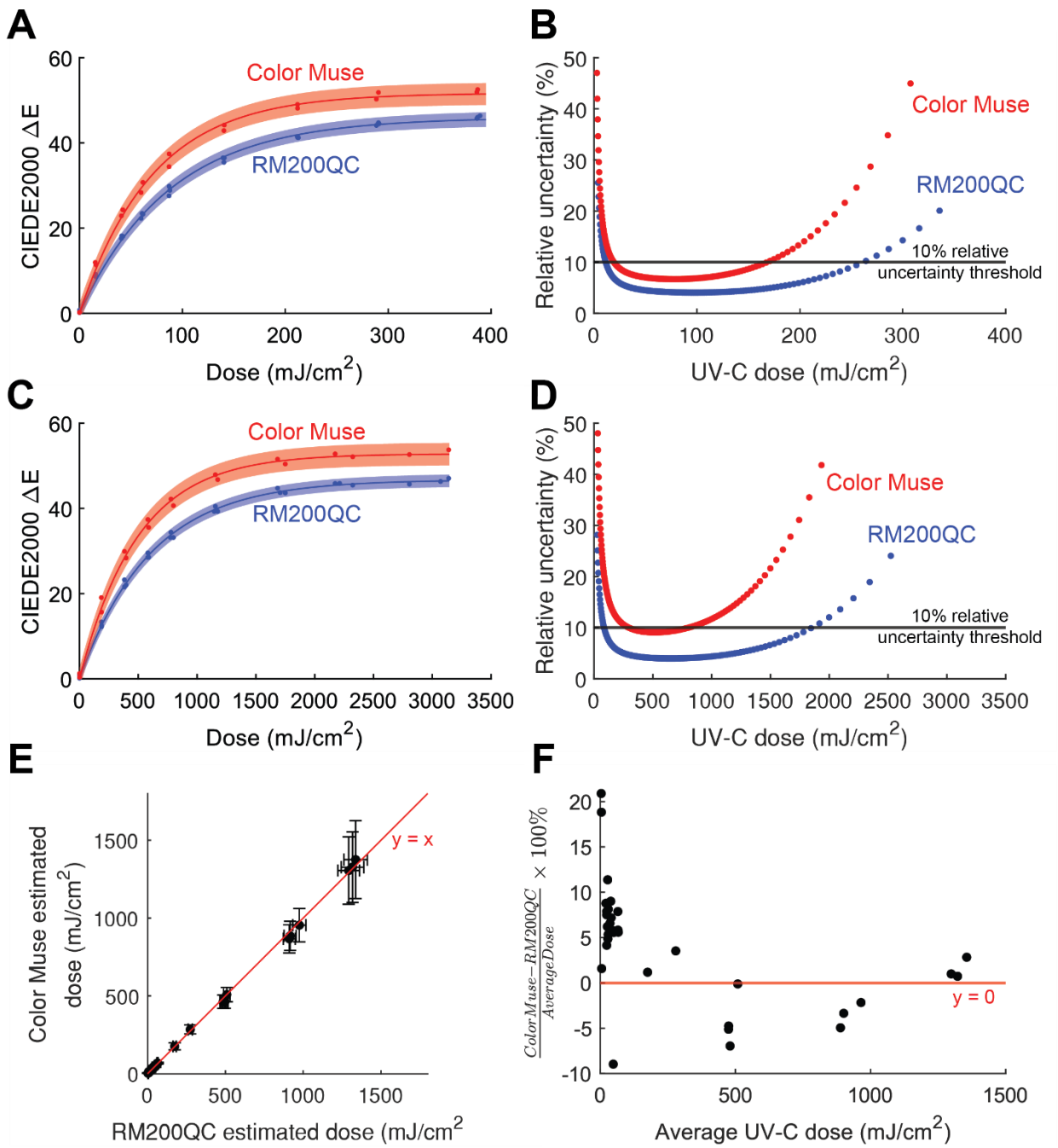

Figure 12.4. UV-C dose quantification from PCI color change. (A) Calibration curve relating UV-C dose to PCI color change (CIEDE2000 ΔE) measured with either the RM200QC spectrocolorimeter (N = 3 replicate data sets) or the Color Muse colorimeter (N = 2 replicate data sets). The shaded regions represent the 95% prediction interval on prediction of PCI color change from measured UV-C dose. Fit function is defined by Su & Grist, et al.[14] based on first-order reaction kinetics. For the RM200QC, R^2 = 0.9976, a = 46.0 (45.3, 46.7), b = 87.4 (83.6, 91.2). For the Color Muse, R^2 = 0.9963, a = 51.7 (52.8, 50.6), b = 71.2 (66.5, 75.9). (B) Relative uncertainty of dose measurement. Relative uncertainty is defined as half the width of the 95% confidence interval on UV-C dose measurements, divided by measured dose. UV-C dose measurements have <10% relative uncertainty from 11.3 – 261.4 mJ/cm^2 (RM200QC) or 19.2 – 168.1 mJ/cm^2 (Color Muse). (C) Calibration curve of PCI covered by a 1.1 mm-thick borosilicate glass attenuator, which extends the dynamic range. PCI color change is measured with either the RM200QC spectrocolorimeter (N = 3 replicate data sets) or the Color Muse colorimeter (N = 2 replicate data sets). For the RM200QC, R^2 = 0.9982, a = 46.7 (46.2, 47.3), b = 605.9 (584.3, 627.5). For the Color Muse, R^2 = 0.9960, a = 52.8

(51.7, 53.9), b = 495.6 (462.9, 528.3). (D) Relative uncertainty of dose measurements with 1.1 mm-thick borosilicate glass attenuator. UV-C dose measurements have <10% relative uncertainty from 85.0 – 1853.2 mJ/cm^2 (RM200QC) or 295.6 – 802.6 mJ/cm^2 (Color Muse). (E) Scatterplot of UV-C doses measured from the same PCI using either the RM200QC or ColorMuse. Error bars represent the uncertainty in the predicted dose, which arises from uncertainty in the calibration fit parameters and uncertainty in the ΔE measurement. (F) Scatterplot of the difference in dose measured by the ColorMuse and RM200QC. N = 34 PCIs.

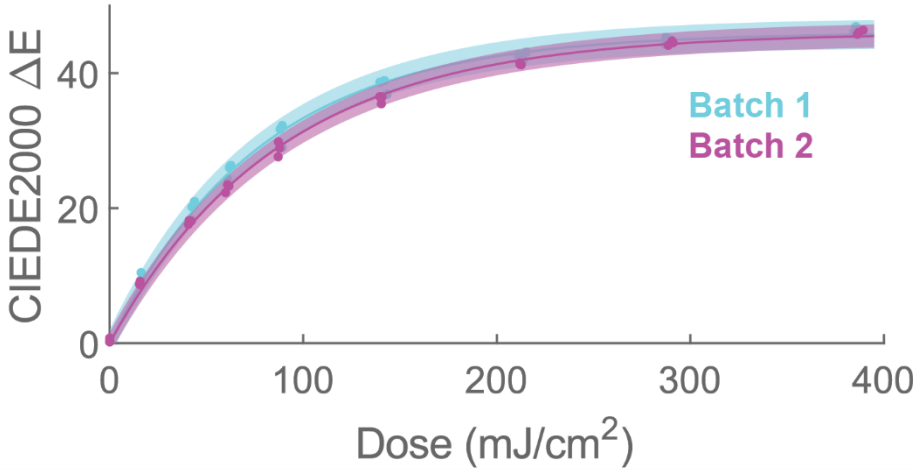

Figure 12.5. PCI calibration curve is batch-dependent. Each curve consists of 3 replicate datasets and was fit to the function based on first-order reaction kinetics defined by Su & Grist, et al.[14] For batch 1, R^2 = 0.9964, a = 46.0 (45.2, 46.8), b = 77.6 (73.5, 81.6). For batch 2, R^2 = 0.9976, a = 46.0 (45.3, 46.7), b = 87.4 (83.6, 91.2). Batch to batch variation may be due to changes in PCI starting color or variation in indicator reaction kinetics.

Optical model. To create a model of the respirator compatible with the optical modeling software, a 3M 1860 N95 with straps removed was scanned using a Creaform Go!SCAN 3D. After additional pre-processing, the N95 was positioned within a CAD model of the UV-C chamber (**Figure 12.6**). The entire assembly was then imported into non-sequential mode in Zemax OpticStudio (Version: 20.3) and exploded into individual parts. Parts not essential to the optical model (e.g., screws, hinges, etc.) were ignored during simulations. UV-C source and surface parameters are listed in **Table 12.1**. The N95 CAD object was converted to an absorbing detector, consistent with a previous study that approximated on-N95 UV-C distribution using an absorbing spherical detector[18], and positioned and/or duplicated to match *in-situ* chamber locations. All simulations were performed with "Use Polarization", "Scatter NSC Rays", "Split NSC Rays" and "Ignore Errors" engaged. Detector data were exported and analyzed using custom MATLAB scripts. Because the optical model may not accurately predict absolute dose due to environmental fluctuations, simulation results were normalized to the maximum value within the analyzed domain (e.g., entire chamber and/or N95(s)).

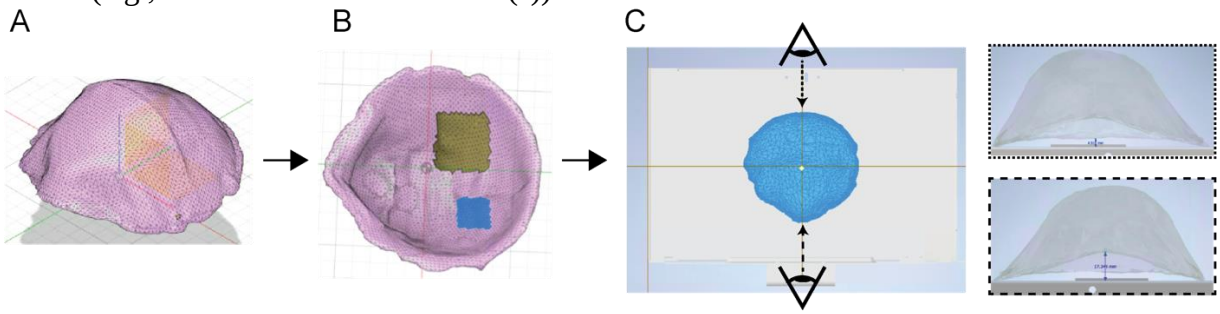

Figure 12.6. Preprocessing of scanned N95 for optical model. (A) Scanned 3M 1860 N95 mesh model is roughly aligned to X-Y plane in Autodesk Fusion 360. B) The inner mesh layer facing the wearer was manually removed prior

to converting the model to a solid and exporting as a .STEP file. C) A CAD model of the Spectronics XL-1000 (kindly provided by Spectro-UV) and modified N95 .STEP file were imported into an Autodesk Inventor assembly. The Spectrolinker-1000 was positioned to align the bottom of the back-left corner of the chamber with the origin. The model N95 was aligned close to the center of the top surface of the chamber floor. The pitch angle of the N95 was adjusted so that the height of the nosepiece and the chin piece approximated values measured in situ. The entire assembly was then imported into the optical modeling software for use.

Table 12.1. Additional optical model specifications

UV-C source information		
Emission	254 nm, monochromatic	
Number of UV-C bulbs	5	
Filament-to-filament length	230 mm	
Diameter	3 mm	
Rays/source tube during simulations	5E7	
Reflective properties applied to chamber surfaces		
Component	% reflective	% diffuse scattering
Top reflector	86	100
Rear panel	20	90
Front door	5	100
Sides and bottom panel	20	90

UV-C dose distribution on chamber floor. UV-C dose distribution across the chamber floor was characterized *in situ* at 15 evenly spaced locations (**Figure 12.7**) using PCIs as described previously[14]; briefly, all 15 PCIs were simultaneously exposed to ~100 mJ/cm^2, then read with the RM200QC within 600 s. Peak UV-C irradiance within a 15 s exposure was also measured at 14 of these locations sequentially using a radiometer (the built-in chamber sensor obstructed placement at one location). Simulated UV-C dose at each location was extracted from the optical model using custom MATLAB scripts.

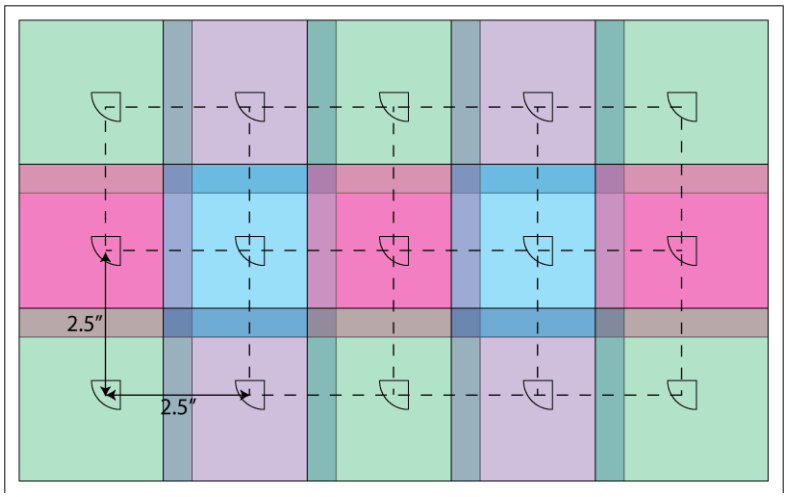

Figure 12.7. Map for *in-situ* measurements on chamber floor. Irradiance and dose were measured at 14 or 15 locations with a radiometer (colored squares) and PCIs (quarter-circles), respectively.

UV-C dose distribution across N95 facepieces. *In situ*: To empirically measure on-N95 UV-C dose, PCIs with backing removed were adhered to the N95 facepiece, exposed, and subsequently removed for color quantification. To facilitate comparison to simulation, each PCI location on the N95 was recorded by measuring the PCI: 1) corner height (C), 2) highest point height if not corner height (lowest point height if corner is highest) (h), 3) rotation along the N95 surface (Φ, **Figure 12.8**), and 4) lateral distance from either the nosepiece-to-chin midline or side-to-side seam. N95 straps were removed to minimize shadowing and variability in N95 tilt. A printed floor map ensured reproducible N95 positioning in the chamber, with nosepieces toward the door (**Figure 12.9**).

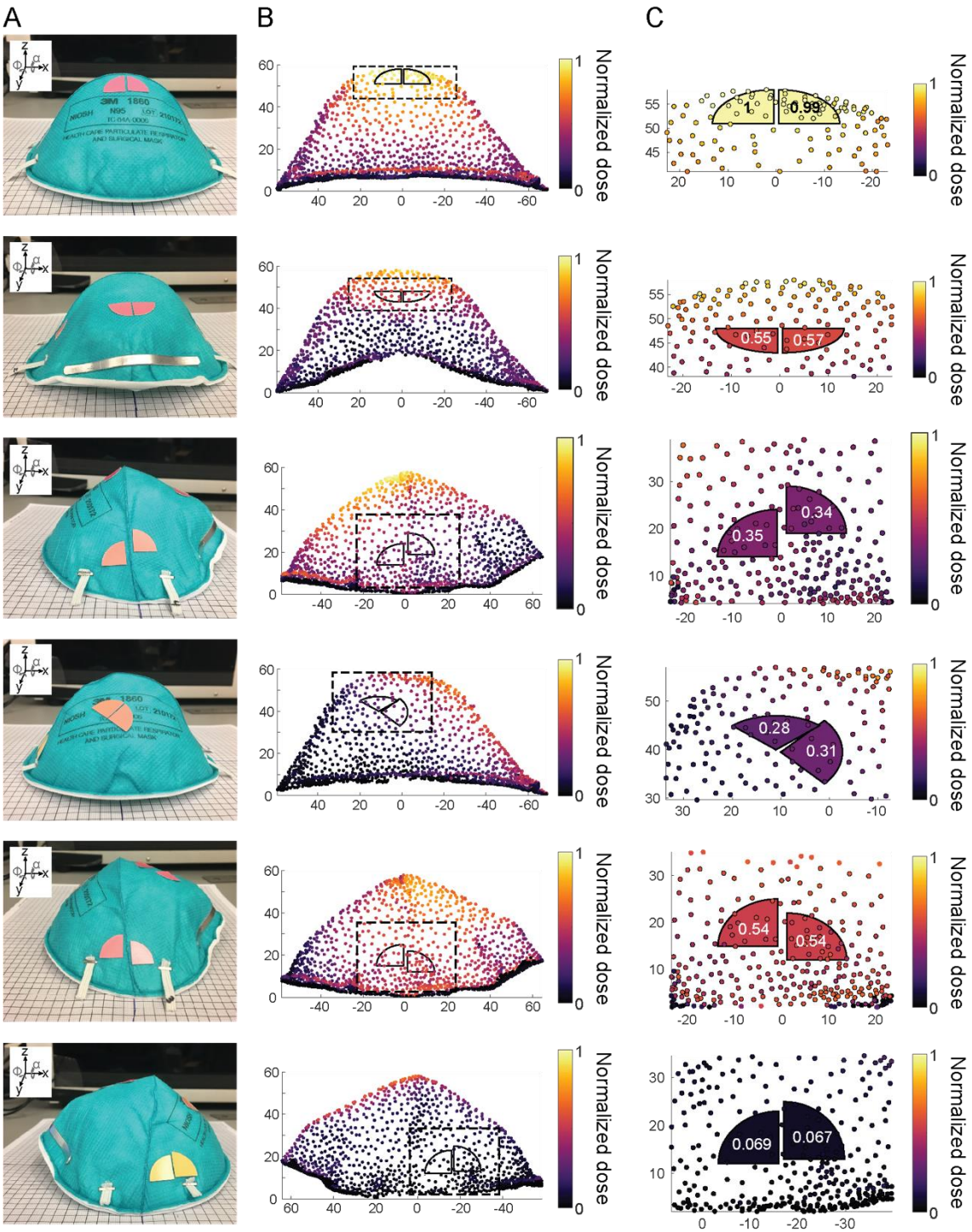

Figure 12.8. Optical model identifies paired measurement sites for in-situ PCI measurements. (A) Images of PCIs placed on N95s taken post-UV-C exposure. While x-y-z axes are independent of view angle, rotational angles α and ϕ are defined relative to the view angle. B) Scatterplots of optical simulation output overlaid with outlines of PCIs estimated to receive similar doses, therefore identifying measurement sites. Dashed rectangular outline indicates area shown in C. C) High resolution plots of the PCIs and on-N95 simulation results from B projected onto a 2D plane. PCIs colored by average dose normalized to the maximum average PCI-measured dose, which is also indicated in overlying text. Axes in B) and C) show distance in mm. Due to N95 curvature, the PCI outline on the 2D projection may differ slightly from the true PCI footprint on an N95 *in situ*. We assume these differences are minimal.

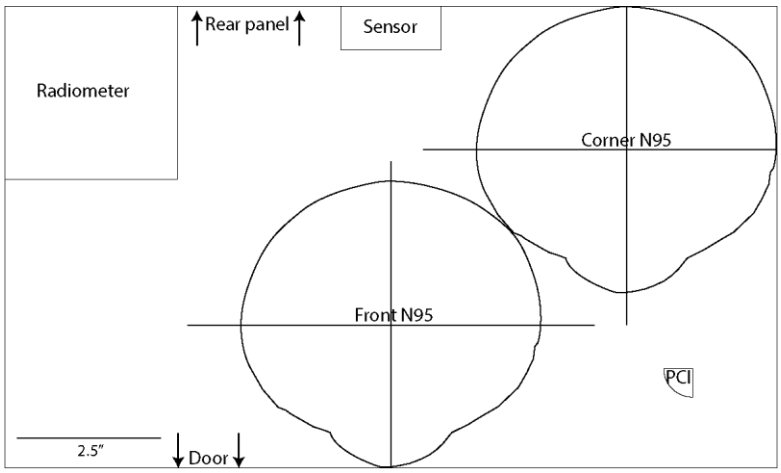

Figure 12.9. Chamber floor map for on-N95 measurements. Map positioned on chamber floor to ensure reproducible placement of all physical components for on-N95 measurements. "Sensor" indicates location of built-in sensor within the chamber.

Optical model: To characterize on-N95 UV-C dose from simulations, average values at specific *in-situ* PCI locations were extracted from the N95 detector simulation data using a custom MATLAB script. Briefly, N95 detector data were imported into MATLAB. The outline of each PCI was plotted on top of the simulated N95 dose map using the spatial parameters described above. The vertical height of the PCI (d) was then defined as |C-h|. The angle of rotation toward the N95 surface (α, **Figure 12.8**) of the PCI was calculated based on geometry (**Eq. 12.1**, **Eq. 12.2**). When the corner is either the highest or lowest part of the PCI:

$$\alpha = cos^{-1}\frac{d}{r} \qquad \textbf{Eq. 12.1}$$

where *r* is the radius of the PCI.
When corner is not the highest or lowest point of the PCI,

$$\alpha = cos^{-1}\frac{d}{r * sin(\Phi)} \qquad \textbf{Eq. 12.2}$$

where Φ is defined as the angle between the horizontal axis and highest PCI point.

The average on-N95 value from simulation was calculated as the mean value of the data points contained within the PCI perimeter, determined using the "inpolygon" function on a 2D projection of N95 data points and PCI outlines (**Figure 12.8**).

Heatmap plots. All heatmaps of UV-C dose or irradiance were generated with the 'inferno' perceptually uniform, colorblind-friendly colormap, which was created by Stéfan van der Walt and Nathaniel Smith and adapted from Python's matplotlib for use in MATLAB by Ander Biguri.[23]

SARS-CoV-2 preparation, handling, and $TCID_{50}$ assay.

Virus preparation and stock titration: SARS-CoV-2 stocks of the strain USA-WA1/2020 were obtained from the Biodefense and Emerging Infections (BEI) Research Resources Repository. Dulbecco's Modified Eagle Medium (DMEM, Sigma-Aldrich) containing 10% fetal bovine serum (FBS),100 U/mL penicillin, and 100 µg/mL streptomycin was used for all cell culture. To produce virus passage 1, SARS-CoV-2 stocks were amplified in Vero-E6 cells (ATCC® CRL-1586™). In brief, to generate passage 1, 50 µl of the BEI stock was inoculated onto confluent T-175 flasks of Vero-E6 cells and allowed to propagate until 50% cytopathic effect (CPE) was achieved (~48 hours post infection) at which time cells were lysed through 1 round of freeze and thaw. CPE was

defined as any virus-induced cell death or change in cell morphology observed using brightfield microscopy. Supernatants were collected and clarified by spinning at 1500 rpm for 5 mins. The clarified viral supernatant was aliquoted and frozen at -80°C. Aliquots were thawed for production of virus passage 2, which was performed as above except using Calu-3 human lung epithelial cells (UC Berkeley Cell Culture Facility). The concentration of virus passage 2 stocks was assessed by 50% tissue culture infectious dose ($TCID_{50}$) assay using Vero-E6 cells and was determined to be 8×10^7 $TCID_{50}$/mL. Passage 2 cells were used for all experiments.

N95 facepiece/coupon inoculation: All coupons or N95 facepiece viral measurement sites were inoculated by pipetting 3 aliquots of 16.67 μL, for a total of 50 μL, of passage 2 virus stock at 8×10^7 $TCID_{50}$/mL onto the N95 material. While most locations on the N95 facepiece can be inoculated, for the hydrophobic N95 model used in this study, we observed that beaded inoculation droplets would roll off of steeply sloped surfaces (e.g., base of the facepiece near the chin or nosepiece), precluding inoculation at some locations. Alternate droplet sizes or N95 orientations during drying may mitigate this challenge. The SARS-CoV-2 inoculation volume was selected to balance drying time and assay sensitivity. Inoculation sites were left to dry at room temperature for 3.5 hours in a biosafety cabinet. For paired on-N95 UV-C dose and SARS-CoV-2 inactivation measurements, where the PCIs were placed on the N95 prior to inoculation, we also verified that the N95s were not exposed to UV-C during the drying process. To do so, a PCI was positioned in the biosafety cabinet next to the N95 respirators while the inoculation sites dried, and the PCI color was measured using the RM200QC spectrocolorimeter before and after the 3.5 hour drying period to verify no change in color.

Virus titration: After irradiation, inoculated coupons or N95 facepiece measurement sites were extracted using 12mm biopsy punches (MedexSupply ACD-P1250). N95 facepiece punches were incubated in stationary 24-well plates containing cell culture medium (DMEM supplemented with 10% fetal bovine serum, 100 U/mL penicillin, and 100 μg/mL streptomycin) for ≥30 minutes. Viable SARS-CoV-2 virus was quantified by $TCID_{50}$ assay by incubating confluent Vero E6 cells in 96 well plates with 10-fold serial dilutions of viral extraction sample at 37°C/5% CO_2. Eight replicate wells were assessed per dilution. Five days after inoculation, CPE was scored visually under brightfield illumination using a 4✕/0.13 NA objective. Wells with CPE exhibited either complete destruction of the cell monolayer, or large areas of cell lysis/cell debris. $TCID_{50}$ was calculated using the Reed-Muench method[24]. The limit of detection of the assay is 3.16 $TCID_{50}$/mL, which was determined by calculating the $TCID_{50}$ at which no CPE is observed in any replicate wells.

All study procedures were approved by the UC Berkeley Committee for Laboratory and Environmental Biosafety and conducted in agreement with BSL-3 requirements.

SARS-CoV-2 dose response on N95 coupons. The UV-C dose response of SARS-CoV-2 was assessed by measuring viral inactivation on 3M 1860 N95 coupons inoculated with SARS-CoV-2 and exposed to different UV-C doses. By mapping UV-C irradiance across the chamber floor, we identified 5 locations of equivalent irradiance at which to place a radiometer, PCI, and 3 inoculated N95 coupons (**Figure 12.10, Figure 12.11**). PCIs and coupons were placed on custom-built platforms to match the height of the radiometer sensor. Platforms were built from laser-cut (HL40-5G-110, Full Spectrum Laser) pieces of 3.175 mm-thick acrylic (McMaster Carr 85635K421), joined with epoxy (J-B Weld 50176). Printed maps on the chamber floor and platforms ensured consistent positioning from run-to-run (**Figure 12.12**).

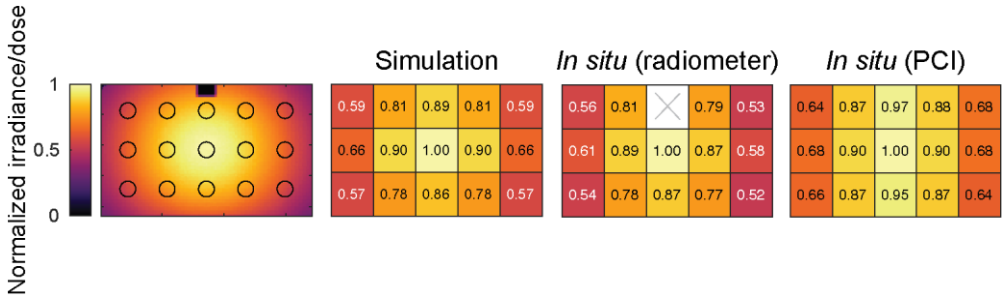

Figure 12.10. Simulation correlates *in-situ* measurements of UV-C distribution across chamber floor correspond. Spatial measurements across chamber floor estimated from simulation and measured *in situ* with a radiometer and PCIs. Leftmost heatmap shows locations from simulation from which values were averaged to compare to *in-situ* measurements. To map UV-C dose distribution on the chamber floor within the optical model, a rectangular detector with the surface area of the chamber floor was positioned at approximately the base height of the diffuser of the physical radiometer (35.175 mm). Small absorbing fiducials were introduced in the back left corner and above the built-in chamber sensor to assist with orientation during data post-processing. The average value within a 25.4 mm diameter circle (diameter of radiometer diffuser) at each *in-situ* position was determined using a custom MATLAB script.

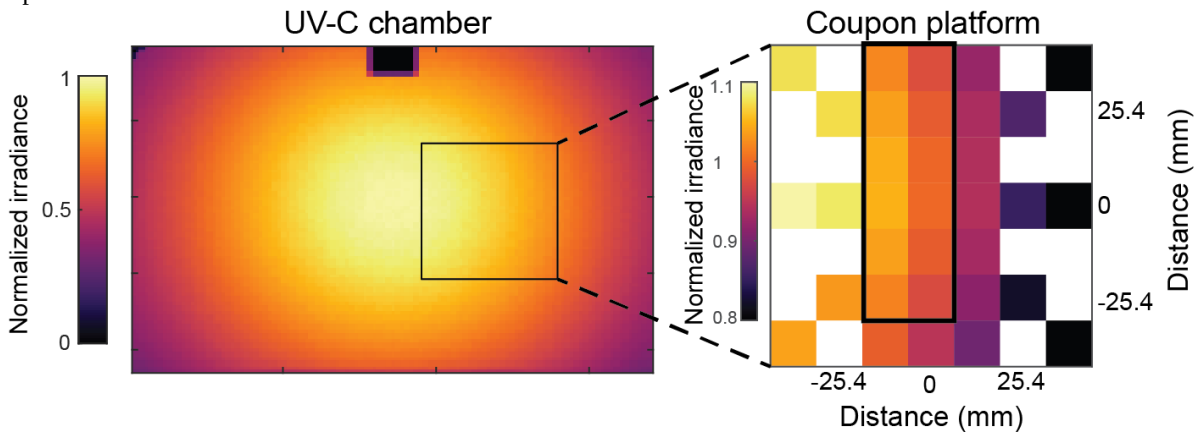

Figure 12.11. In-situ irradiance mapping determines coupon placement. In-situ irradiance mapping using the radiometer at the coupon platform location identifies a 25.4 mm × 63.5 mm region (black outline) where the irradiance varies < 10%. Within this area, 3 N95 coupons can fit for simultaneous exposure. Irradiance on the UV-C chamber heatmap is normalized to the maximum irradiance in the chamber. Irradiance on the coupon platform heatmap is normalized to the irradiance at the center (0 mm, 0 mm) position.

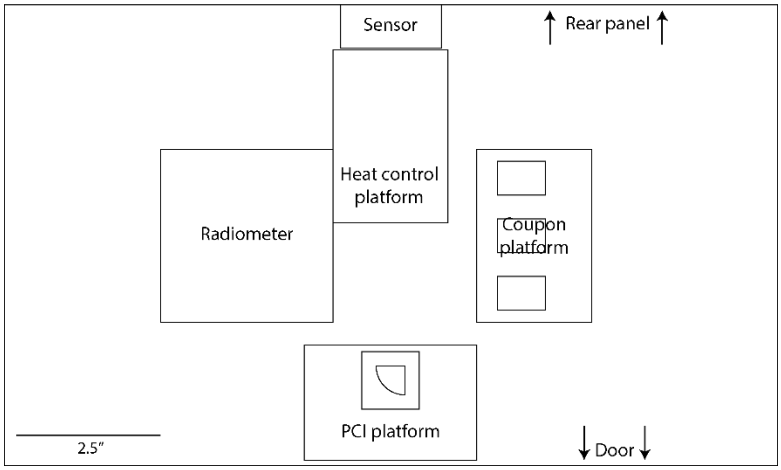

Figure 12.12. Chamber floor map for coupon study. Map positioned on chamber floor to ensure reproducible placement of all physical components involved in coupon study.

For SARS-CoV-2 inactivation experiments, 3 replicate inoculated coupons were simultaneously irradiated with a given UV-C dose. Given the minimal impact of expiration status on UV-C decontamination efficacy (**Figure 12.13**), expired (i.e., past the manufacturer-recommended shelf life) N95s were used for experiments, to preserve non-expired N95s for healthcare workers. Coupons (15 mm × 20 mm) were cut from the edge of N95s to include the raised, sealed seam to minimize layer separation. The seam did not prevent the coupons from lying flat during UV-C exposure. To verify that heating in the UV-C chamber did not contribute to SARS-CoV-2 inactivation, temperature in the UV-C chamber was recorded in preliminary experiments (outside of BSL-3) over time using a USB temperature/RH datalogger placed at the center of the chamber (Digi-Sense UX-20250-42). Additionally, an inoculated 'heating control' coupon was included in the chamber under UV-C-blocking material during some exposures (175, 300, 500 mJ/cm^2), to measure the amount of SARS-CoV-2 inactivation due solely to any increase in chamber temperature. Both a radiometer and PCI (with borosilicate attenuator for doses beyond the PCI upper limit of quantification) were used to quantify *in-situ* UV-C dose applied during each exposure. Exposure time was estimated by dividing the target dose by the irradiance at the coupon platform (~6.4 mW/cm^2 after bulb warm-up). To account for output degradation[14] (**Figure 12.1**), exposure time was optimized by comparing the dose measured by the radiometer during a test exposure to the target dose.

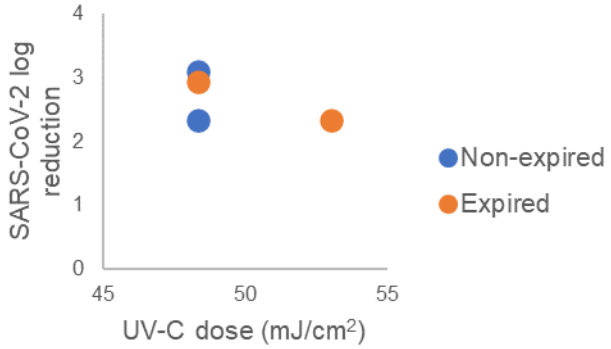

Figure 12.13. SARS-CoV-2 inactivation does not depend on N95 expiration status. No difference in SARS-CoV-2 UV-C response was observed between non-expired and expired 3M 1860 N95 material coupons. N = 2 replicates/condition.

After each exposure, PCI(s) were measured with both the RM200QC and the Color Muse. Biopsies were excised from all irradiated coupons, the non-irradiated heating control coupon, and one unexposed control coupon stored at room temperature outside the UV-C chamber. A $TCID_{50}$ assay was performed to assess SARS-CoV-2 viability.

Paired measurements of UV-C dose and SARS-CoV-2 inactivation on N95s. To simultaneously measure UV-C dose and SARS-CoV-2 inactivation on 3M 1860 N95 facepieces, PCIs (without attenuator) were affixed to N95s at each chosen dose measurement site, and accompanying SARS-CoV-2 inoculation sites outlined in advance to facilitate accurate viral deposition. SARS-CoV-2 was inoculated at each paired inoculation site. After drying, two N95s ('corner' and 'front' N95s) were placed in a UV-C chamber after bulb warm-up. To monitor dose during each exposure, a radiometer and PCI were also placed at their respective positions near the two corners of the chamber floor (**Figure 12.9**). After a 10 s UV-C exposure, PCIs were removed from the N95s and measured with both the RM200QC and the Color Muse. SARS-CoV-2 inoculation sites as well as an unexposed room temperature control coupon were excised following each UV-C exposure.

12.4 Results & Discussion

Measuring UV-C dose and SARS-CoV-2 inactivation on and across N95s. In this study, we sought to understand the impact of N95 shape and placement on SARS-CoV-2 inactivation and how variation in inactivation relates to UV-C dose received across the N95 surfaces (**Figure 12.14A**). Building upon previous work quantitatively relating PCI color change to received UV-C dose[14] and verifying the near-ideal angular response of PCIs[21], we introduce simultaneous measurement of SARS-CoV-2 inactivation and UV-C dose on N95 facepieces. To increase accessibility of the PCI dosimetry method, we also compared the performance of a substantially lower-cost colorimeter to the previously reported spectrocolorimeter (**Figure 12.4**). Applying this PCI dosimetry method, we paired PCI UV-C dose measurements with SARS-CoV-2 inactivation measurements to characterize the received dose and resulting viral inactivation variation across N95 facepiece surfaces.

Towards the study goal of assessing impact of N95 shape and placement on received UV-C dose and SARS-CoV-2 inactivation, we first identified the dynamic range of the UV-C dose-response curve. Only doses within this range will elucidate the variable relationship between UV-C dose and viral inactivation. The physical setup and exposure time of N95s in a decontamination chamber and the SARS-CoV-2 inoculation sites were then optimized to receive doses spanning that dynamic range. To perform this non-trivial optimization, we implemented both *in silico* optical ray-trace modeling and *in-situ* experimental PCI quantification. We iterated between high-resolution modeling predictions and the more accurate on-N95 PCI-based UV-C dose measurements (**Figure 12.14B**).

Building and validating optical model of a UV-C decontamination system. After optically modeling the UV-C decontamination chamber, we observed normalized simulation dose measurements differ from normalized *in-situ* radiometer measurements by an average of 4.7% ± 4.5% at 14 unique locations across the chamber floor (**Figure 12.10**). Assuming spatially invariant fluctuations, the normalized irradiance and normalized dose distribution within the system are equal. Therefore, the terms "normalized irradiance" and "normalized dose" are used interchangeably to compare to *in-situ* results, depending on the *in-situ* measurement approach (i.e., radiometer or PCI). From a 3D scan of a 3M 1860 N95 imported into the virtual UV-C chamber, normalized simulation measurements differ from normalized *in-situ* PCI measurements by an average of 6.0 ± 6.2% across the facepiece centrally positioned near the chamber door ('front N95') (**Figure 12.14C**). The largest discrepancy on the door-facing N95 surface saw simulation underestimate the normalized PCI dose by ~16%. For an N95 positioned in the chamber rear corner ('corner N95'), simulation differed from *in-situ* PCI measurements by an average of 18 ± 25%, with the largest discrepancies again occurring on the wall-facing N95 surfaces (**Figure 12.14C** and **Figure 12.15**). Differences between the simulation and *in-situ* measurements may arise due to N95-to-N95 shape variability (**Figure 12.16**), differences between true and modeled surface properties, and higher relative uncertainty of low-dose PCI measurements. Overall, however, on-N95 dose measurements correlate with simulation measurements at corresponding locations (**Figure 12.14C**). Thus, after validating the agreement between the simulation and *in-situ* measurements across both the chamber floor and an N95 in multiple chamber locations, we coupled the two measurement tools to design and optimize paired UV-C dose and SARS-CoV-2 inactivation experiments, leading to the first demonstration of simultaneous on-N95 viral inactivation and UV-C dose measurements to date.

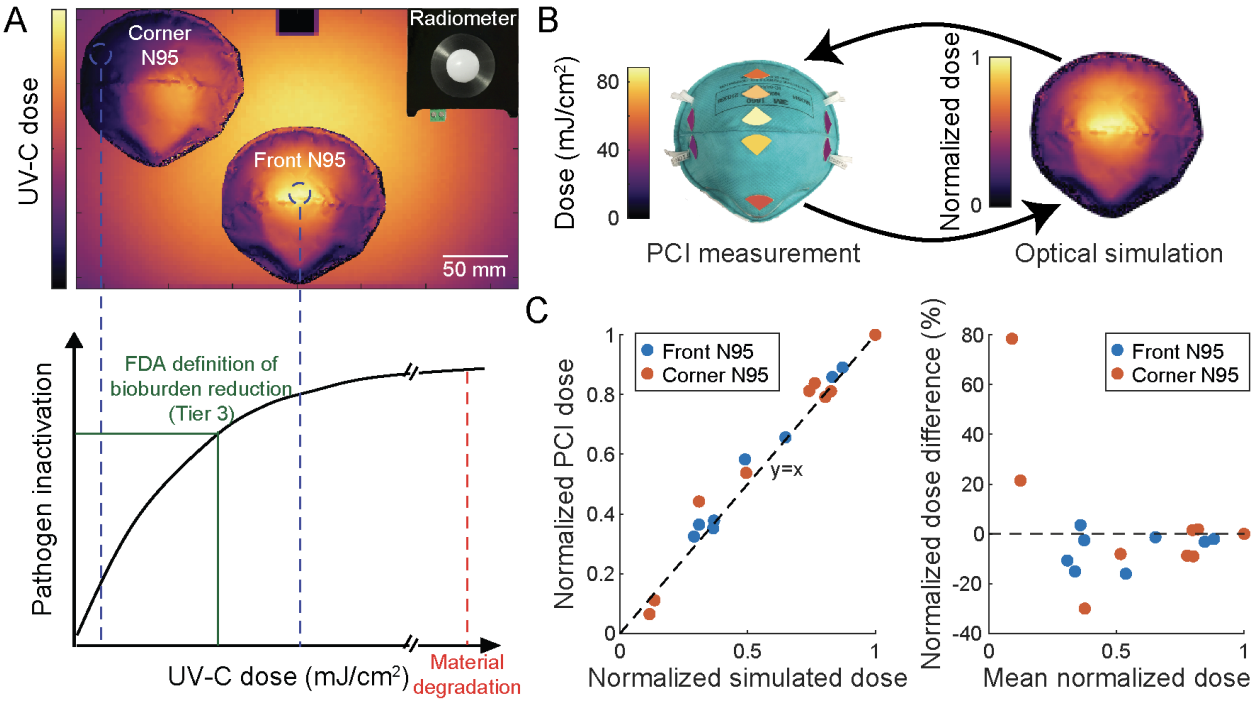

Figure 12.14. Integrated optical modeling and in-situ PCI measurement pipeline for simultaneous and near-coincident on-N95 UV-C dose and viral inactivation measurements. (A) Schematic highlighting how UV-C dose received across complex N95 surfaces can vary substantially, creating a narrow range of UV-C doses that deliver sufficient dose for pathogen inactivation while not exceeding the exposure threshold for material degradation. (B) In-situ PCI measurements and optical simulation results were used in tandem to inform and rapidly iterate on experimental design. (C) Comparison of normalized in-situ PCI and simulated doses at seven discrete locations on N95s in two different chamber positions. Normalized dose difference was calculated as (simulation-PCI)/PCI. Black lines (y = x on left, y = 0 on right) indicate where the data would lie if PCI and simulation measurements were equal. Simulation tends to overestimate normalized in-situ PCI dose at low doses and underestimate in-situ PCI dose at high doses.

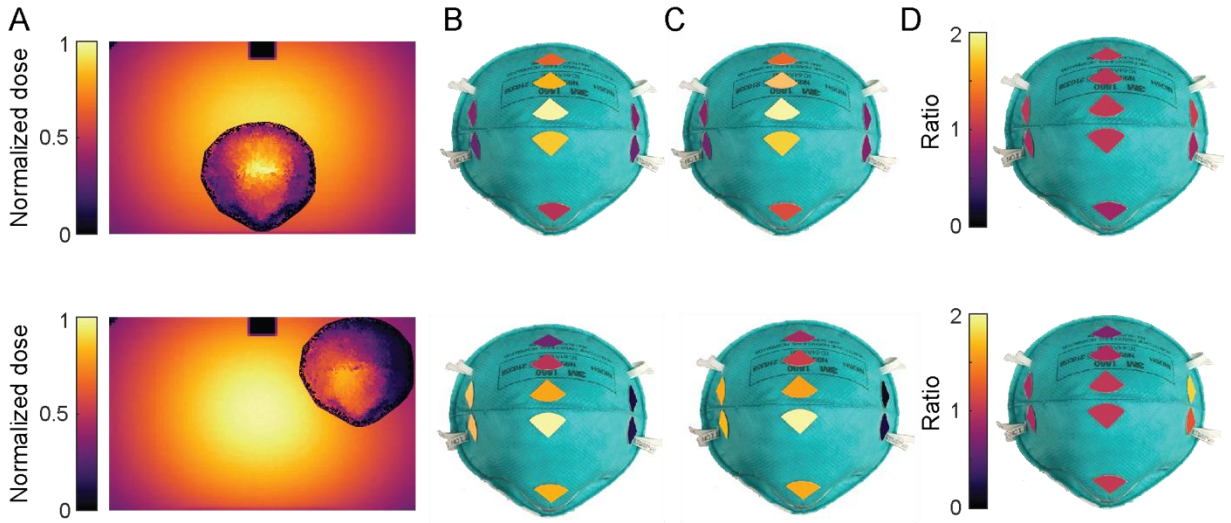

Figure 12.15. Correspondence between simulated and in-situ measured on-N95 UV-C dose distribution using PCIs. (A) High resolution optical model output generated using Delaunay triangulation in Matlab (delaunayTriangulation) represented as heatmaps of UV-C dose across an N95 at the front-center of the chamber (top) and an N95 in the chamber corner (bottom). B) Normalized dose at PCI locations extracted from simulation results. C) In-situ normalized dose measured using PCIs (average of N = 3 replicates). D) Ratio of simulated to in-situ dose.

All values were normalized to the highest on-N95 value, and on-N95 PCIs were false-colored to match color-mapped value. For PCI measurements, exposure times were chosen such that the on-N95 dose was within the dynamic range of the PCIs.

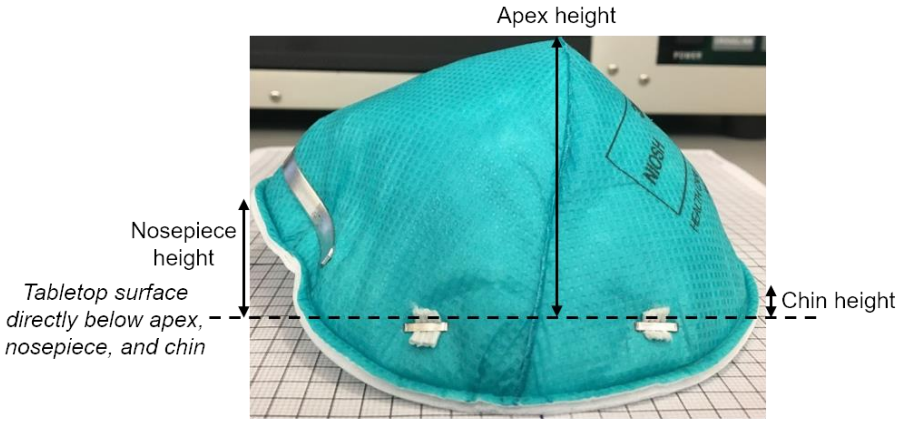

N95	Nosepiece height (mm)	Chin height (mm)	Apex height (mm)
Lot 1, N95 #1 *Used in simulation*	16	5	58
Lot 1, N95 #2	18	2	58
Lot 2, N95 #1	19	7	61
Lot 2, N95 #2	21	8	60
Lot 2, N95 #3	22	5	61
Lot 2, N95 #4	21	7	62

Figure 12.16. N95-to-N95 variation in morphology. Vertical heights from the tabletop to the seam on the nosepiece and chin seam of the N95, as well as to the apex. Heights are measured as the vertical distance from the nosepiece, apex, or chin to the tabletop directly below it.

Establishing dose-response for SARS-CoV-2 viral inactivation by UV-C. In order to quantify the UV-C dose dependence of SARS-CoV-2 viral inactivation without the added complexity of the N95 facepiece shape, we first considered SARS-CoV-2 viral inactivation using UV-C on coupons of N95 material. Simulation and *in-situ* measurements identified and validated five locations in a UV-C decontamination chamber that receive equivalent UV-C irradiance (<5% variation, **Figure 12.20A**) for location-paired UV-C dose and SARS-CoV-2 inactivation measurements on N95 coupons. We simultaneously exposed triplicate coupons inoculated with SARS-CoV-2 while recording the applied dose using both a radiometer and a PCI (**Figure 12.17**). As the dynamic range of the PCIs measured with either color reader was insufficient to measure UV-C doses >~260 mJ/cm^2 (**Figure 12.20B**), for these higher doses we placed 1.1-mm-thick borosilicate glass over the PCI on the flat PCI platform to attenuate incident UV-C irradiance and extend the PCI dynamic detection range. We observed an extended upper limit of quantification (ULOQ) of 1853.2 mJ/cm^2 for the PCI-borosilicate pair when PCI color is measured with the spectrocolorimeter, compared to 261.4 mJ/cm^2 without the attenuator (**Figure 12.4**). When using the lower-cost colorimeter, borosilicate extended the ULOQ from 168.1 mJ/cm^2 to 802.6 mJ/cm^2 (**Figure 12.4**). While the ULOQ of the PCI-borosilicate pair when using the lower-cost colorimeter was lower than some of the UV-C doses included in the SARS-CoV-2 dose-response measurements, we observed good agreement in estimated dose using both color readers to measure all PCIs in SARS-CoV-2 experiments (**Figure 12.4**). Borosilicate was only paired with PCIs on

planar surfaces (not on-N95), as borosilicate transmittance depends on incident angle, yielding non-ideal angular response (see Chapter 11).

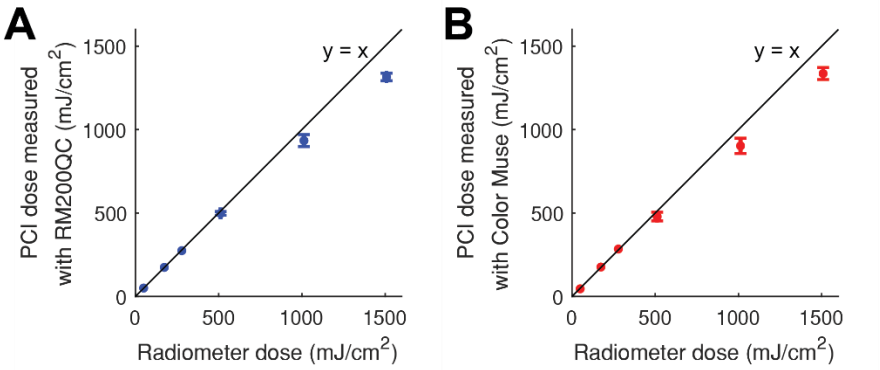

Figure 12.17. Correspondence between radiometer and PCI-measured UV-C doses during coupon experiments. PCI color change was measured with both the (A) RM200QC spectrocolorimeter, and (B) Color Muse colorimeter. For both color readers, N = 1 for radiometer doses <500 mJ/cm^2 and N = 3 for radiometer doses >500 mJ/cm^2. For dose measurements >168 mJ/cm^2, PCIs were coupled to a 1.1 mm-thick borosilicate attenuator. Vertical and horizontal error bars are the standard deviation of the estimated dose measurements. At UV-C doses <1000 mJ/cm^2, the PCI UV-C dose measurements were within 10% of the radiometer measurements. PCIs underestimated dose (compared to the radiometer) up to 13% at ~1500 mJ/cm^2, which may be due to the higher relative uncertainty in this dose range. Due to differences in temperature, humidity, and other environmental factors, the PCI response may also differ in the BSL-3 environment as compared to the non-BSL-3 location where PCI calibration curves were generated. Lastly, doses measured with the PCI-borosilicate stack may be inaccurate due to the non-ideal angular response of borosilicate, which can result in errors if the PCI-borosilicate stack was placed in a different chamber location (receiving a different range of angles of incidence) for dose measurements than the location at which calibration curves were generated.

To elucidate the SARS-CoV-2 dose-response curve, we measured SARS-CoV-2 viral activity from N95 coupons after exposure to applied UV-C doses ranging from 500-1500 mJ/cm^2. The applied UV-C range was selected based on previous results demonstrating that ≥1000 mJ/cm^2 UV-C dose is required for 3-log inactivation of SARS-CoV-2 analogs on the majority of N95 models tested[10,25,11]. For all replicates exposed to 500-1500 mJ/cm^2, we observed >5-log SARS-CoV-2 reduction on N95 coupons (**Figure 12.18**). Furthermore, any remaining virus was below the limit of detection of the $TCID_{50}$ assay for all but one replicate, signifying that lower doses are required to identify the dynamic range of the dose-response curve of our assay.

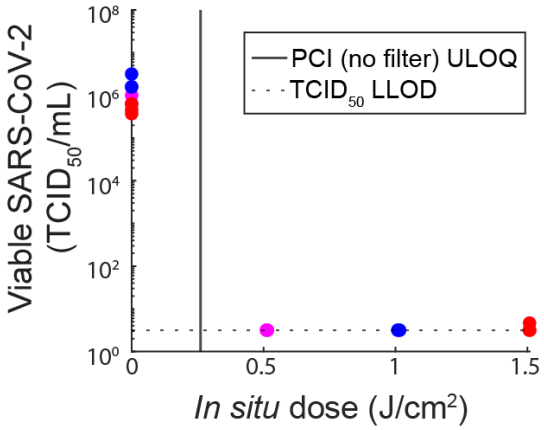

Figure 12.18. 0.5-1.5 J/cm^2 UV-C yields >3-log inactivation of SARS-CoV-2 on N95 coupons. ULOQ = upper limit of quantification. LLOD = lower limit of detection. Colors highlight temporally matched data (control coupons processed at the same time as exposed coupons). N = 3 replicates/condition.

We next assessed an applied UV-C dose range of 50-500 mJ/cm^2. For these lower UV-C doses, we observed an average of >3-log reduction of viable SARS-CoV-2 virus at all doses (**Figure 12.20B**), with no significant differences observed between non-zero UV-C dose conditions (N = 3 replicates, Kruskal-Wallis test with Dunn's multiple comparison test).

We postulate that the >20× higher SARS-CoV-2 UV-C susceptibility observed in this study as compared to previous literature is likely attributable to two factors. First, SARS-CoV-2 was inoculated without a soiling agent (e.g., sweat or sebum surrogates); soiling agents can decrease UV-C inactivation by 1-2 logs.[26,11] Second, the 3M 1860 N95 material was very hydrophobic (water contact angle >90°, **Figure 12.19**), and deposited viral samples 'beaded' on the facepiece surface. Greater UV-C decontamination efficacy has generally been observed on hydrophobic N95 models[11], which we hypothesize may be due to the greater proportion of virus inoculated on the outer N95 layers. Because the outer N95 layers receive more UV-C dose than inner layers[9], inactivation on hydrophobic N95s may more closely resemble nonporous surface decontamination, on which lower UV-C doses (~4.3 mJ/cm^2) have been shown to yield >3-log reduction of SARS-CoV-2[27]. Droplet imbibition into porous matrices is a complex process that depends on properties of the fluid and substrate[28], differences in inoculation volume and solution, and N95 material, all of which may influence the proportion of virus which penetrates into inner N95 layers. Thus, the system scrutinized here is an idealized model system and the SARS-CoV-2 dose response behavior observed is not anticipated to represent SARS-CoV-2 inactivation in clinical settings, where different N95 models and soiling are expected to substantially increase the UV-C dose necessary.

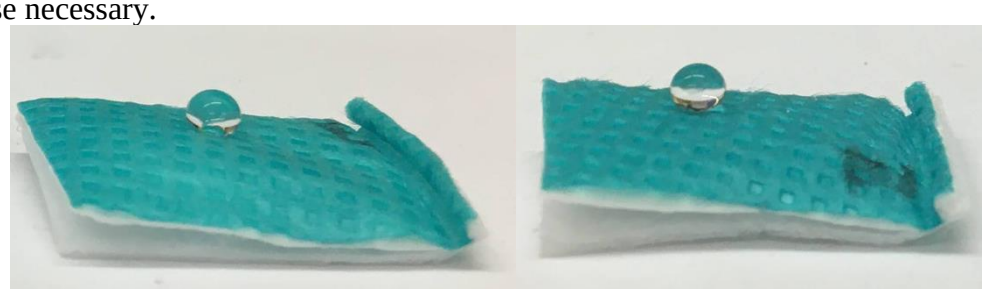

Figure 12.19. 3M 1860 N95 coupons are hydrophobic. A ~10 µL water droplet on expired (right) and non-expired (left) N95 coupons has a contact angle >90°, indicating high hydrophobicity. Additionally, the separation of the layers along the three sides without a seam may cause variable slope with respect to the UV-C source between coupons.

Given the results and precision of the $TCID_{50}$ assay (**Figure 12.20B**), and the anticipated single- or two-stage exponential inactivation of virus with increasing dose[5,16,29], we expect the dynamic range of our measured dose-response curve to exist between 0-50 mJ/cm^2. Thus, we aimed to deliver UV-C doses within this range to map SARS-CoV-2 inactivation differences and UV-C dose nonuniformity to the complex 3D geometry of N95 facepieces (i.e., comparing among facepiece locations).

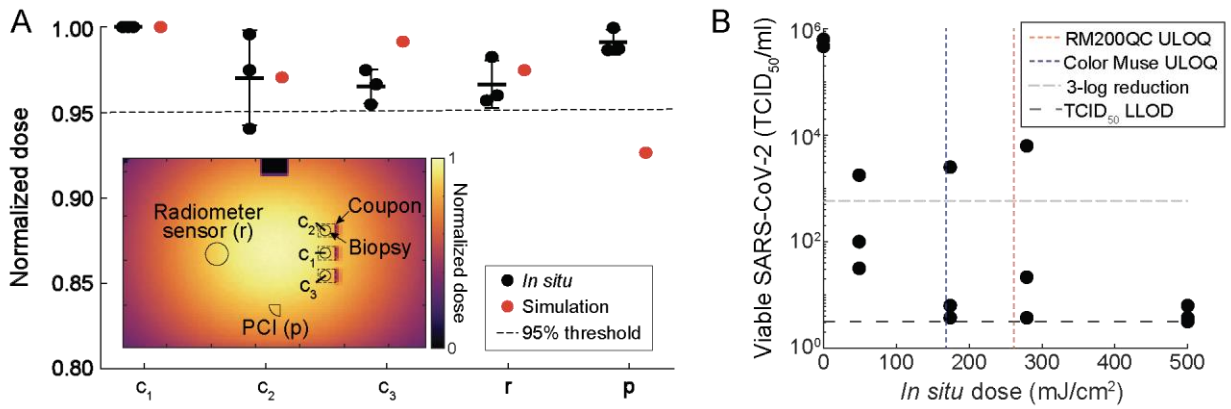

Figure 12.20. Measurement of UV-C dose required for SARS-CoV-2 inactivation on N95 coupons is informed by optical modeling and in-situ PCI dose measurements. (A) Using the optical model and validating in situ, five locations within the decontamination chamber receiving similar UV-C doses (<5% variation between mean in-situ dose measurements at each location) were identified. To inform biopsy location, the optical model also assessed the impact of each coupon seam (modeled as 15 mm wide × 2.5 mm tall × 1 mm-thick absorbing rectangular volumes at the right-hand side of each coupon) on UV-C distribution. In-situ measurements were made using PCIs to simultaneously measure dose received at the PCI and 3 coupon locations while simultaneously recording irradiance with the radiometer. Mean and standard deviation are indicated for the in-situ measurements. (B) SARS-CoV-2 recovery on N95 coupons is dependent on in-situ UV-C dose, measured using a radiometer. During UV-C exposure, the radiometer, PCI, and triplicate N95 coupons were each placed as shown in (A). A borosilicate attenuator was placed on top of PCIs to measure doses >168 mJ/cm^2 due to the limited PCI ULOQ. N=3 replicates per dose. ULOQ = upper limit of quantification. LLOD = lower limit of detection.

Chamber heating does not contribute to SARS-CoV-2 inactivation. To investigate whether heating within the chamber during treatment contributes to SARS-CoV-2 inactivation, we first monitored the chamber temperature during UV-C exposures using a USB temperature datalogger placed inside the chamber. After UV-C bulb warm-up, we measured a chamber temperature of ~27 ^{o}C. Over an exposure time of 200 s, we observe a temperature increase of 0.016 ± 0.001 ^{o}C/second (N = 3 exposures), which corresponds to <3.3 ^{o}C increase over the total cumulative exposure time of all replicates (183 seconds). Thus, we do not anticipate the total temperature increase to contribute to SARS-CoV-2 inactivation, as equivalent SARS-CoV-2 survival after 30 minutes at 22°C and 37°C has been observed[30].

Furthermore, to directly verify that heating in the UV-C chamber did not contribute to SARS-CoV-2 inactivation, we measured SARS-CoV-2 inactivation on inoculated but non-irradiated 'heating control' N95 coupons placed inside the chamber during exposures. Heating control coupons were placed under UV-C-blocking material within the chamber so that the non-irradiated control coupons would be exposed to a similar increase in temperature as irradiated coupons, in order to isolate the effect of chamber heating on SARS-CoV-2 inactivation. Like the exposed and room-temperature unexposed control coupons, the inoculation site on the heating control coupon was excised and processed immediately after each exposure. Compared to control coupons kept outside of the chamber during exposures, we observed no significant difference in viable SARS-CoV-2 $TCID_{50}$/mL (N = 3 replicates, p>0.9999, Wilcoxon matched-pairs signed rank test, **Figure 12.21**). These observations suggest that chamber heating does not contribute to SARS-CoV-2 inactivation, as supported by literature on SARS-CoV-2 stability at measured chamber temperatures.

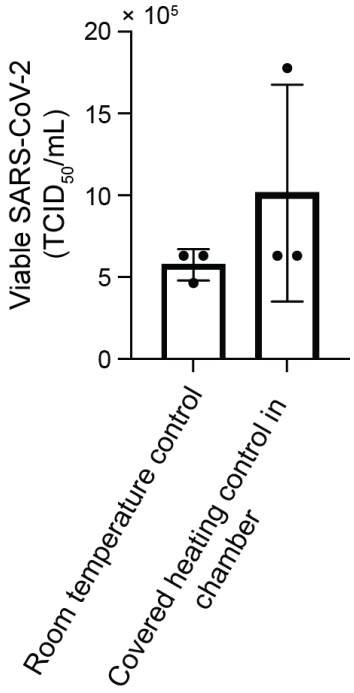

Figure 12.21. Chamber heating does not affect SARS-CoV-2 inactivation. Comparison of SARS-CoV-2 survival on N95 coupons at room temperature and within the chamber shielded from UV-C during illumination. The inoculated heating control coupon was placed on a platform of the same height as the coupon and PCI platforms, and in a location receiving approximately the same irradiance. An acrylic cover which was verified to block all UV-C was then placed on top of the heating control coupon, so that the coupon would be exposed to the temperature rise in the chamber but not to UV-C. A PCI was placed near the heating control coupon, under the acrylic cover, to verify that the heating control coupon is not irradiated with UV-C. $p > 0.9999$, Wilcoxon matched-pairs signed rank test.

On-N95 UV-C mapping informs design of near-coincident UV-C dose and SARS-CoV-2 inactivation measurements. Having established the UV-C dose response of SARS-CoV-2 on flat N95 coupons, we next investigated the magnitude of N95 shape-induced UV-C dose variation, as received UV-C is dependent on incident angle and distance from the UV-C source. Concomitantly, we sought to understand how the nonuniform on-N95 UV-C dose translated to SARS-CoV-2 viral inactivation efficacy. We aimed to map SARS-CoV-2 inactivation differences and UV-C dose nonuniformity across the N95 facepiece by simultaneously quantifying on-N95 dose with *in-situ* PCI measurements and SARS-CoV-2 inactivation via $TCID_{50}$. The tandem approach allowed simultaneous measurement at multiple locations on intact N95 facepieces: a measurement not feasible with radiometers or viral inactivation measurements alone.

Because a PCI placed at the SARS-CoV-2 inoculation site would shadow the virus inoculum, we used optical simulation to identify pairs of adjacent measurement sites on-N95 which receive equal dose. With paired measurement sites, the UV-C dose received by a SARS-CoV-2 inoculation site can be monitored using a PCI placed at the proximal equivalent-dose site. Optical simulation rapidly reports the irradiance distribution across easily tunable N95 configurations with high spatial resolution, facilitating identification of: (1) *locations* to make on-N95 measurements that sample the range of delivered UV-C doses, and (2) *measurement sites* within each location receiving the same dose. Each location must be large enough to house two proximal measurement sites each ~13 mm in diameter.

We first used optical simulation to characterize the UV-C dose distribution across the surface of multiple N95s within the chamber. To increase decontamination system throughput, multiple N95s are often irradiated simultaneously[31,32], but care must be taken to ensure all N95s receive sufficient dose. Additionally, N95s must be separated to prevent cross-contamination. In the studied decontamination system, three N95s can be staggered within the chamber (e.g., two in the back, one in the front). Given the lateral symmetry in dose distribution within the chamber (**Figure 12.1, Figure 12.10**), we characterized UV-C dose distribution across two N95s in the unique positions in this 'maximal-throughput' layout, which we call 'front' and 'corner' (**Figure 12.23A**). From the simulated UV-C dose map across these N95s, we identified six discrete locations (a-f in **Figure 12.23A**) which sample the dose range. At locations a, b, d, and e, UV-C dose measured with PCIs *in situ* is 3.3% ± 7.6% greater than simulated dose (**Figure 12.23A**). At location f, *in-situ* UV-C dose is 46.4% ± 7.6% lower than simulated dose, in line with our previous findings that simulation overestimated *in-situ* dose by 78% near that location (**Figure 12.15**). Similarly, the largest difference between simulated and *in-situ* UV-C dose is at location c, where simulated dose is 26% ± 3% lower than the *in-situ* dose, consistent with our previous finding that simulation underestimated the *in-situ* dose by 16% near the nosepiece of the front N95 (**Figure 12.15**). The discrepancy between simulation and *in-situ* UV-C dose measurements at select on-N95 locations highlights the importance of complementary *in-situ* measurements.

Within each location, the high-spatial-resolution map of simulated dose was used to identify two proposed measurement sites; dose at each site was then measured *in situ* using PCIs. Note that while measurement sites are often proximal to one another, the high-resolution simulation results established that some measurement sites receive the most similar dose when slightly offset (e.g., the sites at location b) due to the irregular N95 facepiece geometry and the off-center positioning of the N95s in the chamber. We observed that for locations receiving normalized UV-C doses >0.34 (normalized to the maximum on-N95 dose), the doses across each proximal pair of PCI and inoculation sites were within 6.0% of each other, both in simulation and when measured *in situ*. For normalized UV-C doses ≤0.34 (at more steeply sloped and/or shadowed locations), the simulated doses at each pair of measurement sites were within 11.1% of each other and the doses measured *in situ* were within 11.8% ± 6.0% of each other (**Figure 12.23B**). Differences between paired sites may be larger at locations with greater curvature (e.g., location e), where PCI angle (and thus, received UV-C dose) is more sensitive to run-to-run variation in PCI placement as well as N95 morphology. At locations with normalized UV-C doses ≤0.34, the higher relative uncertainty of PCI quantification at low doses may also contribute to a greater difference in dose at proximal sites. We quantified a relative uncertainty of ~20% at the lowest-dose (~5 mJ/cm^2) location, compared to a relative uncertainty of ~5% at all other locations when PCIs are measured with the RM200QC (**Figure 12.4B**).

Intra-chamber variation in UV-C dose and SARS-CoV-2 inactivation. Having identified paired on-N95 measurement sites receiving equivalent dose, simultaneous measurements of UV-C dose and SARS-CoV-2 inactivation on intact N95s could be performed. We assessed N95s placed at the front and corner positions in the decontamination chamber and chose an exposure time such that dose received across the N95 surfaces would span the dynamic range of 0-50 mJ/cm^2 determined from the coupon study (**Figure 12.20B**). For analysis, both UV-C dose and SARS-CoV-2 log reduction were normalized to the respective maximum value measured in the system within each replicate UV-C exposure.

UV-C dose and SARS-CoV-2 log reduction correspond well (**Figure 12.23C**) and are positively and linearly correlated ($r^2 = 0.7016$; $p = 1.4428 \times 10^{-5}$) (**Figure 12.23D**). SARS-CoV-2

dose response is still being investigated, but is expected to be primarily log-linear[33,29,34,35] in agreement with other pathogens. While the dose response curve likely has shoulder and/or tailing behavior at the lower and upper ends[5], these nonlinear regions may not be captured with the range and resolution of UV-C doses tested here. The dose required for 90% inactivation (D_{90}) estimated from a linear regression on the dose-response curve ($r^2 = 0.78$) is ~19 mJ/cm^2, higher than the D_{90} of ~1.4 mJ/cm^2 for dried SARS-CoV-2 on a nonporous surface[33], as expected (**Figure 12.22**).

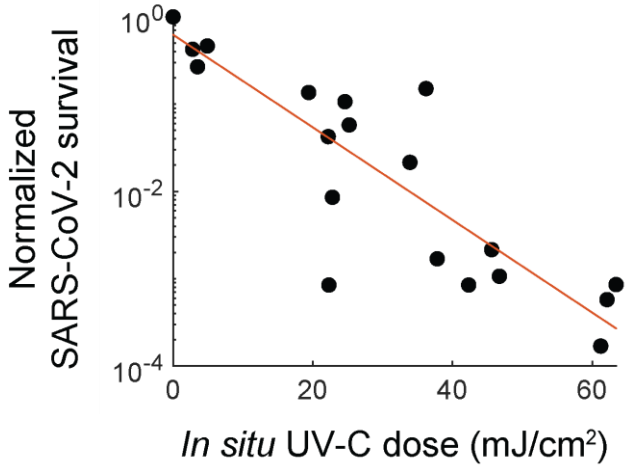

Figure 12.22. Normalized on-N95 SARS-CoV-2dose-response curve for 2 N95 facepieces. Normalized SARS-CoV-2 survival is calculated as $TCID_{50}$/mL divided by the time-matched negative control $TCID_{50}$/mL. Red line illustrates the linear regression on in-situ UV-C dose and log(survival) with equation: y = -0.0531*x - 0.2045 (R^2 = 0.78). Based on linear regression, the estimated D_{90} dose is between 18.83 - 19.03 mJ/cm^2, depending on whether the y-intercept value is ignored or considered, respectively.

Similar to the coupon study, we observe varying SARS-CoV-2 inactivation among replicate inoculation sites receiving similar UV-C dose (1.1 ± 0.8-log difference in inactivation between replicates), which we hypothesize may be due to: (1) the quantal nature of the $TCID_{50}$ assay[36,37], and/or (2) variability in the slope of the coupon surface caused by separation of N95 layers along the three sides without a seam (**Figure 12.19**). Slight variations in the amount of virus inoculated, viral extraction efficiency, and excision area may also contribute to technical variation in measured $TCID_{50}$/mL. To characterize intra-chamber variation, we quantified the fold difference in UV-C dose and SARS-CoV-2 log reduction across both N95 facepieces in the chamber. Simulation predicted a 14.9-fold difference in UV-C dose across the facepieces of both N95s in the chamber, and we measured *in situ* a dose difference of 17.4 ± 5.0-fold. This UV-C dose range yielded an 8.2 ± 1.4-fold difference in SARS-CoV-2 log reduction (from 0.4 ± 0.1-log reduction at location f to 3.4 ± 0.4-log reduction at location a). The observed 2.9 ± 0.2-log difference in SARS-CoV-2 survival across N95s within one chamber is substantial, given the FDA definition of "bioburden reduction" on N95 respirators that requires ≥3-log reduction of various pathogens[7]. To our knowledge, this is the first study to rigorously quantify both UV-C dose and viral inactivation at paired locations on intact N95s, to understand how UV-C dose distribution and resulting decontamination efficacy depend on N95 facepiece shape.

In-process UV-C dose monitoring on chamber floor overestimates minimum on-N95 dose. To assess whether dose measured at a location off-N95 could be used for in-process dose monitoring of decontamination cycles, we characterized the relationship between on-N95 dose and the dose measured on at a specific location on the chamber floor. In-situ dose is often monitored at an off-N95 location in decontamination protocols[38], as on-N95 dose measurements would

shadow the underlying N95 region from irradiation. To test whether UV-C dose monitoring on the chamber floor could serve as a proxy for the lowest dose received by N95s in the chamber, we compared the dose received in two of the lowest-dose locations on the chamber floor to the lowest dose measured on-N95.

Based on the simulation of UV-C dose distribution across the chamber floor (**Figure 12.23A,C**), we anticipated that the corners of the UV-C chamber receive the lowest on-floor dose, and thus we chose to measure dose at two corners using a radiometer and PCI. Compared to the maximum on-N95 dose measured, the doses on the floor in the chamber corners were 49.5% ± 1.6% (radiometer location) and 44.0 ± 0.7% (floor PCI location) of the maximum on-N95 dose, whereas the lowest on-N95 dose measured was 6.0% ± 1.6% of the maximum on-N95 dose (**Figure 12.23C,D**). Thus, in the UV-C chamber tested here, dose monitoring on the chamber floor cannot serve as a proxy for the lowest on-N95 UV-C dose, even if on-floor dose is monitored in the lowest-irradiance locations. As can be seen in the heatmaps and values reported in **Figure 12.23C** and **Figure 12.23D**, steeply sloped regions (particularly on the corner N95) receive several-fold lower dose than the lowest-irradiance location on the chamber floor. If a protocol is tuned only to ensure the on-floor monitoring location receives sufficient dose for decontamination, the N95s will not be fully decontaminated. Instead, care should be taken to quantify the relationship between the lowest on-N95 UV-C dose and the dose received at any in-situ monitoring point. This relationship can then be used to ensure that all N95 surfaces receive at least the on-N95 target dose, as described previously[14].

Intra-N95 variation in UV-C dose and SARS-CoV-2 inactivation. In addition to characterizing intra-chamber variation, we also analyzed UV-C dose and SARS-CoV-2 inactivation variation across each individual N95. On the front N95, the apex (location a) receives the highest dose while the more steeply sloped regions near the base of the sides of the N95 (location b) receive some of the lowest doses that can be measured with our approach, given the footprint of the PCI and SARS-CoV-2 inoculation site. Across the locations sampled on the front N95, simulation predicted a 3.0-fold difference in UV-C dose, and we measured a 2.8 ± 0.4-fold difference in UV-C dose using PCIs *in situ*. This variation in UV-C dose yielded a 2.8 ± 1.5-fold difference in SARS-CoV-2 log reduction (from 1.6 ± 1.2-log reduction at location b to 3.4 ± 0.4-log reduction at location a). While placing the N95 directly in the center of the UV-C chamber rather than offset toward the door would increase UV-C dose uniformity, throughput may be reduced, as the number of N95s that could fit in the chamber without contacting each other would be reduced from three to one.

Across the 3 measured locations on the facepiece of the corner N95, simulation predicted an 8.1-fold difference in UV-C dose and we measured a 10.2 ± 3.3-fold difference in dose. This variation in UV-C dose yielded a 4.9 ± 1.3-fold difference in SARS-CoV-2 inactivation (from 0.4 ± 0.1-log reduction at location f to 2.1 ± 0.7-log reduction at the maximum-dose location on the corner N95, which was either location d or e depending on the replicate). However, because the measurement locations were chosen to evenly sample the range of UV-C doses applied across both (front and corner) N95s, the measured locations on the corner N95 did not capture the maximum corner N95 dose near the apex (**Figure 12.23A,C**). Thus, we expect that the total variation in UV-C dose and resulting viral inactivation on the corner N95 would be even higher than measured here.

We also compared the magnitude of variation in UV-C dose and SARS-CoV-2 inactivation on the front and corner N95s. As compared to the front N95, the corner N95 had greater intra-N95 variation in both UV-C dose and SARS-CoV-2 inactivation. In contrast to the front N95, which had an equal amount of variation (2.8-fold) in UV-C dose and SARS-CoV-2 inactivation, the

difference in UV-C dose (10.2-fold) was greater than the difference in SARS-CoV-2 inactivation (4.9-fold) on the corner N95. We hypothesize that the corner N95 receives UV-C doses which may be in the shoulder of the SARS-CoV-2 survival curve, where SARS-CoV-2 inactivation is not fully log-linear with dose[5]. If the corner N95 receives UV-C doses in this shoulder region, the magnitude of intra-N95 UV-C dose variation will be larger than the amount of variation in SARS-CoV-2 inactivation.

Characterization of UV-C dose distribution across N95s within a decontamination system is valuable for informing decontamination protocols and evaluating throughput. In our system, we observed substantially lower variation in UV-C dose and SARS-CoV-2 inactivation across a single N95, as compared to across both N95s in the chamber, which suggests that approaches to increase decontamination throughput should be carefully considered. Including more N95s in the chamber may not necessarily increase throughput as compared to a single N95 in the center of the chamber, as multiple N95s likely have more nonuniform on-N95 dose because they are more spread out and can shadow each other. Greater UV-C dose nonuniformity increases the exposure time needed for all N95 surfaces to reach the minimally acceptable UV-C dose, which in turn affects the total number of safe reprocessing cycles prior to N95 material degradation (**Figure 12.14A**)[12]. The simulation and *in-situ* dose measurement workflows we demonstrate here help inform N95 positioning within decontamination systems to optimize decontamination cycle time, pathogen inactivation, and the maximum number of safe reuses.

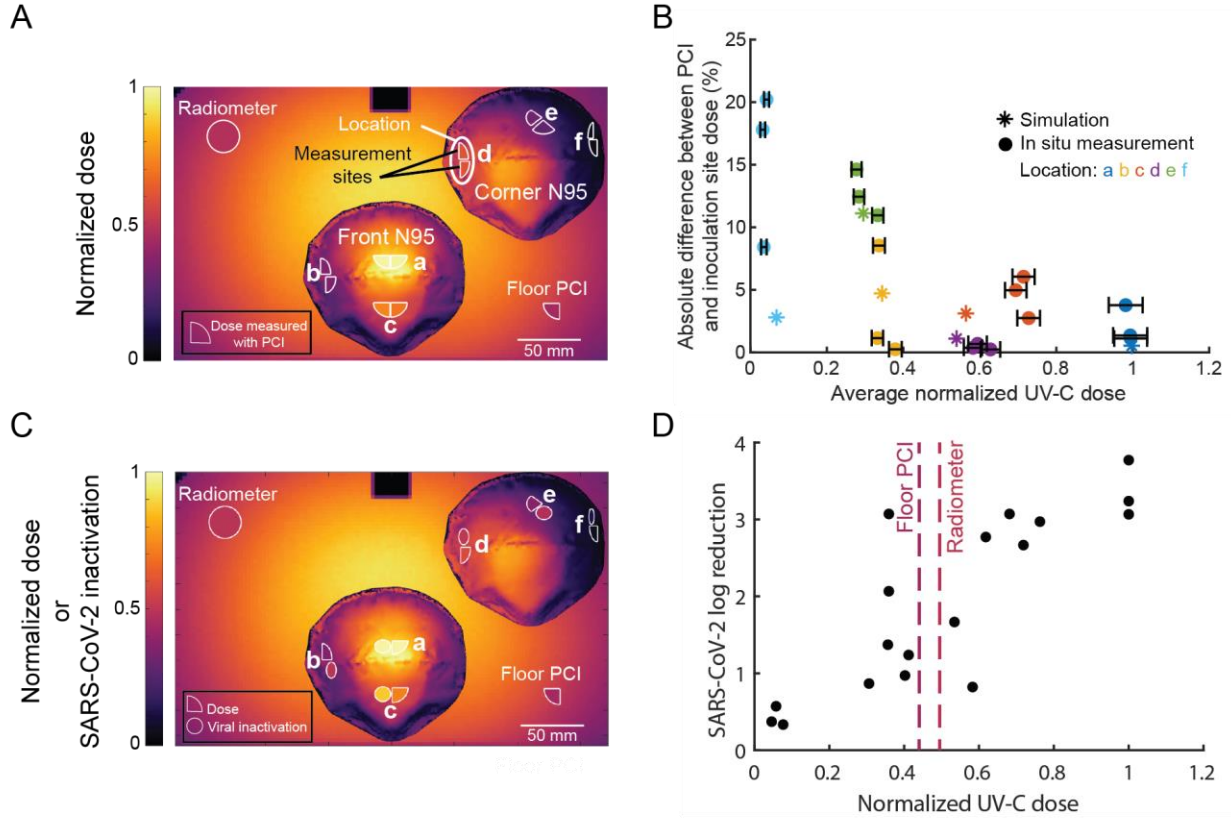

Figure 12.23. Paired on-N95 measurements of UV-C dose and SARS-CoV-2 inactivation show correlated, several-fold variation in dose and inactivation across one decontamination chamber. (A) Optical simulation of UV-C dose distribution over two 3M 1860 N95 facepieces in the UV-C chamber, overlaid with PCIs at paired measurement sites for viral inactivation and dose measurement. Heatmap shows simulated UV-C dose (normalized to the maximum dose in the chamber). PCI fill color represents the mean dose measured with PCIs in situ across triplicate measurements. (B) Comparison of dose differences within paired measurement sites. Data are colored by on-N95

location. Horizontal error bars on measured values represent the error in estimated dose. (C) Average normalized UV-C dose (quarter-circles) and SARS-CoV-2 inactivation (circles) at measured locations on front and corner N95, colored by the normalized value. Values are normalized to measurements at the apex of the front N95. Surrounding heatmap shows simulated UV-C dose. (D) SARS-CoV-2 inactivation on N95 facepieces is proportional to UV-C dose received. Selected locations on two N95 facepieces in the Spectronics XL-1000 UV-C chamber receive a 17.4 ± 5.0-fold difference in UV-C dose, which yields an 8.2 ± 1.4-fold difference in SARS-CoV-2 log reduction.

12.5 Conclusions

In summary, we have demonstrated that the N95 facepiece shape and position within a UV-C decontamination system have substantial influence on the on-N95 UV-C dose distribution and concomitant decontamination efficacy. We introduce a workflow to combine optical modeling and *in-situ* quantitative PCI dosimetry to characterize on-N95 UV-C dose with high spatial resolution, high throughput, and near-ideal angular response. For the first time, we combined simultaneous and robust quantitative UV-C dose measurements with SARS-CoV-2 inactivation measurements at specific locations on N95 respirators to probe the relationship between on-N95 dose and pathogen inactivation within each UV-C exposure. The substantial variation in on-N95 UV-C dose and SARS-CoV-2 inactivation we observed in a single decontamination chamber highlights how nonuniform UV-C dose distribution impacts pathogen inactivation and total UV-C exposure (which influences N95 material degradation and the safe number of decontamination cycles). We further demonstrated that a lower-cost colorimeter accurately quantifies dose from PCIs, making the PCI quantification workflow more accessible. Additional investigation into alternative color metrics may extend the dynamic range of PCIs measured with lower-cost color readers. Future studies are needed to characterize SARS-CoV-2 dose response in more clinically relevant conditions, such as with the addition of soiling agents and on varying N95 models. Extending the dynamic range of PCIs, while maintaining a near-ideal angular response, is also critical for measurement of >~200 mJ/cm^2 UV-C dose on-N95. Overall, the on-N95 UV-C dosimetry approach here facilitates characterization of decontamination protocols of any UV-C system, supporting system-specific validation that is critical to ensuring safe and effective N95 decontamination.

12.6 References

1. Ultraviolet Disinfection Guidance Manual for the Final Long Term 2 Enhanced Surface Water Treatment Rule. 436 (2006).
2. Sun, Z., Fu, J., Li, X., Blatchley, III, E. R. & Zhou, Z. Using Algal Virus *Paramecium bursaria* Chlorella Virus as a Human Adenovirus Surrogate for Validation of UV Treatment Systems. *Environ. Sci. Technol.* **54**, 15507–15515 (2020).
3. Memarzadeh, F., Olmsted, R. N. & Bartley, J. M. Applications of ultraviolet germicidal irradiation disinfection in health care facilities: effective adjunct, but not stand-alone technology. *Am J Infect Control* **38**, S13-24 (2010).
4. Qiao, Y. *et al.* Greater than 3-Log Reduction in Viable Coronavirus Aerosol Concentration in Ducted Ultraviolet-C (UV–C) Systems. *Environ. Sci. Technol.* acs.est.0c05763 (2020) doi:10.1021/acs.est.0c05763.
5. Kowalski, W. *Ultraviolet Germicidal Irradiation Handbook: UVGI for Air and Surface Disinfection*. (Springer Berlin Heidelberg, 2009). doi:10.1007/978-3-642-01999-9.

6. CDC. Decontamination and Reuse of Filtering Facepiece Respirators. *Centers for Disease Control and Prevention* https://www.cdc.gov/coronavirus/2019-ncov/hcp/ppe-strategy/decontamination-reuse-respirators.html (2020).
7. *Recommendations for Sponsors Requesting EUAs for Decontamination and Bioburden Reduction Systems for Surgical Masks and Respirators During the Coronavirus Disease 2019 (COVID19) Public Health Emergency*. https://www.fda.gov/media/138362/download (2020).
8. Tseng, C.-C. & Li, C.-S. Inactivation of Viruses on Surfaces by Ultraviolet Germicidal Irradiation. *J. Occup. Environ. Hyg.* **4**, 400–405 (2007).
9. Fisher, E. M. & Shaffer, R. E. A method to determine the available UV-C dose for the decontamination of filtering facepiece respirators. *J. Appl. Microbiol.* **110**, 287–295 (2011).
10. Mills, D., Harnish, D. A., Lawrence, C., Sandoval-Powers, M. & Heimbuch, B. K. Ultraviolet germicidal irradiation of influenza-contaminated N95 filtering facepiece respirators. *American Journal of Infection Control* **46**, e49–e55 (2018).
11. Heimbuch, B. & Harnish, D. *Research to Mitigate a Shortage of Respiratory Protection Devices During Public Health Emergencies*. https://www.ara.com/wp-content/uploads/MitigateShortageofRespiratoryProtectionDevices_3.pdf (2019).
12. Lindsley, W. G. *et al.* Effects of Ultraviolet Germicidal Irradiation (UVGI) on N95 Respirator Filtration Performance and Structural Integrity. *Journal of Occupational and Environmental Hygiene* **12**, 509–517 (2015).
13. Reifsnyder, W. E. Radiation geometry in the measurement and interpretation of radiation balance. *Agricultural Meteorology* **4**, 255–265 (1967).
14. Su, A., Grist, S. M., Geldert, A., Gopal, A. & Herr, A. E. Quantitative UV-C dose validation with photochromic indicators for informed N95 emergency decontamination. *PLOS ONE* **16**, e0243554 (2021).
15. Grist, S. M. *et al.* Current Understanding of Ultraviolet-C Decontamination of N95 Filtering Facepiece Respirators. *Applied Biosafety* apb.20.0051 (2021) doi:10.1089/apb.20.0051.
16. Fischer, R. J. *et al.* Early Release - Effectiveness of N95 Respirator Decontamination and Reuse against SARS-CoV-2 Virus - Volume 26, Number 9—September 2020 - Emerging Infectious Diseases journal - CDC. doi:10.3201/eid2609.201524.
17. Ozog, D. M. *et al.* The effect of ultraviolet C radiation against different N95 respirators inoculated with SARS-CoV-2. *Int. J. Infect. Dis.* **100**, 224–229 (2020).
18. Wilde, J. P., Baer, T. M. & Hesselink, L. Modeling UV-C irradiation chambers for mask decontamination using Zemax OpticStudio. *Appl. Opt.* **59**, 7596 (2020).
19. Lawal, O. *et al.* Method for the Measurement of the Output of Monochromatic (254 nm) Low-Pressure UV Lamps. *IUVA News* **19**, (2017).
20. Masse, V., Hartley, M. J., Edmond, M. B. & Diekema, D. J. Comparing and optimizing ultraviolet germicidal irradiation systems use for patient room terminal disinfection: an exploratory study using radiometry and commercial test cards. *Antimicrobial Resistance & Infection Control* **7**, 29 (2018).
21. Geldert, A. *et al.* Nonuniform UV-C dose across N95 facepieces can cause 2.9-log variation in SARS-CoV-2 inactivation. *medRxiv* 2021.03.05.21253022 (2021) doi:10.1101/2021.03.05.21253022.
22. Lester, R. A., Parisi, A. V., Kimlin, M. G. & Sabburg, J. Optical properties of poly(2,6-dimethyl-1,4-phenylene oxide) film and its potential for a long-term solar ultraviolet dosimeter. *Phys Med Biol* **48**, 3685–3698 (2003).
23. Biguri, A. *Perceptually uniform colormaps*.

24. Reed, L. J. & Muench, H. A simple method of estimating fifty per cent endpoints. *American Journal of Epidemiology* **27**, 493–497 (1938).
25. Lore, M. B., Heimbuch, B. K., Brown, T. L., Wander, J. D. & Hinrichs, S. H. Effectiveness of Three Decontamination Treatments against Influenza Virus Applied to Filtering Facepiece Respirators. *The Annals of Occupational Hygiene* **56**, 92–101 (2011).
26. Fisher, E. M., Williams, J. & Shaffer, R. E. The Effect of Soil Accumulation on Multiple Decontamination Processing of N95 Filtering Facepiece Respirator Coupons Using Physical Methods. *J Int Soc Respir Prot* **27**, 11 (2010).
27. Chin, A. W. H. *et al.* Stability of SARS-CoV-2 in different environmental conditions. *The Lancet Microbe* **1**, e10 (2020).
28. Das, S., Patel, H. V., Milacic, E., Deen, N. G. & Kuipers, J. a. M. Droplet spreading and capillary imbibition in a porous medium: A coupled IB-VOF method based numerical study. *Physics of Fluids* **30**, 012112 (2018).
29. Kariwa, H., Fujii, N. & Takashima, I. Inactivation of SARS Coronavirus by Means of Povidone-Iodine, Physical Conditions and Chemical Reagents. *DRM* **212**, 119–123 (2006).
30. Chin, A. W. H. *et al.* Stability of SARS-CoV-2 in different environmental conditions. *The Lancet Microbe* **1**, e10 (2020).
31. Zunner-Keating, B. P. *et al.* Rapid implementation of ultraviolet germicidal irradiation and reuse processes for N95 respirators at a health system during the coronavirus disease 2019 (COVID-19) pandemic. *Infect Control Hosp Epidemiol* 1–3 doi:10.1017/ice.2020.1386.
32. Purschke, M. *et al.* Construction and validation of UV-C decontamination cabinets for filtering facepiece respirators. *Appl. Opt., AO* **59**, 7585–7595 (2020).
33. Storm, N. *et al.* Rapid and complete inactivation of SARS-CoV-2 by ultraviolet-C irradiation. *Scientific Reports* **10**, 22421 (2020).
34. Darnell, M. E. R., Subbarao, K., Feinstone, S. M. & Taylor, D. R. Inactivation of the coronavirus that induces severe acute respiratory syndrome, SARS-CoV. *J. Virol. Methods* **121**, 85–91 (2004).
35. Blatchley, E. R., III, Petri, B. & Sun, W. SARS-CoV-2 UV Dose-Response Behavior. (2020).
36. Smither, S. J. *et al.* Comparison of the plaque assay and 50% tissue culture infectious dose assay as methods for measuring filovirus infectivity. *J. Virol. Methods* **193**, 565–571 (2013).
37. Gustafsson, R. K. L., Engdahl, E. E. & Fogdell-Hahn, A. Development and validation of a Q-PCR based TCID50 method for human herpesvirus 6. *Virol J* **9**, 311 (2012).
38. Lowe, J. J. *et al. N95 Filtering Facepiece Respirator Ultraviolet Germicidal Irradiation (UVGI) Process for Decontamination and Reuse*. https://www.nebraskamed.com/sites/default/files/documents/covid-19/n-95-decon-process.pdf (2020).

Chapter 13

Conclusions & Future Directions

In this dissertation, we have contributed to quantitative single-cell biology and pathogen inactivation studies through advancements in two measurement techniques: electrophoretic cytometry for single-cell proteoform characterization, and quantitative UV-C dosimetry for characterization and validation of UV-C decontamination processes. To advance electrophoretic cytometry, we have identified and developed strategies to minimize technical variation in protein abundance and molecular mass measurements, allowing finer biological differences to be distinguished. We have also extended electrophoretic cytometry to new sample types, including embryos, blastomeres, and subconfluent adherent cells, advancing studies of development and cell-microenvironment interactions. Finally, we have combined nucleic acid measurements with cytoplasmic proteoform measurements from the same single cell or cell cluster, establishing a new approach for single-cell multiomic characterization with proteoform specificity.

To advance characterization of UV-C pathogen inactivation, we reviewed the current understanding of UV-C decontamination and best practices in UV-C dose measurement and identified a measurement gap in high-throughput quantification of UV-C dose on nonplanar surfaces such as N95 respirators. To address this measurement gap, we developed and applied a method for quantitative UV-C dose measurement from colorimetric indicators, whose small form factor, ideal angular response, and low cost support high-throughput UV-C dose measurements on N95 surfaces and other complex geometries. Robust quantitative UV-C dose measurement techniques help characterize and mitigate the immense device-to-device and run-to-run variation in UV-C dose output, supporting improved understanding and validation of UV-C decontamination processes.

This dissertation presents several proof-of-concept innovations which could be further improved by increasing the versatility of the approaches to be able to detect a wider range of molecules. For example, while the multimodal electrophoretic cytometry approach described here is fills a unique measurement gap in detection of both nuclear DNA or RNA and cytoplasmic proteoforms from the same cell, alternative approaches which can measure nucleic acids and proteins from both the nuclear and cytoplasmic compartments would be valuable. Methods for selective permeabilization of the nuclear envelope to allow nuclear proteins to electromigrate into the gel while retaining larger nucleic acids in the microwell may be promising, in addition to approaches for *in situ* detection of nucleic acids. There are also many future directions to extend the capabilities of projection electrophoresis for spatial proteomic analysis. To facilitate lysis and solubilization of samples with greater amounts and density of protein, such as confluent cell layers or tissue slices, new sample preparation approaches are key. Inspiration on approaches to isolate and solubilize protein from complex biological samples may be drawn from tissue clearing[1], tissue pixelation[2], expansion microscopy[3], and reversible protein capture and release[4] work, among other fields. Additionally, pathology and other spatial proteomic analysis may be advanced by combining projection electrophoresis of adherent cells or tissues with other histological stains or extracellular matrix analysis. The versatility of the UV-C dosimetry technique described here could also be improved by increasing the dynamic range of the technique, to measure doses needed to inactivate many pathogens on porous substrates which require on the order of J/cm^2.

Future work to extend quantitation capabilities would also be beneficial. Due to unknown, target-dependent protein loss, capture efficiency, and antibody binding efficiency, protein quantitation in electrophoretic cytometry is relative rather than absolute. Incorporation of protein standards or calibration curves may be valuable to facilitate absolute quantitation to compare expression levels of different proteins, as well as increase understanding of how protein molecular mass or subcellular localization influences the level of technical variation in protein abundance measurements. Given the range of emission spectra of UV-C sources and the range of spectral sensitivity of UV-C sensors, establishing standards for the way in which UV-C dose is measured and reported would also improve quantitative comparisons of pathogen inactivation studies and UV-C decontamination protocols.

Finally, is it important to note that there are tradeoffs to any measurement technique; many other approaches can complement the electrophoretic cytometry and UV-C dosimetry techniques described in this dissertation to advance overall understanding of single-cell biology and pathogen inactivation. For example, coupling electrophoretic cytometry with upstream analyses of whole cells (e.g., live-cell imaging) or downstream analyses of extracted proteins (e.g., imaging mass spectrometry) can yield rich multidimensional characterization of single cells. By offering increased wavelength specificity, spectroradiometry complements colorimetric UV-C dosimetry by enabling characterization of a pathogen's susceptibility to different wavelengths (i.e., pathogen action spectrum) and the transmission of different wavelengths through porous materials, which is particularly important to understand and compare the efficacy of different UV-C sources (e.g., pulsed xenon, 222 nm far-UV-C, LEDs, and other emerging germicidal UV sources). The advances covered in this dissertation complement and work in parallel with other measurement techniques to advance quantitative biology and medicine.

References

1. Chung, K. *et al.* Structural and molecular interrogation of intact biological systems. *Nature* **497**, 332–337 (2013).
2. Ganguli, A. *et al.* Pixelated spatial gene expression analysis from tissue. *Nat Commun* **9**, 202 (2018).
3. Chen, F., Tillberg, P. W. & Boyden, E. S. Expansion microscopy. *Science* **347**, 543–548 (2015).
4. Neira, H. D., Jeeawoody, S. & Herr, A. E. Reversible Functionalization of Clickable Polyacrylamide Gels with Protein and Graft Copolymers. *Advanced Functional Materials* **30**, 2005010 (2020).